Rajiv Sharan Mishra · Partha Sarathi De
Nilesh Kumar

Friction Stir Welding and Processing

Science and Engineering

Springer

Friction Stir Welding and Processing

Rajiv Sharan Mishra • Partha Sarathi De
Nilesh Kumar

Friction Stir Welding and Processing

Science and Engineering

Springer

Rajiv Sharan Mishra
University of North Texas
Denton, TX, USA

Nilesh Kumar
University of North Texas
Denton, TX, USA

Partha Sarathi De
Minerals, Metallurgical
and Materials Engineering
Indian Institute of Technology
Bhubaneswar, Odisha, India

ISBN 978-3-319-07042-1 ISBN 978-3-319-07043-8 (eBook)
DOI 10.1007/978-3-319-07043-8
Springer Cham Heidelberg New York Dordrecht London

Library of Congress Control Number: 2014939952

Printed on acid-free paper

Springer is part of Springer Science+Business Media (www.springer.com)

To our Gurus and families

Preface

The field of friction stir welding is approaching 20 years and the idea of a book that could serve as textbook has been around for many years now. The authors have been involved with many previous reviews and edited volumes that have served the friction stir welding and processing community well. The first comprehensive book in the form of an edited volume was published by ASM International in 2007. From 2001, there are also edited proceedings of friction stir welding and processing symposium. Of course, TWI technical meeting and symposium CDs have been a great source of information for this community. As the field grows and number of engineers, students and researchers involved increase, a need has been felt for a book that could serve as a textbook. That was our motivation for putting this book together, which is written to serve as an initial book for students at senior undergraduate level or graduate level. Engineers and researchers getting into the field of friction stir welding may find the book useful as a resource for continuing education. We have purposely kept the book short and avoided the urge to make it a comprehensive review. This book is certainly not aimed at involved researchers in this field or experts in this area, although they may find it helpful as they teach the subject to others. We do hope that such experts will find the book worthy of recommendation. In our desire to finish the book in a timely manner, we have not been able to finish all chapters to the level we had initially wished. We hope and request readers to provide their comments and feedback for future editions.

At the time of completion of this book (April 2014), one of the authors (RSM) has spent exactly 15 years in the field of friction stir welding and processing. He would like to acknowledge the start he got because of encouragement and mentorship from Murray Mahoney and Cliff Bampton. RSM was still a postdoctoral researcher at that time with Amiya Mukherjee at UC-Davis and in the transition phase to a faculty position at the University of Missouri–Rolla (UMR). Amiya's mentorship had helped in starting a small involvement and then transition to UMR. RSM's involvement in the area of friction stir welding and processing really got going when he established his Friction Stir Processing laboratory at UMR. The support from National Science Foundation and DARPA during the early days was very critical. Over the years, many students and postdoctoral researchers

contributed to my understanding of the friction stir process. The authors have learned much of what they know from these interactions in the research group, where Partha and Nilesh at one point were students.

The formation of National Science Foundation's Industry/University Cooperative Research Center was a key development for RSM's group at Rolla. This IUCRC also led to many collaborations and friendships. Bill Arbegast was not only a champion of the technology, he had the vision to bring a large group of researchers together under this umbrella. Over the years, it has been a pleasure to work with and learn from John Baumann, Glenn Grant, Blair Carlson, Chris Smith, Tony Reynolds, Tracy Nelson, Carl Sorensen, Dwight Burford, Yuri Hovanski, Kyu Cho, Kevin Doherty, K. K. Sankaran and many other colleagues under this IUCRC. The support from NSF, DARPA, ARL, ONR, Boeing, General Motors, Pacific Northwest National Laboratory, Pratt & Whitney, Friction Stir Link, Air Force Research Laboratory, Magnesium Elektron North America, NASA-JSC, Naval Surface Warfare Center, inside and outside this center has allowed continuous growth of our work and understanding. Without a sustained support, it would not have been possible to reach this stage where we put together this book!

One of the authors (PSD) also expresses his gratitude to IIT Bhubaneswar for granting him leave to work at the University of North Texas (UNT) for a month in 2013 at the initial stages of the preparation of this book. This stay was made all the more memorable by the complete support and hospitality extended by RSM, NK and their cheerful colleagues at UNT. RSM and NK are very thankful to the University of North Texas for all the support from the time they joined UNT in 2011.

Although we have not listed students and postdoctoral researchers by name, their tireless efforts are very much behind the body of this work. Many of their figures have been cited and sometimes without full acknowledgement. Apologies to all those whose work we could not properly cite.

We are very thankful to Springer, in particular Ania Levinson, for providing opportunity to put this textbook together and pushing us to the finish line. We are sure we tested their patience by missing numerous deadlines!

Finally, none of this would be possible without the support of our families and their sacrifices. So, we close with a big thank you to family members and friends.

Denton, TX, USA — Rajiv Sharan Mishra
Bhubaneswar, Odisha, India — Partha Sarathi De
Denton, TX, USA — Nilesh Kumar
April 14, 2014

Contents

1 Introduction 1
1.1 Solid State Welding 3
1.2 Friction Stir Welding 3
1.3 Taxonomy for Friction Stir Welding and Processing 5
1.4 Overall Applicability of Friction Stir Welding 7
1.5 A Few Illustrative Implementation Examples 8
References 11

2 Fundamentals of the Friction Stir Process 13
2.1 Overview of Macroscopic Processes During FSW 13
2.2 Heat Generation During Friction Stir Process 16
2.2.1 Heat Generation from Frictional Heating 18
2.2.2 Heat Generation from Plastic Deformation 24
2.2.3 Heat Transfer During Friction Stir Process 25
2.3 Experimental Studies on Heat and Material Flow 29
2.4 Material Flow Basics 36
2.4.1 Flow Zones Around the Tool Pin 40
2.4.2 Strain and Strain Rate During FSW 41
2.4.3 Forces During FSW 46
2.5 Material Behavior and Constitutive Equations 50
2.5.1 Determination of Constitutive Equations at High Strain Rates 52
2.6 Forces Around the Pin and Shoulder 53
References 55

3 Fundamental Physical Metallurgy Background for FSW/P 59
3.1 Introduction 59
3.2 Phase Transformation Basics 61
3.2.1 Thermodynamics of Phase Formation 61
3.2.2 Phase Nucleation Kinetics 63
3.2.3 Phase Growth Kinetics 66
3.2.4 Overall Transformation Kinetics 70

3.3 Recovery, Recrystallization and Grain Growth 71
3.3.1 Static Recovery 73
3.3.2 Static Recrystallization 75
3.3.3 Dynamic Recovery 76
3.3.4 Dynamic Recrystallization 77
3.3.5 Grain Growth 78
3.4 Precipitation Transformations 79
3.5 Eutectoid Transformations 83
3.6 Widmanstätten Structures (Adapted from Porter and Easterling (2004)) 85
3.7 Martensitic Transformation 86
3.8 Physical Simulation of FSW 88
3.9 Microstructural Evolution During Friction Stir Welding 89
References 93

4 Friction Stir Welding Configurations and Tool Selection 95
4.1 Joint Configuration 95
4.2 Tool Material Selection 99
4.3 Tool Features 101
4.4 A Conceptual Process Map with Microstructural Domains 107
Additional Reading 107
References 108

5 FSW of Aluminum Alloys 109
5.1 Al Alloys: Background 109
5.2 Friction Stir Process of Aluminum Alloys 112
5.2.1 Friction Stir Welding Tool Design 112
5.2.2 FSW Operational Parameters 114
5.3 Microstructure Evolution During FSW 114
5.3.1 2XXX Alloys 114
5.3.2 5XXX Alloys 116
5.3.3 6XXX Alloys 117
5.3.4 Cast Al-Si Mg Alloys 119
5.3.5 7XXX Alloys 120
5.4 Mechanical Properties After FSW 121
5.4.1 2XXX Alloys 121
5.4.2 5XXX Alloys 126
5.4.3 6XXX Alloys 129
5.4.4 Cast Al-Si-Mg Alloy 132
5.4.5 7XXX Alloys 133
5.5 Microstructure and Mechanical Properties of Friction Stir Spot Welds 139
5.5.1 Macro/Microstructure 139
5.6 Corrosion in FSW Welds 143
References 146

6 Friction Stir Welding of Magnesium Alloys 149
6.1 Magnesium Alloys in Twenty-First Century 149
6.2 Classification of Magnesium Alloys 151
6.3 Welding of Magnesium Alloy 153
6.3.1 Conventional Route of Welding Mg Alloys 154
6.3.2 Friction Stir Welding of Magnesium Alloys 155
6.3.3 Evolution of Microstructure 162
6.3.4 Properties 172
References 184

7 Friction Stir Welding of High Temperature Alloys 189
7.1 Titanium Alloys 190
7.1.1 Introduction and Basic Physical Metallurgy 190
7.1.2 Tool Materials and Related Issue 195
7.1.3 Mechanical Properties of Titanium Alloys 195
7.1.4 Friction Stir Welding of Titanium Alloys 199
7.2 Ferrous Alloy 208
7.2.1 Introduction and Basic Physical Metallurgy of Steels 208
7.2.2 Tool Materials and Related Issues 215
7.2.3 Mechanical Properties of Steel 217
7.2.4 Friction Stir Welding of Steels 219
References 234

8 Dissimilar Metal Friction Stir Welding 237
8.1 Introduction 237
8.2 Issues with Dissimilar Metal Welding 237
8.3 Friction Stir Welding of Dissimilar Metals 240
8.3.1 Friction Stir Welding of Different Alloys with Similar Base Metals and Melting Points 240
8.3.2 Friction Stir Welding of Different Alloys Having Dissimilar Base Metals and Similar Melting Point 243
8.3.3 Dissimilar Metals Having Widely Differing Melting Point 251
References 257

9 Friction Stir Processing 259
9.1 Friction Stir Processing for Superplastic Forming 261
9.1.1 Constitutive Relationship and Microstructural Requirements for Superplasticity 261
9.1.2 Superplastic Flow in Friction Stir Processed Materials 262
9.1.3 Friction Stir Processing as a Technology Enabler for New Concepts 264

9.2 Enhanced Room Temperature Formability via FSP 269
9.3 Friction Stir Processing of Surface Composites and Powder Processing: Approach for Stiffness Limiting Design 272
9.3.1 Localized Surface Modification 273
9.3.2 Processing of Powder Metallurgy Alloys 274
9.3.3 Synergistic Design: Concept of Embedded Structures for Higher Efficiency 276
9.4 Friction Stir Casting Modification: Examples of Approaches for Strength Limiting, Fatigue Limiting and Toughness Limiting Designs 279
9.4.1 Microstructural Refinement 279
9.4.2 Influence on Mechanical Properties 282
9.5 Friction Stir Channeling (FSC) 288
9.6 Ultrafine Grained Materials via Friction Stir Processing 291
References 294

10 Residual Stresses and Mitigation Strategies 297
10.1 Introduction 297
10.1.1 Definition 297
10.1.2 Causes of Residual Stress 297
10.1.3 Types of Residual Stresses 298
10.1.4 Implications of Residual Stresses 299
10.2 Residual Stresses in Welding 301
10.2.1 Residual Stresses in Friction Stir Welding 302
10.3 Measurement of Residual Stresses 305
10.3.1 Hole Drilling 306
10.3.2 X-Ray Diffraction 307
10.3.3 Role of Sample Size in the Measurement of Residual Stresses 309
10.4 Effect of Residual Stress on Properties 310
10.5 Dependence of Residual Stresses on Friction Stir Welding Parameters 311
10.6 Understanding Development of Residual Stresses in Friction Stir Welding 314
10.7 Difference Between Residual Stress Generation in Friction Stir Welding and Fusion Welding 316
10.8 Mitigation of Residual Stresses 317
10.8.1 Active Cooling 317
10.8.2 Mechanical Tensioning 318
10.8.3 Roller Tensioning 319
10.9 Modeling and Simulation of Residual Stresses in Friction Stir Welding 320
References 325

Index 327

Chapter 1
Introduction

Welding and joining of materials is a key step in manufacturing of integrated systems. The present book deals with metallic structures and the joining of these is achieved by either mechanical fastening or metallurgical bonding. Most of the conventional welding processes involve local melting along the joint line and subsequent solidification leads to formation of a joint. Figure 1.1 shows a very generic classification of manufacturing processes and welding/joining of metals falls under consolidation processes. The consolidation/assembly processes can involve joining or mechanical fastening. The selection of joining technique depends on the scale of structures and design considerations. While large aircrafts use mechanical fastening, the shipbuilding uses welding techniques. Smaller systems like automobiles use a large number of techniques including welding and adhesive bonding. The impact of joining techniques on the workpiece is an important consideration. Figure 1.2 shows an overview of metallic material joining and its association with microstructural changes and reliability. The inset in figure is a classic example of liberty ship failure because of improper joining procedure. Another example often cited in welding courses is the Alexander Kielland disaster in the North Sea where a weld failure led to collapse of oil platform. The lessons from these always weave an intricate relationship between design, materials, welding processes and procedures, and final inspection. Residual stresses and related impact on long term service are an integral and important part of the entire scheme. Of course, fundamental understanding of these is critical not only to avoid these occurrences but also to maximize the structural efficiency of the systems.

Metals joining processes can be divided into four basic categories—fusion welding; brazing and soldering; adhesive bonding; and solid state bonding. In fusion welding processes, a portion of the base metals are melted, a filler metal may be introduced, and the pieces of metal are connected by a continuous puddle of liquid metal. After the molten puddle solidifies, the pieces of metal are joined.

R.S. Mishra et al., *Friction Stir Welding and Processing: Science and Engineering*,
DOI 10.1007/978-3-319-07043-8_1,

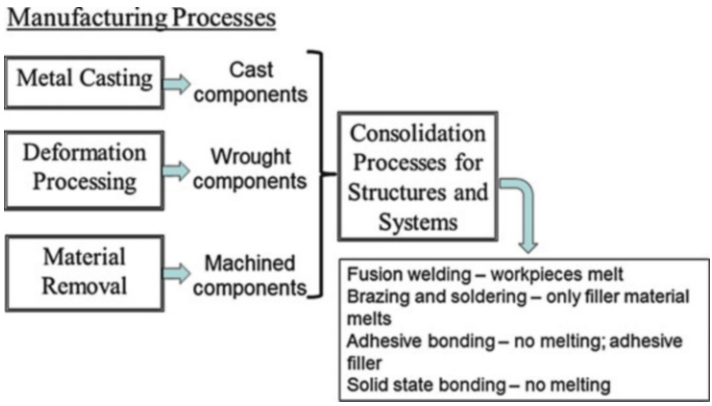

Fig. 1.1 An overview of the manufacturing processes and subset of joining processes for production of integrated systems or structures

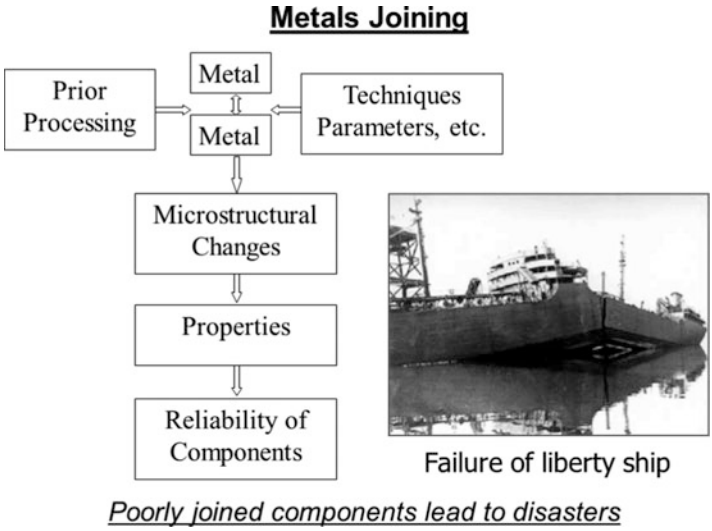

Fig. 1.2 An overview layout of the metallic material joining and the context of process-microstructure-properties-performance approach

Brazing and soldering differ from fusion welding in that only the filler metal melts; the filler metal is drawn into the space between the base metals, alloys with the base metal, and solidifies to produce the bond. In adhesive bonding, the filler material is a glue rather than a molten metal. The solid state bonding processes rely on deformation and/or atom diffusion to produce the bond, with no melting of either the base metal or a filler metal.

1.1 Solid State Welding

In these processes, pressure and deformation provides a significant portion of the bonding. Generally no melting of the base metal is required and filler material is not usually required. Diffusion bonding utilizes a pressure that is great enough to only locally deform the hills and valleys on the abutting surfaces. No gross deformation of the workpiece occurs. Then, at a high temperature below the melting temperature of the workpiece, atoms are allowed to diffuse across the interface to fill in any remaining voids and complete the joining process.

Deformation bonding processes use applied pressures above the yield strength of the work, causing gross deformation, forcing atoms on one surface into intimate contact with atoms on the second surface. Atomic attraction provides the bond. We can provide the pressure to the work by several methods, including cold welding, explosive welding, forge welding, friction welding, hot pressure welding, roll welding, ultrasonic welding, and friction stir welding. Friction stir welding is unique among the deformation based solid state processes because of the way material flows and comes together to produce the joint. If done properly, it leads to exceptional properties and that has been the main reason for its successful implementation in numerous aerospace, automotive and shipbuilding applications. A simple layout of the pressure and time during solid state welding is shown in Fig. 1.3. Friction stir welding involves intense plastic deformation and weld cycle is fairly short.

1.2 Friction Stir Welding

Friction stir welding (FSW) was invented at The Welding Institute (TWI) of UK in 1991 as a solid-state joining technique, and was initially applied to aluminum alloys (Thomas et al. 1991; Dawes and Thomas 1995). The basic concept of FSW is remarkably simple. Figure 1.4 illustrates process definitions for the tool and

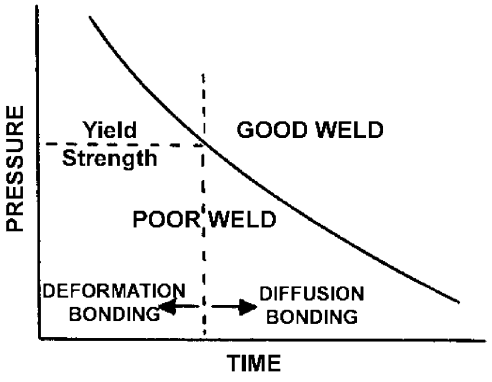

Fig. 1.3 A schematic illustration of pressure and time involved in deformation and diffusion bonding processes. In friction stir welding, the pressure exceeds the yield strength of the workpiece and weld cycle is fairly short

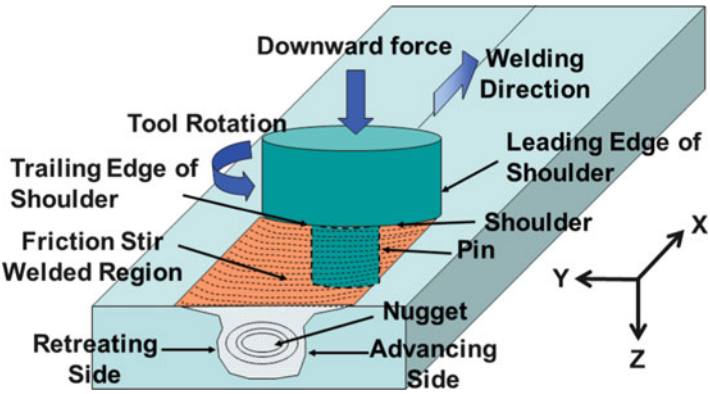

Fig. 1.4 A schematic drawing of friction stir welding in a butt joint configuration

workpiece in a butt joint configuration. A non-consumable rotating tool with a specially designed pin and shoulder is inserted into the abutting edges of sheets or plates to be joined and subsequently traversed along the joint line. The definitions of all terms are included in the taxonomy section. In this illustration, the FSW tool rotates in the counterclockwise direction and travels into the page (or left to right). The advancing side is on the right where the tool rotation direction (sense of tangential velocity) is the same as the tool travel direction and the retreating side is on the left where the tool rotation (sense of tangential velocity) is opposite the tool travel direction. Friction stir processing (FSP) is a generic adaptation of FSW, where the tool is traversed along a desired path to modify the microstructure rather than joining two pieces. Conceptually the FSP runs are similar to bead-on-plate runs. Although most of the fundamental concepts are similar, certain aspects are purposely changed in FSP to achieve the desired processing goal. For example, in friction stir welding one may want to maximize the traverse rate to increase the production rate. If one takes some of the faster examples to date such as traverse rate of 1–3 m/min for Al 5XXX alloys, at a tool rotation rate of 1,000 rpm, this would give advance per revolution as 1–3 mm/rev. The shear gradient in such runs would be very high and resultant microstructural gradient would lead to inhomogeneous grain structure. This may not matter for the joint property in terms of room temperature strength. However, if the intention is to use FSP for superplasticity, the goal would be to obtain fine grains and uniform microstructural distribution. For this, the traverse speed and tool rotation rate needs to be carefully selected to obtain fine and uniform grain size (Fig. 1.5).

The tool serves three primary functions, i.e., (a) heating of the workpiece, (b) movement of material to produce the joint, and (c) containment of the hot metal beneath the tool shoulder. Heating is created within the workpiece by friction between both the rotating tool pin and shoulder and by severe plastic deformation of the workpiece. The localized heating softens material around the pin, and combined with the tool rotation and translation leads to movement of material from the front to the back of the pin thus filling the hole in the tool's wake as the tool moves

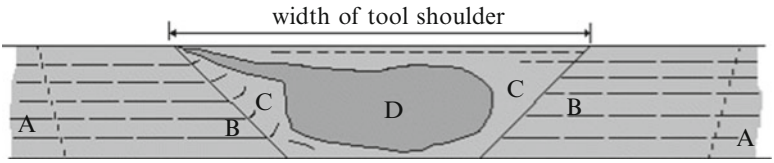

Fig. 1.5 Various microstructural regions in the transverse cross-section of a friction stir welded material (Mishra and Mahoney 2007, reprinted with permission from ASM International)

forward. The tool shoulder restricts metal flow to a level equivalent to the shoulder position, i.e., approximately to the initial workpiece top surface.

As a result of the tool action and influence on the workpiece, when performed properly, a 'solid state' joint is produced, i.e., no melting. Because of various geometrical features on the tool, material movement around the pin can be complex with gradients in strain, temperature, and strain rate (London et al. 2001). Accordingly, the resulting nugget zone microstructure reflects these different thermomechanical histories and is not homogeneous. In spite of the local microstructural inhomogeneity, one of the significant benefits of this 'solid state' welding technique is the fully recrystallized, equiaxed, fine grain microstructure created in the nugget by the intense plastic deformation at elevated temperature (Rhodes et al. 1997; Liu et al. 1997; Jata and Semiatin 2000; Benavides et al. 1999). As will be seen within these chapters, the fine grain microstructure produces excellent mechanical properties, fatigue properties, enhanced formability and exceptional superplasticity.

1.3 Taxonomy for Friction Stir Welding and Processing

Friction stir welding: joining of two workpieces by FSW.

Friction stir processing: use of the friction stir process to modify the microstructure to local region metallurgically.

Tool shoulder: the region of tool in contact with the workpiece surface. To enhance the material flow, tool shoulder can have negative or positive scrolls. A negative scroll is a depression in the shoulder surface and the workpiece material fills this. A positive scroll is a protrusion on the shoulder surface. Both types of scrolls conceptually enhance the material flow inward. The other design choice for the shoulder is concave or convex. Concave shoulders were designed to hold the workpiece material in a cup shape. The convex shoulders are relatively new and they require negative scroll spiral (or groves) to contain the material. The advantage of convex shoulder lies in its ability to tolerate minor variability in workpiece thickness.

Tool pin: also referred to as probe in some literature, the pin of the tool is inserted in the workpiece and it influences the horizontal material flow from front to back, as well as vertical material flow from top to bottom. The most common pin

profiles are cylindrical or conical. The pins can be threaded or have step spiral design. In addition, the flow can be influenced by putting flats or flutes. The overall possibilities of variations can be extremely large.

Advancing side: the tool pin surface rotation direction and the tool traverse direction have the same vectorial sense. Because of the tool's forward movement, the material wants to flow back, but the pin surface rotation opposes that flow on this side of the tool.

Retreating side: the tool pin surface rotation direction and the tool traverse direction have the opposite vectorial sense. The material flow is easier on this side of the tool pin as the pin surface helps the material flow backward.

Leading edge: the front side of the tool. The tool shoulder meets the cold workpiece material in this region. The tool shoulder sweeps the top layer sideways toward the retreating side and this can have implication of the overall material flow and weld nugget appearance.

Trailing edge: the back side of the tool. The trailing part keeps pumping heat in the workpiece after pin has crossed the region. This influences the microstructural evolution after the pin induced deformation.

Tool rotation rate: the rate at which the tool rotates. This has major contribution to the heat input and material flow.

Tool traverse speed: the travel speed of the tool. This impacts the overall thermal cycle.

Tilt angle: the angle between the plane normal of workpiece and the spindle shaft. Typically an angle between 0 and 3° is selected.

Work angle: it is an angle between the spindle shaft and the workpiece normal in the z–y plane. This is rarely used in gantry style machine, but can be useful for robotic machine due to the machine stiffness issues.

Plunge rate: the rate at which the tool is inserted in the workpiece. It controls the rate of heat build-up and force during the start of the process.

Plunge depth: the programmed depth of the pin bottom from the top surface of workpiece. For position-controlled runs, this is a critical number.

Plunge force: the vertical force on the tool when shoulder meets the top surface of workpiece. For force-controlled runs, this is the target force.

Z-axis: the workpiece normal is referred to as the z-axis and this is also the direction of plunge force. A convenient way to look at the forces is from tool's perspective. Vertical up direction is compressive force on the tool.

X-axis: the travel direction is referred to as the x-axis. The tool pin experiences compressive force from front to back.

Y-axis: the direction normal to the travel direction is the plane parallel to the top surface. The tool pin experiences compressive force from retreating side to advancing side because of the imbalance of material flow around the pin.

Unaffected material or parent metal: This is material remote from the weld, which has not been deformed, and which although it may have experienced a thermal cycle from the weld is not affected by the heat in terms of microstructure or mechanical properties.

Heat affected zone (HAZ): In this region, which lies closer to the weld center, the material has experienced a thermal cycle that has modified the microstructure and/or the mechanical properties. However, no plastic deformation occurred in this area.

Thermo-mechanically affected zone (TMAZ): In this region, the friction stir welding tool has plastically deformed material and the heat from the process will also have exerted some influence on the material. In the case of aluminum, it is possible to get significant plastic strain without recrystallization in this region, and there is generally a distinct boundary between the recrystallized zone (weld nugget) and the deformed zones of the TMAZ.

Weld Nugget: The fully recrystallized area, sometimes called the stir zone, referring to the zone previously occupied by the tool pin. The term stir zone is commonly used in friction stir processing where large volumes of material are processed.

1.4 Overall Applicability of Friction Stir Welding

Friction stir welding is considered to be the most significant development in metal joining in decades and in addition is a "green" technology due to its energy efficiency, environmental friendliness, and versatility. As compared to the conventional welding methods, FSW consumes considerably less energy, no consumables are use such as a cover gas or flux, and no harmful emissions are created during welding, thereby making the process environmentally friendly. Further, since FSW does not involve the use of filler metal and because there is no melting, any aluminum alloy can be joined without concern for compatibility of composition or solidification cracking; issues associated with fusion welding. Also, dissimilar aluminum alloys and composites can be joined with equal ease (Murr et al. 1998; Li et al. 2000, 1999).

In contrast to traditional friction welding, a welding process limited to small axisymmetric parts that can be rotated and pushed against each other to form a joint (Cary 1979), friction stir welding can be applied to most geometric structural shapes and to various types of joints such as butt, lap, T-butt, and fillet shapes (Dawes and Thomas 1996). The most convenient joint configurations for FSW are butt and lap joints. A simple square butt joint is shown in Fig. 1.6a. Two plates or sheets with the same thickness are placed on a backing plate and clamped firmly to prevent the abutting joint faces from being forced apart. The backing plate is required to resist the normal forces associated with FSW and the workpiece. During the initial tool plunge, the lateral forces are also fairly large and extra care is required to ensure that plates in the butt configuration do not separate. To accomplish the weld, the rotating tool is plunged into the joint line and traversed along this line while the shoulder of the tool is maintained in intimate contact with the plate surface. Tool position and penetration depth are maintained by either position control or control of the applied normal force. On the other hand, for a lap joint

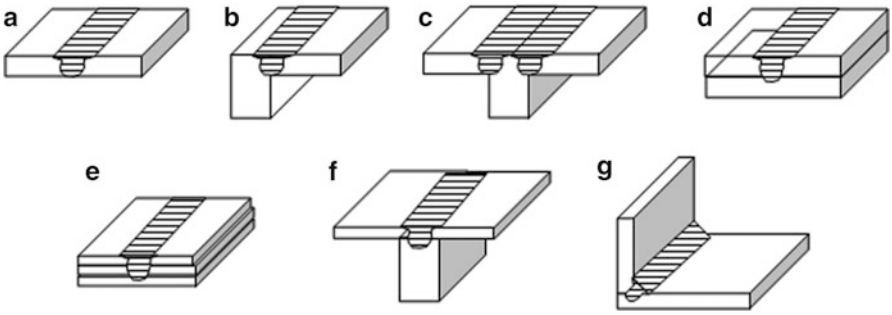

Fig. 1.6 Joint configurations for friction stir welding: (**a**) square butt, (**b**) edge butt, (**c**) T butt joint, (**d**) lap joint, (**e**) multiple lap joint, (**f**) T lap joint, and (**g**) fillet joint (Mishra and Ma 2005, reprinted with permission from Elsevier)

configuration, two lapped plates or sheets are clamped and a backing plate may or may not be needed depending on the lower plate thickness. A rotating tool is vertically plunged through the upper plate and partially into the lower plate and traversed along the desired direction joining the two plates (Fig. 1.6d). However, the tool design used for a butt joint, where the faying surfaces are aligned parallel to the tool rotation axis, would not be optimum for a lap joint where the faying surfaces are normal to the tool rotation axis. The orientation of the faying surfaces with respect to the tool features is very important and is discussed in detail in Chap. 4. Configurations, of other types of joint designs applicable to FSW are discussed in Chap. 4. Additional key benefits of FSW compared to fusion welding are summarized in Table 1.1.

1.5 A Few Illustrative Implementation Examples

The adoption of friction stir welding was fastest in the aerospace industry. This was a classic example of 'technology pull'! The high strength aluminum alloys, such as 2XXX and 7XXX series aluminum alloys are classified as 'nonweldable' by fusion welding techniques. So, when the friction stir welding was invented in 1991, it opened new opportunities to weld high strength aluminum alloys. This obviously led to high level of excitement in the aerospace industry, which saw significant design opportunities. Table 1.2 shows an example of strength levels achieved in initial studies of friction stir welding of 2024Al and 7075Al. Subsequently other attributes of friction stir welding, like defect free welds, lower residual stresses and lower distortion, led to numerous implementations using lower strength aluminum alloys.

The recent examples of commercialization of FSW include joining of front and back section of the iMac monitor, central tunnel assembly of Ford GT, long panels

Table 1.1 Key benefits of friction stir welding (Mishra and Ma 2005, reprinted with permission from Elsevier)

Metallurgical benefits	Environmental benefits	Energy benefits
Solid phase process	No shielding gas required	Improved materials use (e.g., joining different thickness) allows reduction in weight
Low distortion	Minimal surface cleaning required	Only 2.5 % of the energy needed for a laser weld
Good dimensional stability and repeatability	Eliminate grinding wastes	Decreased fuel consumption in light weight aircraft, automotive and ship applications
No loss of alloying elements	Eliminate solvents required for degreasing	
Excellent mechanical properties in the joint area	Consumable materials saving, such as rugs, wire or any other gases	
Fine recrystallized microstructure	No harmful emissions	
Absence of solidification cracking		
Replace multiple parts joined by fasteners		
Weld all aluminum alloys		
Post-FSW formability		

Table 1.2 An example of initial results for 2024Al and 7075Al alloys that led to excitement for implementation of friction stir welding

	Parent material	Gas-shielded arc welded butt joint		Friction stir welding	
Base alloy and temper	Tensile strength (MPa)	Tensile strength (MPa)	% of Parent	Tensile strength (MPa)	% of Parent
2024-T3	485	Nonweldable	–	432	89
7075-T6	585	Nonweldable	–	468	80

for the body of train carriages in Chinese high speed trains, NASA's Orion spacecraft, etc. Figure 1.7 shows a few photographs of implementations in aerospace and locomotive applications. The upper left corner photograph shows a generic curvilinear weld using a robotic friction stir welding machine. The examples from Airbus Group include various configurations, including several relating to replacement of riveting technology by FSW in longitudinal and circumferential joints. The versatility of FSW is quite obvious. Similarly the example from the Shinkansen application is illustrative of a system level solution. Figure 1.8 shows an example of friction stir spot welding used for automotive applications.

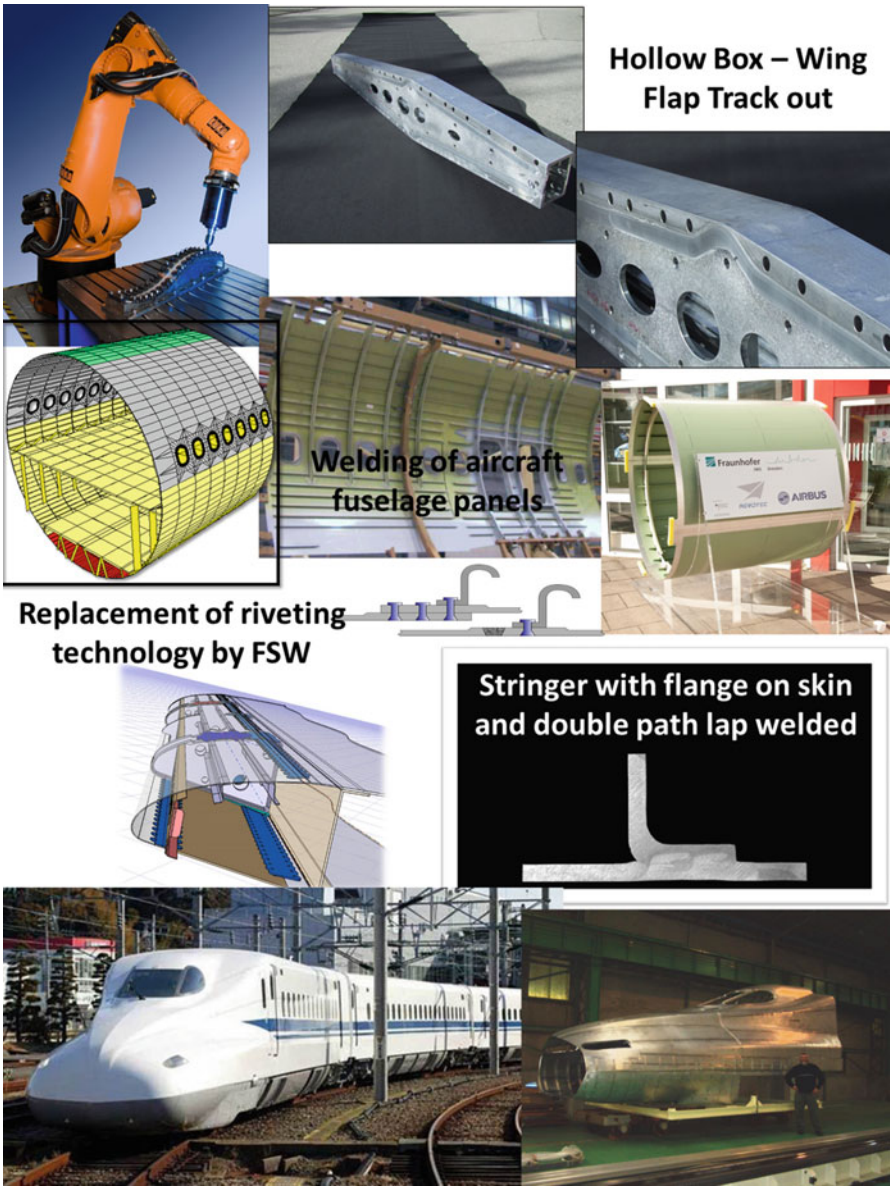

Fig. 1.7 A few illustrative examples of implementation of friction stir welding (all aircraft related photographs courtesy Airbus Group, Ottobrunn, Germany and Shinkansen photographs courtesy Mr. Gilbert Sylva)

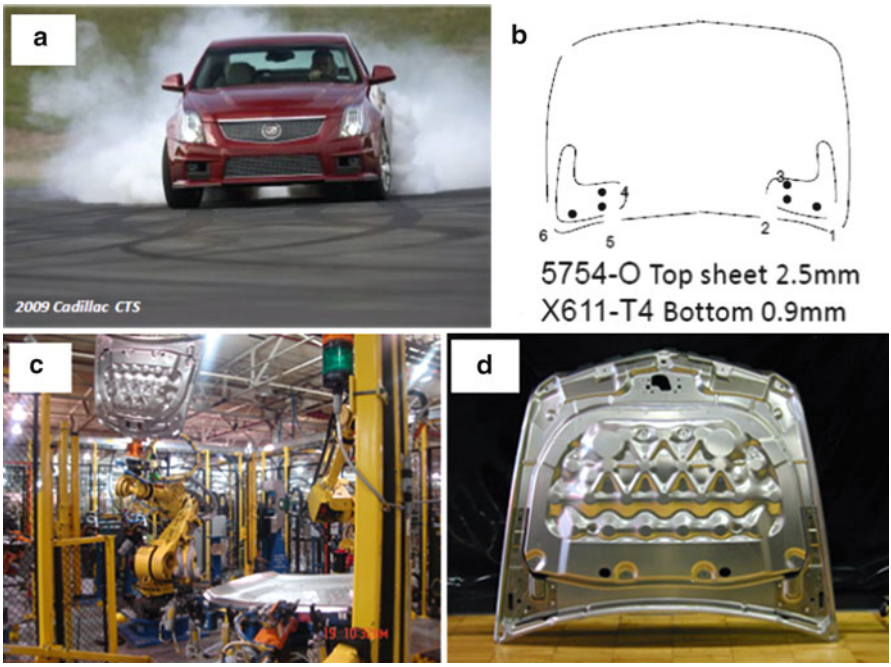

Fig. 1.8 An example of friction stir spot welding used in automotive industries (Figure courtesy Dr. Blair Carlson, General Motors)

References

S. Benavides, Y. Li, L.E. Murr, D. Brown, J.C. McClure, Scripta Mater. **41**, 809 (1999)
H.B. Cary, *Modern Welding Technology* (Prentice Hall, New Jersey, 1979)
C.J. Dawes, W.M. Thomas, Weld. J. **75**, 41 (1996)
C. Dawes, W. Thomas, TWI Bulletin 6 (Nov/Dec 1995), p. 124
K.V. Jata, S.L. Semiatin, Scripta Mater. **43**, 743 (2000)
Y. Li, L.E. Murr, J.C. McClure, Mater. Sci. Eng. **A271**, 213 (1999)
Y. Li, E.A. Trillo, L.E. Murr, J. Mater. Sci. Lett. **19**, 1047 (2000)
G. Liu, L.E. Murr, C.S. Niou, J.C. McClure, F.R. Vega, Scripta Mater. **37**, 355 (1997)
B. London, M. Mahoney, B. Bingel, M. Calabrese, D. Waldron, in *Proceedings of the Third Int. Symposium on Friction Stir Welding*, Kobe, Japan, 27–28 Sept 2001
R.S. Mishra, Z.Y. Ma, Mater. Sci. Eng. R **50**, 1 (2005)
L.E. Murr, Y. Li, R.D. Flores, E.A. Trillo, Mater. Res. Innovat. **2**, 150 (1998)
C.G. Rhodes, M.W. Mahoney, W.H. Bingel, R.A. Spurling, C.C. Bampton, Scripta Mater. **36**, 69 (1997)
W.M. Thomas, E.D. Nicholas, J.C. Needham, M.G. Murch, P. Templesmith, C.J. Dawes, G. B. Patent Application No 9,125,978.8, Dec 1991

Chapter 2
Fundamentals of the Friction Stir Process

2.1 Overview of Macroscopic Processes During FSW

For any manufacturing process, understanding its fundamental process mechanisms is vital for its long-term growth. In this chapter, we will outline the essential characteristics of friction stir process. As pointed out in Chap. 1, unlike fusion-based joining processes, there is no perceptible melting during friction stir welding (FSW). From the operational viewpoint, a friction stir welding run can be divided into three sub-procedures or phases:

(a) plunge and dwell,
(b) traverse, and
(c) retract.

At the start of the plunge phase, both the tool and the workpiece are at ambient temperature (except the region surrounding tool and workpiece interface). When the rotating friction stir tool is gradually inserted into the workpiece, the material is too cold to flow and the rubbing action creates chipping as in any machining process. The rate of insertion determines the rate of temperature rise and extent of plasticity. The process of tool insertion continues until the tool shoulder is in intimate contact with the workpiece surface. At this stage, the entire tool shoulder and pin surface contribute to the frictional heating and the force starts to drop as the metallic workpiece reaches critical temperature for plastic flow. For metals with higher melting point, the rotating tool is sometimes intentionally retained at this position for short durations so as to reach the desired temperature required for plastic flow. This is known as the dwell phase and is typically a fraction of the time required for plunge phase. Typically, the plunge stage is programmed for controlled plunge rate (i.e. vertical position controlled FSW) but it can be also done by controlling the force applied on the tool along its rotation axis (i.e. force controlled FSW). Of course, any combination of displacement and force controlled approach is possible. For a typical FSW run, the vertical force reaches a maximum value in this part of the run and this tends to be critical phase for the tool. It is important to

R.S. Mishra et al., *Friction Stir Welding and Processing: Science and Engineering*,
DOI 10.1007/978-3-319-07043-8_2,

control the rate of heat build-up and in fact, for metals with higher melting point (e.g. steel/titanium) the plunge rate is particularly low so as to generate sufficient heat to plasticize the metal (Refer to Chap. 4 for more discussion on it).

Box 2.1 Friction Stir Spot Welding (FSSW)

FSSW is a new spot welding technique to join overlapping workpieces and intends to replace existing techniques like resistance spot welding. The concept was first developed at Mazda Motor Corporation and Kawasaki Heavy Industry as an extension of FSW for joining Al alloys (Sakano et al. 2001). The method consists of only (a) the plunge and dwell and (c) retract stages of FSW (see Fig. 2.1). Due to absence of stage (b) of FSW (traverse stage) in FSSW, there is no concept of advancing side and retreating side, and the process is considered to be symmetrical.

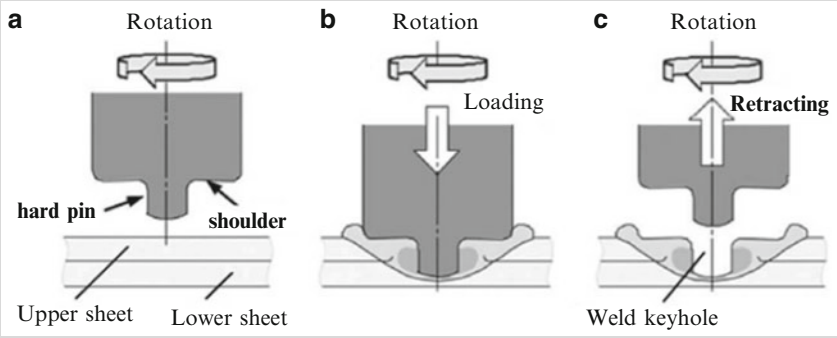

Fig. 2.1 Two different stages (**a**)–(**b**) plunge and dwell and (**c**) retract in FSSW (Yang et al. 2010, reprinted with permission from Elsevier)

The FSSW procedure shown in Fig. 2.1 is known as the plunge type FSSW. Some other variants of FSSW includes (a) refill FSSW (Iwashita 2003), (b) modified refill FSSW (Allen and Arbegast 2005), (c) swing FSSW (Okamoto et al. 2005).

Once the workpiece/tool interface is sufficiently heated up, the tool is traversed along the desired direction to accomplish joining. This is the actual welding phase and can be performed under (a) displacement controlled mode (where tool position with respect to the workpiece surface is held constant) or (b) force controlled mode (normal force applied by the tool to the workpiece is held constant). There are other modes such as power control, torque control, temperature control, etc., on advanced FSW machines available these days. On completion of the joining process, the tool is finally retracted from the workpiece. In Fig. 2.2a, a schematic of the force versus time during friction stir welding is shown.

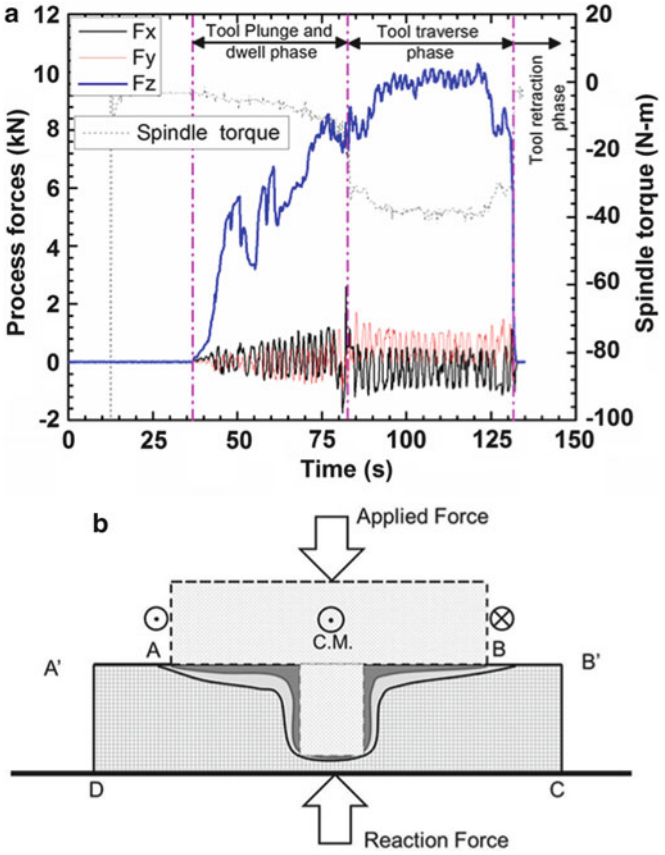

Fig. 2.2 (**a**) The temporal variation of forces F_x, F_y and F_z acting on the tool during friction stir welding. (**b**) Schematic transverse section of friction stir welding tool and workpiece with the tool rotating in counterclockwise direction and is moving out of the plane of the paper with the forces acting

It is instructive here to consider the physical effects occurring at the different positions of the tool/workpiece interface during the traverse phase. Thus, in Fig. 2.2b where the rotating tool shoulder presses on to the workpiece (AB/A′B′ interface), frictional heat generation plasticizes the metal and pushes it downwards. Some fraction of the shoulder generated heat along with the frictional heat generated by the moving and rotating pin softens the metal adjacent to the pin. The softened metal flows around the pin, resulting in joining of the weld seam. In fact, FSW in its pseudo-steady state is conceptually quite similar to thermo-mechanical metalworking of metallic materials (Arbegast 2008). However, a key difference between FSW and elevated temperature metalworking processes is that in metal forming the workpiece is pre-heated to a critical temperature to soften the metal for subsequent deformation without any failure or cracking. But, in FSW the workpieces to be joined are at ambient temperature in the beginning and the heat

generation accomplished through mostly friction is an essential part of the process.[1] In contrast, in most metal forming processes, the aim is to minimize the friction so as to reduce the process energy consumption. The difference between FSW and other metal forming processes are clearly illustrated in Figs. 2.3 and 2.4.

The explanation so far has been directed towards an operational understanding of the process during FSW, and it highlights two key components in FSW process: heat generation and material flow. Figure 2.5 illustrates an overview of the principal process variables (dependent and independent) affecting material flow (deformation) and temperature distribution in FSW, and the physical effects associated with each parameter (the figure is adapted from Colligan and Mishra (2008)). The independent process variables are shown in boxes with bold lines, while the dependent variables are shown in boxes with dashed lines. The linkage between dependent and independent process variables are shown through arrows which pass through respective physical effects shown in dashed boxes in italics. Deducing the effect of independent process variables on the dependent variables through the respective physical effects is, however, more complicated. Nonetheless, simple deductions about the operational effect of different process variables can be made. For example, an increase in tool shoulder diameter and keeping all other independent process variables constant will not only impact the peak temperature and temperature distribution but also will impact the dependent variables, torque and associated power input. It gives a glimpse of the interdependencies and intricacies associated with friction stir welding. Again, increasing the spindle speed (rotation rate) or decreasing the tool travel speed is expected to increase the heat input into the weld as long as the frictional conditions remain unchanged which itself depends on the contact pressure, temperature distribution and shear stress of the workpiece. A generic flow chart of the physical effects in friction stir welding and how they affect the microstructure is shown in Fig. 2.6 (Mishra 2008). Details on how the microstructure is affected will be discussed in Chap. 3.

2.2 Heat Generation During Friction Stir Process

In macroscopic terms the energy flow in FSW is as below (Fig. 2.7). From Fig. 2.7, it is evident that the torque generated at the spindle and weld-arm motor can give a measure of the overall energy required for FSW (Lienert et al. 2002; Khandkar et al. 2003). Again, neglecting other losses (i.e. transmission losses), the electrical power consumed is also a good indicator of the energy trend. But, predictive modeling is practically impossible unless such direct energy measures are correlated to the actual processes in the weld zone, indicating the importance of understanding the heat generation

[1] FSW of pre-heated workpiece is also currently gaining acceptance. Predominantly a heat source like laser beam is used to pre-heat the specimen locally. This reduces the forces during FSW especially for high melting point metals like steel and copper (Kohn et al. 2002).

processes in FSW. The heat generation in FSW arises primarily from two sources, (a) friction between the tool and workpiece surfaces and (b) heat generated during plastic deformation in the bulk of the workpiece.

Box 2.2 A Comparison of Force-Time Profiles for Various Thermo-mechanical Processes

The signature response of any manufacturing process lies in its temporal force and temperature variations. In Fig. 2.3, the reactive body force in the principal loading direction (i.e. F_z) during FSW is compared with other manufacturing processes. The initial force peak characterizes the plunging stage, where the tool processes is more similar to machining process and the work-piece is more or less cold. However, as the heat builds up in and around the tool/work-piece vicinity, the material softens. Consequently the force drops to a more stable steady state characteristic of the actual welding stage unlike metal forming processes where the forces are intermittent type. Recent studies, however, show that the so called steady force state during FSW is in fact complicated with small periodic variations (see Fig. 2.30 in this chapter). The amplitude of these periodic variations is much smaller compared to the average load but nonetheless they carry important information about the process.

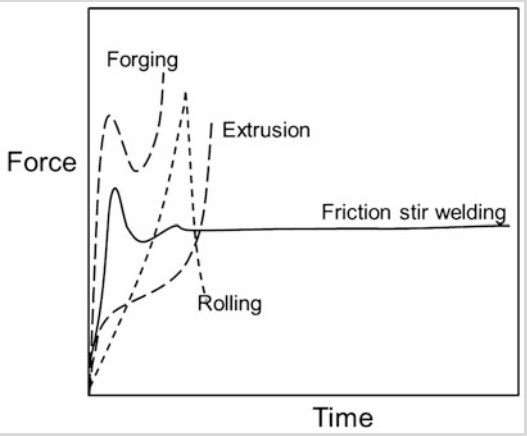

Fig. 2.3 The force versus time curve for different metal working processes and friction stir welding process. The initial sharp increase in force with time followed by a steady state value is typical of FSW and differs significantly from the batch type metalworking operations

Box 2.3 A Comparison of Temperature-Time Profiles for Various Thermo-mechanical Processes

Temperature variation in FSW is quite similar to other joining methods, but is distinctly different from metalworking processes. The effect of this temperature variation with time causes a significantly different effect on the workpiece during FSW. In a metalworking process the temperature variation (along with deformation) is a principal driving force in changing the microstructure of the entire workpiece. But, in FSW the localized temperature (and deformation too) gradient causes a microstructural change in a selected location (i.e. along the welded region) of the workpiece. Consequently, material property is non-uniform, unlike in metalworking processes where the property remains more or less similar throughout.

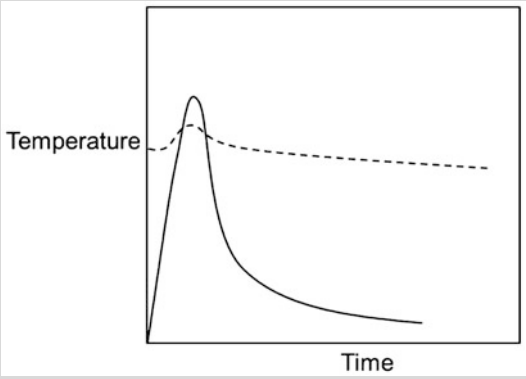

Fig. 2.4 The sharp variation of workpiece temperature (*bold line*) with time in FSW differs significantly from the more steady variation observed in metalworking operations like rolling (*dashed line*)

2.2.1 Heat Generation from Frictional Heating

Considering the frictional heat generation phenomena first: conventionally, friction between any two solids is governed by the following three empirical laws (attributed to the French scientists G. Amonton and C.D. Coulomb),

(a) frictional force (F) is related to the normal load (P) by

$$F = \mu P$$

where μ is the coefficient of static/dynamic friction. Both the static and dynamic coefficients of friction are independent of P,

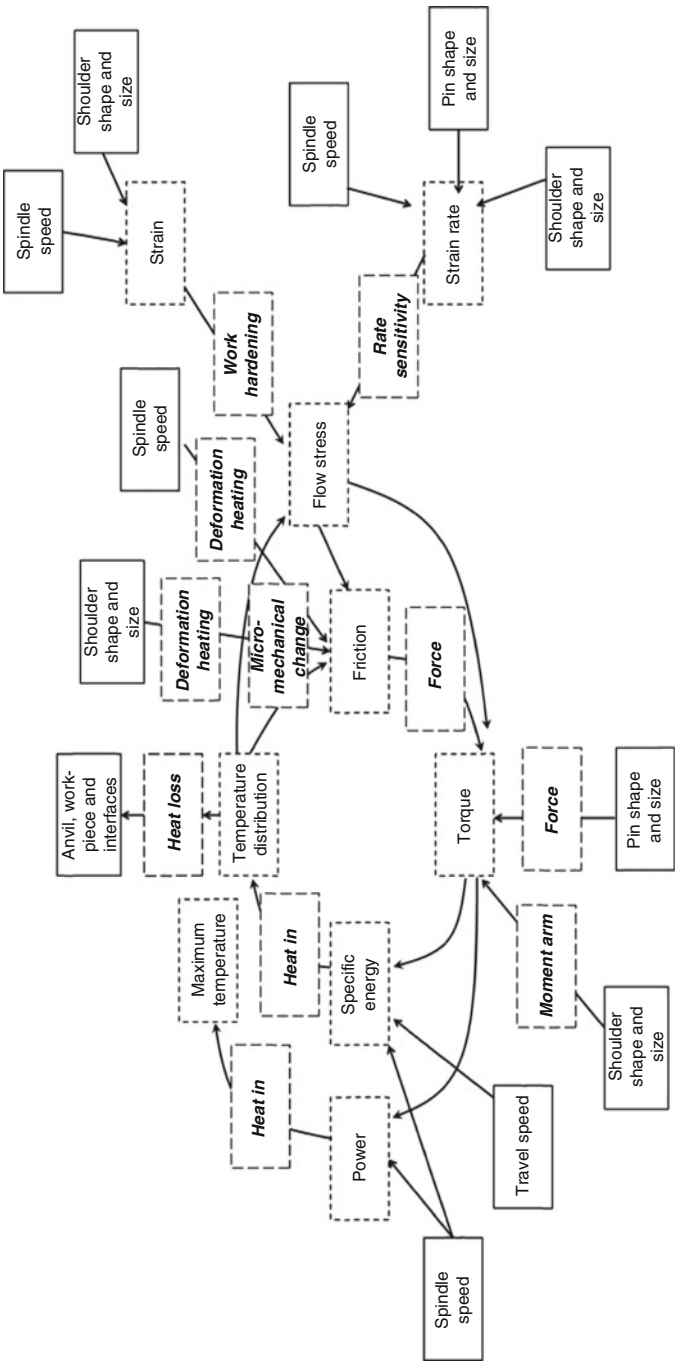

Fig. 2.5 A schematic operational flow chart of FSW with process variables and associated physical effects (Colligan and Mishra 2008, reprinted with permission from Elsevier)

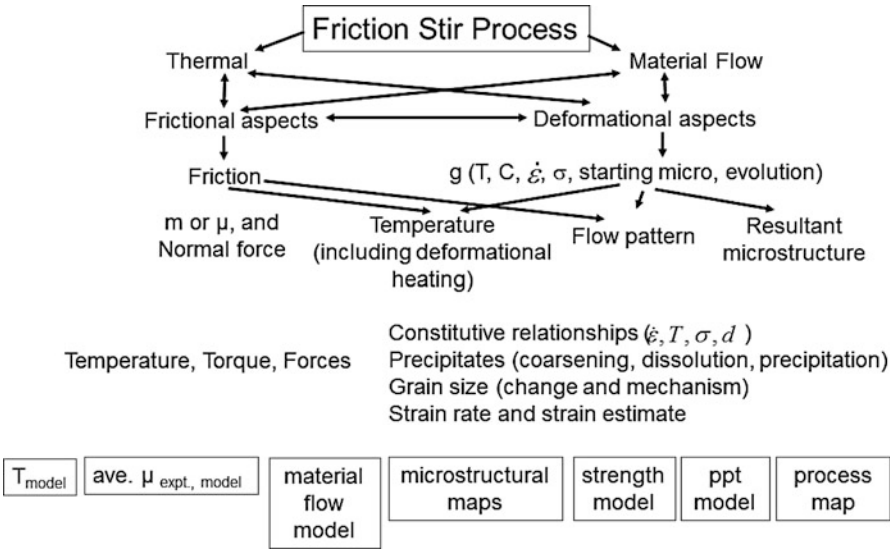

Fig. 2.6 A summary of the physical effects in FSW and how they affect the microstructure (Mishra 2008, reprinted with permission from Elsevier)

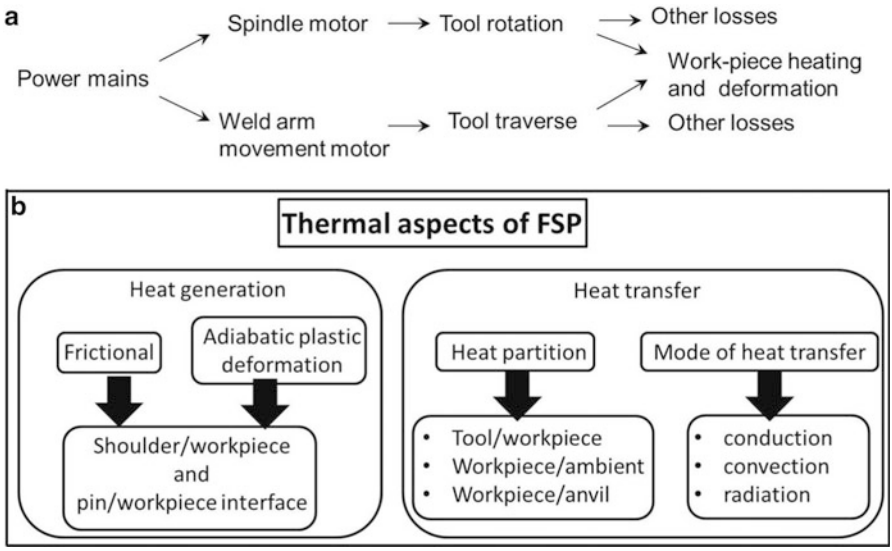

Fig. 2.7 The flow of energy into the workpiece during FSW. (**a**) Energy source and its flow (**b**) nature of heat generation and its utilization

(b) the coefficients of friction are independent of the macroscopic area of contact between the bodies, and
(c) the dynamic coefficient of friction is independent of the relative velocity between the two bodies.

However, exception to the above mentioned rules are frequent and indicate the complexities involved in defining friction. According to our current understanding (Bowden and Tabor 1973), the friction between metals and/or ceramics arises due to (a) interfacial adhesion between asperities on the contacting surfaces and (b) microscopic plastic deformation during relative motion of the contacting surfaces. The frictional energy dissipated during microscopic deformations occurring at the surfaces is entirely converted to heat energy. Thus, in reality the frictional force is influenced by the physical and chemical properties of the interacting surfaces and their dependence on the load, relative velocities and temperature thereof. It is important to note that in FSW these microscopic deformations occur chiefly at the workpiece surface (the tool surface more or less is considered non-deformable although that may not be true for FSW of high temperature materials with refractory metal tools). As a consequence, the heat generated is distributed unequally between the two surfaces (i.e. tool and workpiece) (Bhushan 2002). The extent of this heat partitioning depends on the thermal conductivity, heat capacity, relative velocity and the interfacial area of the tool and workpiece.

From a theoretical viewpoint, this friction can be any of the following.

(a) Coulomb friction

$$\tau = \mu p$$

where τ is the shear stress, p is the pressure and μ is the coefficient of friction.

(b) Constant shear model

$$\tau = m\sigma_y$$

where σ_y is the material yield stress in shear and m is the proportionality constant with m equals to 0 for slipping condition and 1 for sticking condition. In the constant shear model, the workpiece surface in contact with the tool is considered to behave like a material with constant shear strength. The maximum shear strength possible being equal to the yield stress in shear and is equivalent to a situation where the workpiece metal sticks to the tool surface with deformation occurring by sub-surface shearing (i.e. $m = 1$ in equation) (Dieter 1986).

In the remainder of this section, a comprehensive model of heat generation in FSW is presented. Figure 2.8 shows the schematic of a typical FSW tool, with a cylindrical pin of radius R_{pin} (i.e. R_{probe} in figure), and height H_{pin} (i.e. H_{probe} in figure) and a tool shoulder diameter $H_{shoulder}$ (i.e. H_{probe} in figure), the surface of which is at an angle α with the horizontal. The total heat generated at different portions of the tool (Schmidt and Hattel 2005) during welding is sub-divided into the following components depending on the distinct zones of the tool/work-piece interface,

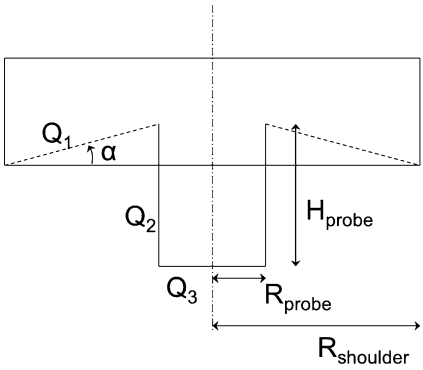

Fig. 2.8 A typical FSW tool with a conical shoulder and a cylindrical unthreaded pin [adapted from (Schmidt and Hattel 2005)]

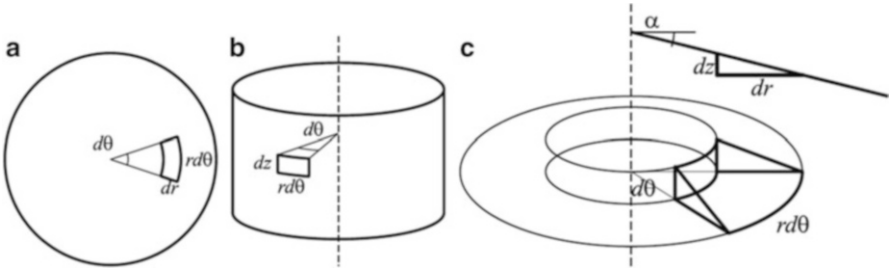

Fig. 2.9 A schematic of the different surface segments of the tool (**a**) pin bottom, (**b**) cylindrical surface of the pin, (**c**) conical surface of the shoulder, and the infinitesimal segments associated with the corresponding segments (Schmidt et al. 2004, © IOP Publishing. Reproduced by permission of IOP Publishing. All rights reserved)

Q_1 = Heat generated at the tool shoulder,
Q_2 = Heat generated at the tool pin,
Q_3 = Heat generated at the tool pin tip.

The general expression for heat generation at each of the different zones of the tool/workpiece interface is,

$$dQ = \omega \cdot r \cdot dF$$

where dQ is the heat generated per unit time, dF is the force acting on the surface at a distance r from the tool centerline and ω is the angular velocity of the tool.

In Fig. 2.9a the horizontal surface of the tool pin is shown. An infinitesimal segment on this surface $dA = r d\theta dr$ is acted upon by the frictional shear stress (τ_{shear}) and generates an infinitesimal amount of heat given as,

$$dQ_3 = \omega \cdot r^2 \cdot \tau_{shear} \cdot d\theta \cdot dr$$

Integrating the above over the tool pin bottom area we get,

Table 2.1 Some other approximate heat generation models used in literature

Assumptions (ref)	Heat generation equation used
1. Heat generated only at shoulder 2. Frictional heating only, i.e. μ is the coefficient of kinetic friction (Chao and Qi 1998)	$Q = \frac{\pi\omega\mu F\left(R_{shoulder}^2 + R_{shoulder}R_{pin} + R_{pin}^2\right)}{45\left(R_{shoulder} + R_{pin}\right)}$
1. The average power (P_{av})is related to measured torque (M_{total}) by $P_{av} = M_{total}\omega$ (Khandkar et al. 2003)	$\dot{q}(r) = \frac{P_{av}r}{(2/3)\pi R_{shoulder}^3 + 2\pi H_{pin}R_{\text{pin}}^2}$
1. The pressure P on tool is calculated from the force (Frigaard et al. 2001)	$q_0 = \frac{4}{3}\pi^2\mu P\omega R_{shoulder}^3$

$$Q_3 = \int_{r=0}^{R_{pin}}\int_{\theta=0}^{2\pi} \omega \cdot r^2 \cdot \tau_{shear} \cdot d\theta \cdot dr$$

$$Q_3 = \frac{2}{3}\pi\tau_{shear}\omega R_{pin}^3$$

In Fig. 2.9b the cylindrical portion of the pin is shown where the infinitesimal segment dA = rdθdz is acted by τ_{shear} and the heat generated is given as,

$$dQ_2 = \omega \cdot R_{pin}^2 \cdot \tau_{shear} \cdot d\theta \cdot dz$$

Integrating the above over the cylindrical surface of the pin,

$$Q_2 = \int_{\theta=0}^{2\pi}\int_{z=0}^{H_{pin}} \omega \cdot R_{pin}^2 \cdot \tau_{shear} \cdot d\theta \cdot dz$$

$$Q_2 = 2\pi\tau_{shear}R_{pin}^2\omega$$

In Fig. 2.9c the conical portion of the tool shoulder is shown where the infinitesimal segment approximated as dA = rdθ (dr + dz) = rdθ (dr + dr tan α) = rdθdr(1 + tan α), is acted upon by the τ_{shear} and heat generated is given as

$$dQ_1 = \omega \cdot r^2 \cdot \tau_{shear} \cdot (1 + \tan(\alpha)) \cdot dr \cdot d\theta$$

Integrating the above over the conical surface of the tool shoulder,

$$Q_1 = \int_{r=R_{pin}}^{R_{shoulder}}\int_{\theta=0}^{2\pi} \omega \cdot r^2 \cdot \tau_{shear} \cdot (1 + \tan(\alpha)) \cdot dr \cdot d\theta Q_1$$

$$= 2\pi(1 + \tan(\alpha))\tau_{shear}\left(R_{shoulder}^3 - R_{pin}^3\right)$$

In the above heat generation model, both ω and τ_{shear} are considered as constant. But, depending on the tool size and the tool rotation conditions these parameters can vary significantly (in terms of r and θ) and the heat generation expressions should be modified accordingly. Some other approximate expressions for heat generation used in literature are presented in Table 2.1. Another aspect worth

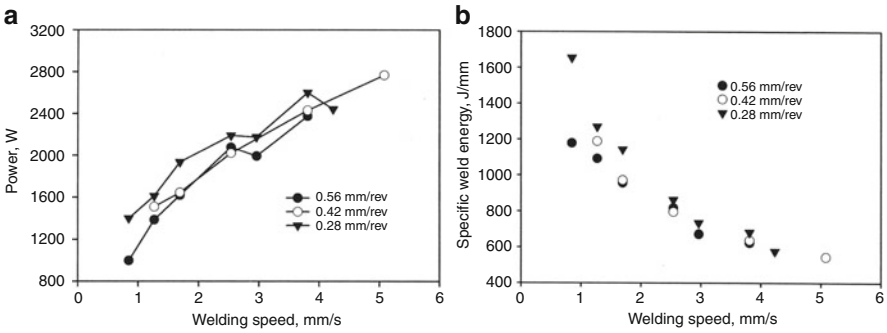

Fig. 2.10 Plots correlating (**a**) Power (W) and (**b**) Specific weld energy (J/mm) as a function of tool traverse speed (mm/s). Here, specific weld energy is defined as the ratio of weld power to the tool traverse speed (Reynolds 2007, reprinted with permission from ASM International)

mentioning is the effect of traverse speed on the weld heat input. Although, the heat generation equations described above are independent of traverse speed, the weld heat input decreases and the power consumed increases with traverse speed increase at constant traverse speed to tool rotation rate ratios (i.e. advance per revolution (APR)) (see Fig. 2.10a). The observation is quite intuitive since in a given time now more material is processed. Also, at higher traverse speed the material ahead of the tool gets less time to preheat resulting in reduced material softening which leads to higher torque and hence higher power requirement to process the material. This aspect can be further illustrated with the help of Fig. 2.10b which gives heat input as a function of the welding speed. As the tool traverse speed increases, the heat input to the weld decreases causing less softening of the material around the tool which in turn increases the demand for higher power.

2.2.2 Heat Generation from Plastic Deformation

Preceding section focused on the heat generation due to friction between the tool and workpiece surface only. However, the localized plastic deformation process occurring in the bulk of the workpiece can also significantly contribute to the heat added to the weld. For example, in a uniaxial tensile test, the total energy (i.e. area under the stress-strain curve) is partially converted to heat, while the remaining is stored in the material microstructure. The amount of this plastic deformation energy which is dissipated as heat can vary between 80 and 100 % of the total input (Hodowany et al. 2000; Kapoor and Nemat-Nasser 1998). Thus, with reference to friction stir welding, the weld power input converted to plastic deformation energy in the bulk can be separated into two parts, (a) fraction stored in the microstructure, and (b) fraction converted to heat. Although, no experimental measurements of these individual fractions have been reported for FSW, the results of numerical simulations predict that the extent of heat obtained from

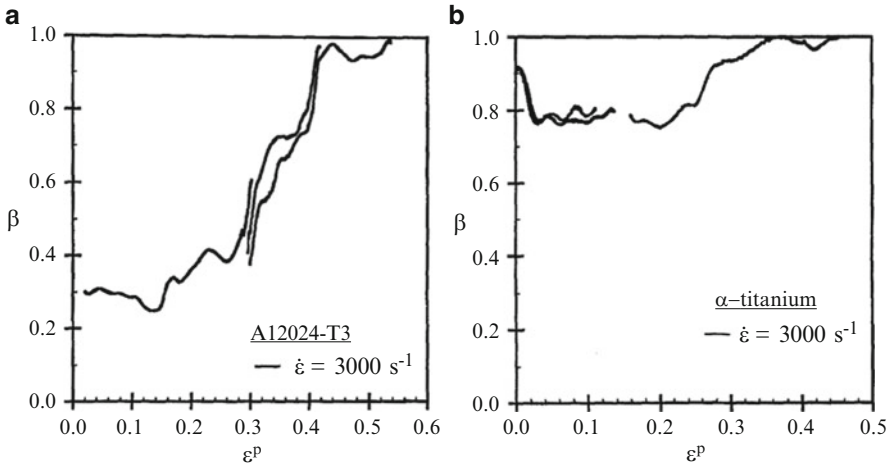

Fig. 2.11 The fraction (β) of plastic deformation energy converted to heat for (**a**) 2024-T3 alloy and (**b**) α-Titanium at strain rates of 3,000 s^{-1} (Hodowany et al. 2000, reprinted with permission from Springer)

bulk plastic deformation can vary between 2 and 20 % (Russell and Shercliff 1999; Colegrove et al. 2000).

In this regard, the experimental measurements on heat dissipation using Kolsky bar and servo-hydraulic testing by Hodowany et al. (2000) of an AA 2024-T3 alloy provide some interesting insight (see Fig. 2.11). The results show that for deformation at low strain levels (~0.4 and below), the Al alloy could store more than 60 % of the input plastic work in its microstructure. However at higher strains, this storage ability diminished and reaches zero at strains >0.5. The results obtained for another metal (α-titanium) were also more or less similar. Additionally, this conversion of plastic deformation work to heat energy is found to be relatively insensitive to the strain rate of deformation (see Fig. 2.12). Thus, for the strain and strain rates prevailing during FSW (see Sect. 2.5), it can be safely assumed that the work done by the applied tool torque is almost totally converted to heat energy.

2.2.3 Heat Transfer During Friction Stir Process

The last section discussed about heat generation in FSW. But, ultimately it is the nature of heat transfer to the workpiece and tool which affects the physical property of the workpiece. In this section, we focus on the mathematical background and physical properties relevant to this heat transfer process. A schematic of the overall heat transfer process in FSW is given in Fig. 2.13 where the energy transfer destination and the principal rate controlling mechanisms associated are shown.

The governing equation for heat transfer is given as,

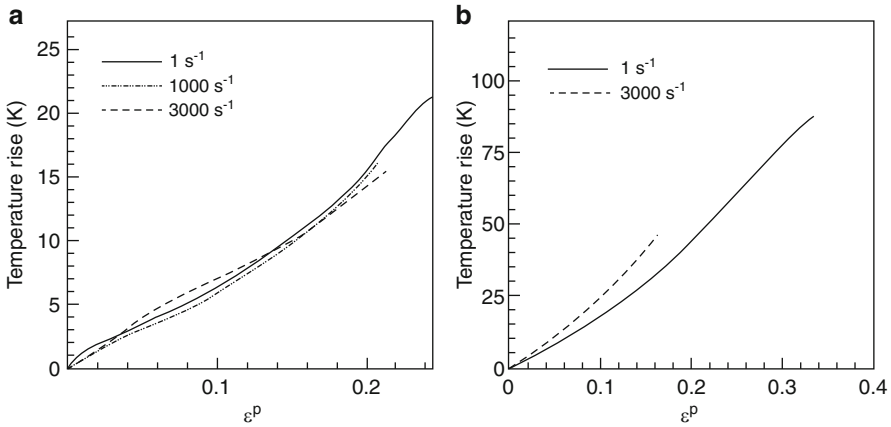

Fig. 2.12 The rate of temperature rise during straining at different strain rates for (**a**) 2024-T3 alloy and (**b**) α-Titanium (Hodowany et al. 2000, reprinted with permission from Springer)

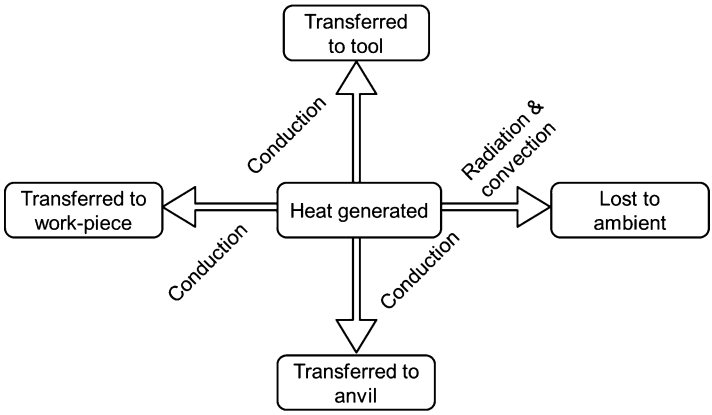

Fig. 2.13 Schematic of the heat transfer processes occurring during friction stir process. Note that in some cases like bobbin tool the heat transferred to the anvil can be neglected. Again, heat transferred to the tool/anvil also depends on the intrinsic conductivity of anvil and tool material. Here, the convective heat transfer from workpiece to anvil/tool is assumed to be rate controlling

$$\frac{\partial}{\partial t}\rho\left(C_pT\right) = -\vec{\nabla}\cdot\rho\vec{u}\left(C_pT\right) - \vec{\nabla}\cdot\left(k\vec{\nabla}T\right) + \dot{q}$$

where ρ is the material density, C_p is the specific heat capacity, T is the temperature, $\vec{u}$ is the velocity, k the thermal conductivity and $\dot{q}$ is the rate of heat generation. If the convective heat transfer is neglected, the equation can be directly solved for temperature distribution by using an appropriate heat generation equation. A typical example of this approach is seen in Frigaard et al. (2001) where the heat generation equation is expressed as,

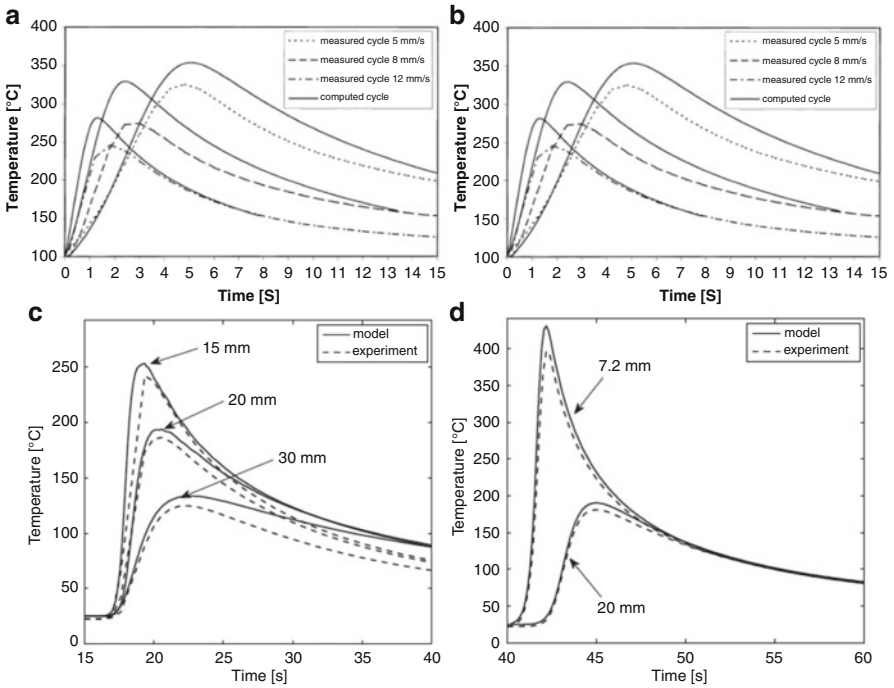

Fig. 2.14 The measured and calculated thermal cycles in (**a**) AA6062, (**b**) AA7108 alloys where the frictional heat from shoulder/workpiece interaction is only considered (Frigaard et al. 2001, reprinted with permission from Springer). The profiles in (**c**) AA 6005-T6 and (**d**) AA 6005-T78 show the measured and calculated thermal cycles where the frictional heat was considered in its entirety (i.e. Q_1, Q_2, Q_3) by measuring the torque on the tool during welding (Simar et al. 2012, reprinted with permission from Elsevier)

$$q_0 = \frac{4}{3}\pi^2 \mu P \omega R^3_{shoulder}$$

where P and μ is assumed to be constant across the shoulder/workpiece interface and heat generation is assumed to be due to friction at shoulder/workpiece interface only (i.e. Q_1). The heat generated due to friction at pin/workpiece (Q_2), pin bottom/workpiece (Q_3) and plastic deformation within workpiece bulk is ignored. A similar thermal model, neglecting the deformation aspect of FSW was solved by Simar et al. (2012) where q_0 is obtained from the measured torque and rotation speed (to give power input) of the tool. In Fig. 2.14 the simulated temperatures during FSW (Frigaard et al. 2001; Simar et al. 2012) is compared with the experimental results. As expected, the error in simulated temperature arising from using pressure relationship (P) to estimate power input is higher compared to the torque input case. Moreover, in both cases the heat transfer phenomenon at the boundaries is either neglected or is accounted for in a simplistic manner leading to errors in the overall prediction. Cho et al. (2013) measured and simulated the thermal cycle in a ferritic stainless steel using a coupled calculation where the heat transfer equation is coupled

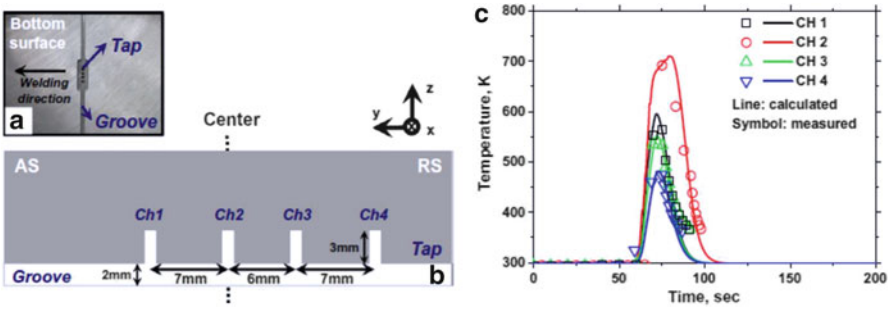

Fig. 2.15 (**a**) Macrograph on bottom surface of specimen showing the actual position of four holes where thermocouples were inserted. (**b**) A schematic of the specimen cross-section. The direction of weld goes into the picture. (**c**) The measured and calculated temperature profile with time. The measured and calculated temperature profile match since the physics of the process was captured in the simulation model (Cho et al. 2013, reprinted with permission from Elsevier)

Table 2.2 The heat transfer coefficient values used by different researchers during simulation of friction stir welding

Reference	Heat transfer coefficient ($W\ m^{-2}\ K^{-1}$)	Material welded
Schmidt and Hattel (2005)	1,000	AA2024-T3
Guerdoux and Fourment (2009)	2,000	AA 6061
Hamilton et al. (2013)	100	AA7042-T6
Nandan et al. (2006)	30	AA6061
Khandkar et al. (2006)	5,000	AA2024/AA 6061
Khandkar et al. (2006)	3,000	AISI 304L
Ulysse (2002)	0	AA 7050-T7451
Jacquin et al. (2011)	400	AA2024-T351
Aval et al. (2011)	1,000	AA 5086-O, AA 6061-T6

with the deformation calculations. Incorporation of the convective heat transfer term results in a more accurate temperature cycle prediction (Fig. 2.15).

Another significant factor influencing the temperature predictions are the boundary conditions selected which includes (a) heat loss to the anvil and (b) heat loss to the tool. Consider the different values of workpiece/anvil convective heat transfer coefficients (Table 2.2) used by researchers in current literature. It is apparent that the heat transfer coefficient value varies significantly depending on the experimental conditions. Although, in most cases a constant convective coefficient is assumed, in reality the heat transfer coefficient changes with time and temperature. This variation in heat transfer coefficient can be easily explained with relation to Fig. 2.16 where the change in initial shape of the workpiece after welding (due to residual stresses generated) is shown schematically. This change in shape depends upon the clamping conditions and workpiece characteristics causing the contact conditions to change during welding. Quite obviously the issues associated in

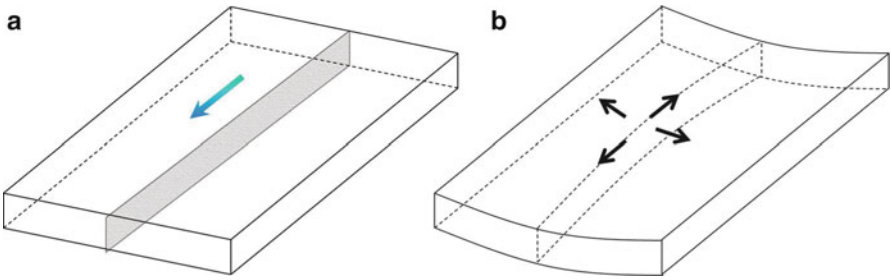

Fig. 2.16 (**a**) Initial shape of the workpieces to be welded. The *shaded region* is the interface while the *arrow* shows welding direction. (**b**) Final shape of the workpiece due to residual stress. The deformation in shape during welding is complicated by the clamping forces

defining the convective coefficient between workpiece and anvil are subjective and difficult to define resulting in differences of heat transfer coefficient values adopted. Nevertheless, considering the average power input during FSW (ranges anywhere between ~1,000 and 3,000 W) an inappropriate choice of heat transfer coefficient can appreciably affect the simulated temperature values.

The heat transfer characteristic between workpiece and tool is significantly different from the workpiece/anvil situation. Owing to the continuous vertical pressure (during steady state welding), the workpiece/tool contact always remains intimate. Consequently, not much variation in convective heat transfer coefficient is expected. The value is also an order of magnitude larger (for example in Guerdoux and Fourment (2009) the value considered is 50,000 W m^{-2} K^{-1}) compared to workpiece/anvil coefficient. Thus, heat transmission to the tool is expected to be easier, although its absolute magnitude is determined by the tool/workpiece interface area which is much smaller compared to the anvil/workpiece case. Consequently, the Neumann boundary conditions can be adopted where,

$$-k\frac{dT}{dz} = -(Q_1 + Q_2 + Q_3)$$

where k is the thermal conductivity of the tool material, while Q_1 Q_2 and Q_3 are as defined earlier. In the next section, material flow during FSW and its consequence on heat generation and transfer is discussed in more details.

2.3 Experimental Studies on Heat and Material Flow

Before, introducing the more quantitative details of friction stir welding, it is worthwhile to summarize the results from an experimental angle. A short summary of some experimental works done by different authors on deformation/material flow during friction stir welding is presented in Table 2.3. Most of these

Table 2.3 Summary of some experimental results on deformation and material flow in friction stir welding (De et al. 2011, reprinted with permission from ASM International)

Study type (ref)	Flow pattern
Steel shots in AA6061-T6 and AA7075-T6 (Colligan 1999)	(a) Steel shots affected by shoulder deposited chaotically and moved downward. (b) Steel shots in pin front deposited continuously behind pin and moved up.
AA5454-H32 marker in AA2195-T8 (Seidel and Reynolds 2001)	(a) Material stirring occurs only at shoulder-affected zone. (b) In pin-affected zone, material moves behind its original position (c) For threaded pins, a secondary vertical flow exists.
Radioactive Ni tracer in AA2219-T8 (Nunes 2001)	(a) Metal rotated around the tool in a thin sliver just beneath shear surface ("wiping flow") in last-in/first-out mode.
Microtexture study in AA6063-T5 (Sato et al. 2001)	(a) Transverse weld section microtexture shows {111} planes as roughly parallel to pin surface. (b) The <110> directions were parallel to transverse direction. (c) Shear type of plastic flow along pin surface.
Microtexture study in AA1100, AA6061-T6, and C458 alloy (Field et al. 2001)	(a) Dominant shear direction is aligned tangent to the rotating direction. (b) Secondary shear direction along tool such that {111} planes are inclined 70° from the dominant shear direction.
Cu foil along faying surface in AA6061-T6 (Guerra et al. 2002)	(a) Advancing side material deposits behind the pin on advancing side. (b) Retreating side material stays on retreating side. (c) Vortex movement within rotational zone associated with the pin.
Microtexture study in AZ61 alloy (Park et al. 2003)	(a) Prominent basal texture (0002) of base material traced an ellipsoid surrounding the pin column (b) The effect was not noticed near the pin shoulder. (c) Onion ring structure and nugget shape associated with the elliptical trace of (0002) texture.
Al-30 vol%SiC and Al-20 vol%W markers AA7050 alloy (London et al. 2003)	(a) Upward movement of material ahead of pin. (b) Markers at advancing side distributed over a much wider region in the wake of weld compared to weld centerline. (c) Downward movement of material due to tool threads.
Microstructural studies on AA2024-T3/2524-T3 (Yang et al. 2004)	(a) Metallurgical bands (low-strain and high strain alternating bands observed on etching) form, which corresponds closely to tool marks. (b) Variation in secondary particle segregation and grain size along bands.
Microstructure studies on AA2024-T3/2524-T3 (Sutton et al. 2004)	(a) Strong correspondence between strain response and metallurgical bands. (b) High strain bands correspond to lower particle density, larger grain size. Reverse is true for lower-strain bands.

(continued)

Table 2.3 (continued)

Study type (ref)	Flow pattern
Textural studies on AA2195-T8 alloy (Schneider and Nunes 2004)	(a) The {111} planes are aligned with the tool rotation axis. (b) Randomly oriented grains in the nugget.
Cu as marker in AA2024-T3 alloys (Schmidt et al. 2006)	(a) Average material flow velocity 0.1-0.3 times the tool rotation speed (b) Three different zones of rotation around the pin are proposed: rotation, transition, and deflection. (c) In rotational zone, material sticks to tool and undergoes multiple rotations. (No Reference Selected)

experiments trace the deformation by using marker materials embedded into the workpiece where its movement after deformation is subsequently analyzed to explain the deformation process. In fact, depending upon the type of marker used, the material flow observed can vary. Therefore, an appropriate choice of marker is critical to get a true representation, the ideal being the one which is similar in physical characteristics to the work-piece material. The results of these experiments can be broadly summarized as (Seidel and Reynolds 2001; Reynolds 2008),

(a) deformation at the tool shoulder and workpiece interface, and
(b) deformation at the tool pin and workpiece interface.

The nature of deformation at tool shoulder/workpiece interface is illustrated schematically in Fig. 2.17a, b, where the FSW tool transfers the marker from advancing side to the retreating side. The marker at the retreating side on the other hand moves to the advancing side. A key difference being—the circular movement of advancing side material is directed vertically downwards into the workpiece while the retreating side material is pushed vertically up towards the workpiece surface. In fact, depending upon the conditions of welding, some of the material may even be pushed out as flash on the workpiece surface.

In Fig. 2.17c, d the nature of material movement due to deformation at the tool pin/workpiece interface is shown. The marker material at the advancing side is moved approximately by the full tool circumference to reach near its original position. The marker material at the retreating side on the other hand is pushed behind the tool. As in the case of tool shoulder/workpiece interface, the movement at the pin/workpiece interface has associated vertical material movement out of its original plane.

A third deformation zone is the interface between tool pin bottom and workpiece. This deformation has some similarity to the tool shoulder/workpiece interface deformation—the difference arising from the workpiece/anvil constraint.

The marker studies by Schmidt et al. (2006), however, exhibits a more complicated material flow pattern during FSW. In this work, the authors welded an Al alloy with a copper strip (0.1 mm thick) positioned between the faying surface in two different configurations (a) faying surface parallel to the welding direction and

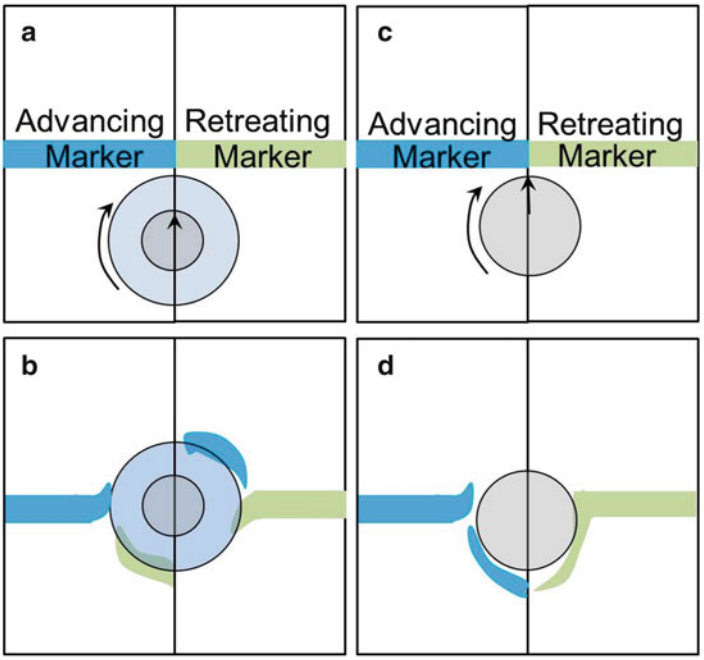

Fig. 2.17 A schematic view of the material transport in the shoulder/workpiece interface region (**a**, **b**) and the pin/workpiece interface region (**c**, **d**)

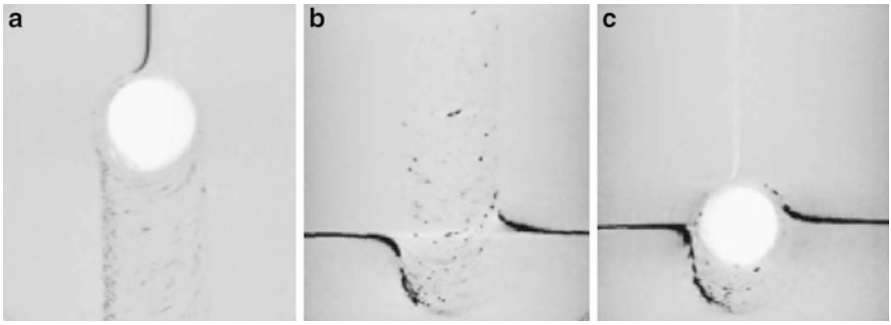

Fig. 2.18 Displacement of marker during friction stir welding (Schmidt et al. 2006, reprinted with permission from Elsevier)

(b) perpendicular to the welding direction. The results of these experiments are presented in Fig. 2.18 where for case (a) the marker material is found to be deposited from the front side to the back side of the tool, while for case (b) the marker material is carried over several probe diameters along the direction of welding. In this particular work the linear tool movement per rotation (also known as "advance per revolution" i.e. (APR)) was 0.3 mm which is larger than the marker dimension used. In similar experiments on Al alloys by Seidel and

Reynolds (2001) using dissimilar aluminum alloy as a marker, material gets transported by a single pin diameter only. However, in this instance the APR used was 0.6 mm while the marker dimension was 1.8 mm. Similar material flow studies by Askari et al. (2001) for an APR of 0.3 mm using SiC markers of 0.8 mm diameter, resulted in displacement of the marker by more than one pin revolution. Thus, depending on the test setup the marker experiments can show different results and is therefore open to multiple interpretations.

Box 2.4 Material Flow During FSSW

Different methods including tracer, dissimilar weld and crystallographic texture variation has been used to investigate material flow in FSSW. Broadly, the material flow in FSSW is considered to be an effect of three different motions: (1) material flow under the shoulder towards the root of the probe along tool surface, (2) flow of material along the pin surface towards the pin bottom, and (3) upward flow of material from the pin bottom towards the shoulder away from pin surface which merges with flow (1)/(2) (Su et al. 2006, 2007; Yang et al. 2010). This is clearly observed in the work of Tozaki et al. where the authors spot welded two different 6000 series alloy sheets (different Cu contents) and obtained its macrostructure (see Fig. 2.19). The effect of different tool probe height and dwell time on the material flow and appearance of the stir zone is also clearly visible.

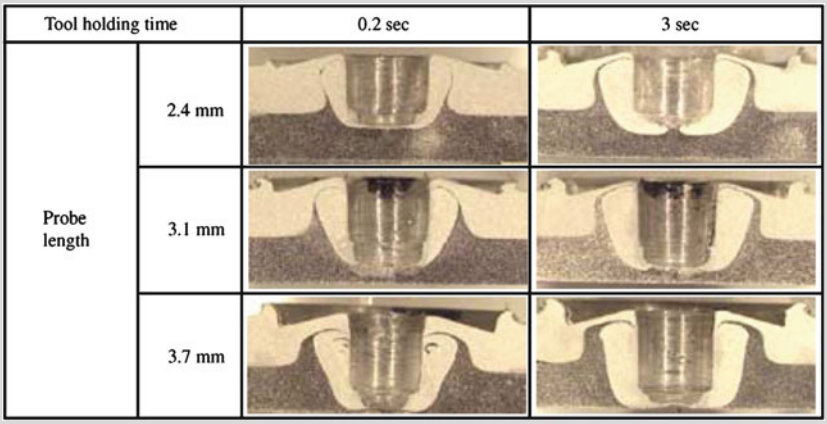

Fig. 2.19 The flow of material during FSSW for different probe length and dwell time. Note that the ingress of lower material (*dark etched region*) towards the probe root can be considered to be a proof of motion (1). The upward movement of lower material can be considered to be a proof of motion (3). The presence of upper material (*light etched region*) below the joint line of two materials can be considered to be a proof of motion (2) (Tozaki et al. 2007, reprinted with permission from Elsevier)

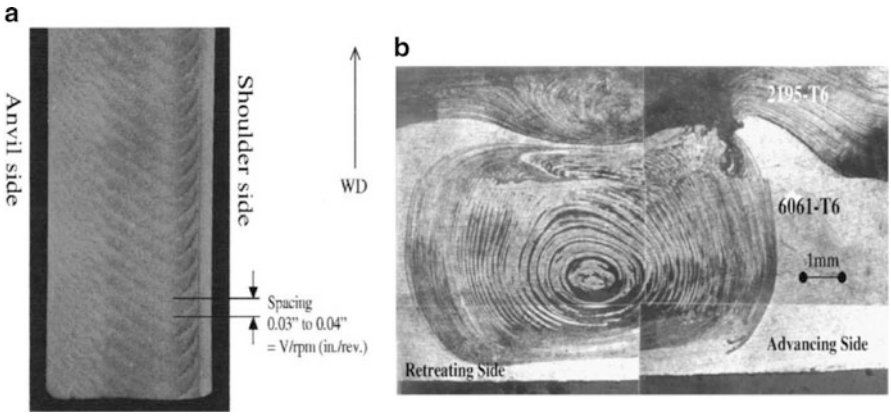

Fig. 2.20 The onion rings/band patterns as observed on the (**a**) lateral section (Schneider and Nunes 2004, reprinted with permission from Springer) and (**b**) transverse section (Guerra et al. 2002, reprinted with permission from Elsevier) of a friction stir weld

So far, we have broadly identified the different deformation zones in a friction stir weld. But on a finer scale this deformation is associated with a more intricate feature generally known as the "metallurgical band" or "onion rings" as shown in Fig. 2.20 and is unique to friction stir welding and related processes. Macroscopically, they are observed as a repetitive pattern on the transverse and lateral section of the weld and arise due to a rhythmic variation in grain size, second phase distribution and/or grain orientation (i.e. texture). The patterns repeat at an interval (as observed in lateral section) equal to the linear distance travelled by the tool during each revolution. Although, the origin of this pattern is still unsolved, recent research on the topic suggests that it is associated with the oscillation of the tool rotation axis about its linear travel axis. More about this will be discussed in a later section of this chapter.

So far we discussed the nature of deformation, but it is worth pointing out that this is intimately connected to the thermal cycle during FSW. It is this thermal cycle which determines the nature of metal flow and depends on

(a) heat generated due to friction between tool shoulder/pin and the workpiece, and
(b) some additional heat produced by the plastic working of the metal already softened by the frictional heat generated.

Assuming a Coulomb friction model, the shear stress between tool and workpiece can be estimated from the measured spindle torque and the surface area of the tool/workpiece interface. The variable p is obtained from the force perpendicular to the workpiece and the tool shoulder diameter. For the constant shear model, one needs to know the strain and temperature conditions in the welded region and the yield stress of the materials for corresponding condition. This requires a thorough knowledge about the constitutive behavior of the metal, more of which will be discussed in a later part of this chapter. In fact, majority of the numerical simulations reported in literature assume a constant shear model with sticking friction condition (i.e. $m \sim 1$). Measurements in FSW based on the Coulomb's law of

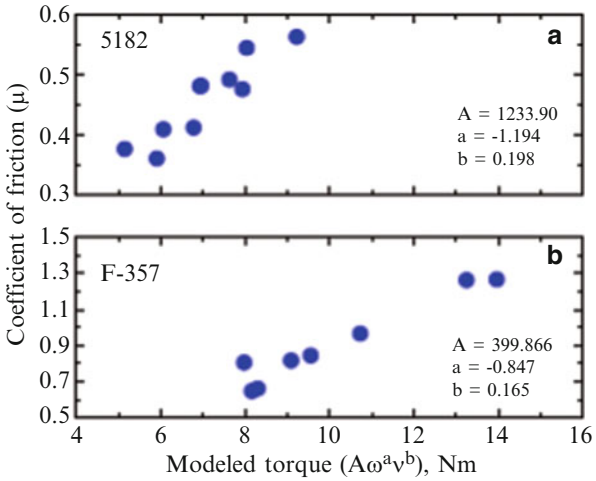

Fig. 2.21 The variation of Coulomb's friction coefficient in FSW measured for two different Al alloys, (**a**) AA 5182 and (**b**) F-357 (Colligan and Mishra 2008, reprinted with permission from Elsevier)

friction show that μ is a function of the material welded and shear stress itself and can vary anywhere between 0.3 and 1.5 (Fig. 2.21). In fact, based on the premise that τ is relatively independent of p, (for all other conditions remaining same) it is argued that the constant shear model is more appropriate. At this point of time, our understanding of the frictional conditions in FSW is, however, less than complete.

Box 2.5 Relation Between Friction and Yield Stress

In metal-working conditions the friction between workpiece and tooling is an important concern and both Coulomb's coefficient and constant shear model approaches have been used. The pressure 'p' in Coulomb's model can equal the uniaxial yield stress or be even higher. However, the shear stress 'τ' cannot exceed the yield stress in shear. This shear yield stress is sometimes related to uniaxial yield stress using Von-Mises' or Tresca criterion.

Any discussion on friction is incomplete without some mention of the temperature ranges during FSW. Direct contact type measurement of temperature in friction stir welded zone is difficult since the thermocouple tends to disintegrate during the deformation.[2] Therefore, most of the direct measurements reported in literature

[2] Direct temperature measurements reported by Rule and Lippold (2013) for Ni-based alloys show peak temperatures in the range of ~1,100 °C. These reports are yet to be verified by other researchers. Nugget zone temperature in the range of 450–530 °C are recorded for AA 7075 alloy friction stir spot welds using thermocouples inserted in tool (Gerlich et al. 2006). These welds are however done at tool rotation speeds of 1,000–3,000 rpm with dwell period varying from 1 to 4 s.

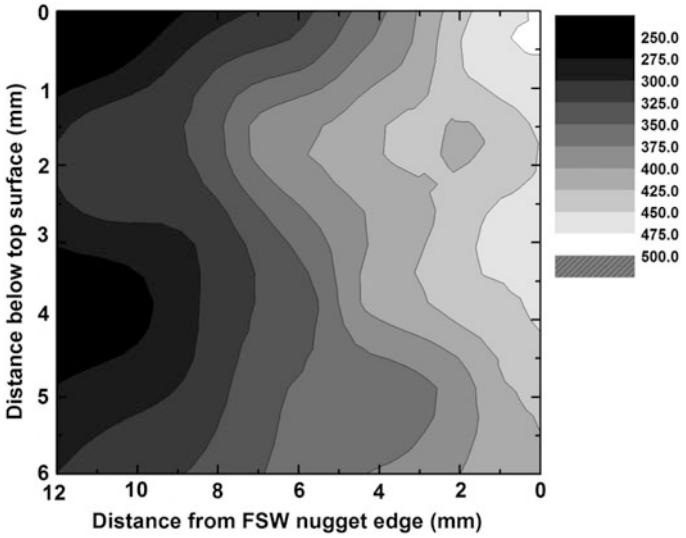

Fig. 2.22 Contour map showing the variation in temperature from *top* to the *bottom* of the workpiece at a region adjacent to the nugget region as measured using thermocouple [adapted from (Mahoney et al. 1998)]

are away from the actual weld region (Fig. 2.22). Non-contact type measurements of the weld surface using infrared thermal imaging systems are however available. The temporal variation in both cases shows a similar trend in that the measured temperatures are below the melting point but above the recrystallization temperature of the workpiece metal. However, the situation can be quite different during dissimilar metal joining where melting can occur depending on the processing conditions (Firouzdor and Kou 2010) and metallurgical interactions.

2.4 Material Flow Basics

Section 2.3 presented the principal characteristics of material flow during FSW. In this section, the theoretical frameworks and its implications thereof with regards to the nature of deformation is discussed. Broadly, these explanations are based on (a) numerical or (b) analytical modeling and are centered on the plastic deformation or the fluid flow approaches. The numerical models are predominantly based on finite element/volume methods while the analytical investigations utilize fluid dynamics except on rare occasions where plastic deformation approach is used (Arbegast 2008). The use of fluid flow approach is merely for the convenience of modeling and does not imply any affirmation of melt formation during FSW. In fact, the absence of (a) typical solidification microstructure (except in some cases of dissimilar metal joining) and (b) the nature of shear stress during FSW confirm the generally accepted solid state deformation model in FSW.

Box 2.6 How Fluid Differs from a Solid

When a shearing force is applied on a solid the shear stress measured is proportional to the strain generated. On the other hand, a fluid flows under the slightest shear stress, i.e. continual application of the stress can result in an infinite strain. Thus, for a fluid, the shear stress is dependent on shear strain rate, i.e.

$$\tau = \mu \frac{dv}{dy}$$

where μ is the coefficient of viscosity and $\frac{dv}{dy}$ is the strain rate. For crystalline solids at high temperature, application of stress leads to creep deformation, when strain accumulates with time. The shear stress also varies with strain rate at high temperatures. But, all such deformations are a consequence of dislocation and point defect interaction (except at very high strain rates $\sim > 10^7$ when adiabatic shear bands form).

Depending upon the deformation conditions the constitutive behavior of metals can exhibit a trend where the strain is independent of the flow stress. Thus, during dynamic recovery of certain metals (more is discussed in Chap. 3) the strain becomes virtually independent of stress. In such instances, the non-Newtonian fluid flow approach has been successfully applied to understand deformation behavior in FSW.

This fluid flow based treatments are based on the premise that materials behave like a incompressible fluid, and rests on the following principles,

(a) conservation of mass (i.e. continuity equation),
(b) conservation of momentum, and
(c) conservation of energy (coupled with (a) and (b) or standalone).

For a non-reactive fluid, with different chemical species this mass conservation in three dimensions is expressed as,

$$\frac{\partial(\rho u X_i)}{\partial x} + \frac{\partial(\rho v X_i)}{\partial y} + \frac{\partial(\rho w X_i)}{\partial z} = 0$$

where, u, v and w are the components of the fluid velocity, $\boldsymbol{V}$ in x, y and z directions, ρ is the density of the fluid and X_i is the mass fraction of species 'i'. In addition to the above convective mass flow, presence of diffusion will result in consideration of diffusive fluxes,

$$\boldsymbol{J_i} = -D_i \nabla X_i$$

and the mass conservation equation becomes,

$$\frac{\partial(\rho u X_i)}{\partial x} + \frac{\partial(\rho v X_i)}{\partial y} + \frac{\partial(\rho w X_i)}{\partial z} + \nabla \cdot \boldsymbol{J_i} = 0$$

For a reactive fluid, with different chemical species, the mass conservation equation assumes a more general form as below,

$$\frac{\partial(\rho X_i)}{\partial t} + \frac{\partial(\rho u X_i)}{\partial x} + \frac{\partial(\rho v X_i)}{\partial y} + \frac{\partial(\rho w X_i)}{\partial z} + \nabla \cdot \boldsymbol{J_i} = A_i$$

where $\frac{\partial(\rho X_i)}{\partial t}$ is the rate of change of mass of the species, X_i per unit volume and A_i is the rate of accumulation of species X_i per unit volume. At this point, it is worth mentioning that kinematics of fluid motion adopts either of the approaches,

(a) Eulerian
(b) Lagrangian

In the Eulerian approach, the change in properties of the fluid at a particular point of the space is recorded as a function of time. Thus, in this approach a concentration change is expressed as $\partial X_i/\partial t|_{x,y,z}$. In the Lagrangian approach, the path of each individual fluid particles are tracked and the temporal change in property (e.g.: concentration) are recorded for the corresponding position with time. The change in concentration with time in Lagrangian approach is represented as DX_i/Dt and is known as material derivative where,

$$\frac{DX_i}{Dt} = \frac{\partial X_i}{\partial t} + u\frac{\partial X_i}{\partial x} + v\frac{\partial X_i}{\partial y} + w\frac{\partial X_i}{\partial z}$$

$$\text{Or, } \frac{DX_i}{Dt} = \frac{\partial X_i}{\partial t} + \vec{v} \cdot \nabla X_i$$

$$\text{Or, } \frac{D\boldsymbol{V}}{Dt} = \left.\frac{\partial \boldsymbol{V}}{\partial t}\right|_{x,y,z} + (\nabla \cdot \boldsymbol{V})\boldsymbol{V}$$

The general conservation of momentum equation is given as (Bird et al. 2007),

$$\frac{\partial}{\partial t}\rho\vec{\boldsymbol{v}} = -\left[\nabla \cdot \rho\vec{\boldsymbol{v}}\vec{\boldsymbol{v}}\right] - \nabla p - \left[\nabla \cdot \vec{\boldsymbol{\tau}}\right] + \rho\vec{\boldsymbol{g}}$$

For constant ρ and μ, expressing $\vec{\boldsymbol{\tau}}$ in terms of Newton's law of viscosity, we get the Navier-Stoke's equation. The material flow during FSW, however, does not follow the Newtonian behavior and choice of proper constitutive behavior is, therefore, critical to a realistic simulation. The typical boundary conditions used during material flow calculations are shown in the Fig. 2.23.

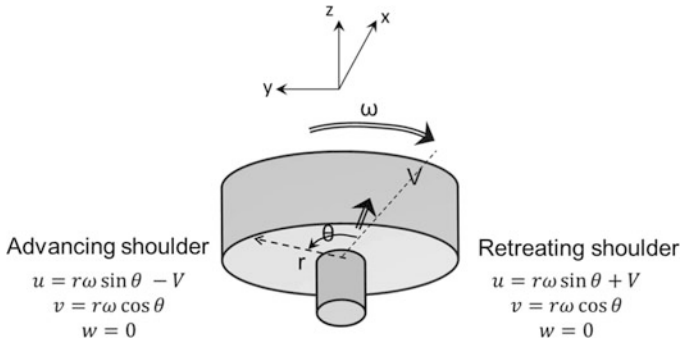

Fig. 2.23 A typical material flow boundary condition adopted at the tool/workpiece interface for fluid flow based simulations (the tool traverse direction is out of the paper towards the reader)

The boundary conditions along the vertical pin surface depends on the pin type (e.g., threaded or smooth) and will be similar to that along the shoulders, except for the velocity along z direction, which can be approximated as,

$$w = t.p. \times \left(\frac{\omega}{2\pi}\right)$$

where, *t.p.* is the thread pitch of the tool. It is apt to mention here that even without the threading some amount of vertical material movement is expected.

Student Exercise

Explain why FSW will have vertical movement even with cylindrical, unthreaded pin.

The strain rate during such fluid flow treatment is calculated based on the effective strain rate $(\dot{\varepsilon})$ and is given as,

$$\dot{\varepsilon} = \left(\frac{2}{3}\varepsilon_{ij}\varepsilon_{ij}\right)^{1/2}$$

where (i,j) = x, y, z and ε_{ij} is the strain which is expressed as below,

$$\varepsilon_{xy} = \frac{1}{2}\left(\frac{\partial v}{\partial x} + \frac{\partial u}{\partial y}\right)$$

$$\varepsilon_{xx} = \frac{\partial u}{\partial x} \text{etc.}$$

The effective stress (σ_e) is calculated from the material constitutive equation and can have the following typical form,

$$\sigma_e = \frac{1}{\alpha}\sinh^{-1}\left(\left(\frac{Z}{A}\right)^{1/n}\right)$$

where

$$Z = \dot{\varepsilon}\exp\left(-\frac{Q}{RT}\right)$$

Z is known as the Zener-Hollomon parameter, Q is the activation energy (or fundamentally more appropriately expressed as temperature dependence), α and A are material constants. The coefficient of viscosity for the material is calculated based on the effective strain rate and effective stress using the following equation (Zienkiewicz et al. 2005),

$$\mu = \frac{\sigma_e}{3\dot{\varepsilon}}.$$

It should be noted that the stress is not directly calculated in the fluid flow approach and the residual stress in the weld cannot be estimated directly by this method. Another, disadvantage of the fluid flow based method is its inability to predict discontinuities (uninterrupted material flow is enforced by the continuity equation), in contrast to practical welds where discontinuities/defects do happen depending upon the friction stir process parameters. The simulation of FSW using the Lagrangian approach holds an edge over the Eulerian approach in this aspect, although its numerical stability is poor compared to the fluid flow based methods. The excessive mesh deformation occurring during FSW simulation (in FEA methods) makes the Lagrangian formulation more difficult to implement. The ALE (arbitrary Lagrangian-Eulerian) technique is a hybrid numerical method where the mesh deformation issue faced by Lagrangian method is overcome by artificially moving the boundaries (i.e. nodes) by some prescribed velocity. The convective terms in the equation are adjusted with reference to this velocity. The ALE method is suitable for analyzing large scale deformations (as in FSW) occurring over a short time period which makes it essential to use mass scaling techniques when longer time durations are required to be investigated (as during steady state welding period). The essential details of the ALE technique are available in reference (Belytchko et al. 1982; van der Lugt and Huetnik 1986).

2.4.1 Flow Zones Around the Tool Pin

The experiments on material flow (see Table 2.3) and the numerical simulation results indicate that material flow in the region adjacent to pin occurs primarily

by shear and can be divided into following zones (Schmidt et al. 2006; Guerra et al. 2002),

(a) rotation zone, and
(b) transition zone and deflection zone.

Box 2.7 Concept of Streamlines in Fluid Flow

A simpler way to understand the material flow is to use the concept of streamlines, which are just a family of curves representing the instantaneous velocity of the fluid. Thus, for an Eulerian description, it connects all the points which have the same velocity at the given time instance. For steady state flow the streamlines are fixed in space and unchanged with time while in unsteady case the streamlines continually changes with time. If, the flow rate between two adjacent streamlines is dψ, then using the continuity concept we get,

$$d\psi = -vdx + udy$$

Again considering flow rate to be a function of position i.e. $\psi = \psi(x, y)$, we get,

$$u = \frac{\partial \psi}{\partial y}, v = -\frac{\partial \psi}{\partial x}$$

The variable ψ is known as the stream function. Knowing the stream function of a flow, the velocity at any point can be calculated.

The rotation zone is positioned immediate to the tool surface where material movement is a combination of transverse and longitudinal displacement (w.r.t workpiece) as well as angular displacement with respect to the tool axis. The transition zone comprises of the sheared layer situated in between the rotation zone and the matrix/shear layer border. Schmidt et al. (2006) defined an additional deflection zone surrounding the transition zone which is characterized by low deformation. The experiments of Guerra et al. (2002) does indeed indicate the presence of two zones, which they characterized as (a) rotation zone and (b) transition zone (see Fig. 2.24). However, a comprehensive understanding about the nature of flow in and around the pin and shoulder of the tool is still lacking.

2.4.2 Strain and Strain Rate During FSW

Due to the complex nature of material flow very limited experimental studies exists on strain and strain rate in FSW. Chen and Cui (2009) estimated the strain and strain rate in an A356 (Al-7Si-0.3 Mg) cast alloy using pin-breaking (modified stop

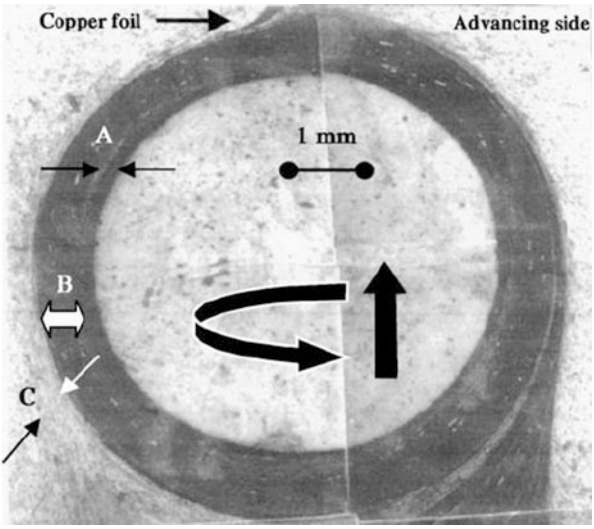

Fig. 2.24 The region *A* indicates the gap between tool and workpiece. The region *B* is the rotation zone, while region *C* is known as the transition zone. The *central white region* shows the position of the pin (Guerra et al. 2002, reprinted with permission from Elsevier)

action) technique. In this work, the shape of a deformed dendrite is traced in the deflection zone and strain is calculated at several points along the trace of the dendrite till the point it entered the shear zone. To calculate the strain an X–Y grid is superimposed on the deformed material and new X and Y position of each point is recorded. The strain is calculated as,

$$\varepsilon = \ln\left(\frac{l}{l_o}\right) = \ln\left(\frac{\sqrt{\Delta x^2 + \Delta y^2}}{\Delta y}\right)$$

The FSW strain rate is estimated by the use of calculated strain and tool traverse speed (v). The expression used to calculate strain rate is given as

$$\dot{\varepsilon} = \frac{\Delta\varepsilon}{\Delta t} = \frac{\Delta\varepsilon}{\Delta y} \times \frac{\Delta y}{\Delta t} = \frac{\Delta\varepsilon}{\Delta y} \times v$$

The results from their study are shown in Fig. 2.25. There is a continuous rise in strain and strain rate as it approaches the shear zone with a maximum strain of 3.5 (Fig. 2.25a) at the shear zone boundary. The maximum shear strain rate value at this point is 85 s^{-1} (Fig. 2.25b). Here, it should be noted that these workers used the deformed material ahead of pin (leading side) to estimate strain and strain rate. In a similar approach, Jata and Semiatin (2000) investigated the grains sheared in the thermo-mechanically affected zone (TMAZ), and an effective strain rate of 10 s^{-1} was reported. Frigaard et al. (2001) estimated the strain rate as 1–20 s^{-1} in aluminum alloys (AA6082-T6 and AA7108-T79) from the relationship between

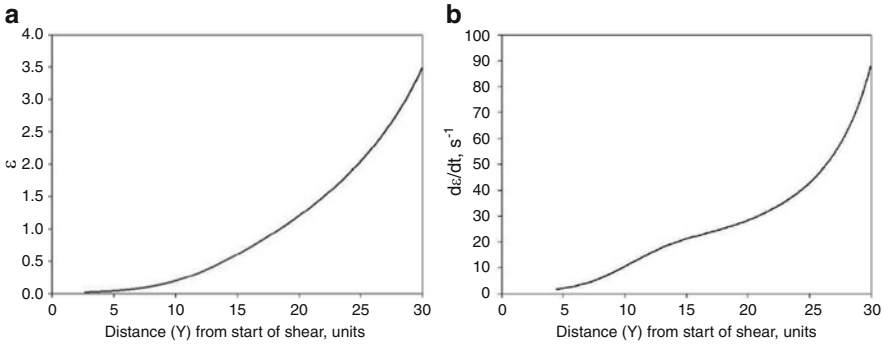

Fig. 2.25 Variation of (**a**) estimated strain and (**b**) strain rate based on the study of deformation of dendrite trunk trace (Chen and Cui 2009, © IOP Publishing. Reproduced by permission of IOP Publishing. All rights reserved)

subgrain size (w) and Zener-Hollomon parameter (Z), using temperatures obtained from heat transfer calculations. The relationship between w and Z given as

$$w = [-0.60 + 0.08\log Z]^{-1}$$

where

$$Z = \dot{\varepsilon} \ \exp\left(\frac{18772}{T_p}\right)$$

and T_p is the peak temperature attained during FSW.

In another study, Mukherjee and Ghosh (2010) used AA5083 plates containing 290 μm thick AA5457 foil in parallel and perpendicular orientations to the tool traverse direction. Using the deformation information of the foil the strain in FSW was estimated to be 4.6. Masaki et al. (2008a, b) estimated the strain rate in AA1050 during FSW using process simulation where AA1050 samples are subjected to plane strain compression at different strain rates (1, 10, and 32 s^{-1}). This is followed by cooling of the deformed material to simulate the cooling cycle during FSW. The grain size obtained from plane strain compression experiments are compared to that obtained during welding and based on grain size equality it is concluded that the strain rate in FSW is 1.8 s^{-1}. It is worth mentioning here that validity of such analysis depends on the accuracy of the temperature measured during FSW process. Some uncertainty in strain rate estimate can also arise due to approximations in the grain size estimate since observed grain sizes in FSW microstructure are usually a result of recrystallization and grain growth. Process simulation done by Chang et al. (2004) assumes a torsion type deformation and the strain rate is calculated as

$$\dot{\varepsilon} = \frac{R_m.2\pi r_e}{L_e}$$

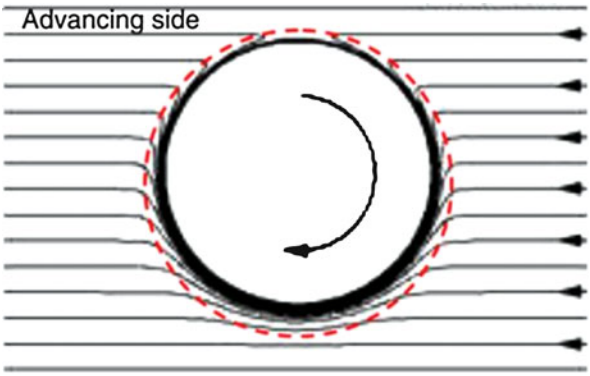

Fig. 2.26 The streamline flow field from 2D computational fluid dynamics model representing material flow around a tool pin (Reynolds 2008, reprinted with permission from Elsevier)

where R_m, r_e, and L_e are average material flow rate, radius, and depth of the dynamically recrystallized zone. The strain rate calculated varies from 5 to 50 s^{-1} for tool rotational rates of 180–1,800 rpm.

Long et al. (2007) and Reynolds (2008) used computational fluid dynamics simulation to model the material deformation as a 2D flow field around the tool pin (Fig. 2.26). The tool rotation is considered to be counterclockwise traversing from left to right while the dashed circle around the pin represents the shear zone boundary.

In this model, it is assumed that each streamline intersecting pin on the leading side of the tool gets transported to the trailing side to a position equal to the respective chord length (directly opposite to its original position). Based on this assumption, Long et al. (2007) came up with the following expression to calculate strain at different points of the FSW shear zone

$$\varepsilon = \ln\left(\frac{l}{APR}\right) + \left|\ln\left(\frac{APR}{l}\right)\right|$$

where

$$l = 2r\cos^{-1}\left(\frac{r-x}{r}\right)$$

Here, l is the maximum stretched length of a material in the shear zone of initial length equal to APR, r and x are the radius of pin and distance of the streamline from the retreating side of the tool, respectively. The estimated strain distribution in the processed zone for an APR of 0.5 mm/rev and a pin diameter of 10 mm is presented in Fig. 2.27 where strain on the retreating side is observed to be zero and reaches a maximum (~8) on the advancing side. The finding corresponds to the experimental observation where shear zone sharply transitions from the base to the advancing side of the weld compared to the gradual transition on the retreating side.

The calculated average strain and strain rate variation with tool rotation is presented in Fig. 2.28 where both the parameters increases with increase in tool rotational rate.

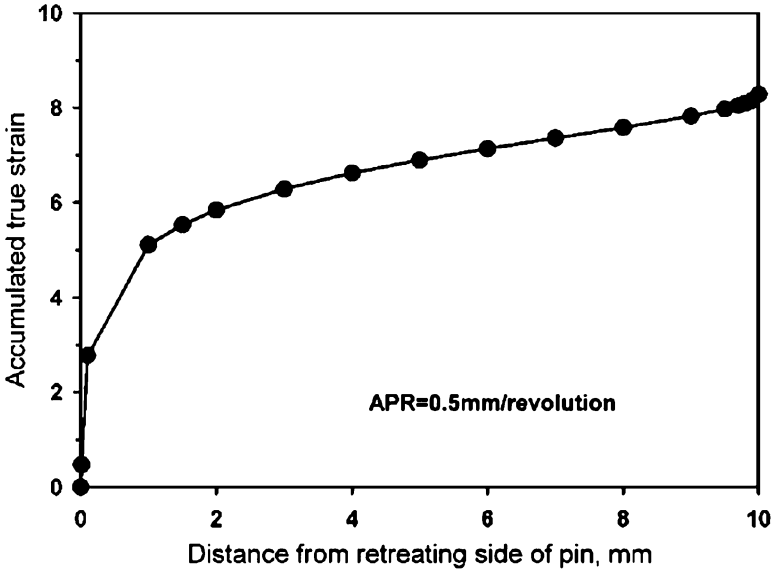

Fig. 2.27 Variation in strain from retreating side to advancing side for APR = 0.5 mm/rev and a tool pin diameter = 10 mm (Long et al. 2007, reprinted with permission from Maney Publishing)

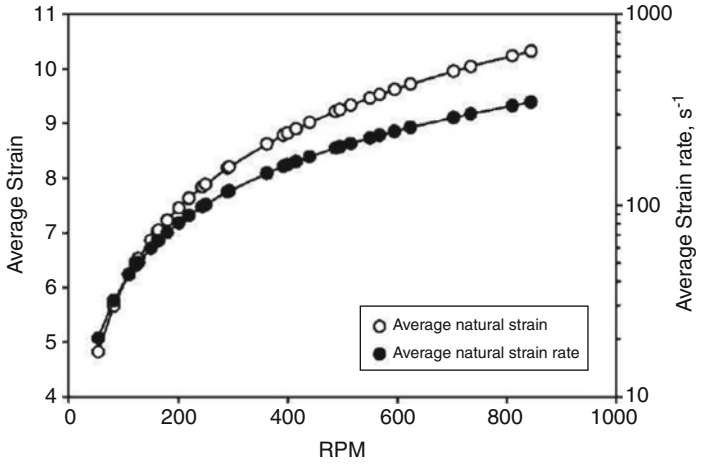

Fig. 2.28 Variation of average strain and strain rate as a function of tool rotational rate (Long et al. 2007, reprinted with permission from Maney Publishing)

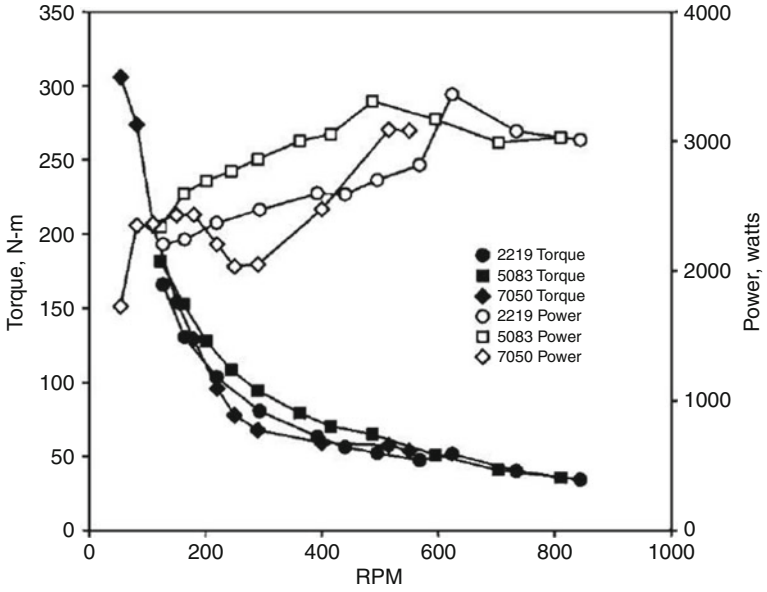

Fig. 2.29 The variation in torque during with tool rotation rate during FSW of three different Al alloys. The traverse speed remained constant (Long et al. 2007, reprinted with permission from Maney Publishing)

The continuum based FEM simulation by Buffa et al. (2006a, b) on the other hand predicts the strain and strain rate to be of the order of 5–7 and 4–8 s^{-1}, respectively. The fluid dynamics based simulation by Nandan et al. (2006) predict a varying strain rate with a value of ~100 s^{-1} near the shoulder and 30 s^{-1} at a distance 4 mm below the surface.

It may be mentioned that all calculations from simulation and experimental estimates involve simplifications and/or assumptions arising due to lack of complete understanding of the process. Hence, while the actual strain and strain rates are expected to be different from the values reported here, in general, the magnitude of strain and strain rates are expected to be in the range of values covered here.

2.4.3 Forces During FSW

The forces and torque generated during joining can give important insight into the nature of ongoing process in FSW. In this regard, the experimental work of Long et al. (2007) on three different Al alloys (AA22119, AA5083 and AA7050) using a force controlled FSW deserves special mention. Some of the key findings of this work can be summarized as

(a) welding torque reduces with decrease in APR (Fig. 2.29), and
(b) the vertical force on workpiece is not a function of torque.

Since, the welding torque is a function of the frictional resistance due to shear stresses (τ_{shear}) generated within the workpiece, this lack of dependence of torque on vertical force suggests that Coulomb's law of friction is not effective during FSW. The trend of torque reaching a uniform value with a decreasing APR implies that the constant shear model of friction may in fact be more suitable. In fact, ALE simulations by Schmidt and Hattel (2005) also suggests that except for the plunge period, plastic deformation contributes substantially to the total heat generation indicating a sticking friction during FSW.

Another significant feature is the correlation between vertical and horizontal forces with the metallurgical band/onion ring formation during FSW (Yan et al. 2007). Figure 2.30 shows the variation in rotation speed, vertical and horizontal forces, displacement and traverse velocity in FSW (without and with welding) in details. Owing to the very nature of the equipment control used in FSW, an intrinsic periodicity in rotation rate, welding speed, and displacement (Dx) is observed even without actual welding (Fig. 2.30a). However as expected, no cyclic variation in forces Fx and Fz (they occur in response to the interaction between tool with workpiece) are observed. The periodicity in the welding speed and displacement of the FSW tool (during free rotation without welding) is identical to the average angular velocity of the tool (e.g. if the tool is rotating at an average 300 rpm, the observed periodicity is 5 cycles/s (=300 rotations/60 s)). The angular velocity of tool itself was however found to be cyclic (e.g. if the average rotation is 300 rpm, the rotation rate itself varying sinusoidally over an upper and lower limit) with a unique periodicity characteristic of the FSW machine used and depends on its electronic controls. It is to be noted here that in some FSW equipment the welding speed and displacement during welding is measured by tracking the movement of workpiece. In such equipment no such periodicity in welding speed and displacement is expected. In Fig. 2.30b the variation in welding speed, displacement, and forces (vertical/horizontal) when actual welding process is carried out are shown. In this instance, unlike in the free rotation state, the horizontal and vertical forces (in addition to welding velocity) are observed to vary in an approximately sinusoidal fashion with a frequency equal to the average angular speed of tool rotation. The tool displacement was however observed to be unaffected by the welding. Further, this periodic variation in forces and welding velocity were independent of the extent of tool run-out although with increased tool run-out the mean value of horizontal force was found to decrease. The most interesting aspect of these findings is that the frequency of periodic variation in forces and welding velocity is identical to the frequency of occurrence of metallurgical banding (i.e. onion ring) formed during the welding (Fig. 2.31). In fact, this leads one to believe that periodicity of the forces in FSW is intrinsic to the material process and metallurgical banding is an intrinsic character of the welding process itself.

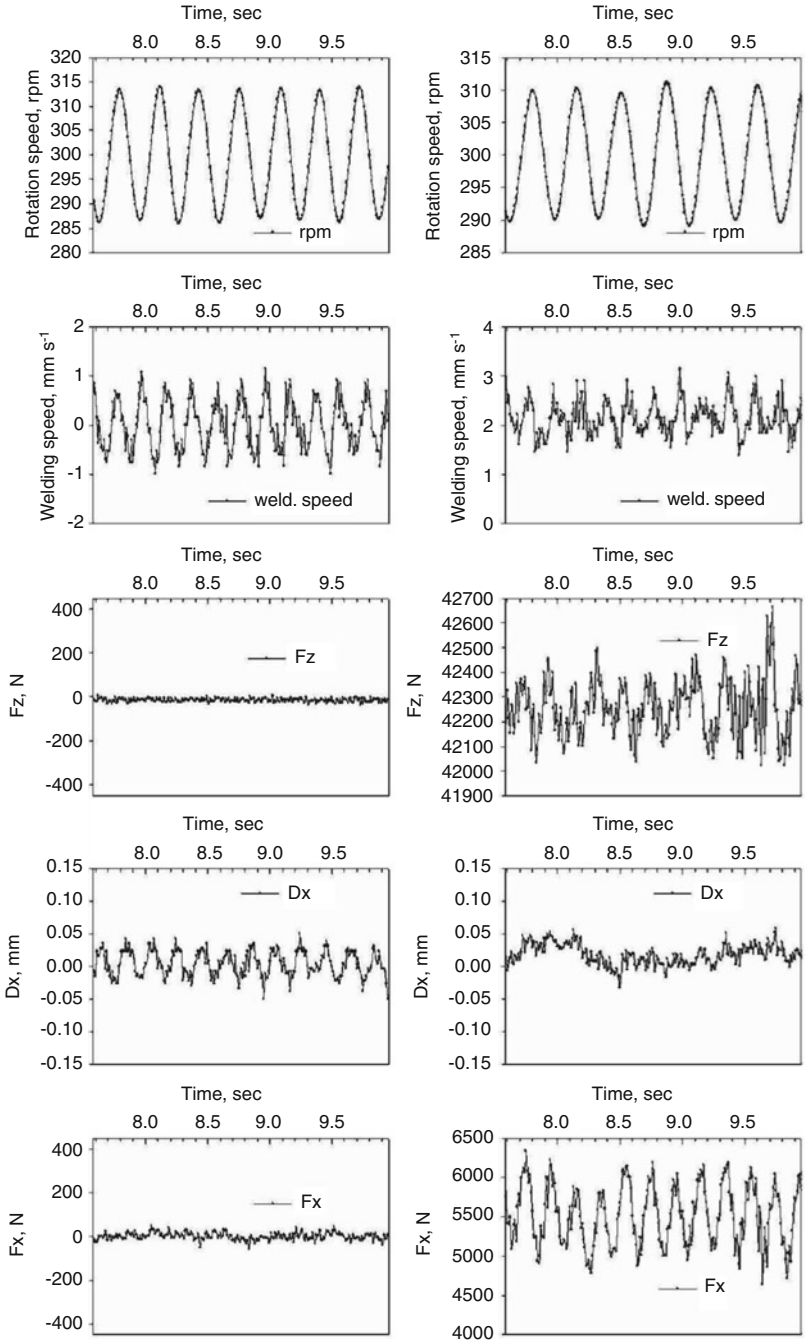

Fig. 2.30 The variation in rotation speed, tool displacement, welding velocity and forces (*vertical* and *horizontal*) during (**a**) free rotation of tool and (**b**) during welding (Yan et al. 2007, reprinted with permission from Maney Publishing)

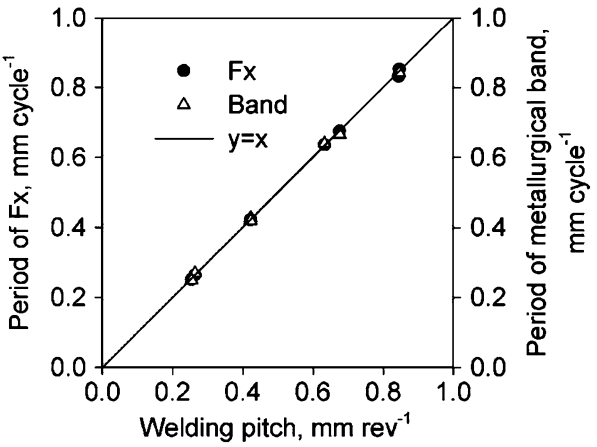

Fig. 2.31 The correlation between the frequency of horizontal force cycle and metallurgical band cycle for different APR values during FSW (Yan et al. 2007, reprinted with permission from Maney Publishing)

Box 2.8 Origin of Tool Run-Out

The main contributor to the tool run-out is misalignment between spindle and tool holder. The eccentricity between the tool and spindle axes leads to run-out. A schematic illustrating various sources leading to tool run-out is shown in Fig. 2.32.

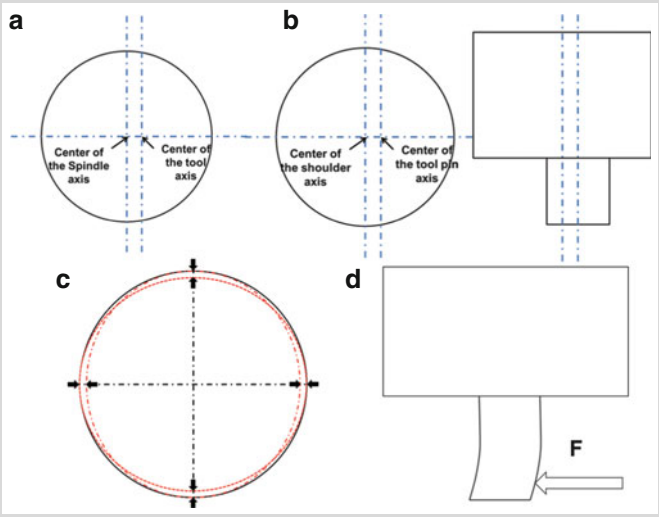

Fig. 2.32 The different sources of tool run-out in friction stir weld (**a**) shift between spindle and tool axis, (**b**) shift between the center of tool pin and shoulder, (**c**) non-parallel spindle and tool axis resulting in wobbling, (**d**) Pin bending (possible in tools with long pin)

2.5 Material Behavior and Constitutive Equations

Understanding the stress-strain relationship of a metal (i.e. the constitutive equation) during FSW is critical to have an insight into the process. The challenge partly stems from the fact that the temperature, strain and strain rate conditions in FSW vary at different positions of the weld. Consequently, the flow stress at different positions varies rendering a constant flow stress approach inadequate. Nevertheless, the customary approach is to model the material using constitutive equations where the material flow behavior is modeled either on a physical or on an empirical basis. Considering the physical approach first: modeling the behavior primarily involves an expression of deformation on the basis of dislocation movements (even though other physical effects like twinning or phase transformations can be involved depending on the material). The strain rate because of dislocation passage through a single crystal can be expressed as,

$$\dot{\gamma} = b\rho\overline{v}.$$

In the above equation deduced by Orowan, $\dot{\gamma}$ is the shear strain rate, b is the Burger's vector of dislocation, ρ is the dislocation density and $\overline{v}$ is the average dislocation velocity. For a given strain (i.e. constant dislocation density) the strain rate is, therefore, dependent on the dislocation velocity which itself depends on the microstructure, temperature and stress, and can be expressed as (Gilman 1969),

$$v = v_s^*\left(1 - e^{-\tau/s}\right) + v_d^* e^{-D/\tau}$$

where v_s^* and v_d^* are limiting velocities, s is the coupling stress, D is called the characteristic drag address and τ is the applied shear stress. The extension of these effects to a polycrystalline material (as is the case for practical welding) requires a consideration for all individual slip systems in the crystals and incorporating the effect of their mutual interactions thereof. The problem however is non-trivial since dislocations are non-equilibrium structures and mechanical deformation is essentially an irreversible process, i.e. path dependent function. Thus, for a given dislocation density, the mobile dislocation velocity depends on the dislocation drag effects which is influenced by the immobile dislocation arrangements governed by the prior deformation history. This effect of deformation history becomes increasingly relevant at high strains and strain rates used in friction stir processes. Consequently, the use of physical based constitutive equations is rare and empirical approaches are more common. In Table 2.4 some examples of the commonly used constitutive equations in FSW are summarized. The correctness of these constitutive models is however determined by the accuracy and suitability of the material constants used for the particular applications. In the next part of this section we briefly discuss one of the common methods used to determine the empirical based constitutive equations.

Table 2.4 Examples of different constitutive material behaviors adapted for FSW modeling.

Equation name (ref)	Equation form
Hansel-Spittel (Guerdoux and Fourment 2009)	$\overline{\sigma} = \sigma_f = K(T)\left(\sqrt{3}\dot{\overline{\varepsilon}}\right)^{m(T)}$
Johnson-Cook (Schmidt and Hattel 2005)	$\sigma_y = \left(A + B\left\|\overline{\varepsilon}^{pl}\right\|^n\right)\left(1 + C\, ln\frac{\dot{\overline{\varepsilon}}^{pl}}{\dot{\varepsilon}_0}\right)\left(1 - \left(\frac{T - T_{ref}}{T_{melt} - T_{ref}}\right)^m\right)$
Sheppard and Wright (Nandan et al. 2006, Cho et al. 2013, Hamilton et al. (2013), Ulysse 2002)	$\sigma_e = \frac{1}{\alpha}\sinh^{-1}\left[\left(\frac{Z}{A}\right)^{1/n}\right]$

Box 2.9 Stress-Strain Behaviour of Metals

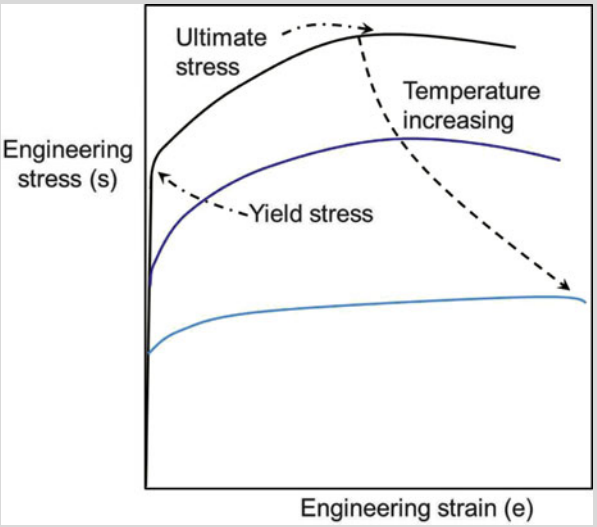

Fig. 2.33 Change in flow stress-strain behavior with temperature

Figure 2.33 shows schematic stress-strain curves during uniaxial tensile test of a polycrystalline material at different temperatures for a constant strain rate. At any temperature, the true plastic stress ($\boldsymbol{\sigma = s(e+1)}$) increases with true plastic strain ($\boldsymbol{\varepsilon = ln(e+1)}$). This is known as strain hardening and is denoted by strain hardening coefficient (n) where true stress is commonly related to true strain by an equation of the form ($\boldsymbol{\sigma = \sigma_0 + K\varepsilon^n}$), where $\boldsymbol{\sigma_0}$, and K are constants. Beyond the ultimate stress (s_u) necking causes an apparent loss in engineering strength, though considering true stress,

(continued)

Box 2.9 (continued)

material still strain hardens or reaches a saturation level. At a given temperature, change in the test strain rate again modifies the stress-strain behavior. This effect of strain rate on stress is known as the strain rate sensitivity (m). The relation between true stress and true strain rate ($\dot{\varepsilon}$) at constant strain and temperature is generally expressed as ($\sigma = C\dot{\varepsilon}^m$), where C is a material constant. The effect of temperature (T) on true stress at constant strain and strain rate is again given as ($\sigma = C_1 exp^{Q/RT}$), where Q is the activation energy for plastic flow and C_1 is the material constant. The equations describing the effect of strain, strain rate and temperature on stress can be further combined to give a general equation (see for example the Johnson-Cook equation). The strain rates for uniaxial tensile tests are in the range of 0.00001–0.1 s^{-1} and are commonly known as quasi-static tests. Such quasi-static tests do not apply to FSW since the magnitudes of strain/strain rates are much lower.

2.5.1 Determination of Constitutive Equations at High Strain Rates

As indicated earlier, the commonly used quasi-static tensile testing methods are unsuitable for higher strain rate testing. This is due to the inertial effects of the test crosshead which causes difficulty in measuring the actual stress and strain conditions. Consequently, measuring the deformation behavior at high strain rates requires specialized testing conditions. The commonly used techniques include (Field et al. 2004),

(a) drop-weight testing,
(b) split-Hopkinson pressure bars or Kolsky bar, and
(c) plate impact.

Of these, split-Hopkinson pressure bar is the most versatile and widely used technique (Fig. 2.34). This method was originally devised for compressive loading conditions (Hopkinson 1914) and has since then been adapted to tensile and torsional conditions also (Harding et al. 1960; Duffy et al. 1971).

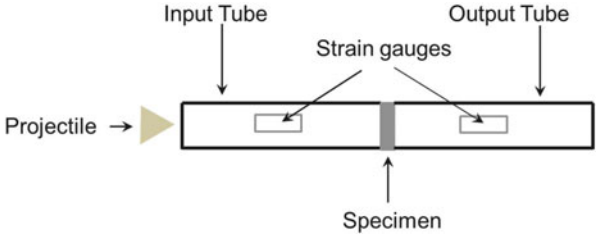

Fig. 2.34 Schematic representation of a split-Hopkinson bar setup

The original version of this method comprises of two solid bars (called input and output bar) where a specimen is placed between the two such that they are in mechanical contact with each other. A projectile at high velocity is fired towards the specimen through the input bar, which on impact creates a compressive uniaxial incident stress wave. Part of this incident stress wave is reflected back from the specimen through the input bar, while the remaining part is transmitted through the output bar. In fact, both the input and output bars are designed in such a way that the reflected/transmitted stress waves are below their elastic deformation limits. The elastic strain (from embedded strain gauges) caused by the transmitted /reflected stress waves are recorded against time in both the input (ε_{refl}) and output (ε_{trans}) bars. Using this information the stress (σ) and the corresponding strain (ε) imposed on the specimen is obtained as follows,

$$\sigma(t) = \frac{AE\varepsilon_{trans}|_t}{A_s}$$

$$\frac{\partial \varepsilon}{\partial t} = \frac{2c_b\varepsilon_{refl}|_t}{l_s}$$

where A is the cross-sectional area of the bar, A_s is the area of the specimen, E is the Young's modulus of the material, c_b is the longitudinal wave velocity in the input/output bar material and l_s is the specimen thickness at the time instant and $\partial\varepsilon/\partial t$ is the specimen strain rate. The stress-strain diagram is further obtained by integrating the strain with time for the corresponding stress. Variations of this technique are used to measure the stress-strain behavior of material at various temperatures under different loading conditions. The data thus obtained are regressed to obtain the material constants for the selected constitutive equation.

2.6 Forces Around the Pin and Shoulder

As we wrap up this chapter, a simple schematic of forces around the pin are shown in Fig. 2.35 along with identification of various quadrants. This nomenclature is use in future chapters to discuss aspects around the pin or in the stir zone. The shear force from the pin surface is always tangential and in this figure marked as τ_s. The shear force visualization is easier and this force is responsible shear layer formation. For a cylindrical pin without any features, this force engages with the material around the pin uniformly. The normal force exerted by the pin in the direction of travel is shown as σ_{pt}. The four quadrants are: Quadrant I-leading-advancing quadrant, Quadrant II-leading-retreating quadrant, Quadrant III-trailing-retreating quadrant and Quadrant IV-trailing-advancing quadrant. This figure can be used to discuss the influence of local forces on the material flow, friction coefficient at tool/workpiece interface, and defect formation.

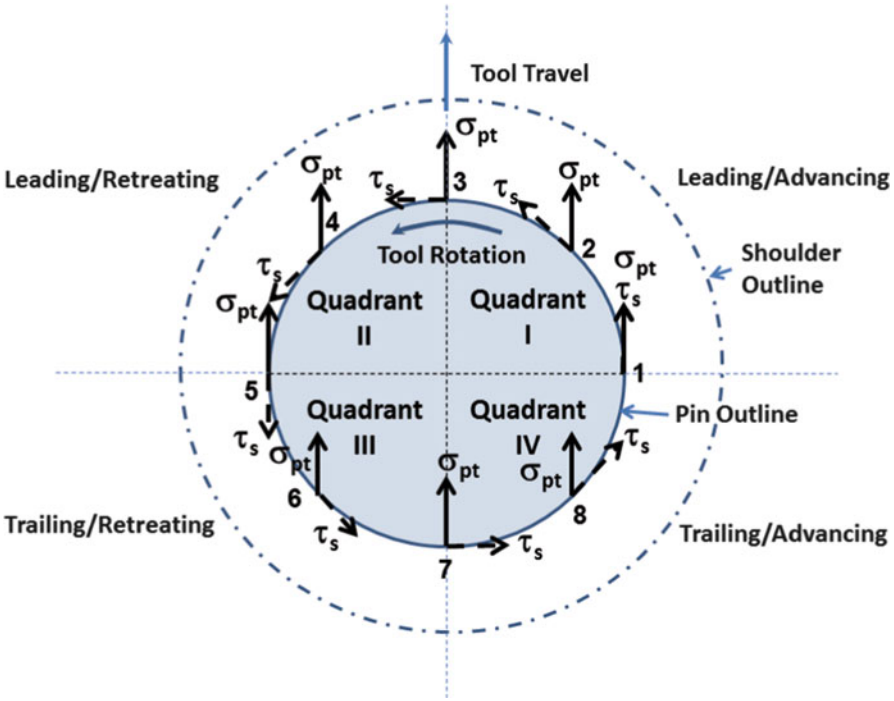

Fig. 2.35 Forces around the pin during friction stir process. The pin cross-section is divided into four quadrants to facilitate discussion of interaction of pin with stir zone material around it

On the leading side, the σ_{pt} force pushes the material to the pin surface and the coupling will enhance the component of pressure dependent friction coefficient. On the other hand, the pin surface σ_{pt} forces on the trailing side exert no pressure on the material flowing behind. This lowers the engagement of flowing workpiece material with the pin surface. This not only would reduce the friction coefficient, but lead to lack of consolidation behind the pin. Although tool design and process parameters are discussed later, for initial concepts let us quickly consider two aspects. First, what happens to these forces if the pin shape is changed from cylindrical to conical. The σ_{pt} forces for a conical surface will have resolved downward component that was missing for the cylindrical pin surface. This will introduce a vertical or downward flow component that helps in enhanced material flow and consolidation. As discussed later in Chap. 4, lack of fill defects form near the bottom of pin between points 8 and 1 on the trailing/advancing side. Second, let us consider tool tilt which is often used to enhanced consolidation behind the tool. Again, a downward force component of σ_{pt} force on the trailing side can be visualized because of the tool tilt.

A more complex aspect is the influence of these forces on material flow. Let us take the pin surface region between points 1 and 2 (referred as 1–2), and compare it with region between points 2 and 3. At point 1, the σ_{pt} force does not have any normal component to the pin surface, and is aligned with the rotational shear

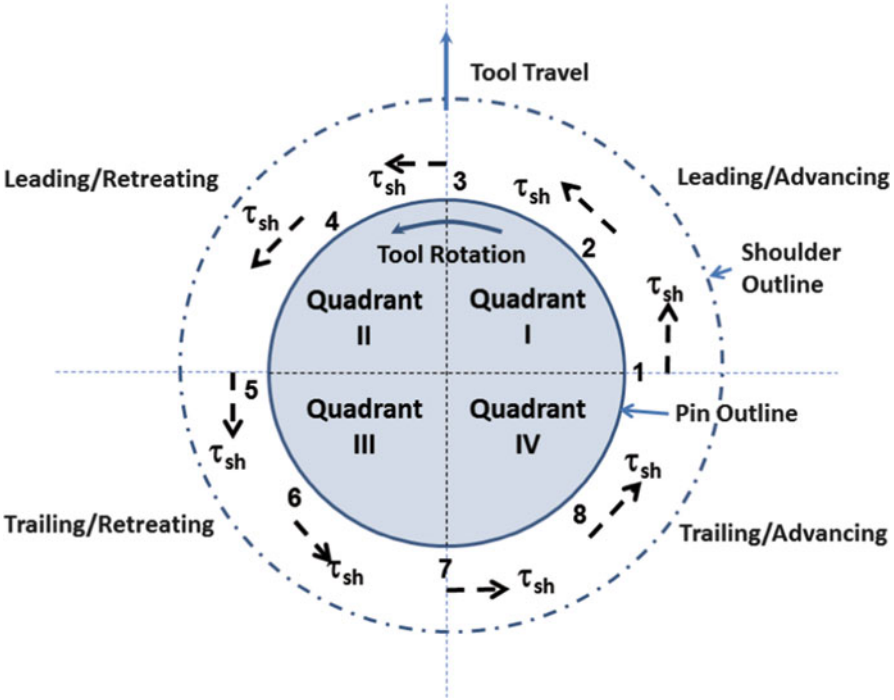

Fig. 2.36 Shoulder shear forces around the tool

component. Both force components oppose flow of material from the advancing side. In 1–2 region, the σ_{pt} force will have a resolved normal component to pin surface and resolved parallel component to pin surface. The pin surface normal component will try to displace the material towards the advancing side. Without going into any details in this chapter, some observations of faying surface hook formation and the length of feature line can be treated as indirect evidence of some material flow on the advancing side. But this gets complicated because of tool run-out and interpretation becomes more challenging. Figure 2.36 shows shear force vectors associated with shoulder. An interesting aspect is that shoulder induced flow in region 4–5–6 leads to change in the top surface shape of the nugget. For thin sheets, the shoulder influenced material flow can dominate the pin surface related flow. Examples of nugget shape are included in the next chapter.

References

C.D. Allen, J.A. Arbegast, Evaluation of friction stir spot welds in aluminum alloys. Paper 2005-01-1252, 2005 SAE World Congress, Society of Automotive Engineers, Detroit, MI, 2005

W.J. Arbegast, A flow-partitioned deformation zone model for defect formation during friction stir welding. Scripta Mater. **58**, 372–376 (2008)

A. Askari, S. Silling, B. London, M. Mahoney, Modeling and analysis of friction stir welding processes, in *Friction Stir Welding and Processing*, ed. by K.V. Jata, M.W. Mahoney, R.S. Mishra, S.L. Semiatin, D.P. Field (Warrendale, PA, TMS, 2001)

H.J. Aval, S. Serajzadeh, A.H. Kokabi, Evolution of microstructures and mechanical properties in similar and dissimilar friction stir welding of AA5086 and AA6061. Mater. Sci. Eng. A **528**, 8071–8083 (2011)

T. Belytchko, D.P. Flanagan, J.M. Kennedy, Finite element methods with user controlled mesh for fluid structure interaction. Comput. Methods Appl. Mech. Eng. **33**, 669–688 (1982)

B. Bhushan, *Introduction to Tribology* (John Wiley and Sons, New York, NY, 2002)

R.B. Bird, W.E. Stewart, E.N. Lightfoot, *Transport Phenomena*, 2nd edn. (John Wiley and Sons, New York, NY, 2007)

F.P. Bowden, D. Tabor, *Friction—An Introduction to Tribology* (Doubleday and Company, Garden City, NY, 1973). Reprinted Krieger Publishing Co., Malabar, FL (1982)

G. Buffa, J. Hua, R. Shivpuri, L. Fratini, A continuum based fem model for friction stir welding—model development. Mater. Sci. Eng. A **419**, 389–396 (2006a)

G. Buffa, J. Hua, R. Shivpuri, L. Fratini, Design of the friction stir welding tool using the continuum based FEM model. Mater. Sci. Eng. A **419**, 381–388 (2006b)

C.I. Chang, C.J. Lee, J.C. Huang, Relationship between grain size and Zener-Holloman parameter during friction stir processing in AZ31 Mg alloys. Scripta Mater. **51**, 509–514 (2004)

Y.J. Chao, X. Qi, Thermal and thermo-mechanical modeling of friction stir welding of aluminum alloy 6061-T6. J. Mater. Process. Manuf. Sci. **7**, 215–233 (1998)

Z.W. Chen, S. Cui, Strain and strain rate during friction stir welding/processing of Al-7 Si-0.3 Mg alloy. IOP Conf. Ser. Mater. Sci. Eng. **4**, 012026 (2009)

H. Cho, S. Hong, J. Roh, H. Choi, S.H. Kang, R.J. Steel, H.N. Han, Three-dimensional numerical and experimental investigation on friction stir welding processes of ferritic stainless steel. Acta Mater. **61**, 2649–2661 (2013)

P. Colegrove, M. Painter, D. Graham, T. Miller, 3-Dimensional flow and thermal modeling of the friction stir welding process, in *Proceedings of Second International Symposium on Friction Stir Welding*, June 2000

K. Colligan, Material flow behaviour during friction stir welding of aluminum. Welding J. Research Supplement, 229s–237s (1999)

K.J. Colligan, R.S. Mishra, A conceptual model for the process variables related to heat generation in friction stir welding of aluminum. Scripta Mater. **58**, 327–331 (2008)

P.S. De, N. Kumar, J.Q. Su, R.S. Mishra, Fundamentals of friction stir welding. *ASM Handbook, Welding Fundamentals and Processes*, vol. 6A (2011)

G.E. Dieter, *Mechanical Metallurgy*, 3rd edn. (McGraw-Hill Co., Boston, MA, 1986)

J. Duffy, J.D. Campbell, R.H. Hawley, On the use of a torsional split Hopkinson bar to study rate effects in 1100-0 aluminum. Trans. ASME J. Appl. Mech. **38**, 83–91 (1971)

D. Field, T. Nelson, Y. Hovanski, K. Jata, Heterogeneity of crystallographic texture in friction stir welds of aluminum. Metall. Mater. Trans. A. **32**, 2869–2877 (2001)

J.E. Field, S.M. Walley, W.G. Proud, H.T. Goldrein, C.R. Siviour, Review of experimental techniques for high rate deformation and shock studies. Int. J. Impact Eng. **30**, 725–775 (2004)

V. Firouzdor, S. Kou, Al-to-Mg friction stir welding: effect of material position, travel speed and rotation speed. Metall. Mater. Trans. A **41**, 2914–2935 (2010)

Ø. Frigaard, Ø. Grong, O. Midling, A process model for friction stir welding of age hardening aluminum alloys. Metall. Mater. Trans. A. **32**, 1189–1200 (2001)

A. Gerlich, G. Avramovic-Cingara, T.H. North, Stir zone microstructure and strain rate during friction stir spot welding. Metall. Mater. Trans. A **37**, 2773–2786 (2006)

J.J. Gilman, *Micromechanics of Flow in Solids* (Mc-Graw-Hill, New York, NY, 1969), p. 179

S. Guerdoux, L. Fourment, A 3D numerical simulation of different phases of friction stir welding. Model. Simul. Mater. Sci. Eng. **17**, 075001 (2009)

M. Guerra, C. Schmidt, J.C. McClure, L.E. Murr, A.C. Nunes, Flow patterns during friction stir welding. Mater. Charact. **49**, 95–101 (2002)

C. Hamilton, M. Kopyscianski, O. Senkov, S. Dymek, A coupled thermal/material flow model of friction stir welding applied to Sc-modified aluminium alloy. Metall. Mater. Trans. A **41**, 1730–1740 (2013)
J. Harding, E.O. Wood, J.D. Campbell, Tensile testing of materials at impact rates of strain. J. Mech. Eng. Sci. **2**, 88–96 (1960)
J. Hodowany, G. Ravichandran, A.J. Rosakis, P. Rosakis, Partition of plastic work into heat and stored energy in metals. Exp. Mech. **40**, 113–123 (2000)
B. Hopkinson, A method of measuring the pressure produced in the detonation of high explosives or by the impact of bullets. Philos. Trans. R. Soc. Lond. A **213**, 437–456 (1914)
T. Iwashita, Method and apparatus for joining, U.S. Patent 6,601,751, 2003
D. Jacquin, B. de Meester, A. Simar, D. Deloison, F. Montheillet, C. Desrayaud, A simple Eulerian thermomechanical modeling of friction stir welding. Journal of Materials Processing Technology **211**, 57–65 (2011)
K.V. Jata, S.L. Semiatin, Continuous dynamic recrystallization during friction stir welding of high strength aluminum alloys. Scripta Mater. **43**, 743–749 (2000)
R. Kapoor, S. Nemat-Nasser, Determination of temperature rise during high strain-rate deformation. Mech. Mater. **27**, 1–12 (1998)
M.Z.H. Khandkar, J.A. Khan, A.P. Reynolds, Prediction of temperature distribution and thermal history during friction stir welding: input torque model. Sci. Technol. Weld. Join. **8**, 165–174 (2003)
M.Z.H. Khandkar, J.A. Khan, A.P. Reynolds, M.A. Sutton, Predicting residual thermal stresses in friction stir welded metals. J. Mater. Process. Technol. **174**, 195–203 (2006)
G. Kohn, Y. Greenberg, I. Makover, A. Munitz, Laser-assisted friction stir welding. Weld. Int. **81** (2), 46–48 (2002)
T.J. Lienert, W. Stellwag, L.R. Lehman, Comparison of heat inputs: friction stir welding vs. arc welding (2002), http://174.122.108.74/conferences/abstracts/2002/011.pdf
B. London, M. Mahoney, W. Bingel, M. Calabrese, R.H. Bossi, D. Waldron, Material flow in friction stir welding monitored with Al-SiC and Al-W composite markers, TMS Annu Meet. 2003. p. 3–12.
T. Long, W. Tang, A.P. Reynolds, Process response parameter relationships in Al alloy friction stir welds. Sci. Technol. Weld. Join. **12**, 311–317 (2007)
M.W. Mahoney, C.G. Rhodes, J.G. Flintoff, R.A. Spurling, W.H. Bingel, Properties of friction stir-welded 7075 T651 aluminum. Metall. Mater. Trans. A **29**, 1955–1964 (1998)
K. Masaki, Y.S. Sato, M. Maeda, H. Kokawa, Experimental estimation of strain rate during FSW of Al-alloy using plain strain compression. Mater. Sci. Forum **580–582**, 299–302 (2008a)
K. Masaki, Y.S. Sato, M. Maeda, H. Kokawa, Experimental simulation of recrystallized microstructure in friction stir welded Al alloy using a plain-strain compression test. Scripta Mater. **58**, 355–360 (2008b)
R.S. Mishra, Preface to the Viewpoint Set on friction stir processing. Scripta Mater. **58**, 325–326 (2008)
S. Mukherjee, A.K. Ghosh, Flow visualization and estimation of strain and strain-rate during friction stir process. Mater. Sci. Eng. A **527**, 5130–5135 (2010)
R. Nandan, G.G. Roy, T. Debroy, Numerical simulation of three-dimensional heat transfer and plastic flow during friction stir welding. Metall. Mater. Trans. A **32**, 1247–1259 (2006)
A.C. Nunes Jr., Wiping metal transfer in friction stir welding, TMS Annu Meet. 2001. p. 235–248
K. Okamoto, F. Hunt, S. Hirano, Development of friction stir welding technique and machine for aluminum sheet metal assembly. Paper 2005-01-1254, 2005 SAE World Congress, Society of Automotive Engineers, Detroit, MI, 2005
S. Park, Y. Sato, H. Kokawa, Basal plane texture and flow pattern in friction stir weld of a magnesium alloy. Metall. Mater. Trans. A Phys. Metall. Mater. Sci. **34A**, 987–994 (2003)
A.P. Reynolds, Microstructure development in aluminum alloy friction stir welds, in *Friction Stir Welding and Processing*, ed. by R.S. Mishra, M.W. Mahoney (ASM International, Materials Park, OH, 2007)

A.P. Reynolds, Flow visualization and simulation in FSW. Scripta Mater. **58**, 338–342 (2008)
J.R. Rule, J.C. Lippold, Physical simulation of friction stir welding and processing of Nickel-base alloys using hot torsion. Metall. Mater. Trans. A **44**, 3649–3663 (2013)
M.J. Russell, H.R. Shercliff, Analytical modeling of microstructure development in friction stir welding, in *Proc. First Int. Symp. on Friction Stir Welding*, June 1999
R. Sakano, K. Murakami, K. Yamashita, T. Hyoe, M. Fujimoto, M. Inuzuka, U. Nagano, H. Kashiki, Development of spot FSW robot system for automobile body members, in *Proceedings of the Third International Symposium of Friction Stir Welding*, Kobe, Japan, TWI, 27–28 Sept 2001
Y. Sato, H. Kokawa, K. Ikeda, M. Enomoto, S. Jogan, T. Hashimoto, Microtexture in the friction-stir weld of an aluminum alloy. Metall. Mater. Trans. A Phys. Metall. Mater. Sci. **32**, 941–948 (2001)
H. Schmidt, J. Hattel, J. Wert, An analytical model for the heat generation in friction stir welding, Model. Simul. Mater. Sci. Eng. **12**, 143–157 (2004)
H. Schmidt, J. Hattel, A local model for the thermomechanical conditions in friction stir welding. Model. Simul. Mater. Sci. Eng. **13**, 77–93 (2005)
H.N.B. Schmidt, T.L. Dickerson, J.H. Hattel, Material flow in butt friction stir welds in AA2024-T3. Acta Mater. **54**, 1199–1209 (2006)
J.A. Schneider, A.C. Nunes Jr., Characterization of plastic flow and resulting microtextures in a friction stir weld. Metall. Mater. Trans. B Process. Metall. Mater. Process. Sci. **35**(2004), 777–783 (2004)
T.U. Seidel, A.P. Reynolds, Visualization of the material flow in AA2195 friction-stir welds using a marker insert technique. Metall. Mater. Trans. A **32**, 2879–2884 (2001)
A. Simar, Y. Brechet, B. de Meester, A. Denquin, C. Gallais, T. Pardoen, Integrated modeling of friction stir welding of 6xxx series Al alloys: process, microstructure and properties. Prog. Mater. Sci. **57**, 95–183 (2012)
P. Su, A. Gerlich, T.H. North, G.J. Bendzsak, Material flow during friction stir welding. Sci. Technol. Weld. Join. **11**, 61–71 (2006)
P. Su, A. Gerlich, T.H. North, G.J. Bendzsak, Intermixing in dissimilar friction stir spot welds. Metall. Mater. Trans. A **38**, 584–595 (2007)
M.A. Sutton, B. Yang, A.P. Reynolds, J. Yan, Banded microstructure in 2024-T351 and 2524-T351 aluminum friction stir welds: part II. Mechanical characterization. Mater. Sci. Eng. A. **364**, 66–74 (2004)
Y. Tozaki, Y. Uematsu, K. Tokaji, Effect of tool geometry on microstructure and static strength in friction stir spot welded aluminum alloys. Int. J. Mach. Tool. Manufact. **47**, 2230–2236 (2007)
P. Ulysse, Three-dimensional modeling of the friction stir welding process. Int. J. Machine Tools Manuf. **42**, 1549–1557 (2002)
J. van der Lugt, J. Huetnik, Thermo-mechanically coupled finite element analysis in metal forming processes. Comput. Methods Appl. Mech. Eng. **54**, 145–160 (1896)
J.H. Yan, M.A. Sutton, A.P. Reynolds, Processing and banding in AA2524 and AA2024 friction stir welding. Sci. Technol. Weld. Join. **12**, 390–401 (2007)
B. Yang, J. Yan, M.A. Sutton, A.P. Reynolds, Banded microstructure in AA2024-T351 and AA2524-T351 aluminum friction stir welds: part I. Metallurgical studies. Mater. Sci. Eng. A. **364**, 55–65 (2004)
Q. Yang, S. Mironov, Y.S. Sato, K. Okamoto, Material flow during friction stir spot welding. Mater. Sci. Eng. A **527**, 4389–4398 (2010)
O.C. Zienkiewicz, R.L. Taylor, J.Z. Zhu, *The Finite Element Method: Its Basis and Fundamentals*, 6th edn. (Butterworth Heinemann, Oxford, 2005)

Chapter 3
Fundamental Physical Metallurgy Background for FSW/P

3.1 Introduction

All metal processing activities involve a combination of deformation and heat transfer where depending on the processing path a variation in microstructure occurs. For a thermo-mechanical process like FSP, variations in process parameters are accompanied by changes in deformation and heat transfer characteristic with consequent variations in the microstructure. In Fig. 3.1a, b the microstructure of an Al alloy (Al-Mg-Si type) obtained through two different casting routes are shown while Fig. 3.1c, d presents the differences in welded macrostructure of a AA356 alloy using the same FSW tool at different operating parameters. As is evident, depending on the processing conditions the microstructure differs drastically with consequent changes on the macrostructure.

All practical processing are conducted at non-equilibrium conditions the preliminary effect of which is reflected in the deviations from equilibrium phase distribution whereby the shape, size and fraction of the phases present get affected. A typical example of this is seen in steel, where depending on the heating and cooling rate during heat treatment the fraction of ferrite and cementite (cementite in steels in reality is a metastable phase) changes along with their morphology. For conditions further away from equilibrium the thermodynamically predicted ferrite/cementite microstructure gives way to a metastable phase like martensite. Thus, any microstructural evolution is intimately connected to phase transformations which determines the origin of all equilibrium and non-equilibrium structures and is the main topic of discussion in this chapter. In the next section the role of thermodynamics on phase transformation is presented.

R.S. Mishra et al., *Friction Stir Welding and Processing: Science and Engineering*,
DOI 10.1007/978-3-319-07043-8_3,

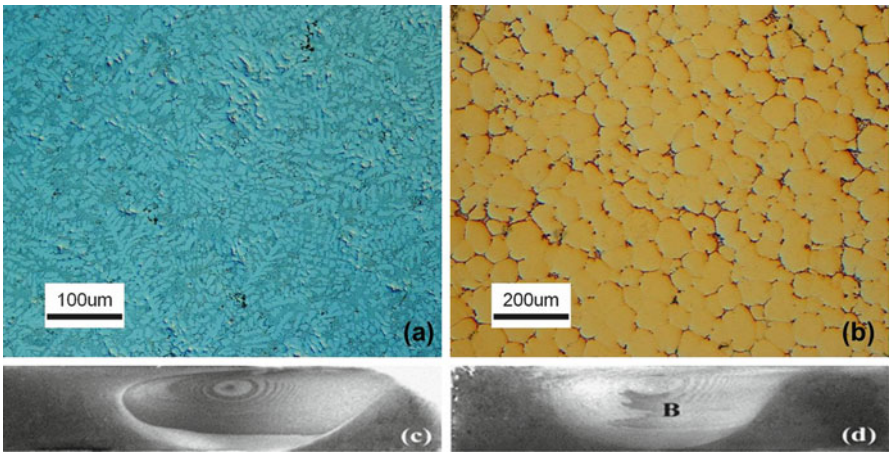

Fig. 3.1 (**a**) Typical dendritic microstructure of a Al-Mg-Si alloy processed using casting route in a copper mould (Animesh, Pvt). (**b**) Equiaxed microstructure in a Al-Mg-Si alloy processed using cooling slope casting technique (Animesh, Pvt). (**c**, **d**) Macrostructures of a friction stir processed AA356 alloy using the same tool at different rotation and welding speeds (Ma et al. 2006)

Box 3.1 Effect of Heating/Cooling Rate on Eutectoid Steel Microstructure

Consider a eutectoid composition Fe-C alloy which is heat treated in two different heating regimes A and B (see Fig. 3.2). In both the regimes the steel is heated above A_1 temperature and held for a certain period of time after which it is cooled again. In regime A the cooling is done at a fast rate (e.g.: cooled using cold water), while in regime B the cooling is done at a slower rate (e.g.: cooled in air). As the steel sample is heated up above A_1 temperature, the carbon existing in carbide phase starts to decompose and gets dissolved in the austenite (γ) phase. When the γ phase is again cooled down, the dissolved carbon diffuses to preferred sites yielding a ferrite-carbide microstructure (Regime B). Now, if the cooling rate is increased to a much higher rate (Regime A), the time available for carbon diffusion (diffusivity decreases with temperature) becomes very limited, resulting in little or no diffusion to the preferred sites. The austenite with excess carbon atoms then changes from its face centered cubic structure to body centered tetragonal martensitic structure. Thus, while thermodynamics play a vital role in microstructure formation, the influence of kinetics (i.e. diffusion) on microstructure formation is of no less significance.

(continued)

Box 3.1 (continued)

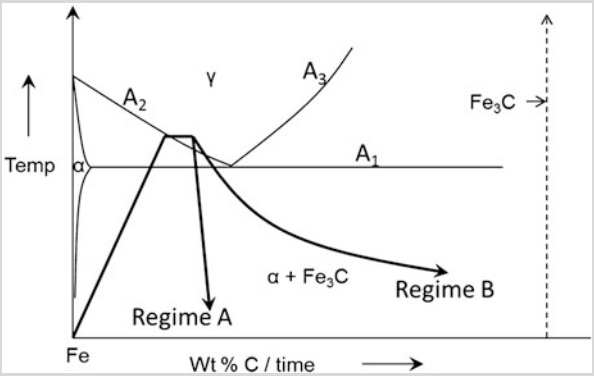

Fig. 3.2 A section of the Fe-C phase diagram showing the metastable cementite phase. Imposed on this phase diagram are the two heating regimes A and B for an eutectoid steel. The two heat treatment regime will result in different microstructure with altogether different phase distribution due to different reaction kinetics

3.2 Phase Transformation Basics

3.2.1 Thermodynamics of Phase Formation

Any discussion of microstructure begins with the concept of phase which can be defined as ". . .portion of the system whose properties and composition are homogenous and which is physically distinct from other parts of the system" (Porter and Easterling 2004). The microstructure of a metal/alloy processed under equilibrium (or near equilibrium) condition consists of phase/phases where the individual fractions of each are determined primarily by their Gibbs free energy (G) and is a function of both temperature (T) and composition. The Gibbs free energy mentioned here is of the volumetric type, i.e. the energy associated with formation of free surfaces is neglected. Consequently, a valid thermodynamic treatment of phase transformation requires it to occur quasi-statically (i.e. infinitely slow) with the following equilibriums (a) thermal (i.e. temperature equality), (b) mechanical (i.e. no stress) and (c) chemical (i.e. chemical potential of each component equal in all phases) being maintained at each stage. Quite obviously, the stringent requirement of equilibrium thermodynamics can never be implemented in practice and practical microstructures are influenced by both thermodynamic and kinetic factors. In the next sections the physical factors controlling the origin of phase transformations is discussed.

Box 3.2 Phase Diagram Construction

Consider a binary system A-B which behaves like a regular solution. The "Gibbs free energy of mixing" (ΔG_m) for the solution comprises of the following contributions:

$$\Delta G_m = \Delta H_m - T\Delta S_m$$

where ΔH_m is the enthalpy change during mixing, ΔS_m is the entropy change during mixing and T is the temperature of mixing. For regular solutions the enthalpy change during mixing is zero. The entropy change during mixing is given as

$$\Delta S_m = RT(X_A \ln X_A + X_B \ln X_B) + \Omega X_A X_B$$

where **Ω** is the "regular solution parameter" and is independent of temperature. For any temperature the stable phase corresponds to the composition with minimum free energy of mixing. In Fig. 3.3a at low temperatures, this minimum in free energy occurs at two different compositions. As the temperature is raised, the two minima's approach each other, until at 1,000 K the minima occurs at one single composition.

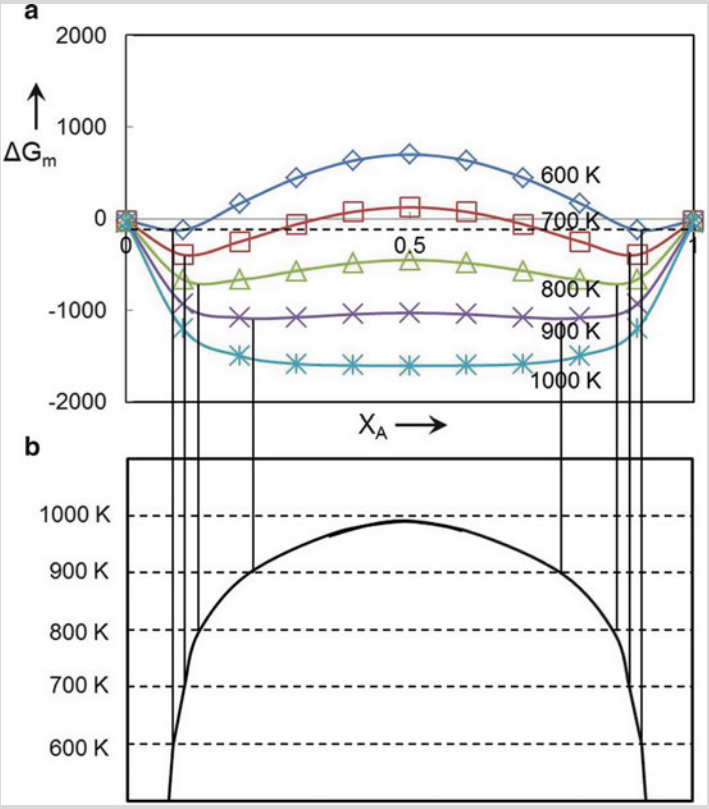

Fig. 3.3 (**a**) The variation of free-energy with temperature and composition for a binary system (A and B component) with regular solution type behavior. (**b**) Construction of the phase diagram construction from F.E. vs. composition curve

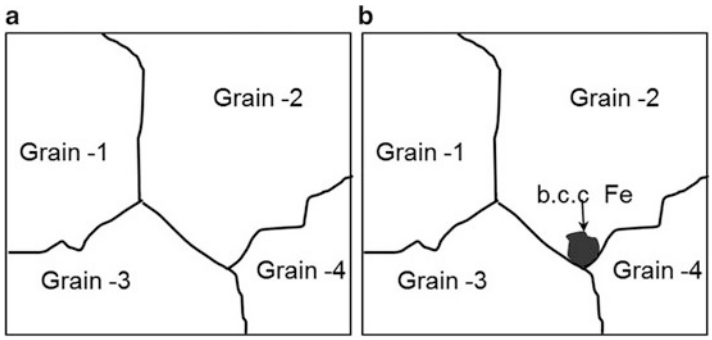

Fig. 3.4 (**a**) Microstructure of polycrystalline f.c.c. iron phase (γ-Fe) which when cooled to a temperature near the polymorphic transformation temperature gives rise to (**b**) Microstructure with b.c.c. iron phase (α-Fe) appearing at preferred locations (e.g.: grain boundary triple junction)

Student Exercise

(a) The free energy versus composition diagram in Fig. 3.3a is for positive Ω value. For negative Ω plot the free energy versus composition diagram at the different temperatures?
(b) Figure 3.3b is a typical example of "miscibility gap" in phase diagram. Can you find out binary phase diagrams showing the same phenomena? (Hint: Consult ASM Handbook volume on Phase Diagrams)

3.2.2 Phase Nucleation Kinetics

As discussed above, phase transformations during practical processing (including FSW) occur under non-equilibrium conditions. Consider, the simple diffusive phase transformation where polycrystalline face-centered cubic (f.c.c.) Fe gets converted to body centered cubic (b.c.c.) crystal structure on cooling. In this transformation atomic movements involved are minimum and no compositional changes are required (polymorphic phase transformation). The principal driving force for such a transformation is the difference in volumetric Gibbs free energy and the final distribution of the b.c.c. phase depends on how and where the phase formation commences. This process of initiation of a new phase with time is the realm of nucleation kinetics.

Consider the chance formation of a b.c.c. Fe phase nuclei in a f.c.c. Fe phase (Fig. 3.4b). The stability of the indicated nuclei is determined by its total Gibbs free energy (ΔG_{total}) which is a sum of (a) Volumetric energy (ΔG_{volume}), (b) Surface energy ($\Delta G_{surface}$), (c) Strain energy (ΔG_{strain}) and (d) Defect energy (ΔG_{defect}). For a spherical nuclei of radius r the volumetric free energy is then expressed as (Porter and Easterling 2004),

$$\Delta G_{volume} = \frac{4}{3}\pi r^3 \, \Delta G_v \tag{3.1}$$

where ΔG_v is the free energy change per unit volume. Justifiably, any such new phase formation must be accompanied with a decrease in ΔG_v leading to a negative ΔG_{volume}. The spherical nucleus thus formed results in the creation of a fresh surface necessitating an additional positive energy supply to overcome the surface tension (γ) forces which constitutes the $\Delta G_{surface}$ and is given as (Porter and Easterling 2004)

$$\Delta G_{surface} = 4\pi r^2 \gamma \tag{3.2}$$

The ΔG_{strain} depends upon the specific volume differences between the parent and product phase and is relevant for solid $\rightarrow$ solid phase transformations. A product phase with higher specific volume compared to the parent phase results in a compressive force on the product increasing the energy required for phase transformation. For a product phase which is coherent with the matrix the strain energy is given as (Porter and Easterling 2004)

$$\Delta G_{strain} = 4\pi r^2 \Delta G_s \tag{3.3}$$

where ΔG_s is the misfit strain energy per unit volume and is expressed as (Porter and Easterling 2004)

$$\Delta G_s^{coherent} \cong 4\mu\delta^2 \cdot V \tag{3.4}$$

where μ is the shear modulus of the parent phase, δ is the "unconstrained lattice misfit" between the parent and product phase and V is the volume of the unconstrained hole in parent phase. For incoherent phases this misfit strain energy is usually considered to be zero, although in certain situations misfit strains do arise and needs to be accounted for.

Box 3.3 Surface Energy ($\Delta G_{surface}$)

Surface energy depends on γ, i.e. surface tension. For coherent surfaces the value of γ is nominal, while incoherent surfaces have the highest γ. Note the contrast with ΔG_{strain} where coherent phases have high misfit strain while incoherent phases have nominal misfit strain (except in special circumstances).

The last (but not the least) contribution to the total energy arises from ΔG defect which accounts for the energy reduction caused by microstructural defects eliminated during nuclei formation. This also forms a basis for classification whereby nucleation processes are distinguished as (1) heterogenous and (2) homogenous. In the heterogenous case nucleation commences at microstructural defects (intrinsic or extrinsic) existing within the material. These defects are associated with high energy and nucleation at these locations leads to a reduction in defect area with a

corresponding decrease in energy calculated as a product of the surface tension associated with the area reduced. The typical defects sites include (a) vacancies, (b) dislocations, (c) stacking faults, (d) grain and interphase boundaries, (e) free surfaces, where the defect energy contribution in each case increases in the aforesaid order. Thus, for a given heterogenous nucleation event the probable sites will be (a) free surface, (b) interphase boundary, (c) grain boundary . . . in this order. In case of homogenous nucleation the defect energy contribution is zero. Consequently, homogenous nucleation of a product phase is more improbable and happens only when compositional fluctuations are thermodynamically favorable. Thus, depending on the precipitate size and the relative energy contributions, a nuclei can either be energetically stable (i.e. further increase in its size leads to decrease in total energy of the microstructure) or unstable where the stability criteria is given as

$$\frac{d\Delta G_{total}}{dr} = 0 \tag{3.5}$$

For a homogenous nucleation the critical nuclei radius (r*) for stability is given as

$$r^* = \frac{2\gamma + 8\mu\delta^2 V}{\Delta G_v} \tag{3.6}$$

The corresponding critical free energy (ΔG^*)of the nuclei is given as,

$$\Delta G^* = \frac{40}{3}\pi\frac{\left(\gamma + 4\mu\delta^2 V\right)^2}{\Delta G_v} \tag{3.7}$$

Student Exercise

Plot the variation of ΔG_{total} as a function of nuclei radius. In the same diagram plot how the other components like ΔG_{volume}, $\Delta G_{surface}$, varies with nuclei radius.

A size increase beyond the critical radius leads to a further decrease in the free energy making it energetically stable.

For any microstructure, the rate at which such stable nuclei's are formed influences the size and distribution of the phases at the end of the transformation process and is of critical importance. For homogenous nucleation this nucleation rate ($I_{nucleation}$) is given as (Porter and Easterling 2004),

$$I_{nucleation} = C_1 \exp\left(\frac{-E}{kT}\right)\exp\left(\frac{-\Delta G^*}{kT}\right) \tag{3.8}$$

Where C_1 is a constant, E is the activation energy required for transferring atoms to the nuclei from parent phase, T is the temperature at which nucleation is occurring and k is the Boltzmann's constant. For heterogenous nucleation the expression for

nucleation rate is similar to Eq. (3.8) except for the constant C_1 which is a function of the nucleation sites activated for the particular transformation process.

Box 3.4 Effect of Temperature on Nucleation

The energy E required to move the atoms from parent phase to nuclei is approximately constant. Thus, the first exponential term in Eq. 3.8 increases as T increases. The value of ΔG^* on the other hand increases since ΔG_v increases with T. So, the second exponential term in Eq. (3.8) increases as T decreases. Nucleation is maximized at an intermediate temperature and declines if the temperature is higher/lower than the optimum.

Nucleation for phase transformation during friction stir process is influenced by the high strains imparted to the work-piece. Depending on the metal and the temperature this strain can result in the following events

(a) Retention of the strain in the form of dislocation structures.
(b) Recovery (full or partial) of the dislocation structures to form sub-boundaries within the original grains.
(c) Recrystallization of the matrix to form fine grains followed by grain growth.

The presence of copious defects, in the form of dislocations, sub-boundaries and grain boundaries makes heterogenous nucleation an inevitable part of phase transformation during friction stir process.

Another important effect of the strain imparted during FSP is its effect on the diffusivity of atoms. Dislocations and grain boundaries trigger a significant extent of grain boundary/ pipe diffusion in addition to the usual lattice diffusion processes and is particularly significant at low temperatures. This along with the availability of heterogenous nucleation sites promotes the formation of phases at a much lower temperature which ordinarily is viable only at high temperatures.

3.2.3 Phase Growth Kinetics

The nucleation process is followed by growth where the product phase forms at the expense of the parent phase i.e. the product/parent phase boundary (more commonly called "interface") migrates into the parent phase. This migration velocity depends upon the nature of the parent/product interface and is broadly classified as (Porter and Easterling 2004),

(a) Glissile interface and
(b) Non-glissile interface

For a glissile interface this migration is effected by line defect (i.e. dislocations) movement caused by internal shear forces acting on the dislocations existing at the interface. The movement of such glissile interface is less sensitive to the temperature and is considered to be of athermal nature.

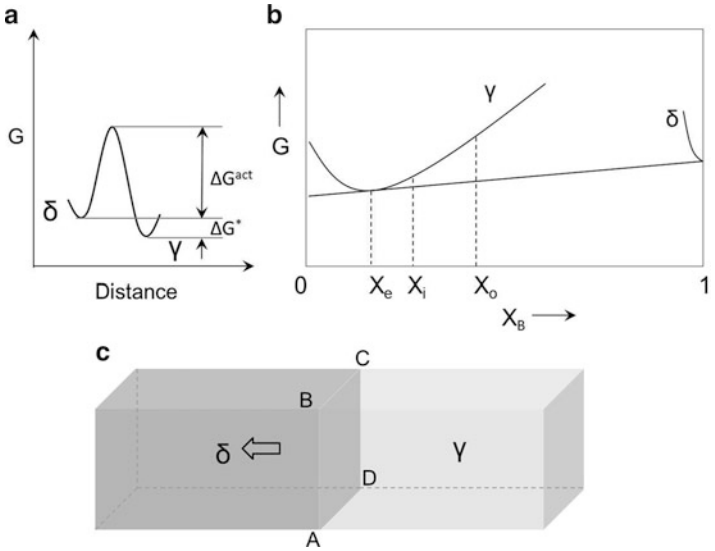

Fig. 3.5 (**a**) Atoms jump across the interface ABCD (in (**c**) by overcoming the activation barrier. (**b**) Free energy variation of the phases where δ is the parent phase and γ is the product phase. The mean composition of the material is X_0, X_i is the composition at the interface and X_e is the composition of γ in equilibrium with δ. (**c**) The product phases γ grows at the expense of δ (Adapted from Porter and Easterling (2004))

On the other hand, non-glissile interface migration occurs through atomic jumps happening across the boundary which results in an overall lowering of the system energy (by ΔG^{*}) (Fig. 3.5a). The migrating atom however needs to overcome an initial energy barrier (ΔG^{act}) known as the activation energy for migration (Fig. 3.5a) before it can get transferred across the interface. It is appropriate to mention here that atoms in a lattice are always vibrating about their mean position due to thermal energy which becomes zero only at absolute zero temperature. The vibration amplitude of atoms varies with time and there is always a finite probability for an atom to overcome the activation barrier.

In Fig. 3.5c the atoms are shown to jump from phase δ to phase γ across the ABCD interface causing it to move in the left direction. If the atoms in phase δ are vibrating with a frequency ν_1 and there are n_1 atoms per unit area of the interface which are in a favorable position to overcome the activation barrier and form phase γ, the effective flux of atoms from phase δ to γ is given as (Porter and Easterling 2004)

$$J_{\delta\to\gamma} = A_1\nu_1 n_1 \exp\left(-\frac{\Delta G^{act}}{RT}\right) \tag{3.9}$$

where A_1 is an accommodation factor determining how many atoms jumping from the δ phase (i.e. parent) finds a suitable position to get attached to the γ phase. Just

as atoms jump from δ to γ phase there will also be atoms which can jump from the γ phase to the δ phase. The flux of such reverse jumps is (Porter and Easterling 2004),

$$J_{\gamma\to\delta} = A_2\nu_2 n_2 \exp\left(-\frac{(\Delta G^{act} + \Delta G^{*})}{RT}\right) \tag{3.10}$$

The overall flux (J_{net}) of atoms across the interface is then given as (Porter and Easterling 2004),

$$J_{net} = A_1\nu_1 n_1 \exp\left(-\frac{\Delta G^{act}}{RT}\right)\left\{1 - \exp\left(-\frac{\Delta G^{*}}{RT}\right)\right\} \tag{3.11}$$

In the above derivation the product $A_1\nu_1 n_1$ is considered to be equal to the product $A_2\nu_2 n_2$. This can be rationalized as follows: if the phases are under equilibrium condition, i.e. ΔG^{*} is equal to zero then no growth will occur, which will imply that $A_1\nu_1 n_1 = A_2\nu_2 n_2$. Assuming that the interface movement is happening under slight deviations from equilibrium (i.e. $\Delta G^{*} \to 0$), the equality condition then still remains tenable (Porter and Easterling 2004). A net flux of atom from δ to γ will imply that the interface ABCD (Fig. 3.5c) is moving with a velocity V. If the molar volume of Avogadro number atoms ($N_{avogadro}$) is given as V_{molar}, then volume of each atom is given as $V_{molar}/N_{avogadro}$ and the number of atoms moving per unit area per unit time (i.e. flux) across the interface ABCD is given as (Porter and Easterling 2004)

$$\frac{V \times N_{avogadro}}{V_{molar}} = A_1\nu_1 n_1 \exp\left(-\frac{\Delta G^{act}}{RT}\right)\left\{1 - \exp\left(-\frac{\Delta G^{*}}{RT}\right)\right\} \tag{3.12}$$

For $\Delta G^{*} \to 0$, the interface velocity is then simplified as (Porter and Easterling 2004),

$$V = \frac{A_1\nu_1 n_1 V_{molar}}{N_{avogadro}} \cdot \frac{\Delta G^{*}}{RT} \exp\left(\frac{-\Delta G^{act}}{RT}\right) \tag{3.13}$$

where the interface mobility M is defined as (Porter and Easterling 2004),

$$M = \frac{A_1\nu_1 n_1 {V_{molar}}^2}{RTN_{avogadro}} \cdot \exp\left(\frac{-\Delta G^{act}}{RT}\right) \tag{3.14}$$

resulting in the expression,

$$V = M \cdot \frac{\Delta G^{*}}{V_{molar}} \tag{3.15}$$

From the equilibrium phase diagram and interface structure (Fig. 3.5b, c) it is to be noted that this phase growth (γ → δ) involving movement of B and A atoms will occur

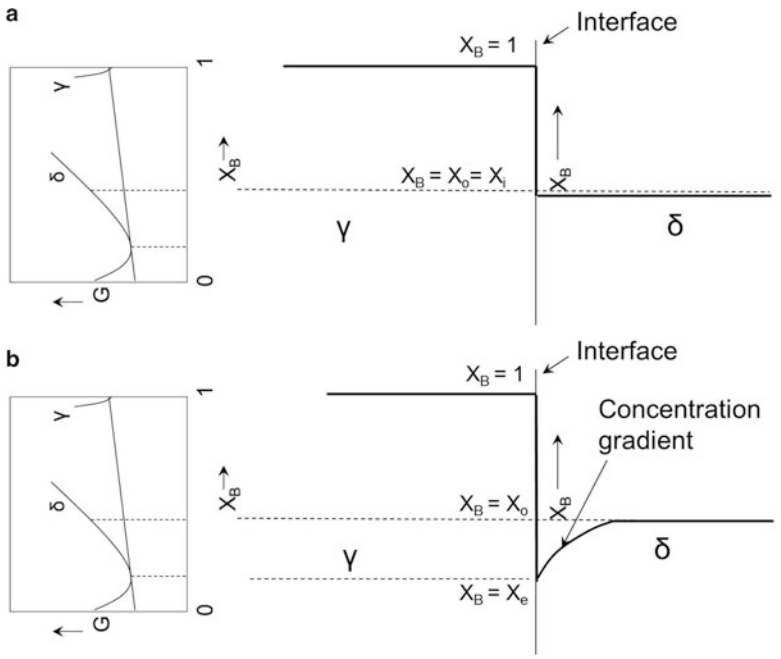

Fig. 3.6 (**a**) Concentration profile of atoms when the product phase γ grows from parent phase δ where interface nature is the determining factor for phase growth. Diffusion within δ is considered to be infinitely fast. (**b**) Concentration profile where diffusivity of atoms is the determining factor for phase growth. The interface transfer is considered to be infinitely fast. In each case the equilibrium phase diagram is shown (Adapted from Porter and Easterling (2004))

in a "First in first out" fashion, where the region adjacent to the interface serves as the initial source/sink of the atoms. This can result in additional local non-equilibrium situation, resulting in a compositional imbalance (see Fig. 3.6b). Figure 3.6a depicts a condition where phase growth is happening under interface control.

Box 3.5 Interface Structure

The structure of solid/solid interfaces can generally be classified into two types (a) interface between same phase or (b) interface between dissimilar phases. The interface between same phases can be broadly classified into (1) low angle boundaries, (2) high angle boundaries. In low angle boundaries the atomic match at the boundary region is good and these types of boundaries are called coherent interfaces. For high angle boundaries the atomic match is poor (except in special cases e.g. coherent twin boundaries) and interfaces are incoherent in nature. Similarly, interface between dissimilar phases can be coherent, incoherent or semi-coherent in nature. Generally diffusion across incoherent interfaces is easy compared to coherent interfaces or diffusion in the lattice itself.

Student Exercise

Can you guess how other phases present as a particle in the microstructure affect interface movement?

The situation pertains to a case where atomic diffusivity is high enough such that atoms moving in/out across the interface are immediately replenished from positions further away from interface. So availability of requisite atoms is not the rate limiting factor for growth. In Fig. 3.6b the circumstances are different as seen by the concentration gradient appearing in the parent phase. Here atomic diffusivity controls the transport of atoms to the region near the interface (interface mobility M is considered to be high enough so as not be a rate controlling factor). Thus, phase growth rate is limited by the availability of requisite atoms in the proper proportion. In such situations the ΔG^* value will also get affected since interfacial composition variation will affect the surface free energy. The phase growth will no longer be a simple function as represented by Eq. (3.13). The conditions are further complicated when both diffusivity of atoms and interface mobility together controls the phase growth.

As in the case of phase nucleation, the conditions prevailing during friction stir process can significantly affect the phase growth. The introduction of defects in the form of dislocations and grain boundaries and the associated improvement in diffusivity is expected to make interface movement controlled phase growth more probable.

Something to Think

In fusion welding alloying elements are added to the welded zone to change the microstructure and property. Do you think that the same can be done for friction stir welding?

3.2.4 Overall Transformation Kinetics

Based on our previous discussion it is apparent that the overall kinetics for phase transformation is determined cooperatively by (a) the number of nuclei's initially present, (b) the nucleation rate determining the number of nuclei's added with time and (c) growth rate of the stable nuclei's. A simple approach to the problem is to assume that the nuclei's are distributed randomly and grows without affecting the growth of others. For transformations of the type $\beta \rightarrow \gamma$ or $\delta \rightarrow \varepsilon + \theta$, where the parent phase is completely converted to the product phase, the above assumptions forms the basis of Avrami equation which is variously known as Johnson-Mehl-Avrami or Johnson-Mehl-Avrami-Kolgomorov (JMAK) equation.

The isothermal phase transformations kinetics using Avrami equation considers two particular situations (a) site saturation (no further nucleation is happening, i.e. nucleation rate is zero) or (b) constant nucleation rate (I) where nuclei's are added at a constant rate. Consider an event of site-saturation where N is the total number of nuclei distributed randomly in a unit volume. Here the nuclei's are considered to be growing in a spherical fashion (i.e. equal growth rate in all directions) where the radius of each growing nuclei at time 't' is given by $r = Vt$ where V is the interface velocity. The fraction of product phase already formed is 'f' where some of the nuclei's have stopped growing since they impinge on their neighbours. The number 'n' of nuclei's which are still growing is then given as $n = N(1 - f)$, where the radius increase causes an increase in fraction transformed 'df' and is expressed as,

$$df = 4\pi V^2 t^2 N(1 - f)dr \tag{3.16}$$

i.e.

$$df = 4\pi V^3 t^2 N(1 - f)dt \tag{3.17}$$

Integrating and simplifying we get,

$$f = 1 - \exp\left(-\frac{4}{3}\pi V^3 N t^3\right) \tag{3.18}$$

In fact, depending on the conditions of nucleation and nuclei growth different expressions for fraction transformed can be obtained and the general form for Avrami equation is given as,

$$f = 1 - \exp(-kt^n) \tag{3.19}$$

where k and n are constants which depends on the nature of transformation.

3.3 Recovery, Recrystallization and Grain Growth

All metal working processes involve a combination of heat and strain input where depending on the progression of these inputs these processes can be broadly classified as shown in Fig. 3.7. The recovery, recrystallization and grain growth phenomena occurring during metal working processes vary intimately with this sequence. Thus, a hot working process is characterized by dynamic recovery/dynamic recrystallization while a cold-work-anneal process is distinguished by static recovery/static recrystallization. The position of friction stir process is unique in the sense that heat and strain inputs are done simultaneously (see Fig. 3.8).

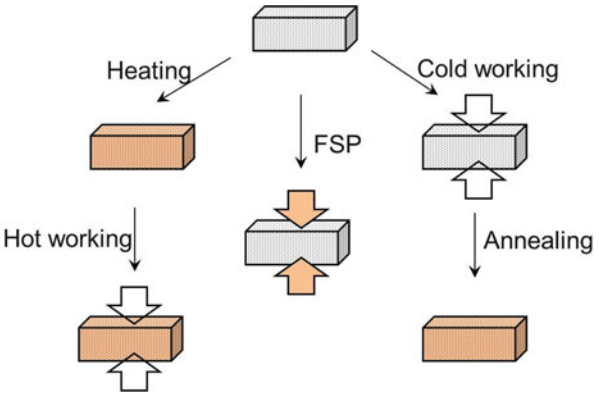

Fig. 3.7 A classification of the metal working processes based on the heat and strain input sequences during processing. FSP is a hybrid between hot and cold working

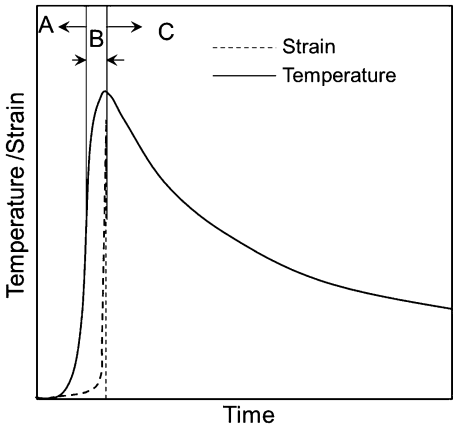

Fig. 3.8 The schematic variation of temperature and strain in the nugget zone of a friction stir process. The region A is the period when the FSP tool is approaching the observed region. Region B is the period when the FSP tool traverses the observed region. Region C is the period when the FSP tool is moving away from the observed region

Table 3.1 Different physical processes occurring during friction stir process

Zone A	Zone B	Zone C
Static recovery	Dynamic recovery	Static recovery
Static recrystallization	Dynamic recrystallization	Static recrystallization
Grain growth	Grain growth	Grain growth

Consequently, the type of recovery, recrystallization processes occurring in FSP is a combination of both cold and hot working.

Based on the temperature/strain variation with time, a friction stir process can be broadly classified into three zones (A to C), where zones A and C involve a temperature cycle while zone B involve a simultaneous combination of temperature and strain regime (Fig. 3.8). Table 3.1 presents the different physical processes which can occur in these three zones where the extent of their incidence depends on the dislocation kinetics of the metal/alloy processed and the temperature and strain conditions present. The remaining part of this section explains each of these processes and the phenomena occurring therein.

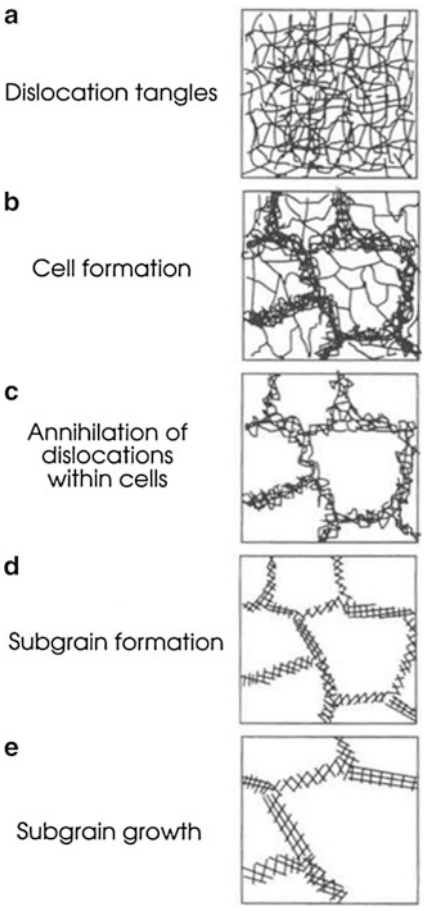

Fig. 3.9 The various microstructural changes occurring during static recovery process. Although the processes are shown sequentially, in practice they can happen simultaneously (Humphreys and Hatherly 2002, reprinted with permission from Elsevier)

3.3.1 Static Recovery

Plastic deformation in metals results in an increase in the dislocation and vacancy density with a resultant change in the physical properties. Subjecting such deformed metal to high temperatures results in static recovery/recrystallization whereby excess dislocations and vacancies are removed causing a restoration of their physical properties. The extent of recovery/recrystallization will however depend on the nature of the metal and the strain and temperature conditions associated therein. In Fig. 3.9a schematic of the various microstructural features occurring during a static recovery process is shown. The principal driving force for these microstructural changes is slip/climb type of dislocation movements which causes dislocations to annihilate each other (when dislocations have opposite burgers vector) and create more complex three dimensional dislocation structures (e.g. cell walls). Further recovery processes results in a rearrangement of these

dislocation structures into stable arrays forming walls of dislocations within the individual grain itself. The walls (also known as sub-grain boundaries) enclose three dimensional volumes known as subgrains where each subgrain consists of the same phase that are oriented differently in space. These sub-grain boundaries differ from the normal grain boundaries in their (1) internal structure, (2) surface energy and (3) orientation gradients (across the boundary) and are also termed as low-angle boundaries, while the normal grain boundaries are designated as high angle boundaries. It is to be recognized that these low angle/high angle boundaries are nothing but an interface (see Sect. 2.3), which separates same phases having different spatial. The surface energy of these low angle boundaries (γ_{LAB}) are lesser than that of high angle boundaries and is given as (Read 1953)

$$\gamma_{LAB} = \gamma_{HAB} \frac{\theta}{\theta_{HAB}} \left(1 - \ln \frac{\theta}{\theta_{HAB}}\right) \tag{3.20}$$

where γ_{HAB} is the surface energy of high angle boundary with an orientation difference of $\theta_{HAB} \sim 15^{\circ}$. For a subgrain of effective radius (R) the surface energy per unit volume for the subgrain is then given as (Humphreys and Hatherly 2002)

$$E_{SUB} \approx \alpha \frac{\gamma_{LAB}}{R} \tag{3.21}$$

where α is a constant. Further recovery causes a reduction in the total energy stored at the subgrain boundaries through subgrain growth where the effective driving pressure (P) acting on the boundary is given by the expression for E_{SUB}. The velocity of a subgrain boundary is expressed by Eq. (3.15) where M is substituted by $M_{subgrain}$, the mobility of the subgrain boundary, while the driving force $\frac{\Delta G^*}{RT}$ is substituted by P. Depending on the nature of the subgrain boundary, the boundary mobility is considered to be either a constant or a function of the orientation gradient existing across the boundary.

So far our discussion on recovery is applicable only for single phase metals. The presence of second phase particles further influences recovery where these particles interact with (a) dislocations and (b) low angle boundaries. Thus, second phase particles impede dislocation movement with an opposing shear stress (τ_{or}) (for phases having incoherent interface with matrix) which is expressed as (Humphreys and Hatherly 2002),

$$\tau_{Or} = \frac{Gb}{\lambda} \tag{3.22}$$

where G is the shear modulus, b is the burgers vector of the dislocation and λ is the inter-particle distance. This opposing shear stress is significant only when the particle spacing is small i.e. in the range of few nanometers. The effect of second phase particles on low angle boundaries occurs through the Zener drag effect (P_Z) which reduces the driving pressure (P) by (Porter and Easterling 2004),

$$P_Z = \frac{3f_v\gamma_{LAB}}{2r} \tag{3.23}$$

where f_v is the volume fraction of second phase and r is the radius of the second phase particles. Thus, second phase particles effectively reduces the sub-grain growth and promotes dislocation preservation within a microstructure.

3.3.2 Static Recrystallization

As already discussed, static recovery causes a dislocation rearrangement resulting in a subgrain structure. On the other hand, during static recrystallization dislocations in the deformed microstructure reorganizes itself to form a new set of strain-free grains separated from each other by high angle grain boundaries. Here the deformed (i.e. strained) grains can be considered to be the parent phase, while the recrystallized (i.e. strain free) grains constitute the product. A significant difference between static recrystallization and conventional phase transformation is: in conventional phase transformation volume free energy change caused by crystal structure modification is the primary driving force for interface movement. But, in static recrystallization both the parent and product phases have the same crystal structure, and the driving force for interface movement is the strain energy (ΔG_{strain}) existing within the deformed grains where (Humphreys and Hatherly 2002),

$$\Delta G_{strain} = \alpha\rho_{dis}Gb^2 \tag{3.24}$$

α is a constant and ρ_{dis} is the density of dislocation within the deformed grains. An additional factor, which affects recrystallization is the surface energy contribution resulting from a change ingrain radius (R) which is given as (Humphreys and Hatherly 2002)

$$\Delta G_{surface} = \frac{2\gamma_m}{R} \tag{3.25}$$

For two phase alloys an additional effect on the driving force for recrystallization arises from the second phase particle distribution and is given by Eq. (3.23).

One key difference between conventional phase transformation and recrystallization is, in conventional case nuclei's of product phase arises from compositional fluctuations at the atomic level while the same is inapplicable for recrystallization. The origin of the first strain free region (i.e. the nucleus for recrystallized grain) from the parent deformed structure remains a controversial topic in recrystallization. The currently accepted understanding is "Nucleation of recrystallization is considered to be no more than discontinuous subgrain growth at sites of high strain energy and orientation gradient" (Humphreys and Hatherly 2002). Thus, nucleation of recrystallized grains occurs typically at microstructural in homogeneities like prior grain boundaries,

transition bands, shear bands and second phase particles (for two phase alloys). Homogenous nucleation of recrystallized grains is considered to be inconceivable.

Any further growth of the recrystallized grains follow the general interfacial controlled phase growth kinetics where the grain boundary velocity (V_{HAB}) is expressed as,

$$V_{HAB} = M_{HAB}P \tag{3.26}$$

where M_{HAB} is the high angle grain boundary mobility and P the driving force for movement which depends on ΔG_{strain}, $\Delta G_{surface}$ and P_z. But, as the recrystallization progresses, the ΔG_{strain} and $\Delta G_{surface}$ value decreases causing a reduction in the driving pressure.

A simple representation of the recrystallization kinetics is given by the JMAK equation (Eq. (3.18)), where the fraction transformed (X_v) is expressed as (Humphreys and Hatherly 2002),

$$X_v = 1 - \exp(-kt^n) \tag{3.27}$$

where n is equal to 4 (considering three dimensional grain growth). The accuracy of the model is however limited since the basic assumptions of the JMAK derivation i.e. (a) random nucleation sites and (b) constant growth rate are not exactly applicable for practical recrystallization. A more accurate description of the recrystallization phenomena is possible by using the Monte Carlo simulation and cellular automata techniques, detailed references for which may be found in the Rollett (1997).

3.3.3 Dynamic Recovery

The dynamic recovery phenomena occurs during the deformation process itself and results in a subgrain structure typical of static recovery. However, unlike in static recovery not much is known about the intervening steps which lead to the subgrain microstructure. The stress-strain curve for a dynamically recovered metal shows an initial increase in stress with strain. This is followed by a plateau region where the stress remains independent of the strain (Fig. 3.10). The stress (σ_s) during dynamic recovery depends on the applied strain rate ($\dot{\varepsilon}$) and temperature (T) and can be represented by the following constitutive equation (McQueen et al. 2011),

$$A \sinh(\alpha\sigma_s)^n = \dot{\varepsilon} \exp\left(\frac{Q}{RT}\right) = Z \tag{3.28}$$

where A, α and n are material constants. The subgrain size (d_s) developed during dynamic recovery is given as (McQueen et al. 2011),

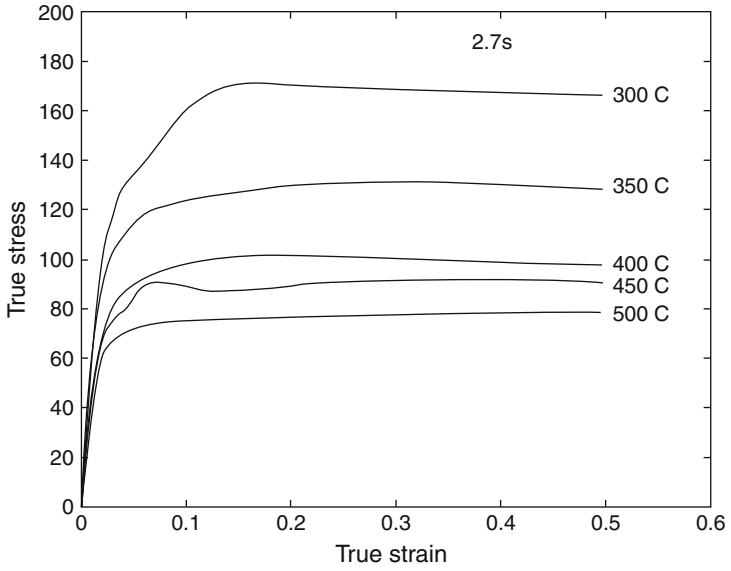

Fig. 3.10 The stress-strain curve (hot compression test) for a AA 6061 alloy with 15 % SiC at 2.7 s^{-1} strain rate. The stress-strain curve shows an initial rise in stress with strain, followed by a plateau and is typical of dynamic recovery (Ganesan et al. 2004, reprinted with permission from Elsevier)

$$d_s^{-1} = a + b \log Z \tag{3.29}$$

where a and b are material constants. The above equation is valid for a constant Z condition and gives the subgrain size after a steady state stress is achieved. Typically, pure Al alloys exhibit dynamic recovery while for solute strengthened and precipitation strengthened Al alloys a combination of dynamic recovery and dynamic recrystallization is observed (McQueen et al. 2011).

Student Exercise

To increase the strength of the weld region one possible way is to decrease the grain growth period (see Fig. 3.8). Do you think the grain growth period can be indefinitely reduced by increasing the traverse speed?

3.3.4 Dynamic Recrystallization

During dynamic recrystallization the initial straining of the grains results in recrystallization whereby new strain free grains are formed. Continued application of strain introduces new dislocations into the recrystallized grains forming subgrains inhibiting their further growth. With additional straining these subgrains furnish

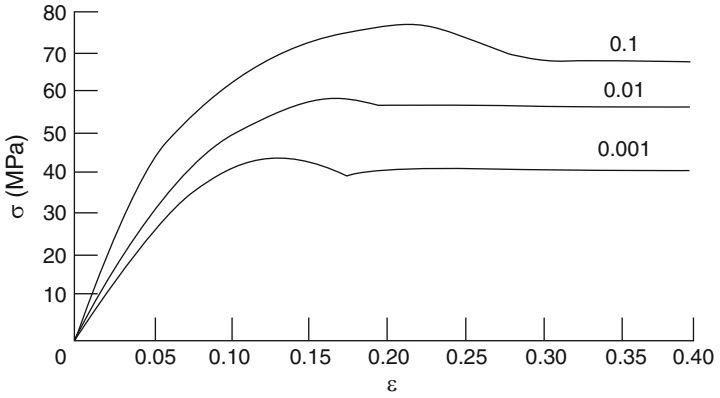

Fig. 3.11 Stress-strain diagram of recrystallized Ni at 1,000 °C for grain size of 30 μm. Note the initial peak followed by a decrease in stress to reach a steady state region. This is typical of dynamic recrystallization (Poliak and Jonas 1996, reprinted with permission from Elsevier)

fresh nucleation sites for recrystallization. Thus, with continued straining the microstructure undergoes a series of recrystallization events and recrystallization of this type is also known as discontinuous dynamic recrystallization. A typical stress-strain behavior for such dynamically recrystallized metal is shown in Fig. 3.11.

The constitutive equation used to represent such recrystallization behavior is same as Eq. (3.27) and the steady state grain size (d_s) obtained during the process is given in terms of Z or σ as (McQueen et al. 2011),

$$d_s^{-1} = A + B \log Z \tag{3.30}$$

Or,

$$\sigma_s = C + D\, d_s^p \tag{3.31}$$

where A, B, C, D and p are constants.

3.3.5 Grain Growth

As already discussed in the Sect. 3.2 any grain in a polycrystalline material is associated with a positive surface energy (Eq. (3.25)). Consequently, a grain size increase (alternatively thought of as "curvature reduction") reduces the total energy stored in a microstructure. This curvature reduction is the principal driving force for grain growth. Thus, if two grains adjacent to each other have a different radius, the larger radius grain grows at the expense of the smaller where atoms get transferred

by a process similar to that discussed in the Sect. 2.3. The grain growth phenomena can then be expressed as (Humphreys and Hatherly 2002)

$$\frac{dR}{dt} = \frac{\alpha M \gamma_{HAB}}{R} \tag{3.32}$$

and the temporal change in grain size expressed as (Humphreys and Hatherly 2002),

$$R_f^2 - R_i^2 = \alpha M \gamma_{HAB} t \tag{3.33}$$

The above parabolic kinetics predicted for grain growth is however in variance with actual experiments where the exponent for R is found to be between 2 and 3 (Humphreys and Hatherly 2002). This difference has been ascribed to various non-idealities which includes (Humphreys and Hatherly 2002)

(a) Non-equiaxed initial grain structure.
(b) Texture formation—resulting in non-uniform γ_{HAB}.
(c) Presence of small amounts of second phase/solutes which impedes grain boundary movement.

In fact, the effect of second phase on grain growth is very much similar to its effect on subgrain growth where the driving pressure for boundary movement is reduced by the drag effect of the second phases. For a constant second phase shape, dimension and volume fraction, this gives rise to a limiting grain size (D_{Zener}) which is known as the Zener limit and is expressed as (Porter and Easterling 2004),

$$D_{Zener} = \frac{4r}{3f_v} \tag{3.34}$$

where r and f_v have the usual meaning.

Something to Think

The final grain size in the welded region is a function of recrystallization and grain-growth. The finer the grain size, higher will be the strength. If the original grain size in workpiece is ~50 μm, calculate the volume fraction of second phase required to reduce the grain size to ~0.2 μm. Do you think it is feasible?

3.4 Precipitation Transformations

Precipitation transformation forms the basis of high strength alloys where strengthening is achieved by the means of second phases finely distributed within the matrix. These finely distributed precipitates resist the slip motion of dislocations causing an increase in the yield strength. Schematically, precipitation reaction can be expressed as,

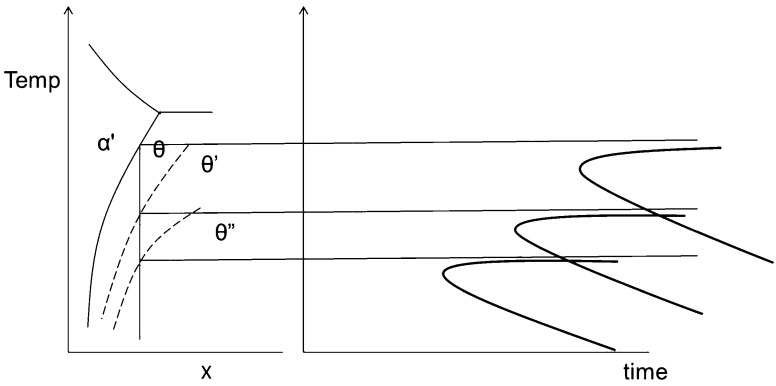

Fig. 3.12 Precipitation hardening phenomena where the alloy is cooled rapidly from the α′ region to the two phase (α + θ) region. Rapid cooling results in formation of an initial supersaturated solution of α. The supersaturated solution initially decomposes into the metastable phases θ″ and θ′. The time temperature transformation curve for each of the phases is also shown (Adapted from Porter and Easterling (2004))

$$\alpha' \rightarrow \theta + \alpha$$

where α′ is a supersaturated solution phase, θ is a stable or metastable phase and α is a saturated phase which has the same crystal structure as the supersaturated α′ phase. Figure 3.12 shows the phase diagram representation for precipitation reaction where a sample is cooled rapidly from its solutionizing temperature to a lower temperature preserving the excess solutes in the α phase. A further controlled temperature rise of this supersaturated solution (i.e. aging process) causes a separation of the excess solute atoms from α phase to form metastable or stable phases. Based on the mechanism of precipitation this solute atom separation is further classified into (Christian 2002)

(a) Spinodal decomposition
(b) Continuous precipitation reaction
(c) Discontinuous precipitation reaction

For a spinodally decomposing system the free-energy variation is similar to that shown in Fig. 3.1a where below certain temperatures the singular phase dissociates into multiple phases with different composition.

This decomposition of the single phase into multiple phases is unique in the sense that it occurs spontaneously. To understand this, consider Fig. 3.13, where the free energy versus composition for a thermodynamic system with miscibility gap along with its first and second derivative is shown. In the compositional region BB′ (second derivative of ΔG_m with composition negative) consider an alloy of composition A whose free energy is given by the point X on the free energy versus composition curve (Fig. 3.13). This same composition phase when decomposed into two different phases of composition A_1 and A_2 (the proportion of each phase

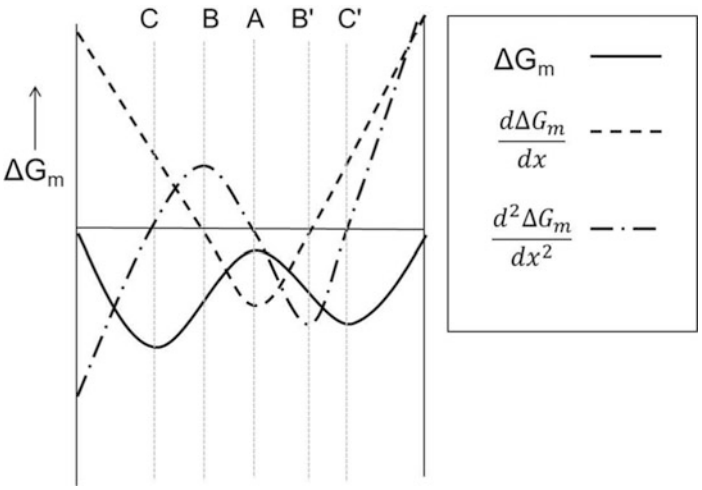

Fig. 3.13 Free energy versus composition diagram for a system with miscibility gap (Fig. 3.1). In the region BB′ spinodal decomposition happens, while in the region BC and B′C′ the precipitation process is diffusion based

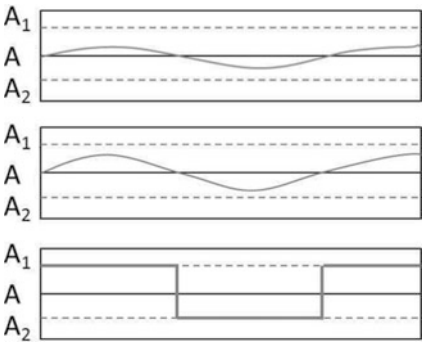

Fig. 3.14 The kinetics of spinodal decomposition showing how the initial small fluctuation from composition A amplifies, resulting in decomposition into two phases with composition A_1 and A_2 (Adapted from Porter and Easterling (2004))

being maintained so that the average composition is same as A—Lever rule) results in a phase mixture whose total free energy is lower than that of the single phase (see Fig. 3.13). Thus, any small compositional fluctuation in such microstructures leads to a negative volumetric free energy change (ΔG_{volume}) which increases the fluctuation even further (Fig. 3.14). This spontaneous formation of new phases is particularly favorable when the surface free energy ($\Delta G_{surface}$) and strain energy (ΔG_{strain}) contributions are negligible and results in homogenous phase nucleation. Such homogenous nucleation condition is particularly feasible when the "unconstrained lattice misfit"—δ (see Eq. (3.4)) is very low and the interface is coherent with a minimum surface free energy. Precipitation reactions of this type are known as spinodal transformations.

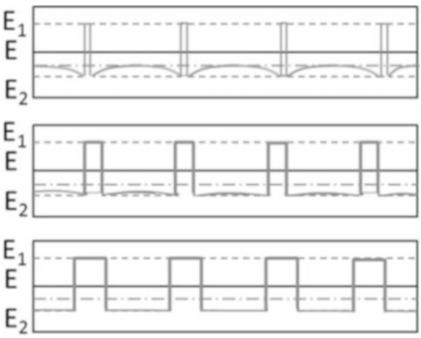

Fig. 3.15 The kinetics of continuous precipitation, showing the formation of a stable nuclei's of a phase with composition E_1 from the initial composition E. The further growth of nuclei's occur through diffusion process (Adapted from Porter and Easterling (2004))

A distinguishing feature of such reactions is that atomic movement happens from both "high to low" and "low to high" concentrations. In the spinodal region, precipitates nucleate homogenously producing a very small inter-particle distance. In certain alloys where atomic diameters of solute and solvent atoms are similar (e.g. Ag-Al alloys) spinodal decomposition results in the formation of clusters of atoms (also known as GP (Guinier-Preston) zones) where the excess solute segregates in a random fashion. These coherent clusters/GP zones create resistance to dislocation movement causing matrix strengthening. The maximum strengthening achieved when stronger metastable intermediate phases (also called as transition phases) with coherent/semi-coherent interfaces are formed.

In the compositional region BC and B′C′ the precipitation process is very different from that of the spinodal region. Thus, for an alloy of composition E, a small composition fluctuation in the microstructure actually raises the system volume free energy (see Fig. 3.13), although final decomposition into the two terminal compositions E_1 and E_2 will lead to a net decrease in energy. This unfavorable energetics means that compositional fluctuations by itself cannot lead to the terminal compositions E_1 and E_2 unlike in spinodal decomposition where fluctuations get amplified. Thus, formation of a stable nuclei from the fluctuations can proceed only through normal downhill diffusion process (i.e. atom movement from higher to lower concentration, see Fig. 3.15) making homogenous nucleation unlikely with precipitation initiated mainly at dislocations or at grain boundaries.

In discontinuous precipitation system (also known as cellular precipitation) the supersaturated solution (i.e. α') precipitates a saturated solution (i.e. α) and a stable phase (θ) (Porter and Easterling 2004). Morphologically, the microstructure for a discontinuously formed precipitate is similar to the eutectoid microstructure (i.e. lamellar structure) although its exact mechanism is still not understood unambiguously.

As in the case of grain growth (see Sect. 3) the precipitates formed always intend to minimize their curvature. This implies that a bigger precipitate tends to grow larger at the expense of the smaller ones which results in an increase in inter-particle

distance with consequent lowering of strength. This precipitate growth kinetics is controlled either by (a) diffusion of atoms from one particle to other through the matrix or (b) transfer of atoms across the interface between matrix and precipitate (Ballufi et al. 2005). The first case (i.e. (a)) results in diffusion-limited coarsening, while the second case (i.e. (b)) is known as source-limited coarsening (Ballufi et al. 2005). For diffusion-limited coarsening the mean precipitate size grows as (Ballufi et al. 2005),

$$\langle R(t)\rangle^3 - \langle R(0)\rangle^3 = K_{diffusion}t \tag{3.35}$$

is where $\langle R(t)\rangle$ is the mean particle radius at time t, $\langle R(0)\rangle$ is the initial mean particle radius and $K_{diffusion}$ is the rate constant for diffusion-limited coarsening. For a source-limited coarsening the mean precipitate size grows as (Ballufi et al. 2005),

$$\langle R(t)\rangle^2 - \langle R(0)\rangle^2 = K_{source}t \tag{3.36}$$

where K_{source} is the rate constant for source limited coarsening. It is to be noted that precipitate dissolution kinetics follows the same kinetics as precipitate coarsening.

3.5 Eutectoid Transformations

Eutectoid reaction is another important phase transformation phenomena which happens in the solid state. Schematically the eutectoid reaction is expressed as $\alpha \rightarrow \beta + \gamma$, where the phase α gives rise to two stable phases β and γ. An important example of such reaction is in steel where

$$\gamma \text{ (austenite)} \rightarrow \alpha \text{ (ferrite)} + Fe_3C \text{ (cementite)}$$

with the ferrite and cementite phase appearing as a lamellar microstructure. The reaction starts by nucleation of either α or Fe_3C at the austenite grain boundary (as determined by the boundary characteristics) where the nuclei comprises of a semicoherent interface with one of the grain (γ_1), while its interface with the other grain (γ_2) is incoherent (see Fig. 3.16a) (Porter and Easterling 2004). Consequently, the α/Fe_3C phase starts growing into the γ_2 grain. Assuming the nucleated phase as cementite, this growth is accompanied by a decrease in C concentration in the region adjacent to the cementite phase. This leads to α phase nucleation in the adjacent region, the growth of which is again followed by carbon rejection leading to re-nucleation of cementite (see Fig. 3.16b, c). The alternate carbon rejection and absorption leads to a sideways nucleation process forming a lamellar eutectoid colony, which continues to grow into the austenite grain.

The growth of a eutectoid colony is very similar to the growth of lamellar eutectic and occurs in a cooperative fashion where C atoms rejected by ferrite and Fe atoms

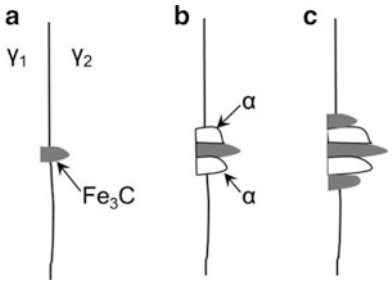

Fig. 3.16 Nucleation of pearlite in steel. Initially a cementite (Fe_3C) nuclei forms at the grain boundary separating the two grains (γ_1 and γ_2). The flat interface with grain γ_1 indicates that the interface is semicoherent. The curved interface with grain γ_2 indicates incoherent interface. The formation of cementite with local depletion of C in austenite grains results in nucleation of ferrite (α) phase. The process repeats itself resulting in pearlite colony formation (Adapted from Porter and Easterling (2004))

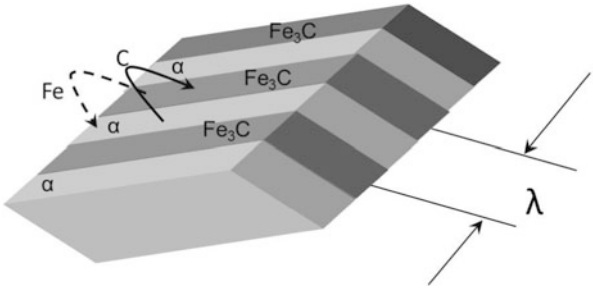

Fig. 3.17 A schematic three dimensional view of eutectoid lamella (pearlite). The atomic movement occurring during the growth process is also shown

rejected by the Fe_3C phase moves laterally across the tips of the lamella (Fig. 3.17) (Porter and Easterling 2004). The rate at which the eutectoid lamella grows therefore depends on the diffusivity of the C and Fe atoms at the transformation temperature. For an interlamellar spacing of S the total α/Fe_3C interface per unit volume of the eutectoid is given as $2S^{-1}$. The free energy change associated per unit mole of γ ($\Delta G(S)$) conversion is then given as (Porter and Easterling 2004),

$$\Delta G(S) = -\Delta G_0 + \frac{2\gamma_{interface} V_m}{S} \tag{3.37}$$

where ΔG_0 is the free energy change for eutectoid reaction where inter-lamellar distance is very large (i.e. interfacial energy contribution is minimum) while $\gamma_{interface}$ is the surface energy of the lamellar interface. The above reaction can take place only if $\Delta G(S)$ is negative, which means that the eutectoid transformation should occur below the equilibrium temperature (i.e. undercooling is required). If the variation of ΔG_0 with undercooling is expressed as (Porter and Easterling 2004),

$$\Delta G_0 = \frac{\Delta H \cdot \Delta T}{T_{Eutectoid}} \tag{3.38}$$

where ΔH is the enthalpy change at eutectoid temperature $T_{Eutectoid}$ and ΔT is the under cooling, the minimum lamella spacing at a given temperature is proportional to the under cooling. The growth rate (V) of a neutectoid colony can therefore be expressed as (Porter and Easterling 2004)

$$V = kD_c^{\gamma}(\Delta T)^2 \tag{3.39}$$

where k is a constant while D_c^{γ} is the coefficient of diffusivity of C in austenite. The above squared dependence of lamellar interspacing on undercooling is typical of eutectoid systems where the diffusing solute atoms are in the interstitial sites (e.g. in pearlitic steel) (Porter and Easterling 2004). The lamellar interspacing varies as the third power of undercooling, when solute atoms are of the substitutional type (Porter and Easterling 2004).

3.6 Widmanstätten Structures (Adapted from Porter and Easterling (2004))

In the Fe-C phase diagram (Fig. 3.18), the formation of pro-eutectoid ferrite from austenite is another example of diffusional transformation where the product formed is an equilibrium structure. Depending upon the transformation conditions the structure of the ferrite formed can however vary significantly (see Fig. 7.20). At small undercooling below the A_3 temperature (point (a) in Fig. 3.18) the ferrite

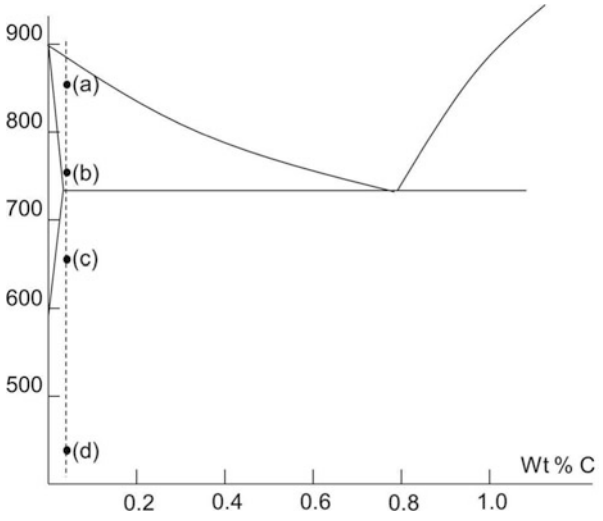

Fig. 3.18 The Fe corner of Fe-Fe_3C phase diagram. For a steel of the given composition (*dotted line*) quenching from the austenite region to different holding temperatures (point *a* to *d*) results in the formation of different ferritic structures (Adapted from Porter and Easterling (2004))

nucleates at the austenitic grain boundaries. As in the case of nucleation during pearlite formation, the ferrite formed will have both semi-coherent and incoherent interfaces with all the interfaces growing at more or less similar velocities. This leads to the growth of lumpy (more precisely called "Grain-boundary allotriomorphs") ferrite structures and is a characteristic of high transformation temperatures. Increasing the undercooling to lower temperatures (points b, c in Fig. 3.18) results in the formation of plate like ferrite structures which happens due to the relative immobility of the semi-coherent interfaces. In this situation the incoherent interface grows in preference to the semi-coherent interface forming "Widmanstätten plates". At still higher undercooling, the austenite to ferrite transformation happens through a "massive transformation" process where the austenite gets transformed to ferrite with the same composition, resulting in massive ferrite phases. During massive transformation no long range diffusion processes occur and the product phase growth is controlled by atomic transfer across the interfaces.

Still further undercooling renders the austenite to ferrite transformation kinetics infeasible and a completely new metastable phase martensite forms (point (d) in Fig. 3.18). The martensitic phase transformation process is discussed in more details in the next section.

3.7 Martensitic Transformation

The phase transformation processes discussed so far involve thermally aided atomic movement either in the long or short atomic ranges. Martensitic transformation is an unique process where atomic movements occurs over fractional atomic distances and are athermal in nature. Thus, quenching (to prevent C atom diffusion) of steel from its austenitic phase field (face-centered cubic structure) to a low temperature in the range of point (d) (Fig. 3.18), results in martensite (body centered cubic structure) formation. But, unlike austenite to ferrite transformation which can proceed to completion isothermally, conversion to martensite does not occur isothermally and the fraction transformed depends only on the extent of undercooling. In fact, above a certain temperature (known as "Martensite start temperature" or M_s) the martensite transformation does not occur at all. The driving force for martensite formation $\Delta G(\gamma \rightarrow a')$ at M_s is given as (Porter and Easterling 2004)

$$\Delta G(\gamma \rightarrow a') = \Delta H(\gamma \rightarrow a') \frac{T_0 - M_s}{T_0} \tag{3.40}$$

where $\Delta H(\gamma \rightarrow a')$ is the enthalpy change at M_s, T_0 is the temperature at which the free energy of austenite and martensite phase are equal. On the other hand, if quenching is done below a certain temperature (known as "Martensite finish temperature" or M_f), the austenite to martensite conversion reaches its completion.

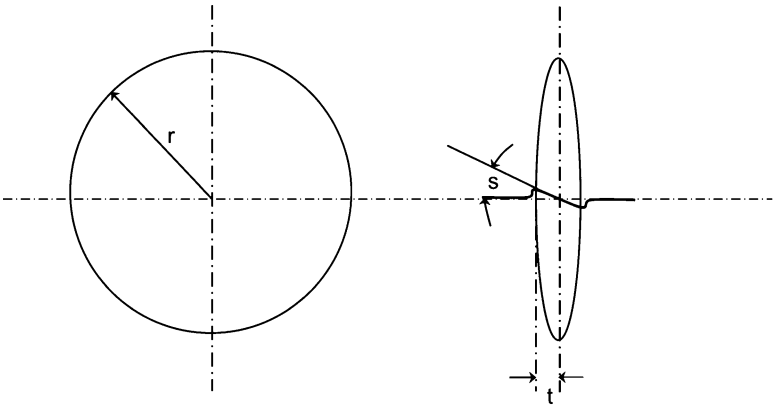

Fig. 3.19 A schematic of the lens shaped martensite nuclei formed. The shear strain s applied on the habit plane is also shown (Adapted from Porter and Easterling (2004))

Both M_s and M_f temperature depends on the alloy composition with M_s in case of steel given as (Andrews 1965),

$$M_s(^\circ C) = 539\text{-}423C\text{-}30.4Mn\text{-}12.1Cr\text{-}17.7Ni\text{-}7.5\ Mo$$

The free energy of a fully coherent martensite nuclei formed in a matrix of austenite (i.e. homogenous nucleation) is thus expressed as (Porter and Easterling 2004),

$$\Delta G = A_{vol}\gamma + V_{vol}\Delta G_{strain} - V_{vol}\Delta G(\gamma \rightarrow a') \tag{3.41}$$

Where V_{vol} is the volume of the lens of martensite nuclei, A_{vol} is the surface area of the martensite lens, γ is the interfacial surface tension. Here the martensite lens is considered as a thin ellipsoid with radius r and semi-thickness t which is formed by simple shear s parallel to the plane of the ellipsoid disc (Fig. 3.19). The critical free energy barrier to homogenous nucleation and the corresponding dimensions of the ellipsoid (r* and t*) is then given as (Porter and Easterling 2004),

$$\Delta G^* = \frac{512}{3} \cdot \frac{\gamma^3}{[\Delta G(\gamma \rightarrow a')]^4} \cdot \left(\frac{s}{2}\right)^4 \mu^2 \pi \tag{3.42}$$

$$t^* = \frac{2\gamma}{\Delta G(\gamma \rightarrow a')} \tag{3.43}$$

and

$$r^* = \frac{16\gamma\mu(s/2)^2}{(\Delta G(\gamma \rightarrow a'))^2} \tag{3.44}$$

where μ is the shear modulus of the austenite phase. Current research indicates that martensite nucleates heterogeneously on individual dislocations existing in the microstructure (Porter and Easterling 2004). Alternately, it has been proposed that the elastic strain field of dislocations reduces the free energy barrier for homogenous nucleation of martensite (Sinclair and Mohamed 1978; Porter and Easterling 2004). Once the nucleation barrier is overcome, the volume free energy causes the marteniste plates to grow rapidly across the grain until hampered by other martensite plates or grain boundary.

Student Exercise

You are planning to friction stir weld a plain low-carbon steel structure. Can you estimate the microstructure?

The microstructural observation of martensite formation reveals some unique features

(a) Martensite forms in a narrow lens shaped region within the grains and are oriented at specific directions only.
(b) The boundary region between the martensite and austenite phase (also called as "habit plane") is macroscopically undistorted, and is free of any plastic deformation. This happens despite the fact that the parent and product crystal structures are different and is associated with a volumetric change.

In fact, based on the above observations the transformation can be assumed to be a combination of simple shear on the habit plane accompanied by dilation normal to the habit plane (Porter and Easterling 2004). Researchers have proposed various theories for a physical explanation of the above observations, the details of which can be obtained from the following reference (Christian 2002).

3.8 Physical Simulation of FSW

Different constitutive materials behavior for modeling FSW were discussed in Chap. 2, which covered the relationship of flow stress with temperature, strain and strain rate in materials. This inter-relationship is produced by phase transformations, recovery, recrystallization and grain growth depending on the thermo-mechanical conditions prevailing during FSW. A proper choice of constitutive relation is therefore a critical component in FSW simulation. Among the different experimental methods used to determine constitutive equations, hot torsion testing is particularly relevant since deformation in FSW is considered to have a significant torsional component. As an example, the process simulation by Chang et al. used expressions for torsional deformation to simulate FSW (Chang et al. 2004) and later hot torsion testing using Gleeble® has been used to simulate FSW microstructure itself.

Such microstructure reproduction for thermo-mechanical processes using controlled deformation experiments forms the basis of physical simulations and can throw significant light on the process investigated.

Thus, Rule and Lippold successfully replicated the TMAZ structure in Ni-base alloys using hot-torsion testing where the number of revolutions (i.e. total strain) and revolution rate (i.e. strain rate) controls the microstructure (Rule and Lippold 2006). The experiments, however, failed to reproduce the stir zone microstructure. Similar physical simulation using a combination of compressive stress and thermal cycling in Gleeble® successfully replicated the heat affected zone microstructure (Genevois et al. 2006). It needs to be mentioned that the similarity in microstructure does not imply that the deformation path in the physical simulation and FSW is same. The effect of compressive (effect of shoulder pressing on workpiece) and extrusion forces (effect of tool movement) existing in stir zone is not accounted for in the hot torsion experiments. This probably explains why Rule and Lippold were unable to reproduce the stir zone microstructure, while the HAZ zone microstructure was successfully reproduced by Genevois et al.

3.9 Microstructural Evolution During Friction Stir Welding

The inter-relationships of independent and dependent processing parameters and their physical effects on microstructural evolution are important (see Figs. 2.5 and 2.6 for an example). Each of the dependent and independent processing parameters was discussed at length in Chap. 2. A general discussion on microstructural evolution was incorporated in this chapter up to Sect. 3.6. This section focuses on microstructural evolution during FSW/P.

As a result of friction stir welding the processed regions or welded zones undergo microstructural changes. A pictorial overview of such microstructural evolution across different zones is presented in Fig. 3.20. As expected the base material retains its original/starting microstructure. The microstructural evolution in HAZ takes place under the influence of thermal cycle only. Hence, static recovery and recrystallization, grain growth, precipitate nucleation, growth, and dissolution will take place depending on the starting microstructure and processing conditions. For example, if a precipitation hardenable metallic material such as 2XXX and 7XXX series aluminum alloys is subjected to friction stir welding and processing in solutionized and quenched condition, precipitate nucleation and its growth are most likely to happen in HAZ. Figure 3.21 explains this aspect with the help of a schematic binary phase diagram. If the starting microstructure (X_0) is quenched from single phase zone, it will have all the solutes in solid solution. Now, if the thermal cycle is such that peak temperature remains within two phase zone ($\alpha + \beta$), the β phase will nucleate and grow from α phase during heating and cooling cycle. But, if peak temperature exceeds the solvus line, no precipitate would exist at

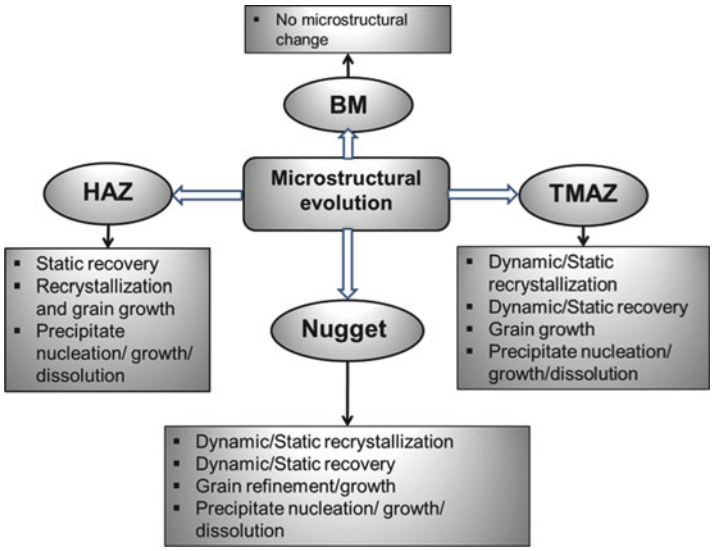

Fig. 3.20 A schematic of microstructural evolution in different zones of friction stir processed/ welded material

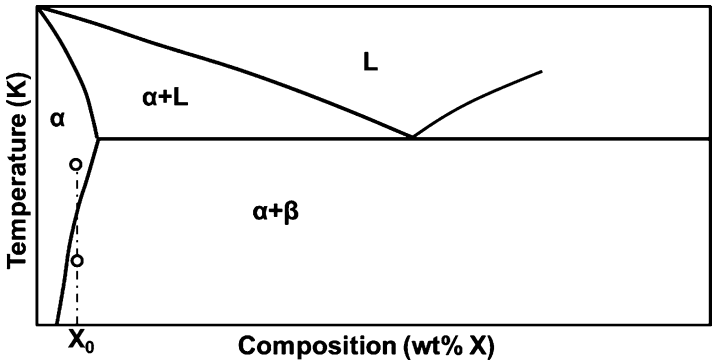

Fig. 3.21 Precipitate evolution in HAZ of friction stir welded/processed material

the peak temperature of the thermal cycle. During cooling cycle the extent of precipitation of β phase in HAZ would depend on the cooling rate. For such a system, the knowledge of phase equilibrium, precipitate nucleation kinetics, its growth and coarsening becomes important to quantify such microstructural change in HAZ under different circumstances. If work hardenable materials such as 5XXX series aluminum alloy are subjected to friction stir welding and processing in H temper, then in that case thermal cycle might cause static recovery of deformed state, static recrystallization, and grain growth.

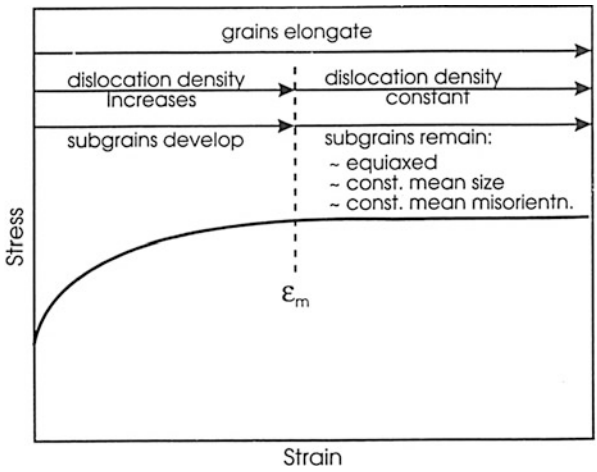

Fig. 3.22 A schematic stress-strain curve summarizing the evolution of microstructure during dynamic recovery (Humphreys and Hatherly 2002, reprinted with permission from Elsevier)

The interpretation of microstructural evolution in HAZ is relatively straightforward due to the presence of thermal cycle only. The material in TMAZ is also plastically deformed and deformation condition is comparable to hot-working of metallic material. Hence, in the interpretation of microstructural evolution the accurate knowledge of strain, strain rate, and thermal cycle is pivotal not only for a priori guess of possible microstructure after FSW/P but also for microstructural modeling in this zone. Since this zone resembles hot-deformation metal working process, dynamic recovery/recrystallization followed by static recovery/recrystallization, grain growth, and/or precipitate nucleation, growth, and/or coarsening should be expected. Like HAZ, observation of various physical phenomena in this zone would depend on starting microstructure and processing parameters. Unlike HAZ, the plastic deformation would cause development of dislocation-based substructures in this zone. Readers are referred to the sections dealing with dynamic recovery and recrystallization of this chapter to get an insight to how these phenomena control the evolution of microstructure. A summary of possible microstructural changes during dynamic recovery is presented in Fig. 3.22. Microstructural examination during FSW/P of TMAZ shows elongated grains and recovered microstructure consistent with the summary presented in Fig. 3.22.

The most difficult part of microstructural evolution during FSW/P is in the nugget. Nugget represent a highly dynamic and turbulent zone marked by complex material flow, presence of different states of stresses (and cyclic forces), varying strain and strain rates around the rotating and traversing tool. Chapter 2 discusses all these aspects in greater detail. Moreover, the microstructure elements which evolve in the material volume while in the shear layer (Stage I) around the tool pin and under the shoulder gets altered once deposited on the trailing side of the tool. They get modified due to combined action of thermal and deformation field first (Stage II) and at later stages due to thermal field alone (Stage III). Hence, the discussion of microstructural evolution should involve all three stages in the nugget. To further explain it, a schematic of grain size evolution in the nugget is presented in Fig. 3.23.

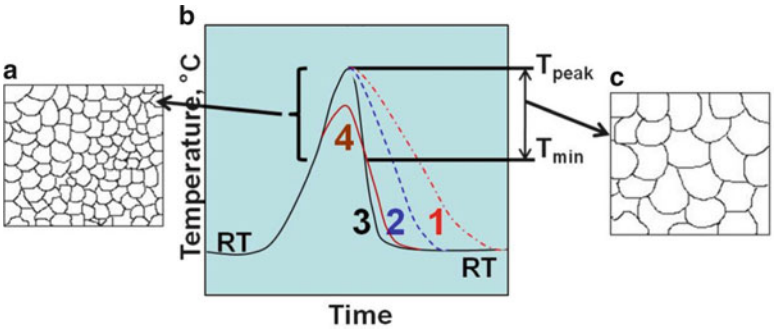

Fig. 3.23 A schematic illustration of grain size evolution in the nugget (**a**) Microstructure evolved during Stage I (**b**) Various thermal profiles for obtaining different microstructure (see text for details) and (**c**) Final microstructure (at the end of Stage III) (Kumar and Mishra 2012, reprinted with permission from Elsevier)

Figure 3.23a can represent stage I of microstructural evolution in the nugget, i.e., the microstructural evolution within the shear layer and just deposited on the trailing side of the tool. It will be assumed that by the time material volume got deposited on the trailing side of the tool, the nucleation and growth of the recrystallized grain was over. It is very difficult to retain this microstructure since it gets modified during stage II and stage III of microstructural evolution as described above. However, there have been some attempts to retain this microstructural state by a few researchers by using techniques like the use of external quenching media to arrest the modification of microstructure, i.e., by eliminating stage II and stage III. Average grain size as small as <100 nm has been reported in the nugget (Kumar and Mishra 2012, 2013). During stage II under the combined action of stress and thermal cycle, the microstructure would undergo repeated grain growth, dynamic recovery, and dynamic recrystallization similar to the one taking place in TMAZ. Once it is out of the deformation zone of the tool pin, stage III would set in which static recovery, static recrystallization, and grain growth occur, similar to that taking place in HAZ. The time of residence of a material volume being thermo-mechanically deformed in Stages I, II, and III would depend on the processing parameters, which in turn governs the final grain size. It is known that slower tool traverse speeds lead to coarser grains compared to that at higher tool traverse speed (Mishra and Ma 2005). For the sake of discussion, if it assumed that only stage I and stage III are present during grain size modification in the nugget, the final grain size can be tweaked depending on the thermal cycle. There are two ways of doing it—one by changing the peak temperature (curves 1 and 4 in Fig. 3.23b) and second by modifying the cooling rate. By imposing external forced cooling arrangement one can change the cooling rate from curve 1 to curve 3 depending on the kind of cooling arrangement (Fig. 3.23b). Peak temperature can also be reduced by changing processing parameters such as tool traverse speed (by increasing), tool rotation rate (by reducing), etc. (Fig. 3.23b). The intention behind these is to cut-down on resident time at T_{peak} and T_{min} (minimum temperature required for grain growth) to minimize grain growth during stage III. The grains after stage III are shown in Fig. 3.23c.

References

Animesh, Pvt, Private collections of Dr. A. Mandal, IIT Bhubaneswar

K.W. Andrews, Empirical formulae for the calculation of some transformation temperatures. J. Iron Steel Inst. **203**, 229–248 (1965)

R.W. Ballufi, S.M. Allen, W.C. Carter, *Kinetics of Materials* (John Wiley and Sons, New Jersey, 2005)

C.I. Chang, J.C. Lee, J.C. Huang, Relationship between grain size and Zener-Holloman parameter during friction stir processing in AZ31 Mg alloys. Scripta Mater. **51**, 509–514 (2004)

J.W. Christian, *The Theory of Transformations in Metals and Alloys, Vols. 1 and 2*, 3rd edn. (Elsevier Science Ltd., Oxford, 2002)

G. Ganesan, K. Raghukandan, R. Karthikeyan, B.C. Pai, Development of processing maps for 6061 Al/15% SiC_p composite materials. Mater. Sci. Eng. A **369**, 230–235 (2004)

C. Genevois, D. Fabrègue, A. Deschamps, W.J. Poole, On the coupling between precipitation and plastic deformation in relation with friction stir welding of AA2024 T3 aluminium alloy. Mater. Sci. Eng. A **441**, 39–48 (2006)

F.J. Humphreys, M. Hatherly, *Recrystallization and Related Annealing Phenomena*, 1st edn. (Elsevier Science Ltd., U.K., 2002)

N. Kumar, R.S. Mishra, Thermal stability of friction stir processed ultrafine grained Al-Mg-Sc alloy. Mater. Charact. **74**, 1–10 (2012)

N. Kumar, R.S. Mishra, Ultrafine grained Al-Mg-Sc alloy via friction stir processing. Metall. Mater. Trans. A **44**, 934–945 (2013)

Z.Y. Ma, S.R. Sharma, R.S. Mishra, Effect of friction stir processing on the microstructure of cast A356 aluminum. Mater. Sci. Eng. A **433**, 269–278 (2006)

H.J. McQueen, S. Spigareli, M.E. Kassner, E. Evangelista, *Hot Deformation and Processing of Aluminum Alloys* (CRC Press, Boca Raton, FL, 2011)

R.S. Mishra, Z.Y. Ma, Friction stir welding and processing. Mater. Sci. Eng. R **50**, 1 (2005)

E.I. Poliak, J.J. Jonas, A one-parameter approach to determining the critical conditions for the initiation of dynamic recrystallization. Acta Mater. **44**, 127–136 (1996)

D.A. Porter, K.E. Easterling, *Phase Transformations in Metals and Alloys*, 2nd edn. (CRC Press, Boca Raton, FL, 2004)

W.T. Read, *Dislocations in Crystals* (McGraw-Hill, New York, NY, 1953)

A.D. Rollett, Overview of Modeling and Simulation of Recrystallization. Prog. Mater. Sci. **42**, 79–99 (1997)

J.R. Rule, J.C. Lippold, Physical simulation of friction stir welding and processing of nickel-base alloys using hot torsion. Metall. Mater. Trans. A **44**, 3649–3663 (2006)

R. Sinclair, H.A. Mohamed, Lattice imaging study of a martensite-austenite interface. Acta Metall. **26**, 623–628 (1978)

Chapter 4
Friction Stir Welding Configurations and Tool Selection

The basic goal of any joining technique is to perform welding in as many configurations as possible to enhance the design space for components and structures. This chapter is split into two main sections: joint configurations and tool selection guidelines. There may be some overlap in these areas, and those are dealt with some minor comments wherever needed. Also, some discussion on defect formation during the friction stir process is included.

4.1 Joint Configuration

Most joints during friction stir welding can be classified into three basic categories, (a) butt, (b) lap, and (c) fillet. Most of the other joints can be visualized as a combination of these. Within these joint configurations, a few others have been shown in Fig. 4.1 to help the discussion of certain aspects of the friction stir process. Some defects are specific to a particular type of joint. For example, in the early years of friction stir welding, cylindrical pin tools without any features were commonly used for butt welds. These usually showed a 'lazy S' pattern of original faying surface oxide film. With pin features, the faying surface is distributed more effectively and the remanence of faying surface is usually not observable by normal cross-section metallography.

The butt joints shown in Fig. 4.1a–e are based on specific requirements and essentially use the same basic concept of welding from one side. The point of difference is that in friction stir joints material flow is different on the advancing and retreating sides (see Figs. 2.17 and 2.18). A temperature gradient from top (crown) to bottom (root) of the weld also exists. Combination of these factors results in property variations and defect formation for welds outside the process window. Right from the early days of friction stir welding, a relative language of 'hot' and 'cold' runs developed. It is easy to visualize these in terms of tool rotation

R.S. Mishra et al., *Friction Stir Welding and Processing: Science and Engineering*,
DOI 10.1007/978-3-319-07043-8_4,

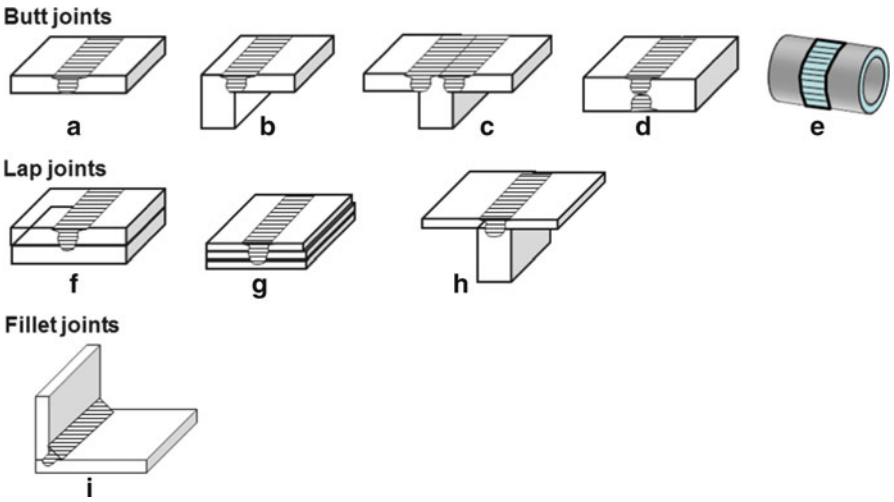

Fig. 4.1 Joint configurations for friction stir welding: (**a**) single side square butt, (**b**) edge butt, (**c**) T butt joint, (**d**) double side square butt used for thick plates, (**e**) tubular welds with single side butt joint, (**f**) lap joint, (**g**) multiple lap joint, (**h**) T lap joint, and (**i**) fillet joint

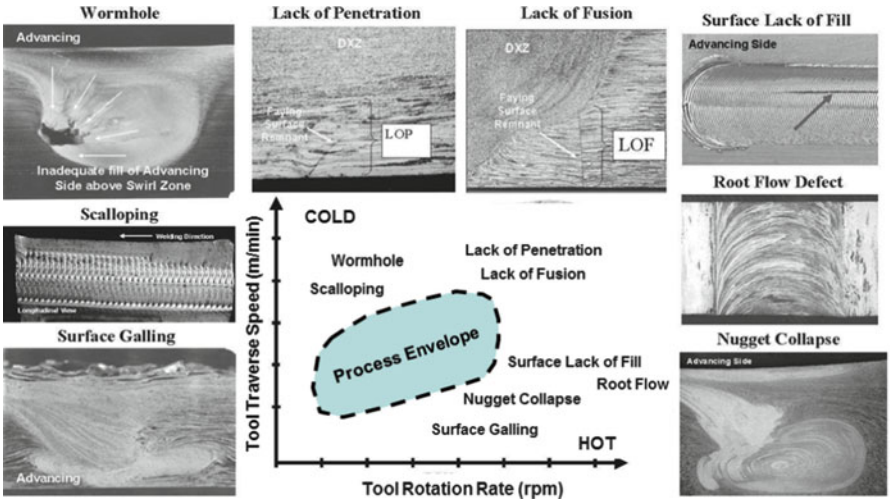

Fig. 4.2 Relationship of regions of various defect types with process envelope for defect-free welding (Arbegast 2007, reprinted with permission from Elsevier)

rate and tool traverse speed. As the tool rotates at higher rate, more heat energy is transferred to the workpiece (see Fig. 2.5). Conversely, faster tool traverse speed reduces the time to build up heat. In fact, in many ways friction stir process is 'self-regulating'. The optimum process window for a given tool can be small for difficult to flow materials. Figure 4.2 shows a defect formation map from Arbegast (2007).

The map is for conceptual illustration purposes and it is possible to observe exceptions to this based on the features of the tool. The defects can be broadly classified as, (a) material flow related, (b) geometrical aspect related, and (c) lack of surface constraint related. Wormhole formation at the bottom of the advancing side is quite common and clearly results from lack of material flow. In Fig. 4.2 it is represented as a 'cold' run defect. It should be noted that changing the pin profile from cylindrical to conical reduces this defect. So, the readers should use this map as a first level conceptual tool and expect to see defects in other regions of the chart depending on the tool, workpiece material and process conditions.

The surface lack of fill defect results primarily from lack of constraint from tool shoulder where the hot material finds it easier to flow out and form flash than to be constrained under the shoulder and complete the proper material flow. On the other hand, the defects listed for regions under the pin have more of a geometrical nature. For example, in butt weld configurations, the runs are made in so called kissing pass mode. That is, the bottom of the pin is close to the anvil but not too close. The material flow under the pin is responsible for removing the original faying surface. For colder runs, the material flow under the pin is very limited and it will lead to lack of penetration defect. Similarly, if the tool pin is not centered properly, the remaining faying surface may not bond completely or get forged tightly together. This can be a particular concern for robotic friction stir welding where the lower stiffness of robotic arm may result in inaccurate tool position for colder runs with significant lateral forces.

The butt weld joints shown in Fig. 4.1b, c have concerns with support from the bottom. If the anvil is designed to provide complete support, then the material flow and temperature issues are similar to the conventional flat butt weld. However, if it is not possible to fully support the bottom surface, then colder runs are likely to result in better runs as the bottom part of the workpiece becomes self-supporting. The double sided butt welds (Fig. 4.1d) are similar to single sided butt weld for all the mechanical aspects of friction stir welding. Metallurgically, it produces a region of heat affected zone in the overlapping area. The circular welding of tube in butt weld configuration (Fig. 4.1e) needs both mechanical and metallurgical consideration. A hollow tube that cannot be internally supported would require pin length to be shorter than the tube wall thickness. Again, colder runs would be more favorable as it will support the forging load (vertical force) that the tool applies. A more critical issue is the exit hole with traditional friction stir welding tool. If an exit hole is allowed by the designer, then the runs do not require much extra attention other than the tilt angle incorporation by using an offset at the place where tool is plunged. That is, instead of using plunge at the top of the tube, the plunge can be slightly offset to include the tilt angle. On the other hand, if an exit hole is unacceptable as a part of the component, then a ramp approach can be used to take the tradition fixed pin tool off from the tube surface. Such approaches are more of engineering challenge and don't have any fundamental process barrier.

The lap joints in friction stir welding (Fig. 4.1f–h) create some non-intuitive material flow related issues. Again, in the early days of the friction stir welding, it was not realized that material from quadrant I (leading-advancing side) gets

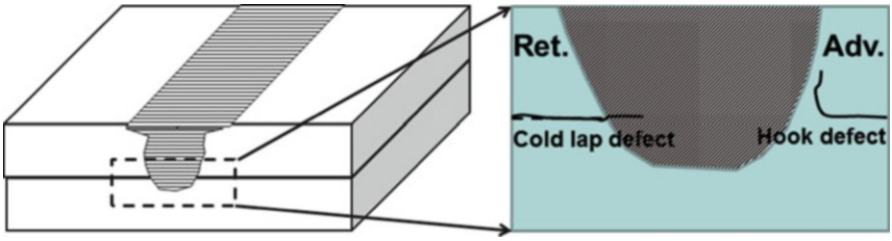

Fig. 4.3 Examples of faying surface related basic defect formation in friction stir lap welds, (**a**) cold lap defect, and (**b**) hook formation

deposited in quadrant IV (trailing-advancing side) (see Fig. 2.17a, b). This aspect of material flow and the processing strain gradient across the nugget from retreating to advancing side leads to two basic types of defects in lap welds, shown in Fig. 4.3. The advancing side hook defect formation is shown here in much more pronounced way to highlight this. The level of this does depend on the processing details, particularly the type of features on pin. A key fundamental aspect is that if one measures the length of the hook feature and extrapolates linearly along the original faying surface, it will extend in the space occupied by the nugget region. An interpretation of this is related to the oxide film at the faying surface being pushed out to the advancing side. Details of this can be understood in the following basic steps. First, the material incorporating the faying surface ahead of the pin is pushed up because of the combination of force and higher space at the leading side for friction stir runs with titled tools (of course, this won't apply to 0° tilt runs). Some part of the lifted faying surface near the advancing side then is pushed backward on the advancing side and finally forged down at the trailing side to give the final appearance. On the other hand, the faying surface that gets broken on the retreating side gets deposited behind the tool close to the original faying surface location. This cold lap defect extends inside the nugget. These defects have important implications on the performance of the joint and mechanics of crack growth during lap shear test can dominate the microstructural aspects. Some comments have been made later in this chapter regarding the control of these defects with selection of pin features and shoulder geometry.

In the discussion of the lap joints, the material flow related defect formation was not revisited, but as in butt welds all the material flow related volumetric defects like worm hole and surface breaking lack of fill defects are possible. The fillet weld (Fig. 4.1i) is a special case where keeping with the autogenous nature of the process, an inclined region has to be present to support the shoulder. This type of joint has not been pursued much, particularly in the published work. It is also possible to come up with many other configurations but the discussion of the joints shown in Fig. 4.1 allows conceptual grasp of various type of the joints. Next we discuss the tool types and some common basic features.

4.2 Tool Material Selection

In this section we discuss the basic conceptual approach of tool material selection and then build towards the tool features and the framework for selection. The idea is to provide a foundational discussion which would then allow the readers and researchers to develop their own detailed formulation for such exercise.

Figure 1.4 schematically shows tool and labels different part of a friction stir welding tool along with illustration of the friction stir welding process. The tool has been shown again in Fig. 4.4 and illustrates the different aspects of the tool vividly.

At the start of the friction stir process, a 'cold tool' plunges into a 'cold workpiece'. Figure 2.1 illustrates the variation in plunge force at different stages of friction stir welding. A sharp rise in plunge force should be noted during tool plunge into the workpiece. Therefore, this initial period is very demanding for the tool. Figure 4.5 shows a very simplistic approach to this discussion. Let us pick two workpiece examples for this discussion, (a) an aluminum alloy, and (b) a titanium alloy. The aluminum alloy represents a lower melting temperature material, and it is possible to find a large number of metallic alloys that are comparatively stronger (Refer to Table 5.6 and Table 6.2 for tool materials used in the processing of Al- and Mg-based alloys). The tool material needs six basic characteristics, (1) strength at ambient temperature and process temperature, (2) fatigue life at process temperature, (3) fracture toughness, (4) wear characteristics, (5) long term thermal stability, and (6) chemical stability (no or limited reaction with workpiece). In the case of aluminum alloys, popular tool materials have been H13 tool steel and MP159 cobalt base superalloy. Both these tool materials would be classified as tool material A type in Fig. 4.5. That is, their strength is higher than the workpiece at all temperatures. The tool material can still have issues. Wear is a particular concern and weaker material can still induce wear particularly in certain condition. An illustrative example is wear of tool materials during very long welds of AA5083 alloy. Based on the quality of AA5083 alloy, it can have a significant volume fraction of constituent particles, which are hard intermetallic phases. These can inflict significant wear on the tool pin, particularly the features on the pin. Another critical

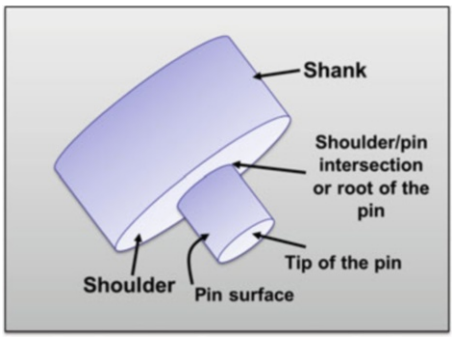

Fig. 4.4 A friction stir welding tool

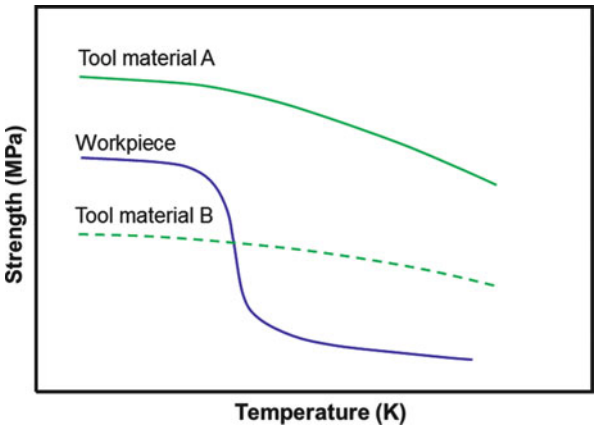

Fig. 4.5 An illustration of variation of strength of material with temperature

aspect of tool in industrial setting is life. Unlike the research setting where a number of short runs are made to develop the process for a particular configuration, production runs involves miles of runs with a tool. Here, fatigue properties become very important. A simple example can be discussed using AA5083 alloy. AA5083 or AA 5XXX alloys are used for flat deck applications in ships. This was one of the initial applications of friction stir welding. It we consider that the tool temperature reaches 500 °C, one can calculate the stress at the pin root based on the lateral load on the pin. If the tool is made of H13 tool steel, one can find the life for the calculated peak stress at pin root by taking the S-N curve data at 500 °C.

The tool material selection becomes more challenging for high temperature materials, like steels, nickel base alloys and titanium alloys. For this discussion, let us consider titanium alloys. This will be discussed further in high temperature chapter, but at this stage a basic context can be developed. Two types of tool materials have been used by a number of researchers and we will consider those for this example, (a) WC-Co cermet tools, and (b) W-La_2O_3 tools. The strength of WC-Co tool is higher than the titanium alloys at all temperatures, and, therefore, this combination would be tool material A and workpiece. On the other hand, the W-La_2O_3 alloy is not stronger than titanium alloys at room temperature; however, at high temperature strength is higher. So, this combination would be tool material B and workpiece in Fig. 4.5. In this case the major concern for the tool is in the plunge stage. The plunge rate should be such that the titanium alloy is heating at temperature where it is weaker than the W-La_2O_3 alloy. Overall, tool deformation and wear are major concerns. For all high temperature tool materials wear and reactivity comes into play, sometimes together. This is particularly so when wear mechanisms are linked with reaction of tool material with workpiece or atmospheric oxygen and subsequent removal of reaction product(s) from the tool surface under shear forces. Reaction products like WO_3 vaporizes on formation which will leave the surface of tool made of W always exposed to atmospheric oxygen. Ellingham diagram is an effective way of knowing relative tendency of the formation and stability of oxides of various pure metals. It is shown in Fig. 4.6.

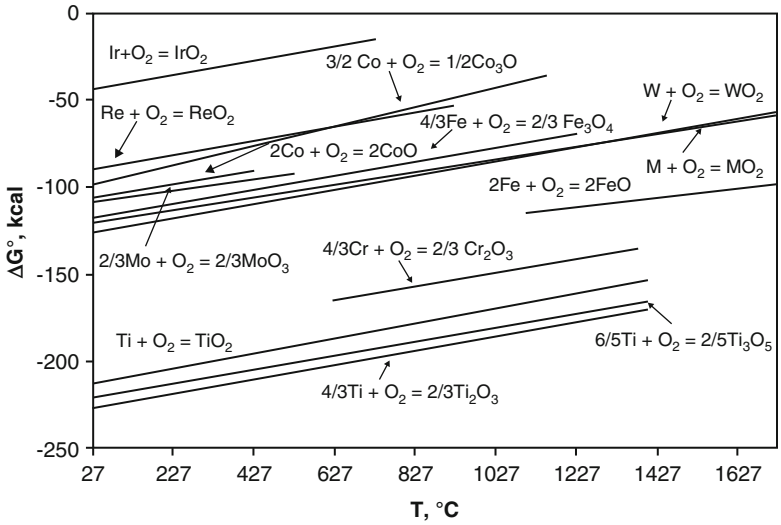

Fig. 4.6 Ellingham diagram showing relative tendency of formation and stability of high melting point pure metals

The coupling between the workpiece and tool material also depends on the surface interaction and the resultant ***friction***. Although, a qualitative dependence can be deduced between the tool material-workpiece coupling and nugget size, no framework exists for proper discussion for tool material selection. In general, ceramic and cermet tools result in smaller nugget size, implication being that the friction coefficient is lower and the shear layer is thinner. Table 4.1 summarizes different attributes expected in different class of materials commonly used as tool material.

4.3 Tool Features

Tool geometry and features are the most important ways of controlling material flow. Figure 4.7 shows very simple framework for discussion. Mishra and Ma (2005) and Fuller (2007) have reviewed tool features and readers should follow up with those reviews to get some more idea of the extent of possibilities. The present discussion is focused on a few illustrative examples towards the basics of tool design and resultant material flow.

As mentioned in the previous chapter, the tool shoulder has maximum impact on the temperature. The shoulder also restrains plasticized workpiece material from flowing out. Some of the original tool designs used to use a tool shoulder diameter to pin diameter ratio of 4:1. The recent trend is to lower the ratio in the range of 3:1 to 2:1 to control the heat input. Conventionally, the shoulder used can be flat,

Table 4.1 Tool materials and their attributes (*Source*: ASM Handbook, Vol 6A, Welding fundamentals and Processes, T. Lienert et al (Eds.), Friction Stir Welding Tool Designs by Carl D. Sorensen, reprinted with permission from ASM International)

	Tool material class				
Material attributes	Tool steels	Superalloys	Refractory metals	Carbides, cermets, and ceramics	Superabrasives
Strength (room temperature)	Good	Excellent	Excellent	Excellent	Excellent
Strength (at processing temperature)	Good	Very good	Excellent	Good	Excellent
Fatigue strength	Very good	Excellent	Very good	Excellent	Very good
Fracture toughness	Very good	Very good	Very good	Good	Poor to good
Wear resistance	Good	Good	Very good	Good	Excellent
Chemical inertness	Good	Very good	Good	Good	Excellent
Availability	Excellent	Very good	Very good	Very good	Very good
Cost	Excellent	Very good	Poor to acceptable	Good	Poor to acceptable

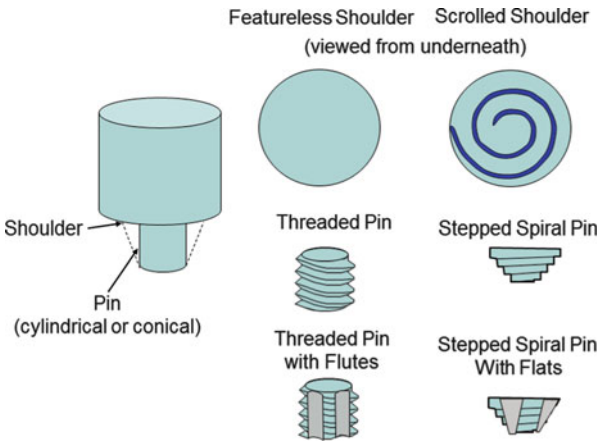

Fig. 4.7 An illustration of basic tool shoulder and pin features

concave (very common) or convex (has to have scroll). A featureless shoulder is used for runs with tool tilt angle. That means there is more open room in front of the tool, and the back of the tool does the forging of material behind the pin. The front part of the shoulder is preheating the workpiece, and the depth to which workpiece gets heated-up will vary based on the thermal conductivity of the workpiece. Ideally, the material in front of the pin should be preheated to the temperature where its flow stress decreases sufficiently to keep the tool forces low. Because of the temperature gradient from the root of pin to tip of the pin, the workpiece strength is highest at the bottom of the pin. The pin gets loaded like a cantilever beam, and rotating fatigue that the pin experiences in very similar to a rotating

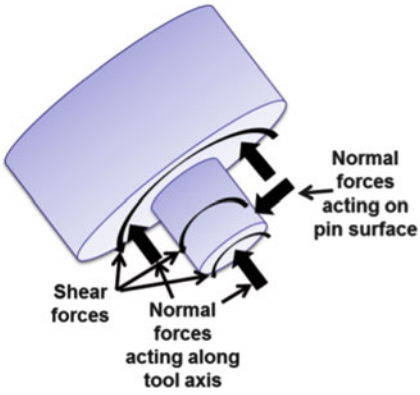

Fig. 4.8 A simplified pictorial representation of various forces acting on different regions of a friction stir welding tool

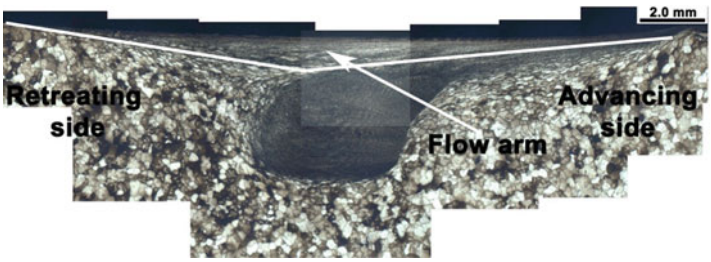

Fig. 4.9 Flow arm present in cast A201 (Al-Cu alloy). The processing of the material was carried out at tool rotation rate 1,000 rpm, tool traverse speed 1.7 mm/s, tool tilt angle 2.5°, and plunge depth ~3.5 mm; Etchant used to reveal the grain structure: Tucker's reagent

beam bending fatigue specimen. Therefore, most of the time pin failure occurs at the root of the pin. To aid readers visualize various forces acting on the tool, a schematic of the tool has been shown in Fig. 4.8. It shows shear and normal forces acting on the shoulder and tip of pin. On cylindrical surface, normal forces are acting opposite to the direction of the tool movement. It should be noted that this normal force on the vertical surface of the tool would be acting over the entire length of the pin. The distribution and magnitude of such forces would be heavily influenced by a large number of friction stir welding parameters.

Getting back to the shoulder's influence on the material flow, the shear forces (refer back to Chap. 2) of a featureless shoulder would tend to push the material at an inclined angle. The overall impact of shoulder influenced flow can be quite large. For example, for relatively hotter runs, the shoulder can move the material from retreating side to behind the pin at the top. This is the origin of nugget shape with a top flow arm going towards the advancing side. An example of it is shown in Fig. 4.9.

The scrolls on a flat shoulder can be machined as positive (feature extending out from the surface) or negative. Conceptually both types help in bringing the material inward. This has major impact on reducing the volumetric defects that were

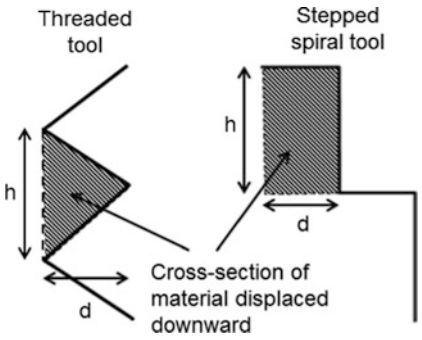

Fig. 4.10 Illustration of displacement of volume by pin feature for a threaded tool and stepped spiral tool

discussed in relation with material flow. The workpiece material is restricted from flowing out even for hotter runs. Additionally, the scroll shoulder tools can be run without tilt, which is very helpful for runs on curved surfaces. However, to stabilize mechanical stability of the tool, it is better to run with some tilt angle (0.25–0.5°). The convex shoulder scrolls are always negative. The convex shoulder tool is designed to accommodate slight various in sheet thickness of the material. Because of its geometry, the region of workpiece surface engaged with tool shoulder varies.

The pin shape and features on the pin greatly influence the material flow. Two common pin shapes are, cylindrical and truncated conical. Pin features are primarily added to promote vertical flow of material besides breaking up the flow as will be discussed later in this section. First, let us consider the vertical flow. The pin length for such discussion needs to be considerably longer than the shoulder induced shear layer thickness. Therefore, all the discussion to follow will be for pin length 3 mm and longer. For a featureless cylindrical pin, while the material flows from front of the pin to the back, there is no downward push. Such tools have very small region for good runs. Changing the pin profile from cylindrical to truncated conical create some resolved downward force component and therefore, downward material flow. This aspect is critical for high temperature materials. For example, some of the work on titanium alloys is done with WC cermet tools and generally these are featureless. Generally the conical profile results in better process window. The stress at the tip of the pin during plunge cycle can be simply estimated by considering the plunge force and contact area. Comparison of this stress with the flow stress of the tool material at temperature of friction stir can give an indication of chances of pin deformation or failure. Mushrooming of W based tool is often observed when used for high temperature materials.

The next part of the tool pin discussion is the selection of features. Let us examine the threaded pin profile and compare that with the stepped spiral profile. Figure 4.10 shows an illustration of displaced volume by a pin feature for threaded tool and stepped spiral tool. The marked cross-section is the area that is displaced downwards in each rotation. This displaced volume can be approximated by considering an effective radius (the rigorous calculation should use inner and outer radii of the pin using the feature depth). This volume for a pin with outer radius of R and inner radius of r would be,

$$\frac{1}{2}h \times d \times \left(2\,\pi\left(\frac{R+r}{2}\right)\right) \quad \text{for threaded tool, and} \tag{4.1a}$$

$$h \times d \times \left(2\,\pi\left(\frac{R+r}{2}\right)\right) \quad \text{for stepped spiral tool.} \tag{4.1b}$$

where h is thread pitch or step height and $d = (h^2/4 + (R-r)^2)^{1/2}$ for threaded tool or width of the step for stepped spiral tool. At first glance with this approximate estimate, it is clear that the stepped spiral will have larger downward throw of material (by a factor of two for stepped spiral tool in comparison with threaded tool). This downward flow of material can be compared with the horizontally displaced volume by the forward motion of the tool. The horizontally displaced volume will be the same for both the features selected here. A rough estimate of the horizontally displaced volume for one revolution of tool can be given as

$$h \times \frac{tool\ traverse\ rate\ in\ mm/min}{too\ rotation\ rate\ in\ rpm} \times \left(2\,\pi\left(\frac{R+r}{2}\right)\right) \quad \text{for both type of tools.} \tag{4.2}$$

Comparison of the horizontally displaced volume (Eq. (4.2)) with vertically displaced volume (Eq. (4.1)) gives a preliminary idea about extent of mixing of material during the run. The ratio in Eq. (4.2) tool traverse rate/tool rotation rate is termed as advanced per revolution (APR).Hence, dividing Eq. (4.2) by Eq. (4.1), we get $\alpha(APR)/d$ where α is equal to 1 for stepped spiral tool and 2 for threaded one. This is particularly important relationship for friction stir processing where microstructural uniformity and intense mixing may be desired. Even for friction stir welding, such a simple calculation can allow a correlation between the nugget profile with process parameters. From this relationship, it is evident that

$$\alpha(APR)/d < 1 \tag{4.3}$$

would be required for vertical component of the material volume to be larger than that of horizontal component.

Next consideration is that of additional features on the pin. Again, the intent is not to be comprehensive but illustrative, so that the readers can interpret various reported results that they will come across. In the preceding paragraphs, we established some faying surface related defect formation and we considered horizontal and vertical displacement of material as a result of tool traverse and tool rotation. For many joints it is desirable to break up the faying surface so that the indications of remnant oxide film are not detectable during cross-section examination. Figure 4.7 shows two additional features marked flats and flutes. The concept behind this is to disrupt the material flow as much as possible. When a threaded or a spiral tool is displacing material, the flow can be monotonic. By putting the flats or flutes, two things happen. First, as the additional features rotate, the horizontal

Table 4.2 The key tool features and the different design variations incorporated by researchers and the possible advantages of using the features (Fuller 2007)

Tool feature	Design variation		Advantage
Shoulder	Convex with scroll	Curved geometry	Allows joining of different thickness work-pieces. Scroll contains material within shoulder
		Tapered geometry	-do-
	Concave (standard design)	Smooth surface	Concavity preserves material within shoulder region. Requires tool tilt.
		Scrolled surface	Allows welding without tool tilt. Minimizes normal tool force and thickness reduction in weld zone.
Pin	Cylindrical	Flat bottom	Easier too machine. Commonly used design
		Round bottom	Reduces tool wear during plunge and improves joining at weld root.
		With flats	Increased plastic strain and temperature in nugget region
	Conical	Threaded cone	Low transverse force compared to cylindrical pins.
		Stepped spiral	Robust design and used for high temperature materials welding
		With flats	Increased plastic strain and temperature in nugget region
	Whorl		Reduces transverse force on tool
	MX Triflute		Refined version of whorl pin
	Threadless		Useful in aggressive tool wear situation
	Retractable		Allows closure of exit hole

cross-section can be visualized to pulsate and the surface flow is affected by local volume. Second, the continuity of the downward flow is broken. In the earlier discussion, we considered the material in the thread or spiral feature moves downwards in a continuous fashion. Although the reality has more complications, for the basic treatment here we ignore those. By incorporating additional features, the material in the thread or the spiral is forced to come out and get displaced discontinuously because of the additional features.

In Table 4.2, variety of tool design features developed and the apparent implications of these features on the welding process are summarized.

The last aspect of this short discussion is the importance of sticking of workpiece material at the tool surface. Let us consider the threaded tool again. If the workpiece material has good affinity for sticking to the tool, then the shear forces that would result in continuous displacement of material downwards may not be sufficient. In this case the primary tool pin feature would lose its effectiveness. The guideline then would be to make features that have larger shear forces at the tool/workpiece interface. For example, a coarser thread would be better than finer thread (Eq. (4.3)). If the threads become ‘gummed’ up, then the pin would effectively behave as a cylinder!

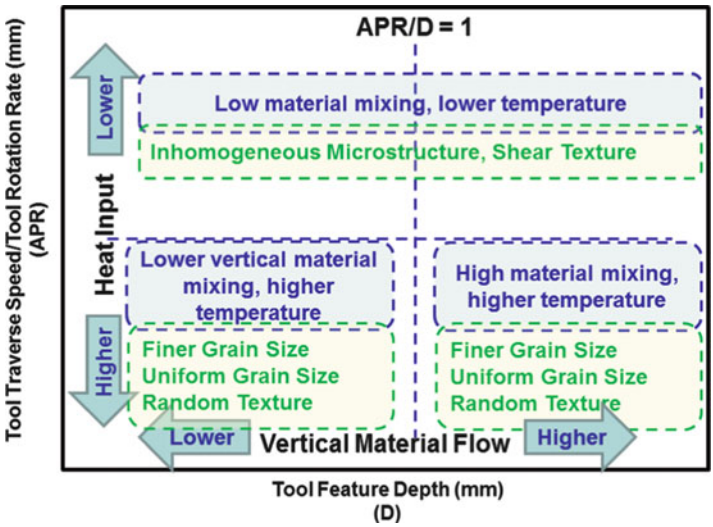

Fig. 4.11 An example of conceptual map showing various domains as a function of process parameter and tool feature

4.4 A Conceptual Process Map with Microstructural Domains

At this stage a generic map can be visualized. The readers are cautioned that the boundaries of these domains are intended to just help with the thought process regarding tool feature design and process parameter selection. They should be guided by the overall goal of a particular friction stir welding or processing runs. Figure 4.11 shows a version that highlights domains of material mixing coupled with heat input and likely microstructural evolution. Of course, systematic work would be needed for quantitative develop such maps with well-defined domains. These maps will also be material dependent as the rate of recovery, recrystallization and grain growth will dictate the final microstructure.

Additional Reading

A. Arora, M. Mehta, A. De, T. DebRoy, Load bearing capacity of tool pin during friction stir welding. Int. J. Adv. Manuf. Technol. **61**, 911–920 (2012)

T. DebRoy, A. De, H.K.D.H. Bhadeshia, V.D. Manvatkar, A. Arora, Tool durability map s for friction stir welding of an aluminum alloy. Proc. R. Soc. A **468**, 3552–3570 (2012). doi:10.1098/rspa.2012.0270

C.B. Fuller, Friction stir tooling: tool materials and design, Ch. 2, in Friction Stir Welding and Processing, ed. by R.S. Mishra, M.W. Mahoney (ASM International, Materials Park, OH, 2007), pp. 7–35

M. Mehta, A. Arora, A. De, T. DebRoy, Tool geometry for friction stir welding—optimum shoulder diameter. Metall. Mater. Trans. A **42**, 2716–2722 (2011)
R. Rai, A. De, H.K.D.H. Bhadeshia, T. DebRoy, Review: friction stir welding. Sci. Technol. Weld. Join. **16**, 325–342 (2011)
C.D. Sorensen, Friction stir welding tool designs, in *Welding Fundamentals and Processes*, ed. by T. Lienert et al., vol. 6A (ASM Handbook, Novelty, OH, 2011)
Y.N. Zhang, X. Cao, S. Larose, P. Wanjara, Review of tools for friction stir welding and processing. Can. Metall. Quart. **51**, 250–261 (2012)

References

W.J. Arbegast, Application of friction stir welding and related technologies, Ch. 13, in *Friction Stir Welding and Processing*, ed. by R.S. Mishra, M.W. Mahoney (ASM International, Materials Park, OH, 2007), pp. 273–308
C.B. Fuller, Friction stir tooling: tool materials and design, Ch. 2, in *Friction Stir Welding and Processing*, ed. by R.S. Mishra, M.W. Mahoney (ASM International, Materials Park, OH, 2007), pp. 7–35
R.S. Mishra, Z.Y. Ma, Friction stir welding and processing. Mater. Sci. Eng. R **50**, 1–78 (2005)
C.D. Sorensen, Friction stir welding tool designs, in *Welding Fundamentals and Processes*, ed. by T. Lienert et al., vol. 6A (ASM Handbook, Novelty, OH, 2011)

Chapter 5
FSW of Aluminum Alloys

Aluminum, the third largest element available on the earth's crust is the second highest consumed metal by weight and stands a distant second to iron and its alloys. The lower consumption by weight is in a large part a consequence of its low density, and is one of the prime advantages of this metal. This low density combined with the attractive strength properties of modern Al alloys makes it ideal for structural applications. The other distinctive properties of Al and its alloys include high ductility, low electrical resistance and high corrosion resistance. Such combination of desirable properties along with low density makes Al and its alloys an ideal replacement for steel, though the relatively high cost and low weldability has limited its scope to more niche applications.

The high cost of Aluminum and its alloys is primarily on account of the energy intensive extraction process which is envisaged to be countered by an efficient recycling process in the near future (Green 2007). The low weldability on the other hand is a consequence of its intrinsic oxidative character which makes economical fusion based joining methods inefficient to use. The invention of friction stir process has changed this scenario making Al alloy joining a much simpler activity. The rest of this chapter discusses the application of FSW process to different Al alloys and the microstructural/mechanical/corrosion characteristics of such joints.

5.1 Al Alloys: Background

Pure Al, is a silvery white metal of high electrical conductivity the practical application of which is however very limited. In Table 5.1 the strength of polycrystalline pure Al is presented. As is evident, despite a high ductility, the mechanical strength of such pure Al is low making it structurally unusable. Consequently, Al is used mostly in an alloyed form where the different alloying elements, imparts the desired mechanical strength. In Fig. 5.1 the different alloying elements and the combinations used are shown. These alloying elements exist in solid solution or as secondary phases impeding dislocation motion which increases the yield and tensile

R.S. Mishra et al., *Friction Stir Welding and Processing: Science and Engineering*,
DOI 10.1007/978-3-319-07043-8_5,

Table 5.1 The yield and tensile strength of pure Al (adapted from Hatch 1984)

Al (% purity)	Yield strength (MPa)	Tensile strength (MPa)
99.6 % (polycrystalline)	30	70

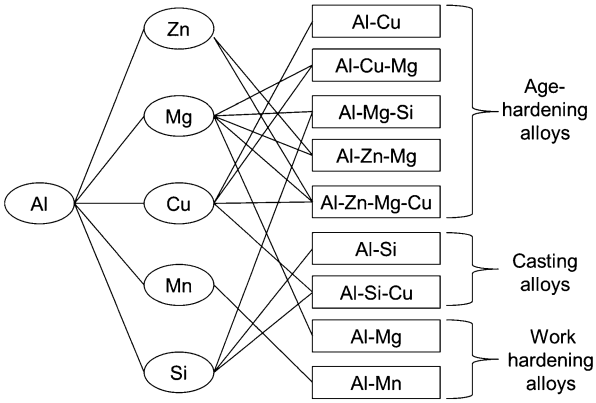

Fig. 5.1 Different combinations of elements used in Al alloys for the purpose of strengthening (Adapted from Hatch (1984))

Table 5.2 The commercial designations of "Aluminum Association" for different Al alloys

AA designation	Possible composition of the alloy (Al base, with next major alloying elements in following order)
2XXX	Al-Cu; Al-Cu-Mg
3XXX	Al-Mn
4XXX	Al-Si
5XXX	Al-Mg
6XXX	Al-Mg-Si
7XXX	Al-Zn-Mg; Al-Zn-Mg-Cu

strength of Al rendering it into a mechanically usable form. A third group of Al alloys are the Al-Si and Al-Si-Cu type where strengthening is achieved through a combination of finely dispersed Si eutectic phase and precipitation processes. The Al alloys strengthened through solid solution process are categorized as "work-hardening" alloys while those strengthened through precipitation are known as the "heat treatable" alloys (see Fig. 5.1). Additionally, the solute and secondary phases present restricts the grain boundary movement (both low and high angle) which inhibits recrystallization and grain growth improving the high temperature performance of such alloys (see Chap. 3).

In Table 5.2 the commercial designation of (Aluminum Association (AA)) of different Al alloys are presented. Based on the strengthening levels achieved the work-hardened and precipitation strengthened alloys are further classified into different tempers. Thus, 3XXX and 5XXX Al alloys strengthened by imparting

Table 5.3 Temper designations applicable for 3XXX and 5XXX series Al alloys (adapted from Hatch 1984)

Temper designation	Treatment sequence
F	In as fabricated state (mechanical property variable)
O	Annealed and has the lowest strength
H1	Work hardened. The degree of work-hardening is indicated by the second digit where strength increases in the following order H12, H14, H16, H18. The hardening at H18 is equivalent to that obtained after 75 % reduction in area
H2	Work hardened → partially annealed. The degree of strength is indicated by the second digit and increases in the following order H22, H24, H26, H28
H3	Work hardened → partially stabilized by heating to low temperatures. The degree of strength is indicated by second digit and increases in the following order H32, H34, H36, H38
H112	Work hardened during the fabrication process itself. The product requires to meet minimum mechanical property requirement
H321	Work hardened during fabrication process by controlling the hot and cold working processes
H116	Special work hardening temper which is corrosion resistant

Table 5.4 The different temper designations applicable for 2XXX, 6XXX and 7XXX Al alloys (adapted from Hatch 1984)

Temper designation	Treatment sequence
F	In as fabricated state (mechanical property variable)
O	Annealed and has the lowest strength
W	After solution heat treatment and applies to alloys which age significantly at room temperatures
T	All other heat treatments (except F, O, W) which produces stable tempers
T1	Cooled from an elevated temperature shaping process → naturally aged to stable temper
T2	Cooled from an elevated temperature shaping process → cold worked → naturally aged to stable temper
T3	Solution heat-treated → cold worked → naturally aged to stable temper
T4	Solution heat treated → naturally aged to stable temper
T5	Cooled from an elevated temperature shaping process → artificially aged
T6	Solution heat treated → artificially aged
T7	Solution heat treated → aged beyond the maximum strength
T8	Solution heat treated → cold worked → artificially aged
T9	Solution heat treated → artificially aged → cold worked
T10	Cooled from an elevated temperature shaping process → cold worked → artificially aged

mechanical strain (i.e. work hardening) to the products (in the form of sheets or plates) are assigned tempers ranging from H1 to H3 as shown in Table 5.3. The different temper designations for 2XXX, 6XXX and 7XXX alloys strengthened through a combination of solutionizing and aging heat treatment are given in Table 5.4. Evidently, the choice of product temper depends on the property

requirements for a particular application. The use of processes like FSW however, changes the temper characteristics in and around the joined region. Understanding these unavoidable microstructural changes occurring during friction stir process is therefore of critical importance and will be a matter of discussion in this chapter.

5.2 Friction Stir Process of Aluminum Alloys

The principal FSW variables which are under operator control include tool design and the tool movement parameters. However, factors like machine characteristics, work-piece thickness and control mechanisms will also affect the weld quality. For example, everything remaining same (i.e. tool design, tool movement, work-piece thickness), a different welding machine will result in a finite possibility of weld quality variation. In this respect, the welding parameters for FSW behave as a typical "path variable". The reason for this is simple: no two welding machines are similar. Factors like machine stiffness, tool eccentricity and control precision will vary from one machine to another and in most published literature these aspects are unaccounted for. Nonetheless, in a repetitive welding scenario, development of a process envelop facilitates quality welding. In the next sub-sections the choice of FSW tool and possible methodology in selecting the tool movement parameters for Al alloys are discussed.

5.2.1 Friction Stir Welding Tool Design

Ideally, the choice of FSW tool design parameters (see Sect. 1.3 for definitions) needs to be derived from integrated thermo-mechanical and microstructure models. But, the lack of realistic models continue to be a roadblock in this effort and tool design still continues to be empirical/semi-empirical in nature. In Table 4.2, a variety of tool design features developed and the apparent implications of these features on the welding process are summarized.

The materials commonly used for FSW of Al alloys are tool steels which possesses a combination of high temperature strength and toughness. The choice is determined partly by the approximate temperature reached during welding of Al alloys (~400–500 °C). Therefore, any tool steel with a tempering temperature higher than 500 °C is an ideal choice. The other aspect to consider is the peak force achieved during tool plunge which is a combination of compressive and tensile forces. This can lead to tool breakage especially in concave shoulder tools which requires a tilted orientation for its operation. In Table 5.5 the tempering temperature and hardness for two commonly used tool materials are given. The ultimate choice is however determined by factors like (a) run length, (b) machinability of material vis-à-vis tool design complexity and (c) cost factors.

The other critical design factor is the dimension of the tool features like (a) shoulder diameter, (b) pin diameter and (c) pin length. Among the afore-

Table 5.5 The tempering temperatures, hardness and fracture toughness of some materials used to manufacture FSW tools

Material	Tempering temperature (°C)	Hardness	Hardening temperature (°C)	Reference
H13	540–650 for 1 h	29–50 HRC	995–1,040 °C	(Matweb)
MP159	663 for 4 h	1,895 MPa	1,038–1,052	(Latrobe)

Table 5.6 Dimensions of tool features used for different Aluminum alloys

Shoulder diameter (mm)	Pin diameter (mm)	Shoulder diameter/pin diameter	Material welded	Reference
20	7	2.8	6061 T6	Fahimpour et al. (2012)
16	6	2.7	2024 T6	Genevois et al. (2005)
18	5	3.6	5083 O	Peel et al. (2003)
10	4	2.5	5083 H18	Gan et al. (2008)
10	4	2.5	6111 T4	Gan et al. (2008)
23	8.2	2.8	2024 T3	Sutton et al. (2004)
19.1	7.87	2.4	7050 T7	Fuller et al. (2010)
10	3	3.3	6016 T4	Rodrigues et al. (2009)

mentioned design dimensions, the choice of pin length is the simplest and is determined by the thickness to be welded. As a rule of thumb, a pin length of approximately 0.85–0.95 of the work-piece thickness is used. The choice of shoulder and pin diameter is however complicated by factors like

(a) work-piece dimension (i.e. its capacity to act as a heat-sink)
(b) desired joint efficiency (i.e. joint strength as a fraction of the parent material strength)
(c) expected tool forces (i.e. mechanical integrity of tool)

In Table 5.6, some tool dimensions reported in published literature is reproduced. As it may be observed that the shoulder diameter varies over a wide range and is chiefly determined by (a) work-piece thickness, (b) work-piece dimensions. A higher work-piece thickness entails a higher shoulder diameter, so that sufficient heat to plasticize the metal through work-piece thickness is generated. Similarly, for the same work-piece thickness, larger overall dimensions will result in a higher heat loss. Again, for a given shoulder diameter, larger heat is generated at higher tool rotations and lower tool traverse speeds. Therefore, no straightforward method to estimate the optimum shoulder diameter exists.

Quite similarly, no quantitative methodology to determine the pin diameter exists. Ideally, a smaller pin diameter is preferable as it reduces the heat affected zone dimensions. On the other hand, a smaller pin is more prone to fracture, especially during the initial plunging period when the axial force on the pin is at its highest. Thus, as a rule of thumb a pin diameter of approximately 1/3 the shoulder diameter is usually used. Accurate modeling/simulation of FSW is however expected to reduce these uncertainties about tool design in the future.

5.2.2 FSW Operational Parameters

Once a tool is designed for a particular welding situation the selection of FSW operation parameters is the next step. A cursory glance at published literature shows that no clear-cut methodology exists in this regard. The choice of FSW operation parameters is therefore based on some broad objectives which can be expressed mathematically as

$$\text{Objective function} = \text{Maximize}\begin{Bmatrix}\text{joint efficiency}\\ \text{defect free weld}\\ \text{welding time}\end{Bmatrix}$$

where "joint efficiency" can be defined as the strength of the joint compared to the parent material where strength is defined either by tensile property or hardness. Defining the metric for "defect free weld" on the other hand involves the use of non-destructive testing methods like ultrasound technique and is more qualitative in nature. The "welding time" is important especially for extensive welding jobs a typical example of which maybe in the ship-building or aviation industry. For any practical welding operation the ultimate objective is the reliability of the weld which is achieved through a combination of the three functions mentioned above. At present no standard welding code is available in published literature to achieve the same. Thus, selection of process parameters is still determined based on experimental studies and is expected to be so in the near future.

5.3 Microstructure Evolution During FSW

As already mentioned, microstructure evolution determines the final joint properties after FSW. In the rest of this section the microstructure of different Al alloys and their evolution during FSW is discussed.

5.3.1 2XXX Alloys

The 2XXX series are a Cu based precipitation hardening alloy where the precipitates formed depends on the overall alloy composition. For pure Al-Cu alloys the precipitation sequence is given as,

$$\alpha(\text{Supersaturated}) \rightarrow \alpha + \text{G.P. zone} \rightarrow \alpha + \theta'' \rightarrow \alpha + \theta'$$

where α is the Al matrix phase while θ'' and θ' are the metastable phases. In Al-Cu-Mg alloys the precipitates depends on the Cu:Mg ratio. For a Cu:Mg ratio less than 5 (Bakavos et al. 2008; Ringer et al. 1996), the precipitation progresses as,

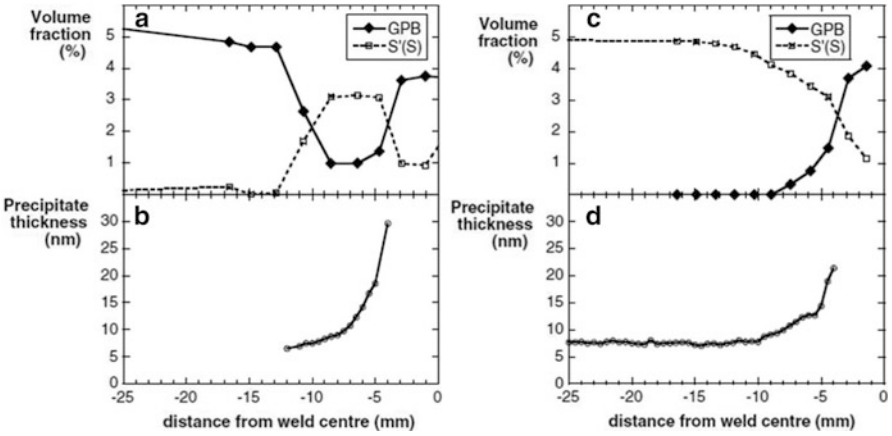

Fig. 5.2 Distribution of the different phases and their volume fractions at the advancing side of friction stir welded (**a**, **b**) AA2024-T351 and (**c**, **d**) AA2024-T6 alloy (Genevois et al. 2005, reprinted with permission from Elsevier)

$$\alpha(\text{Supersaturated}) \rightarrow \alpha + \text{Cu-Mg co-clusters} \rightarrow \alpha + \text{G.P. zone} \rightarrow \alpha + \text{S (Type I or Type II)}$$

where type-II is the stable incoherent phase. The semi-coherent type-I phase is formed when the solution treated and quenched alloy is cold worked before aging (Wang and Starink 2007). At higher Cu:Mg ratios the precipitation progresses as (Ringer et al. 1996),

$$\alpha(\text{Supersaturated}) \rightarrow \alpha + \text{G.P. zone} \rightarrow \alpha + \theta'' \rightarrow \alpha + \theta'$$

where for high Mg (>0.3 wt%) and Mg:Si ratio (>0.2) the θ' phase is converted to Ω phase which improves the hardening characteristics (Bakavos et al. 2008). Presence of Ag (~0.1 wt%) in such alloys further promotes the formation of Ω phase.

The bulk of FSW work on 2XXX alloys has been on AA2024 which is a Al-Cu-Mg alloy with low Cu:Mg ratio. Friction stir welding this alloy in T351 temper results in a nugget with GP zone microstructure, the fraction of which progressively reduces towards the TMAZ with a corresponding increase in the incoherent S phase. The absence of GP zone in the TMAZ indicates that the initial GP zone existing in the T3 state transform into the S phase. The GP zone fraction again increases towards the HAZ and reaches its maximum in the base metal (BM) region (Fig. 5.2) (Genevois et al. 2005). Similar investigations on AA2024-T6 alloy show a continuous decrease in the GP zone fraction from the base metal into the weld nugget with a corresponding increase in the S phase (Fig. 5.2) (Genevois et al. 2005). Another typical feature is the presence of metallurgical bands (onion ring structures) within the nugget region (see Chap. 2). Sutton et al. (2004) revealed that these bands in AA2024-T351 and AA2524-T351 alloys are due to periodic deposition of particles composed of Al, Cu, Mg and Fe indicating a constituent

particle type origin. These particles are associated with a fine grain microstructure which alternates with a band of coarse grained structure and can be observed in both transverse and longitudinal sections of the weld. The electron-backscattering diffraction (EBSD) studies on AA2024-T351 alloys indicate that these grains in the nugget region are composed of high angle grain boundaries which indicate a dynamic recrystallization type origin.

5.3.2 5XXX Alloys

As mentioned earlier, the 5XXX alloys are solid-solution hardened systems with Mg as the primary alloying element. The maximum Mg solubility in Al (14.9 wt% at 450 °C) determines the upper limit of solid-solution strengthening in such alloys. Further strength increases are determined by the temper of the alloy and is achieved by a combination of cold working/annealing (Table 5.3). Thus, essentially 5XXX alloys are of the single phase type, though some Al_3Mg_2 and Al_6Mn type dispersed second phases do exist. The Al_3Mg_2 phase forms both intra-granularly as well as at the grain boundaries and causes preferential Mg depletion in the grain boundary (Goswami et al. 2010). The Al_6Mn phase originates during the molten stage of Al extraction and is un-dissolvable in the solid state making it an effective dispersoid to prevent high temperature grain growth (for mechanism see Chap. 3). Additionally, depending on the alloy composition (especially Fe and Si content) other secondary phases can also form.

Friction stir welding of AA5083 (O temper) alloy results in a recrystallized nugget region where a considerable increase in size and volume fraction of the Al_6(MnFe) type dispersed phases is observed (Fig. 5.3) (Sato et al. 2001). This is ascribed to the growth and precipitation of these phases at the FSW temperatures (Sato et al. 2001).

Peel et al. (2003) investigated the grain boundary structures in AA5083-H19 alloy (i.e. cold worked) and noted that FSW leads to a dynamically recrystallized nugget microstructure. At regions beyond the nugget (~5 mm on either side including TMAZ and beyond) the microstructure consists of original dynamically recovered parent structure interspersed with localized recrystallized areas and is a consequence of the initial alloy temper. The dislocation density in H19 temper is highest which combined with the elevated temperature conditions of FSW initiates recrystallization in the nugget zone and beyond (Peel et al. 2003). Similar investigations on AA5083 alloy in the O temper reveals the presence of a dynamically recovered TMAZ zone only (Sato et al. 2001).

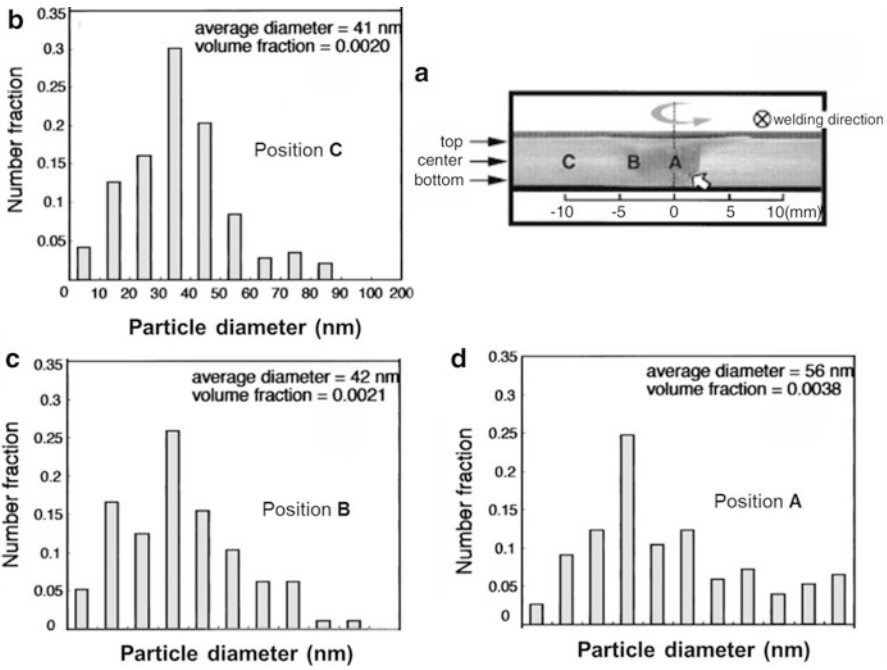

Fig. 5.3 The different positions (A, B, C) in a weld of AA5083 alloy (**a**) and the distribution of small particles (Al_6Mn type) at the different weld positions (**b**) at position C (**c**) at position B and (**d**) at position A. Note the particle coarsening and volume fraction increase in the nugget region (Sato et al. 2001, reprinted with permission from Springer)

5.3.3 6XXX Alloys

The Al-Mg-Si alloys are an important precipitation hardening system with application both in its wrought and cast form. The precipitation sequence in these alloys is given as,

$$\alpha(\text{super-saturated}) \rightarrow \text{G.P. zone} \rightarrow \beta''(\text{needle}) \rightarrow \beta'(\text{rod}) \rightarrow \beta(\text{platelet})$$

where β'', β' are the metastable precursor phases of the equilibrium phase β (Mg_2Si) and occurs for high Mg:Si ratios (>1.0) with the maximum strengthening obtained at the β'' precipitation stage (Edwards et al. 1994; Chakraborti and Laughlin 2004). At lower Mg:Si ratio Si is the equilibrium precipitate.

For 6XXX series alloys with high Mg:Si ratio and small Cu additions the precipitation sequence changes to,

$$\alpha(\text{super-saturated}) \rightarrow \text{G.P. zone} \rightarrow \beta'' \rightarrow Q' \rightarrow Q(\text{lath})$$

Friction stir welding of AA6063-T5 dissolves all β'' precipitates in the nugget while a few rod shaped precipitates remains un-dissolved in the TMAZ region

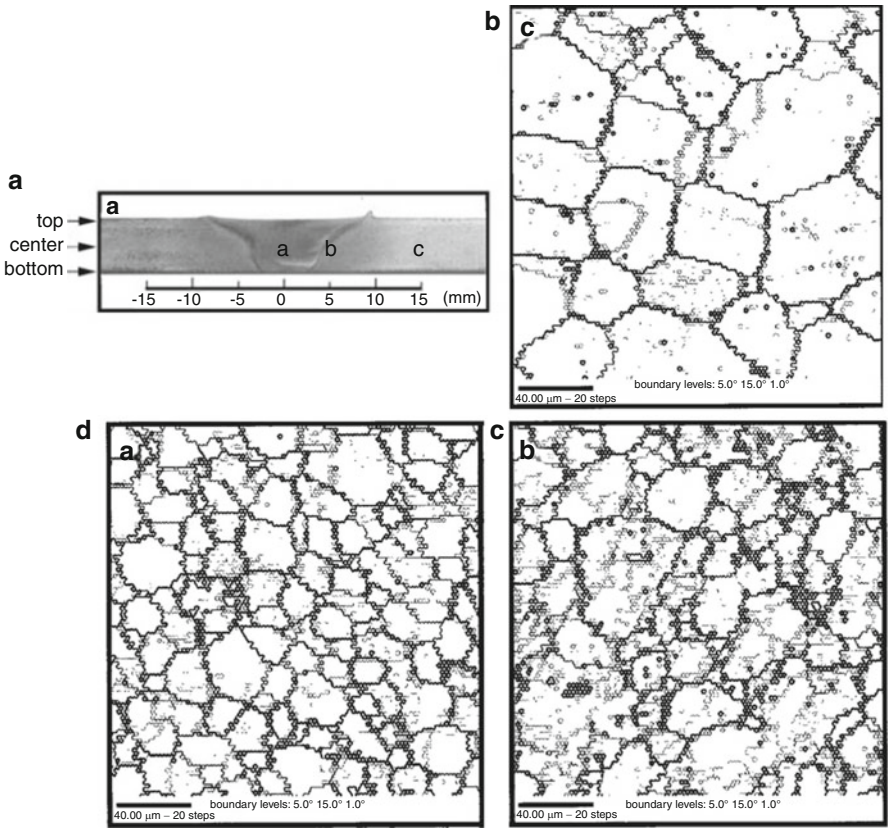

Fig. 5.4 (**a**) The different positions (a, b, c) in the weld of AA6063-T5 alloy. The microstructural maps shown in (**b**), (**c**) and (**d**) correspond to positions c, b, a and were obtained using Electron back-scattered diffraction technique. The *dark lines* are high angle grain boundaries and the *grey lines* indicate low angle grain boundaries (Sato et al. 1999a, reprinted with permission from Springer)

(Sato et al. 1999a). Post-weld aging results in re-precipitation of GP zone and β″ precipitates with resultant improvement in weld properties (Sato et al. 1999b). The volume fraction of precipitate formed is highest in the nugget followed by the TMAZ region. A more detailed discussion on the effect of post-weld aging is presented in Sect. 5.4.2. Detailed grain structure analysis of the AA6063-T5 weld suggests that the nugget comprises of a dynamically recrystallized zone which is surrounded by a dynamically recovered TMAZ followed by the base metal microstructure (Fig. 5.4).

The AA6063 alloy discussed above is a typical ternary Al-Mg-Si alloy of the high Mg:Si ratio type. Gallais et al. (2008) investigated the precipitate distribution after friction stir welding of AA6056 (T4 and T78 temper) which is a typical quaternary Al-Mg-Si-Cu alloy. For both tempers, the original needle shaped β″ precipitates (low volume fraction in T4 and more in T78) dissolves in the nugget zone giving rise to a single phase microstructure. The β″ precipitates in the HAZ are coarsened

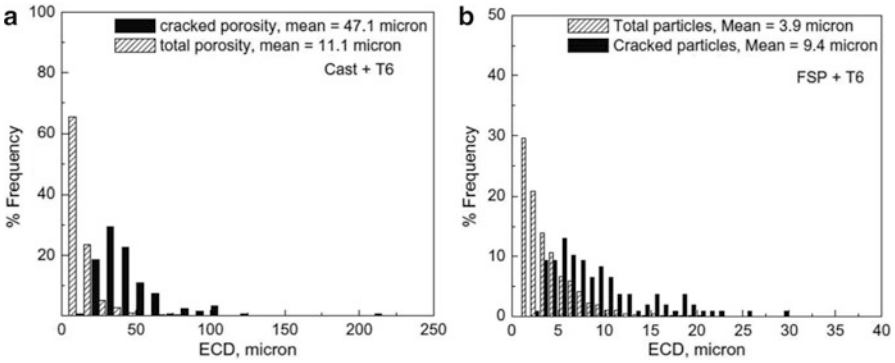

Fig. 5.5 (**a**) The porosity distribution in a as cast Al-Mg-Si alloy which acts as potential stress raisers during fatigue. After friction stir process the porosities are eliminated and the Si particles act as the controlling factor for crack initiation (**b**) distribution of Si particles after processing. The distribution of cracked porosities in (**a**) and particles in (**b**) show higher mean ECD. This clearly indicates that defects of higher size controls the fatigue property. (Jana et al. 2010, reprinted with permission from Elsevier)

compared to the base metal indicating the effect of FSW temperature cycle. The TMAZ microstructure comprises of coarse Q precipitate nucleated heterogeneously on the dispersoids with attendant mechanical property degradation. It is to be added that dispersoids are unaffected by FSW and has a composition similar to the parent microstructure (Al_7Cu_2Fe and (Al, Fe, Si) phases) (Feng et al. 2010).

5.3.4 Cast Al-Si Mg Alloys

The alloys discussed so far mostly concerns the wrought Al alloys. Another important class is the Al-Si-Mg alloys used in die-casting applications. The chemical composition of these alloys varies with Si between 6 and 10 % and Mg between 0.3 and 0.6 %. The microstructure comprises of acicular Si distributed in the aluminum matrix. One principal defect in such die-cast microstructure is porosity (Fig. 5.5a), which causes a deterioration in the dynamic mechanical properties. Jana et al. investigated the effect of friction stir process on porosity and Si particles, where these microstructural attributes are approximated as an ellipse and then defined in terms of an equivalent critical diameter (ECD = (Major diameter/minor diameter)$^{0.5}$) (Jana et al. 2010). Friction stir process completely eliminates porosities with high mean ECD making Si particles with low mean ECD the controlling microstructural feature (Fig. 5.5b) with a concomitant improvement in the fatigue property. Another observation is its effect on Si particle size and shape where friction stir process decreases the mean particle size making the particle size distribution narrower and decreases the particle aspect ratio (Jana et al. 2010). This reduces the statistical uncertainties in the microstructure making mechanical property much more predictable.

5.3.5 7XXX Alloys

The Al-Zn-Mg alloys are one of the early precipitation hardening systems which despite its potential to achieve high strength is less popular due to low corrosion resistance. Consequently, the commonly used 7XXX series alloys are of Al-Zn-Mg-Cu type, where Cu is added to improve its corrosion resistance. The precipitation sequence of such quaternary alloys is given as

$$\text{Al(super-saturated)} \rightarrow \text{G.P. zone(I or II)} \rightarrow \eta' \rightarrow \eta$$

where η' is the metastable precursor of the equilibrium η phase. Additionally, depending on the alloy composition small amounts of equilibrium T and S phases are also formed. For a Cu-free alloy the η phase composition is given as $MgZn_2$ which in the presence of Cu is composed of exactly 33 at% Mg, 10–15 at% Al , approximately 13 % Cu and the balance as Zn (Marlaud et al. 2010). Aging at low temperatures (~120 °C) results in an η phase devoid of Cu while higher aging temperatures (135–160 °C) increases the Cu fraction where the final Cu content is proportional the initial Cu concentration in the alloy (Marlaud et al. 2010). Another complexity is the different types of G.P. zone formation (I and II) depending on the aging temperature. The type-I G.P. zone with AuCu(I) structure forms when aging is done between room temperature to ~150 °C and is independent of the quenching temperature after solution heat treatment (Berg et al. 2001). According to Sha and Cerezo (2004) the type-I G.P. zone nucleates homogenously (see Chap. 3). The type-II G.P. zone nucleates at vacancy rich clusters and forms only when quenching temperature is above 450 °C and aging temperature is above 70 °C (Berg et al. 2001). As in other Al alloys, special additions are done in 7XXX alloys to form dispersoids. The elements used for this purpose are Zr and Cr which forms Al_3 Zr and Al_7Cr respectively.

A comprehensive transmission electron microscopy (TEM) analysis of a AA7050-T651 friction stir weld conducted by Su et al. (2003) observe that the nugget microstructure consists of fine η precipitates in addition to type-I G.P. zone structures. The TMAZ region of the weld on the other hand exhibits coarse η phase located at the grain boundary or within the grain itself. Selected Area Diffraction analysis reveals traces of type-I GP zone at selected areas of the TMAZ. However, unlike in the parent/HAZ no evidence of type-II G.P. zone or η' precipitate is observed in the nugget/TMAZ microstructure. The η' precipitates in the HAZ are also significantly coarser compared to the parent microstructure which has the highest density of η' phase. A considerable increase in the particle free zone (PFZ) at the grain boundary regions of the HAZ microstructure is also detected. FSW also converts Al_7Cu_2Fe phase present as rod/bar shaped particles in the parent microstructure to blocky shape in the nugget region though a minimal effect on Al_3Zr dispersoids is observed. As in other Al alloys the grain boundary and dislocation structures in the nugget is atypical of a dynamically recrystallized microstructure while the TMAZ zone reveals a typical dynamically recovered

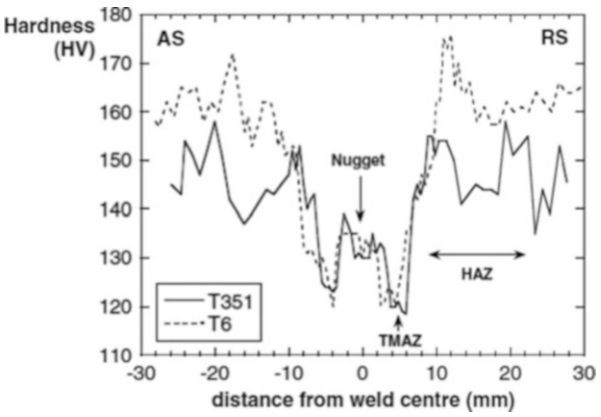

Fig. 5.6 The variation in micro-hardness of a friction stir welded AA2024 alloy in T351 and T6 state (Genevois et al. 2005, reprinted with permission from Elsevier)

microstructure consisting of cell, subgrains and regions of high dislocation density (Su et al. 2003). This is in contrast to the parent metal which predominantly consists of low angle boundary structures characteristic of a partially recrystallized microstructure.

In this regard, it may be added that in any experiment a considerable time lag between FSW operation and microstructural characterization exists. In most cases this information is unavailable which makes it difficult to pinpoint the temporal origin of GP zone in nugget and TMAZ zone. Fuller et al. (2010) investigated the effect of natural aging on friction stir welded AA7050 in T7651 temper. The results show that with prolonged natural aging the microstructure in nugget zone changes from a type-I G.P. zone structure to a combination of G.P. zone (type-II) with some fraction of η' and η precipitates (Fuller et al. 2010).

5.4 Mechanical Properties After FSW

The previous section elaborated on the effect of FSW on microstructure of different Al alloys. In the present section the consequence of this microstructure on the mechanical properties is discussed.

5.4.1 2XXX Alloys

Micro-hardness measurements on a friction stir welded AA2024 T3/T651 alloy (Fig. 5.6) shows that the hardness in the nugget zone is approximately 30 HV lower than the parent material irrespective of the initial temper (Genevois et al. 2005). The lowest hardness is observed in the TMAZ zone from where the hardness again rises into the HAZ except for an intervening region where a relative drop in hardness occurs

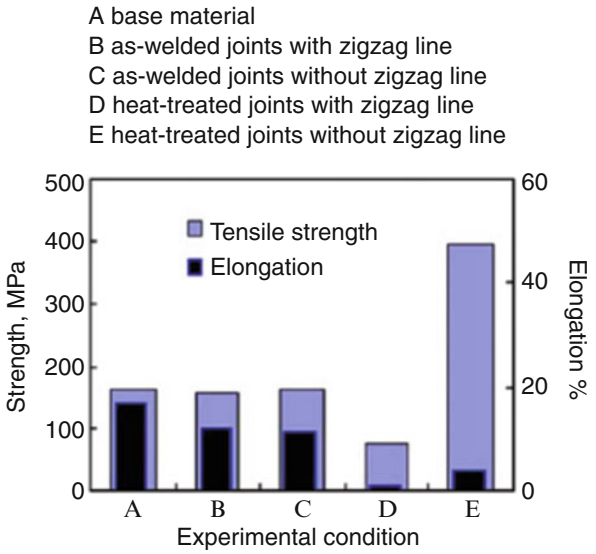

Fig. 5.7 The tensile properties of a friction stir welded AA2219 alloy in O temper, both with and without lazy-S in the as-welded as well as heat-treated condition (Liu et al. 2006, reprinted with permission from Elsevier)

(Genevois et al. 2005, Jones et al. 2005). This microhardness results agree with the microstructural observation of the weld zone where the hardness lows corresponds to lower volume fractions of S′ phase (see Fig. 5.2). Similar measurements on AA2024 in T351 temper by Bussu and Irving (2003) show a very similar trend. The AA2024 alloy discussed so far is a 2XXX series alloy with low Cu:Mg ratio. The microhardness pattern of welded AA2017 (high Cu:Mg ratio)—in T351 temper exhibit the "W" shape similar to that of AA2024 alloy where the two troughs of the W are located in the TMAZ and the crest occurs in the nugget zone. In fact, this W shape is a typical pattern for the precipitation hardening Al alloys, although depending on the welding conditions other profiles can also be obtained.

Genevois et al. (2006) measured the effect of this microhardness variation on tensile property using miniature tensile specimens. The tensile results show that the TMAZ region constitutes the weak link in the overall weld mechanical property. Another microstructural feature influencing mechanical behavior is the remnant oxide lines (alternatively called "Lazy S") present in the nugget. The surface of all Al alloys are coated with a very thin and tenacious oxide coating (due to its high reactivity with oxygen in air), which under improper welding conditions leave a clearly traceable pattern of oxide debris. Liu et al. investigated the effect of these oxide lines on a AA2219 alloy in O temper (Liu et al. 2006) and observed that in the as-welded condition the effect of this remnant oxide on mechanical property is minimal. A post-weld aging heat treatment however severely degrades the tensile properties due to micro-crack formation along the oxide line (Fig. 5.7). It is worth pointing out that any tensile property deterioration associated with lazy-S formation will also degrade the dynamic mechanical properties of the weld. Another aspect of interest is the effect of metallurgical banding on the overall tensile property. Sutton et al. (2004) investigated this effect on a AA2024-T351 weld using digital imaging

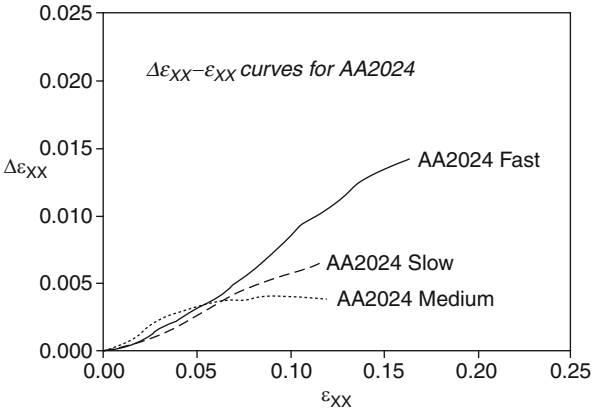

Fig. 5.8 The difference in strain between the HSB and LSB regions for three different FSW parameters. The metallurgical band width varies from (a) Fast—0.34 mm, (b) Medium—0.25 mm and (c) Slow—0.17 mm (Sutton et al. 2004, reprinted with permission from Elsevier)

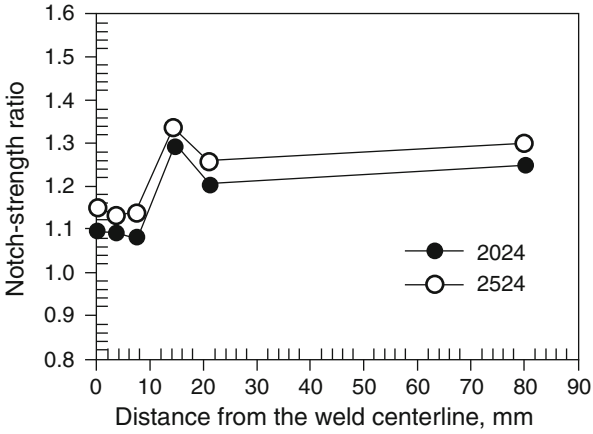

Fig. 5.9 The variation in notch tensile strength of a friction stir welded AA2024 and AA2524 alloy in T351 temper. The notches were placed at different positions from the weld centerline (Yan et al. 2006, reprinted with permission from Elsevier)

correlation techniques on miniature tensile specimens, where the localized surface deformation within the bands were recorded during testing. The authors classified the bands into two types (a) Low strain band (LSB) and (b) High strain band (HSB) where the LSB with higher micro-hardness has a high secondary particle density and smaller grain size compared to the HSB. It is observed that at low plastic strains both the LSB and HSB deform identically though at higher plastic strains the HSB deforms more compared to the LSB (Fig. 5.8) (Sutton et al. 2004). Notch tensile experiments on friction stir welded AA2024-T351 alloy with notches placed at different distances from the weld center to the advancing side show an appreciable notch tensile strength reduction in the nugget compared to the parent (Yan et al. 2006). Fractographic evidence indicates that the particle rich portions in the metallurgical bands act as preferential sites for void nucleation with resultant loss in mechanical property (Yan et al. 2006). However, the tensile strength of AA2024 friction stir weld is in general notch insensitive (Fig. 5.9) (Yan et al. 2006).

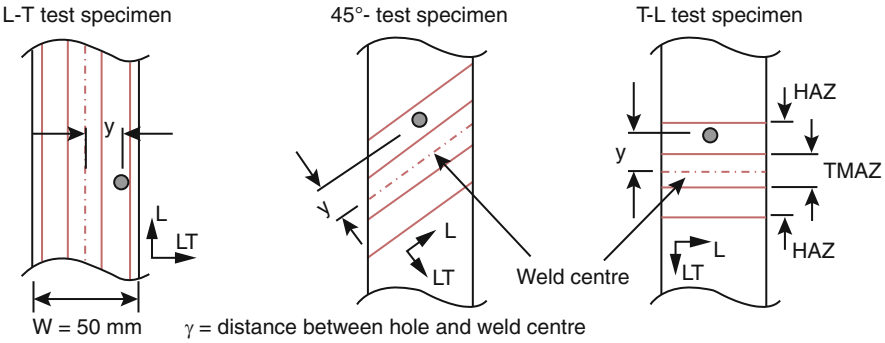

Fig. 5.10 The different orientations of center-hole fatigue specimens used to study fatigue crack initiation in AA2024-T3 welds (Lemmen et al. 2011, reprinted with permission from Elsevier)

The fatigue behavior of weld joints is another important aspect which needs special attention. Conventionally, fatigue failure is classified into three stages (a) crack initiation, (b) crack growth and (c) final failure. The crack initiation stage comprises of ~80 % of the fatigue life while final failure forms an insignificant part of the total.

Understanding the origin of fatigue crack initiation in friction stir welds is therefore of critical importance. Lemmen et al. (2011) studied the fatigue crack initiation phenomenon in a AA2024-T3 weld where center hole fatigue specimens in different orientations are used to investigate the sensitivity of different weld zones (Fig. 5.10). Fatigue loads with R ratio of 0.1 and stress amplitudes ranging between 60 and 100 MPa are applied using a servo-hydraulic machine at a frequency of 10 Hz. After every 2,500 cycle a marker load with R ratio of 0.7 at constant maximum stress is applied for 5,000 cycles to simplify the identification of fatigue crack initiation site. The authors observed that besides residual stress, microstructure determines the fatigue crack initiation with cracks initiated preferentially on the advancing side of TMAZ with mean stress point controlling its location (Lemmen et al. 2011). The crack initiation is however unaffected by metallurgical banding though depending on specimen orientation the stage-II crack propagation during fatigue is affected (Lemmen et al. 2011).

Bussu and Irving (2003) investigated the effect of residual stress on fatigue crack propagation in a AA2024 alloy in T351 temper where a surface crack tension (SCT) and a compact tension (CT) specimen oriented with respect to the weld is used (Fig. 5.11). Although the authors did not explicitly mention the crack position in their SCT and CT specimens, based on their description it is safe to assume that the cracks were machined on the advancing side of the weld. Thus, for SCT specimens the semi-circular cracks are machined perpendicular to the weld either at the joint line or at a distance of 11 and 28 mm into the advancing side. For the CT specimen the chevron cracks are machined parallel to the weld, either along the joint line or at distances of 6 and 28 mm into the advancing side. For the SCT specimen crack propagation is fastest for the sample with crack 11 mm away from the joint line, the slowest

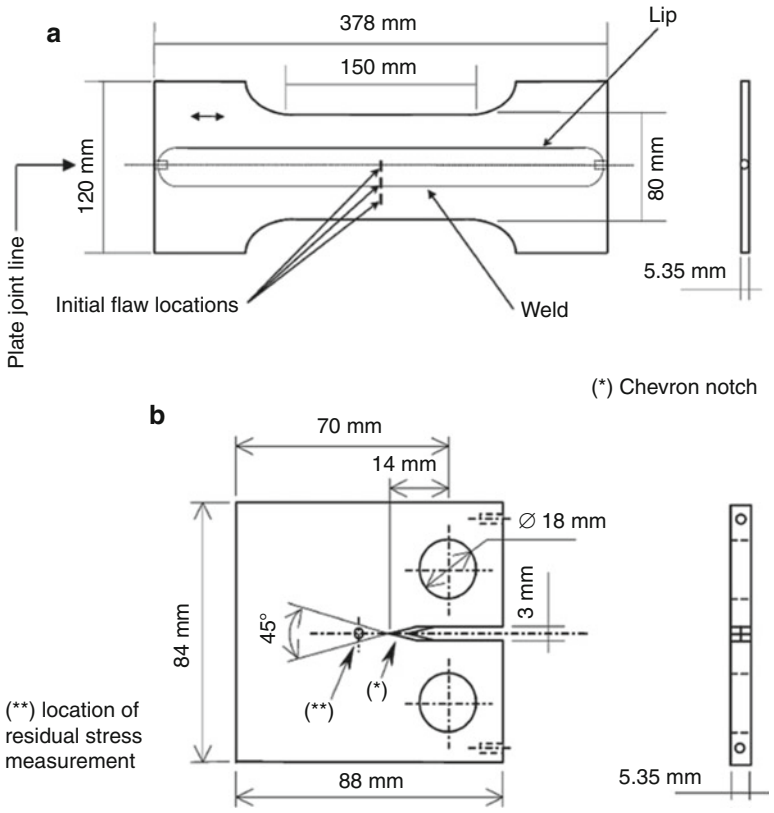

Fig. 5.11 (**a**) Surface crack tension specimen used to evaluate the effect of residual stress on fatigue crack propagation. In each case the surface cracks were machined at different location from weld centerline. (**b**) Compact tension specimen used to evaluate fatigue crack propagation. In each case the chevron crack was located at different distance from weld centerline (Bussu and Irving 2003, reprinted with permission from Elsevier)

observed for the sample with crack 28 mm into the advancing side. For the CT specimen the sample with crack 28 mm into the advancing side exhibits the fastest crack propagation, the slowest observed for sample with crack 6 mm into the advancing side. The authors repeated the same tests on stress relieved (2 % plastic strain) weld samples and observed that unlike in non-stress relieved samples no difference in crack propagation is observed. This lead to the conclusion that the residual stresses existing after FSW significantly affects fatigue crack propagation.

Milan et al. (2008) performed a detailed residual stress evaluation in both longitudinal and transverse direction of AA2024-T3 friction stir welds using the cut-compliance technique. The residual stress in the weld is observed to be a combination of compressive/tensile stresses (Fig. 5.12). These compressive residual stresses significantly reduce the propagation rate of transverse and longitudinal fatigue cracks though an accelerated behavior is observed in the weld zone.

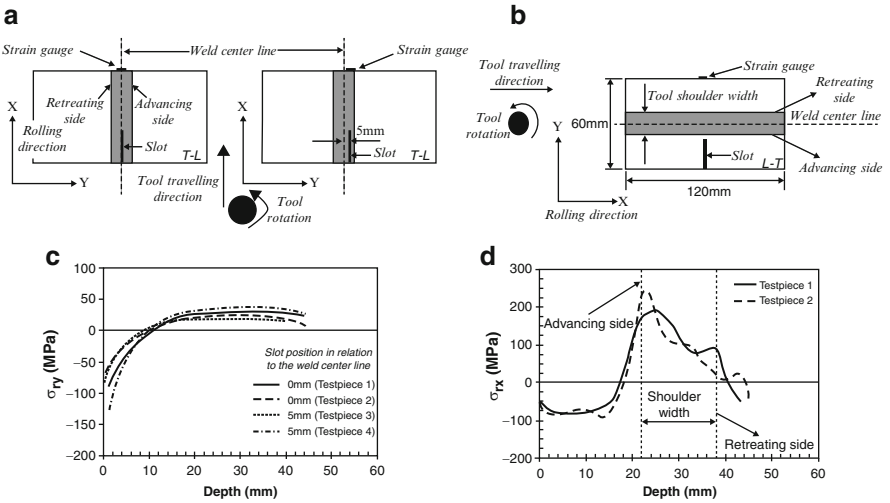

Fig. 5.12 (**a**, **b**) The weld specimens of AA2024-T3 used to evaluate residual stress using cut-compliance technique. (**c**, **d**) The residual stress distribution in the weld in transverse and longitudinal direction (Milan et al. 2008)

5.4.2 5XXX Alloys

For precipitation hardening systems the effect of FSW on the mechanical properties of the weld is mainly due to its effect on the pre-existing hardening precipitates. In a solid solution hardening system like 5XXX series the effect of FSW on the mechanical property arises due to its effect on the prior dislocation structures in the microstructure. Thus, depending on the alloy temper the micro-hardness profile in a 5XXX series alloy can vary significantly. The effect can be explained based on the fact that nugget region in FSW is essentially a dynamically recrystallized region, while TMAZ region is a dynamically recovered zone. Consequently, after FSW the nugget becomes essentially free of dislocation structures while dislocations in the TMAZ and adjoining region recover to form cells and sub-grain structure. The initiation of these microstructural events again depends on the initial dislocation density in the parent microstructure where the effect is maximum for H1 temper and decreases for the H2 and H3 tempers respectively. The consequence is visible in the micro-hardness profile of friction stir welded AA5083 alloys in the O and H19 temper (Fig. 5.13). The micro-hardness across the weld of AA5083-O alloy is uniform with no loss in joint efficiency while for H19 temper the hardness is lowest in the nugget, TMAZ and adjoining region. The discrepancy is explained by the fact, that in O temper dislocation content is least and dislocation density change after FSW is effectively negligible. Rather, depending on the position of micro-hardness measurement a slight hardening (probably due to grain boundary strengthening) is observed. For the H19 temper initial dislocation content is high and FSW reduces dislocation density significantly causing a pronounced softening in the weld region.

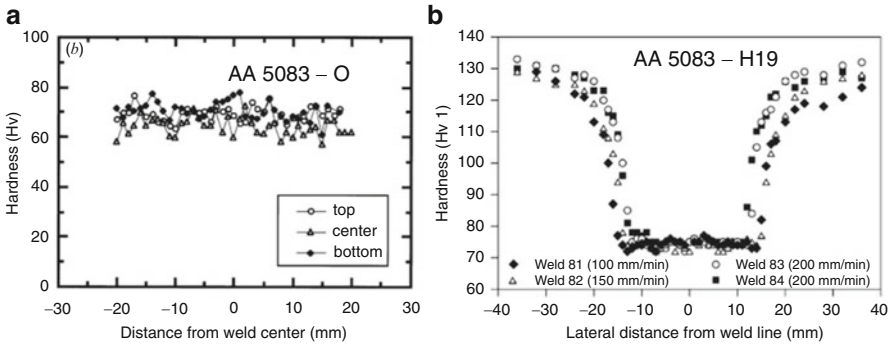

Fig. 5.13 (**a**) The micro-hardness variation in a welded AA5082-O alloy (Sato et al. 2001, reprinted with permission from Elsevier). (**b**) The micro-hardness variation in a welded AA5083-H19 alloy (Peel et al. 2003, reprinted with permission from Elsevier)

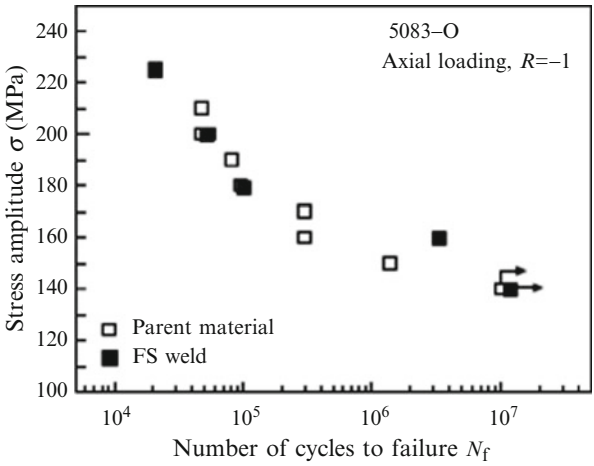

Fig. 5.14 The variation in S-N life for a AA5083 alloy in O temper and after friction stir welding. As in the case of micro-hardness distribution, no variation in fatigue life is observed (Uematsu et al. 2009, reprinted with permission from Elsevier)

The above results of weld micro-hardness are easily extended to infer the tensile property. For the O temper welds the tensile property will be similar to the parent material while a degraded property for H1, H2 and H3 tempers is expected. In many weld joints the bend property is of critical importance. Sato et al. (2004) investigated the effect of lazy-S line in a AA5052-O weld joint. No significant effect of the dispersed oxide particles on the root-bend property is observed.

As in case of tensile property, the effect of FSW on fatigue depend on the temper of the alloy welded. The fatigue behavior of AA5083-O welds evaluated by Uematsu et al. (2009) shows no perceptible differences in the high cycle fatigue life (Fig. 5.14). Dickerson and Przydatek investigated the effect of root flaw on the high cycle fatigue life of friction stir welded AA5083 in both O and H321 temper in a resonance fatigue testing machine at 170 Hz and R of 0.1(Dickerson and Przydatek 2003). The fatigue life of AA5083-O alloy is found to be unaffected

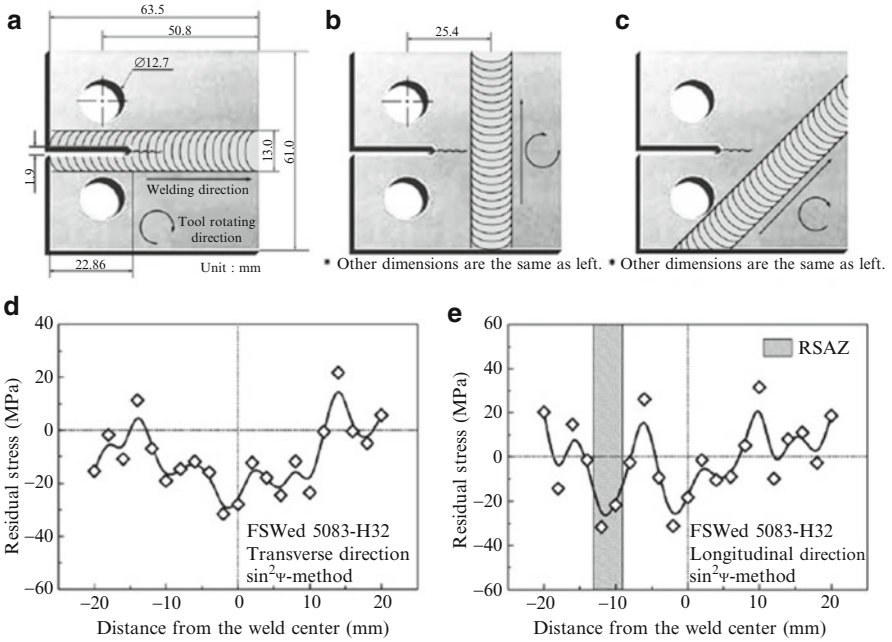

Fig. 5.15 (**a**–**c**) The different orientations of C-T specimen used to evaluate fatigue crack propagation in a AA5083-H32 alloy. Residual stress in the transverse (**d**) and longitudinal (**e**) direction of the weld, measured using X-ray diffraction technique (Kim et al. 2008, reprinted with permission from Elsevier)

by the root flaw, though a significant decrease in fatigue life for the H321 weld is observed. It is to be noted that the effective length of root flaw in the O temper fatigue specimen is of the order of 0.35 mm while in H321 specimen the length is 1 mm. This leads to an apparently misleading conclusion that a flaw of 0.35 mm in the weld will not affect the fatigue property. It maybe affirmed that any root flaw is expected to adversely affect the mechanical properties of the weld irrespective of its temper. However, for flaw sizes in the microstructurally small crack domain no significant effect on fatigue property is expected (Suresh 2004). Although the authors do not mention any information about the grain boundary distribution and or grain size in the respective alloys, it is expected that the observed effect is essentially a consequence of small crack behavior. As in other alloys, FSW creates residual stresses within the weld region which affects the fatigue crack propagation. Kim et al. (2008) investigated the fatigue crack propagation behavior in a AA5083-H32 alloy using CT specimens at different orientations with respect to the weld (Fig. 5.15a–c). The residual stresses on the top surface in transverse (T direction is perpendicular to weld) and longitudinal (L direction is parallel to weld) orientations were evaluated using X-ray diffraction (Fig. 5.15d, e). The compressive residual stresses in the weld are found to retard the crack propagation rate during fatigue ($R = 0.1$ and 0.8). Beyond a certain K value the propagation rate however accelerates in the fine grained nugget region of specimens (for constant stress intensity

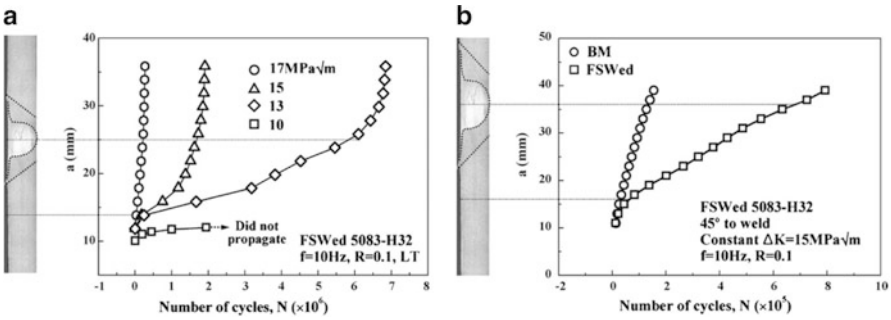

Fig. 5.16 (**a**) The fatigue crack propagation rate in a LT orientation CT specimen of AA5083-H32 alloy weld for constant stress-intensity tests. (**b**) The fatigue crack propagation rate in a 45° orientation CT specimen of AA5083-H32 alloy weld for constant stress intensity tests (Kim et al. 2008, reprinted with permission from Elsevier)

(K) tests at R = 0.1) with LT orientation (Fig. 5.16a). The effect is however not observed in the CT sample with welds oriented at an angle of 45° to the crack (Fig. 5.16b). Overall, it is therefore safe to conclude that compressive residual stresses due to FSW retards fatigue crack propagation in the long crack regime. Beyond a certain stress intensity factor, the crack however relieves the residual stress and microstructure effect becomes dominant whereby finer grain size in the nugget accelerates the crack propagation rate.

5.4.3 6XXX Alloys

In this section the mechanical characteristics of friction stir welded 6XXX alloys is discussed. Figure 5.17 shows the variation in micro-hardness of a Cu free 6XXX alloy (AA6063-T5) weld (Sato et al. 1999b). Sato et al. (1999b) classified the weld into four regions with the maximum hardness observed in the base metal (BM), from where it decreases to a minimum (MIN) before registering a slight increase in the nugget region (SOF(0)). No significant difference in hardness profile between the top, middle and bottom portion of the weld is observed. Post-weld aging of the weld at 175 °C results in an increase in the micro-hardness.

A maximum hardness increase is observed in the SOF(0) followed by the MIN, LOW and BM region causing a shift in minimum hardness to the LOW region (Fig. 5.18). This improvement in the weld micro-hardness is a consequence of progressive precipitation of metastable phases as shown in Fig. 5.19. Similar micro-hardness study by Gallais et al. (2007) in a Cu containing 6XXX alloy (AA6056) in T4 condition followed by post weld natural aging exhibits multiple LOW region in the HAZ/TMAZ zone (Fig. 5.20a). The T78 condition shows the characteristic micro-hardness variation seen in AA6063-T5 alloy (see Figs. 5.17 and 5.20b). The hardness reduces continuously into the TMAZ as a consequence of heterogenous precipitation of Q phase on dispersoids indicating temperatures in the range of

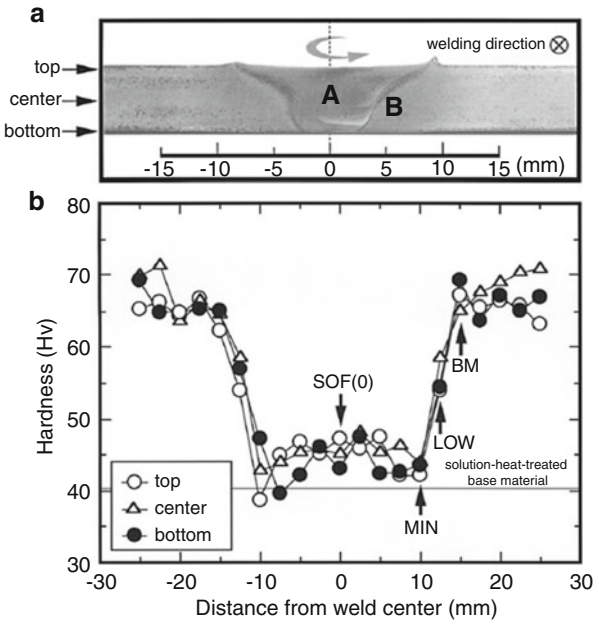

Fig. 5.17 (**a**) The macrostructure of a AA6063-T5 weld showing the location of micro-hardness line scans conducted across the weld. (**b**) Micro-hardness variation at different depths of the weld. Based on the hardness, different weld zones are identified (Sato et al. 1999b, reprinted with permission from Springer)

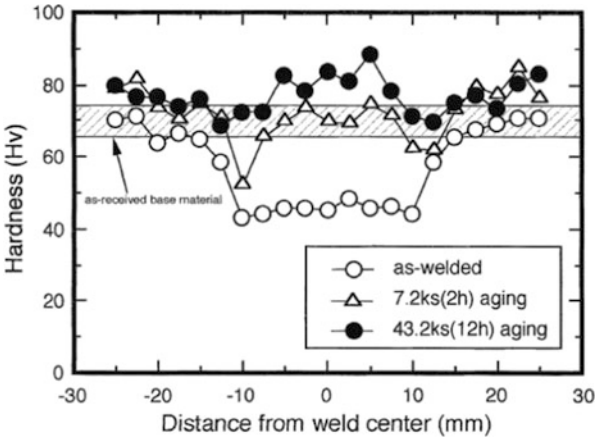

Fig. 5.18 The variation in micro-hardness due to post-weld aging of a AA6063-T5 alloy at 175 °C for 2 and 12 h. The maximum hardness gain is in the SOF (0) region (see Fig. 5.17) (Sato et al. 1999b, reprinted with permission from Springer)

300–400 °C during FSW. In T4 condition, dissolution of GP zone causes an initial hardness drop in the HAZ3 region (Fig. 5.20a) followed by a hardness rise in the HAZ2 zone due to homogenous precipitation of the β″ phase. This is followed by a hardness decrease due to Q phase precipitation on dislocations in the TMAZ region. It is worth noting that similar multiple hardness minima are observed in the AA2024 weld at T3 state (see Fig. 5.6). Although, Genevois et al. (2006) has not analyzed the microstructural factors behind this multiple hardness drop,

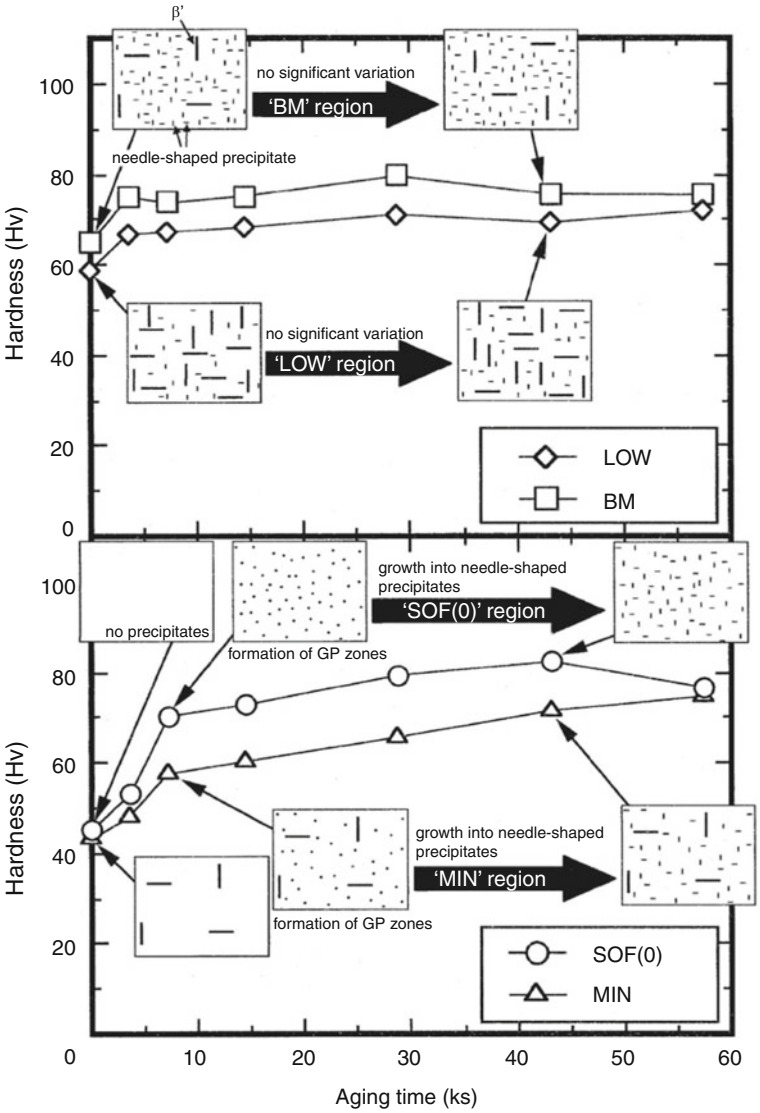

Fig. 5.19 A schematic of the precipitation occurring at different positions of the AA6063-T5 weld shown in Fig. 5.17 for different aging times (Sato et al. 1999b, reprinted with permission from Springer)

considering the similarity between T3 and T4 tempers, GP zone reversion is the likely reason behind this phenomenon.

In addition to the microhardness Gallais et al. (2007) also measured the uniaxial tensile properties from different portions of the weld. Tensile samples machined parallel to the weld direction at different positions with respect to the weld centerline shows tensile strength which follows the trend in micro-hardness.

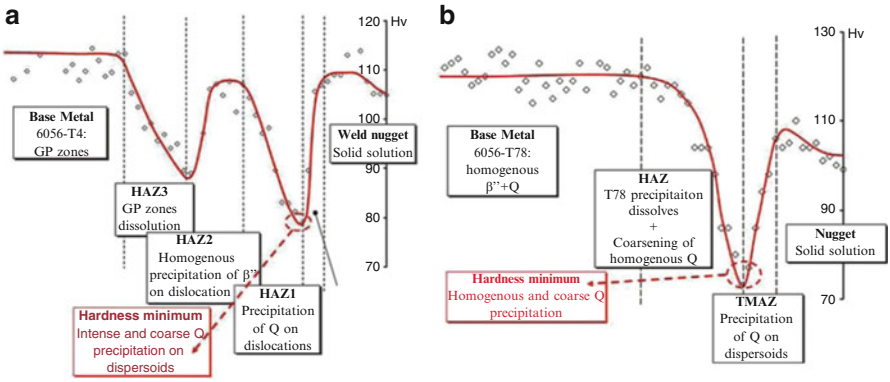

Fig. 5.20 The variation in micro-hardness at the advancing side of a welded AA6056 alloy with the precipitates occurring at different zones (**a**) for alloy with T4 temper (**b**) for alloy with T78 temper (Gallais et al. 2007, reprinted with permission from Springer)

The authors also measured the tensile properties after a post weld T78 aging heat treatment of 175 °C for 6 h, followed by 210 °C for 5 h. The heat treatment improved the tensile property of the nugget zone (compare Fig. 5.21a, b) while minimum changes occurred at the hardness minima position (Fig. 5.21c).

Kim et al. (2008) studied the effect of FSW on the fatigue property of AA6061 in T651 temper using CT specimen in three different orientations (Fig. 5.15a–c). The residual stress pattern measured for the AA6061 weld (Fig. 5.22a, b) is similar to that of AA5083-H32 alloy (Fig. 5.15d, e). At low stress intensity factors the TL specimen show significantly reduced fatigue crack propagation rate compared to the base metal. It is further observed that the decrease in propagation rate is not solely determined by the residual stress. Thus, the residual stress corrected propagation rate of base metal at $R = 0.1$ differs considerably (Fig. 5.22c) from the TL specimen and is ascribed to the reduced crack closure in the fine grained nugget region. This difference between residual stress corrected propagation rate of base metal and TL specimen is however minimized at higher R ratio (0.8), since crack closure effect becomes less prominent with an increase in R. In fact, constant stress-intensity factor crack propagation tests in AA6061-T651 alloy show a very similar behavior to that of AA5083-H32 alloy (see Figs. 5.16 and 5.23). Thus, residual stress combined with grain size effect on crack closure will be a major controlling factor in Al alloy fatigue crack propagation.

5.4.4 Cast Al-Si-Mg Alloy

As already discussed in Sect. 5.3.4, friction stir process significantly changes the microstructure in cast Al-Si-Mg alloys and eliminates casting porosities with consequent improvement in the fatigue life (Fig. 5.24) (Jana et al. 2010). In the

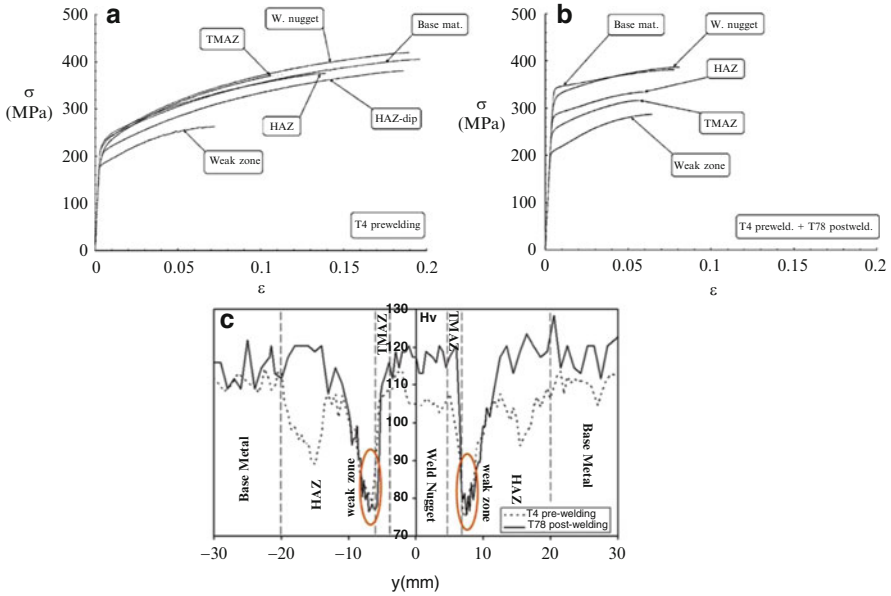

Fig. 5.21 The tensile curve for specimens drawn from different weld locations of AA6056 alloy (**a**) T4 temper (pre-weld), (**b**) T4 temper pre-weld followed by T78 temper post-weld, (**c**) hardness profile across the weld for T4 temper (pre-weld) and T4 temper pre-weld followed by T78 temper post weld (Gallais et al. 2007, reprinted with permission from Springer)

as-cast alloy porosities act as fatigue crack initiator while in the friction stir processed alloy the Si/matrix interface acts as the crack initiator. In the processed alloy the fatigue crack propagates along the particle matrix interface compared to the mixed mode failure in the as-cast alloy.

5.4.5 7XXX Alloys

The mechanical characteristic of friction stir welded 7XXX alloy is very similar to the precipitation hardened Al alloys discussed earlier. In Fig. 5.25 the temporal variation in micro-hardness of two different 7XXX alloys in T651 temper are shown. As in the case of 2XXX and 6XXX alloys the hardness variation shows the typical "W" shaped profile. Natural aging treatment increases the hardness with the hardness minima at the HAZ/TMAZ boundary moving into the HAZ zone. This trend in hardness change with aging is similar to that observed in AA6061-T6 alloy (Fig. 5.18). An important point to note is that the original T6 strength is largely recovered by natural aging. Fuller et al (2010) also measured the tensile properties of the welded AA7050-T651 and AA7075-T651 plates at different stages of natural

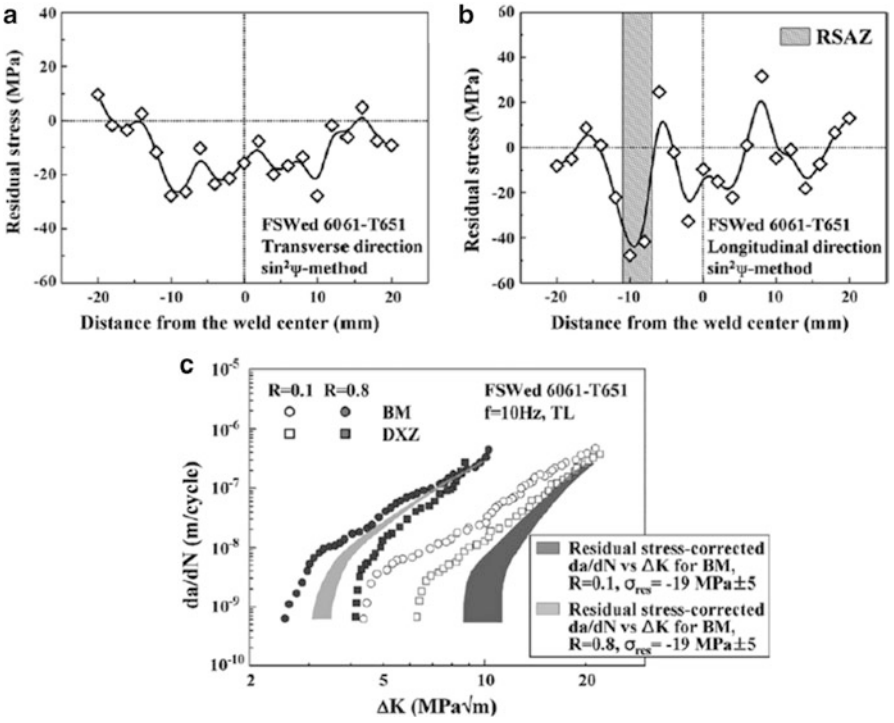

Fig. 5.22 The variation in residual stress across the (**a**) transverse and (**b**) longitudinal direction of a AA6061-T651 weld. (**c**) The effect of residual stress on fatigue crack propagation in specimens for base metal (BM) and from nugget (DXZ) at different R values (Kim et al. 2008, reprinted with permission from Elsevier)

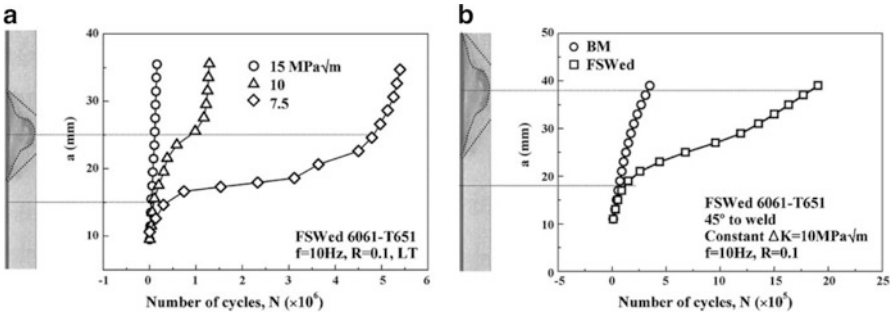

Fig. 5.23 The fatigue crack propagation in welded AA6061-T651 specimens in two different orientations (**a**) LT and (**b**) 45° orientations (see Fig. 5.15a–c) (Kim et al. 2008, reprinted with permission from Elsevier)

aging (Fig. 5.26). After natural aging for ~8 years the tensile property of the welds almost equals that of the parent T651 temper. The tensile tests conducted on two different joint thicknesses (~6.4 and 3.2 mm) for the AA7075-T651 alloy shows that this strength recovery is best for the thinner plate joint.

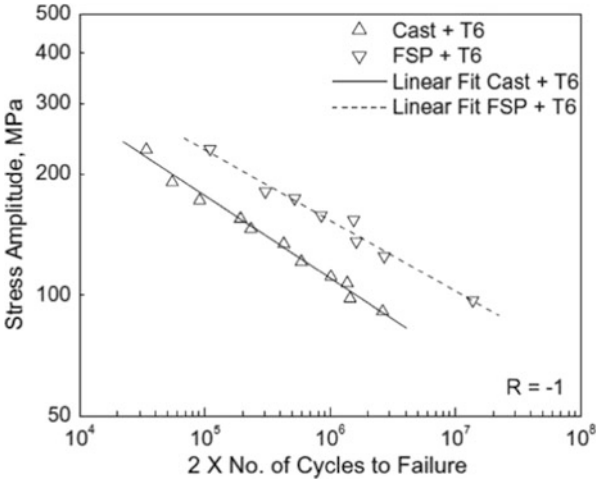

Fig. 5.24 The S-N curve for a Al-Si-Mg alloy in (a) as cast + T6 aging condition and (b) after friction stir processing + T6 aging condition (Jana et al. 2010, reprinted with permission from Elsevier)

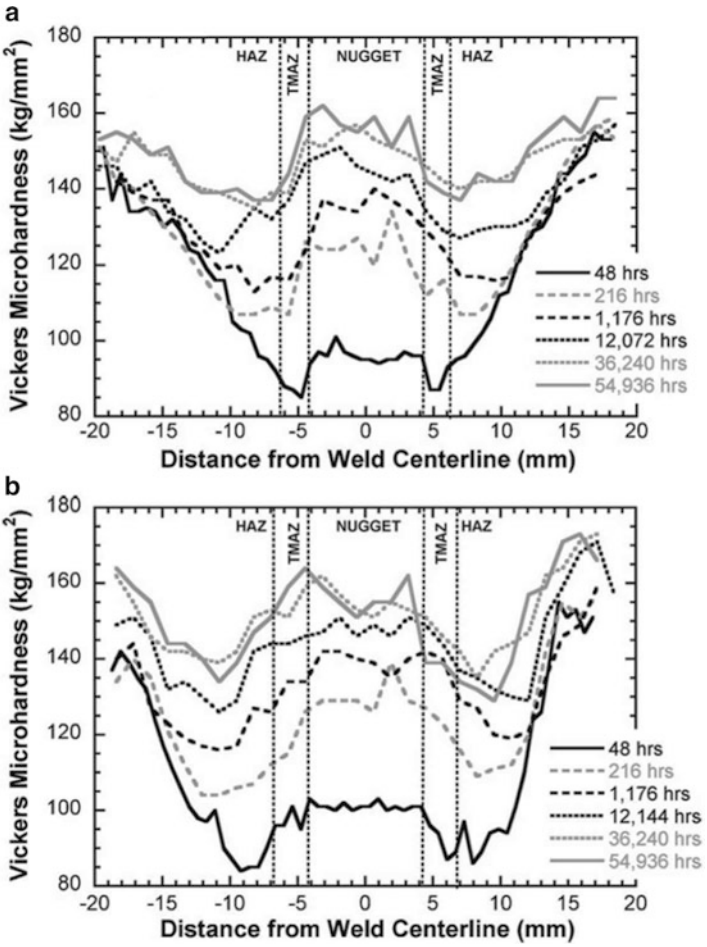

Fig. 5.25 The variation in microhardness of an (a) 7050-T651 and (b) 7075-T651 alloy weld at different stages of natural aging (Fuller et al. 2010, reprinted with permission from Elsevier)

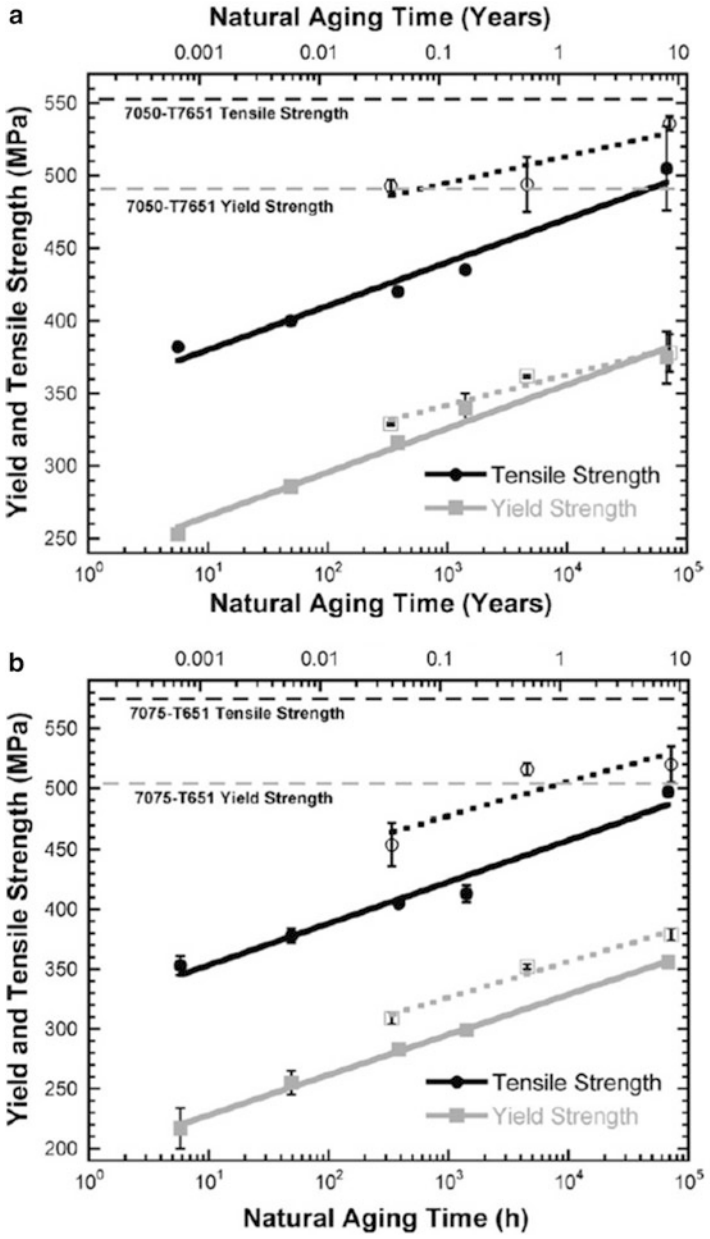

Fig. 5.26 The variation in tensile property of (**a**) AA7050-T651 and (**b**) AA7075-T651 weld with natural aging. The solid data points indicate weld property in transverse direction while the open data points are weld property in the longitudinal direction (i.e. nugget region) (Fuller et al. 2010, reprinted with permission from Elsevier)

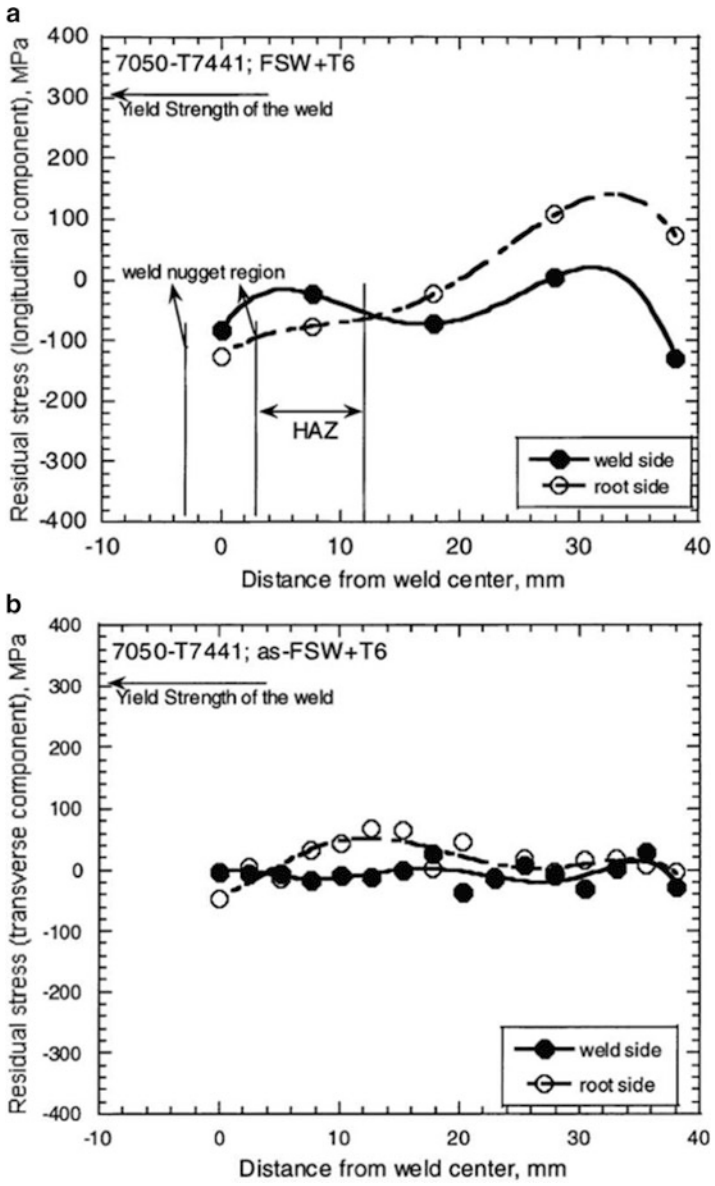

Fig. 5.27 The variation in residual stress in a AA7050-T7441 weld in (**a**) longitudinal direction and (**b**) transverse direction (Jata et al. 2000, reprinted with permission from Springer)

Jata et al. (2000) investigated the fatigue strength of AA7050-T7441 welds where the effect of microstructure and residual stresses in the weld on fatigue crack propagation rate is measured after a T6 post-weld aging treatment. Figure 5.27 illustrates the residual stress at both the top and bottom surfaces of the joint.

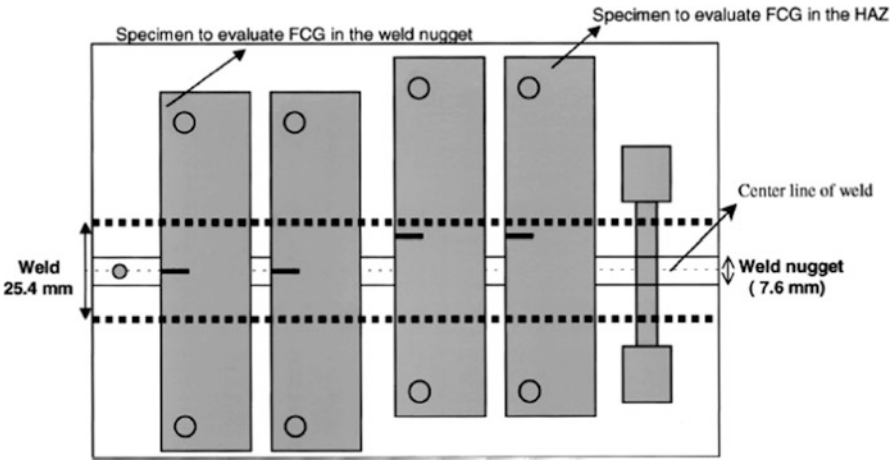

Fig. 5.28 The location of the eccentrically loaded single edge crack tension specimen used to study fatigue crack propagation in a AA7050-T7441 weld (Jata et al. 2000, reprinted with permission from Springer)

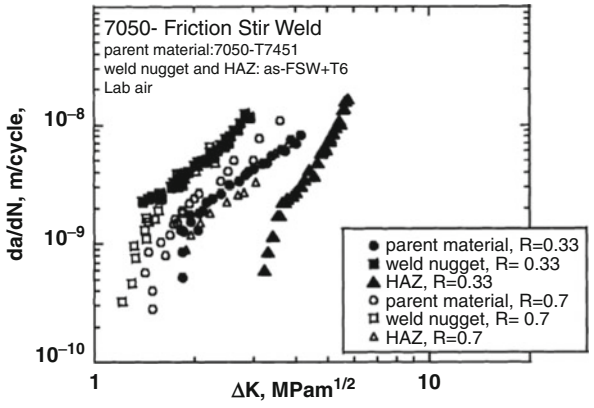

Fig. 5.29 The fatigue crack propagation rate for the eccentrically loaded single edge tension specimens at two different R ratios of 0.33 and 0.7 (Jata et al. 2000, reprinted with permission from Springer)

Fatigue crack propagation rates at different regions of the welds are tested using eccentrically loaded single edge tension specimens with notches machined at different positions (Fig. 5.28). The fatigue crack propagation rate in the heat affected zone is retarded, while the nugget zone shows an accelerated behavior with respect to the parent material (Fig. 5.29). The faster crack propagation in the nugget region is ascribed to the fine grained microstructure which diminishes crack closure effect resulting in an inter-granular type of failure. This difference is more pronounced in tests with low R ratio indicating that crack closure effect due to residual stress affects the crack propagation rate considerably.

John et al. (2003) investigated the effect of specimen geometry on fatigue crack propagation rate in FSW joints. At low R ratios the center-crack specimen geometry

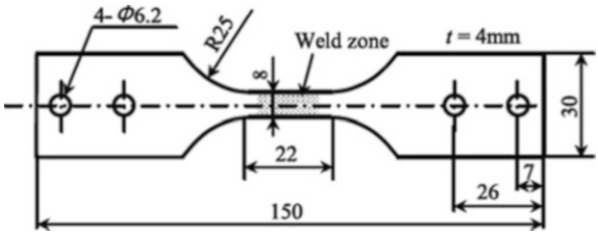

Fig. 5.30 The specimen used to study the fatigue characteristics in a AA7075-T6 specimen (Uematsu et al. 2009, reprinted with permission from Elsevier)

exhibits accelerated crack propagation compared to compact tension and eccentrically loaded single edge specimens. Based on this result the authors conclude that residual stress effect on crack propagation rate is influenced by the specimen geometry. Consequently, the choice of proper specimen geometry is expected to be critical for appropriate FSW weld evaluation.

Uematsu et al. investigated the high cycle fatigue behavior of AA7075-T6 welds using flat specimens at 10 Hz with $R = -1$ with the weld zone located in the center as shown in Fig. 5.30 (Uematsu et al. 2009). Although, the as-welded hardness have the typical W shaped profile of precipitation hardened alloys in T6 temper, the high cycle fatigue life of the weld specimens are unaffected and is similar to that of the parent material (Fig. 5.31). Post fatigue hardness measurement reveals that the weld hardness improves with cyclic loading, which is instrumental in improving the fatigue life (Fig. 5.30).

5.5 Microstructure and Mechanical Properties of Friction Stir Spot Welds

As discussed previously, FSSW is a variation of FSW where only the plunge and dwell phase of FSW is in effect. Although several methods of FSSW has evolved over time (see Box 2.1 in Chap. 2), our discussion in this section will be confined to the more popular variant used i.e. FSSW with keyhole.

5.5.1 Macro/Microstructure

As in normal FSW, a section of the friction stir spot weld has three identifiable regions i.e. nugget, TMAZ and HAZ. However, unlike in FSW, the nugget region in FSSW is characterized by a keyhole left by the tool pin. In Fig. 5.32 a typical friction stir spot weld macrostructure for an AA7075 alloy is shown. The change in microhardness across such welded section for an AA7075 alloy is shown in Fig. 5.33. The apparent similarity of microhardness variation of FSSW AA7075 with the microhardness variation shown for FSW AA7075 in Fig. 5.25b is quite clear, except for the hardness magnitude, which is similar to that after ~1,000 h

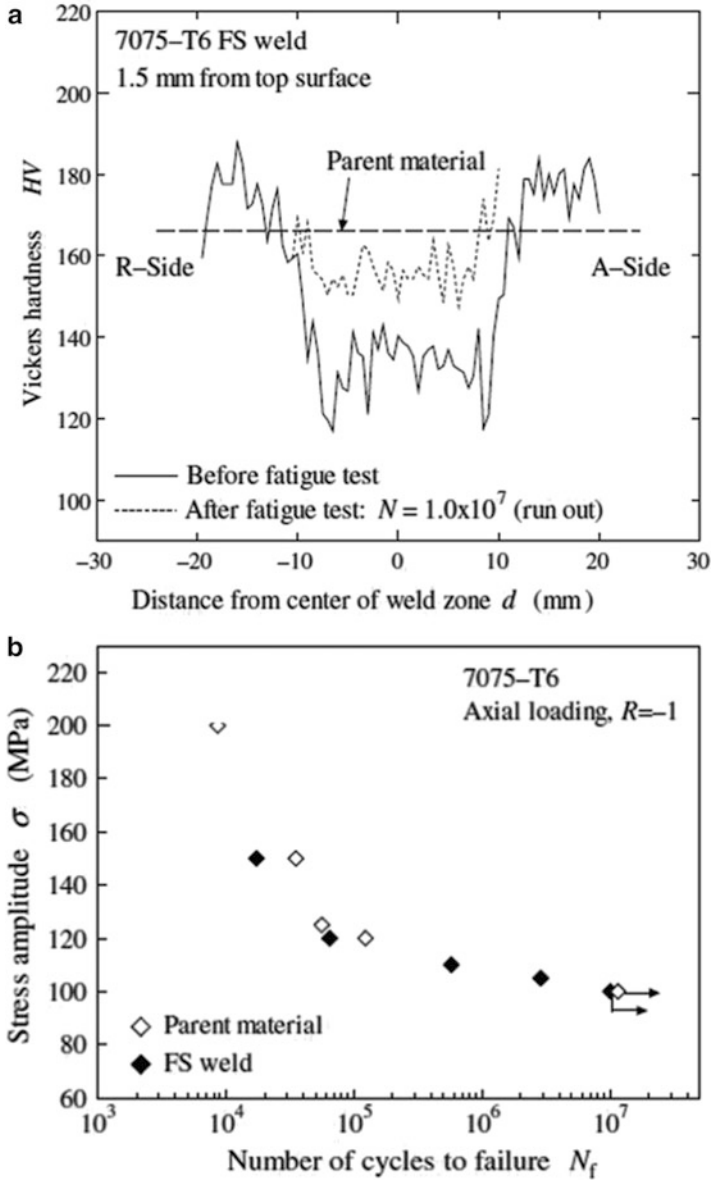

Fig. 5.31 (**a**) The change in microhardness across the AA7075-T6 weld for fatigue testing at R = −1, showing a hardening of the original nugget zone. (**b**) The S-N curve of both the parent, material and FSW weld (Uematsu et al. 2009, reprinted with permission from Elsevier)

natural aging after FSW. This difference is quite anticipated, since, unlike in FSW, the friction stir spot welding involves considerable dwell time (solutionizes precipitates) followed by faster cooling due to lower overall heat input into the joint (i.e. faster cooling due to the cold workpiece mass). It may be added that the

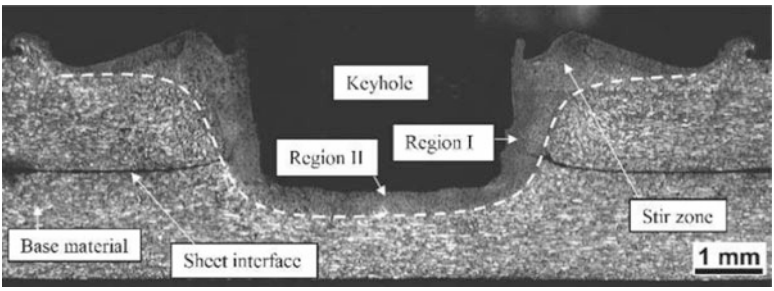

Fig. 5.32 A typical macrostructure for a friction stir spot welded alloy (AA7075) of a lap welded joint. The zones deformed under the influence of pin and shoulder are identified as Region I/II and stir zone (Gerlich et al. 2006, reprinted with permission from Springer)

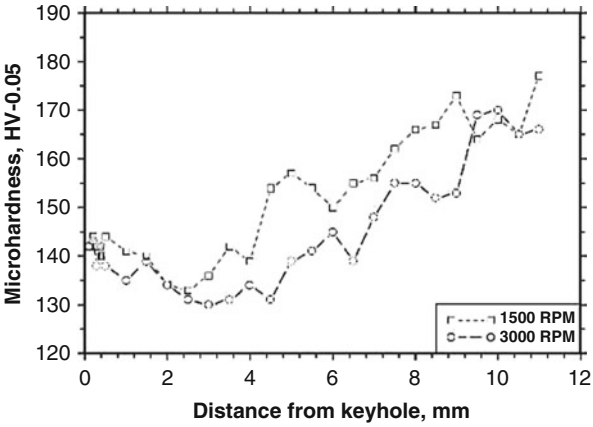

Fig. 5.33 The hardness variation in the FSSW joint starting from region-I (see Fig. 5.31) in a horizontal direction from the surface adjoining the keyhole (Gerlich et al. 2006, reprinted with permission from Springer)

influence of microstructure on the weld mechanical properties of keyhole FSSW is insignificant. Rather, a substantial effect of material flow on mechanical properties is observed. This importance of material flow can be understood from the critical features of a FSSW macrostructure (Fig. 5.34) which are identified as, (a) unbonded region of height h_h or the hook defect, (b) a partially unbonded as well as a smaller fully bonded region within the nugget zone as identified by the hook width (h_w), and (c) reduced thickness of top sheet (T_{eff}). In fact, three features mentioned markedly influences the mechanical properties of friction stir spot welded structures. The morphology of these features again depends on the tool design and the process parameters of FSSW. Thus, mechanical properties of friction stir spot welds (Fig. 5.35) in an AA5754 O-temper alloy done using concave, flat and convex shoulder show significant variation in its static strength (Badrinarayan et al. 2009a). The highest static strength is obtained using concave shoulder tool and is ascribed to the higher effective thickness (T_{eff}) of the top sheet. Similarly, changing the tool pin profile from cylindrical to triangular in a concave shoulder tool resulted in

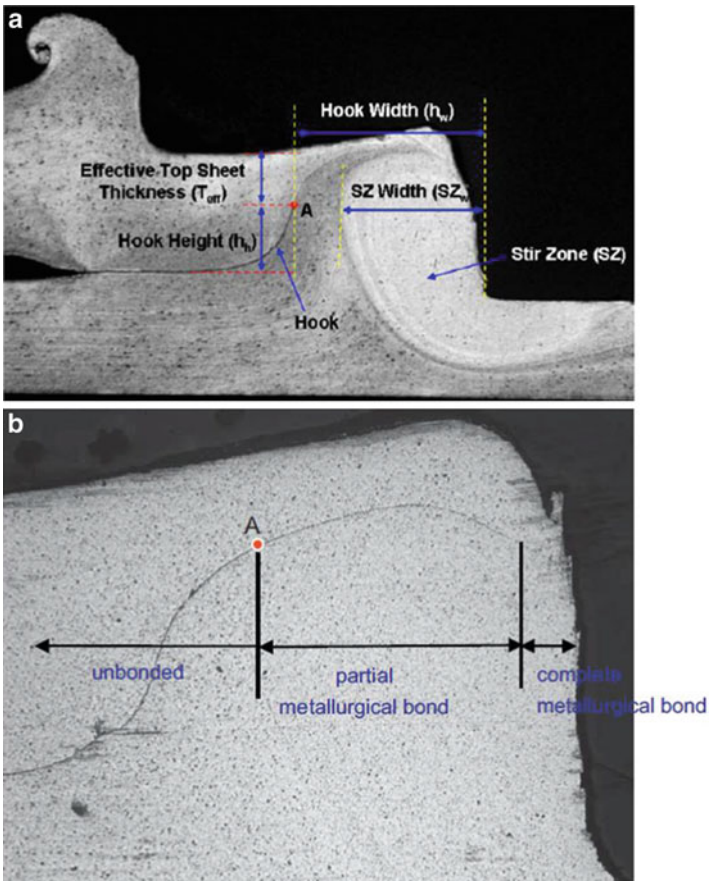

Fig. 5.34 The critical features of a FSSW joint welded using concave tool (**a**) as visualized in the macrostructure and (**b**) nature of bonding at different positions of the features (Badrinarayan et al. 2009a, reprinted with permission from Elsevier)

higher static strength (Fig. 5.36) during cross-tension testing. The triangular pin profile (FSSW-T in Fig. 5.36) results in reduced volume displacement in upwards direction from the lower sheet. Consequently, the hook formed points upward unlike in cylindrical tool (FSSW-C) where it ingresses downward into the stirred zone (Fig. 5.36). This downward hook serves as a crack initiator during tensile testing and results in a shear type failure through the nugget zone.

The static tensile tests on spot welded Al-Mg-Si alloy using flat shouldered tool (Uematsu et al. 2008) also results in crack initiation from the hook. It was further observed that refill type spot welds resulted in ~30 % improvement in static strength (Uematsu et al. 2008). Fatigue tests conducted on spot welded AA6111-T4 lap shear specimens indicate that kinked cracks growing into the bottom sheet from the hook and bending of the unsupported top sheet determines the fatigue life (Lin et al. 2008a, b).

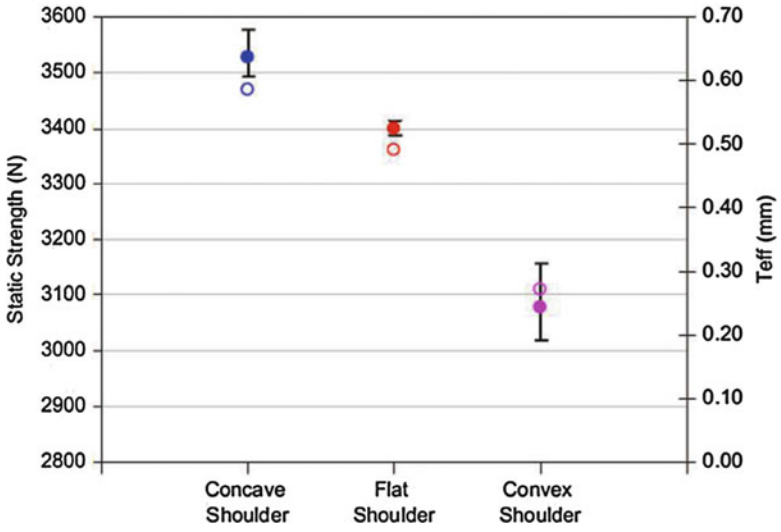

Fig. 5.35 The variation in static strength of a friction stir spot welded Al alloy for FSSW tools with concave, flat and convex shoulder. The corresponding reduction in T_{eff} is also plotted. The tool plunge depths are same in all cases (Badrinarayan et al. 2009a, reprinted with permission from Elsevier)

5.6 Corrosion in FSW Welds

Apart from the mechanical strength, the corrosion property of welded joints is another important feature which is deeply influenced by microstructure. The types of corrosion which are so affected include (Fontana 1986)

(a) Pitting corrosion
(b) Intergranular corrosion
(c) Stress corrosion cracking

The pitting corrosion is distinguished by localized effect where holes are formed in the metal through anodic reaction accelerated by the presence of Cl^- and H^+ ions. The pits initiate at locations where corrosion rates are high, which for Al alloys can be precipitate free zones or coarse precipitates (Paglia and Buchheit 2008).

In intergranular corrosion the grain boundary regions are attacked preferentially while the grain interiors are relatively unaffected. This is mainly caused by enrichment or depletion of specific elements in the grain boundary region, and is generally associated with the formation of grain boundary precipitates or precipitate free zones.

Stress corrosion cracking is initiated by the concurrent presence of tensile stresses and specific corrosion medium with crack propagation occurring by both intergranular and transgranular means (Fontana 1986). The stress corrosion cracks generally propagate in a direction perpendicular to the tensile stresses which may

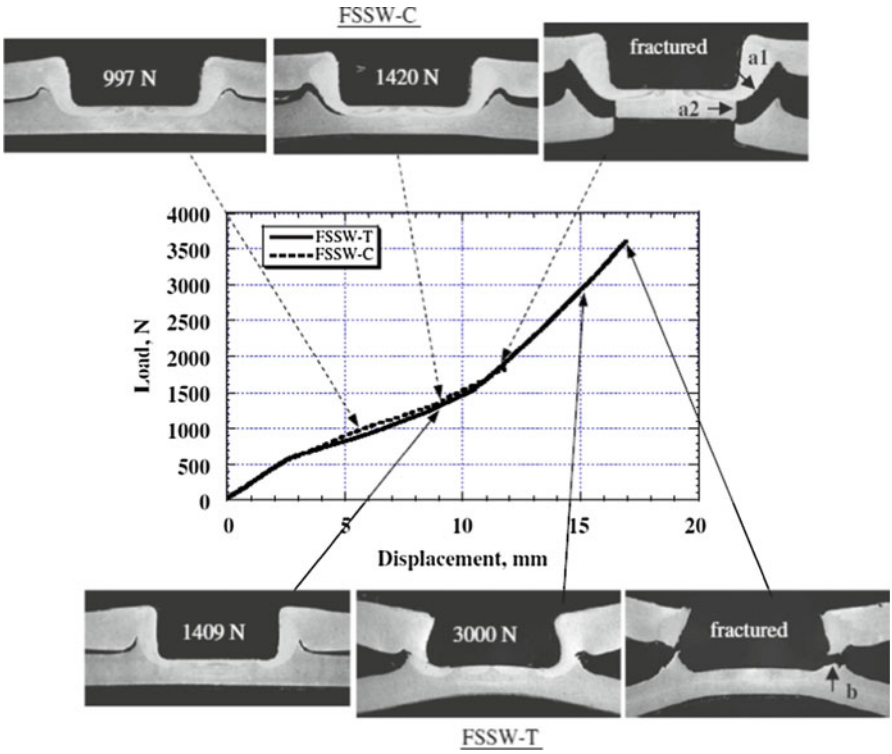

Fig. 5.36 The variation in strength of FSSW using concave shouldered tool with triangular and cylindrical pin. The cylindrical pin weld show low strength compared to the triangular. Note the nature of progress in failure for each case. The bent hook in cylindrical pin case results in severance of the lower sheet. For triangular tool the hook is smaller and the failure propagates through the stir zone causing increased resistance to failure (Badrinarayan et al. 2009b, reprinted with permission from Elsevier)

be of the externally applied or residual type (Fontana 1986). The vulnerability of a metal to stress corrosion is therefore influenced by its chemical composition, grain orientation, precipitate distribution and other associated microstructural factors.

Quite evidently, depending on the FSW conditions and the consequently evolved microstructure, the corrosion property of friction stir welded joints vary significantly. Corrosion tests conducted on a welded AA2219-T8 alloy indicates that the nugget and TMAZ region show a better corrosion resistance compared to the parent microstructure (Bala Srinivasan et al. 2010). The open-circuit potential measurements and immersion tests (ASTM G110-93) indicate that the nugget and TMAZ regions are in fact cathodic compared to the parent (Bala Srinivasan et al. 2010). This is attributed to the dissolution and coarsening of precipitates in the nugget and TMAZ region. The slow strain rate tensile tests performed in air and 3.5 % NaCl solution to evaluate stress-corrosion cracking resistance indicates that the no such corrosion behavior is also expected (Bala Srinivasan et al. 2010).

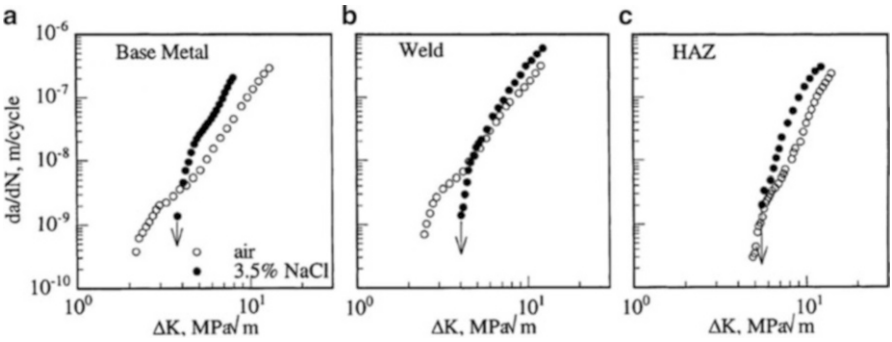

Fig. 5.37 Effect of environment on crack propagation rate in CT specimens on AA7050-T7451 welds (**a**) notch in the base metal, (**b**) notch in the nugget region, (**c**) notch in the HAZ region (Pao et al. 2001, reprinted with permission from Elsevier)

Xu and Liu (2009) investigated the corrosion property of welded AA2219 alloy in O temper using conventional polarization and electrochemical impedance tests. The authors observed that the Al_2Cu particles present in the microstructure makes it prone to pitting type of corrosion. The cathodic nature of the Al_2Cu particles combined with their large sizes in the base metal (compared to the nugget) makes the nugget more corrosion resistant compared to the parent (Xu and Liu 2009).

Similar work on welded AA2024-T3 alloys investigated using electrochemical cells and immersion test techniques show that S phase (Al_2CuMg) precipitated in the nugget/TMAZ/HAZ region act as cathode (Jariyaboon et al. 2007) which promotes intergranular corrosion. Again, depending on the FSW parameters, it is also observed that the corrosion resistance of the nugget increases when a higher angular velocity of the tool is used. The nugget becomes cathodic while the HAZ region becomes anodic and corrosion prone and is a consequence of the reduced size of S phase in the nugget at higher angular velocities.

Wadeson et al. (2006) investigated the corrosion resistance of welded AA7108-T79 using ASTM G34 EXCO and electrochemical measurements. As in the case of 2XXX alloys (S phase precipitation) the coarse $MgZn_2$ equilibrium phase (100 nm long and 20 nm wide) at the grain boundaries increases intergranular corrosion in the TMAZ region (Wadeson et al. 2006). Fatigue crack growth experiments conducted on AA7050-T7451 weld using CT specimens (notches in nugget, base metal and HAZ) show that the threshold stress intensity (K_{th}) for fatigue crack growth is higher in 3.5 % NaCl solution compared to that in air and is irrespective of the notch position (Fig. 5.37). This has been attributed to increased crack closure effect arising out of corrosion products formed during stage-I crack propagation period. The stage-II crack propagation zone is distinguished by a low growth rate in the HAZ zone while the base metal and nugget region exhibits higher crack propagation rate.

References

H. Badrinarayan, Y. Shi, X. Li, K. Okamoto, Effect of tool geometry on hook formation and static strength of friction stir spot welded aluminum 5754-) sheets. Int. J. Mach. Tools Manuf. **49**, 814–823 (2009a)

H. Badrinarayan, Q. Yang, S. Zhu, Effect of tool geometry on static strength of friction stir spot-welded aluminium alloy. Int. J. Mach. Tools Manuf. **49**, 142–148 (2009b)

D. Bakavos, P.B. Pragnell, B. Bes, F. Eberl, The effect of silver on microstructural evolution in two 2XXX series Al-alloys with a high Cu:Mg ratio during aging to a T8 temper. Mater. Sci. Eng. A **491**, 214–223 (2008)

S.P. Bala, K.S. Arora, W. Dietzel, S. Pandey, M.K. Schaper, Characterisation of microstructure, mechanical properties and corrosion behavior of an AA2219 friction stir weldment. J. Alloys Compd. **492**, 631–637 (2010)

L.K. Berg, J. Gjonnes, V. Hansen, X.Z. Li, M. Knutson-Wedel, G. Waterloo, D. Schryvers, L.R. Wallenberg, GP-Zones in Al-Zn-Mg alloys and their role in artificial aging. Acta Mater. **49**, 3443–3451 (2001)

G. Bussu, P.E. Irving, The role of residual stress and heat affected zone properties on fatigue crack propagation in friction stir welded 2024-T351 aluminum joints. Int. J. Fatigue **25**, 77–88 (2003)

D.J. Chakraborti, D.E. Laughlin, Phase relations and precipitation in Al-Mg-Si alloys with Cu additions. Prog. Mater. Sci. **49**, 389–410 (2004)

T.L. Dickerson, J. Przydatek, Fatigue of friction stir welds in aluminium alloys that contain root flaws. Int. J. Fatigue **25**, 1399–1409 (2003)

G.A. Edwards, G.L. Dunlop, M.J. Couper, in *Final-Scale Precipitation in Al Alloy 6061*. The 4th international conference on aluminum alloys, Atlanta, GA, USA (1994), pp. 628–635

V. Fahimpour, S.K. Sadrnezhaad, F. Karimzadeh, Corrosion behavior of aluminum 6061 alloy joined by friction stir welding and gas tungsten arc welding methods. Mater. Des. **39**, 329–333 (2012)

A.H. Feng, D.L. Chen, Z.Y. Ma, Microstructure and low-cycle fatigue of a friction-stir-welded 6061 aluminum alloy. Metall. Mater. Trans. **41**, 2626–2641 (2010)

M.G. Fontana, *Corrosion Engineering, Edition 2005* (Tata McGraw-Hill, New York, NY, 1986)

C.B. Fuller, M.W. Mahoney, M. Calabrese, L. Micona, Evolution of microstructure and mechanical properties in naturally aged 7050 and 7075 Al friction stir welds. Mater. Sci. Eng. A **527**, 2233–2240 (2010)

C. Gallais, A. Simar, D. Fabregue, A. Denquin, G. Lapasset, B. de Meester, Y. Brechet, T. Pardoen, Multiscale analysis of the strength and ductility of AA6056 aluminum friction stir welds. Metall. Trans. A **38**, 964–981 (2007)

C. Gallais, A. Denquin, Y. Brechet, G. Lapasset, Precipitation microstructures in an Aa6056 aluminum alloy after friction stir welding: characterisation and modelling. Mater. Sci. Eng. A **496**, 77–89 (2008)

W. Gan, K. Okamoto, S. Hirano, K. Chung, C. Kim, R.H. Wagoner, Properties of friction-stir welded aluminum alloys 6111 and 5083. J. Eng. Mater. Technol. **130**, 031007-1-031007-2 (2008)

C. Genevois, A. Deschamps, A. Denquin, B. Doisneau-cottignies, Quantitative investigation of precipitation and mechanical behavior for AA2024 friction stir welds. Acta Mater. **53**, 2447–2458 (2005)

C. Genevois, A. Deschamps, P. Vacher, Comparative study on local and global mechanical properties of 2024 T351, 20204 T6 and 5251 O friction stir welds. Mater. Sci. Eng. A **415**, 162–170 (2006)

A. Gerlich, G. Avramovic-cingara, T.H. North, Stir zone microstructure and strain rate during friction stir spot welding. Metall. Mater. Trans. A **37**, 2773–2786 (2006)

R. Goswami, G. Spanos, P.S. Pao, R.L. Holtz, Precipitation behaviour of the β phase in Al-5083. Mater. Sci. Eng. A **527**, 1089–1095 (2010)

J.A.S. Green, *Aluminum Recycling and Processing for Energy Conservation and Sustainability* (ASM International, Novelty, OH, 2007)

J.E. Hatch, *Aluminum: Properties and Physical Metallurgy* (ASM International, Materials Park, 1984)

S. Jana, R.S. Mishra, J.B. Baumann, G. Grant, Effect of friction stir processing on fatigue behavior of an investment cast Al-7Si-0.6 Mg alloy. Acta Mater. **58**, 989–1003 (2010)

M. Jariyaboon, A.J. Davenport, R. Ambat, B.J. Connolly, S.W. Williams, D.A. Price, The effect of welding parameters on the corrosion behaviour of friction stir welded AA2024-T351. Corros. Sci. **49**, 877–909 (2007)

K.V. Jata, K.K. Sankran, J.J. Ruschau, Friction-stir welding effects on microstructure and fatigue of aluminum alloy 7050-T7451. Metall. Trans. A **31**, 2181–2192 (2000)

R. John, K.V. Jata, K. Sadananda, Residual stress effects on near-threshold fatigue crack growth in friction stir welds in aerospace alloys. Int. J. Fatigue **25**, 939–948 (2003)

M.J. Jones, P. Heurtier, F. Montheillet, D. Allehaux, J.H. Driver, Correlation between microstructure and microhardness in a friction stir welded 2024 aluminium alloy. Scripta Mater. **52**, 693–697 (2005)

S. Kim, C.G. Lee, S.-J. Kim, Fatigue crack propagation behavior of friction stir welded 5083-H32 and 6061-T651 aluminum alloys. Mater. Sci. Eng. A **478**, 56–64 (2008)

H.J.K. Lemmen, R.C. Alderliesten, R. Benedictus, Evaluating the fatigue initiation location in friction stir welded AA2024-T3 joints. Int. J. Fatigue **33**, 466–476 (2011)

P.-C. Lin, J. Pan, T. Pan, Failure modes and fatigue life estimations of spot friction welds in lap-shear specimens of aluminum 6111-T4 sheets. Part 2: welds made by a flat tool. Int. J. Fatigue **30**, 90–105 (2008a)

P.-C. Lin, J. Pan, T. Pan, Failure modes and fatigue life estimations of spot friction welds in lap-shear specimens of aluminum 6111-T4 sheets. Part 1: welds made by a concave tool. Int. J. Fatigue **30**, 74–89 (2008b)

H.J. Liu, Y.C. Chen, J.C. Feng, Effect of zigzag line on the mechanical properties of friction stir welded joints of an Al-Cu alloy. Scripta Mater. **55**, 231–234 (2006)

T. Marlaud, A. Deschmaps, F. Bley, W. Lefebvre, B. Baroux, Influence of alloy composition and heat treatment on precipitate composition in Al-Zn-Mg-Cu alloys. Acta Mater. **58**, 248–260 (2010)

M.T. Milan, W.W. Bose Filho, C.O.F.T. Ruckert, J.R. Tarpani, Fatigue behavior of friction stir welded AA2024-T3 alloy: longitudinal and transverse crack growth. Fatig. Eng. Mater. Struct. **31**, 526–538 (2008)

C.S. Paglia, R.G. Buchheit, A look in the corrosion of aluminum alloy friction stir welds. Scripta Mater. **58**, 383–387 (2008)

P.S. Pao, S.J. Gill, C.R. Feng, K.K. Sankaran, Corrosion-fatigue crack growth in friction stir welded Al 7050. Scripta Mater. **45**, 605–612 (2001)

M. Peel, A. Steuwer, M. Preuss, P.J. Withers, Microstructure, mechanical properties and residual stresses as a function of welding speed in aluminium AA5083 friction stir welds. Acta Mater. **51**, 4791–4801 (2003)

S.P. Ringer, K. Hono, I.J. Polmear, T. Sakurai, Nucleation of precipitates in aged Al-Cu-Mg-(Ag) alloys with high Cu:Mg ratios. Acta Mater. **44**, 1883–1898 (1996)

D.M. Rodrigues, A. Loureiro, C. Leitao, R.M. Real, B.M. Chaparro, P. Vilaca, Influence of friction stir welding parameters on the microstructural and mechanical properties of AA 6016-T4 thin welds. Mater. Des. **30**, 1913–1921 (2009)

Y.S. Sato, H. Kokawa, M. Enomoto, S. Jogan, Microstructural Evolution of 6063 Aluminum during friction stir welding. Metall. Trans. A **30**, 2429–2437 (1999a)

Y.S. Sato, H. Kokawa, M. Enomoto, S. Jogan, T. Hashimoto, Precipitation sequence in friction stir weld of 6063 aluminum during aging. Metall. Trans. A **30**, 3125–3130 (1999b)

Y.S. Sato, F. Yamashita, Y. Sugiura, S.W.C. Park, H. Kokawa, Microstructural factors governing hardness in friction-stir welds of solid solution-hardened Al alloys. Metall. Mater. Trans. **32**, 3033–3042 (2001)

Y.S. Sato, F. Yamashita, Y. Sugiura, S.H.C. Park, H. Kokawa, FIB-assisted TEM study of an oxide array in the root of a friction stir welded aluminium alloy. Scripta Mater. **50**, 365–369 (2004)
G. Sha, A. Cerezo, Early stage precipitation in Al-Zn-Mg-Cu alloy (7050). Acta Mater. **52**, 4503–4516 (2004)
J.Q. Su, T.W. Nelson, R. Mishra, M. Mahoney, Microstructural investigation of friction stir welded 7050-T651 aluminum. Acta Mater. **51**, 713–729 (2003)
S. Suresh, *Fatigue of Materials*, 2nd edn. (Cambridge University Press, Cambridge, 2004)
M.A. Sutton, B. Yang, A.P. Reynolds, J. Yan, Banded microstructure in 2024-T351 and 2524-T351 aluminum friction stir welds, Part II. Mechanical characterization. Mater. Sci. Eng. A **364**, 66–74 (2004)
Y. Uematsu, K. Tokaji, Y. Tozaki, T. Kurita, S. Murata, Effect of re-filling probe hole on tensile failure and fatigue behaviour of friction stir spot welded joints in Al-Mg-Si alloy. Int. J. Fatigue **30**, 1956–1966 (2008)
Y. Uematsu, K. Tokaji, H. Shibata, Y. Tozaki, T. Ohmune, Fatigue behavior of friction stir welds without neither welding flash nor flaw in several aluminium alloys. Int. J. Fatigue **31**, 1443–1453 (2009)
D.A. Wadeson, X. Zhou, G.E. Thompson, P. Skeldon, L.D. Oosterkamp, G. Scamans, Corrosion behaviour of friction stir welded AA7108 T79 aluminium alloy. Corros. Sci. **48**, 887–897 (2006)
S.C. Wang, M.J. Starink, Two types of S phase precipitates in Al-Cu-Mg alloys. Acta Mater. **55**, 933–941 (2007)
W. Xu, J. Liu, Microstructure and pitting corrosion of friction stir welded joints in 2219-O aluminum alloy thick plate. Corros. Sci. **51**, 2743–2751 (2009)
J. Yan, M.A. Sutton, A.P. Reynolds, Notch tensile response of mini-regions in AA2024 and AA2524 friction stir welds. Mater. Sci. Eng. A **427**, 289–300 (2006)

Chapter 6
Friction Stir Welding of Magnesium Alloys

6.1 Magnesium Alloys in Twenty-First Century

Magnesium is the eighth most abundant element (%molar) in earth crust. Although Mg came into existence in its elemental form 1808 when Sir Humphrey Davy isolated it from its compound, it was not until 1886 when its industrial production started. To put it in perspective, the invention of Hall-Heroult process same year enabled economical production of aluminum feasible. The production of Mg however remained limited, to a few tons per year until the start of twentieth century.[1] Its production soared to ~228,000 ton per year worldwide by 1943–1944 due to its demand in various military operations during World War II declining to ~10,000 ton per year after the war (King 2007). Figure 6.1 shows a graphical overview of world production of Mg from 1983 till 2010. In 1983, the primary Mg production reached 200,000 ton which remained same till 2000. However, from year 2000 onward a surge in production can be noted (Fig. 6.1). This is due to the increase in magnesium production in China as well as a change in method of data collection by the International Magnesium Association (IMA) from year 2000 onward. Overall, a recent surge in interest in Mg alloys is observed. The main driver for such renewed interest is the transportation industries where weight reduction to improve fuel efficiency has become very important (due to increased governmental regulation on fuel emissions to tackle global warming). In fact, as per one report (Magnesium Vision 2020 2006),[2] North American automotive industries have projected to replace 630 lb of ferrous and aluminum components with 350 lb per vehicle of magnesium parts by 2020 from its current use of an average of ~12 lb per vehicle. The decision of South Korean government to spend close to 90 million

[1] http://www.intlmag.org/faq.html.

[2] http://www.uscar.org/commands/files_download.php?files_id = 240.

R.S. Mishra et al., *Friction Stir Welding and Processing: Science and Engineering*,
DOI 10.1007/978-3-319-07043-8_6,

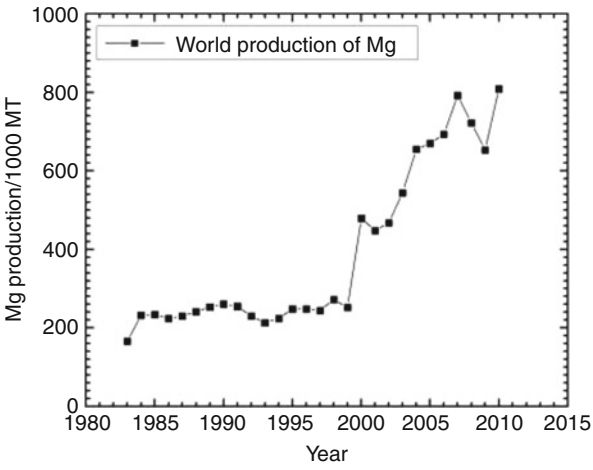

Fig. 6.1 World magnesium production year wise (http://www.intlmag.org/statistics.html)

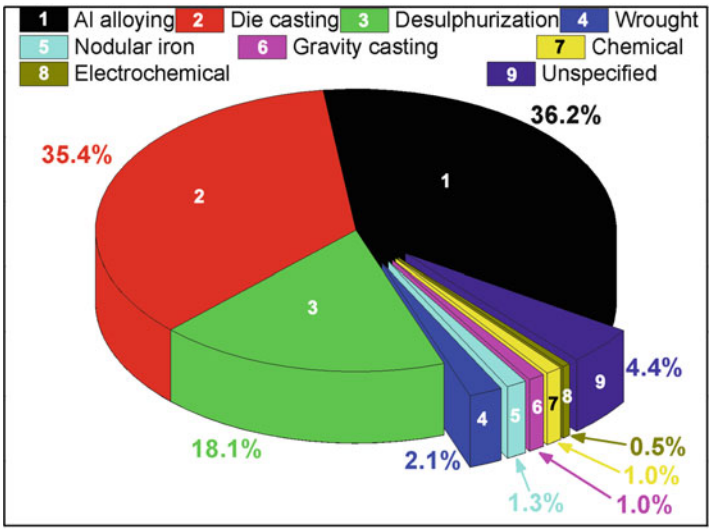

Fig. 6.2 Pie chart showing distribution of Mg usage in 2003 as reported by International Magnesium Association (King 2007)

US dollars on research and development activities related to future magnesium technologies is another example of the surge in interest worldwide in magnesium.[3] Hence, the production of primary Mg is expected to grow in the coming years.

Figure 6.2 shows the use of Mg based on the data published by IMA for 2003 (King 2007). As can be noted, the major portion (~72 %) of Mg shipments are for

[3] http://www.hzg.de/public_relations/press_releases/031069/index_0031069.html.en.

alloying addition in Al alloys and for manufacturing Mg components by diecasting technique. The majority of the die cast components (~85–90 %) are used in automotive industry (Edgar 2000). Close to 20 % is for use in desulphurization process during steel/iron making while wrought Mg alloy constituted just 2.1 % of the total shipment. As per Magnesium vision 2020, the development of low-cost wrought alloys, economical metalworking processes for Mg, non-die casting processes, cost-effective fastening with sufficient load carrying capacity, and appreciable galvanic corrosion resistance will be key technical enablers for achieving its targeted goal of 340 lb of Mg usage in vehicles by 2020 in North America (Magnesium Vision 2020, 2006).

6.2 Classification of Magnesium Alloys

Magnesium alloys are generally classified by the convention laid down by ASTM.[4] As per this system, Mg alloys are represented by two letters which represent two major alloying elements present. It is followed by two digit numbers which represent the amount of the two major alloying elements in the same order. These two numbers are followed by one letter indicating the modification of the alloy containing the same two principal alloying elements. The fourth part—a combination of a letter and two or more numbers—designates the temper of the alloy. For example, AZ31B-H24 means that this alloy contains 3 % of aluminum and 1 % of zinc as major alloying elements. The letter 'B' following AZ31 indicates second modification of the alloy. H24 indicates that the alloy is work hardened and annealed to retain half the hardness or strength in fully strain hardened condition. Table 6.1 summarizes the different alloys and temper designations as outlined in ASTM standard B296. The classification of Mg alloys by ASTM standard is applicable to both cast and wrought alloys. It can be noted that aluminum alloys are designated as per the specifications of Aluminum Association (AA) under the auspices of American National Standards Institute, and as per AA, the nomenclature for cast and wrought aluminum alloys are slightly different.[5]

Magnesium and its alloys are also represented by Unified Numbering System (UNS) for metals and alloys. As per this system a particular metal or an alloy is represented by a letter followed by five digits. For Mg and its alloys, UNS number is M1xxxx. UNS numbers ranging from M10001 to M19999 are reserved for Mg and its alloys. However, the classification system developed by ASTM is most widely used.

Magnesium alloys can also be grouped together based on their preferred processing route for manufacturing a semi-finished or finished product form (Fig. 6.3).

[4] ASM speciality handbook: Magnesium and magnesium alloys (Avedesian and Baker 1999).

[5] ASM speciality handbook: Aluminum and aluminum alloys (Davis & Associates 1993).

Table 6.1 The alloy and temper designation as per ASTM standard; Adapted from ASM Metals Handbook—Magnesium and Magnesium Alloys (see footnote 4)

Part I: two letter designation of two major alloying elements	Part II: two numbers indicating amounts of two major alloying elements in the same order	Part III: order of the modification of the alloy consisting of the same amount of two major alloying elements	Part IV: thermo-mechanical processing history of the alloy in order to introduce or control certain property (-ies)
Aluminum (A), Bismuth (B), Copper (C), Cadmium (D), Rare earth (E), Iron (F), Magnesium (G), Thorium (H), Zirconium (K), Lithium (L), Manganese (M), Nickel (N), Lead (P), Silver (Q), Chromium (R), Silicon (S), Tin (T), Yttrium (W), Antimony (Y), Zinc (Z)	The two numbers indicating composition of two major alloying elements are rounded off to their nearest integer.	First compositions, registered ASTM: A Second compositions, registered ASTM: B Third compositions: C High purity, registered ASTM: D High corrosion resistant, registered ASTM: E Not registered with ASTM: X1	As fabricated: F Annealed: O Strain hardened (applicable to wrought products only): H (subdivisions H1, H2, and H3 which are followed by one or more digits); Solution heat-treated: W (unstable temper); Thermally treated to produce stable temper other than F, O, or H: T (subdivisions T1, T3,. . .,T10 which may be followed by one or more digits)

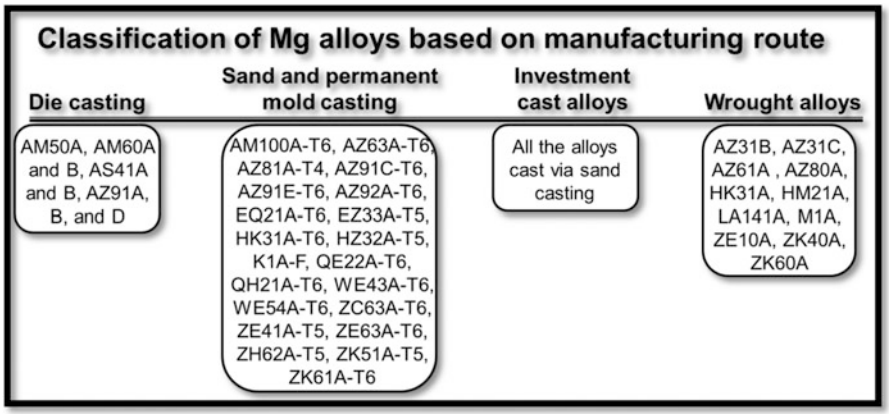

Fig. 6.3 Grouping of commercially available cast and wrought Mg alloys based on their suitable manufacturing routes (data collected from ASM Speciality Handbook—Magnesium and Magnesium Alloys (see footnote 4))

An alloy containing same principal alloying elements can be processed using more than one manufacturing route depending on exact composition of the alloy and also the design requirement for the alloy. For example, investment casting route can be adopted instead of sand casting if design requirement demands high dimensional tolerances or very good surface finish. Similarly, AM50A and AM60A are suited for die casting applications whereas AM100A is more amenable for sand and permanent casting techniques.

A further classification of Mg alloys is based on their strengthening mechanisms. Broadly, Mg alloys can be grouped into two categories—(1) Solid solution strengthened (SSS) alloys, and (2) precipitation/dispersion strengthened (PS/DS) alloys. Grain boundary strengthening or Hall-Petch strengthening is a well-recognized means of improving the strength of polycrystalline materials and can be applied to both SSS and PS/DS alloys to improve their strength further. In addition, magnesium alloys can show significant textural strengthening which leads to anisotropic mechanical properties.

6.3 Welding of Magnesium Alloy

The current resurgence in research and development activities for Mg alloys to broaden their application base has led researchers to investigate the joining of cast and wrought components. Hence, other than traditional ways of joining a constant search for evaluating performance of new joining techniques is being attempted.

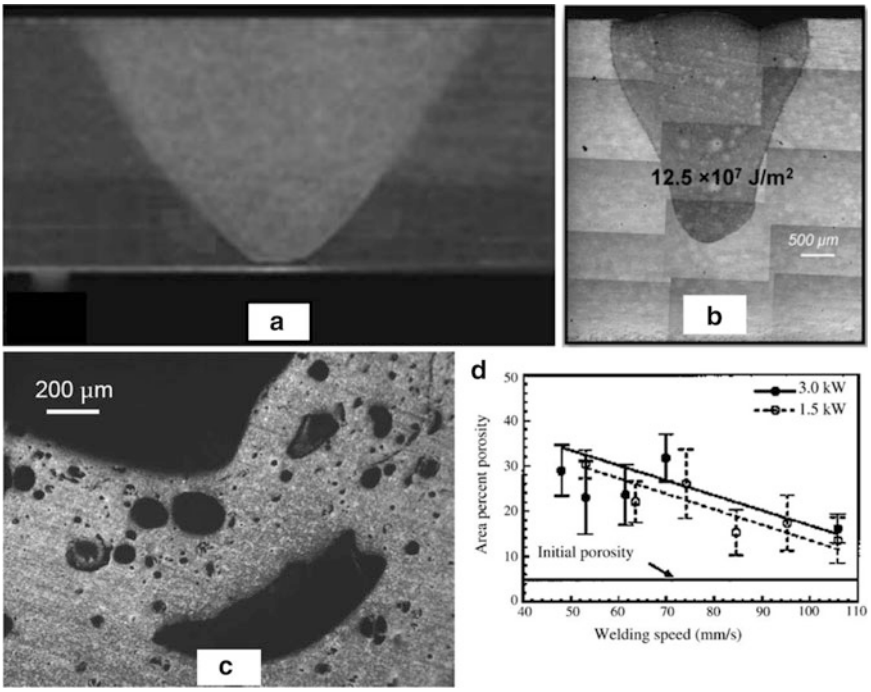

Fig. 6.4 (**a**) Tungsten inert gas welded AZ31B (Liu et al. 2007, reprinted with permission from Springer), (**b**) Laser welded WE43 alloy (Santhanakrishnan 2013, reprinted with permission from Springer), (**c**) Porosities in fusion welded Mg-8Al alloy (Czerwinski et al. 2011), and (**d**) Effect of laser welding speed on porosities (Cao et al. 2006, reprinted with permission from Elsevier)

6.3.1 Conventional Route of Welding Mg Alloys

Traditionally, Magnesium and its alloys are welded using conventional fusion and solid state techniques. Metal inert gas (MIG), tungsten inert gas (TIG), laser beam welding (LBW), and electron beam (EB) welding techniques are some prime examples of fusion welding techniques (Czerwinski et al. 2011). Representative examples for fusion welded magnesium alloy weld zone profile for TIG welded AZ31B (Liu et al. 2007) and laser beam welded WE43 (Mg-4Y-3Nd) is shown in Fig. 6.4 (Santhanakrishnan et al. 2013). In Fig. 6.4c (Czerwinski et al. 2011) the presence of gas porosity is conspicuous in Mg-8Al welded using fusion welding technique. The variation in fraction of porosity in a laser welded 6.0 mm AM60B alloy as a function of welding speed is shown in Fig. 6.4d (Cao et al. 2006). The presence of various types of porosities is one of the common defects observed in fusion welded magnesium alloys. Other defects include hot cracking and oxide formation during fusion welding due to the affinity of magnesium for oxygen.

In the face of such limitations solid-state joining has proved useful in overcoming some of the problems of fusion based techniques. Friction welding, diffusion bonding, ultrasonic welding, electromagnetic welding, etc., are some examples of solid state

joining methods employed for various magnesium alloys (Czerwinski et al. 2011). Although these techniques are capable of getting rid of defects like hot cracking in fusion welding, they lack versatility. For example, friction welding technique requires at least one component to have circular cross-section. Similarly, ultrasonic welding and electromagnetic welding are mostly suitable for thin sheets. In that regard, friction stir welding occupies a space between fusion welding and conventional solid state welding. It is capable of welding components having very simple to complex geometries and it offers all the benefits associated with conventional solid state joining techniques.

6.3.2 Friction Stir Welding of Magnesium Alloys

6.3.2.1 Process Parameters

Friction Stir Welding Tool

Chapter 4 provides a more detailed treatment of the role of tool in friction stir welding. The scope of this section is to provide a summary of tool designs and materials used for friction stir welding of Mg alloys (Table 6.2). Various grades of tool steel have been used as tool material for Mg alloys. Since the peak temperature during friction stir welding are usually below 95 % of absolute melting point of the material, the use of tool steel works well for materials like Mg alloys (Sorensen 2011). Almost all the tools reported in literature uses threaded cylindrical pin geometry. Very few investigations have been carried out using truncated conical pin or pin with flats on it. To gain an insight into quantitative relationship between different aspects of the tool, various parameters have been plotted in Fig. 6.5. It is evident from Fig. 6.5a that the majority of the data points (shoulder diameter, pin diameter) cluster around the line $d_p = 0.4d_s$ where d_p and d_s are pin and shoulder diameters, respectively. The ratio of pin diameter to shoulder diameter plotted in Fig. 6.5b shows that the ratio lies between 0.28 and 0.46 with an average of ~0.40 (the slope of line drawn in Fig. 6.5a. As shown in Fig. 6.5c, in general, there exists a proportional relationship between pin height and shoulder diameter. Figure 6.5d, e shows that no relation between pin height and pin diameter exists. For a given pin height there exists a range of pin diameter and pin height (h) is generally smaller than pin diameter ($h/d_p < 1$).

Welding Parameters

Tool rotation rate and tool traverse speed are the two most important welding parameters in friction stir welding of any material. For Mg alloys, Fig. 6.6 gives a snapshot of different tool rotation rates and traverse speeds used to join Mg alloys. Tool rotation rate and the traverse speed as high as 3,500 rpm and 10,000 mm/min have been used to join Mg alloys. The figure in the inset of Fig. 6.6 shows the

Table 6.2 Summary of tools used in the welding of Mg alloys

Tool material	Hardness	Feature on the pin	Shoulder dia (mm)	Pin diameter (mm)	Pin height (mm)	Reference
Tool steel	62 HR_C	Cylindrical, threaded (1/4–20)	19	6.3	–	Esparza et al. (2002)
Tool steel	62 HR_C	Cylindrical, threaded (1/4–20)	19	6.3	1.9	Esparza et al. (2003)
D2 (SKD11)		–	–	–	–	Lee et al. (2003)
–	–	Cylindrical, threaded, 1.5 mm pitch	18	6	6	Chang et al. (2004)
SKD61	–	–	12	4	–	Tsujikawa et al. (2006)
65Mn steel	–	–	–	–	–	Wang and Wang (2006)
–	–	Cylindrical	18	6	6	Wang et al. (2006)
H-13	–	–	19	6.35	5.72	Woo et al. (2006)
Steel	–	Cylindrical, threaded	20	2.5	2.4	Cavaliere and De Marco (2007)
–	–	Cylindrical, threaded	13	5	1.7	Kannan et al. (2007)
Carbon tool steel SKH9	–	Cylindrical	14	6	2.8	Mironov et al. (2007)
–	–	Coniform threaded	22	6	5.7	Xie et al. (2007)
–	–	–	19	6.35	–	Afrin et al. (2008)
–	–	Cylindrical, threaded	18	6	3.8	Dobriyal et al. (2008)
–	–	Cylindrical, threaded	13, 10	4, 5	–	Commin et al. (2009)
Tool steel	–	Cylindrical, threaded	15	5	3.9	Liao et al. (2009)
–	–	Cylindrical, threaded	20	6	5.7	Xie et al. (2009)
SKD61	–	Cylindrical	15	5	4.9	Yu et al. (2009)

H13	52	Conical (truncated), 30° angle	12, 19	6, 5 (near shoulder)	1.7, 2.9	Bruni et al. (2010)
–	–	Cylindrical, threaded	–	3.2	1.7	Chowdhury et al. (2010)
High carbon steel	70	Cylindrical, threaded	18	6	5.7	Padmanaban and Balasubramanian (2010a)
–	–	Cylindrical, threaded	18,20,24	8	5.9	Yang et al. (2010)
Die steel	–	Cylindrical, threaded	16	7	4.7	Yu et al. (2010)
H13	–	Cylindrical, threaded, ¼–20 (0.8 mm pitch)	19.1	6.4	4.5	Cao and Jahazi (2011)
–	–	Cylindrical, threaded, 1 mm pitch	18	6	5	Dhanapal et al. (2011)
Tunsten-moly high speed steel (SW7M)	–	–	24	8	5.8	Miara et al. (2011)
H13	–	–	19.1	6.4	5.7	Woo and Choo (2011)
SKD61 tool steel	–	Cylindrical, threaded	15	5	3.8	Chen et al. (2012)
H13	–	Cylindrical, flat	12.7	6.4	3.1	Darras (2012)
H13	–	Threaded	12	6 (at root), 3 (at tip)	3	Fu et al. (2012)
HotVar 55Cr10Mo23V9 (hot working steel)	–	Tapered, threaded	17	5 (at root), 3 (at tip)	1.8	Huetsch et al. (2012)
High carbon steel	–	Cylindrical	18	6	5.9	Razal Rose et al. (2012)
–	–	Cylindrical, threaded	15	5	5.7	Xin et al. (2012)
–	–	Cylindrical, threaded	24	8	5.9	Yang et al. (2013)

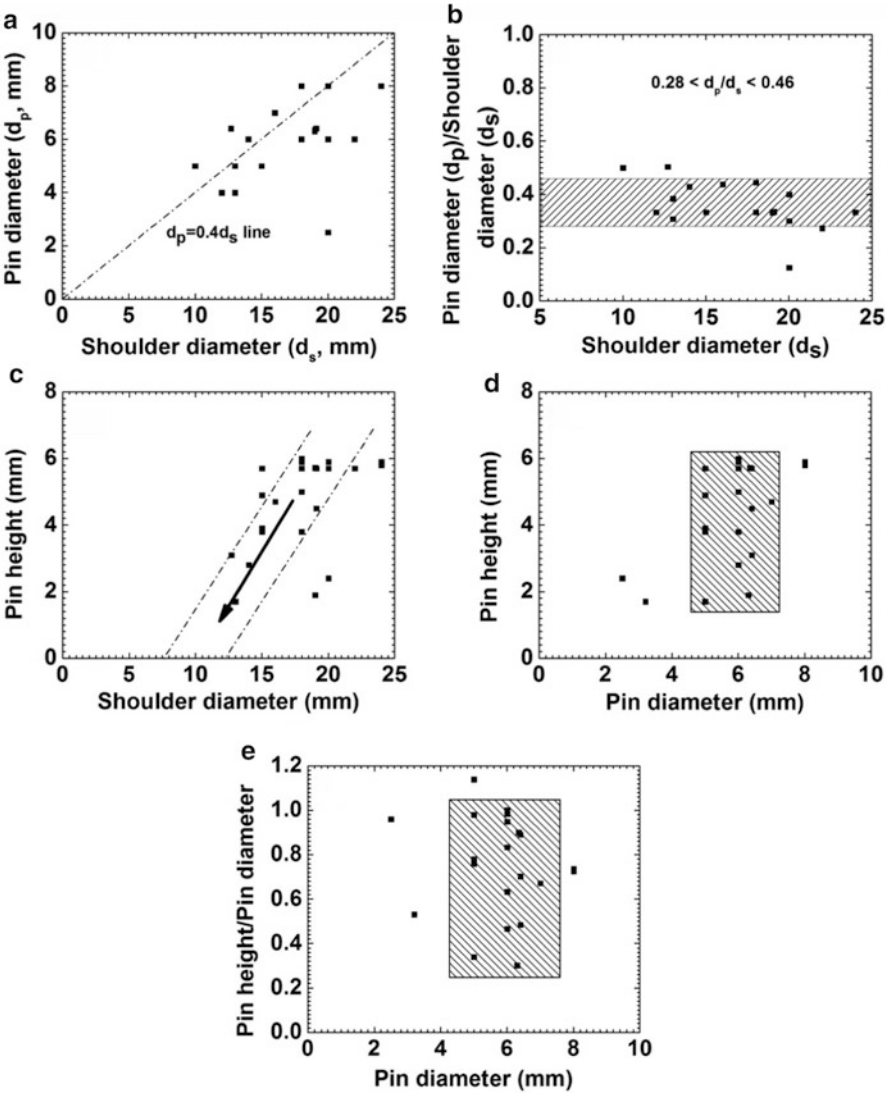

Fig. 6.5 Relationship between different parameters of friction stir welding tool (Esparza et al. 2002; Esparza et al. 2003; Lee et al. 2003; Chang et al. 2004; Tsujikawa et al. 2006; Wang and Wang 2006; Wang et al. 2006; Woo et al. 2006; Cavaliere and De Marco 2007; Kannan et al. 2007; Mironov et al. 2007; Xie et al. 2007; Afrin et al. 2008; Dobriyal et al. 2008; Commin et al. 2009; Liao et al. 2009; Mironov et al. 2009; Xie et al. 2009; Yu et al. 2009; Chowdhury et al. 2010; Padmanaban and Balasubramanian 2010a; Yang et al. 2010; Yu et al. 2010; Cao and Jahazi 2011; Dhanapal et al. 2011; Miara et al. 2011; Woo and Choo 2011; Chen et al. 2012; Darras 2012; Fu et al. 2012; Huetsch et al. 2012; Razal Rose et al. 2012; Xin et al. 2012; Yang et al. 2013)

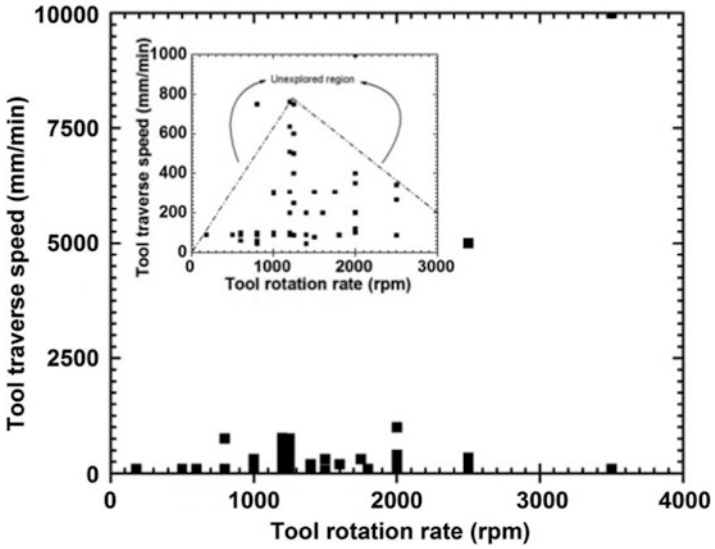

Fig. 6.6 Pictorial representation of tool rotation rate (rpm) and tool traverse speed (mm/min) used for friction stir welding to access process window (Esparza et al. 2002; Esparza et al. 2003; Lee et al. 2003; Park et al. 2003a; Park et al. 2003b; Chang et al. 2004; Wang et al. 2006; Woo et al. 2006; Jang et al. 2007; Mironov et al. 2007; Pareek et al. 2007; Xie et al. 2007; Xie et al. 2008; Liao et al. 2009; Mironov et al. 2009; Xie et al. 2009; Yu et al. 2009; Chowdhury et al. 2010; Yang et al. 2010; Woo and Choo 2011; Yang et al. 2011; Darras 2012; Huetsch et al. 2012; Razal Rose et al. 2012; Xin et al. 2012; Yang et al. 2013)

process window boundary used for Mg alloys with the majority of the tool rotation rate restricted to 3,000 rpm and the tool traverse speed limited to 800 mm/min respectively.

Temperature

Processing parameters including tool and workpiece material properties govern the thermal history of the joint which includes peak temperature, heating, and cooling rates of thermal profile. Understanding these parameters is essential since they control various aspects of microstructural evolution in the nugget, TMAZ, and HAZ. Typical thermal profiles measured at different locations (Fig. 6.7a) of the weldments are included in Fig. 6.7b. It shows that the peak temperature drops on moving away from the weld centerline. The rise in temperature is not observed until the tool has reached very close to the point at which temperature is being measured. After the tool moves away from the point of interest, the temperature starts reducing exponentially.

Far field peak temperature can be predicted using the analytical expression assuming point heat source and is given as

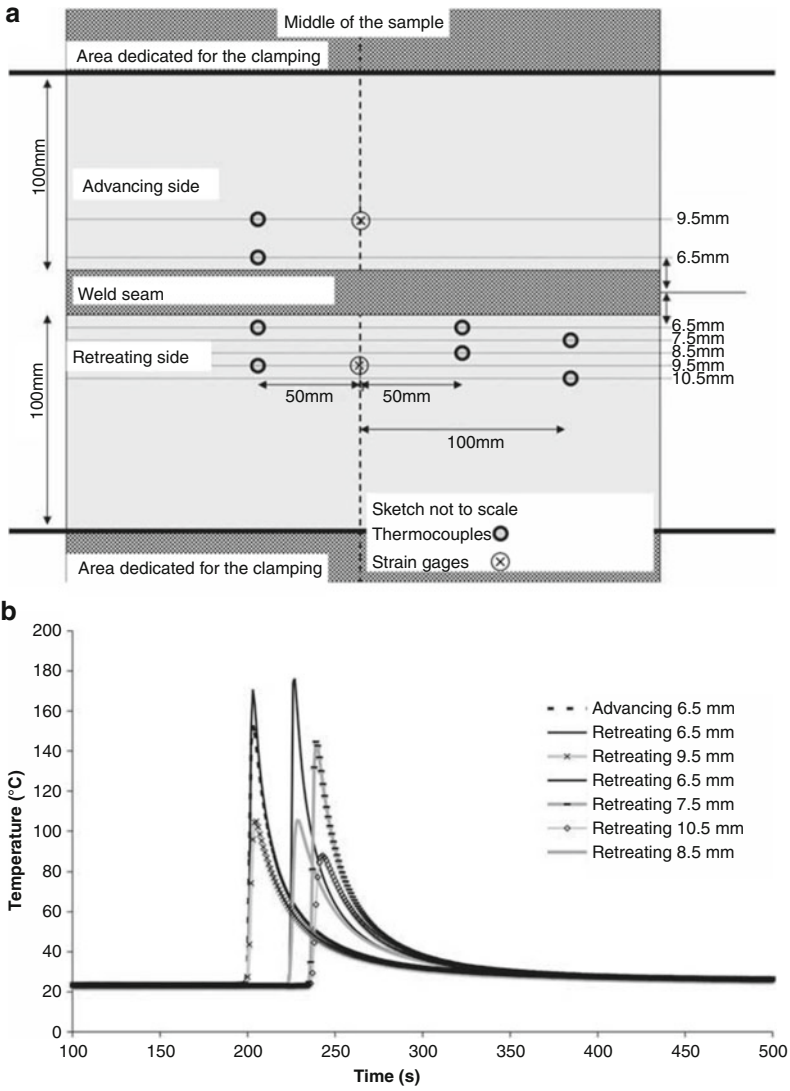

Fig. 6.7 (**a**) *Top view* showing the position of thermocouples (*open circles*) for thermal profile measurement and (**b**) thermal profiles corresponding to the locations shown in (**a**) (Commin et al. 2009, reprinted with permission from Elsevier)

$$T = T_{\mathrm{o}} + T_{\mathrm{source}} erfc\left(\frac{x}{2\sqrt{(k/\rho c_{\mathrm{p}})t}}\right) \tag{6.1}$$

where T_{o}, T_{source}, k, ρ, and c_{p} are room temperature, temperature of the source, thermal conductivity, density, and specific heat capacity, respectively. The Eq. (6.1) was used to fit the peak temperatures measured at different locations on advancing

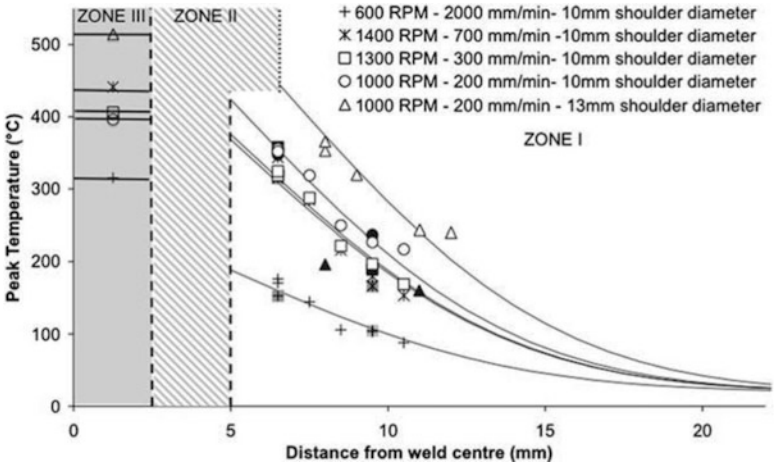

Fig. 6.8 Peak temperature distribution in different zones as a function of processing parameters (Commin et al. 2009, reprinted with permission from Elsevier). The *solid lines* in zone I were predicted using Eq. (6.1) whereas in Zone III by Chang et al. (2004)

side of AZ31B alloy for the data points shown in Fig. 6.8 whereas Chang model (Chang et al. 2004) was used to predict the peak temperature in the nugget as a function of tool rotation rate and tool shoulder diameter. The peak temperature in the nugget (zone III) increases with increase in tool rotation rate and tool shoulder diameter.

Processing Window

Figure 6.9 shows the processing window for five different Mg alloys: AZ91D, AZ61, AS41, AE42, and AZ31. As can be seen in this figure, the processing window for AZ91D and AZ61 is very narrow while AZ31 possesses the broadest window. Thus, the chemistry of the alloy plays an important role with regards to the process window within which it can be welded defect-free. A decrease in Al content with consequent lowering of strength is suggested to increase the processing window (Yu et al. 2009). It also shows that a tool rotation rate of 1000 rpm or above is required to get a defect-free weld. It should be mentioned here that the region beyond the dashed lines shown in Fig. 6.6 is an unexplored region and information about quality of weld in that region is unavailable. Hence, magnesium alloys are generally processed at higher weld power as compared to aluminum alloys. As shown in Fig. 6.6, most of the magnesium alloys are processed at a tool rotation rate greater than 500 rpm. There are many aluminum alloys which can be easily welded at a tool rotation rate below 500 rpm.

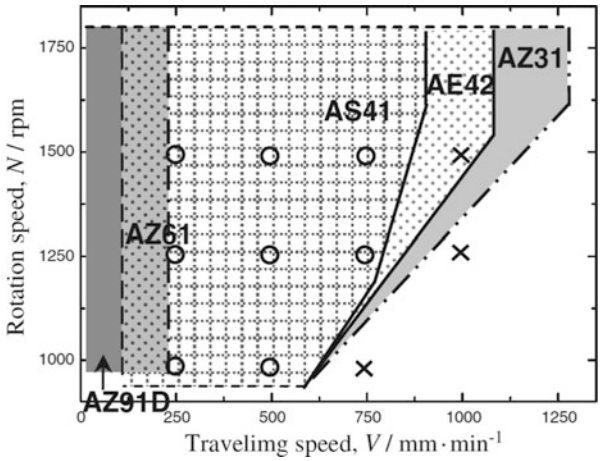

Fig. 6.9 Processing window of different Mg alloys (O: defect-free, x: defect) (Yu et al. 2009, reprinted with permission from Elsevier)

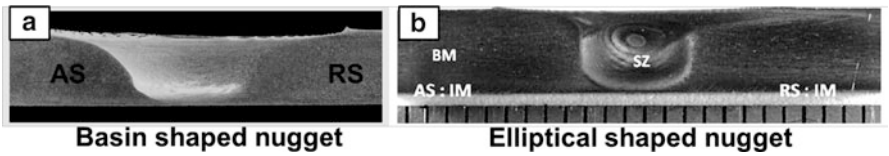

Fig. 6.10 Images illustrating basin- and elliptical-shaped nugget in (**a**) RE3Zn2Zr (Miara et al. 2011) and (**b**) $Al_6Mn_{0.5}Ca_2$ alloys (Chen et al. 2012, reprinted with permission from Elsevier). RE3Zn2Zr alloy was processed at 355 rpm tool rotation rate and 280 mm/min tool traverse speed. The tool rotation rate and tool traverse speed were 1,100 rpm and 300 mm/min, respectively

6.3.3 Evolution of Microstructure

6.3.3.1 Nugget Zone

The shape, size, and various microstructural features related to nugget zone are discussed in greater details in the following sections.

Shape of the Nugget Zone

In Fig. 6.10 examples of two types of nugget shape are shown for magnesium alloys. There are several macroscopic features which can be noted from these figures. The transition region on the advancing side is, in general, sharper than that on the retreating side. Figure 6.10a, b support this observation. The other feature which can be noted in nugget zone of Fig. 6.10b is the presence of several elliptical rings. As discussed in the Chap. 2, these are commonly referred to as "onion ring" due to their resemblance to sectioned onion.

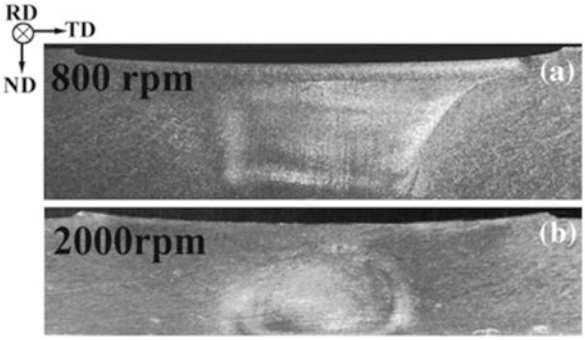

Fig. 6.11 Effect of change of tool rotation rate on the shape of the nugget in AZ31 alloy (Yang et al. 2013, reprinted with permission from Springer)

For a given tool geometry, changes in processing parameters alter the shape of the nugget significantly. For example, Yang et al. (2013) processed AZ31 at different tool rotation rates ranging from 800 rpm to 2,000 rpm and a corresponding change in nugget shape is observed (Fig. 6.11).

Grain Size

As mentioned before, high temperature coupled with extensive plastic deformation during friction stir welding causes a significant grain refinement due to dynamic recrystallization. Mishra and Ma (2005) tabulated the average grain size obtained during friction stir welding and processing of aluminum alloys where the average grain size is observed to vary in the range of 1–20 μm. With the application of special cooling arrangements, grain sizes in the range of 25–100 nm can be obtained (Su et al. 2006, Rhodes et al. 2003). Figure 6.12 illustrates significant grain refinement in the weld nugget zone of an AZ31B alloy using a cylindrical threaded tool (62 HRC hardness) (Esparza et al. 2002). The shoulder and pin diameters of the tool used was 19 mm and 6.3 mm, respectively. The tool traverse speed used was 60 mm/min while the tool rotation rate varied between 800 and 1,000 rpm. The average grain size of starting alloy (including twin boundaries) was reported to be 175 μm. After welding, the average grain size in the nugget zone reduced to 25 μm. Figure 6.12b shows the heterogeneous grain structure in the TMAZ region where a combination of fine and coarse grains including twin boundaries are present.

It should be noted that friction stir welding results in significant grain refinement in general. However, nugget with average grain size larger than the base material is also possible. Thus, Lee et al. (2003) reported an average grain size of 92 μm in the nugget zone of AZ31B-H24 alloy at 2,500 rpm tool rotation rate and 87 mm/min tool traverse speed. In another study, Jang et al. (2007) observed that the average grain size increased to 9 μm when AZ31B-H24 was processed at

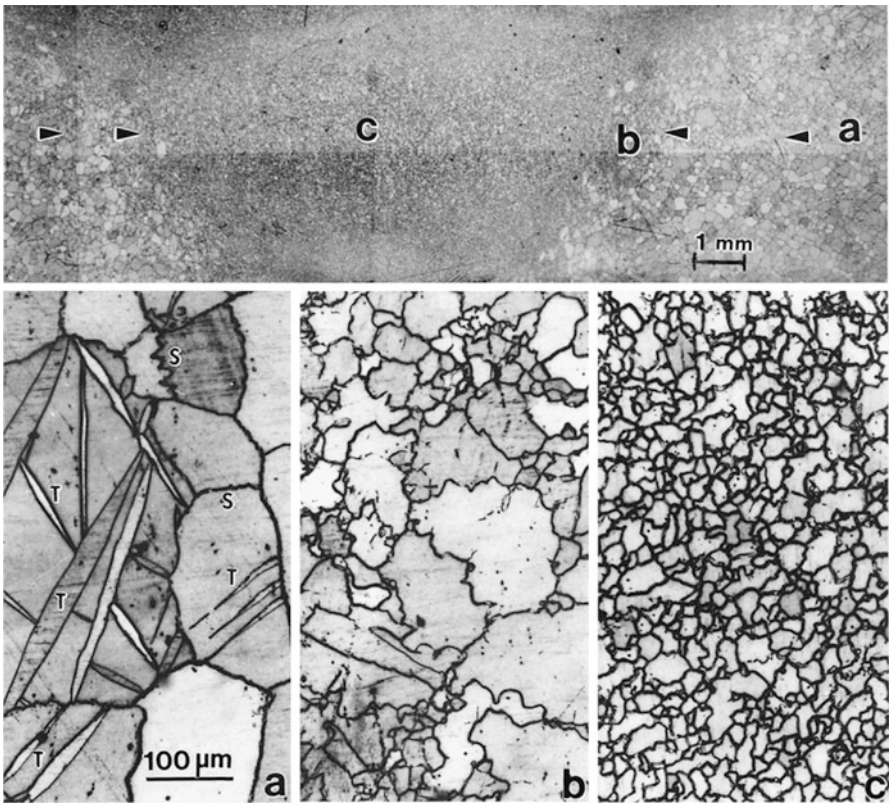

Fig. 6.12 An illustration of grain refinement in AZ31 magnesium alloy. *Top part* shows the transverse cross-section of the welded material; labels (**a**), (**b**), and (**c**) shows the locations where optical microscopy was carried out; (**a**) Base material, (**b**) transition zone, and (**c**) nugget zone (Esparza et al. 2002, reprinted with permission from Kluwer Academic Publishers)

1,600 rpm tool rotation rate and 200 mm/min tool traverse speed. The average grain size of the base material was close to 6 µm. A summary of the average grain size values after friction stir welding of Mg alloys are tabulated in Table 6.3. As in Al alloys, the grain size in the nugget region of majority of Mg alloys varies between 1 and 10 µm.

The variation of average grain size for various Mg alloys reported in published literature as a function of two most important FSP parameters - tool rotation rate and tool traverse speed—and its ratio (ω/v) is illustrated in Fig. 6.13. In general, a decrease in average grain size with decrease in tool rotation rate and with increase in tool traverse velocity is observed (Fig. 6.13a, b). A decrease in ω/v results in decrease in average grain size. In fact, this observation is also true for aluminum alloys. The large scatter in the average grain size is a consequence of the dependence of strain, strain rate and temperature on the processing parameters (see Sect. 2.5).

Table 6.3 Average grain size for various magnesium alloys obtained during friction stir welding under different processing conditions

Material	Thickness (mm)	Tool geometry	Rotation rate (rpm)	Traverse speed (mm/min)	Grain size (μm)	Reference
AZ31B		Cylindrical, threaded	800	60	25	Esparza et al. (2002)
AM60	20	Cylindrical, threaded	2,000	120	10, 15	Esparza et al. (2003)
AZ31B-H24	4	–	1,250–2,500	87–342	33–92	Lee et al. (2003)
AZ91D	2	–	800–1,800	90–750	0.9–5.4	Park et al. (2003a)
AZ61	6.3	Cylindrical, threaded	–	–	11	Park et al. (2003b)
AZ31	10	Cylindrical, threaded	180–1,800	90	2.6–7.5	Chang et al. (2004)
AZ31B	–	Cylindrical	800–1,400	45, 90	2.6–6.1	Wang et al. (2006)
AZ31B-H24 and -T4	4.8	–	1,600	200	9	Jang et al. (2007)
ZK60	3, 6	M6	600–2,000	100–400	1.2–7.0	Mironov et al. (2007)
AZ31B-H24	3.2	–	1,500, 2,000	78–204	12.8, 12.0	Pareek et al. (2007)
Mg-Zn-Y-Zr	6	Coniform, threaded	800	100	6.8	Xie et al. (2007)
AZ31B-H24	5.0	–	500–1,000	60–240	8.5–10.2	Afrin et al. (2008)
ZK60	8	Coniform, threaded	800	100	5.3	Xie et al. (2008)
AZ31B	4	Cylindrical, threaded	1,250	250–750	11.3	Liao et al. (2009)
ZK60A	3	Cylindrical, threaded	600	100	2	Mironov et al. (2009)
AZ61	2.5	–	475	75	5–15	Srinivasan et al. (2009)
ZK60 and ZK60-Y	6	Cylindrical, threaded	1,200	100	8.5, 6.7	Xie et al. (2009)
AZ31B-H24	2	Cylindrical, threaded	1,000	300	5.4	Chowdhury et al. (2010)
AZ31	6.3	Cylindrical, threaded	800	100	10, 13, 19	Yang et al. (2010)
AZ31B	6.5	–	600	60	17	Woo and Choo (2011)

(continued)

Table 6.3 (continued)

Material	Thickness (mm)	Tool geometry	Rotation rate (rpm)	Traverse speed (mm/min)	Grain size (μm)	Reference
Mg-Zn-Y-Zr	6	–	600–1,200	100	3.2–4.6	Xie et al. (2011)
AZ31B-H24	2	Cylindrical threaded and conical truncated	2,000	350, 100	10, 14	Yang et al. (2011)
AMX60	4	Cylindrical, threaded	1,100	200–400	1.3, 2.6	Chen et al. (2012)
AZ31B	3.2	Cylindrical, no feature	1,200–1,750	305–762	7.8–9.1	Darras (2012)
AZ31	2	Tapered, threaded	2,000–3,500	1,000–10,000	2.4–3.8	Huetsch et al. (2012)
AZ61A	6	Cylindrical	1,200	90	9	Razal Rose et al. (2012)
AZ31	6	Cylindrical, threaded	800	90	12	Xin et al. (2012)
AZ31	6.3	Cylindrical, threaded	800–3,500	100	18–25	Yang et al. (2013)

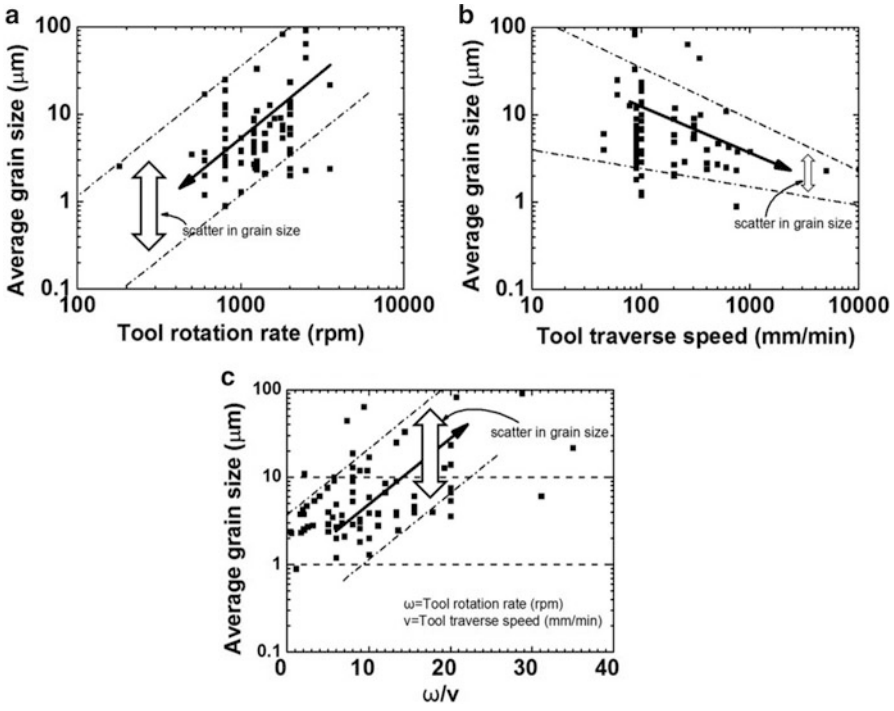

Fig. 6.13 Variation of average grain size as a function of tool rotation rate (ω) (**a**), tool traverse speed (v) (**b**), and their ratio ω/v (**c**). The *dash-dotted* lines in the figure show lower and upper bound of majority of the data as a function of these parameters. The *dashed line* in (**c**) represents majority of average grain size lies within this bound (Esparza et al. 2002; Esparza et al. 2003; Lee et al. 2003; Park et al. 2003a; Park et al. 2003b; Chang et al. 2004; Wang et al. 2006; Woo et al. 2006; Jang et al. 2007; Mironov et al. 2007; Pareek et al. 2007; Xie et al. 2007; Xie et al. 2008; Liao et al. 2009; Mironov et al. 2009; Xie et al. 2009; Yu et al. 2009; Chowdhury et al. 2010; Yang et al. 2010; Woo and Choo 2011; Yang et al. 2011; Darras 2012; Huetsch et al. 2012; Razal Rose et al. 2012; Xin et al. 2012; Yang et al. 2013)

Grain Size Variation Across Different Zones

The last section discussed the average grain size in the nugget zone. However friction stir welding modifies average grain size in the TMAZ and HAZ zones also (Fig. 6.14). The figure combines the data reported by Lee et al. (2003) and Liao et al. (2009) on friction stir welding of AZ31B. The grain size variation data across different zones reported by Afrin et al. (2008) also shows a similar trend. The work of Lee et al. illustrates a significantly coarser nugget region which decreases into the BM. Liao et al. processed AZ31B obtained from two different routes—roll compaction processed (RCP) and conventional hot extrusion (CHE). The grain size in friction stir welded AZ31B produced by RCP route shows no noticeable variation unlike the one produced using conventional hot extrusion technique. This illustrates the importance of initial microstructure on the final grain size across different zones of welded components.

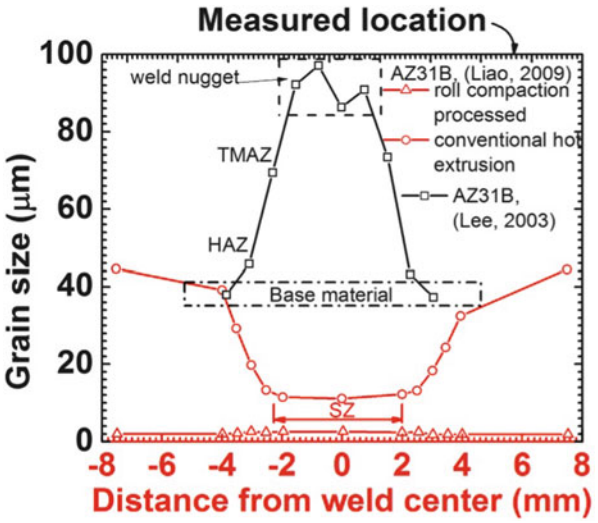

Fig. 6.14 Variation of average grain size across the welded region adapted from Lee et al. (2003) and Liao et al. (2009) on their work on AZ31B alloy

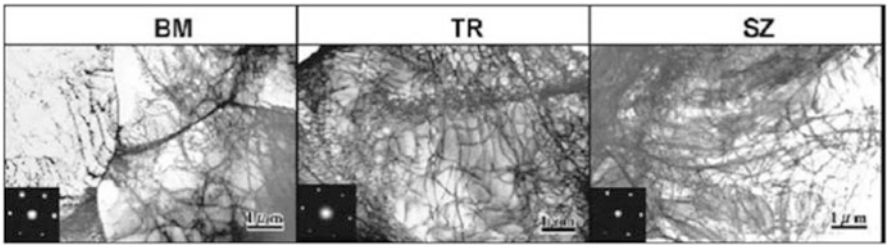

Fig. 6.15 Comparison of dislocation density evolution in different zones of friction stir welded alloy AZ31 (Park et al. 2003a, reprinted with permission from Elsevier)

Dislocations

As mentioned earlier, FSW involves intense plastic deformation at very high temperatures. The appearance of deformation controlled microstructural features like dislocation forest/cells/boundaries depend on the nature of material. Thus, friction stir welding of aluminum alloys (high stacking fault energy) results in dynamic recovery with a low dislocation density (nugget region) (See discussion about 7XXX/5XXX alloys in Chap. 5). The lower stacking fault energy of magnesium alloys results in reduced dynamic recovery which under similar processing conditions may lead to high dislocation density in the form of forest dislocations or even dislocation structures such as cells or low angle grain boundaries. Figure 6.15 compares the dislocation density across different zones of friction stir welded

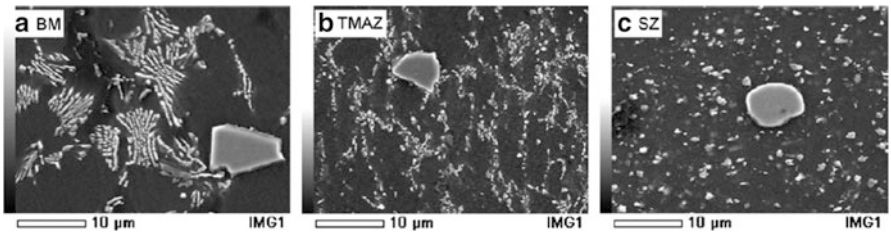

Fig. 6.16 Micrographs showing distribution of particles in different friction stir welded zones in AE42 alloy, (**a**) BM, (**b**) TMAZ, and (**c**) SZ (Yu et al. 2009, reprinted with permission from Elsevier)

AZ31 (Park et al. 2003a). The stir zone (SZ) or nugget representing dynamically recrystallized region has a dislocation density which is similar to that observed in transition region (TR) and base material (BM).

Effect of FSW on Precipitates and Dispersoids

As in aluminum alloys, the size, morphology, volume fraction, and the distribution of precipitates depends on the processing parameters. As discussed in Chap. 3, one of the following things can happen with regards to precipitates in precipitation strengthened magnesium alloys: (a) if the alloy is in solutionized condition and is followed by friction stir welding, the nugget may still remain in solutionized condition, or solutes may partially or fully precipitate out; (b) if the alloy is in under-aged condition, it might get fully aged/over-aged, or partially/fully dissolve/partially or fully reprecipitate. Hence, an adequate knowledge of the thermo-mechanical condition is essential to understand the state of precipitate evolution during friction stir welding. The dispersoids which are resistant to dissolution can get reduced in size due to the severe plastic deformation conditions existing in the nugget zone. This is amply illustrated in the scanning electron microscope images of particle distribution (Fig. 6.16) observed in BM, TMAZ, and SZ of a friction stir welded AE42 alloy (Yu et al. 2009). The AE42 alloy has two types of precipitates: lamellar-shaped $Al_{11}RE_3$ and coarse $Al_{10}RE_2Mn_7$ particle. As one progresses from BM to SZ, the lamellar-shaped $Al_{11}RE_3$ particles get finer in size with a more or less homogeneously distribution. Similarly, the $Al_{10}RE_2Mn_7$ particles reduce in size with its original sharp features assuming an almost elliptical shape.

Texture

Texture plays a very important role in the plastic deformation and fracture of magnesium alloys. Due to dominance of basal slip system during plastic deformation of magnesium at low and elevated temperatures, the basal slip system

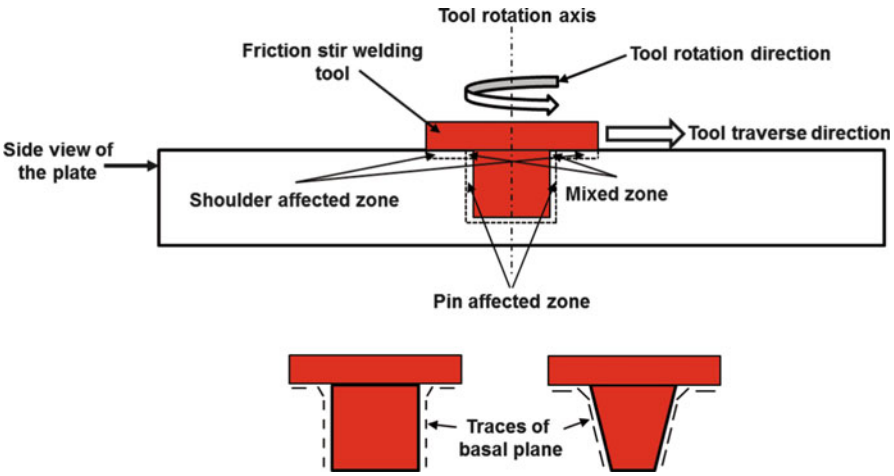

Fig. 6.17 (**a**) Side view of friction stir welding process showing different deformation zones at weld centerline around the tool and (**b**) traces of basal planes in different deformation zones

tends to align itself with the pin surface of the friction stir welding tool. This can be visualized with the aid of the schematic drawn in Fig. 6.17. The three different idealized zones around the rotating FSW tool are shown in Fig. 6.17a. In Fig. 6.17b the trace of these basal planes are shown where the orientation of the planes are observed to vary with the zone position. In the shoulder affected zone, they are parallel to the shoulder plane while in the pin affected zone, the planes are parallel to the pin surface. In the mixed zone the orientation of the basal planes is somewhere in between the orientation of these planes in the other two zones.

Pole figures are an effective way to illustrate the effect of friction stir welding on texture development in different zones. Figure 6.18a shows the idealized texture of a hot-rolled (or extruded) magnesium alloy. The texture shown in Fig. 6.18b represents the basal plane parallel to the surface of a cylindrical pin. All the reported studies so far supports this observation on the texture development in magnesium alloys during FSW (Park et al. 2003a; Woo et al. 2006; Suhuddin et al. 2009; Mironov et al. 2009; Fonda and Knipling 2011; Yang et al. 2013; Chowdhury et al. 2013). In literature this texture has been termed as B-fiber texture observed during simple shear deformation of hexagonal close packed material (Mironov et al. 2009; Fonda and Knipling 2011). In fact, the presence of B-fiber texture indicates that shear is a dominant plastic deformation mode during friction stir welding of not only hcp materials but also in fcc and bcc materials (Fonda and Knipling 2011).

Figure 6.18a represents the texture of the shoulder affected region. In its idealized form this coincides with the base material {0002} texture though other pole figures such as {10-10} and {11-20} in general are different from the base material texture. In some instances the high compressive stresses just

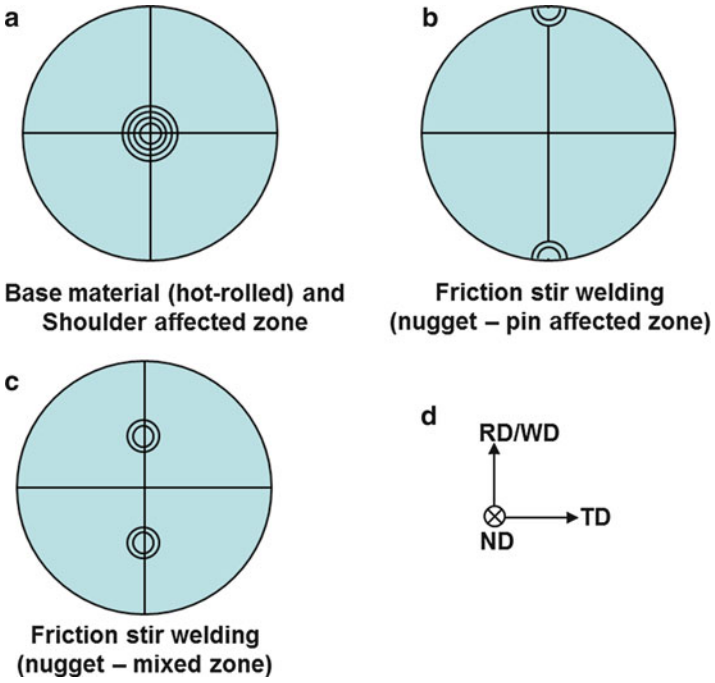

Fig. 6.18 Pole figure showing {0002} poles for magnesium alloy, (**a**) Shoulder affected zone, (**b**) Nugget - pin affected zone, (**c**) Nugget - mixed zone, and (**d**) Frame-of-reference

beneath tool shoulder promotes a random texture. Thus, Park et al. (2003a) observed a relatively weak basal plane texture in the upper part of nugget. The texture evolved during friction stir welding has a tendency to get modified due to the continued deformation and microstructural changes taking place on the trailing side of tool. In another work, Suhuddin et al. (2009) have shown by using a "stop-action technique" that just beneath the tool shoulder the {0002} pole figure was similar to Fig. 6.18a. It was also shown by Suhuddin et al. that this texture changed due to further deformation of the material in the shoulder affected zone on the trailing side of the tool. {0002} pole figure for mixed zone is shown in Fig. 6.18c. Since, it corresponds to an orientation in between pin- and shoulder-affected zones, the poles lie on WD/ND line. In certain instances the texture description as mentioned above can significantly differ from the simple picture presented here. This is particularly true in alloys containing a large volume fraction of second phase where these particles can stimulate nucleation of new grains leading to weak or random texture.

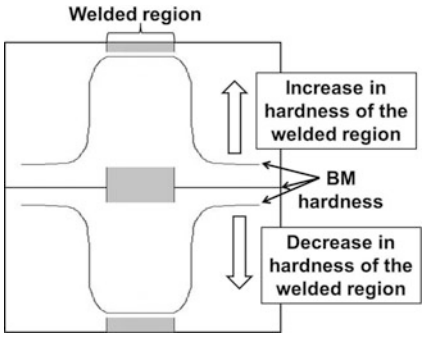

Fig. 6.19 A schematic of possible variations of hardness across the welded region (containing BM, HAZ, TMAZ, and nugget) for Mg alloys

Student Exercise

Redraw Fig. 6.17b for the case where basal planes are parallel to the surface of truncated conical pin as shown in Fig. 6.17a. Compare it with the pole figure shown in Fig. 6.18b. Now draw a cylindrical pin having threads on it. Show the traces of basal planes on the pin surface. Draw {0002} pole figures for both the surfaces of a thread.

6.3.4 Properties

6.3.4.1 Mechanical Properties

Hardness

As in Al alloys, three basic scenarios exists for the hardness distribution across the weld bead in Mg alloys—(1) better (higher), (2) same as, or (3) lower than the base hardness. These three situations are shown in Fig. 6.19 schematically where case (1) and (2) imply 100 % joint efficiency. It is a desirable situation for any welded components but is difficult to achieve in high strength alloys. For example, it is quite possible to attain 100 % joint efficiency in 3XXX and 5XXX series non-heat treatable Al alloys. However, heat-treatable alloys such as 2XXX and 7XXX friction stir welded alloys show significantly lower joint efficiency (De and Mishra 2011). Although, Fig. 6.19 shows a plateau in hardness profile in the welded region, in real components the shape of the hardness curves might be different. In aluminum alloys, W-shaped and V-shaped hardness profiles have been reported. In the cases where W-shaped hardness profiles have been reported, the minimum in hardness appears at either nugget/TMAZ or TMAZ/HAZ interface. For V-shaped hardness profile, the minimum in hardness appears at the center of the nugget. Such profiles have been reported for Mg alloys too. Figure 6.20 provides experimental evidence of such hardness profiles in some Mg alloys where alloy temper,

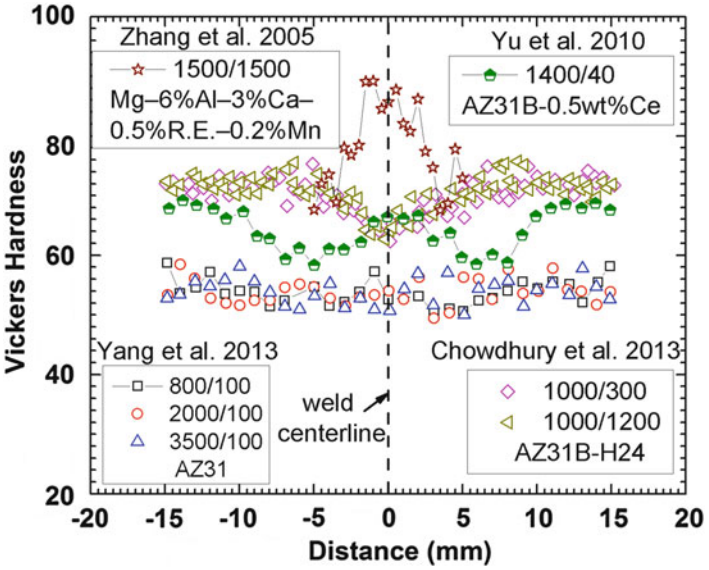

Fig. 6.20 Variation of hardness across the welds showing different shaped profiles in Mg alloys (Zhang et al. 2005; Yu et al. 2010; Yang et al. 2013; Chowdhury et al. 2013)

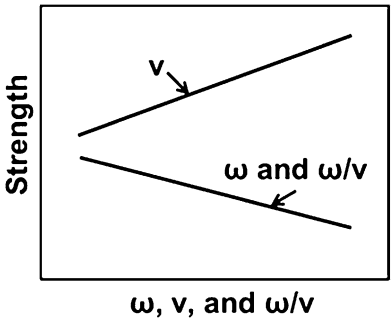

Fig. 6.21 A schematic showing variation in the strength of the friction stir weldments as a function of tool rotation rate (ω), tool traverse velocity (ν) and their ratio ω/ν

chemistry, and processing parameters play a major role in shaping the hardness profile. In few instances it is observed that the location of hardness minimum across the weld and fracture coincides as is later discussed in Sect. 6.2.4.1.4.

Strength and Ductility

In Fig. 6.21, the variation in the strength of friction stir welds as a function of tool rotation rate (ω), tool traverse speed (ν), and their ratio (ω/ν) is shown. According to this an increase in tool traverse speed results in an increase in the strength of the welded material. An increase in tool rotation rate or ω/ν results in a decrease in the

strength of welded material. However, experimental works on friction stir welded Mg alloys shows different type of trend. For example, Wang and Wang (2006) carried out butt welding of AZ31 alloy at two different tool rotation rates and five different tool traverse velocity. At 1,500 rpm, the tensile strength increases up to 75 mm/min after which increase in tool traverse speed show a decrease in the tensile strength. At 950 rpm, the tensile strength increases up to 90 mm/min tool traverse speed beyond which a drop in strength is observed. In another friction stir welding study carried out on AZ31B-H24 alloy, Pareek et al. 2007 changed tool traverse speed from 180 to 480 mm/min at tool rotation rates of 1,500 and 2,000 rpm. At both tool rotation rates, the change in tool traverse speed did not alter the yield strength of the joints while a difference of ~10–20 MPa is observed for joints made at 1,500 and 2,000 rpm. In fact, the alloy welded at higher tool rotation rate (2,000 rpm) shows higher yield strength compared to the weld made at lower tool rotation rate (1,500 rpm). A similar trend is observed for the tensile strengths of this material indicating a weak dependence of strength on the processing parameters (ω and ν). In the work of Afrin et al. (2008) on AZ31B-H24 alloy, an increase in tool rotation rate from 500 to 1,000 rpm results in a decrease in the strength of the material. A change in tool traverse speed from 60 to 240 mm/min increases the strength of the welded structure. Bruni et al. (2010) studied the variation of joint strength as a function of ω/ν for two different sheet thicknesses. For the thicker sheet ultimate tensile strength of the alloy first increased and then decreased with increase in ω/ν. In the thinner sheet, the tensile strength remained more or less same upto 60 mm/min before increasing to a peak value followed by a decrease with increase in ω/ν ratio. In another work Chowdhury et al. (2010) found that yield strength and ultimate tensile strength of AZ31B-H24 alloy decreased linearly with increase in ω/ν ratio as shown schematically in Fig. 6.21.

The discussion above indicates that a wide range of trends has been observed by individual researchers with respect to variation in strength as a function of the above mentioned parameters. The trends observed are based on small set of experiments conducted by individual researchers. Hence, a large number of data points on strength versus these processing parameters were plotted and are shown in Fig. 6.22. The variation of yield strength with tool rotation rate does not show any trend in Fig. 6.22. In fact, for a given tool rotation rate, the yield strength of the alloy (AZ31B) varied considerably. To investigate the reason for such a large variation, a set of data points shown within rectangular box in Fig. 6.22a is replotted in Fig. 6.22b. All the data plotted in Fig. 6.22b correspond to AZ31 alloy. The number following the filled black rectangular symbols represent tool traverse speed. Data points 1, 2, 5, and 6 carry words TC, SC, SQ, and TRI which denote different tool profiles. It is evident from this figure that for a given tool traverse speed the yield strength of welded structure can vary by two fold. It is a significant variation. The variation of yield strength with tool traverse speed is shown in Fig. 6.22c. Overall, it appears that yield strength increases with increase in tool traverse speed. However, here also a wide variation in yield strength can be noted for a given tool traverse speed. Figure 6.22d shows almost no dependence of yield strength on the ratio of tool rotation rate and tool traverse speed. Hence, strength of the welded

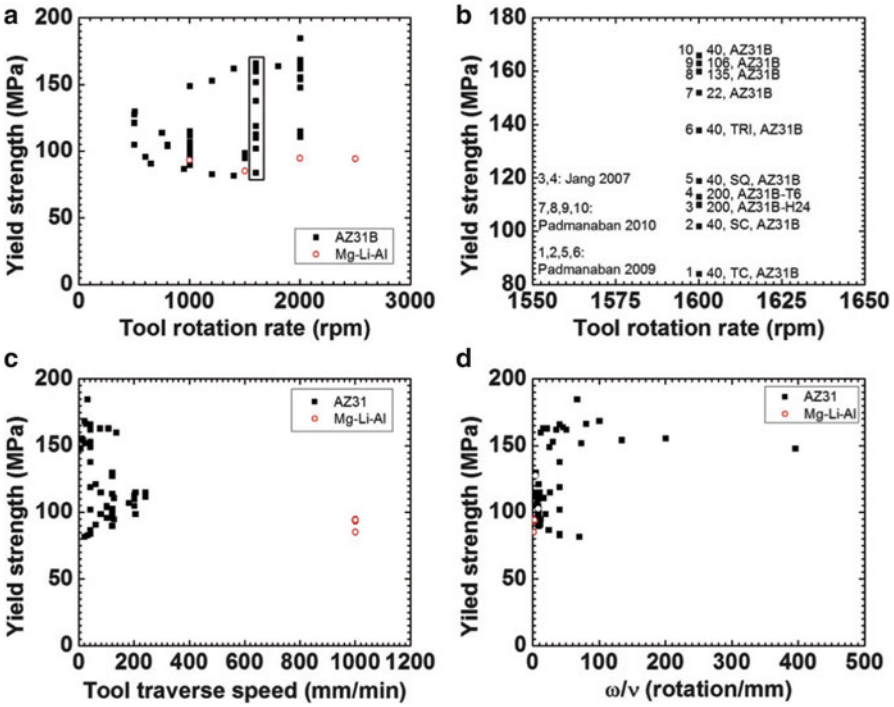

Fig. 6.22 The variation of yield strength of friction stir welded joints as a function of various processing parameters; (**a**) yield strength vs. tool rotation rate, (**b**) magnified view of the data points in rectangular box in (**a**), (**c**) yield strength vs. tool traverse velocity, and (**d**) yield strength vs. ratio of tool rotation rate and tool traverse speed (Tsujikawa et al. 2004; Gharacheh et al. 2006; Tsujikawa et al. 2006; Afrin et al. 2007; Jang et al. 2007; Pareek et al. 2007; Afrin et al. 2008; Padmanaban and Balasubramanian 2009; Cao and Jahazi 2009; Padmanaban and Balasubramanian 2010a; Yang et al. 2010)

material depends on large number of parameters. For a given tool rotation rates, tool traverse speed or the ratio of tool rotation rates and tool traverse speed, a change in other parameters such as tool tilt, tool pin profile, or workpiece thickness can change the final outcome of the weld significantly. Hence, no trend appears to emerge between strength of the weld and processing parameters such as tool rotation rates, tool traverse speeds, etc.

The strength data included above is obtained by testing tensile samples transverse to the welding direction where the gage length includes nugget, TMAZ, HAZ, and the base material. When such samples are tested the deformation is non-uniform along the length of the sample due to microstructural differences that exist across these zones. Hence, elongation-to-failure for the samples tested along the transverse direction is an average response of all the zones. The variation of elongation-to-failure as a function of processing parameters ω and ν is included in Fig. 6.23. A careful observation of Fig. 6.23a (elongation to fracture versus tool

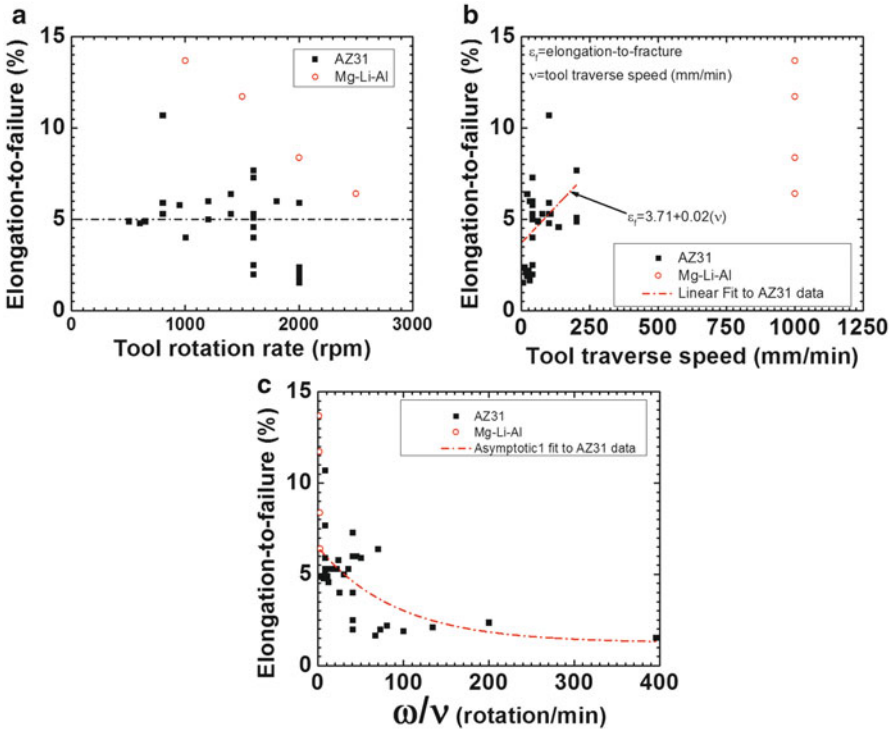

Fig. 6.23 The variation of ductility of friction stir welded joints as a function of various processing parameters; (**a**) elongation-to-failure vs. tool rotation rate, (**b**) elongation-to-failure vs. tool traverse velocity, and (**c**) elongation-to-failure vs. ratio of tool rotation rate and tool traverse speed (Tsujikawa et al. 2004; Gharacheh 2006; Tsujikawa et al. 2006; Afrin et al. 2007; Jang et al. 2007; Pareek et al. 2007; Afrin et al. 2008; Padmanaban and Balasubramanian 2009; Cao and Jahazi 2009; Padmanaban and Balasubramanian 2010a; Yang et al. 2010)

rotation plot) reveals that majority of the data points belonging to AZ31 alloy clusters around a horizontal dash-dotted line drawn at 5 %. Similarly, Fig. 6.23b (elongation-to-failure versus tool traverse speed) also does not provide any well-defined relationship. The plot in Fig. 6.23c (elongation-to-failure versus ω/ν), shows an asymptotic decrease in ductility with increase in the ratio ω/ν. Hence, in Mg alloys, the correlation of strength and ductility with the processing parameters such as tool rotation rate or tool traverse speed is weaker. It is to be mentioned that most of the results are based on the data points for AZ31alloy. A well-defined pattern might emerge in future as other Mg alloy systems are explored for friction stir welding.

Joint Efficiency

The change in load bearing capacity of a welded structure is quantified in terms of joint efficiency which is defined as the ratio of the strength of the welded structure to the strength of the base material. Ideally, a 100 % joint efficiency is always sought though in reality joint efficiencies are always lower. In conventional welding techniques such as arc welding the heat affected zone is the weakest spot in the entire structure. The high temperatures (above melting point) attained during welding process is considered to be the main reason for this lowering in efficiency. The joint efficiencies of AZ31 alloy (which is the most widely studied system by friction stir welding technique) is shown in Fig. 6.24 as a function of tool rotation rate, tool traverse speed and ω/ν where joint efficiency is defined based on both the yield and ultimate tensile strength of the alloy. Depending on the processing parameters used a joint efficiency from 20 % to ~100 % with no well-defined correlations between joint efficiency and processing parameters is observed. For a given processing parameter there is quite a large range of joint efficiencies and is probably a consequence of other joining variables (See Sect. 2.5, Chap. 2). Hence, selecting proper processing parameters is of utmost importance to obtain 100 % joint efficiency. It is quite evident that further research on welding of advanced high strength magnesium alloys is needed.

Fracture Behavior of the Joint

Majority of the failure in transversely tested tensile samples occur at the TMAZ and NZ interface, though in some cases weldments have failed in NZ or HAZ region. Figure 6.25 shows examples of fractured samples in different Mg alloys. Thus, fracture in AZ31B-H24 alloy (Fig. 6.25a) occurs at TMAZ and NZ interface on the advancing side of the weld (Afrin et al. 2008). Afrin et al. (2008) reported that out of 15 samples tested 14 failed in this fashion with the failure plane oriented at ~45° with the tensile axis. This is attributed to unfavorable basal texture orientation in the nugget with respect to the loading axis. Figure 6.25d, e also indicate that fracture occurs at the NZ and TMAZ interface on advancing side (Yang et al. 2010). However, in this instance the fracture was attributed to the lowest hardness exhibited by the weldments at this location. In Fig. 6.25b (Xie et al. 2009) and Fig. 6.25f (Yang et al. 2010) the fracture is located in the stir zone. In the case of Fig. 6.25b, the lowest hardness was found to be in the stir zone and the fracture location was described based on lowest strength of the stir zone. However, for Fig. 6.25f (Yang et al. 2010) the minimum hardness is in the TMAZ region indicating that factors other than hardness (possibly texture) affects the fracture of the joints. The fracture location and orientation shown in Fig. 6.25c for alloy ZK60-Y (Xie et al. 2009) is very similar to those shown in Fig. 6.25a, d, e. However, the location of fracture in Fig. 6.25c was in HAZ which had the lowest hardness region in the entire weldment. Hence, it appears that strength and texture of different zones play important role in the fracture of the welded structures.

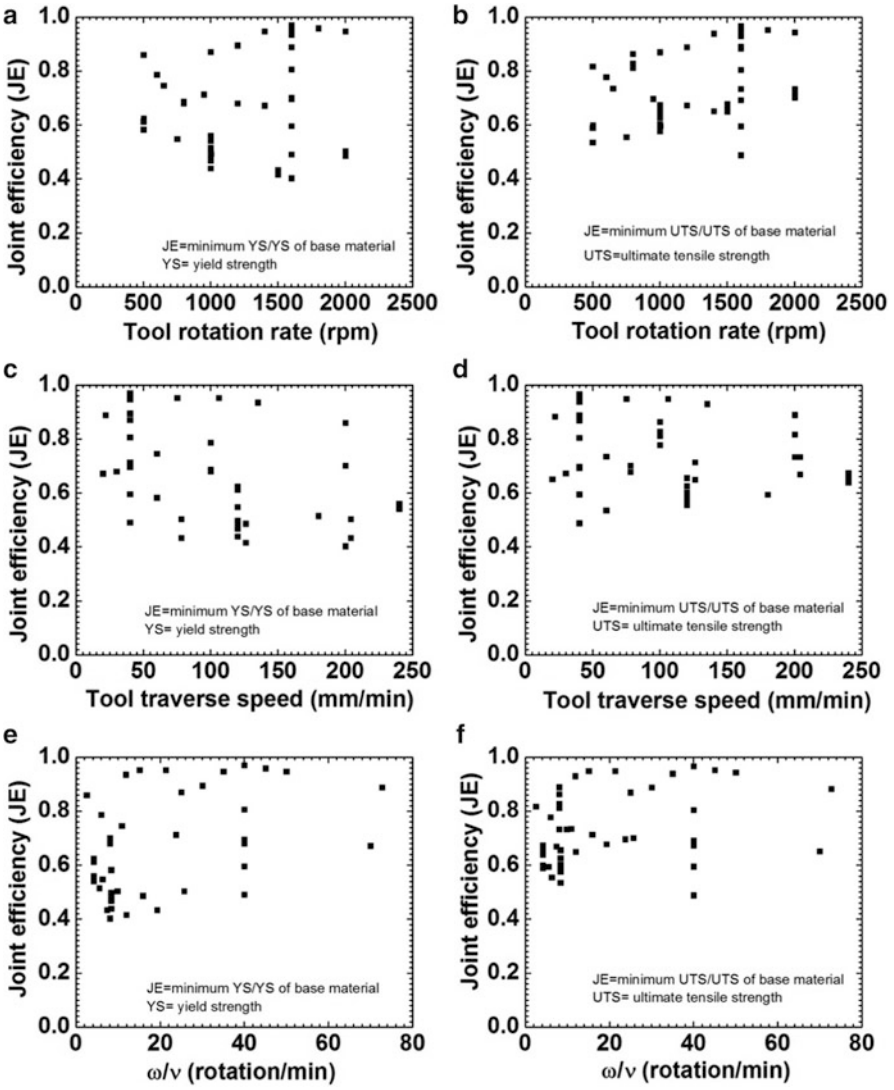

Fig. 6.24 The variation of joint efficiency of magnesium alloy AZ31 as a function of processing parameters—tool rotation rate (ω), tool traverse speed (ν), and ratio ω/ν. Joint efficiency has been defined as the ratio of minimum yield strength in the welded structure to the yield strength of the alloy (Tsujikawa et al. 2004; Gharacheh 2006; Afrin et al. 2007; Jang et al. 2007; Pareek et al. 2007; Afrin et al. 2008; Padmanaban and Balasubramanian 2009; Padmanaban and Balasubramanian 2010a; Yang et al. 2010)

Commin et al. (2012) studied the in-plane and out-of-plane plastic deformation using Speckle interferometry full field method to understand the conditions of failure at zone transition (mostly NZ/TMAZ interface) region. Figure 6.26 presents the speckle deformation maps for welds made using 10 and 13 mm shoulder

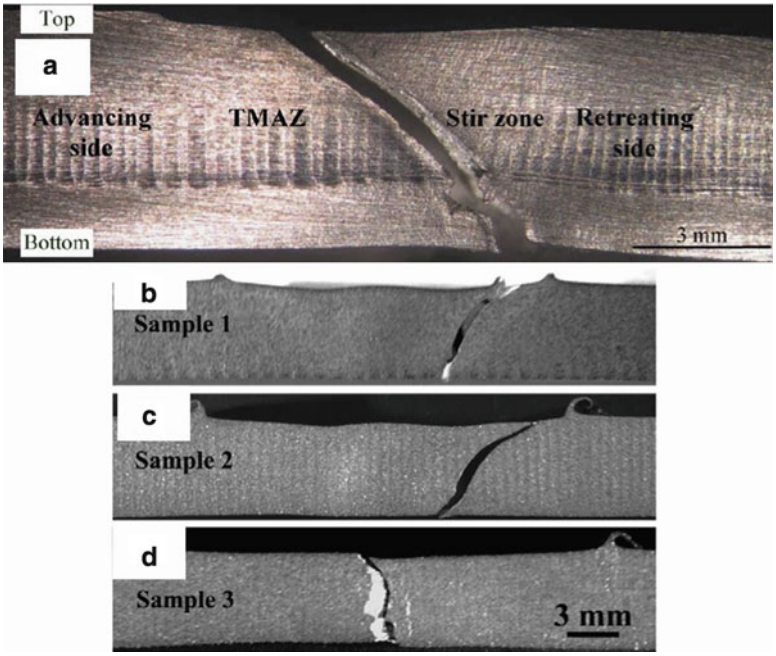

Fig. 6.25 Fracture locations of (**a**) AZ31B-H24 alloy (Afrin et al. 2008, reprinted with permission from Elsevier); (**b**), (**c**), and (**d**) AZ31 (Yang et al. 2010, reprinted with permission from Elsevier)

diameters respectively. The analysis was carried out on the top surface of the weld and the speckle deformation maps show the distribution of strain component ε_{22}. The intensity of this strain component is evident in the TMAZ region for both the welds. In both the cases advancing side (identified by letter A) shows higher strain localization which will promote fracture of such welded components in TMAZ region and is consistent with the experimental observation on friction stir welded Mg samples. The experiments carried out on transverse cross-section also show a similar strain accumulation in the advancing side of TMAZ (Fig. 6.26c).

Fatigue

A good fatigue life for a given loading condition is essential for various structural components used in transportation industries (Friedrich and Mordike 2006). Therefore, before FSW is adopted by industries to join Mg alloys, the fatigue properties of the welded components need a thorough evaluation. Very few such studies exist and most of it is limited to cyclic deformation behavior evaluation of friction stir welded AZ-series Mg alloys (Tsujikawa et al. 2004; Padmanaban and Balasubramanian 2010b; Padmanaban et al. 2011). In Fig. 6.27 the fatigue data of

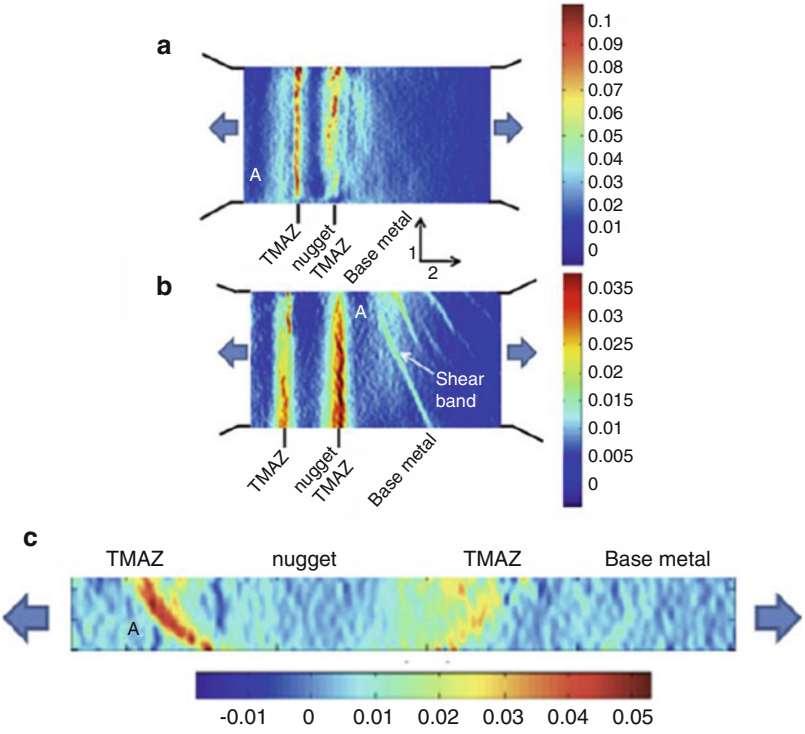

Fig. 6.26 Speckle interferometry results showing distribution of ε_{22} strain on top surface of the weld made using shoulder diameter (**a**) 10 mm and (**b**) 13 mm; (**c**) the distribution of ε_{22} strain on transverse cross-section of another weld; materal: AZ31 (Commin et al. 2012, reprinted with permission from Elsevier)

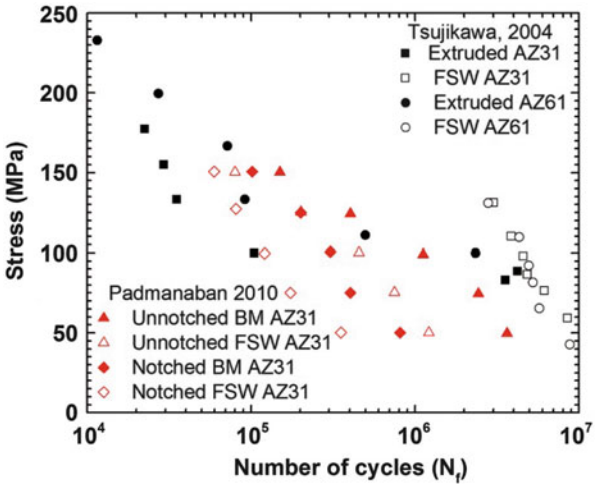

Fig. 6.27 S-N curve showing influence of friction stir welding in AZ-series Mg alloys (Tsujikawa et al. 2004; Padmanaban and Balasubramanian 2010b)

AZ31 and AZ61 alloys reported by Tsujikawa et al. (2004) and Padmanaban and Balasubramanian (Padmanaban and Balasubramanian 2010a) is compiled. Tsujikawa et al. (2004) reported an increase in fatigue life as a consequence of friction stir welding. However, AZ31 and AZ61 alloys show the same fatigue life in friction stir welded condition unlike in as-extruded condition where fatigue life of AZ31 is better than AZ61 alloy. The result of Padmanaban and Balasubramanian (Padmanaban and Balasubramanian 2010b) on AZ31 alloy shows opposite to what is reported by Tsujikawa et al. (2004). A decrease in fatigue life of notched and unnotched AZ31 fatigue samples is noted (Fig. 6.27). It should be remembered that the joint efficiencies of AZ31 and AZ61 were 75 % and 83 %, respectively, calculated using yield strength of the base metal and welded material in the work of Tsujikawa et al. (2004). For unnotched AZ31 sample tested by Padmanaban and Balasubramanian (Padmanaban and Balasubramanian 2010b) the weld efficiency was about 97 %.

6.3.4.2 Corrosion Behavior

Despite possessing attractive combination of thermal, mechanical, electrical, and magnetic properties, Mg and its alloys present little resistance to corrosion. Table 6.4 gives the relative nobility of various metals and alloys in the sea water where magnesium and its alloys occupy the anodic end of the series rendering it highly susceptible to galvanic corrosion (one among many types of corrosion). The severity of corrosion increasing with the distance between a metal or alloy with magnesium in the galvanic series. For example, the rate of corrosion of Mg-Fe couple will be higher than that of Mg-Al couple.

Pourbaix diagram (E-pH) is very widely used to know the thermodynamic potential of corrosion of a material in corrosion science. Figure 6.28 compares the corrosion property of Fe, Al, and Mg metals. Compared to Fe and Al, the E-pH range within which corrosion occurs in Mg is significantly larger. Sometime, metals and alloys protect themselves by forming tenacious oxide or hydroxide films which act as barriers between metal surface and surroundings creating a region of passivation. In the case of Fe and Al alloys a true passivation region exists in certain E-pH range (region labeled $Al_2O_3 \cdot H_2O$). However, for Mg and its alloys, magnesium hydroxide ($Mg(OH)_2$) forming at high pH fails to provide strong protection against continuing corrosion. The compressive rupture of $Mg(OH)_2$ film is another hindrance towards effective protection on exposed Mg surface. $Mg(OH)_2$ film has lower molar volume compared to Mg metal which results in compressive stresses within the hydroxide film formed on the surface of the Mg metal.

The chemistry, impurity content and processing route has also a major influence on the corrosion rate of Mg and its alloys. The chemistry of magnesium alloys especially the presence of impurities like Fe, Cu, Ni has significant influence on the corrosion behavior. The differences in processing history for the same alloy can also affect the corrosion behavior of the alloy. Thus, friction stir welding process also causes a significant change in the corrosion behavior of the alloy. In the nugget region, the

Table 6.4 Galvanic series in seawater at 25 °C (77 °F) for different metals and their alloys (ASM Handbook, Volume 13A, Corrosion: Fundamentals, Testing, and Protection, reprinted with permission from ASM International)

Corroded end (anodic, or least noble)	Protected end (cathodic, or most noble)
1. Magnesium	26. Chlorimet 2
2. Magnesium alloys	27. Copper alloy C27000 (yellow brass, 65 % Cu)
3. Zinc	28. Copper alloys C44300, C44400, C44500 (admiralty brass)
4. Galvanized steel or galvanized wrought iron	29. Copper alloys C60800, C61400 (aluminum bronze)
5. Aluminum alloys	30. Copper alloy C23000 (red brass, 85 % Cu)
6. 5052, 3004, 3003, 1100, 6053, in this order	31. Copper C11000 (ETP copper)
7. Cadmium	32. Copper alloys C65100, C65500 (silicon bronze)
8. Aluminum alloys	33. Copper alloy C71500 (copper nickel, 30 % Ni)
9. 2117, 2017, 2024, in this order	34. Copper alloy C92300, cast (leaded tin bronze G)
10. Low-carbon steel	35. Copper alloy C92200, cast (leaded tin bronze M)
11. Wrought iron	36. Nickel 200 (passive)
12. Cast iron	37. Inconel alloy 600 (passive)
13. Ni-Resist (high-nickel cast iron)	38. Monel alloy 400
14. Type 410 stainless steel (active)	39. Type 410 stainless steel (passive)
15. 50–50 lead-tin solder	40. Type 304 stainless steel (passive)
16. Type 304 stainless steel (active)	41. Type 316 stainless steel (passive)
17. Type 316 stainless steel (active)	42. Incoloy alloy 825
18. Lead	43. Inconel alloy 625
19. Tin	44. Hastelloy alloy C
20. Copper alloy C28000 (Muntz metal, 60 % Cu)	45. Chlorimet 3
21. Copper alloy C67500 (manganese bronze A)	46. Silver
22. Copper alloys C46400, C46500, C46600, C46700 (naval brass)	47. Titanium
23. Nickel 200 (active)	48. Graphite
24. Inconel alloy 600 (active)	49. Gold
25. Hastelloy alloy B	50. Platinum

grains are equiaxed, precipitates and dispersoids are significantly refined and homogeneously distributed, and the dislocation density, in general, is relatively low. The microstructure in TMAZ and HAZ however differ significantly from the nugget. Therefore, different regions are expected to have different corrosion behavior in the same corrosive atmosphere. But, detailed study about the corrosion response of different zones of friction stir welded Mg alloys is as of now unavailable. There are some studies pertaining to stress corrosion cracking behavior of AZ-series alloys where a significant loss of tensile strength and ductility is observed in friction stir

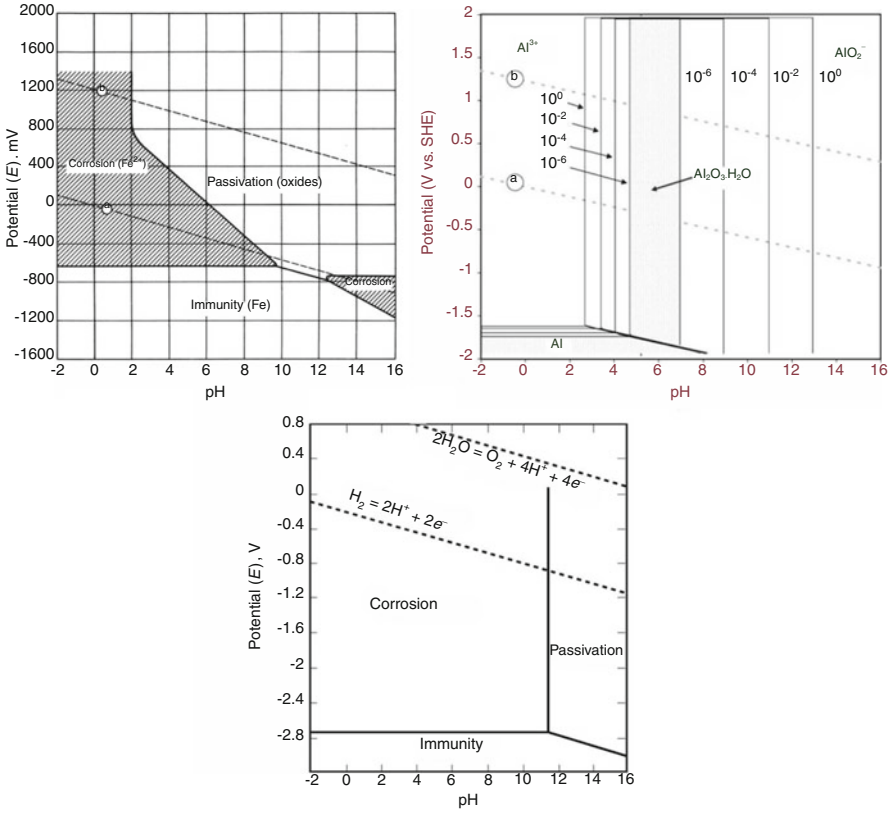

Fig. 6.28 Pourbaix diagram (Potential versus pH) to illustrate the relative resistance of (**a**) Fe (Volume 13A, Corrosion: Fundamentals, Testing, and Protection), (**b**) Al (Volume 13B, Corrosion: Materials), and (**c**) Mg corrosion in water. (http://www.asminternational.org/content/ASM/StoreFiles/06494G_Chapter_Sample.pdf, reprinted with permission from ASM International)

weldments as compared to base material (Srinivasan et al. 2009). In general friction stir welding results in significant grain refinement and change in crystallographic texture of Mg alloys. Unfavorable basal plane orientation (for example, basal plane perpendicular to tensile axis) can lead to crack nucleation and hydrogen build-up ahead of the crack-tip which assists crack propagation. With grain refinement, hydrogen diffusivity is expected to be higher due to increase in grain boundary area per unit volume. Literature provides preliminary evidence of hydrogen-assisted cracking in fine grained material (Argade et al. 2012).

Inferior stress-corrosion cracking resistance of friction stir welds does not however imply that all other forms of corrosion behavior will be worse compared to base material. As discussed previously, friction stir welding results in a better homogenization of microstructure and second phase particles. This is expected to have positive effect on pitting corrosion or galvanic corrosion. In the case of pitting corrosion, refinement and homogenous distribution of second phases results in a

significant decrease in the pit size. Several small pits may be a desirable design attribute than having a critically large size pit. However, a meaningful conclusion regarding the corrosion behavior of friction stir welds can be drawn only when significant amount of data is available. Thus, necessary research and development activities will be critical for the successful adoption of friction stir welded Mg alloys by industries.

References

N. Afrin, D.L. Chen, X. Cao, M. Jahazi, Strain hardening behavior of a friction stir welded magnesium alloy. Scripta Mater. **57**(11), 1004–1007 (2007)

N. Afrin, D.L. Chen, X. Cao, M. Jahazi, Microstructure and tensile properties of friction stir welded AZ31B magnesium alloy. Mater. Sci. Eng. A **472**(1–2), 179–186 (2008)

G.R. Argade, W. Yuan, K. Kandasamy, R.S. Mishra, Stress corrosion cracking susceptibility of ultrafine grained AZ31. J. Mater. Sci. **47**(19), 6812–6822 (2012)

M.M. Avedesian, H. Baker, ASM International, *Magnesium and Magnesium Alloys. ASM Speciality Handbook* (ASM International, Materials Park, 1999)

C. Bruni, A. Forcellese, F. Gabrielli, M. Simoncini, Effect of the ω/v ratio and sheet thickness on mechanical properties of magnesium alloy FSWed joints. Int. J. Mater. Form. **3**, 1007–1010 (2010)

X. Cao, M. Jahazi, Effect of welding speed on the quality of friction stir welded butt joints of a magnesium alloy. Mater. Des. **30**(6), 2033–2042 (2009)

X. Cao, M. Jahazi, Effect of tool rotational speed and probe length on lap joint quality of a friction stir welded magnesium alloy. Mater. Des. **32**(1), 1–11 (2011)

X. Cao, M. Jahazi, J.P. Immarigeon, W. Wallace, A review of laser welding techniques for magnesium alloys. J. Mater. Process. Technol. **171**(2), 188–204 (2006)

P. Cavaliere, P.P. De Marco, Friction stir processing of AM60B magnesium alloy sheets. Mater. Sci. Eng. A **462**(1–2), 393–397 (2007)

C.I. Chang, C.J. Lee, J.C. Huang, Relationship between grain size and Zener-Holloman parameter during friction stir processing in AZ31 Mg alloys. Scripta Mater. **51**(6), 509–514 (2004). Accessed 10 Oct 2011

J. Chen, H. Fujii, Y. Sun, Y. Morisada, K. Kondoh, K. Hashimoto, Effect of grain size on the microstructure and mechanical properties of friction stir welded non-combustive magnesium alloys. Mater. Sci. Eng. A **549**, 176–184 (2012)

S.M. Chowdhury, D.L. Chen, S.D. Bhole, X. Cao, Tensile properties of a friction stir welded magnesium alloy: effect of pin tool thread orientation and weld pitch. Mater. Sci. Eng. A **527** (21–22), 6064–6075 (2010)

S.H. Chowdhury, D.L. Chen, S.D. Bhole, X. Cao, P. Wanjara, Friction stir welded AZ31 magnesium alloy: microstructure, texture, and tensile properties. Metall. Mater. Trans. A **44A**(1), 323–336 (2013)

L. Commin, M. Dumont, J.-E. Masse, L. Barrallier, Friction stir welding of AZ31 magnesium alloy rolled sheets: influence of processing parameters. Acta Mater. **57**(2), 326–334 (2009)

L. Commin, M. Dumont, R. Rotinat, F. Pierron, J.-E. Masse, L. Barrallier, Influence of the microstructural changes and induced residual stresses on tensile properties of wrought magnesium alloy friction stir welds. Mater. Sci. Eng. A **551**, 288–292 (2012)

F. Czerwinski, Chapter 21. Magnesium alloys—design, processing and properties; welding and joining of magnesium alloys (2011)

B.M. Darras, A model to predict the resulting grain size of friction-stir-processed AZ31 magnesium alloy. J. Mater. Eng. Perform. **21**(7), 1243–1248 (2012)

P.S. De, R.S. Mishra, Friction stir welding of precipitation strengthened aluminium alloys: scope and challenges. Sci. Technol. Weld. Join. **16**(4), 343–347 (2011)
A. Dhanapal, S. Rajendra Boopathy, V. Balasubramanian, Developing an empirical relationship to predict the corrosion rate of friction stir welded AZ61A magnesium alloy under salt fog environment. Mater. Des. **32**(10), 5066–5072 (2011)
R.R. Dobriyal, B.K. Dhindaw, S. Muthukumaran, S.K. Mukherjee, Microstructure and properties of friction stir butt-welded AE42 magnesium alloy. Mater. Sci. Eng. A **477**(1–2), 243–249 (2008)
R.L. Edgar, Global overview on demand and applications for magnesium alloys, in *Magnesium Alloys and Their Applications*, ed. by K.U. Kainer (Wiley-VCH Verlag GmbH, Weinheim, 2000), pp. 3–8
J.A. Esparza, W.C. Davis, E.A. Trillo, L.E. Murr, Friction-stir welding of magnesium alloy AZ31B. J. Mater. Sci. Lett. **21**(12), 917–920 (2002)
J.A. Esparza, W.C. Davis, L.E. Murr, Microstructure-property studies in friction-stir welded, thixomolded magnesium alloy AM60. J. Mater. Sci. **38**(5), 941–952 (2003)
R.W. Fonda, K.E. Knipling, Texture development in friction stir welds. Sci. Technol. Weld. Join. **16**(4), 288–294 (2011)
H.E. Friedrich, B.L. Mordike, *Magnesium Technology: Metallurgy, Design Data, Applications* (Springer, New York, 2006)
R.D. Fu, H.S. Ji, Y.J. Li, L. Liu, Effect of weld conditions on microstructures and mechanical properties of friction stir welded joints on AZ31B magnesium alloys. Sci. Technol. Weld. Join. **17**(3), 174–179 (2012)
M.A. Gharacheh, A.H. Kokabi, G.H. Daneshi, B.S. Amirkhiz, R. Sarrafi, The influence of the ratio of "rotational speed/traverse speed" (ω/ν) on mechanical properties of AZ31 friction stir welds. Int. J. Mach. Tool. Manufact. **46**(15), 1983–1987 (2006)
L.L. Huetsch, J. Hilgert, K. Herzberg, J. dos Santos, N. Huber, Temperature and texture development during high speed friction stir processing of magnesium AZ31. Adv. Eng. Mater. **14**(9), 762–771 (2012)
J.R. Davis & Associates, ASM International, *Aluminum and Aluminum Alloys. ASM Specialty Handbook* (ASM International, Materials Park, 1993)
Y.H. Jang, S.S. Kim, C.D. Yim, C.G. Lee, S.J. Kim, Corrosion behaviour of friction stir welded AZ31B mg in 3.5% NaCl solution. Corrosion. Eng. Sci. Tech. **42**(2), 119–122 (2007)
B.M. Kannan, W. Dietzel, R. Zeng, R. Zettler, J.F. dos Santos, A study on the SCC susceptibility of friction stir welded AZ31 Mg sheet. Mater. Sci. Eng. A **460**, 243–250 (2007)
J.F. King, Materials perspective magnesium: commodity or exotic? Mater. Sci. Technol. **23**(1), 1–14 (2007)
W.B. Lee, Y.M. Yeon, S.B. Jung, Joint properties of friction stir welded AZ31B-H24 magnesium alloy. Mater. Sci. Tech. **19**(6), 785–790 (2003)
J. Liao, N. Yamamoto, K. Nakata, Effect of dispersed intermetallic particles on microstructural evolution in the friction stir weld of a fine-grained magnesium alloy. Metall. Mater. Trans. A **40A**(9), 2212–2219 (2009)
L.M. Liu, Z.D. Zhang, G. Song, L. Wang, Mechanism and microstructure of oxide fluxes for gas tungsten arc welding of magnesium alloy. Metall. Mater. Trans. A **38**(3), 649–658 (2007)
Magnesium Vision 2020 USAMP, *Magnesium Vision 2020: A North American Strategic Vision for Magnesium* (USAMP 2006) http://www.uscar.org/commands/files_download.php?files_id=240
D. Miara, A. Pietras, K. Mroczka, Microstructure and properties of friction stir butt-welded magnesium casting alloys. Arch. Metall. Mater. **56**(3), 749–758 (2011)
S. Mironov, Y. Motohashi, R. Kaibyshev, Grain growth behaviors in a friction-stir-welded ZK60 magnesium alloy. Mater. Trans. **48**(6), 1387–1395 (2007)
S. Mironov, Y. Motohashi, R. Kaibyshev, H. Somekawa, T. Mukai, K. Tsuzaki, Development of fine-grained structure caused by friction stir welding process of a ZK60A magnesium alloy. Mater. Trans. **50**(3), 610–617 (2009)

R.S. Mishra, Z.Y. Ma, Friction stir welding and processing. Mater. Sci. Eng. R. Rep. **50**(1–2), 1–78 (2005)

G. Padmanaban, V. Balasubramanian, Selection of FSW tool pin profile, shoulder diameter and material for joining AZ31B magnesium alloy—an experimental approach. Mater. Des. **30**(7), 2647–2656 (2009)

G. Padmanaban, V. Balasubramanian, An experimental investigation on friction stir welding of AZ31B magnesium alloy. Int. J. Adv. Manuf. Tech. **49**(1–4), 111–121 (2010a)

G. Padmanaban, V. Balasubramanian, Fatigue performance of pulsed current gas tungsten arc, friction stir and laser beam welded AZ31B magnesium alloy joints. Mater. Des. **31**(8), 3724–3732 (2010b)

G. Padmanaban, V. Balasubramanian, G. Madhusudhan Reddy, Fatigue crack growth behaviour of pulsed current gas tungsten arc, friction stir and laser beam welded AZ31B magnesium alloy joints. J. Mater. Process. Technol. **211**(7), 1224–1233 (2011)

M. Pareek, A. Polar, F. Rumiche, J.E. Indacochea, Metallurgical evaluation of AZ31B-H24 magnesium alloy friction stir welds. J. Mater. Eng. Perform. **16**(5), 655–662 (2007)

S.H.C. Park, Y.S. Sato, H. Kokawa, Effect of micro-texture on fracture location in friction stir weld of mg alloy AZ61 during tensile test. Scripta Mater. **49**(2), 161–166 (2003a)

S.H.C. Park, Y.S. Sato, H. Kokawa, Microstructural evolution and its effect on Hall-Petch relationship in friction stir welding of thixomolded mg alloy AZ91D. J. Mater. Sci. **38**(21), 4379–4383 (2003b)

A. Razal Rose, K. Manisekar, V. Balasubramanian, Influences of welding speed on tensile properties of friction stir welded AZ61A magnesium alloy. J. Mater. Eng. Perform. **21**(2), 257–265 (2012)

C.G. Rhodes, M.W. Mahoney, W.H. Bingel, M. Calabrese, Fine-grain evolution in friction-stir processed 7050 aluminum. Scripta Mater. **48**(10), 1451–1455 (2003)

S. Santhanakrishnan, N. Kumar, N. Dendge, D. Choudhuri, S. Katakam, S. Palanivel, H.D. Vora, R. Banerjee, R.S. Mishra, N.B. Dahotre, Macro and microstructural study of laser processed WE43 (Mg-Y-Nd) magnesium alloy. Metall. Mater. Trans. B **44**, 1190–1200 (2013)

P.B. Srinivasan, R. Zettler, C. Blawert, W. Dietzel, A study on the effect of plasma electrolytic oxidation on the stress corrosion cracking behaviour of a wrought AZ61 magnesium alloy and its friction stir weldment. Mater. Char. **60**(5), 389–396 (2009)

C.D. Sorensen, Friction stir welding tool designs, in *ASM Handbook, Volume 6A: Welding Fundamentals and Processes*, ed. by T. Lienert, T. Siewert, S. Babu, V. Acoff (ASM International, Materials Park, 2011)

J.Q. Su, T.W. Nelson, C.J. Sterling, Grain refinement of aluminum alloys by friction stir processing. Philos. Mag. **86** (2006); Article Taylor & Francis Ltd

U.F.H.R. Suhuddin, S. Mironov, Y.S. Sato, H. Kokawa, C.W. Lee, Grain structure evolution during friction-stir welding of AZ31 magnesium alloy. Acta Mater. **57**(18), 5406–5418 (2009)

M. Tsujikawa, H. Somekawa, K. Higashi, H. Iwaskai, T. Hasegawa, A. Mizuta, Fatigue of welded magnesium alloy joints. Mater. Trans. **45**(2), 419–422 (2004)

M. Tsujikawa, Y. Abe, S.W. Chung, S. Oki, K. Higashi, I. Hiraki, M. Kamita, Cold-rolled Mg-14 mass % Li-1 mass % Al alloy and its friction stir welding. Mater. Trans. **47**(4), 1077–1081 (2006)

Y.N. Wang, C.I. Chang, C.J. Lee, H.K. Lin, J.C. Huang, Texture and weak grain size dependence in friction stir processed Mg-Al-Zn alloy. Scripta Mater. **55**(7), 637–640 (2006)

X. Wang, K. Wang, Microstructure and properties of friction stir butt-welded AZ31 magnesium alloy. Mater. Sci. Eng. A **431**(1–2), 114–117 (2006)

W. Woo, H. Choo, Softening behaviour of friction stir welded Al 6061-T6 and Mg AZ31B alloys. Sci. Technol. Weld. Join. **16**(3), 267–272 (2011)

W. Woo, H. Choo, D.W. Brown, P.K. Liaw, Z. Feng, Texture variation and its influence on the tensile behavior of a friction-stir processed magnesium alloy. Scripta Mater. **54**(11), 1859–1864 (2006)

G.M. Xie, Z.Y. Ma, L. Geng, R.S. Chen, Microstructural evolution and mechanical properties of friction stir welded Mg-Zn-Y-Zr alloy. Mater. Sci. Eng. A **471**(1–2), 63–68 (2007)
G.M. Xie, Z.Y. Ma, L. Geng, Effect of microstructural evolution on mechanical properties of friction stir welded ZK60 alloy. Mater. Sci. Eng. A **486**(1–2), 49–55 (2008)
G.M. Xie, Z.Y. Ma, L. Geng, Effect of Y addition on microstructure and mechanical properties of friction stir welded ZK60 alloy. J. Mater. Sci. Technol. **25**(3), 351–355 (2009)
G.M. Xie, Z.Y. Ma, Z.A. Luo, P. Xue, G.D. Wang, Effect of rotation rate on microstructures and mechanical properties of FSW mg-zn-Y-zr alloy joints. J. Mater. Sci. Technol. **27**(12), 1157–1164 (2011)
R. Xin, B. Li, A. Liao, Z. Zhou, Q. Liu, Correlation between texture variation and transverse tensile behavior of friction-stir-processed AZ31 mg alloy. Metall. Mater. Trans. A **43A**(7), 2500–2508 (2012)
J. Yang, B.L. Xiao, D. Wang, Z.Y. Ma, Effects of heat input on tensile properties and fracture behavior of friction stir welded Mg-3Al-1Zn alloy. Mater. Sci. Eng. A **527**(3), 708–714 (2010)
Q. Yang, X. Li, K. Chen, Y.J. Shi, Effect of tool geometry and process condition on static strength of a magnesium friction stir lap linear weld. Mater. Sci. Eng. A **528**(6), 2463–2478 (2011)
J. Yang, D. Wang, B.L. Xiao, D.R. Ni, Z.Y. Ma, Effects of rotation rates on microstructure, mechanical properties, and fracture behavior of friction stir-welded (FSW) AZ31 magnesium alloy. Metall. Mater. Trans. A **44A**(1), 517–530 (2013)
L. Yu, K. Nakata, J. Liao, Microstructural modification and mechanical property improvement in friction stir zone of thixo-molded AE42 mg alloy. J. Alloys Compd. **480**(2), 340–346 (2009)
S. Yu, X. Chen, Z. Huang, Y. Liu, Microstructure and mechanical properties of friction stir welding of AZ31B magnesium alloy added with cerium. J. Rare Earths **28**(2), 316–320 (2010)
D. Zhang, M. Suzuki, K. Maruyama, Microstructural evolution of a heat-resistant magnesium alloy due to friction stir welding. Scr. Mater. **52**, 899–903 (2005)

Chapter 7
Friction Stir Welding of High Temperature Alloys

High temperature alloys pose an interesting challenge to friction stir welding. In the previous chapters on aluminum and magnesium alloys, we dealt with matrix elements that do not undergo allotropic transitions. This implies that the microstructural changes were limited to grain size and precipitates. Among high temperature alloys of industrial significance, the present chapter is limited to titanium alloys and steels. Both alloy systems involve complexity of phase transformation, and therefore peak temperature as well as cooling rate during friction stir welding makes a significant difference. Nickel base alloys and copper alloys are not covered in this book, but much of what is discussed applies to those. Students and readers can apply the treatment of alloys covered in this book to nickel and copper alloys by selecting the right type of physical metallurgy.

For high strength aluminum alloys, friction stir welding is considered to be an enabling technology as it can weld non-weldable (classification based on fusion welding) 2XXX and 7XXX alloys. For titanium alloys and steels, a number of fusion welding techniques produce acceptable weld performances. In such cases, an immediate question is, why should we consider friction stir welding? The answer has to lie in the combination of performance of friction stir welds and the fact that wrought microstructure avoids the issues of cast microstructure related defects which is an essential part of fusion welding process. The performance of welds not only includes properties, but also distortion and residual stresses. As will be highlighted in Chap. 10, residual stresses are very different in friction stir welding and the detailed mechanisms for fusion and friction stir welding differ. Once we move beyond the question of justification for using friction stir welding, then the focus shifts to details of the process.

As emphasized earlier, the friction stir process inherently couples heat input and material flow, which is accomplished by rotation and movement of the tool. Chapter 4 dealt with tools and a major aspect that is applicable to this chapter is the criticality of tool material. Our selection of titanium alloys and steels also illustrates this aspect. Later in this chapter, reference to the polycrystalline cubic boron nitride (PCBN) tool for steels will come. While the PCBN tool is an excellent

R.S. Mishra et al., *Friction Stir Welding and Processing: Science and Engineering*,
DOI 10.1007/978-3-319-07043-8_7,

material for steel welds, the reactivity of BN with titanium completely rules it out for titanium alloys. In addition to reactivity and thermal stability the role of diffusion at high temperatures in promoting growth of a reaction layer and subsequent wear of tools is also a pertinent issue. The issue of tool material selection is however less of a focus in this chapter and the main emphasis is placed on the microstructural aspects of welding.

7.1 Titanium Alloys

7.1.1 Introduction and Basic Physical Metallurgy

The basic classification for titanium alloys are:

- α alloys,
- near-α alloys,
- α + β alloys,
- near-β alloys, and
- β alloys.

Ti-6Al-4V alloy is an α + β alloy. At ambient temperature it contains some beta phase. The importance of this classification lies in the types of microstructure that result from these.

7.1.1.1 Alloy Chemistry and Phase Transformation

Titanium alloys have some of the highest specific structural properties because of its high strength and low density (4.5 g/cc). Pure titanium has hexagonal closed packed (hcp) crystal structure at low temperatures which transforms to body centered cubic (bcc) crystal structure above 882 °C. The alloying elements influence this beta transition temperature and accordingly they are classified as α- or β-stabilizer. Aluminum is the most common α-stabilizer used and interstitial elements like O and N which are readily soluble stabilizes the alpha phase. The β-stabilizers are classified as (a) β isomorphous, or (b) β eutectoid. Figure 7.1 shows the effect of alloying elements on phase diagram and is an adaption of a figure from the book on Titanium by Lütjering and Williams (2007). The readers should refer to this book for details of most of the physical metallurgy of titanium alloys described in this chapter. The alloying elements listed in Fig. 7.1 will become the basis of discussion of some of the results. The neutral elements like Sn are considered as α-stabilizer when present with Al.

The beta transus temperature is very important for friction stir welding and processing of titanium alloys. The crystal structure transformation impacts the diffusivity and flow stress of titanium alloys. Figure 7.2 shows the change in

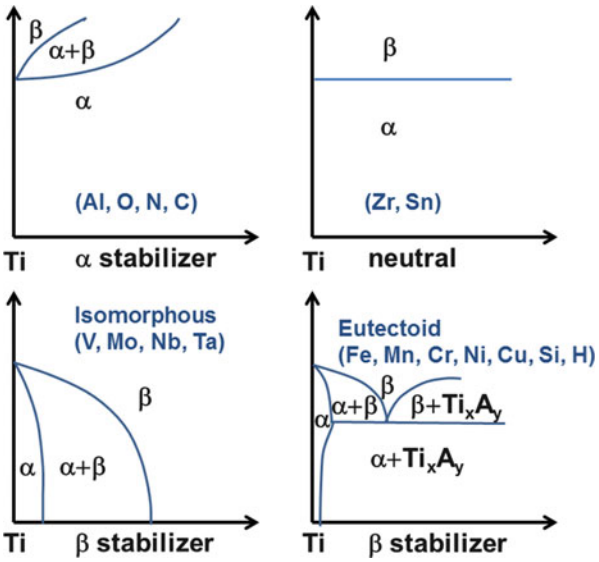

Fig. 7.1 A schematic illustration of effect of alloying elements on phase diagram of titanium alloys (Adapted from Lütjering and Williams 2007)

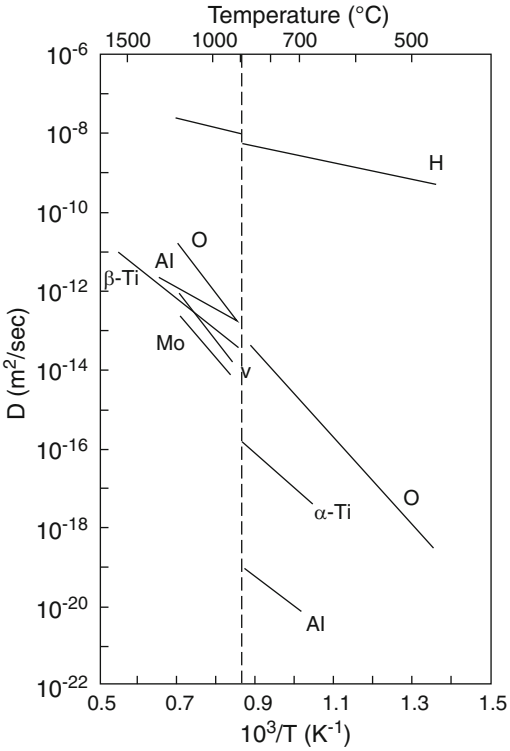

Fig. 7.2 Variation of diffusivity for various elements in α and β phases (Lütjering and Williams 2007, reprinted with permission from Springer). Note the jump in diffusivity of some key alloying element like Al across the beta transus temperature

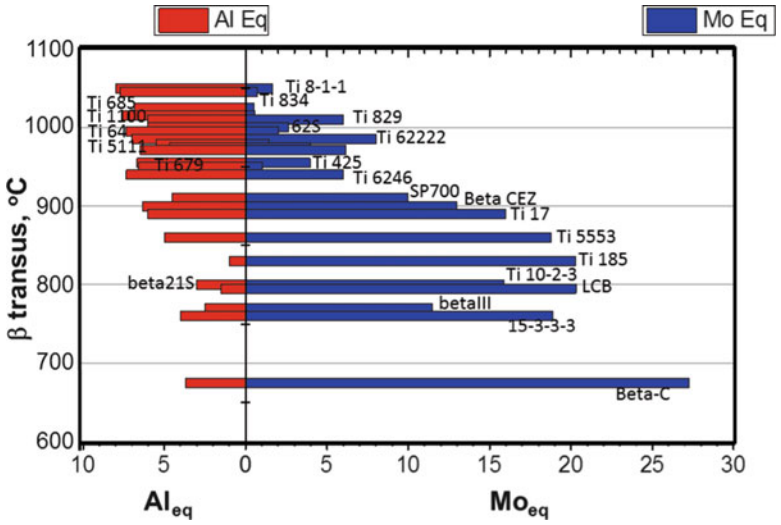

Fig. 7.3 A plot showing the values for Al_{eq} and Mo_{eq} for various titanium alloys and its relationship with the β transus

diffusion rate of various alloying elements. Key thing to note is a jump in diffusivity values across the beta transus temperature, particularly for key alloying element like Al. This plays a key role in material flow.

Any commercial titanium alloys in general contain several alloying elements. Two empirical relationships are used to club together the net effect of alloying elements into α stabilizing elements and β stabilizing elements as (Lütjering and Williams 2007),

$$[Al]_{eq} = [Al] + 0.17\ [Zr] + 0.33\ [Sn] + 10\ [O], \text{ and}$$

$$[Mo]_{eq} = [Mo] + 0.2\ [Ta] + 0.28\ [Nb] + 0.4\ [W] + 0.67\ [V] + 1.25\ [Cr] + 1.25\ [Ni] + 1.7\ [Mn] + 1.7\ [Co] + 2.5\ [Fe].$$

Figure 7.3 shows the values of Al_{eq} and Mo_{eq} plotted with beta transus for many commercial alloys. Some bars are not identified because of lack of space, but the overall pattern emerges. Figure 7.4 plots the same data with a beta stability index that brings out the correlation between the beta transus and composition quite clearly. The process parameters during friction stir welding and processing are selected to control the peak temperature and resultant microstructure is discussed with reference to beta transus temperature. This will be highlighted in the subsequent sections. Most of the results reported so far are for Ti-6Al-4V alloy, which is the workhorse of titanium alloys.

The last step in establishing the framework for discussion is the critical cooling rate from the peak temperature to retain the beta microstructure. Figure 7.5 is based on an empirical correlation from Yolton et al. (1979) and depicts the ability

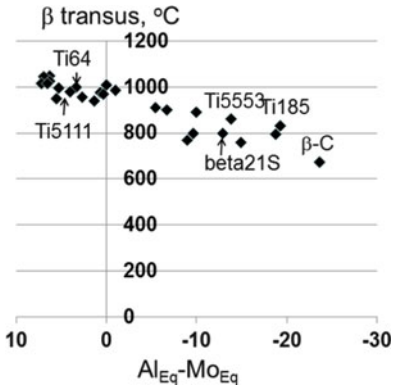

Fig. 7.4 A beta stability map showing the beta transus temperature for all the alloys shown in Fig. 7.3. A better correlation emerges in this plot

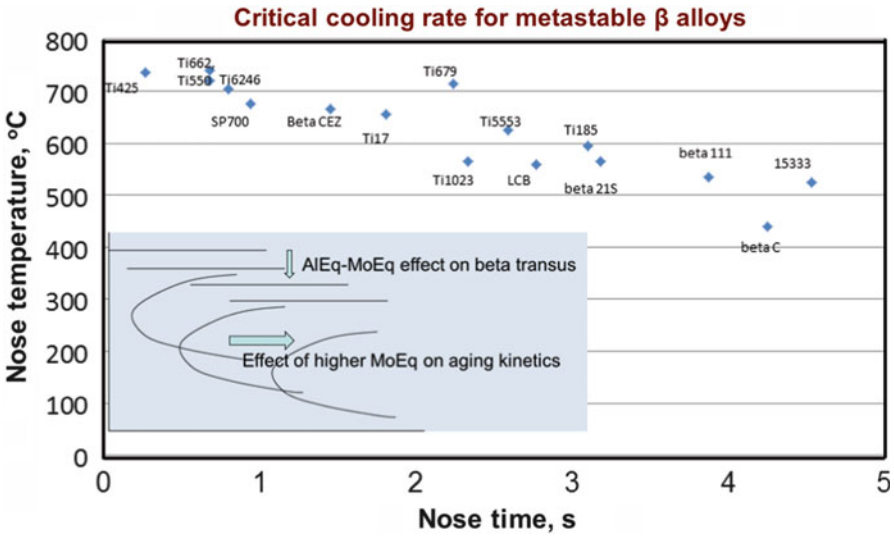

Fig. 7.5 Variation of nose temperature and time for various titanium alloys. Note that near alpha alloys like Ti-6Al-4V are not on this plot as the nose time calculation leads to negative values. This plot can be used to determine the possibility of retaining beta phase during cooling from friction stir process peak temperature

to quench in the beta phase from the friction stir process peak temperature. Note that many near alpha alloys are not on this plot because the calculation gives a negative value of nose time. The implication being that such titanium alloys will always transform from beta to alpha phase during cooling. For these alloys the morphology of transformed microstructure becomes an important consideration for properties.

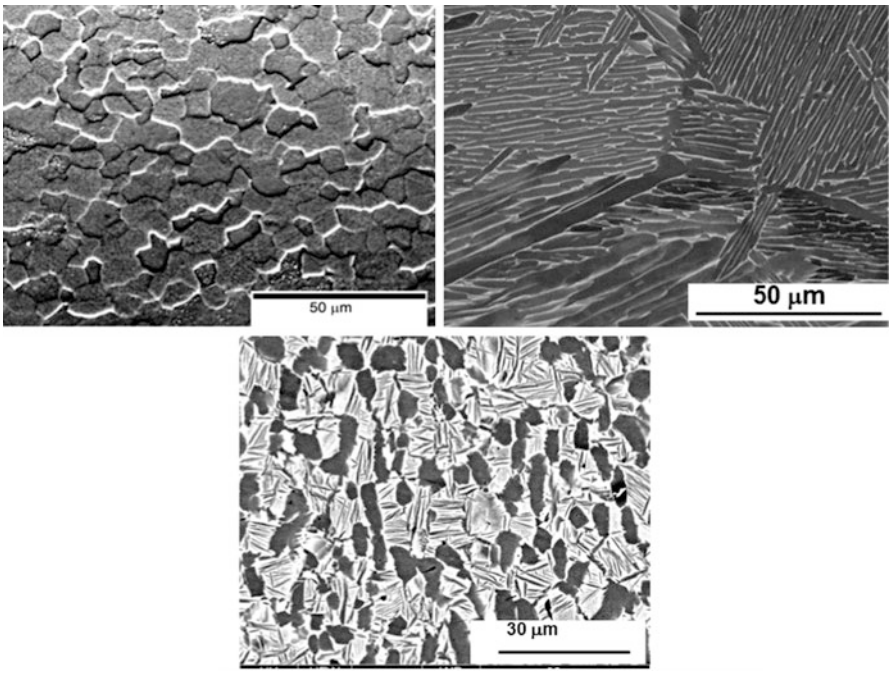

Fig. 7.6 Examples of three basic types of microstructure observed in titanium alloys, (**a**) fully equiaxed grains, (**b**) fully lamellar microstructure in an alpha + beta alloy cooled from above beta transus, and (**c**) a duplex microstructure in an alpha + beta alloy processed in two phase field. The dark equiaxed particles in (**c**) are referred to as primary alpha particles

7.1.1.2 Basic Microstructural Framework

This short section lays out the foundation for microstructural evolution in various titanium alloys. Two separate tracks are important to keep in mind during this discussion. First, given the relevance of Ti-6Al-4V alloy for the titanium alloys and the fact that it is an $\alpha + \beta$ alloy with several microstructural variants, an understanding of such alloy is important. Second, considering the details of the friction stir process, maximum strength-ductility is possible in near-beta alloys, such as Ti-6Al-2Sn-4Zr-6Mo, which has not been explored.

The microstructure of titanium alloys can be classified into three basic types; (a) equiaxed grain morphology, (b) fully lamellar morphology, and (c) duplex microstructure (essentially a mixture of lamellar and equiaxed microstructure). The simplest microstructure, of course, is the equiaxed morphology (Fig. 7.6a). Grains in beta titanium alloys are equiaxed and this would be applicable to friction stir process as well. Fully lamellar microstructure evolves during cooling from temperatures above beta transus (Fig. 7.6b). The size of colonies and width of lath depends on the cooling rate. The most unique microstructure applicable to titanium alloy is the duplex microstructure shown in Fig. 7.6c. The dark particles in this

figure are referred to as primary α particles. This microstructure results from high temperature processing of alpha + beta alloys in the two-phase field. The volume fraction of the primary alpha particles depends on the temperature and act as pinning points for the beta grains at that temperature. The beta grains transform to lamellar alpha during cooling. The beta phase at ambient temperature is confined to interlamellar regions and grain boundaries. The starting microstructure for friction stir welding and processing is likely to be one of these and will be used as the framework for microstructural evolution discussion.

7.1.2 Tool Materials and Related Issue

Unlike in previous chapters, the tool aspect is discussed up front since it limits the operating window for friction stir process. Table 7.1 lists some of the tool materials reported for titanium alloys up to 2011. It is not an extensive list and certainly better tool materials are being developed. W based alloys and WC cermet are the most common and recent use of a new cobalt-base superalloy has given very good results. Wear of tools is a major issue as is the rate of tool traverse speed. W is an alpha stabilizer and other than contamination and stress concentration concerns, incorporation of W containing particles can lead to formation of alpha phase if the alloy is taken to high temperature after welding or processing.

7.1.3 Mechanical Properties of Titanium Alloys

Figure 7.7 shows an overview of strength and ductility in titanium alloys. It is instructive to keep the range of 800–1,200 MPa in mind for discussion of property change after friction stir welding. Typical value of hardness for Ti-6Al-4V alloy is around 325 HVN. Depending on the starting microstructure, Ti-6Al-4V can have yield strength values between 850 and 1,100 MPa and an elongation of approximately 10%. A key point to note is that the near-beta and beta alloys are often referred to as high strength titanium alloys, but the typical strength values are only around 1,200 MPa. The strength values can be increased by aging. Most of the time, α_2 (Ti_3Al) is the phase responsible for strengthening of alpha titanium alloys. In alpha + beta alloys also α_2 particles can strengthen the alpha phase. The interfacial layer of beta phase can strengthen from secondary precipitation of alpha in the beta layer. The beta titanium alloys are strengthened by the ω/β' phase. Most of the discussion in literature on ω phase formation during aging of beta alloys is based on isomorphous phase diagram. Very few beta alloys have high content of eutectoid elements. Solid solution strengthening also contributes to the strength of titanium alloys, although this contribution will remain unchanged during friction stir welding. For alloys processed above beta transus, the prior beta grain size is usually quite coarse. As will be presented later, during friction stir welding the prior beta grain size can be kept fine.

Table 7.1 Some published tool materials used for FSW of titanium alloys

Author	Tool material	Processed material	Tool geometry and dimension (mm)	Processing parameters	Tool wear
Ramirez and Juhas (2003)	CP W	Ti-6Al-4V	–	275 rpm	–
Lee et al. (2005)	TiC	CP Ti	–	1,100 rpm 500 mm/min	–
Reynolds et al. (2005)	W-25 % Re	Timetal 21S	–	200 rpm 50–300 mm/min	–
Lienert et al. (2007)	CP W	CP Ti, Ti-6Al-4V, Ti-15V-3Cr-3Al-3Sn	Pin L-6.4; Pin D-7.9; Sh. D-15	275 rpm Up to 100 mm/min	–
Pilchak et al. (2007a)	W-Re	Ti-6Al-4V	Pin L-1.27; Pin D-5; Sh. D-19	100 rpm 4 ipm	–
Pilchak et al. (2007b)	W-Re	Ti-6Al-4V	–	100/150 rpm 5/10 ipm	–
Zhang et al. (2008a)	Mo based tool	Ti-6Al-4V	Pin L-2; Pin D-5.1-3; Sh. D-15; Geo.- Taper pin, convex shoulder	300–600 rpm 60 mm/min	–
Zhang et al. (2008b)	PCBN	Ti-6Al-4V	Pin L-2; Pin D-5.1-3; Sh. D- 15; Geo.- Taper pin, convex shoulder	200 rpm 50 mm/min	Tool pin diameter decreased, severe wearing happened due to chemical reactivity

Pasta and Reyonds (2008)	W-25% Re	Ti-6Al-4V	Pin D- 5; Sh. D-15	150 rpm 100 mm/min	–
Kumar et al. (2009)	WC-Co	Ti-6Al-4V	Pin L-1.1; Pin D-4; Sh. D-10	800–1,200 rpm 1 ipm	–
Querin et al. (2009)	WC-Co	Ti-6Al-4V	Pin L-4.3; Pin D-8.9-0, 15.5-10; Sh. D-15.5, 19.1; Geo.-Tapered 45 and 60°	400 rpm 4–5 ipm	–
Liu et al. (2009)	W-Re	Ti-6Al-4V	Pin L-1.8; Pin D-6-4; Sh. D-11; Geo.-Taper pin	400 rpm 4 ipm	–
Zhou et al. (2009)	W-Re	Ti-6Al-4V	Pin L-1.8; Pin D-6-4; Sh. D-12; Geo.-Taper pin	400 rpm 2 ipm	Tool pin diameter decreased, severe wearing happened due to chemical reactivity
Edwards and Ramulu (2010)	W-La2O3	Ti-6Al-4V	Pin L-2.8-13.3; Sh. D-19-32	150 rpm 100 mm/min	–
Pilchak et al. (2010)	W-La2O3	Ti-6Al-4V	Pin L-9.9; Pin D-15; Sh. D-25	120–800 rpm 50.8–203.2 mm/min	–
Liu et al. 2010	W-Re	Ti-6Al-4V	–	300–600 rpm 1–5 ipm	–
Sato (2011)	Co based tool	CP Ti Ti-6Al-4V	Pin L-1.7; Pin D-3.5–6.5; Sh. D-15; Geo.-Taper pin	200 rpm 100 mm/min	Pin was hardly deformed or worn, shoulder surface became rough

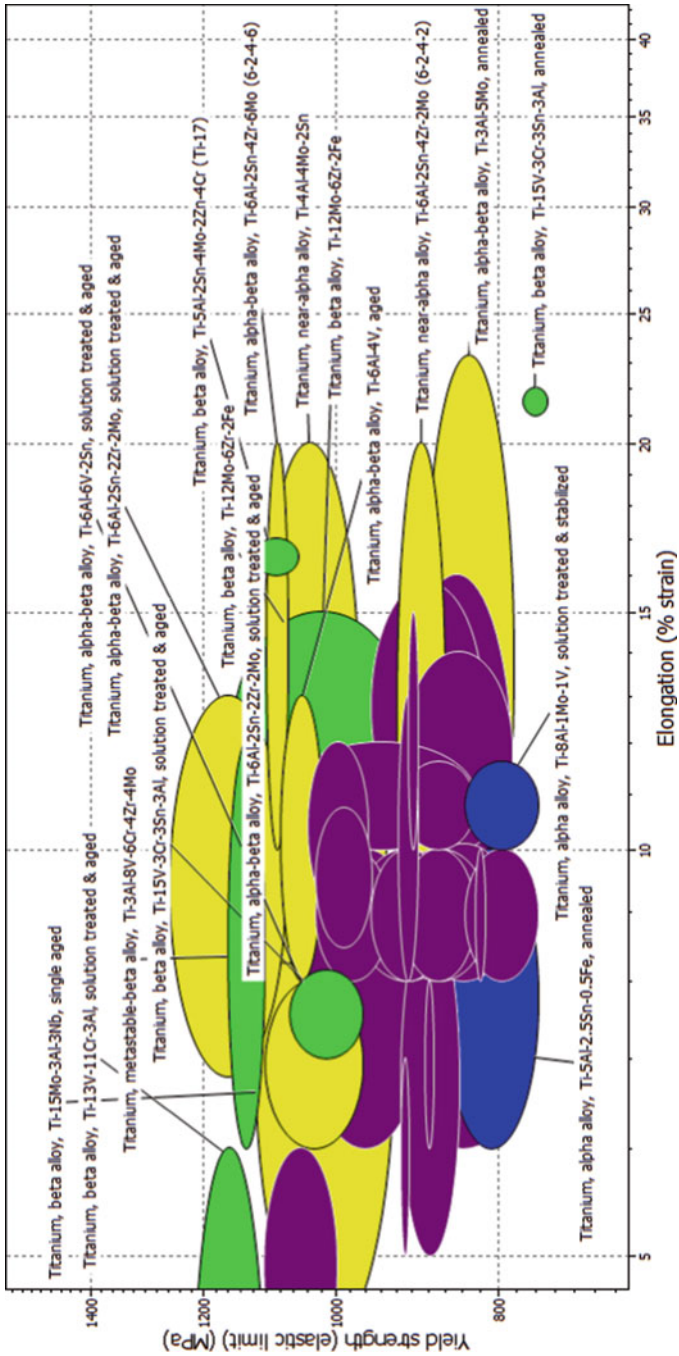

Fig. 7.7 An overview of yield strength and elongation of titanium alloys. Some of the alpha + beta and beta alloys are marked to give a comparative feel for the property space they occupy

Table 7.2 Comparison of thermal properties of titanium with iron and aluminum

	Coefficient of linear thermal expansion (10^{-6} K^{-1})	Thermal conductivity (W m^{-1} K^{-1})	Specific heat capacity (J kg^{-1} K^{-1})
α Titanium	8.4	20	523
Ti-6Al-4V	9.0	7	530
Fe	11.8	80	450
Al	23.1	237	900

7.1.4 Friction Stir Welding of Titanium Alloys

The field is growing and certainly enough literature is available to give confidence about its viability. There are also some technological successes, but we will focus here primarily on a short presentation of results and basic discussion of microstructure and properties. Instead of making sub-sections for different types of titanium alloys, Ti-6Al-4V will be taken as the primary example. Then in each we will compare the response or results of others titanium alloys in comparison to Ti-6Al-4V. The basic framework can also be thought in terms of a comparison of results for α + β alloys with α and β alloys. Readers are encouraged to read a review by Lienert et al. (2007) for further information.

7.1.4.1 Peak Temperature During Friction Stir Welding

The peak temperature during friction stir welding has direct bearing on the phase transformation and related variation of microstructure across the weld. The thermal properties of titanium are quite different from aluminum, as summarized in Table 7.2. The coefficient of linear thermal expansion is related to development of residual stresses and this is dealt with in Chap. 10. The thermal conductivity and specific heat capacity are directly related to the thermal profile that develops and the size of each zone in the cross-section of the weld.

We have selected the work of Edwards and Ramulu (2010) and Pilchak and Williams (2011) for the discussion of thermal cycle. Both the studies used W-1La_2O_3 alloy with ~25 mm diameter shoulder; the pin size and profile were different but we can ignore that at this juncture of discussion. An interesting aspect is that Edwards and Ramulu (2010) measured the temperature by embedding thermocouple in the workpiece, whereas Pilchak and Williams (2011) measured the temperature inside the tool at two locations (one at the top of the pin and other at a location ~12.7 mm above the first thermocouple). Thermal cycle at a given point can be obtained by the approach of Edwards and Ramulu (2010), while the peak temperature change along the run is measured in the work of Pilchak and Williams (2011). Figure 7.8 shows results of peak temperature and thermal profile of a point taken from these studies. The most critical thing to note is that the peak temperature at lowest tool rotation rate is below the beta transus. As discussed later, this gives a microstructure that contains equiaxed alpha phase. Most of the reported

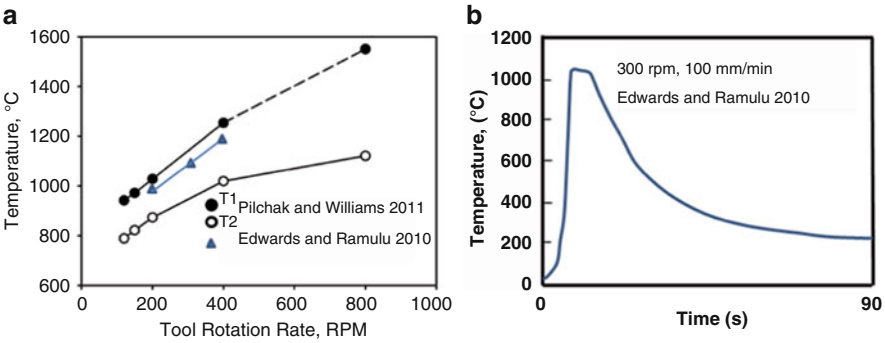

Fig. 7.8 (**a**) Peak temperature measured in workpiece and tool in Ti-6Al-4V alloy with 25.4 mm shoulder W-La_2O_3 tool. (**b**) A thermal cycle for one of the runs depicted in (**a**)

works in literature on Ti-6Al-4V alloy have the peak temperature above the beta transus. From Fig. 7.8b it is possible to calculate an approximate cooling rate in the critical temperature range of 700–850 °C where transformation from beta to alpha would occur. The cooling rate for this condition is above 2,000 °C/min. This is quite fast cooling and is discussed further in the next section of microstructural evolution.

7.1.4.2 Microstructural Evolution During Friction Stir Welding

The sequence of mechanical deformation and microstructural events changes at various locations in the cross-section of a Ti-6Al-4V friction stir weld. This is even more so because the exact nature depends on the peak temperature being above or below the beta transus. Let us start with the basic four regions defined in the previous chapters; stir zone or nugget, thermomechanical affected zone (TMAZ), heat affected zone (HAZ) and the parent material. In this chapter, for both titanium alloys and steels, the classic definition of TMAZ may not hold in all conditions. The reasons for the same and how it complicates the final microstructural interpretation are discussed below. To keep the discussion simple, only two cases of peak temperature below beta transus and above beta transus are considered for an $\alpha + \beta$ alloy. Readers should note that if we take a fully alpha alloy, this discussion would apply, except that the microstructure will be either nearly fully alpha or nearly fully beta. For beta alloys with enough alloying elements to stabilize beta phase at ambient temperature, the discussion would be the simplest as there is no phase transformation involved. The effect of shoulder heating on coarsening of refined microstructure and adjoining regions in the trailing region becomes important.

Case I: Peak Temperature Below the Beta Transus

When peak temperature is below the beta transus, the microstructure consists of alpha and beta phases, and the volume fraction of these phases is governed by the exact temperature. In such a case the microstructural refinement in the nugget

region is retained. The first thing we do is to exclude the discussion about shoulder shear influenced top layer which would be as deep as a few hundreds of microns depending on the local temperature and tool-workpiece sticking coefficient. Note that while the tool is moving forward, the leading side material under the shoulder is being swept from advancing to retreating side. On the other hand, the trailing side material under the shoulder is moving from the retreating side to advancing side (see Chap. 2, Sect. 2.4). This thin layer at the top continues to be deformed even when the pin has already passed from a location (for the central region) and the temperature continues to drop. So, the last part of the central region under the shoulder can be deformed at significantly lower temperature than the rest of the material underneath this layer. Closer examination of this layer always shows much finer microstructure. In Ti-6Al-4V alloy, this layer can have very fine equiaxed alpha microstructure.

Next, we move to a layer which is only influenced by the pin. For thicker materials, this constitutes the major volume of stir zone. In the shear layer adjacent to the pin on the trailing side, the microstructure partially recrystallizes. Note that as the shear layer moves from quadrant I (advancing-leading) to quadrant IV (advancing-trailing), the microstructure undergoes multiple rounds of local recrystallization. Based on the critical strain for recrystallization, the first incidence of local recrystallization comes while the material is still on the leading side of the pin. Considering the first recrystallized grain, it grows and is simultaneously strained. Again, when it reaches the critical local strain, it will recrystallize. Thus, conceptually one can envision multiple rounds of recrystallization, concurrent strain and growth of phases, particularly if the true strain values reach 20–40 according to some simulation (Buffa et al. 2013) predictions. Observation of dislocation structure in some grains in as welded condition validates the notion that different points in the stir zone are at different stages of microstructural evolution. Both alpha and beta phases are in deformed condition in the shear layer just behind the pin, i.e. on the trailing side. Then the microstructure goes through a very fast recovery and growth during the short period it is still under the shoulder when heat is still being generated. The cooling cycle then results in the final microstructure. Figure 7.9 shows an example of nugget microstructure for a Ti-6Al-4V alloy run made at 800 rpm with a 10 mm diameter shoulder WC-Co tool. Clearly the microstructure did not exceed the beta transus of ~995 °C for this alloy. The TMAZ and HAZ of these specimens shows variation of beta phase as a function of location.

Case II: Peak Temperature Above the Beta Transus

The beta transus temperature is approximately reported in the range of 980–1,000 °C. For the sake of discussion we take the value as 995 °C in this chapter. Most of the discussion is based on a recent work of Su et al. (2013) which used a smaller W-La_2O_3 tool with 10 mm shoulder, pin diameter of 6.3 mm and a relatively short pin of 1.7 mm. The results do vary with the tool dimension and the extrapolation of this information to larger tool should be done with specific

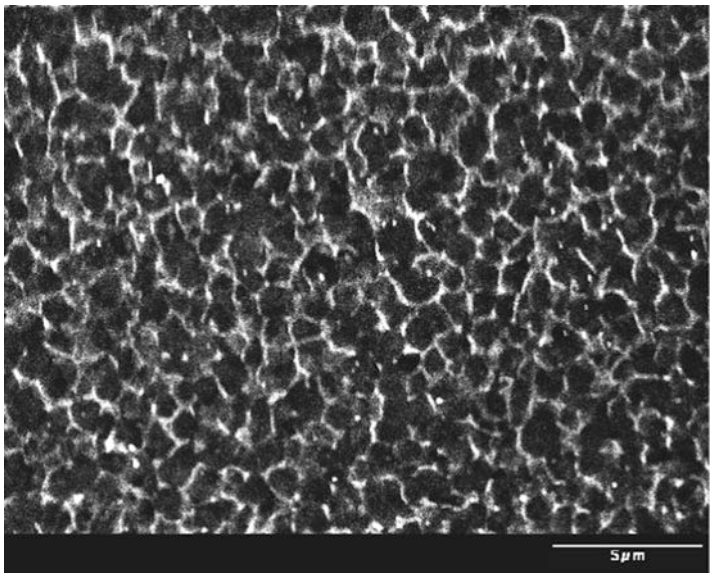

Fig. 7.9 A scanning electron micrograph of Ti-6Al-4V alloy nugget after friction stir welding at 800 rpm and 25 mm/min using a WC-Co tool with 10 mm diameter shoulder. Note the fine and equiaxed alpha grains, indicative of peak temperature being lower than beta transus

consideration of temperature and strain. The gradient in microstructural evolution across the weld is divided into two domains; TMAZ above beta transus and below beta transus. The TMAZ layers in aluminum alloys are wide and diffuse on the retreating side and narrow and sharp on the advancing side. This is mainly related to the imbalance of material flow, and the exact size also depends on the variation of local flow strength of material with temperature. The observations in Ti-6Al-4V are different and discussed below for the two subsets. When the temperature exceeds the beta transus in the TMAZ, the signature pattern of deformation can be wiped off by subsequent microstructural evolution. Pilchak and Williams (2011) have also used the term transition zone (TZ) rather than TMAZ to better express this region. For the rest of the chapter we are referring this to TMAZ, but defining this zone is not always easy and one has to look for other signatures to estimate the boundary of such a zone.

Figure 7.10 shows the cross-section of a specimen processed at 900 rpm and 1 ipm, along with an illustrative temperature profile from the pin surface to base material. In this case the HAZ has three different microstructural regions. A summary of various regions is listed in Fig. 7.10 and some microstructural examples are shown in Fig. 7.11. A key thing that is denoted in Fig. 7.10 is the temperature of 750 °C. Above 750 °C, the amount of vanadium in beta is not high enough to suppress the transformation back to alpha. On the other hand, if the coarsened beta below 750 °C has V content higher than 15 %, it stabilizes the bcc phase (Su et al. 2013). The microstructure in the nugget, TMAZ and part of HAZ is that of transformed β. The transformed α phase satisfies the Burgers orientation relationship with β phase defined by

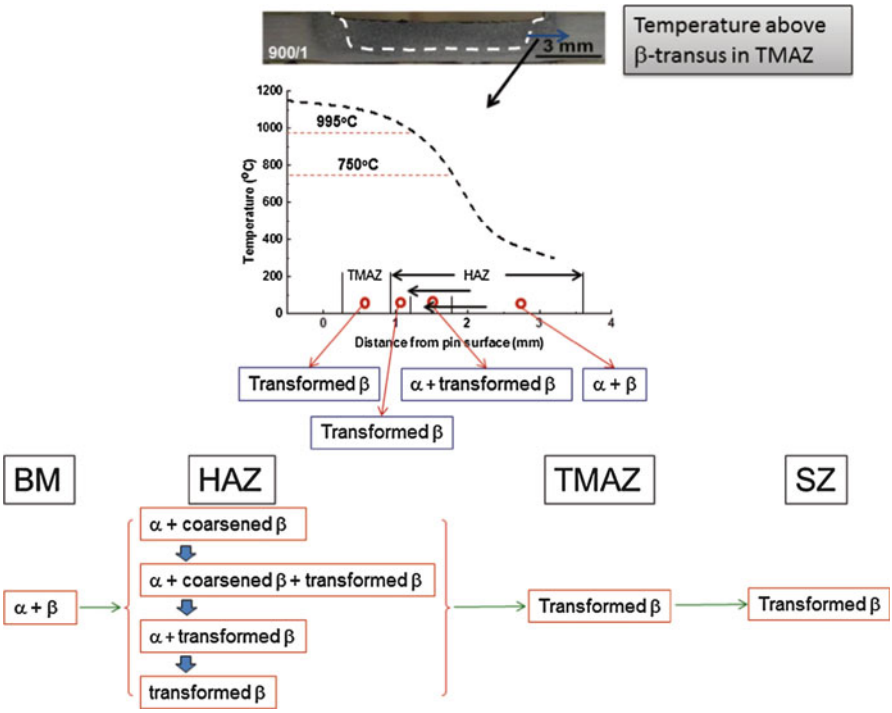

Fig. 7.10 An example of variation of various zones across the weld when the TMAZ gets completely replaced by subsequent microstructural evolution above beta transus. The HAZ also has a gradient microstructure that covers the range from base material microstructure to transformed beta

$$\{0001\}_{\alpha}//\{110\}_{\beta} \text{ and}$$
$$< 11\text{-}20>_{\alpha}// < 111>_{\beta}.$$

According to this relationship, a bcc crystal can transform to 12 hexagonal variants with respect to the parent β crystal. Figure 7.12 shows higher magnification micrographs from the nugget region of two different runs; 900 rpm/1 ipm and 900 rpm/4 ipm. The processing parameters directly influence the peak temperature and the first impact of this is on the prior beta grain size. Although we will not go into any textural detail in this chapter, the shear deformation can lead to simple shear texture in the β phase. This can also influence the variant selection during $\beta \rightarrow \alpha$ transformation and final texture in the nugget. Su et al. (2013) observed that in these runs there was no particular variant selection, i.e. a random distribution of phases exists. Three distinct morphologies can be seen in Fig. 7.12, (a) grain boundary α, (b) lamellar α + β colonies and (c) acicular α laths. As mentioned earlier, the cooling rate in the nugget can be quite high (>2,000 °C/min). The entire cooling rate framework can be defined between 1 °C/min for furnace cooling and 8,000 °C/min for water quenching (Lütjering and Williams 2007). A change from a colony or

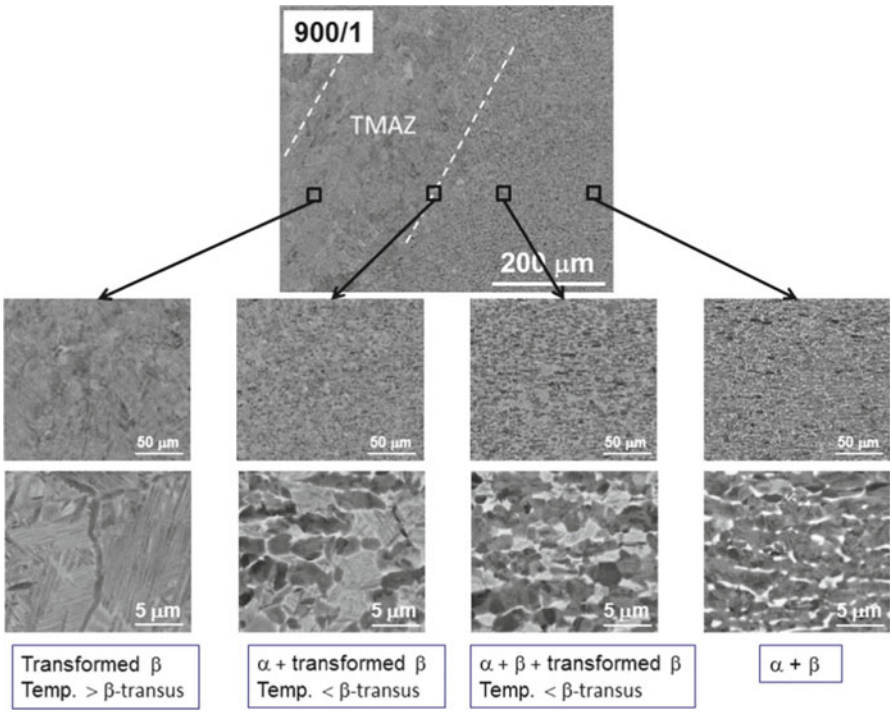

Fig. 7.11 Examples of microstructures at various locations across the weld. Comparison of HAZ microstructure with the parent microstructure clearly shows the increase in beta phase volume fraction and transformed beta. The TMAZ has fully transformed lamellar alpha

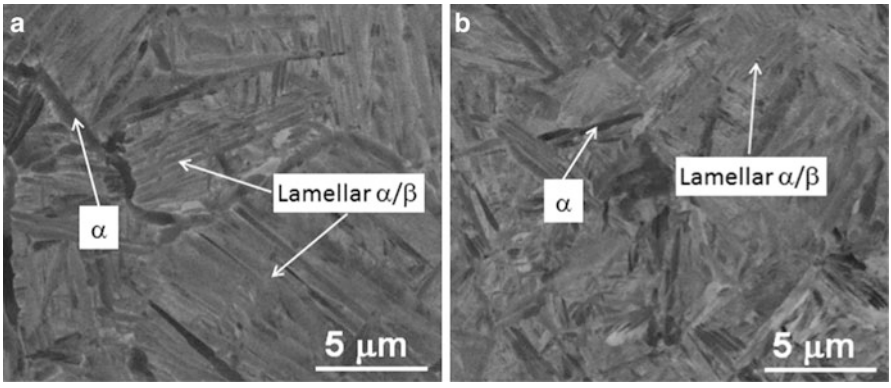

Fig. 7.12 Higher magnification micrographs of the SZs in samples processed at, (**a**) 900 rpm/1 ipm and (**b**) 900 rpm/4 ipm (From Su et al. 2013)

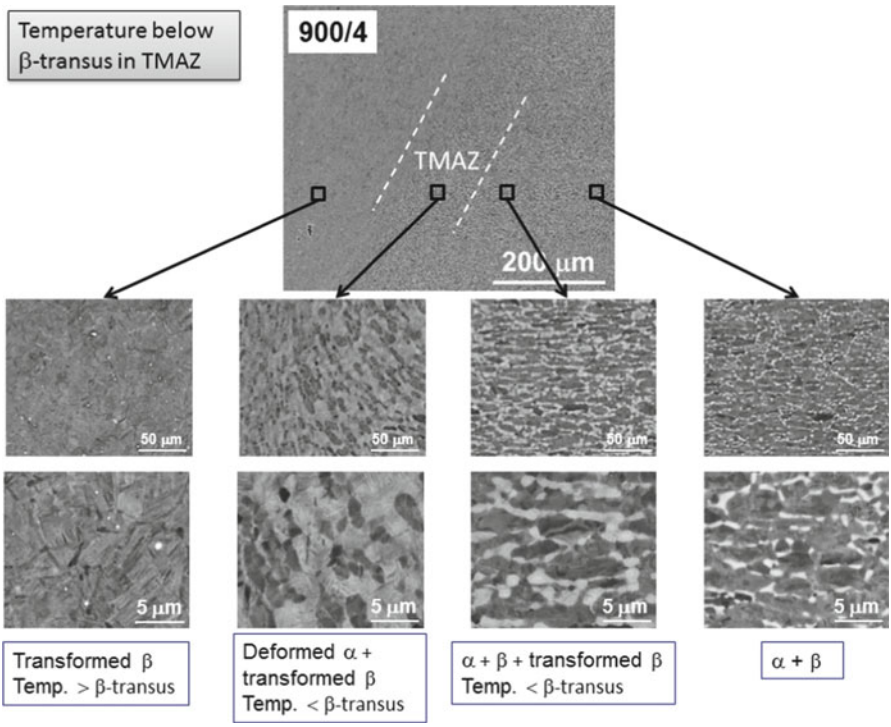

Fig. 7.13 Examples of microstructures at various locations across the weld for a run where part of the TMAZ was below the β transus. Deformed α is visible in the TMAZ and upward flow pattern can also be observed

Widmanstatten type of microstructure to a martensitic structure occurs at cooling rate faster than 1,000 °C/min (Lütjering and Williams 2007). The microstructural example shown in Fig. 7.12 is consistent with the rough estimate of cooling rate and overall expectation of microstructure in Ti-6Al-4V alloy. Figure 7.13 shows an example where the peak temperature at some location in the TMAZ is below β transus, and therefore the deformed α and upward flow pattern are visible.

7.1.4.3 Mechanical Behavior

The strengthening mechanisms applicable for titanium alloys are:

(a) solid solution strengthening,
(b) grain boundary and/or interfacial strengthening, and
(c) precipitation strengthening.

For beta alloys that retain bcc crystal structure at ambient temperature, the primary strengthening mechanisms are solid solution strengthening and grain

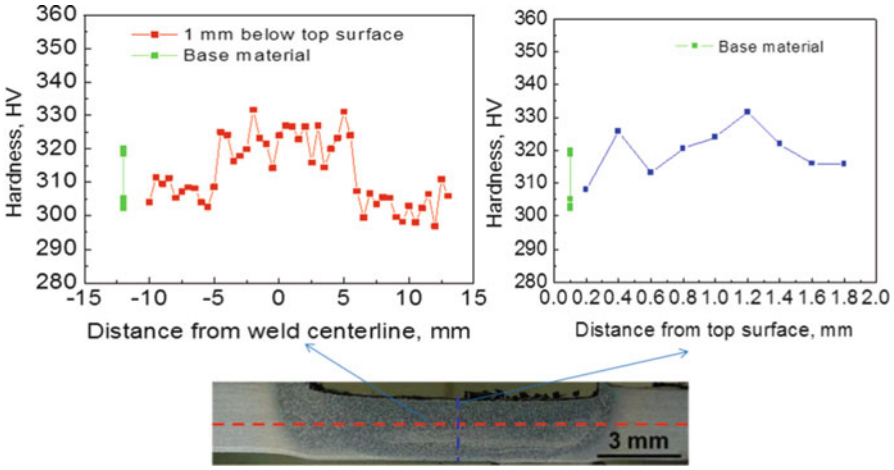

Fig. 7.14 Hardness profile across the stir zone and from top to bottom for a specimen welded at 900 rpm and traverse speed of 1 ipm. Note that the hardness is comparable or better than the base material at all locations

boundary strengthening in as friction stir welded condition. These alloys can be aged to add a component of precipitation strengthening. Similarly, alpha alloys that do not have much of beta stabilizing alloying elements, the as friction stir welded microstructure has solid solution strengthening and grain boundary strengthening. The grain boundary strengthening becomes interfacial strengthening for $\alpha+\beta$ alloys, because of the microstructural range we discussed in the last section. The microstructure can range from fully equiaxed to fully lamellar or any combination of those. The precipitation can also be complex and retained beta can have secondary alpha transformation. This creates complexity in developing quantitative relationship between microstructure and strength.

Figure 7.14 shows hardness profiles from top to bottom and left to right through the stir zone. A noteworthy aspect is that the hardness is not below the parent material at any location. Table 7.3 gives a summary of yield strength (YS), ultimate tensile strength (UTS) and elongation. Values of primary beta grain size are included as well to show the correlation between process parameters and prior beta grain size in the stir zone. The UTS values are as high as ~1,150 MPa while maintaining ductility similar to the parent material. This level of strength in titanium alloys is referred as 'high strength' in literature.

So far, most of the results related to mechanical properties in literature are related to Ti-6Al-4V alloy. Microstructural studies on β alloys have been reported but not mechanical properties. Near-β alloys like Ti-6Al-2Sn-4Zr-6Mo (Ti-6246) can be friction stir welded under conditions that can completely retain the beta phase. These can, of course, be subsequently aged. But to just show a potential of friction stir welding and processing to produce titanium alloys with exceptional local properties, Fig. 7.15 shows a preliminary data for Ti-6246 in as friction stirred condition. The microstructure shows transformation of duplex microstructure to

Table 7.3 A summary of tensile test results of the SZ in the FSP samples (Su et al. 2013, reprinted with permission from Elsevier)

Sample	Prior β grain (μm)	YS (MPa)	UTS (MPa)	Elongation (%)
Base material	–	941.8 ± 24.7	1,014.7 ± 4.55	23.1 ± 1.3
1,000 rpm/1 ipm	38	936.8 ± 20.5	1,042.9 ± 15.0	23.1 ± 2.9
1,000 rpm/2 ipm	32	1,050.4 ± 14.9	1,132.7 ± 4.3	20.0 ± 1.5
1,000 rpm/4 ipm	27	1,058.6 ± 4.9	1,150.8 ± 3.2	19.9 ± 0.5
900 rpm/1 ipm	25	945.8 ± 4.1	1,098.5 ± 6.4	23.6 ± 0.7
900 rpm/2 ipm	21	1,042.2 ± 4.7	1,130.6 ± 4.3	22.0 ± 0.3
900 rpm/4 ipm	12	1,067.4 ± 31.4	1,156.2 ± 0.0	21.7 ± 0.7
800 rpm/1 ipm	20	1,002.2 ± 30.1	1,079.3 ± 12.9	22.0 ± 2.0
800 rpm/2 ipm	17	1,015.3 ± 12.5	1,110.3 ± 5.3	23.2 ± 1.2

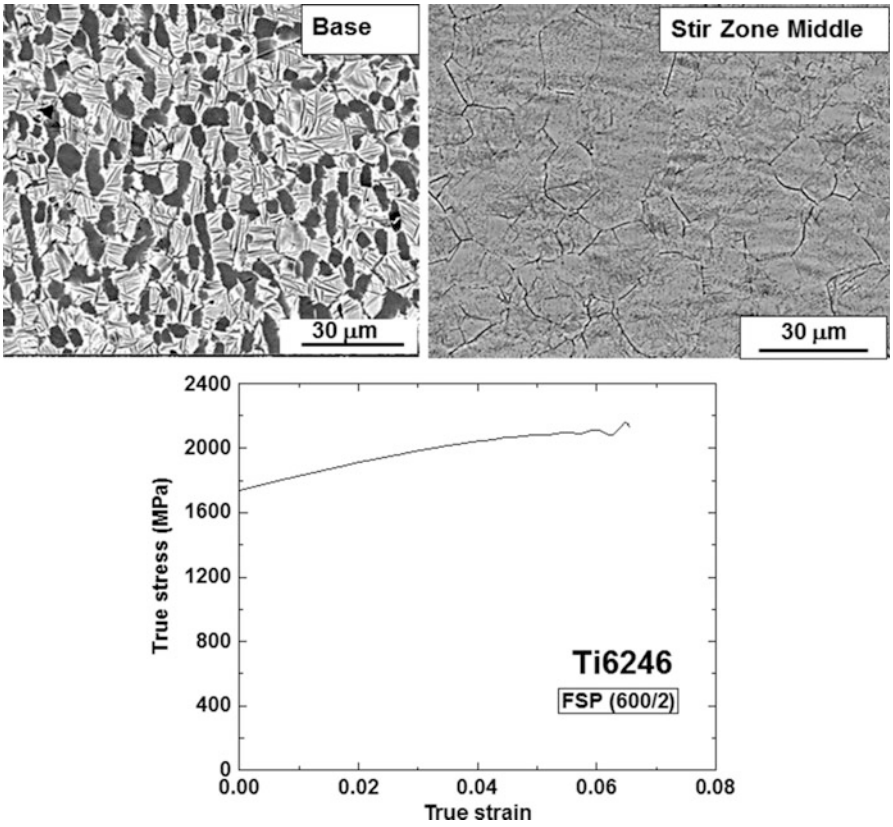

Fig. 7.15 An example of microstructural evolution during friction stir welding of Ti-6Al-2Sn-4Zr-6Mo and exceptional strength-ductility combination (Dutt and Mishra, unpublished research). Note that this type of domain is completely unexplored at the time of publication of this book

nearly fully retained beta. The corresponding strength values are exceptional, ~1,740 MPa YS, ~2,000 MPa UTS, while having ductility of >6 %. Such strength-ductility combination is clearly well above anything that can be obtained by conventional thermo-mechanical processing (see Fig. 7.7). Part of this success is related to the type of microstructure created during friction stir process.

7.2 Ferrous Alloy

7.2.1 Introduction and Basic Physical Metallurgy of Steels

7.2.1.1 Classification and Designation

Ferrous alloys are one of the most important commercial metallic alloys. However, the friction stir welding of ferrous alloys has been very difficult so far due to prohibitively high tool cost and poor tool life (due to excessive wear and thermal fatigue related failures of the tool). This section is devoted to friction stir welding of steels. A summary of physical metallurgy of steels is presented first to assist readers in deciding what all factors to consider in processing of engineering materials like steels.

A part of Fe-C phase diagram is presented in Fig. 7.16. The solid line corresponds to Fe-Fe_3C phase diagram and broken lines to Fe-C phase diagram. As pointed out in Chap. 2, Fe_3C is a metastable phase and it will eventually transform to graphite phase. In steels, graphite is usually not encountered. The presence of elements such as Si and higher content of carbon promote formation of graphite and is observed mostly in cast iron. The phase diagram show many important phases—Ferrite, Austenite, Cementite (Fe_3C), and δ-Fe. Elemental iron exists in body centered cubic (BCC) form up to 910 °C and is termed as ferrite (α-Fe). Above this temperature, it transforms into austenite (γ-Fe) which has face centered cubic crystal structure. The γ-Fe is stable up to 1,394 °C. Once heated above this temperature, it again converts into BCC crystal structure which is termed as δ-Fe which melts at 1,538 °C. The lines Ac_1, Ac_3, and Ac_{cm} are designated as maximum temperature at which ferrite-cementite, ferrite-austenite, and austenite-cementite co-exist when heated-up. The letter 'c' in Ac_i ($i = 1, 3, cm$) stands for *chauffant*, a French word for heating. Similarly, when cooling condition exists, 'c' is replaced by 'r' which stands for *refroidisant*, again a French term for cooling. Readers should also bear in mind that A_2 (Curie temperature) and A_4 (γ-Fe transforms to α-Fe) transformation temperature also exists in addition to the critical temperatures mentioned above. From phase transformation point of view these transformation temperatures are very important, and it should always be borne in mind while carrying out any kind of thermo-mechanical processing of steels. Later on its significance with respect to friction stir welding and processing of steels is discussed.

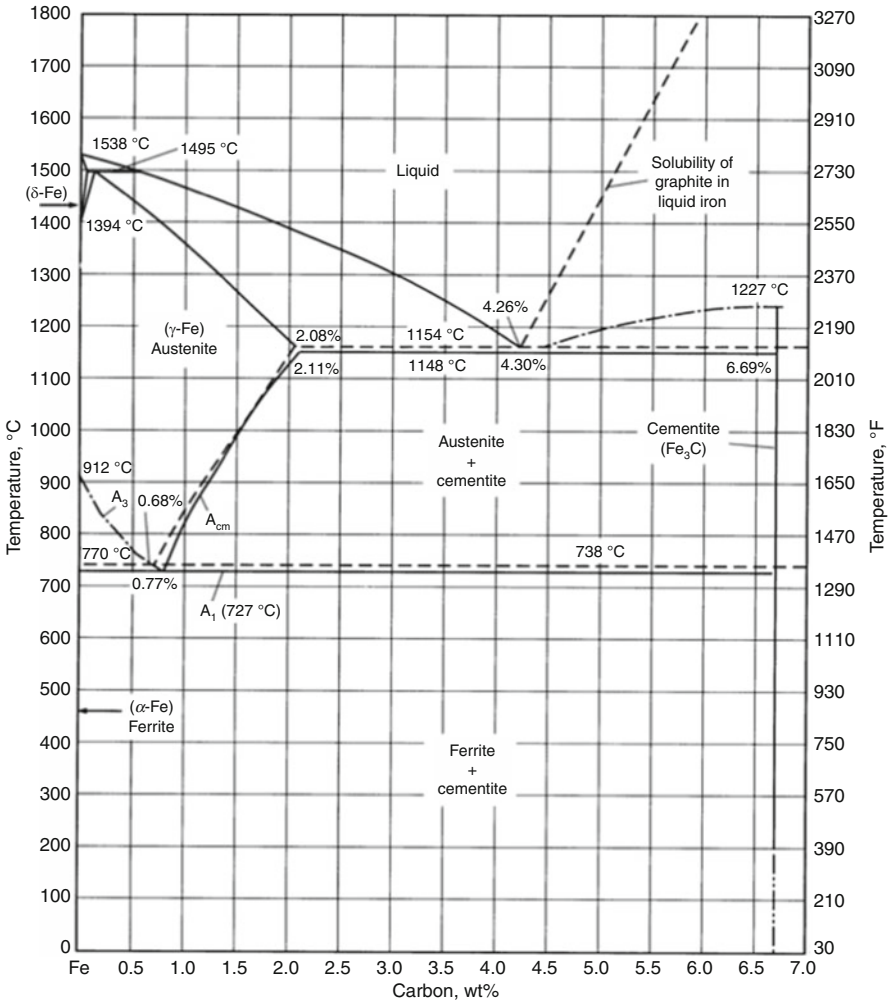

Fig. 7.16 Fe-C phase diagram (ASM Handbook; Volume 1, Properties and Selection: Irons, Steels, and High-Performance Alloys → Microstructures, Processing, and Properties of Steels → Iron-Carbon Phase Diagram, reprinted with permission from ASM International)

Figure 7.17 pictorially classifies ferrous alloys limited to 2 wt% carbon content and they are termed as steels. It shows that steels can be classified into plain carbon steel and alloy steel. Plain carbon steels can further be classified into low-carbon steel, medium-carbon steel, high-carbon steel and ultrahigh-carbon steel. The content of carbon is shown in Fig. 7.17 adjacent to each type of plain-carbon steels. Alloy steels can be further be classified into low-alloy steel (total alloying content <8.0 wt%) and high-alloy steel (total alloying content >8.0 wt%). It should be

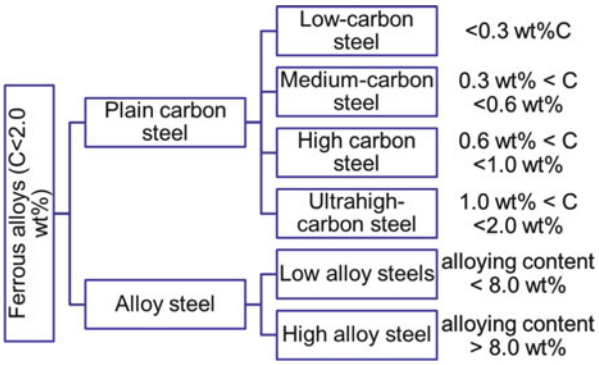

Fig. 7.17 Classification of steels (ASM Handbook; Volume 1, Properties and Selection: Irons, Steels, and High-Performance Alloys → Classification and Designation of Carbon and Low-Alloy Steels → Classification of Steels, reprinted with permission from ASM International)

noted here that steels can also be classified in a number of ways such as microstructure-based (e.g., pearlitic steel) and de-oxidation practice based classifications (e.g., rimmed steel).

Different organizations and countries across the world have developed their own designation system for steels. Here, the designation system developed by American Iron and Steel Institute (AISI) and Society of Automotive Engineers (SAE) will be discussed along with Unified Numbering System (UNS) of designating steels. The SAE-AISI designation system is included in Table 7.4. As per this system any steel is represented by four digit numbers. First two digits of the number designate the primary alloying elements present in the steel. The last two digits represent fraction of carbon in weight percentage when the number comprising last two digits are divided by hundred. For example, steel 1018 is a low carbon steel where carbon is present is about 0.18 wt%. But, it should be remembered that in 1018 steel carbon can vary in the range 0.14–0.20 wt%. UNS system of designating steel is given in Table 7.5. It shows numbering system followed not only for steels but also for cast iron. It is an alphanumeric system where a class of steel is designated by a letter followed by a five digit number. The SAE-AISI 1018 steel is designated as G10180. Since the same steel is designated differently under different designation system in use across the world, UNS system uniquely identifies such alloys.

7.2.1.2 Basic Microstructural Framework

Austenite, ferrite, cementite, pearlite, bainite, and martensite are the important phases/microstructural constituents frequently encountered in steels. In addition to this, several types of precipitates (carbides, nitrides, etc.) depending on the alloying addition and inclusions are also present in steels. In this section, a summary of microstructural evolution under different processing conditions is

Table 7.4 SAE-AISI system of designating steels (ASM Handbook: Volume 1, Properties and Selection: Irons, Steels, and High-Performance Alloys → Classification and Designation of Carbon and Low-Alloy Steels → Designations for Steels, reprinted with permission from ASM International)

Numerals and digits	Type of steel and nominal alloy content (%)	Numerals and digits	Type of steel and nominal alloy content (%)	Numerals and digits	Type of steel and nominal alloy content (%)
Carbon steels		*Nickel-chromium-molybdenum steels*		*Chromium (bearing)steels*	
10*xx*[a]	Plain carbon (Mn 1.00 max)	43*xx*	Ni 1.82; Cr 0.50 and 0.80; Mo 0.25	50*xxx* 51*xxx* 52*xxx*	Cr 0.50 Cr 1.02 Cr 1.45 } C 1.00min
11*xx*	Resulfurized	43BV*xx*	Ni 1.82; Cr 0.50; Mo 0.12 and 0.25; V 0.03 min	*Chromium-vanadium steels*	
12*xx*	Resulfurized and rephosphorized	47*xx*	Ni 1.05; Cr 0.45; Mo 0.20 and 0.35	61*xx*	Cr 0.60, 0.80, and 0.95; V 0.10 and 0.15 min
15*xx*	Plain carbon (max Mn range: 1.00–1.65)	81*xx*	Ni 0.30; Cr 0.40; Mo 0.12	*Tungsten-chromium steel*	
Manganese steels		86*xx*	Ni 0.55; Cr 0.50; Mo 0.20	72*xx*	W 1.75; Cr 0.75
13*xx*	Mn 1.75	87*xx*	Ni 0.55; Cr 0.50; Mo 0.25	*Silicon-manganese steels*	
Nickel steels		88*xx*	Ni 0.55; Cr 0.50; Mo 0.35	92*xx*	Si 1.40 and 2.00; Mn 0.65, 0.82, and 0.85; Cr 0 and 0.65
23*xx*	Ni 3.50	93*xx*	Ni 3.25; Cr 1.20; Mo 0.12	*High-strength low-alloy steels*	
25*xx*	Ni 5.00	94*xx*	Ni 0.45; Cr 0.40; Mo 0.12	9*xx*	Various SAE grades
Nickel-chromium steels		97*xx*	Ni 0.55; Cr 0.20; Mo 0.20	*Boron steels*	
31*xx*	Ni 1.25; Cr 0.65 and 0.80	98*xx*	Ni 1.00; Cr 0.80; Mo 0.25	*xx*B*xx*	B denotes boron steel
32*xx*	Ni 1.75; Cr 1.07	*Nickel-molybdenum steels*		*Leaded steels*	
33*xx*	Ni 3.50; Cr 1.50 and 1.57	46*xx*	Ni 0.85 and 1.82; Mo 0.20 and 0.25	*xx*L*xx*	L denotes leaded steel
34*xx*	Ni 3.00; Cr 0.77	48*xx*	Ni 3.50; Mo 0.25		
Molybdenum steels		*Chromium steels*			
40*xx*	Mo 0.20 and 0.25	50*xx*	Cr 0.27, 0.40, 0.50, and 0.65		
44*xx*	Mo 0.40 and 0.52	51*xx*	Cr 0.80, 0.87, 0.92, 0.95, 1.00, and 0.05		
Chromium-molybdenum steels					
41*xx*	Cr 0.50. 0.80. and 0.95; Mo 0.12, 0.20, 0.25, and 0.30				

[a] The *xx* in the last two digits of these designations indicates that the carbon content (in hundredths of a percent) is to be inserted

Table 7.5 UNS system of designating steels (Reprinted, with permission, from the Handbook of Comparative World Steel Standards, 4th edition, copyright ASTM International, 100 Barr Harbor Drive, West Conshohocken, PA 19428)

UNS designation	Description
Ferrous metals	
Dxxxxx	Specified mechanical properties steels
Fxxxxx	Cast irons
Gxxxxx	SAE and Former AISI carbon and alloy steels (except tool steels)
Hxxxxx	AISI H-steels
Jxxxxx	Cast steels
Kxxxxx	Miscellaneous steels and ferrous alloys
Sxxxxx	Heat and corrosion resistant (stainless) steels
Txxxxx	Tool steels
Welding filler metals	
Wxxxxx	Welding filler metals, covered and tubular electrodes classified by weld deposit composition

presented to help in evaluation of microstructural evolution during friction stir welding and processing.

It is important to know what alloying elements do to different phases seen in Fe-C phase diagram. As one can quickly make out from Fig. 7.16, addition of C expands the austenitic region. Hence, different alloying additions lead to different effects on the phase stability and are shown pictorially in Fig. 7.18. These alloying elements are generally described based on what they do to γ phase field. At present they are classified into four different types:

(a) Open γ field: addition of elements such as Ni, Mn, Mo, etc. cause γ field to stabilize up to room temperature if added in sufficient quantity (Fig. 7.18a),
(b) Expanded γ field: addition of elements such as C, N, Cu, Zn, etc. leads to existence of γ field in much broader region (Fig. 7.18b),
(c) Closed γ field: addition of elements like Si, Al, Be, Ti, V, Cr, Mo, etc., leads to existence of γ field in a closed loop and causes merger of BCC phases α and δ (Fig. 7.18c) and
(d) Contracted γ field: addition of elements like B, Nb, Zr, etc. leads to contraction of γ field and expansion of α field (Fig. 7.18d).

It indicates that at a given processing temperature different alloys would possess different deformation characteristics. Hence, in terms of friction stir welding of different alloys, it would call for different welding strategy to obtain a successful weld.

Austenite becomes the starting point for a number of microstructural phases observed in steels and this point is further illustrated pictorially through Fig. 7.19. It shows that austenite may transform into a variety of phases depending on alloy chemistry and processing history of the alloy. With regard to friction stir welding and processing, this chart illustrates two main points: first, during heating cycle, if condition is adequate for austenite formation, phases such as pearlite, bainite,

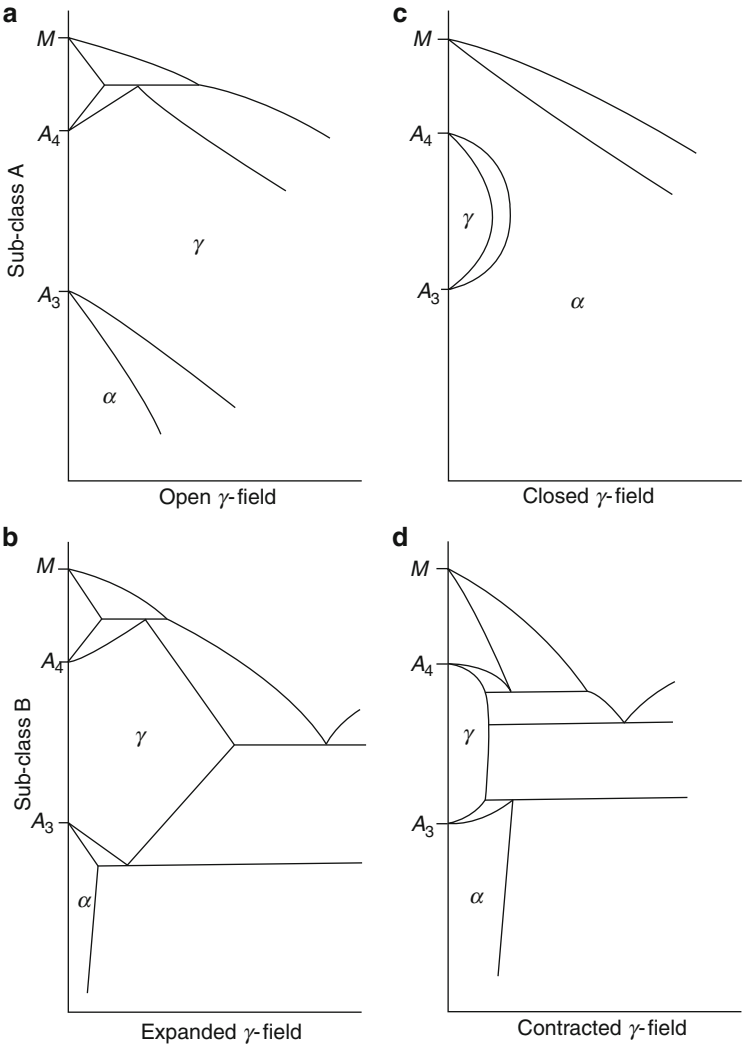

Fig. 7.18 Effect of alloying addition on Fe-C phase diagram (Bhadeshia and Honeycombe (2006), reprinted with permission from Elsevier)

martensite, etc. would get transformed into austenite. Second point is related to transformation of austenite phase during cooling cycle to its parent phase if processing condition allows it to happen. This point should be considered while discussing phase transformation and its influence on mechanical and other properties in all the zones, i.e., nugget, TMAZ, and HAZ.

Proeutectoid phases in plain carbon steels are ferrite and cementite. Here, ferrite needs special attention. It generally exists in equiaxed form when it nucleates from austenite grains during air cooling after thermo-mechanical processing such as hot-rolling. However, proeutectoid ferrite and ferritic microstructure can exist in

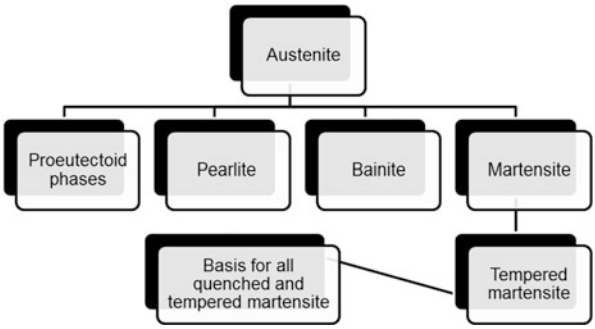

Fig. 7.19 Austenite as starting point for many commercially important phases (Courtesy Dr. K. K. Sankaran)

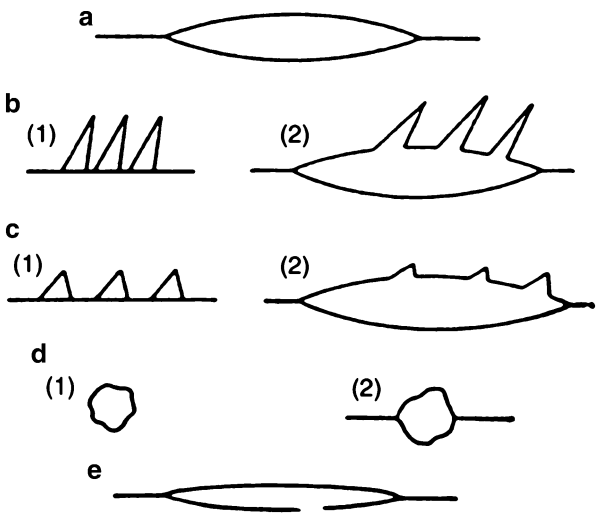

Fig. 7.20 Different morphologies commonly encountered in ferritic steels, (**a**) grain boundary allotriomorph, (**b**) Widmanstätten (1) primary side plates (2) secondary side plates, (**c**) Widmanstätten saw teeth nucleated on (1) grain boundary (2) grain boundary allotriomorph, (**d**) idiomorphs (1) within grain (2) on grain boundary, and (**e**) Widmanstätten interagranular plates (Krauss 2005, reprinted with permission from ASM International)

many different morphological states depending on the cooling rates and alloy chemistry. These various morphologies are shown in Fig. 7.20 and this classification is based on Dubé system.

Figure 7.21 shows a relationship between cooling rate and various austenite transformation products for Fe-0.01 wt%C steel. It is clear that different types of ferritic phases can be introduced as a function of cooling rate. At sufficiently high cooling rate austenite phase transforms into martensitic phase. The martensite start temperature is significantly influenced by carbon content and alloying.

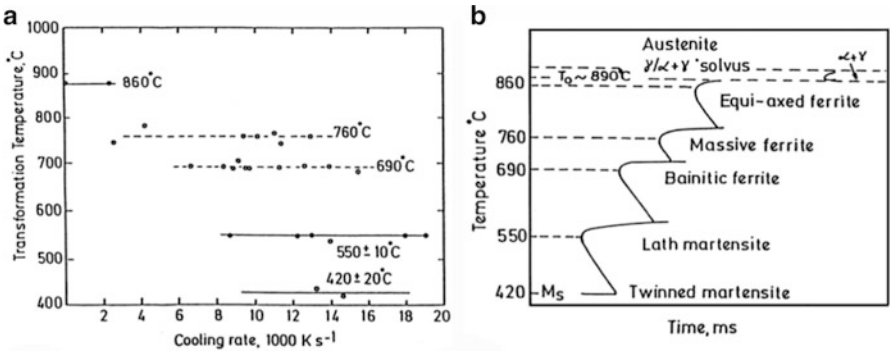

Fig. 7.21 (**a**) Transformation start temperatures and cooling rates and (**b**) corresponding transformation products of austenite for an Fe-0.01% C alloy (Krauss 2005, reprinted with permission from ASM International)

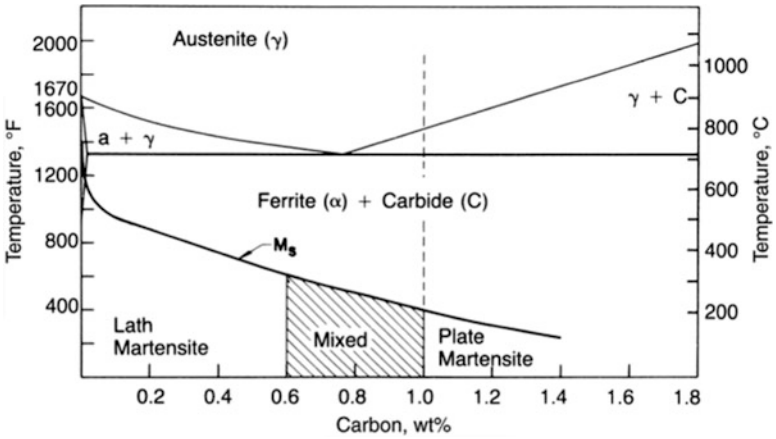

Fig. 7.22 The variation of martensite start temperature (M_S) as a function of carbon content in steels (Krauss 2005, reprinted with permission from ASM International)

Figure 7.22 shows that as carbon content of the steels increases, the martensite start temperature decreases. Hence, a higher undercooling would be required to accomplish austenite-martensite phase transformation for high carbon steels.

7.2.2 Tool Materials and Related Issues

As mentioned in the beginning of the Sect. 7.2, the tool wear and fracture have been one of the biggest hindrances in the success of friction stir welding of steels. However, a great stride has been made in the past one decade or so on the tool

Table 7.6 Summary of tool materials and geometries used for FSW of steels (Cam 2011, reprinted with permission from Maney Publishing)

Material	Thickness (mm)	Tool material	Pin geometry
Structural steels			
AISI 1012	1.6	WC-based material	Columnar without threads
AISI 1018	6.4	Mo- and W-based alloys	Standard (cylindrical with threads)
AISI 1035	1.6	WC-based material	Columnar without threads
DH-36	6.4	W-based alloy	Columnar slightly tapered
DP590, TRIP 590	...	PcBN	Tool with a convex scrolled shoulder
IF-steel	1.6	WC-based material	Columnar without threads
High C steels			
1070	1.6	WC-based material	Columnar without threads
CK5 (0.85 wt-%C)	1.6	WC-based material	...
1 wt-%C	2.3	PcBN	Tapered
Ferritic stainless steels			
12 % Cr (1.4003)	12.0	W-based alloy	Tapered with three flats
Austenitic stainless steels			
304	2.5	Cold-work steel[b] coated with TiN	Conical with threads
304	2.0	PcBN	Cylindrical[c]
304	6.0	PcBN	Columnar without threads
304L	3.2	W-based alloy	...
304L	6.4	PcBN	Tapered with three flat surfaces
304L	15.0	PcBN	Truncated (a convex shoulder[d])
NSSC 270[a]	6.0	PcBN	Step spiral tool with a convex shoulder
Duplex stainless steels			
SAF 2507	4.0	PcBN	Columnar without threads
SAF 2205	2.0	WC-based material	Columnar without threads

[a] Superaustenitic steel (please note that W-based alloy is W-25Rh and WC-based material is WC-Co)
[b] X155CrVMo12-1
[c] No information on pin surface details
[d] Shoulder surface with spiral pattern

development front for welding steels. Table 7.6 provides summary of some the tools used for welding/processing steels. It provides information on the workpiece welded and its thickness, tool material, and pin geometry.

Coming back to the tool wear and fracture issue, Chap. 4 detailed the issues related to the performance of the tools used for processing high melting point materials such as Ti alloys and steels. The welding of such materials presents very harsh environment for the tool. Figure 8.3 in Chap. 8 compares the softening behavior of AA 6061-T6 and SS 301. During FSW of aluminum alloys peak temperature is generally around 400–500 °C. At such temperatures the flow stress of aluminum alloy is less than 10 MPa. However, SS301 shows an yield strength in excess of 600 MPa. Hence, to process such a material the temperature should be in

excess of 900 °C. At such a high temperature, tool steel generally used for processing aluminum and magnesium alloys cannot be used. Hence, as shown in Table 7.6, most of the tool materials are based on refractory metals or ceramics.

It was also pointed out in Chap. 2 that most of the tool wear and fracture occur during the plunge stage. Hence, some of the suggestions like controlling the plunge rate should be followed for extended use of a tool in such harsh environment. Another alternative to it would be to heat the workpiece entirely or locally to bring down the plunge force on the tool during the plunge stage. The integration of a secondary heating element(s) to friction stir welding is opening up door to a new way of joining such hard-to-weld materials and is termed as "hybrid friction stir welding" techniques. The aim of such integration is not only to improve the longevity of the tool but also to have a greater control over microstructural evolution during the welding. In one study it was shown that it was possible to bring down plunge force by 10 %, side force by 110 % and torque by 30 % by induction heating of 1018 steel (Tweedy et al. 2005).

The wear of the tool during the processing of steels leads to another issue which is incorporation of worn-out tool material into the nugget of the steel workpiece. For example, in a study where super-austenitic stainless steel was double-sided friction stir welded using W-based tool, the nugget was found to be contaminated with W. Figure 7.23 includes two SEM images showing different levels of W debris in the nugget of the welded zone. Figure 7.23c, d show electron dispersion spectroscopy spectra corresponding to W-enriched region and base material. The presence of W-peak in Fig. 7.23c should be noted which is absent in Fig. 7.23d. Contamination of the weld nugget should be avoided as much as possible as contaminants might react and form reaction product(s) detrimental to mechanical properties of the weld nugget. One way of getting around the problem of contamination of the weld nugget is to coat the tool with an appropriate material. For example, Ohashi et al. (2009) prevented the weld nugget contamination with Si and N coming from the wear of Si_3N_4 tool by coating the tool with TiC/TiN.

7.2.3 Mechanical Properties of Steel

One of the reasons for very diverse use of steels is a wide range of strength values obtainable in this class of material. The crystal structure and chemistry of the steels allow it to be subjected to a diverse set of thermo-mechanical processing routes and to possess a great variety of microstructural features. The yield strength-elongation chart included in Fig. 7.24 shows that strength can vary from as small as ~200 to ~2,000 MPa in steels.

Overall, the following strengthening mechanisms contribute towards the yield strength of the steel:

(a) Friction stress (Peierls-Nabarro stress)
(b) Solid solution strengthening (interstitial and substitutional)

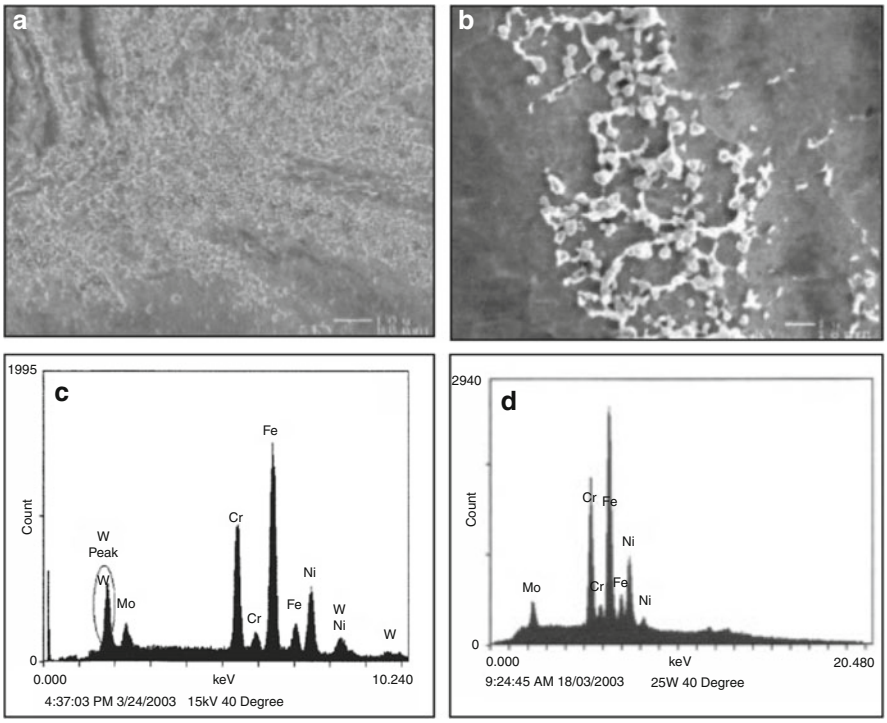

Fig. 7.23 W-enrichment in the weld nugget as a result of the wear of the tool during friction stir welding of superaustenitic stainless steel (Klingensmith et al. 2005, reprinted with permission from the American Welding Society, Miami, FL)

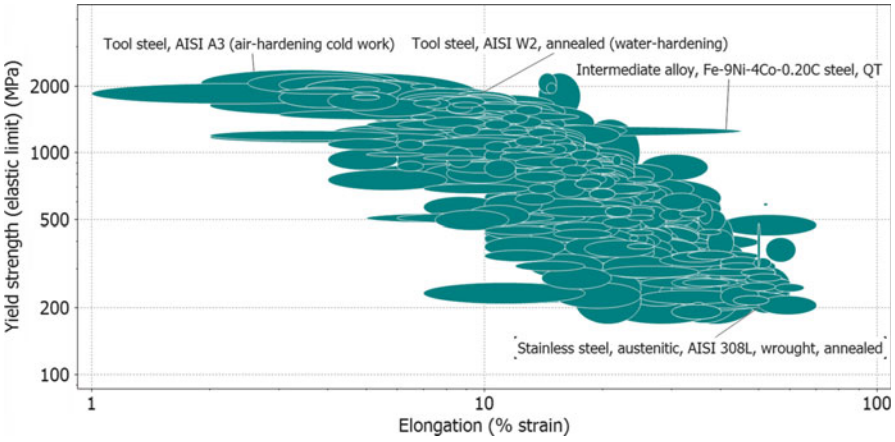

Fig. 7.24 Strength-ductility chart showing wide range of strength available in steels

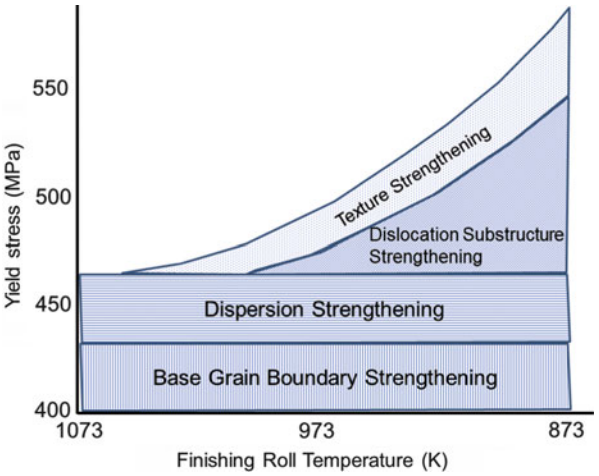

Fig. 7.25 The yield strength of ferrite steel. Schematic illustration of various strengthening mechanisms contribution towards the total strength of the alloy

(c) Dislocation strengthening
(d) Precipitation strengthening
(e) (Sub)-grain (or twin) boundary or Hall-Petch strengthening, and
(f) Texture strengthening.

Not all strengthening mechanisms will be operative in all types of steels at all times. By varying the contribution from each strengthening mechanisms, a range of properties can be introduced in steels in a controlled manner. For example, in well annealed condition, steel will have no contribution coming from dislocation strengthening mechanism to its yield strength. Moreover, in the same alloy, different processing routes or conditions will result in different level of contribution from the same type of strengthening mechanisms to the yield strength of the alloy. Figure 7.25 is included to show how some of the strengthening mechanisms mentioned above contribute towards the total strength of ferrite steel. It also shows influence of processing on the microstructure variation and its influence on the change in yield strength through the change in contribution from each strengthening mechanism. Here in this particular condition, it shows that with decrease in finishing rolling temperature, the contribution coming from ferrite sub-grain and texture strengthening increase whereas dispersion and grain boundary strengthening remain constant. This aspect will be highlighted briefly when discussing the evolution of microstructure and its influence on the mechanical properties of friction stir welded or processed steels.

7.2.4 Friction Stir Welding of Steels

Like FSW/P of Ti-alloys, this field is still growing and full of positive and negative sentiments about the viability of this technique for steels. Due to availability of steels in great many microstructural and thermo-mechanical processing states, it would not

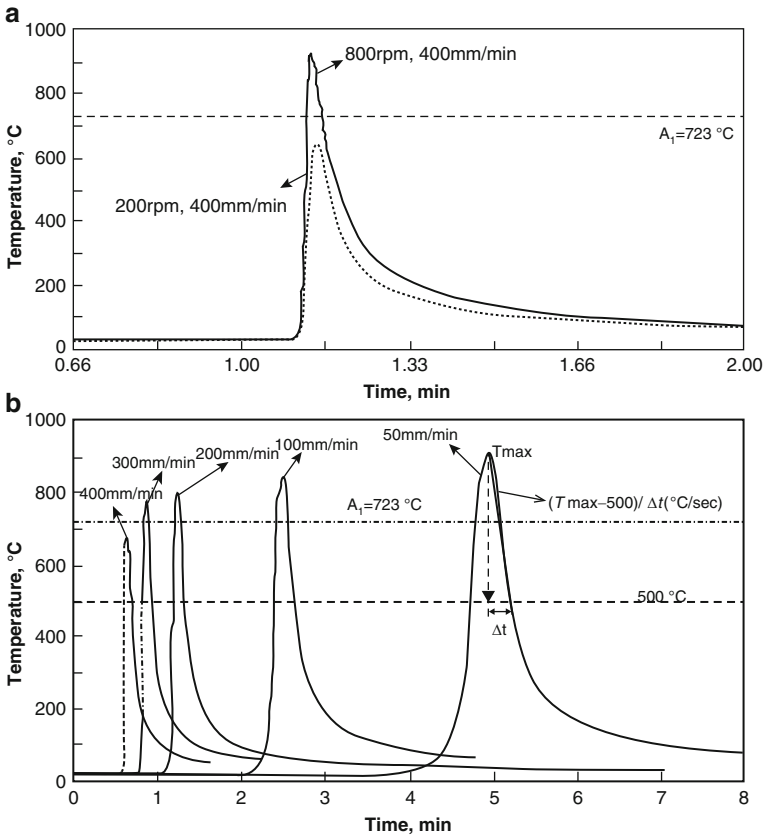

Fig. 7.26 (**a**) Thermal history measured in high carbon steel (0.7 wt%C) as a function of tool rotation rates (adapted from Cui et al. 2007a), and (**b**) thermal history measured in medium carbon steel (0.5 wt%C) as a function of tool rotation rates (adapted from Cui et al. 2007b)

be possible to cover friction stir welding aspects of all these steels. Moreover, not all types of steels have been used for friction stir welding and processing purpose. The discussion will be limited to plain-carbon steels and austenitic stainless steel. The idea behind choosing examples based on these alloys is to enable readers in setting-up welding and processing procedures based on types of steel and what to expect at the end of welding and processing as a function of processing parameters.

7.2.4.1 Peak Temperature

Temperature measurement using thermocouples inserted in the workpiece or the tool indicates that peak temperature during processing can reach up to as high as 1,200 °C. Figure 7.26 shows the variation of thermal profiles of the weld nugget as a

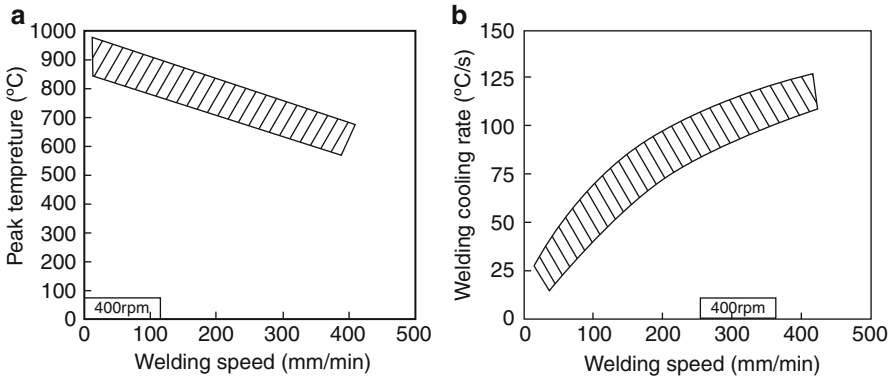

Fig. 7.27 Effect of tool traverse speed on (**a**) peak temperature and (**b**) cooling rate for plain carbon steel (adapted from Cui et al. 2007b)

function of tool rotation rates and tool traverse speeds. In each case the thermocouple was placed on the weld centerline towards the bottom of the plate and just outside the nugget. Figure 7.26a shows dependence of thermal profile on tool rotation rate. By reducing the tool rotation rate a peak temperature below critical temperature A_1 was observed. In the nugget a temperature higher than this is expected as these values represent temperature measurement just outside the nugget. Similarly, Fig. 7.26b shows dependence of thermal history on tool traverse speed. As expected, an increase in tool traverse speed resulted in a decrease in peak temperature. Temperature as high as 900 °C can be noted in Fig. 7.26b.

Figure 7.27 shows peak temperatures and cooling rates measured for different plain carbon steels as a function of welding speed. As expected a decrease in peak temperature with increasing tool traverse speed can be noted (Fig. 7.27a). The calculation of average cooling rates for these steels from the cooling portion of the thermal profiles show cooling rates reaching as high as 125 °C/s which is sufficient for the formation of phases like martensite, bainite, etc.

7.2.4.2 Microstructure Evolution and Mechanical Properties

Interstitial-Free Steel

Figure 7.28a shows the microstructure of the base IF-steel which was subjected to friction stir welding. It is a single phase material and essentially contains ferrite. The EBSD map of the base material is shown in Fig. 7.28b. Based on dominance of one color (blue), it can be stated that initial microstructure was heavily textured. The friction stir welding was carried out in butt configuration. The welding was carried out at two different tool traverse speed: 100 mm/min and 400 mm/min. In each case the tool rotation rate was 400 rpm. A WC material based tool was used to make both welds. The EBSD maps from the nugget zone are shown in Fig. 7.28c, d.

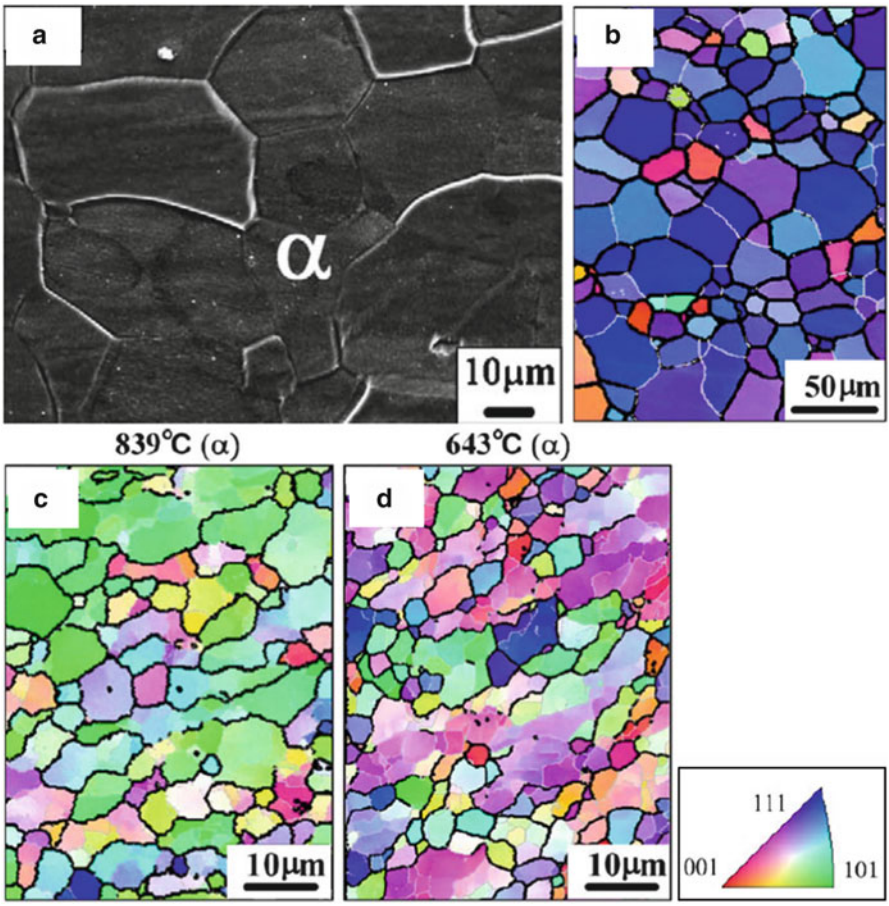

Fig. 7.28 Interstitial-free steel, (**a**) SEM image of the base material showing single phase ferrite (α), (**b**) EBSD map of base material, (**c**) IF-steel welded at 400 rpm and 100 mm/min, and (**d**) IF-steel welded at 400 rpm and 400 mm/min (Fujii et al. 2006, reprinted with permission from Elsevier)

Figure 7.28c corresponds to the weld made at the tool rotation rate of 400 rpm and tool traverse speed of 100 mm/min and Fig. 7.28d corresponds to the weld made at the tool rotation rate of 400 rpm and tool traverse speed of 400 mm/min. Due to differences in tool traverse speed, the EBSD map in Fig. 7.28c corresponds to a weld made with higher heat input compared to the EBSD map shown in Fig. 7.28d. Grey lines correspond to low angle grain boundaries (misorientation angle 2–15°) which appear to be in higher quantity for the run made at lower heat input. The temperature measurement also supports this observation. The peak temperature measured was 643 °C and 839 °C for the welds made at 400 mm/min and 100 mm/min, respectively. Here in this case no phase transformation was observed under the processing condition chosen. But, if temperature is in excess of 913 °C, ferrite will transform to austenite. However, during cooling cycle possibility of

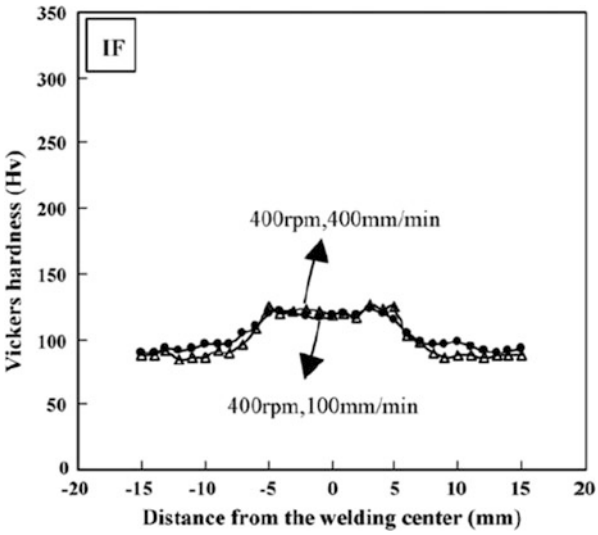

Fig. 7.29 The microhardness variation across the weld nugget on the transverse cross-section of the friction stir weld of IF steel (Fujii et al. 2006, reprinted with permission from Elsevier)

formation of ferrite from austenite is very high since a very high cooling rate is required to obtain martensite in IF-steel. In pure iron a cooling rate of 35,000 °C/s is required to transform austenite to martensite.

Due to significant grain refinement in the nugget, the strength of the nugget is expected to be higher than that of the base material. In the base material the average grain size was ~24 μm which reduced to 5–6 μm in the nugget after welding. The hardness profiles taken on transverse cross-section across the welded zones are shown in Fig. 7.29. As expected, it shows microhardness values to be higher than that of the base material. There are possibly two factors which are contributing towards this improvement in hardness or strength—one, grain refinement and second, either dislocation or sub-grain boundary strengthening. Sub-grains can be noted in Fig. 7.28 (grey lines representing low angle grain boundaries).

Low-Carbon Steel

Figure 7.30 has been included here to illustrate the effect of friction stir welding on microstructure evolution in different zones of the weld. The weld was made at 1,000 rpm tool rotation rate and tool traverse speed was 12.6 mm/min. The shank of the tool was made of DESNIMET-180 (W-3.5Ni-1.5Fe) and the shoulder and the pin were made of CY-16 (a complex carbide material consisting of WC-8TiC-10.5NbC and TaC-8.5Co). Figure 7.30a shows polygonal ferrite and very small scale unresolved pearlite appearing as darker regions in the micrograph. The pin affected region in the nugget showed same set of phases but at larger scale (Fig. 7.30b). HAZ-1 consisted of ferrite + pearlite phases and HAZ-2 tempered martensite.

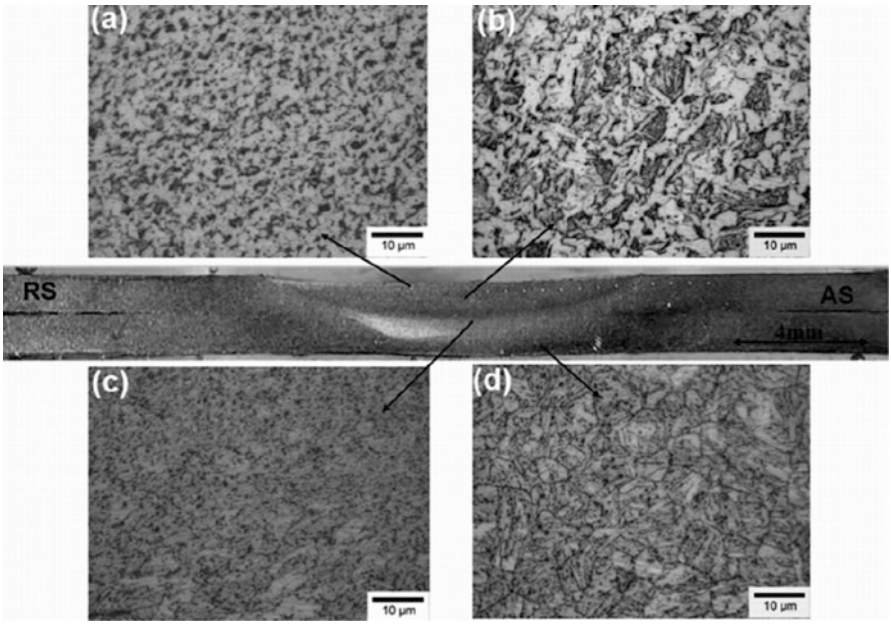

Fig. 7.30 Optical macrograph and micrographs for M190 steel lap weld made at tool rotation rate 1,000 rpm and tool traverse speed 12.6 mm/min; (**a**) shoulder affected zone of the nugget, (**b**) pin affected zone of the nugget, (**c**) HAZ-1, and (HAZ-2) (Ghosh et al. 2011, reprinted with permission from Elsevier)

The effect of increased cooling rate on microstructural evolution during friction stir welding of M190 steel is presented in Fig. 7.31. All the processing parameters in this case were same as the last one except that a forced air cooling arrangement was incorporated on the top side of the plate behind the welding tool. The shoulder affected nugget zone showed a tempered martensitic structure. It should be noted here that this tempered martensitic microstructure does not derive directly from the martensitic phase present in the base material. But, the material in the nugget transforms to austenite during welding and sufficient cooling rate causes martensite to form and which eventually get transformed to tempered martensite. It does not get sufficient time to get transformed to ferrite and pearlitic microstructure as was the case for Fig. 7.30a due to a higher cooling rate.

High Carbon Steel

The result based on butt-welding of SAE-AISI 1070 steel is included in Fig. 7.32. The starting microstructure consisted of mostly pearlite and a small amount of ferrite. The tool rotation rates and tool traverse rates were systematically changed to modify two parameters:

(a) peak temperature in the nugget, and
(b) cooling rate.

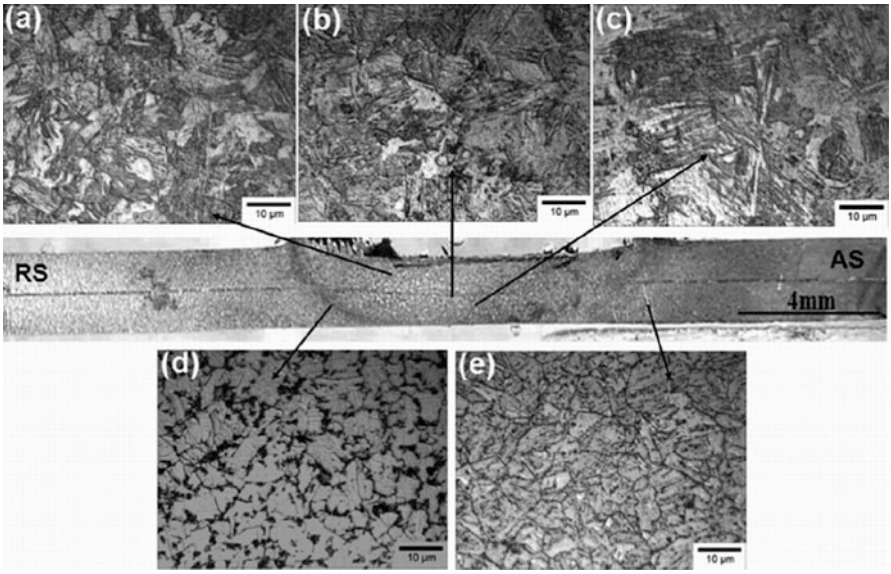

Fig. 7.31 Optical macrograph and micrographs for M190 steel lap weld made at tool rotation rate 1,000 rpm and tool traverse speed 12.6 mm/min by incorporating forced air cooling arrangement at the top of the plate on the trailing side of the tool; (**a**) shoulder affected zone of the nugget, (**b**) pin affected zone of the nugget, (**c**) HAZ-1, and (**d**) HAZ-2 (Ghosh et al. 2011, reprinted with permission from Elsevier)

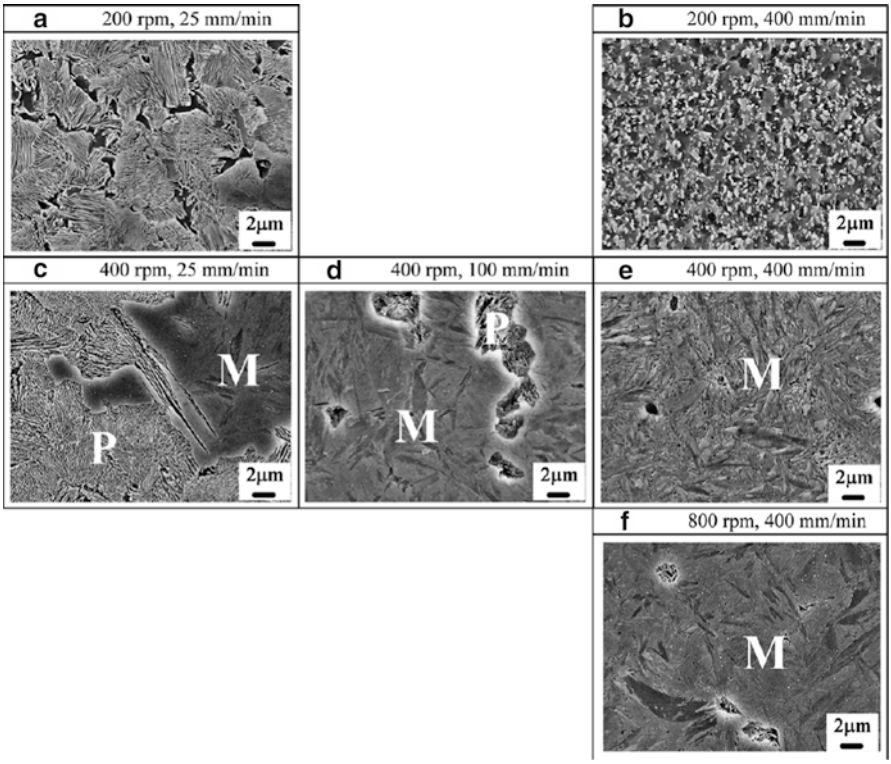

Fig. 7.32 Friction stir butt-welding of high carbon steel SAE-AISI 1070 showing effect of processing parameters on microstructure evolution in the weld nugget (Cui et al. 2007a, reprinted with permission from Elsevier)

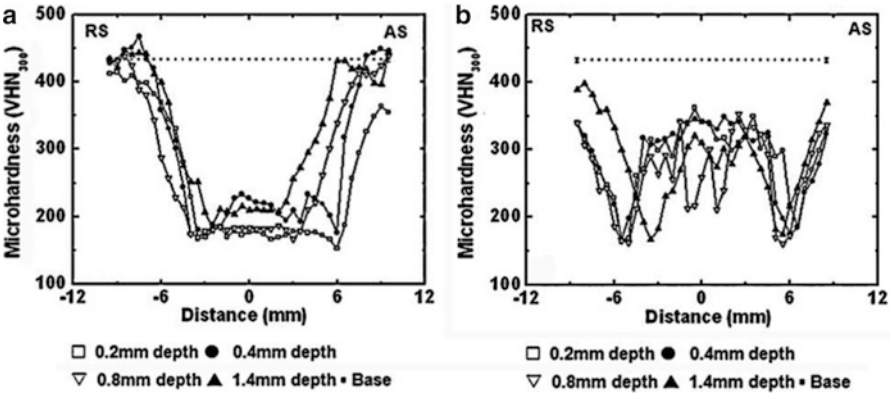

Fig. 7.33 Microhardness profiles on the transverse cross-section of M190 steel lap weld made at tool rotation rate 1,000 rpm and tool traverse speed 12.6 mm/min (**a**) in absence of forced air cooling and (**b**) in presence of forced air cooling. The microhardness measurements were taken at different depths on the same section (Ghosh et al. 2011, reprinted with permission from Elsevier)

The SEM micrograph shown in Fig. 7.32a corresponds to a case where cooling rate is low enough to cause the formation of same set of phases as in the base material. However, the scale of ferrite and pearlite was finer than that observed in base material. After changing the tool traverse speed from 25 to 400 mm/min resulted in peak temperature to be below A_1. Obviously, a subcritical temperature would not facilitate any kind of phase transformation. Hence, under this set of processing parameters, only refinement of the ferrite and pearlite microstructure took place (Fig. 7.32b). However, instead of changing tool traverse speed, once tool rotation rate was changed from 200 to 400 rpm while maintaining the tool traverse speed at 25 mm/min, it showed formation of pearlite along with a small fraction of martensite (Fig. 7.32b). This suggests that peak temperature in the nugget exceeded A_3 which caused formation of austenite phase which during cooling transformed back to mainly pearlite. But, cooling rate was sufficient to cause formation of martensite too. The fraction of martensite progressively increased once the tool traverse speed was changed from 25 to 400 mm/min (Fig. 7.32c–e). Similarly, at 400 rpm tool rotation rate, fully martensitic structure in the weld nugget can be observed at tool traverse speed of 100 mm/min and higher (Fig. 7.32c–e).

Micrographs shown in Sects. 7.2.4.2.2 and 7.2.4.2.3 highlight the role of peak temperature and cooling rates in the microstructural development during welding of steels. Because of this, mechanical properties are also affected significantly. Microhardness variation shown in Fig. 7.33, taken on the transverse cross-section of friction stir welded mild steel, shows a decreased hardness in the nugget of the weld. Figure 7.33a corresponds to the case presented in Fig. 7.30 and Fig. 7.33b to that in Fig. 7.31. It was shown in Fig. 7.30 that nugget contained mostly ferrite and pearlite and HAZ tempered martensite. Because of the presence of a softer phase in the nugget compared to martenite in base material, the low hardness in the nugget is an expected behavior. In the latter case (Fig. 7.31), since martensitic phase is

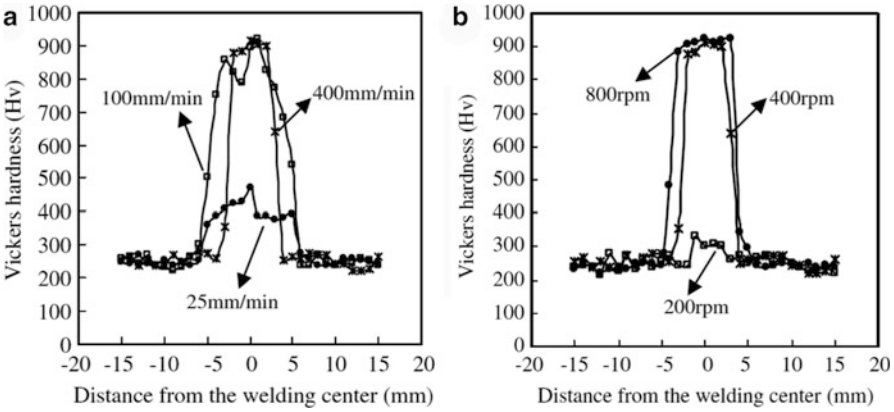

Fig. 7.34 Microhardness variation of a friction stir welded high carbon steel (0.7 wt%C) (Cui et al. 2007a, reprinted with permission from Elsevier)

present in the weld nugget, the hardness in the nugget should be higher than the former case given that the alloy is same in both cases. In both conditions the lowest hardness values were same because HAZ contained similar (ferrite + pearlite) microstructures.

Actually the role of peak temperature and cooling rates are so profound in friction stir welding and processing of steels that it forces us to think in a new direction. In the welding or processing of aluminum and magnesium based alloys generally a systematic change in strength or hardness is observed if processing parameters such as tool rotation rate, tool traverse speeds, etc. are changed systematically (increasing or decreasing). Figure 7.34 shows how this scenario is different in the case of steels. It shows the microhardness variation on the transverse cross-section of friction stir welded high carbon steel (0.7 wt%C). Figure 7.34a corresponds to a weld made at 400 rpm and at different tool traverse speeds as indicated in the figure. A more than two times increase in hardness values of the nugget can be noted on changing the tool traverse speed from 25 to 100 mm/min. Although the jump in microhardness values is quite phenomenal, this kind of trend is also observed in Al and Mg based alloys. However, Fig. 7.34b shows quite an opposite trend than that observed in Al and Mg based alloys as a function of increasing tool rotation rates. In Al and Mg based alloys, higher heat input associated with higher tool rotation rates result in lower hardness or strength. However, in steels it can be quite opposite depending on peak temperature and cooling rates. Figure 7.34b shows microhardness variation on the transverse cross-section for the same alloy but now as a function of tool rotation rates. The tool traverse speed in this case is 400 mm/min and tool rotation rates are indicated in the figure. At 200 rpm, weld nugget show slightly higher hardness than that of base material. However, on increasing the tool rotation rates to 400 and 800 rpm, the microhardness values change by almost threefold. As mentioned earlier, higher tool rotation rates represent higher heat input and an increase in hardness of the nugget is quite contrary to

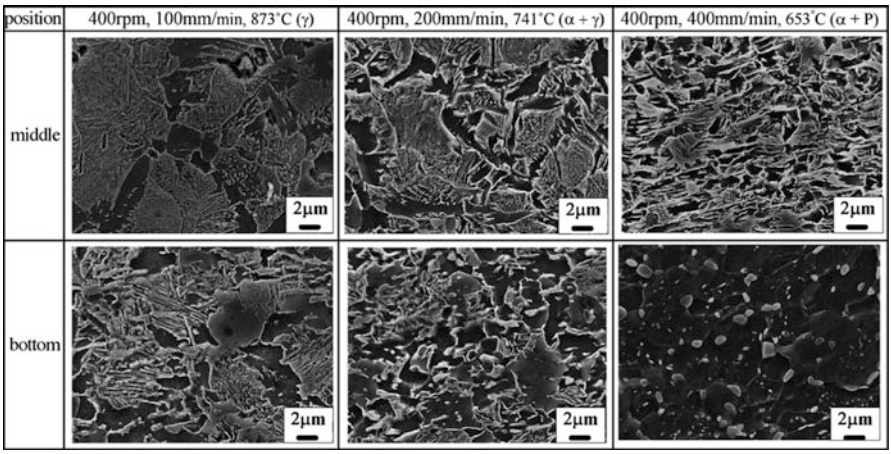

Fig. 7.35 The role of critical temperature in microstructural evolution of a medium carbon steel (0.35 wt%C) (Fujii et al. 2006, reprinted with permission from Elsevier)

our understanding based on friction stir welding and processing of aluminum and magnesium based alloys. However, in the case of steels it should be noted that increasing tool rotation rates causes peak temperatures to increase which can also result in higher cooling rates at certain combinations of tool rotation rates and tool traverse speeds. Thus, it may result in the formation of phases such as martensite, which have very high strength/hardness compared to ferritic or pearlitic phases.

Role of A_1/A_3 Temperatures in FSW/P

It is evident from the micrographs presented in Figs. 7.30, 7.31, and 7.32 that the peak temperature coupled with cooling rate plays a pivotal role in microstructural development in different welded zones, i.e., nugget, TMAZ, and HAZ. The presence of multiple HAZs is also a result of positional and temporal dependence of peak temperature and cooling rates. When peak temperature is restricted below A_1, it leads to modification of existing phases in terms of morphology and size. In some cases, some non-equilibrium phases might transform to more stable ones. But, once temperature during processing has surpassed A_3 or A_{cm} (more appropriately Ac_1 or Ac_3), the resulting phase(s) in different zones will depend on the kinetics of the process being governed by the cooling curve. The role of critical temperature is further illustrated in Fig. 7.35. It shows a medium carbon steel containing 0.35 wt% C which has been welded in a controlled manner so that the peak temperature in the nugget in below A_1, above A_3 and between A_1 and A_3. It should be noted here that temperature were measured from the bottom of the plate at the weld centerline and thermocouple were placed very close to the nugget. Hence, in the nugget, the peak temperature is expected to be little higher than the one shown in Fig. 7.35 for each condition. The peak temperature recorded at 400 rpm and 400 mm/min was 653 °C

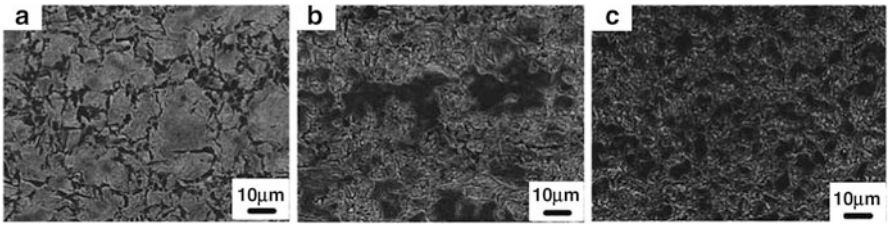

Fig. 7.36 Evolution of microstructure in the weld nugget of medium carbon steel (0.35 wt%C) as a function of processing parameters (adapted from Cui et al. 2007b)

which is below A_1. Since, peak temperature was below A_1, as stated before only morphological and size change should be observed in the processed zone. The microstructure inside the nugget near the bottom shows microstructure very similar to the base material except the ferrite grain size. Due to relatively higher temperature in the upper part of the nugget (but still lower than A_1) deformation is more severe which leads to a different size (smaller) and morphology of ferrite and pearlite phase.

The peak temperature measurement at 400 rpm and 200 mm/min showed a temperature of 741 °C. This temperature is between A_1 and A_3. Hence, in this case ferrite and cementite would combine to form austenite. During cooling cycle of the weld, this austenite can transform back to a number of phases as shown in Fig. 7.19. In this case, it transformed to proeutectoid ferrite and pearlite due to the prevailing cooling condition. In the case where the steel was welded at 400 rpm and 100 mm/min, again ferrite would combine with cementite or pearlite would transform into austenite since the peak temperature is now 873 °C which is above A_3. The transformation might be partial or complete depending on time provided for the transformation to take place. Similar to the last case, here also the austenite might transform to many other phases depending on the prevailing cooling condition. Figure 7.35 shows formation of ferrite and pearlite under this condition.

The Role of Initial Microstructure

Figure 7.36 shows the result of friction stir welded medium carbon steel. The difference between this steel and the steel used for the weld results shown in Fig. 7.35 is the starting microstructure. The starting microstructure in the previous case was ferrite and globular cementite as a result of spheroidization heat treatment. However, this alloy contains ferrite and pearlite obtained by annealing heat treatment. In this case friction stir welding at 400 rpm and 25 mm/min resulted in ferrite and pearlite containing microstructure in the weld nugget. However, the steel processed at 100 mm/min and 400 mm/min (tool rotation rates same in both the cases) showed presence of martensite indicating that temperature exceeded A_1 and cooling rate to be sufficiently high for martensite formation. The temperature

measurement carried out in the same fashion as before indicates that at 400 rpm and 100 mm/min temperature exceeded 900 °C. The measured peak temperature corresponding to 400 rpm and 400 mm/min is close to 675 °C which is below A_1. But, the presence of martensite in the weld nugget suggests that temperature in fact exceeded A_1. The processing in ferrite + pearlite two phase zone cannot give rise to martensite phase. Hence, a peak temperature above A_1 (or A_3) can be speculated. It should be remembered that the steel with spheroidized Fe_3C when processed at 100 mm/min and 200 mm/min (tool rotation rate 400 rpm in both cases), the peak temperatures were 873 °C and 741 °C, respectively. It indicates that austenite formed at these temperatures should have transformed to martensite but it actually did not happen which is not the case when Fe_3C is present in the form of pearlite (a lamellar structure of ferrite and cementite). Hence, this discrepancy is possibly related to carbon distribution in the alloy. In the case where C is tied-up with spheroidized Fe_3C, when temperature exceeds A_1, the time is not sufficient for complete dissolution of C in austenite due to highly non-equilibrium nature of friction stir welding. Hence, effectively a lower level of carbon might exist in the austenite phase which would require a relatively higher cooling rate for martensite to form. Due to fine scale of ferrite and cementite platelets in pearlite, carbon does not have to travel a long distance for the homogenization of austenite phase and it might result in relatively higher carbon content in the austenite phase within friction stir welding heating cycle. Relatively higher carbon content might be causing formation of martensite under similar peak and cooling condition since a relatively lower cooling rate is required for martensite to form.

Welding of HSLA, Ferritic, Austenitic, and Duplex Stainless Steels

As shown in Fig. 7.18, it is possible to retain austenite phase down to room temperature. It is even possible to retain ferrite phase up to very high temperature by suitable alloying additions. In such cases, ideally speaking, there is no phase change in different weld zones during friction stir welding, except changes in morphology and scale of the existing microstructure and introduction of some dislocation based structures. In one sense, the microstructural evolution is like aluminum and magnesium alloys where there is no crystal structure change of the matrix as a function of peak temperature and cooling rate.

Figure 7.37 shows the microstructure corresponding to the base material and the nugget of friction stir welds made at 400 and 800 rpm for a superaustenitic stainless steel (Fe-0.016C-0.48Si-0.49Mn-0.023P-0.001S-17.78Ni-19.82Cr-6.13Mo-0.20 N-0.63Cu). Very coarse grain and presence of twins can be observed in the base material (Fig. 7.37a). A significant grain refinement can be noted from the OIM images shown in Fig. 7.37b, c. In austenitic stainless steel, there is a possibility of formation of δ-ferrite if temperature during welding is high enough for its formation. An example of such kind of phase transformation in the nugget of an austenitic stainless steel 304 is shown in Fig. 7.38.

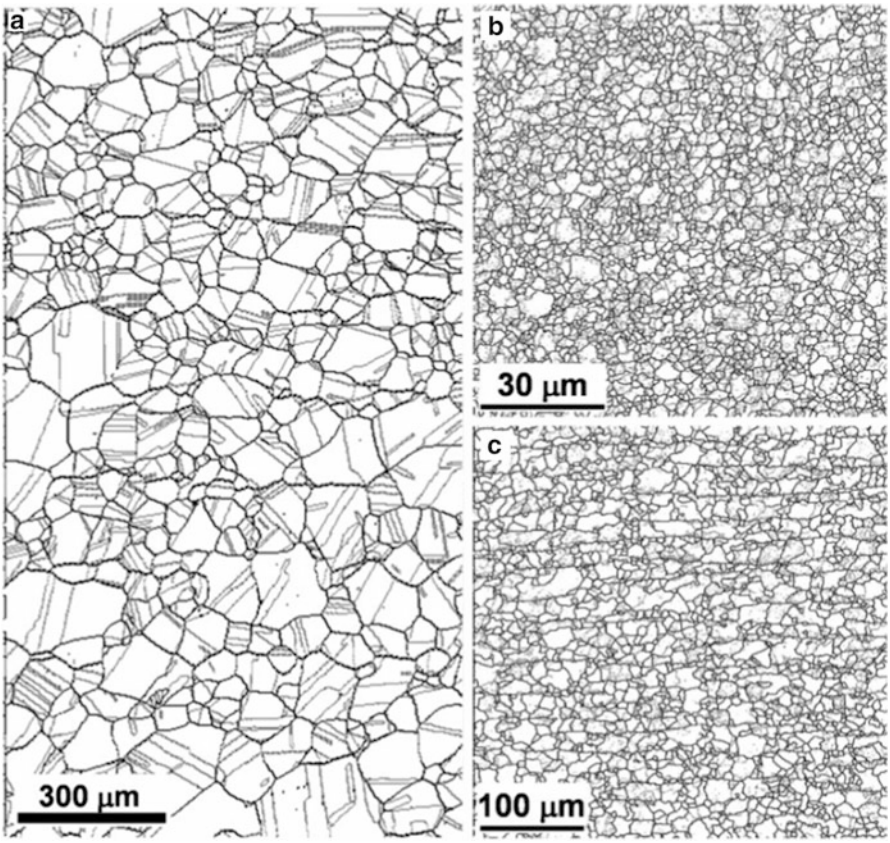

Fig. 7.37 Influence of friction stir welding on the microstructure of a superaustenitic stainless steel (Sato et al. 2009, reprinted with permission from Maney Publishing)

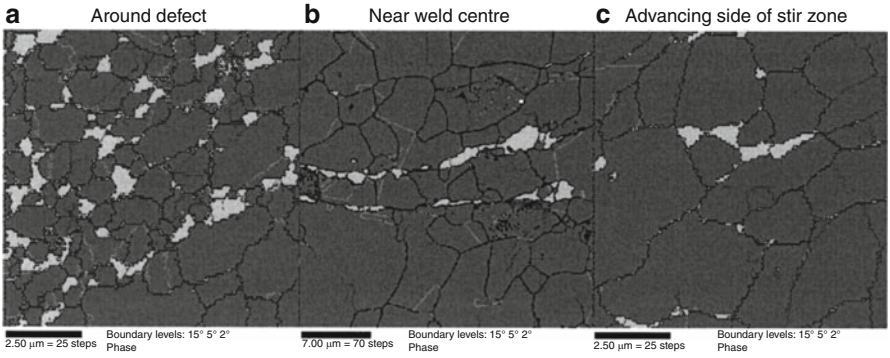

Fig. 7.38 Formation of δ-ferrite in the friction stir welded nugget of 304 austenitic stainless steel (Park et al. 2005, reprinted with permission from Maney Publishing)

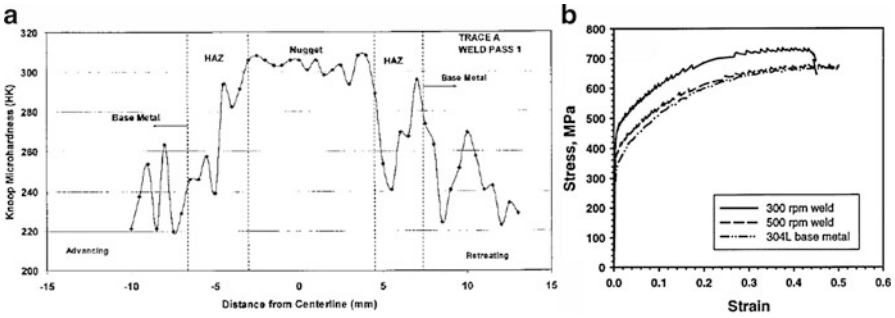

Fig. 7.39 (**a**) Microhardness profile on the transverse cross-section of a double sided welded superaustenitic stainless steel (Al-6XN: 2022Cr-6.0-7.0Mo-23.5-25.5Ni) (Klingensmith et al. 2005, reprinted with permission from the American Welding Society, Miami, FL), and (**b**) engineering stress-engineering strain curves for 304L stainless steel for base material and welded material (Reynolds et al. 2003, reprinted with permission from Elsevier)

Microstructural modifications of such alloys have large influence on their mechanical properties. As a result of grain refinement the nugget region shows hardness and strength either similar to or higher than the base region. Figure 7.39a shows hardness distribution across the weld on the transverse cross-section of a double-sided weld of a superaustenitic stainless steel Al-6XN. A higher hardness in the nugget compared to the base material should be noted for this particular weld. In this particular case, the grain size for base material was about 63 μm and after FSW in the nugget it was about 5.9 μm. Hence, the improvement in the hardness can be attributed to grain size refinement. Figure 7.39b shows the engineering stress-engineering strain curves for 304 L stainless steel. The samples were longitudinally oriented with respect to the weld and were machined entirely from the weld nugget. It shows that both the welds showed better yield strength than that of the base material. Moreover, the ductility was also very similar to the base material.

Foregoing discussion on microstructural evolution and mechanical properties indicate that a clear understanding of phase transformation is necessary to control the weld properties in steels. A general framework with respect to plain carbon steel has been presented in the next section which will help practitioner of this technology understand microstructural evolution in different zones of friction stir welds.

7.2.4.3 Microstructural Evolution Framework for Friction Stir Welding and Processing of Steels

Figure 7.40 schematically shows different zones in a friction stir weld. For simplicity only one HAZ zone has been shown here. Experimental finding suggests that more than one HAZ might exist depending upon exact processing condition. A temporal evolution of temperature in each zone is also shown in the same figure. As experimentally observed, the maximum peak temperature is shown for the nugget. A material volume in HAZ experiences the lowest peak temperature. In this

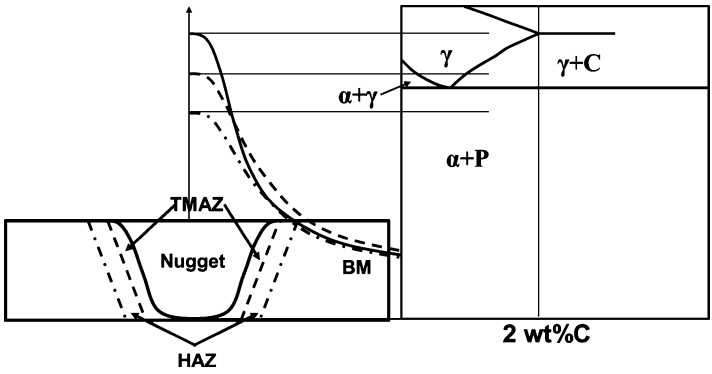

Fig. 7.40 A schematic illustration of microstructural evolution in different zones of the friction stir weld

particular case, it is shown that the nugget temperature exceeds critical temperature A_3 for almost all plain carbon steels used in most of the practical applications. Hence, in such a case the microstructure in the nugget would rely on the cooling rate in this zone and CCT (continuous cooling transformation) diagram should be consulted to get information regarding the expected microstructure in the nugget. In some cases, the actual microstructure may be slightly different from the expected one due to large strain and strain rate involved during the welding process.

TMAZ would develop a range of microstructures depending on exact chemistry of the steel. If the chemistry of the alloy is such that it reaches two phase region $\alpha + \gamma$, then final microstructure would consist of α phase and a transformed product of γ which would depend on the rate of cooling existing in that zone. Under different cooling conditions, a range of microstructure can be expected in this zone. Since, the phase α cannot undergo phase transformation, it can exist in fully recrystallized, partially recrystallized, recovered state, or a combination of recrystallized and recovered states. If chemistry is such that it reaches single phase γ, the final microstructure in TMAZ would depend on exact cooling condition, and like nugget, a CCT curve would be helpful in understanding what type of phase to expect under the prevailing processing condition.

The thermal profile of the HAZ suggests that temperature never crossed critical temperature A_1 in this particular case. Hence, the final microstructure will be more or less similar to the starting microstructure except that high temperature would cause morphology and size to change. In the case of martensitic steel, it would get tempered under the influence of high temperature as is shown in Figs. 7.30 and 7.31.

This particular illustration suggests that mechanical properties of the weld can be controlled in precise manner by controlling the evolution of microstructure in different zones of the weld. The processing parameters can be varied in a systematic manner to control peak temperature and cooling rates in different zones to control the microstructure evolution to obtain pre-determined distribution of mechanical properties across the welded zones. This approach can be developed not only for plain carbon steels but also for other types of steels such as duplex steel, austenitic steels, etc.

References

H.K.D.H. Bhadeshia, R. Honeycombe, Steels - Microstructure and Properties, Elsevier (2006)
G. Buffa, A. Ducato, L. Fratini, FEM based prediction of phase transformations during Friction Stir Welding of Ti-6Al-4V titanium alloy. Mater. Sci. Eng. A **581**, 56 (2013)
G. Cam, Friction stir welded structural materials: beyond Al-alloys. Int. Mater. Rev. **56**, 1–48 (2011)
L. Cui, H. Fujii, N. Tsuji, K. Nogi, Friction stir welding of a high carbon steel. Scr. Mater. **56**, 637–640 (2007a)
L. Cui, H. Fujii, N. Tsuji, K. Nakatak, K. Nogi, R. Ikeda, M. Matsushita, Transformation in stir zone of friction stir welded carbon steels with different carbon contents. ISIJ Int. **47**, 299–306 (2007b)
A.K. Dutt and R.S. Mishra, unpublished research (2014)
P. Edwards, M. Ramulu, Identification of process parameters for friction stir welding Ti-6Al-4V. J. Eng. Mater. Technol. **132**, 1–10 (2010)
H. Fujii, L. Cui, N. Tsuji, M. Maedac, K. Nakata, K. Nogi, Friction stir welding of carbon steels. Mater. Sci. Eng. A **429**, 50 (2006)
M. Ghosh, K. Kumar, R.S. Mishra, Friction stir lap welded advanced high strength steels: microstructure and mechanical properties. Mater. Sci. Eng. A **528**(28), 8111–8119 (2011)
G. Krauss, *Steels: Processing, Structure, and Performance* (ASM International, Materials Park, 2005)
S. Klingensmith, J.N. DuPont, A.R. Marder, Weld. J. **84**, 77s–85s (2005)
N. Kumar et al., The effects of friction stir welding on the microstructural evolution and mechanical properties of Ti-6Al-4V alloy, in *Friction Stir Welding and Processing V* (TMS, Warrendale, 2009), pp. 45–53
W.B. Lee, C.Y. Lee, W.S. Chang, Y.M. Yeon, W.B. Jung, Microstructural investigation of friction stir welded pure titanium. Mater. Lett. **59**, 3315–3318 (2005)
T.J. Lienert, Microstructure and mechanical properties of friction stir welded titanium alloys, in *Friction Stir Welding and Processing*, ed. by R.S. Mishra, M.W. Mahoney (ASM International, Materials Park, 2007), pp. 123–154. ISBN-13: 978-0-87170-840-3
H.J. Liu et al., Microstructural evolution mechanism of hydrogenated Ti-6Al-4V in the friction stir welding and post-weld dehydrogenation process. Scr. Mater. **61**, 1008–1011 (2009)
H. Liu et al., Study of the key issues of friction stir welding of titanium alloy. Mater. Sci. Forum **638–642**, 1185–1190 (2010)
G. Lütjering, J.C. Williams, *Titanium* (Springer, Berlin, 2007). ISBN 978-3-540-71397-5
R. Ohashi, M. Fujimoto, S. Mironov, Y.S. Sato, H. Kokowa, Sci. Technol. Weld. Join. **14**(3), 221–227 (2009)
S. Park, Y. Sato, H. Kokawa et al., Microstructural characterisation of stir zone containing residual ferrite in friction stir welded 304 austenitic stainless steel. Sci. Technol. Weld. Join. **10**, 550 (2005)
S. Pasta, A.P. Reyonds, Residual stress effects on fatigue crack growth in Ti-6Al-4V friction stir weld. Fatig. Fract. Eng. Mater. Struct. **31**, 569–580 (2008)
A.L. Pilchak et al., The relationship between friction stir weld parameters and microstructure in investment cast Ti-6Al-4V, in *Stir Welding and Processing IV* (TMS, Warrendale, 2007), pp. 419–427 (2007b)
A.L. Pilchak, M.C. Juhas, J.C. Williams, Observations of Tool-Workpiece Interactions during Friction stir welding of Ti-6Al-4V. Metall. Mater. Trans. A **38A**(2), 435–437 (2007a)
A.L. Pilchak et al., Microstructure evolution during friction stir welding of mill-annealed Ti-6Al-4V. Metall. Mater. Trans. A **11** (2010)
A.L. Pilchak and J.C. Williams, Microstructure and texture evolution during friction stir processing of fully lamellar Ti-6Al-4V, Metall. Mater. Trans. A. **42A**, 745 (2011)
J.A. Querin et al. Effect of weld tool geometry on friction stir welded Ti-6Al-4V, in *Trends in Welding Research* (ASM International, Materials Park, 2009), pp. 108-112

A.J. Ramirez, M.C. Juhas, Microstructural evolution in Ti-6Al-4v friction stir welds. Mater. Sci. Forum **426–432**, 2999–3004 (2003)

A. Reynolds, W. Tang, T. Gnaupel-Herold, H. Prask, Structure, properties, and residual stress of 304L stainless steel friction stir welds. Scr. Mater. **48**, 1289 (2003)

A.P. Reynolds, E. Hood, W. Tang, Texture in friction stir welds of Timetal 21S. Scr. Mater. **52**, 491–494 (2005)

Y.S. Sato, N. Harayama, H. Kokawa, H. Inoue, Y. Tadokoro, S. Tsuge, Evaluation of microstructure and properties in friction stir welded superaustenitic stainless steel. Sci. Technol. Weld. Join. **14**, 203 (2009)

Y. Sato, M. Miyake, H. Kokawa, T. Omori, K. Ishida, S. Imano, S. Park, S. Hirano, in *Development of Co-Based Alloy FSW Tool for High-Softening-Temperature Materials, Friction Stir Welding and Processing VI*, ed. by R.S. Mishra, M.W. Mahoney, Y. Sato, Y. Hovanski, R. Verma. 2011 TMS annual meeting, pp. 1–9 (2011)

R.S. Mishra, M.W. Mahoney, S.X. McFadden, N.A. Mara, A.K. Mukherjee, High strain rate superplasticity in a friction stir processed 7075 al alloy. Scr. Mater. **42**, 163 (1999)

J. Su, J. Wang, R.S. Mishra, R. Xu, J.A. Baumann, Microstructure and mechanical properties of a friction stir processed Ti-6Al-4V alloy. Mater. Sci. Eng. A **573**, 67–74 (2013)

B.M. Tweedy, W. Arbegast, C. Allen, in *Friction Stir Welding and Processing III*, ed. by K.V. Jata et al.(TMS, Warrendale, 2005), pp. 97–104

C.F. Yolton, F.H. Froes, R.F. Malone, Alloying element effects in metastable beta titanium alloys. Metall. Trans. A **10**, 132–134 (1979)

Y. Zhang, Y.S. Sato, H. Kokawa, S.H.C. Park, S. Hirano, Microstructural characteristics and mechanical properties of Ti-6Al-4V friction stir welds. Mater. Sci. Eng. A **485**, 448–455 (2008a)

Y. Zhang, Y.S. Sato, H. Kokawa, S.H.C. Park, S. Hirano, Stir zone microstructure of commercial purity titanium friction stir welded using pcBN tool. Mater. Sci. Eng. A **488**, 25–30 (2008b)

L. Zhou et al., The stir zone microstructure and its formation mechanism in Ti-6Al-4V friction stir welds. Scr. Mater. **61**, 596–599 (2009)

Chapter 8
Dissimilar Metal Friction Stir Welding

8.1 Introduction

The varied requirements of different regions or parts in a structure often require the use of different materials to meet the design expectation. So, the use of different materials in a given engineering system is a norm not an exception. Thus, to improve the fuel efficiency, automobile industry is encouraging the use of a combination of light metals like Al and Mg alloys. The increased use of light metal parts will necessitate their joining with existing structural member and most probably with dissimilar metals.

Figure 8.1a shows a turbocharger impeller as an example of dissimilar metal welding (http://www.ptreb.com/Industries/Automotive/Turbocharger_Impeller_Welding/). A magnified view of the joint region is shown in Fig. 8.1b. The shaft of the turbocharger impeller is made of carbon steel (because of good machinability, toughness, and hardenability) which was joined to the impeller made of Inconel (due to good high temperature properties and corrosion resistance) using electron beam welding (Bailey 1986). Thus, different materials in a dissimilar joint can be either metals with same base element but different chemical compositions or altogether different base metals. Welding between different aluminum alloys or different ferrous alloys, are examples where base material is same. Welds between aluminum and magnesium alloys or aluminum alloys and ferrous alloys, etc., fall in the category where base materials are different.

8.2 Issues with Dissimilar Metal Welding

Both, fusion and non-fusion welding techniques are utilized for dissimilar metal welding. Irrespective of the welding techniques, the differences in the chemistry of the materials, their melting points, thermal conductivity, coefficient of thermal

R.S. Mishra et al., *Friction Stir Welding and Processing: Science and Engineering*, 237
DOI 10.1007/978-3-319-07043-8_8, © Springer International Publishing Switzerland 2014

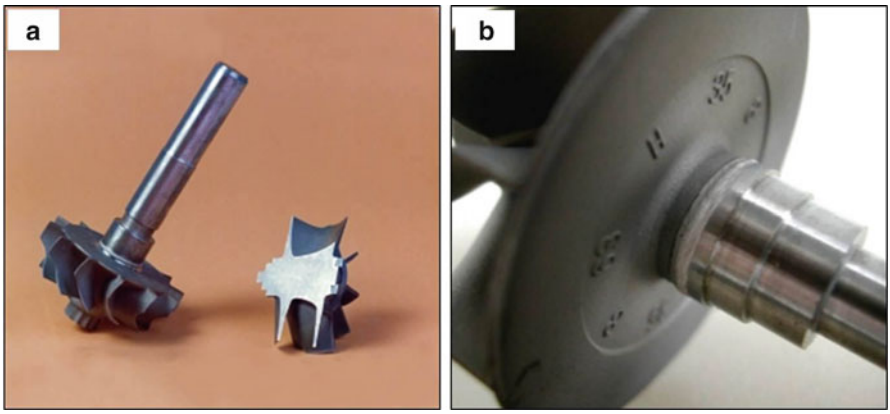

Fig. 8.1 (**a**) Turbocharger impeller and its cross-sectional view, and (**b**) magnified view of the welded location showing joint between shaft and impeller (http://www.ptreb.com/Industries/Automotive/Turbocharger_Impeller_Welding/; last accessed on 11 November 2013)

expansion, etc., pose a serious challenge in obtaining sound joints meeting the design requirements.

In fusion welding technique the chemistry of the resulting weld is accounted for by the use of filler material. The use of such filler material is non-existent in solid state joining techniques (because typically they are autogenous). However, prevention of brittle intermetallic phases remains a challenge in both types of welding categories and a judicious selection of dissimilar metals is required so that mechanical and corrosion properties meet the expectations of the designers. A survey of phase diagram often gives a better picture about the compatibility of materials under considerations for dissimilar welding. For example, Fig. 8.2 shows Fe-Al binary phase diagram (Volume 3, Alloy Phase Diagrams → Al (Aluminum) Binary Alloy Phase Diagrams → Al-Fe (Aluminum-Iron)) which is relevant for dissimilar welding of ferrous alloys to aluminum, a commercially important dissimilar joint. It shows that Fe and Al are immiscible in each other and tend to form intermetallic compounds such as $FeAl_3$ and Fe_3Al.

For materials with differing melting points, fusion welding leads to initial melting of the low melting point alloy. This can cause compositional changes due to evaporation of low melting point elements leading to inferior welds. Although, melting is not an issue in solid-state welding of similar metals and alloys, widely differing material softening characteristics poses its own sets of challenge. Solid state welding between materials of widely differing melting points may lead to melting of low melting point material. Even if gross melting is avoided, incipient melting of low temperature phases present is possible. The differences in softening characteristics (drop of flow strength with temperature) of the materials being welded can also lead to insufficient material mixing resulting in undesirable weld characteristics. Figure 8.3 shows the variation of yield strength of 6061Al-T6 and SS304 stainless steel as a function of temperature. It is evident that for a given

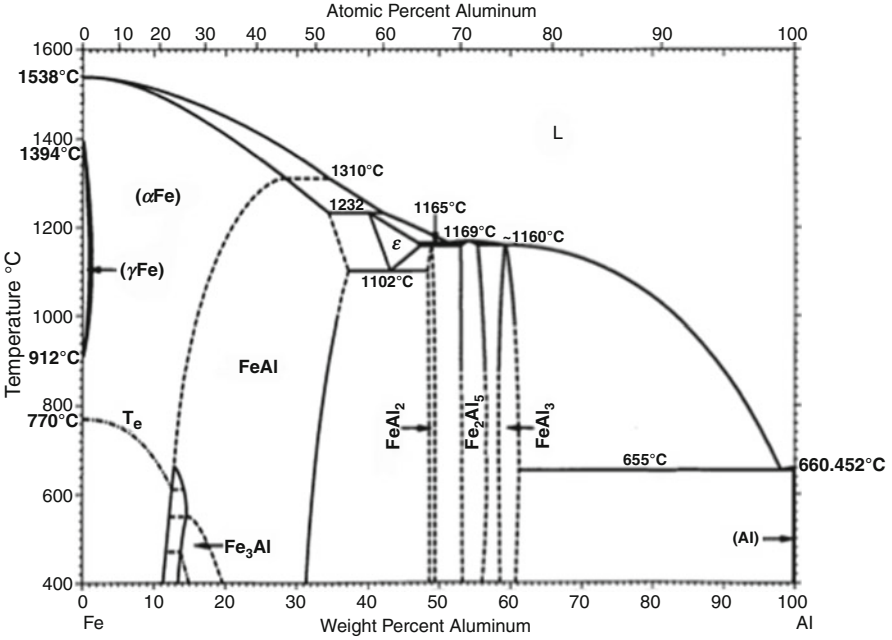

Fig. 8.2 Fe-Al binary phase diagram (ASM Handbook, Volume 3, Alloy Phase Diagrams → Al (Aluminum) Binary Alloy Phase Diagrams → Al-Fe (Aluminum-Iron), reprinted with permission from ASM International)

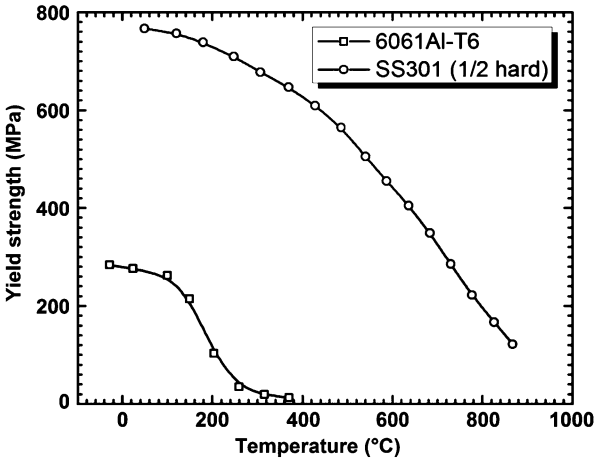

Fig. 8.3 Yield strength of 6061Al-T6 (ASM Handbook, Volume 2, Properties and Selection: Nonferrous Alloys and Special-Purpose Materials → Properties of Wrought Aluminum and Aluminum Alloys → 6061 Alclad 6061) and SS301 alloys as a function of temperature (ASM Handbook, Volume 1, Properties and Selection: Irons, Steels, and High-Performance Alloys → Elevated-Temperature Properties of Stainless Steels → Product Forms)

temperature both the materials possess different strength which will lead to differences in their flow characteristics during solid-state welding. Later, it will be seen that a positional dependence of weld formation in friction stir welding of dissimilar metals also exists.

Thus, differences in the physical properties of metals and alloys call for a meticulous design of welding strategy to obtain a sound quality joint. The next section focuses on dissimilar metal joining using friction stir welding and will highlight the opportunities and challenges for friction stir welding of dissimilar metals.

8.3 Friction Stir Welding of Dissimilar Metals

Friction stir welding has been explored to a great extent for joining not only similar metals/alloys but also dissimilar metals/alloys. Dissimilar metal joining using friction stir welding in this section will be discussed under three very broad categories and encompasses dissimilar welding of many metallic materials.

8.3.1 Friction Stir Welding of Different Alloys with Similar Base Metals and Melting Points

Typical combinations which fall under this category include—aluminum-aluminum alloys, magnesium and magnesium alloy, ferrous-ferrous alloys where the base material remains same and they differ only in terms of major alloying elements and their concentrations. For example, both AA2024 and AA5052 alloys have aluminum as a base metal but the major alloying elements are Cu and Mg, respectively (see Chap. 5). Although, the melting points (to be precise, solidus and liquidus temperatures) of these alloys are very similar, the second phases present in each may have different melting point. In the following section, although, welding between only dissimilar aluminum alloys is considered this will provide a good insight into the welding of other dissimilar materials mentioned above.

8.3.1.1 Welding of Aluminum Alloys with Other Aluminum Alloys

Figure 8.4 shows the transverse cross-sectional image of dissimilar weld created between 1.0 mm AA5182 and AA6061 sheets (Leal et al. 2008). A cylindrical tool of 10.0 mm shoulder diameter with a concave (8° from vertical) profile, 3.0 mm cylindrical tool pin with left-handed thread, and 0.9 mm pin height was used. A tool rotation rate of 1,800 rpm, tool traverse speed of 160 mm/min, and a tool tilt angle of 2.5° was used to prepare the weld. Figure 8.4a, b presents the top view (location: 0.25 mm above the weld root) and a transverse cross-section of the weld.

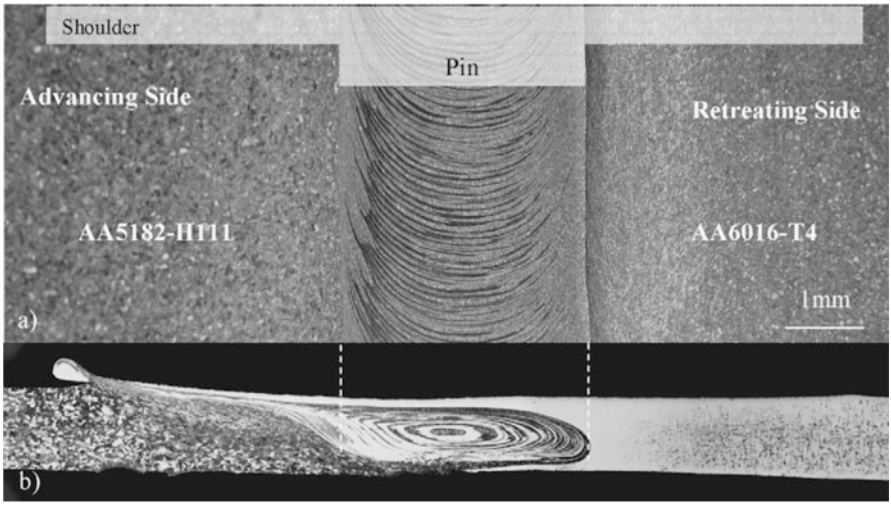

Fig. 8.4 (**a**) Horizontal cross-section of a dissimilar weld between 5182Al and 6016Al alloys, and (**b**) transverse cross-section of the same weld showing intercalated layers of the alloys (*brighter* region 6016Al and *darker* region 5182Al) in the onion ring (Leal et al. 2008, reprinted with permission from Elsevier)

The transverse cross-section shows the onion ring pattern (see Chap. 2) with intercalated AA5182 (darker layer) and AA6016 (brighter layer) alloys. Similar intercalated structure are reported by Ouyang and Kovacevic (2002), Shigematsu et al. (2003), Park et al. (2010), Palanivel et al. (2012).

Figure 8.5 illustrates the role of welding parameters in joint formation. The welding was carried out between AA5052 and 5J32Al—an aluminum alloy designation of Kobe Steel (Al-5.68wt%Mg-0.2wt%Cu) equivalent to AA5023; at two different tool rotation rates of 1,000 and 1,500 rpm and tool traverse speeds varying between 100 and 400 mm/min in the steps of 100 mm/min. The welds made at 1,000 rpm and 100–400 mm/min, show very little mixing between AA5052 and 5J32Al alloys. However, the welds made at 1,500 rpm at 100–400 mm/min show better mixing of these alloys (Song et al. 2011).

The difference in material mixing is mostly related to ease of material flow at different temperatures. It may be mentioned that temperature increases with increase in tool rotation rates and can lead to a better material mixing of the alloys (see Chap. 2).

In fact, even position of the alloy, i.e., whether an alloy occupies advancing side or retreating side of the weld also affects material mixing. This positional dependence of material mixing during dissimilar material welding has been studied by many, a representative example of which is included in Fig. 8.6 (Park et al. 2010). The figure shows dissimilar friction stir welds between AA5052-H32 and AA6061-T6 alloys made at 2,000 rpm tool rotation rate and 100 mm/min tool traverse speed at a tool tilt angle of 3°. The shoulder diameter, pin diameter, and pin height were 10, 4, and 1.7 mm, respectively. The difference in the extent of material mixing is

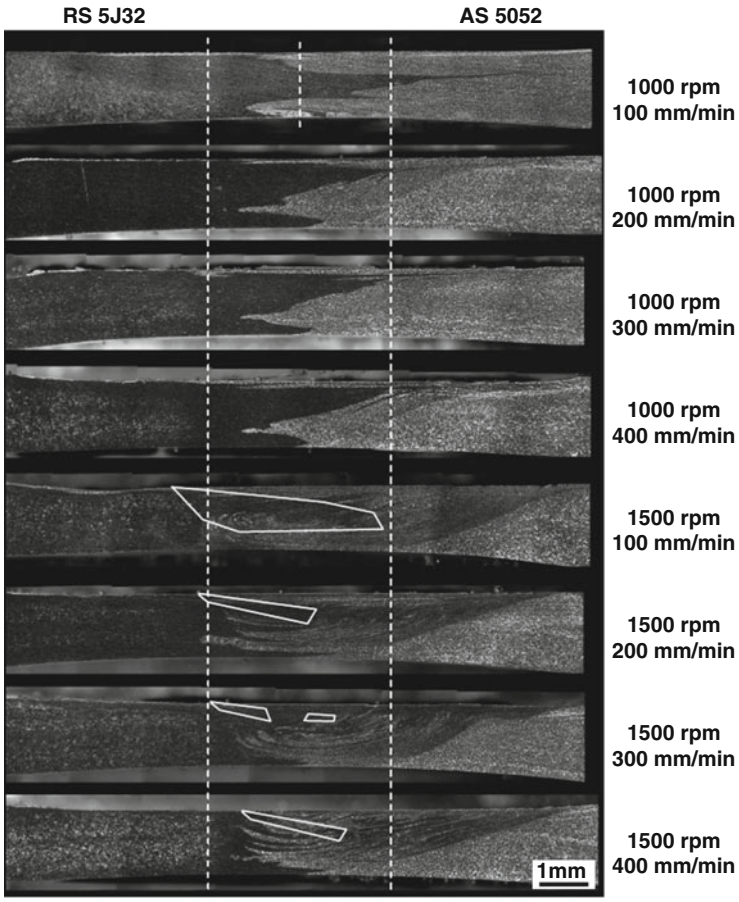

Fig. 8.5 Friction stir dissimilar welds between 5052Al and 5J32Al showing effect of tool rotation rates and tool traverse speeds on material mixing (Song et al. 2010)

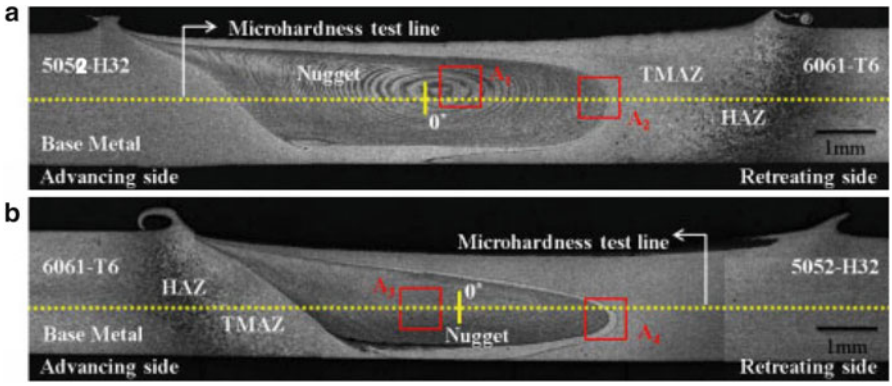

Fig. 8.6 The effect of material positioning on the level of material mixing during friction stir dissimilar welding of 5052Al-H32 and 6061Al-T6 alloys (Park et al. 2010, reprinted with permission from Maney Publishing)

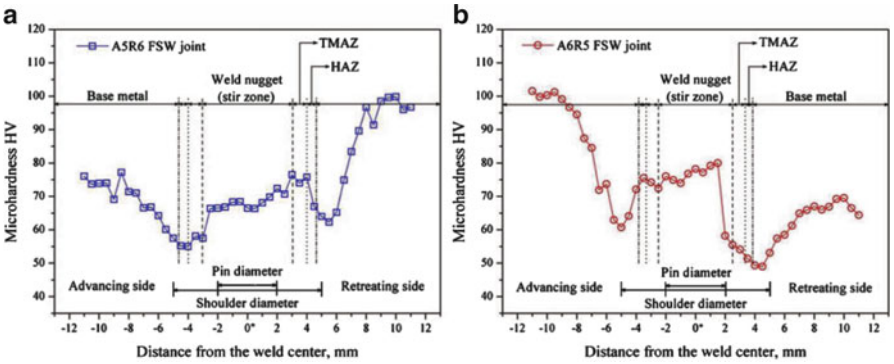

Fig. 8.7 Microhardness profile along the dotted (yellow) horizontal lines shown in Fig. 8.6 for the weld (**a**) A5R6 (5052Al-H32 on advancing side and 6061Al-T6 on the retreating side) and (**b**) A6R5 (6061Al-T6 on advancing side and 5052Al-H32 on the retreating side) (Park et al. 2010, reprinted with permission from Maney Publishing)

quite evident from Fig. 8.6. Based on elemental analysis of different regions within the squared region shown in Fig. 8.6a, it was concluded that the darker and lighter onion ring regions were AA5052-H32 and AA6061-T6, respectively. In the instance where AA5052-H32 is on the retreating side of the weld (Fig. 8.6b), the nugget region predominantly consisted of AA6061-T6 alloy.

This difference in material mixing results in different mechanical properties as evident from the microhardness measurement (Fig. 8.7) carried out at locations along the dotted horizontal lines in Fig. 8.6 (Park et al. 2010). In both cases the hardness minimum occurs in the HAZ of AA5052 alloy. The variation in microhardness within nugget is less when AA6061 T6 is on advancing side compared to the case where it was on the retreating side. The tensile tests on specimens aligned transverse to the welding direction resulted in fracture at the location of minimum hardness for both the welds. It may be added that literature shows conflicting results on the effect of material arrangement on the strength of welds.

8.3.2 Friction Stir Welding of Different Alloys Having Dissimilar Base Metals and Similar Melting Point

In terms of average strength, magnesium alloys are weaker than aluminum alloys. Hence, welding of dissimilar magnesium alloys in itself poses little or no challenge. Thus, the tools used for welding aluminum alloys can be used for magnesium alloys without worrying about tool wear. Again, melting point of pure aluminum and magnesium are quite similar. Therefore the real challenge in joining aluminum and magnesium alloys is posed by the widely differing chemistry. To highlight the issue the Al-Mg binary phase diagram is shown in Fig. 8.8 (Volume 3, Alloy Phase

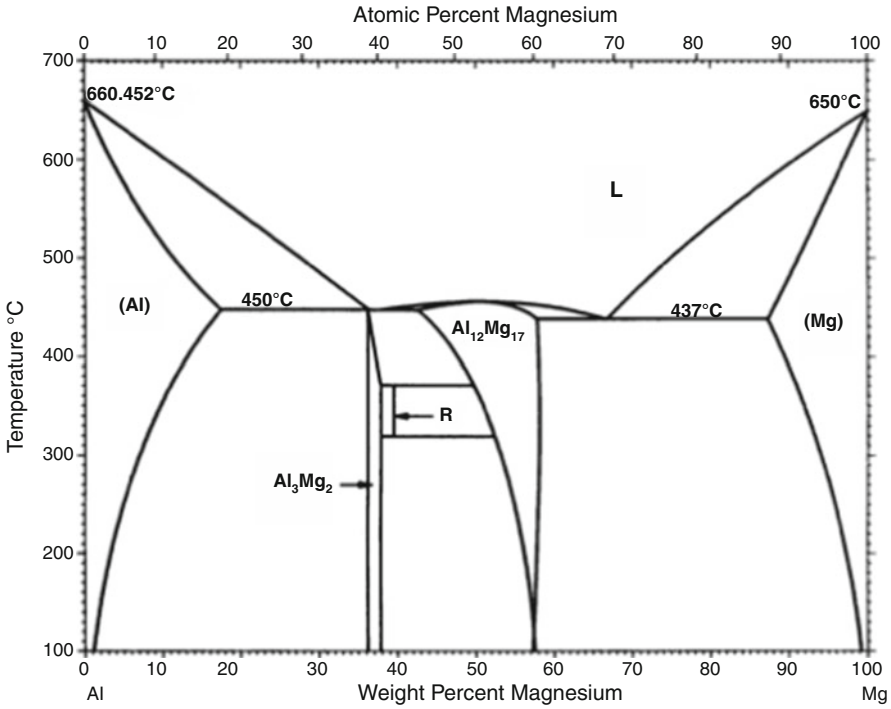

Fig. 8.8 Binary Al-Mg phase diagram (ASM Handbook, Volume 3, Alloy Phase Diagrams → Al (Aluminum) Binary Alloy Phase Diagrams → Al-Mg (Aluminum-Magnesium), reprinted with permission from ASM International)

Diagrams → Al (Aluminum) Binary Alloy Phase Diagrams → Al-Mg (Aluminum-Magnesium)). The equilibrium diagram indicates five different phases—two terminal solid solutions Al(Mg) and Mg(Al), and three intermetallic compounds, $\beta(Al_3Mg_2)$, R, and $\gamma(Al_{12}Mg_{17})$. The phase diagram indicates that if pure Al and Mg are welded together and equal proportion of both the materials (wt.%) are present in the weld nugget, this would lead to formation of $\beta(Al_3Mg_2)$ and $\gamma(Al_{12}Mg_{17})$ phases at room temperature. In reality, during friction stir welding of dissimilar metal, the material flow is very complex and a non-equilibrium condition exists during processing. Hence, joining of Al and Mg, results in a non-equilibrium microstructure. Hence, different regions of the weld are expected to consist of different phases. The phase diagram shown in Fig. 8.8 also highlights another issue associated with dissimilar welding—the melting of intermetallic phases. For example, Al(Mg) and Al_3Mg_2 would react and form liquid at 450 °C. During friction stir welding depending on processing parameters temperature can reach in excess of 500 °C. This accompanied by the high shear forces involved during friction stir welding can lead to liquation cracking. Incipient melting of low melting phases and liquation cracking have been reported even for welding of similar metals, and widely differing chemistry actually accentuates the problem.

The discussion above highlights the challenges in joining dissimilar materials which vary considerably in their chemical compositions. To overcome these

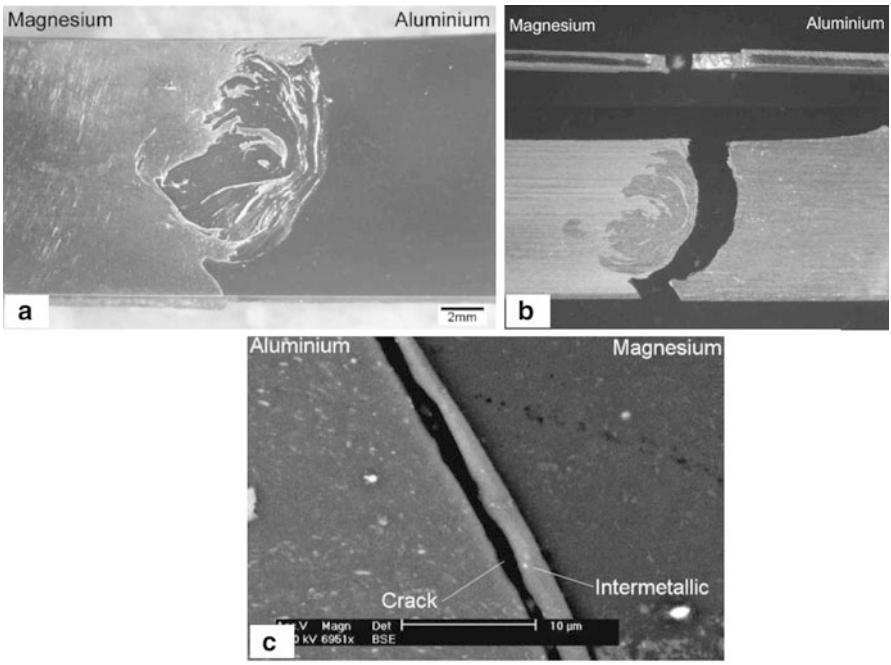

Fig. 8.9 (**a**) A dissimilar friction stir weld between AZ31B (retreating side) and 6061Al (advancing side), (**b**) fractured weld as a result of side bend test, and (**c**) location of the crack in the weld (McLean et al. 2003, reprinted with permission from Maney Publishing)

difficulty one therefore needs to judiciously choose the welding parameters such as position of tool from the weld interface, positioning of the materials (whether advancing or retreating side), tool rotation rates, tool traverse speed, etc.

8.3.2.1 Welding of Aluminum Alloys with Magnesium Alloys

Figure 8.9 shows a friction stir dissimilar weld between AZ31B and AA6061 alloys (McLean et al. 2003) where AZ31B is on the retreating side. As in the case of dissimilar Al alloy welding, a positional dependence of material flow is also observed. Thus, transverse cross-section in Fig. 8.9 shows intercalated layers of these two alloys. Side bend testing resulted in fracture along the interface at very low loads. The fractured sample is shown in Fig. 8.9b. Energy dispersive X-ray spectroscopy of the fractured surface revealed a thin, continuous layer of $Al_{12}Mg_{17}$, with the fracture occurring at aluminum/$Al_{12}Mg_{17}$ interface. In Fig. 8.9c, an SEM image of the cracks at AA6061/$Al_{12}Mg_{17}$ interface is shown. The continuous intermetallic layer is speculated to be formed by reaction melting and re-solidification of $Al_{12}Mg_{17}$ phase.

There are several other published works which show very sharp interface between Mg and Al alloy in the weld nugget indicating lack of mixing and presence

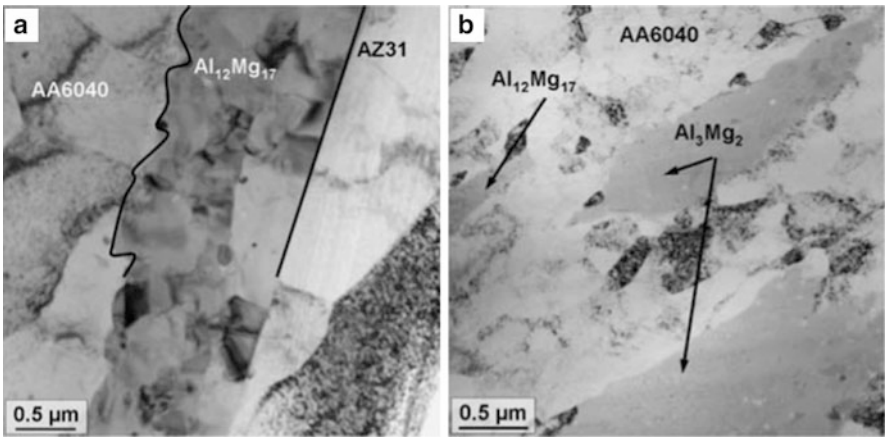

Fig. 8.10 (**a**) TEM micrograph showing microstructure at the interfacial region of 6040Al and AZ31 weld and (**b**) grains containing nano-sized Al_3Mg_2 precipitates (Kostka et al. 2009, reprinted with permission from Elsevier)

of intermetallic compounds. The work of Kostka et al. (2009) reported the presence of nano-sized Al_3Mg_2 precipitates in addition to $Al_{12}Mg_{17}$. Kostka et al. (2009) joined AA6040 and AZ31 at 1,400 rpm and 225 mm/min. The TEM image of the interface region between AA6040 and AZ31 in the weld nugget is shown in Fig. 8.10. The various phases identified using selected area diffraction (SAD) pattern from different regions are shown in Fig. 8.10. The comprehensive SAD patterns for each phase are shown in Fig. 8.11.

As mentioned earlier for Al and Mg alloys dissimilar welding, the position of the material influences the level of mixing between these alloys. Firouzdor and Kou (2010a) welded 6061Al and AZ31B by switching their sides at 1,400 rpm tool rotation rate and 38 mm/min tool traverse speed. The transverse macrostructure corresponding to this weld is shown in Fig. 8.12a with microstructure from two different regions of the nugget (indicated by the arrows) shown in Fig. 8.12b, c. In addition to intercalated layers of AA6061 and AZ31B, intermetallic phase Al_3Mg_2 (labeled as β) are noted.

Figure 8.13 shows the transverse cross-section of the same set of alloys (as in Fig. 8.12) where AZ31B is present on advancing side of the weld. Other processing parameters remaining the same as in the last case, for which the transverse cross-section is shown in Fig. 8.13a. It indicates slightly better mixing than in Fig. 8.12a. Micrographs in Fig. 8.13b, c show a finer scale of intercalated layers of the two alloys although Al_3Mg_2 (labeled as β) phases are present in this case too.

To study the effect of tool rotation rate on weld formation, Kwon et al. (2008) welded AA5052 and AZ31B alloys at 1,000, 1,200, and 1,400 rpm tool rotation rates. The aluminum alloy is placed on the advancing side of the weld. The transverse cross-sections corresponding to each tool rotation rate are shown in Fig. 8.14. A careful comparison of the three welds shown in Fig. 8.14 indicates that within this processing envelop the extent of material mixing is approximately similar.

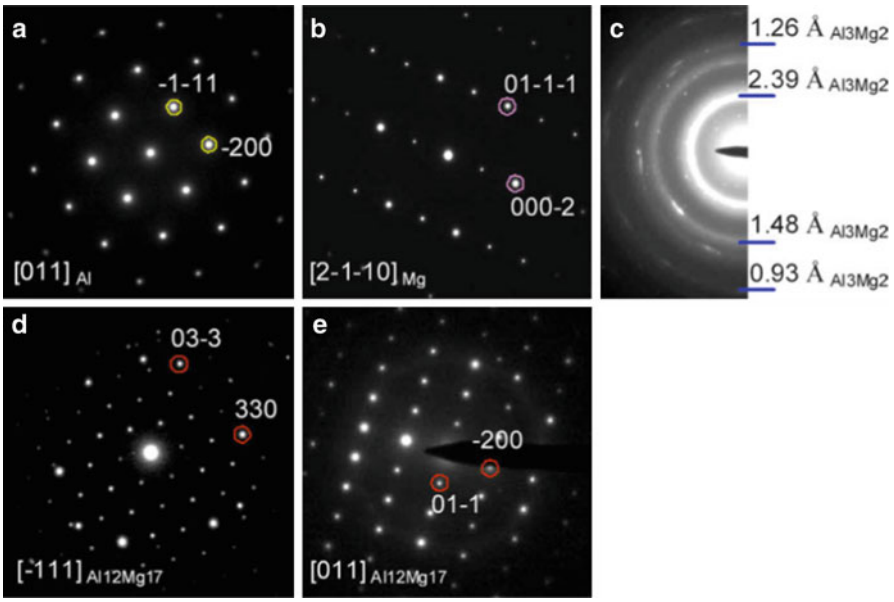

Fig. 8.11 SAD pattern of (**a**) 6040Al, (**b**) AZ31, (**c**) nano-sized Al_3Mg_2, (**d**, **e**) $Al_{12}Mg_{17}$ (Kostka et al. 2009, reprinted with permission from Elsevier)

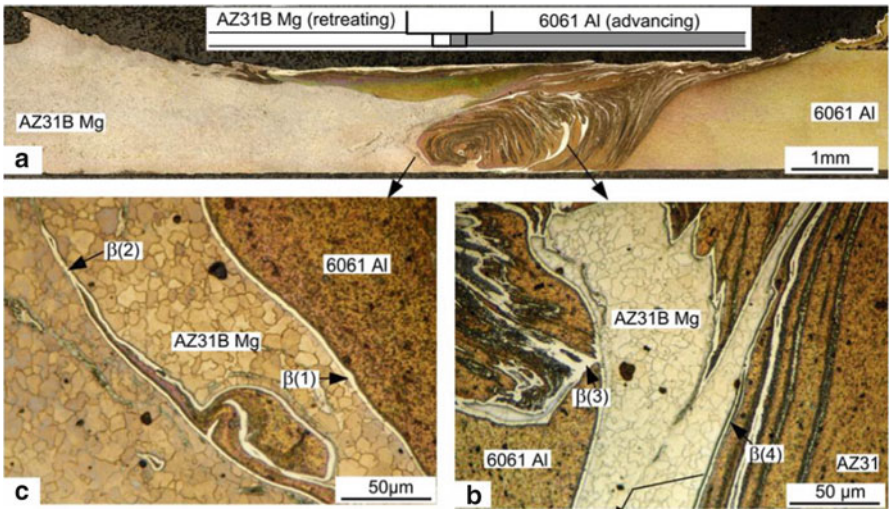

Fig. 8.12 Friction stir dissimilar weld between AZ31B (retreating side) and 6061Al (advancing side) processed at 1,400 rpm and 38 mm/min tool rotation rate and tool traverse speed, respectively, (**a**) transverse cross-section, (**b**, **c**) showing micrographs corresponding to different regions in the weld nugget (Firouzdor and Kou 2010a, reprinted with permission from Springer)

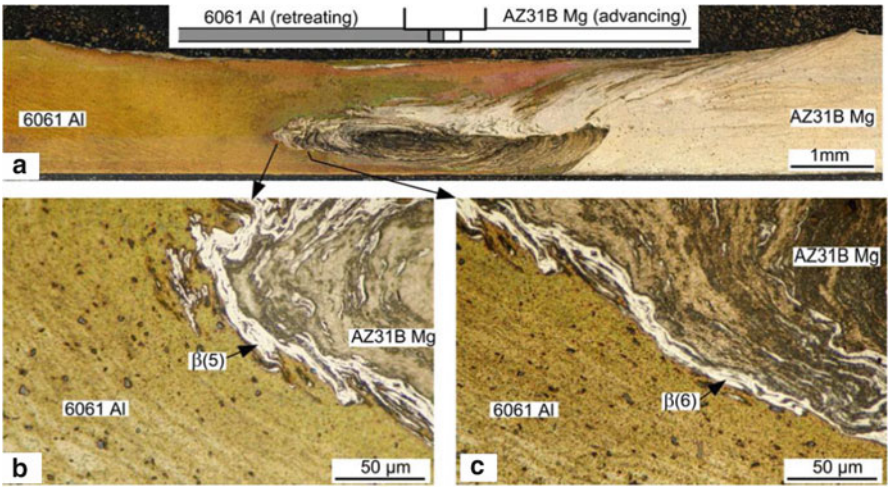

Fig. 8.13 Friction stir dissimilar weld between AZ31B (advancing side) and 6061Al (retreating side) processed at 1,400 rpm and 38 mm/min tool rotation rate and tool traverse speed, respectively, (**a**) transverse cross-section, (**b**, **c**) showing micrographs corresponding to different regions in the weld nugget (Firouzdor and Kou 2010a, reprinted with permission from Springer)

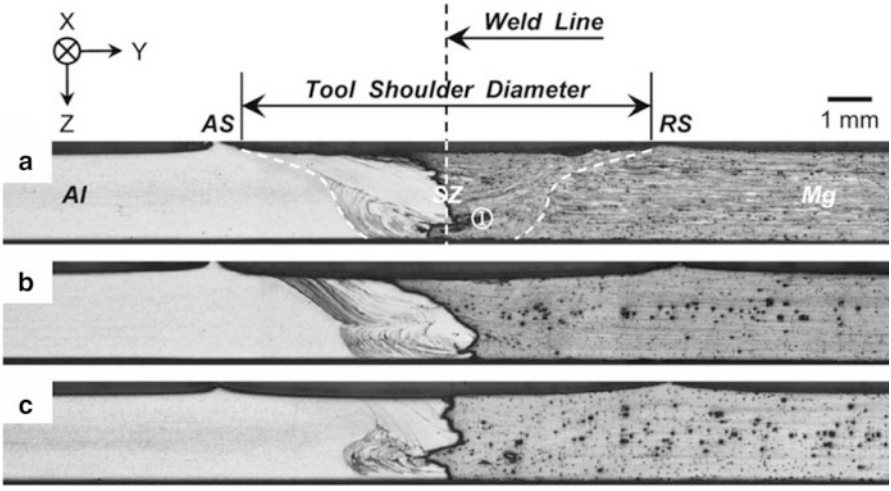

Fig. 8.14 Friction stir dissimilar welds of 5052Al and AZ31B alloys; (**a**) 1,000 rpm, (**b**) 1,200 rpm, and (**c**) 1,400 rpm (Kwon et al. 2008, reprinted with permission from Elsevier)

The effect of tool offset on material mixing and resulting mechanical properties is addressed by Liang et al. (2013). Figure 8.15 shows the results of friction stir welds between AA6061 and an Mg alloy having 1 wt% Al and 1 wt% Zn. The transverse cross-section shown in Fig. 8.15a corresponds to the condition where tool is offset by 1 mm from the weld centerline into the Mg side. Figure 8.15b represents the case where the tool is offset into Al by the same amount. For the weld

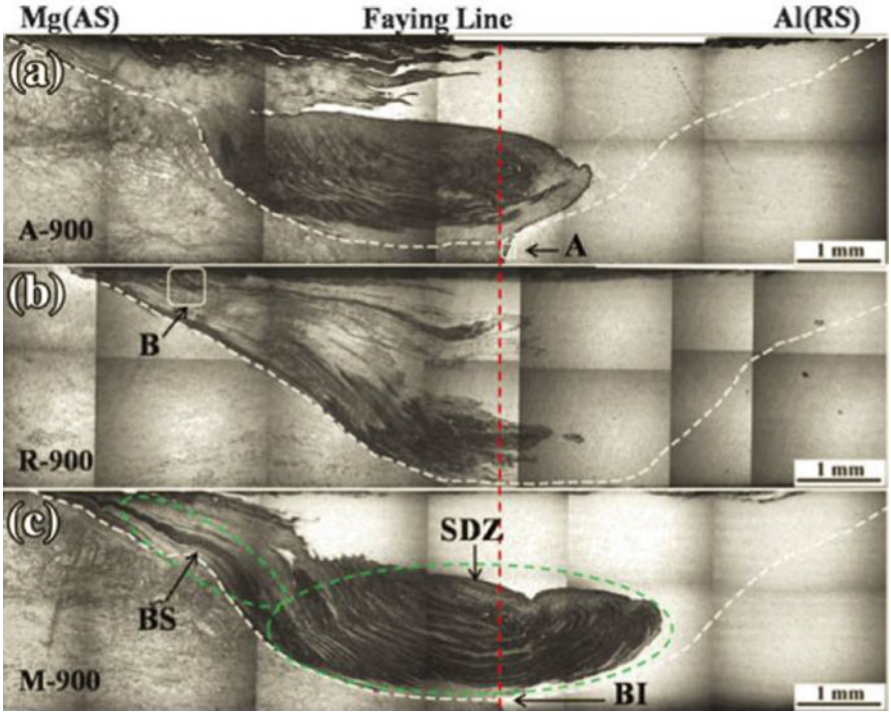

Fig. 8.15 Effect of tool offset on the joint formation between Mg and Al dissimilar weld, (**a**) 1 mm offset toward Mg side, (**b**) 1 mm offset toward Al side, and (**c**) welding with no offset (Liang et al. 2013, reprinted with permission from Springer)

shown in Fig. 8.15c, the welding is carried out without any offset. The weld nugget with 1 mm offset into Mg alloy results in higher volume fraction of Mg alloy in the nugget. A smaller volume fraction of Mg alloy in the nugget is observed for the case where tool offset is 1 mm into Al alloy. The weld made with no offset (Fig. 8.15c shows higher proportion of Al alloy in the nugget compared to the case shown in Fig. 8.15a and is relatively smaller compared to the case shown in Fig. 8.15b).

Different volume fractions of Al and Mg alloys in the nugget also results in different plastic deformation behavior. Figure 8.16 shows engineering stress-strain curves corresponding to the three welds included in Fig. 8.15. The weld M-900 (weld carried out with no tool offset) possessed maximum ductility. The specimen, in which tool offsets are used, show similar ductility and is very small compared to the ductility shown by M-900 weld. The modes of tensile failure are different in each case.

Although, the M-900 weld exhibits higher ductility compared to the rest, overall ductility is much lower compared to the base materials (Al and Mg alloys). In fact, literature confirms that Al and Mg alloy dissimilar welds possess very limited ductility. The effect of tool rotation rates on the strength, ductility, and joint efficiency of AZ31B-O and AA5052-O dissimilar welds is shown in Fig. 8.17 (Shigematsu et al. 2009). The tensile sample orientation is perpendicular to the welding direction and an overall lowering in tensile strength and elongation after

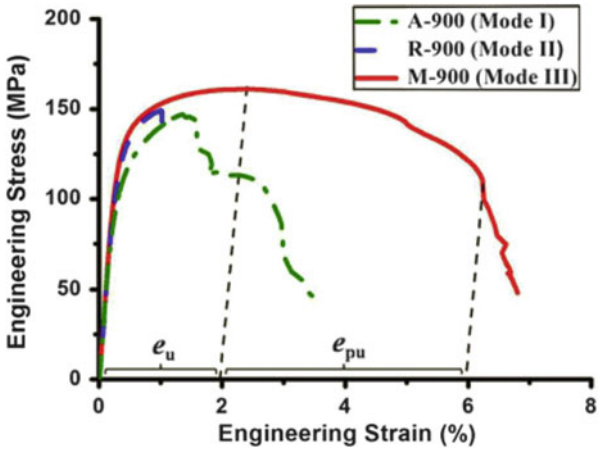

Fig. 8.16 Effect of tool offset on the plastic deformation behavior of Al and Mg alloys dissimilar welds (Liang et al. 2013, reprinted with permission from Springer)

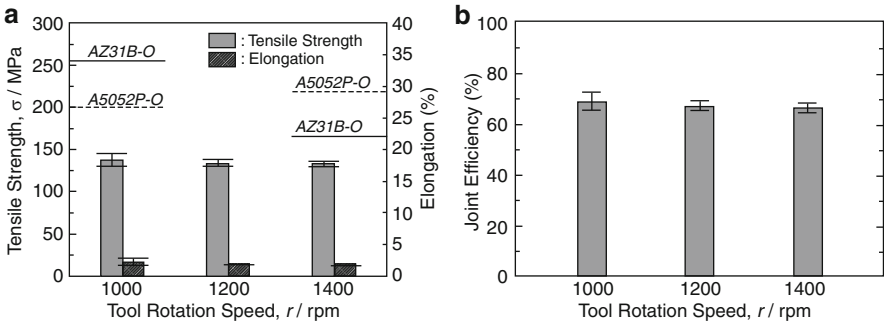

Fig. 8.17 Friction stir dissimilar welds of 5052Al-AZ31B, (**a**) tensile strength and elongation and (**b**) joint efficiency as a function of tool rotation rates (adapted from Shigematsu et al. 2009)

welding is observed. The joint efficiency remained unaffected by different tool rotation rates (Fig. 8.17b). Similar study by Shigematsu et al. on the effect of tool traverse speed on strength, elongation, and joint efficiency showed almost similar response as shown in Fig. 8.17.

Such inferior mechanical properties of the weldments can be related to the formation of intermetallic compounds (e.g. $Al_{12}Mg_{17}$) which are present in continuous network form. As mentioned earlier, the formation of continuous network may be attributed to constitutional liquation and shearing of the film during dissimilar Al and Mg alloys welding. Figure 8.18a presents the transverse cross-section of the weld made between AZ31B-H24 and AA6061-T6 alloys in lap configuration (Firouzdor and Kou 2010b). The weld interface shows the presence of Al_3Mg_2 near AA6061 alloy and $Al_{12}Mg_{17}$ towards AZ31B alloy (Fig. 8.18b) with very fine cracks at the AA6061 and $Al_{12}Mg_{17}$ interface. The proximity of these intermetallic

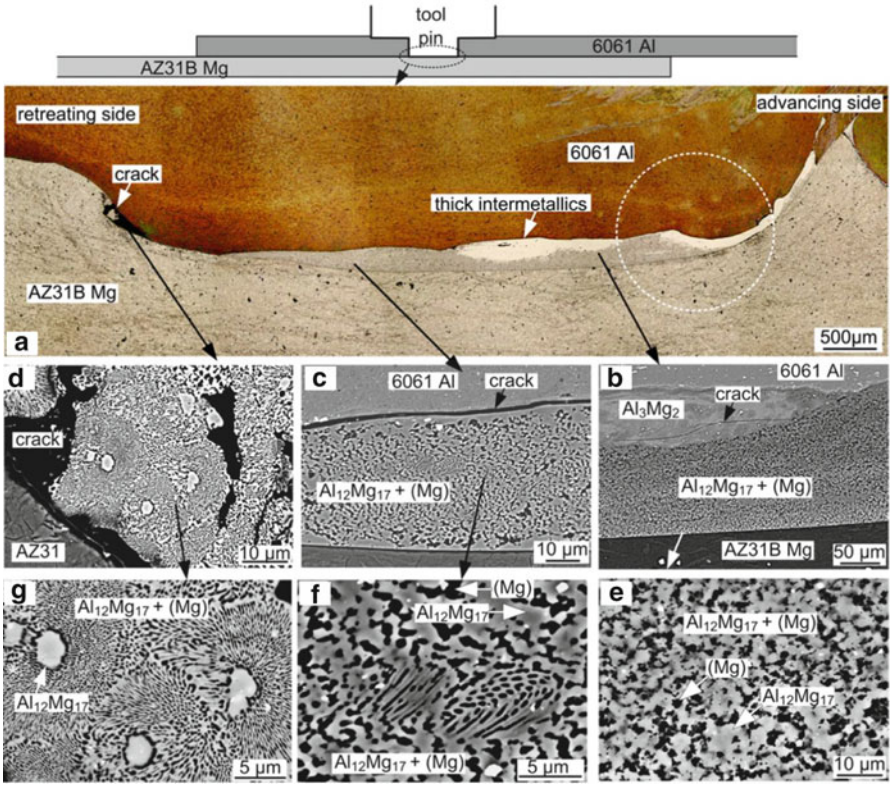

Fig. 8.18 (**a**) Transverse cross-section of the dissimilar friction stir weld between AZ31B-H24 and 6061Al-T6 alloys, (**b–e**) micrographs showing different phases and features of the different region of the weld as indicated (Firouzdor and Kou 2010b, reprinted with permission from Springer)

compounds with aluminum rich region and magnesium rich region, respectively, is consistent with our expectation based on Al-Mg binary phase diagram. The resemblance of microstructures shown in Fig. 8.18c–e to a solidified microstructure is indicative of liquation during welding.

8.3.3 Dissimilar Metals Having Widely Differing Melting Point

So far two scenarios in dissimilar metal welding are considered. In this section a third scenario will be considered wherein the base metal of the alloy differ from each other entirely and have substantial difference in their melting point. The welding of Al/Mg alloys to Cu/Ti/ferrous alloys are few examples which fall in this category. In the next subsection the welding of aluminum alloys to ferrous alloys are discussed.

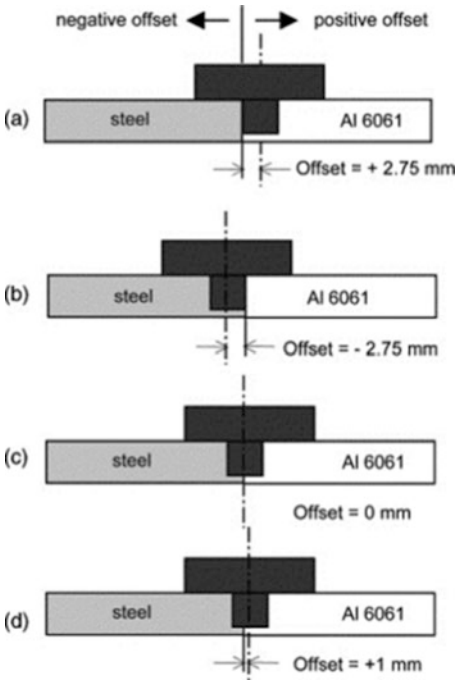

Fig. 8.19 A schematic of tool pin position with respect to weld centerline (Chen and Kovacevic 2004, reprinted with permission from Elsevier)

8.3.3.1 Welding of Aluminum Alloys with Ferrous Alloys

As mentioned before, owing to considerably different thermo-mechanical and physical properties of Al and steels, it is very difficult to join them in usual manner to obtain a sound joint economically. It is possible to use tools made of WC or pCBN to weld such dissimilar metals in usual manner, i.e., the tool positioned at weld centerline. However, the use of such expensive tools makes the process uneconomical. Moreover, excessive heat generated on the steel side melts aluminum alloys. It is not possible to use tools made of tool steel in usual way to weld aluminum and steel combination due to excessive wear and eventual damage of the tool. However, this difficulty has been overcome by researchers by studying positional dependence of the tool made of tool steel on joint properties.

So far, FSW of Al/Steel in butt and lap configurations has been reported in literature. Chen and Kovacevic reported the weldability of AA6061 and 1018 steel (Chen and Kovacevic 2004) using tool steel tool for a number of tool positions with respect to weld centerline. A schematic describing the various tool positions is included in Fig. 8.19.

A tool offset of +1 mm (Fig. 8.19d) results in the formation of sound weld but only up to a limited portion along the weld length. The macrostructure of transverse cross-section for weld with +1 mm offset in given in Fig. 8.20. Since, +1 mm of the tool pin was all the time in contact of steel, it resulted in excessive tool wear leading up to the breakage of the tool. The progressive wear of the tool during welding might have resulted in defective weld formation at later portion of the weld.

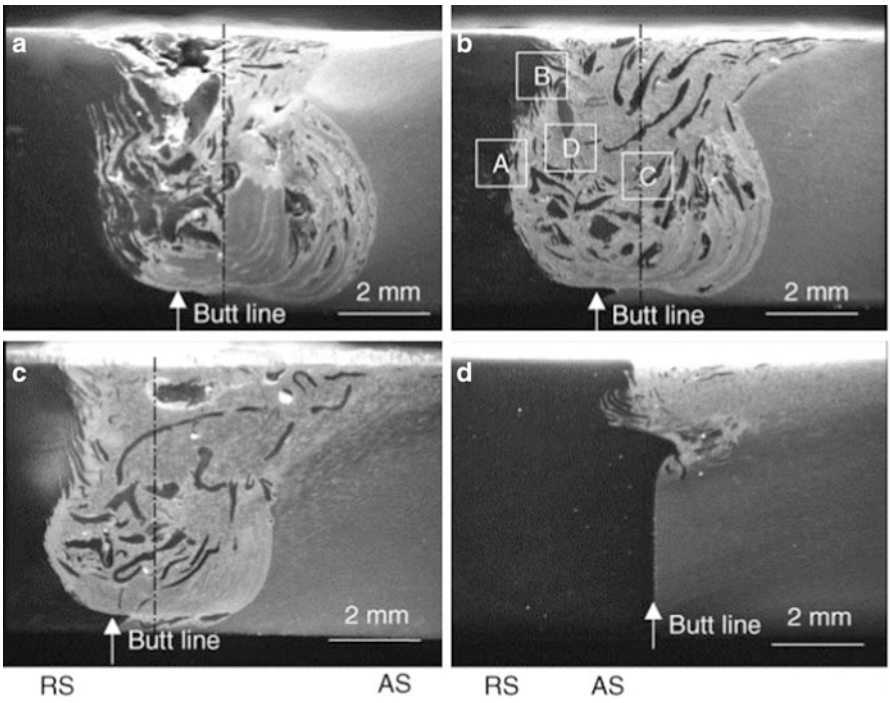

Fig. 8.20 Macrostructure of Al/Steel weld at (**a**) 20 mm, (**b**) 45 mm, (**c**) 80 mm, and (**d**) 120 mm along longitudinal direction for the weld with +1 mm tool offset (Chen and Kovacevic 2004, reprinted with permission from Elsevier)

To avoid the excessive wear and eventual breakage of the tool, in another study where 6013Al-T4 was welded to X5CrNi18-10 stainless steel, a sound weld was obtained by positioning the tool towards aluminum side so that the tool barely touched the stainless steel plate (Uzun et al. 2005). The transverse cross-section of the weld made between these two alloys is shown in Fig. 8.21. It shows stainless steel particles embedded in the aluminum alloy matrix. The presence of stainless steel in aluminum matrix in the form shown in Fig. 8.21 is a consequence of different flow behavior of aluminum and steel, limited solubility of iron and aluminum in each other, and faster processing kinetics. The bonding between the aluminum and steel is another issue as the presence of micro-cracks has been reported at the aluminum/steel interface.

The results of similar experiments by Kimapong and Watanabe (2004) using AA5083 and SS400 mild steel is presented in Fig. 8.22. It is found that tool offset corresponding to 0.2 mm (Fig. 8.22c) results in a sound weld formation with a maximum tensile strength which is, however, lower than the tensile strength of Al alloy. Kimapong and Watanabe also reported the presence of several intermetallics in the processed region.

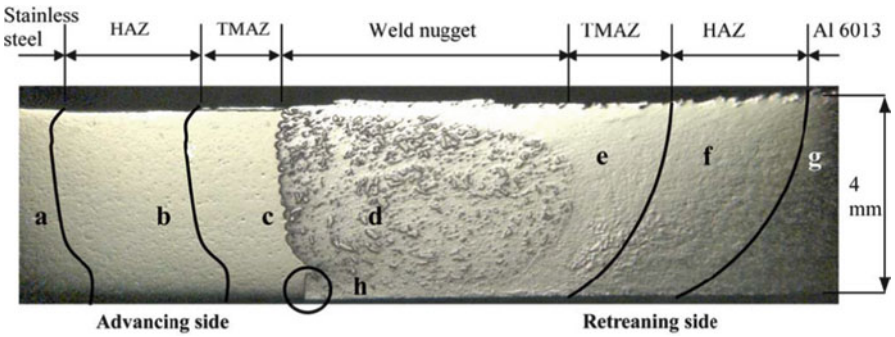

Fig. 8.21 Macrostructure of Al/Steel dissimilar weld (Uzun et al. 2005, reprinted with permission from Elsevier)

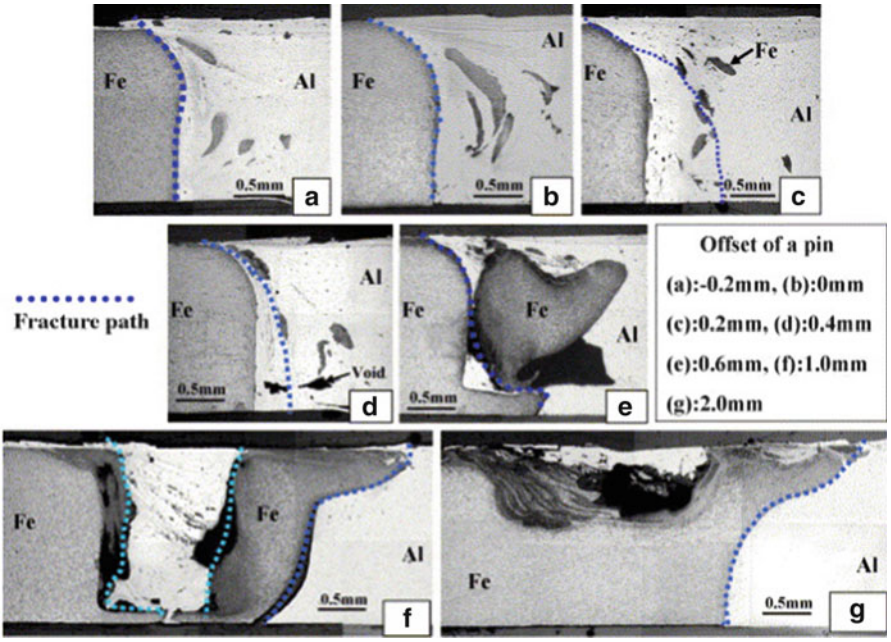

Fig. 8.22 The effect of tool offset on weld quality and fracture location (Kimpong and Watanabe 2004, reprinted with permission from the American Welding Society, Miami, FL)

Interfacial Reaction

Figure 8.2 shows that different phases may exist as a result of reaction between Al and steel. It depends on the chemistry of the materials being joined, time, temperature, and kinetics of the reaction. According to this phase diagram intermetallic phases Fe_3Al, FeAl, $FeAl_2$, Fe_2Al_3, and $FeAl_3$ might be present as a reaction product. It is quite possible to have more than one reaction products in the welded zone (Fig. 8.18b).

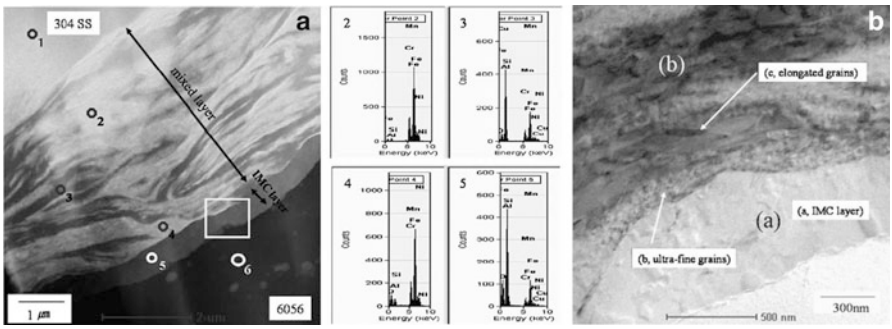

Fig. 8.23 TEM image showing interfacial reaction products developed during friction stir welding of SS304 and 6056Al (Lee et al. 2006, reprinted with permission from Elsevier)

Lee et al. (2006) studied the interfacial reaction in the friction stir welding of austenitic stainless steel (SS 304) and aluminum alloy (6056Al). Figure 8.23a shows four different regions: stainless steel, intermediate, intermetallic, and aluminum alloy regions. The presence of different regions was ascertained using EDS analysis. The EDS spectrums from regions 1 and 6 (marked with O_1 and O_6, respectively) are not shown in Fig. 8.23a. The mixed region shows presence of Fe-rich phase (regions O_2 and O_4) and Al-rich phase (region O_3). In addition to this, closer look at intermetallic compound layer (region shown by rectangular box in Fig. 8.23a) revealed ultrafine grained Al alloy phase sandwiched between elongated Fe-rich phase and intermetallic compound. Based on the strong astigmatism present, it was concluded that Fe-rich phase was ferritic, which may be a result of high temperature, high strain rate deformation, and due to the presence of ferrite stabilizer Al. The intermetallic compound was reported to be Al_4Fe phase.

Material Position

The positional dependence of the material plate on weld quality has also been noted in few works on the joining of dissimilar metals. In one such work by Watanabe et al. (2006), dissimilar metal welding between steel (SS400) and Al (5083Al) was carried out by rotating the tool in clockwise and anti-clockwise directions. In other words, the welding was done by placing steel plates on advancing and retreating sides, alternatively. It is shown schematically in Fig. 8.24. The presence of steel plate is shown to be on advancing side in Fig. 8.24a and on retreating side in Fig. 8.24b. In this work it was noted that aluminum alloy did not bond with steel plate when steel plate was present on the retreating side of the tool (Fig. 8.24b). It should be noted here that the tool is entirely present in aluminum plate and barely touches steel plate. When steel is present on the advancing side of the tool (Fig. 8.24a), aluminum flowing around the tool gets pressed (forged) against the steel and it results in bond formation between both materials. However, when steel is present on the retreating side this is not the case. Now, the material volume

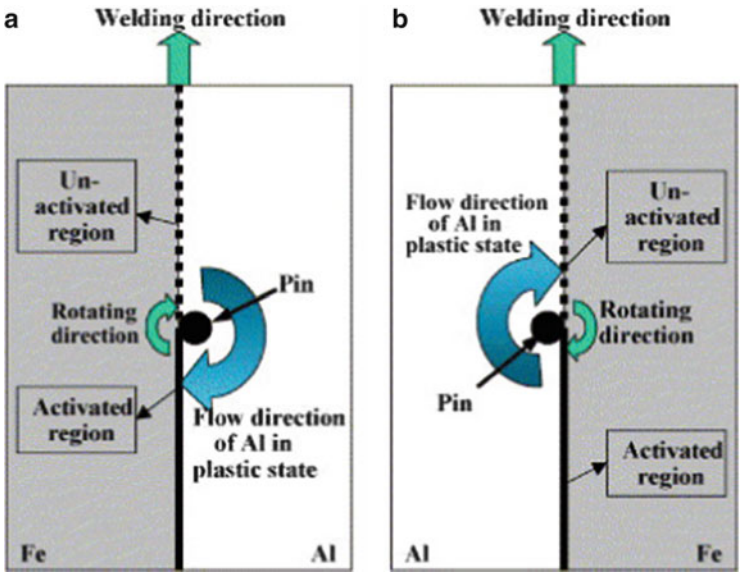

Fig. 8.24 The role of clockwise and counter-clockwise tool rotation on weld formation between Al and steel (Watanabe et al. 2006, reprinted with permission from Elsevier)

already deposited on steel side experiences shear forces acting in the direction opposite to the tool movement at tool pin and steel interface. The local forces discussed in Chap. 2 can be used to visualize this. It results in peeling off of the already deposited aluminum alloy. It, therefore, prevents a sound weld formation when steel is present on the retreating side of the tool.

Mechanical Properties

Figure 8.25a shows the strength of the joint made between 5083Al and SS400 as a function of tool offset (Watanabe et al. 2006). Clearly, the tool offset of +0.2 mm resulted in maximum tensile strength of the joint under these processing conditions. Although lower strength than that obtained for offset +0.2 mm, even the tool offset +0.4 mm appears to induce moderately good tensile strength in the joint. Uzun et al. (2005) have investigated the fatigue properties of 6013Al/X5CrNi18-10 dissimilar metal welding. The result has been shown in Fig. 8.25b. Evidently, the fatigue properties of the welded plate are similar to base 6013Al alloy. The tensile test and fatigue properties results of these researchers indicate that it is quite possible to get sound weld possessing good mechanical properties.

In summary, current research related to Al and steel welding is limited to the development of processing strategy which can lead to a sound joint with minimal tool wear and maximum joint efficiency. Hence, a need to develop innovative welding strategies to successfully weld Al and steel exists. In fact, the same is

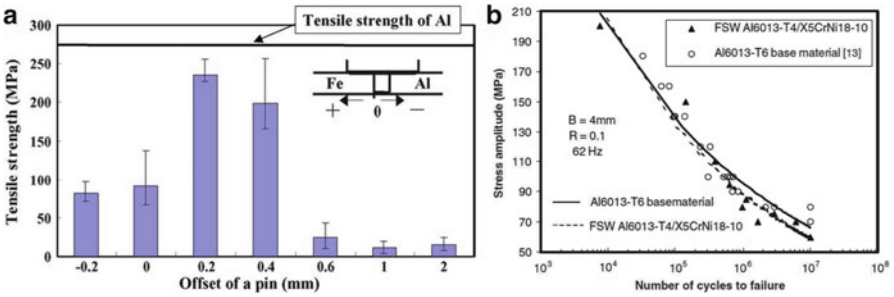

Fig. 8.25 (**a**) Tensile strength of 5083Al/SS400 weld (Watanabe et al. 2006, reprinted with permission from Elsevier) and (**b**) S-N curve corresponding to 6013/X5CrNi18-10 weld and its comparison with the S-N curve of base 6013Al alloy (Uzun et al. 2005, reprinted with permission from Elsevier)

applicable for the welding of Al/titanium and Al/copper joints. Thus, a successful outcome in Al/Steel welding research can play a major role in the progress of dissimilar metal joining.

References

N. Bailey, *Welding Dissimilar Metals* (The Welding Institute, Crampton & Sons Limited, Swaston, Cambridge, 1986), pp. 16–19

C.M. Chen, R. Kovacevic, Joining of Al 6061 alloy to AISI 1018 steel by combined effects of fusion and solid state welding. Int. J. Mach. Tool. Manufact. **44**, 1205–1214 (2004)

V. Firouzdor, S. Kou, Al-to-Mg friction stir welding: effect of material position, travel speed, and rotation speed. Metall. Mater. Trans. A **41A**(11), 2914–2935 (2010a)

V. Firouzdor, S. Kou, Formation of liquid and intermetallics in Al-to-Mg friction stir welding. Metall. Mater. Trans. A **41A**(12), 3238–3251 (2010b)

K. Kimapong, T. Watanabe, Friction stir welding of aluminum alloy to steel. Welding J. 277S–282S(10) (2004)

A. Kostka, R.S. Coelho, J. dos Santos, A.R. Pyzalla, Microstructure of friction stir welding of aluminium alloy to magnesium alloy. Scr. Mater. **60**(11), 953–956 (2009)

Y.J. Kwon, I. Shigematsu, N. Saito, Dissimilar friction stir welding between magnesium and aluminum alloys. Mater. Lett. **62**(23), 3827–3829 (2008)

R.M. Leal, C. Leitao, A. Loureiro, D.M. Rodrigues, P. Vilaça, Material flow in heterogeneous friction stir welding of thin aluminium sheets: effect of shoulder geometry. Mater. Sci. Eng. A **498**(1), 384–391 (2008)

W.-B. Lee, M. Schmuecker, U.A. Mercardo, G. Biallas, S.-B. Jung, Interfacial reaction in steel–aluminum joints made by friction stir welding. Scr. Mater. **55**, 355–358 (2006)

Z. Liang, K. Chen, X. Wang, J. Yao, Q. Yang, L. Zhang, A. Shan, Effect of tool offset and tool rotational speed on enhancing mechanical property of Al/Mg dissimilar FSW joints. Metall. Mater. Trans. A **44A**(8), 3721–3731 (2013)

A.A. McLean, G.L.F. Powell, I.H. Brown, V.M. Linton, Friction stir welding of magnesium alloy AZ31B to aluminium alloy 5083. Sci. Technol. Weld. Joi. **8**(6), 462–464 (2003)

J.H. Ouyang, R. Kovacevic, Material flow and microstructure in the friction stir butt welds of the same and dissimilar aluminum alloys. J. Mater. Eng. Perform. **11**(1), 51–63 (2002)

R. Palanivel, P. Koshy Mathews, N. Murugan, I. Dinaharan, Effect of tool rotational speed and pin profile on microstructure and tensile strength of dissimilar friction stir welded AA5083–H111 and AA6351–T6 aluminum alloys. Mater. Des. **40**, 7–16 (2012)

S.-K. Park, S.-T. Hong, J.-H. Park, K.-Y. Park, Y.-J. Kwon, H.-J. Son, Effect of material locations on properties of friction stir welding joints of dissimilar aluminium alloys. Sci. Technol. Weld. Joi. **15**(4), 331–336 (2010)

I. Shigematsu, Y.-J. Kwon, K. Suzuki, T. Imai, N. Saito, Joining of 5083 and 6061 aluminum alloys by friction stir welding. J. Mater. Sci. Lett. **22**(5), 353–356 (2003)

I. Shigematsu, Y.-J. Kwon, N. Saito, Dissimilar friction stir welding for tailor-welded blanks of aluminum and magnesium alloys. Mater. Trans. **50**(1), 197–203 (2009)

S-W. Song, B-C. Kim, T-J. Yoon, N-K. Kim, I-B. Kim and C-Y. Kang, Effect of Welding Parameters on Weld Formation and Mechanical Properties in Dissimilar Al Alloy Joints by FSW, Materials Transactions, **51**, 1319 (2010)

H. Uzun, C. Dalle Donne, A. Argagnotto, T. Ghidini, C. Gambaro, Friction stir welding of dissimilar Al 6013-T4 to X5CrNi18-10 stainless steel. Mater. Des. **26**, 41–46 (2005)

T. Watanabe, H. Takayama, A. Yanagisawa, Joining of aluminum alloy to steel by friction stir welding. J. Mater. Process. Technol. **178**, 342–349 (2006)

Chapter 9
Friction Stir Processing

The intrinsic nature of friction stir process has two basic components as highlighted in previous chapters, material flow and microstructural evolution. The development of friction stir processing as a generic metallurgical tool for microstructural modification and a broader manufacturing technology is connected to these. Even though the adaption of these friction stir process based technological variants is slow, the potential of these is limitless. The focus of this chapter is to illustrate the linkages of basic friction stir process attributes to some illustrative examples of new technology development. The chapter is by no means comprehensive because many ideas can be built on these basics and each one can have its own niche area of application.

We start off with an overview Fig. 9.1 from Mishra and Mahoney (2007) that serves as a basic illustration. The material flow can be treated as the overarching aspect of all friction stir attributes other than temperature, but the split attributes listed are to facilitate visualization of microstructural evolution and development of the derivative processes, referred to as friction stir technologies. We have listed only (a) microstructural refinement, (b) homogenization and (c) primary particle breakdown, but other keywords can be used to describe the impact of friction stir process on key 'enabling' microstructural aspect for a particular friction stir technology. Let us take the first paper (Mishra et al. 1999) using the keyword 'friction stir processing' and related patent (Mishra and Mahoney 2004). As discussed in a bit more detail in the next section, fine grain size is a key enabling microstructural feature for superplasticity, as fine grain size is a necessary requirement for structural superplasticity. So, the sections below are setup with what are the key enabling microstructural aspect(s) and/or friction stir attribute(s) that leads to the development of a particular friction stir technology. The intention is that readers will not only find these examples illustrative, but also a foundational material that they can then use to develop additional friction stir technologies to broaden this generic processing tool. Significant part of the text presented below is based on an earlier review of Mishra and Mahoney (2007).

Another way to look at the opportunities of using friction stir processing is to consider a very well accepted set of design approaches and the materials science

R.S. Mishra et al., *Friction Stir Welding and Processing: Science and Engineering*,
DOI 10.1007/978-3-319-07043-8_9,

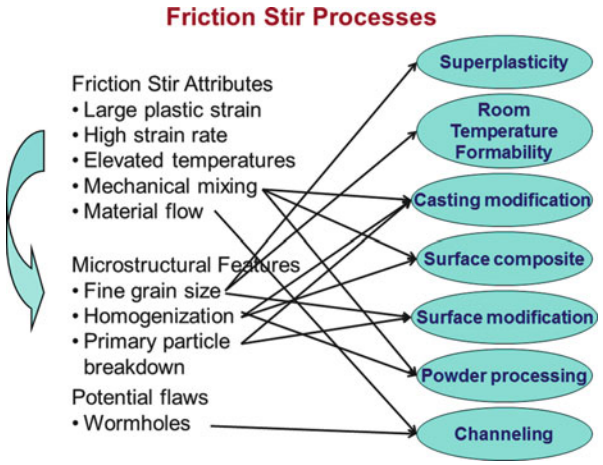

Fig. 9.1 An illustration of the evolution of microstructural features because of the basic friction stir process attributes, and its linkage to various emerging friction stir processing technologies (Mishra and Mahoney 2007, reprinted with permission from ASM International)

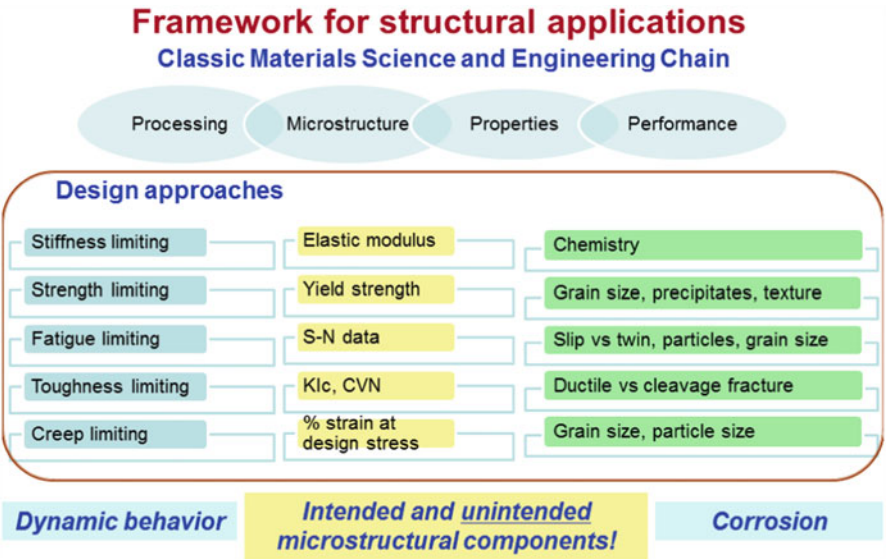

Fig. 9.2 A layout depicting the materials science and engineering chain along with five commonly used design approaches. The design approaches are linked with key materials properties and what they depend on

and engineering chain. Figure 9.2 shows this broad framework including dynamic and corrosion properties. A new keyword that is included is 'unintended microstructure'. A way to understand this is to think of how materials are used for engineering applications. The designer sets the performance goal and specifies

material that would meet the requirement. When a material is ordered, composition and minimum guaranteed properties are specified. A process may also be specified as a part of the design specification. What microstructure would give the properties is not a concern of the designer. The material composition combined with some typical manufacturing processing steps lead to 'intended' microstructure. A common observation is that impurity elements lead to unintended constitutive particles. One way to limit that is to specify tighter compositional control which has implication on price. Number of engineering failures are a result of these unintended microstructure or microstructural flaws. Friction stir processing can be used to modify these microstructural features, particularly the regions where finite element modeling tools show higher vulnerability.

9.1 Friction Stir Processing for Superplastic Forming

Superplasticity is an ability of a material to exhibit >200 % elongation in tension. Historically, a key aspect of the superplastic materials is also the low flow stress. In fact, the original development of superplastic forming in 1960s by Backofen et al. (1964) attracted more attention because it was gas forming of a metallic component. This gives an impression of ease of forming because one can conceptually visualize this as equivalent to glass blowing. Of course, once the formed metallic component cools down to room temperature, its properties are that of any structural metallic material. Superplastic forming grew rapidly in 1970s and 1980s, because of its ability to create 'unitized' components. Unitized components lower the number of parts that is used for a system. Aerospace industries were among the first adopters in spite of a major drawback of slow forming rate (strain rate of 10^{-4}–10^{-3} s^{-1}). Last 20 years or so there has been a large increase in efforts related to high strain rate superplasticity (strain rate $>10^{-2}$ s^{-1}).

9.1.1 Constitutive Relationship and Microstructural Requirements for Superplasticity

The mechanism of structural superplasticity has been established to be grain boundary sliding. The high temperature deformation based on grain boundary sliding can be represented by a generic constitutive relation (Nieh et al. 1997),

$$\dot{\varepsilon} = \frac{ADGb}{kT}\left(\frac{\sigma}{G}\right)^{n}\left(\frac{b}{d}\right)^{p} \tag{9.1}$$

where $\dot{\varepsilon}$ is strain rate, G shear modulus, b Burgers vector, σ applied stress, d grain diameter (size), D appropriate diffusivity, n stress exponent, p inverse grain size exponent, and A is a microstructure and mechanism dependent dimensionless constant.

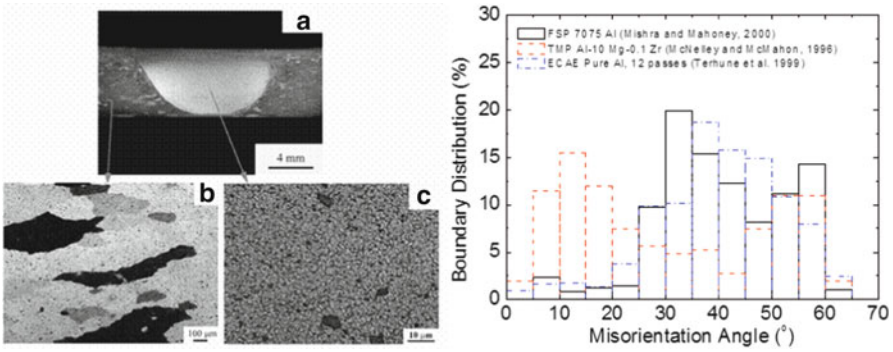

Fig. 9.3 Example of fine grain size in the friction stir processed nugget of Al7075 alloy. The grain boundary misorientation distribution shows the effectiveness of friction stir processing in producing high angle boundaries (Mishra and Mahoney 2007, reprinted with permission from ASM International)

Often in superplasticity literature, the strain rate sensitivity exponent ($m = \partial \log\sigma / \partial \log\dot{\varepsilon}$) is used instead of the stress exponent (n), shown in Eq. (9.1). However, 'm' is just the reciprocal of 'n'. Higher m values mean a greater resistance to external neck formation, and hence increased ductility. Generally, an m value of ~0.5 and a p value of 2–3 imply deformation by grain boundary sliding. The most important microstructural features that govern the overall superplastic behavior are:

(a) fine grain size (<15 μm),
(b) equiaxed grain shape,
(c) presence of very fine second phase particles to inhibit grain growth, and
(d) large fraction of high angle grain boundaries.

Friction stir process results in fine grain size and large fraction of high angle grain boundaries in aluminum alloys under a very wide range of processing conditions. Figure 9.3 shows grain refinement in Al7075 and a distribution of boundary misorientation. As mentioned in the initial chapters, because of large strain, high strain rate and high temperature, dynamically recrystallized microstructure with fine grain size evolves during friction stir process. It is typical to observe >90 % of grain boundaries with high misorientation (>15°). As discussed further, this microstructure is ideal for superplastic flow and forming.

9.1.2 Superplastic Flow in Friction Stir Processed Materials

In this section the examples of superplastic flow have been divided into conventional and non-conventional aluminum alloys. Conventional alloys are essentially commercial aluminum alloys that are readily available in various forms. In this context, a distinction between friction stir welding and friction stir processing needs to be made, particularly with regards to future possibilities. When friction stir welding is considered as a potential solution for an existing design of structure, it is important to keep

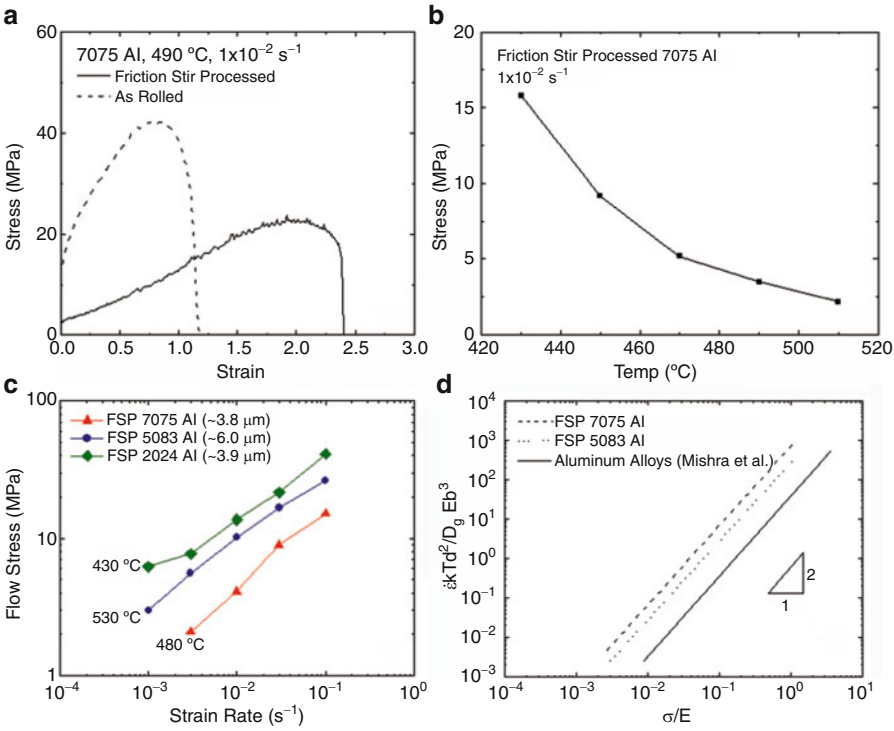

Fig. 9.4 (**a**) A comparison of flow curves for Al7075 alloy in as-rolled and as-FSP conditions at 10^{-2} s^{-1} strain rate. (**b**) The variation of flow stress data with temperature showing very low initial flow stresses. (**c**) A comparison of stress-strain rate behavior for three different commercial aluminum alloys. All of them show stress exponent close to 2 at the temperature selected. (**d**) A plot of normalized strain rate against normalized stress showing faster kinetics in FSP condition for both Al7075 and Al5083 alloy. For comparison a line for all conventionally processed aluminum alloys is included (Mishra and Mahoney 2007, reprinted with permission from ASM International)

the alloy selection same as original. On the other hand if a new system is being designed from ground up, and friction stir processing is a potential path, alloys with higher amount of dispersoids can be considered. In the examples presented in this section, Al-Zn-Mg-Sc and Al-Mg-Zr alloys are included. These are experimental alloys with considerable volume fraction of Al_3Sc and Al_3Zr, respectively, which effectively pins the grain boundaries at high temperatures for microstructural stability.

Figure 9.4 shows results for commercial aluminum alloys from three alloy series. The fine grained microstructure in friction stir processed condition leads to lower flow stress and much faster deformation kinetics. Figure 9.5 captures the variation of elongation with strain rate and temperature for these alloys. A remarkable part of this data set is the high strain rate range and wider temperature range over the superplasticity is observed. The comparison with as-rolled 6.3 mm thick rolled Al7075 alloy sheet is instructive in lack of superplasticity in sheets that are thicker and not particularly processed for superplasticity. So, fundamentally it highlights two limitations of conventional superplasticity; lower strain rate and

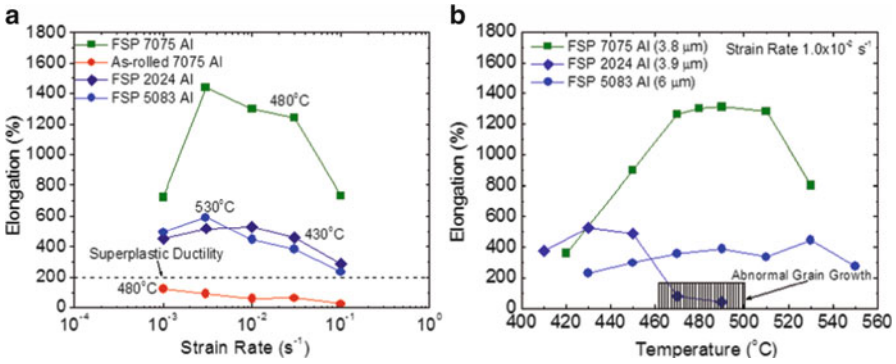

Fig. 9.5 Variation of elongation with (**a**) strain rate, and (**b**) temperature, showing high strain rate superplasticity

thinner sheets. In the plot against temperature, a region of abnormal grain growth is marked. This sets the upper limit for superplasticity in friction stir processed material. The abnormal grain growth aspect is different from conventionally processed aluminum alloys. It results from unique as-processed friction stir microstructure that contains strain gradients and microstructural gradients that can lead to microstructural instability at the higher end of temperature range.

Even better results are observed for unconventional aluminum alloys that contain very fine thermally stable second phase particles. Figure 9.6 shows results for two alloys containing Al_3Sc and Al_3Zr particles (Charit and Mishra 2005; Ma et al. 2010). An exceptional aspect of these results is that the peak elongation values are at strain rates higher than 10^{-2} s^{-1}, which is considered as the transition to high strain rate superplasticity. This has very important implications on total forming time and energy used in forming. Figure 9.7 adds additional information of grain size refinement to ultrafine region (<1 μm) in a single pass. The advantage of ultrafine grained microstructure is that the lowest temperature for high strain rate superplasticity drops to ~200 °C. This is still close to 0.6 T_m for this alloy. However, traditionally aluminum alloys do not show such low temperature superplasticity. Of course, the thermal stability at the higher temperature becomes an issue for such a fine microstructure. The main learning point from these results is that one needs to consider alloy chemistry, processing conditions, and design approaches in a holistic manner to take advantage of full potential of friction stir processing for superplasticity.

9.1.3 *Friction Stir Processing as a Technology Enabler for New Concepts*

This section is primarily taken from a previous review by Mishra and Mahoney (2007). Apart from the opportunity of achieving high strain rate superplasticity in commercial alloys, FSP offers several new opportunities as a 'technology enabler' (Mishra and Mahoney 2001; Mishra 2004; Mishra et al. 2004). Some of these possibilities are briefly described below (Mishra 2004).

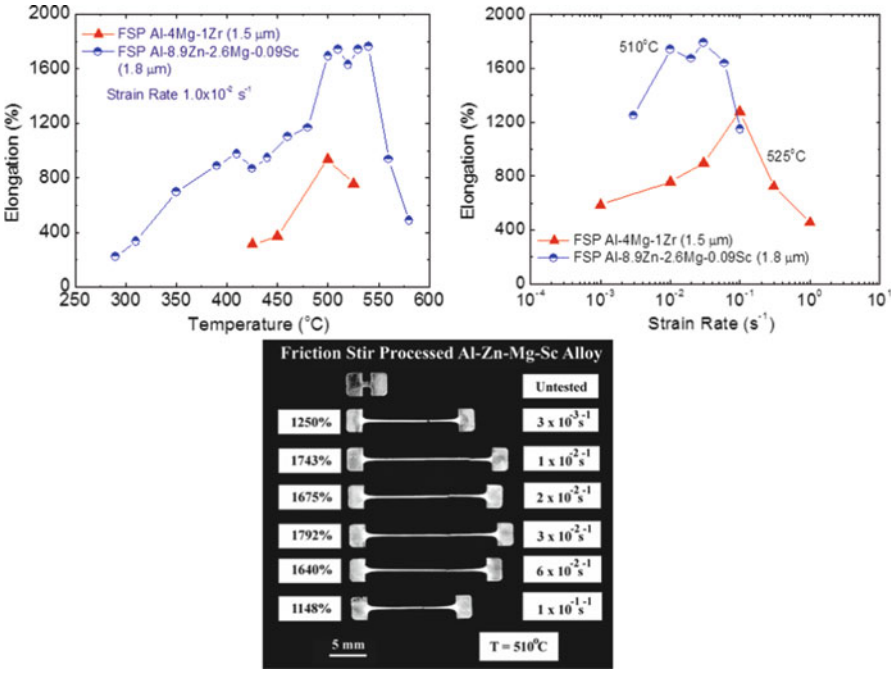

Fig. 9.6 Superplastic elongation data for two non-conventional aluminum alloys with very fine thermally stable particles. Note the peak elongation is at strain rate $>10^{-2}\ s^{-1}$, which is considered as transition to high strain rate

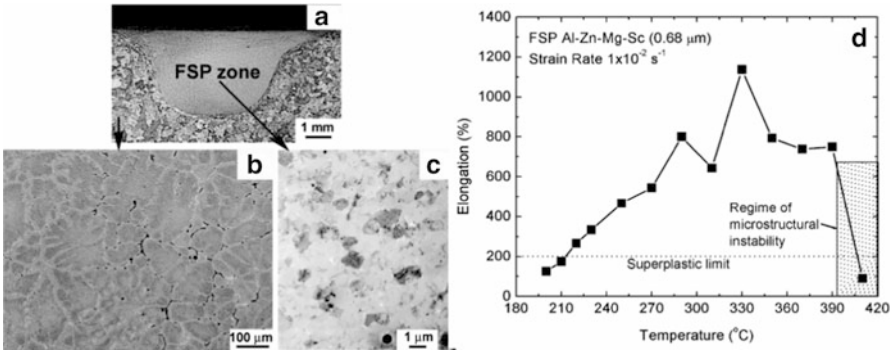

Fig. 9.7 Example of refinement of a cast Al-Zn-Mg-Sc alloy to ultrafine grained microstructure in one pass and associated high strain rate superplasticity at a very wide temperature range. Note the lower temperature limit of superplasticity. It also shows that the ultrafine grained microstructure limits the higher temperatures

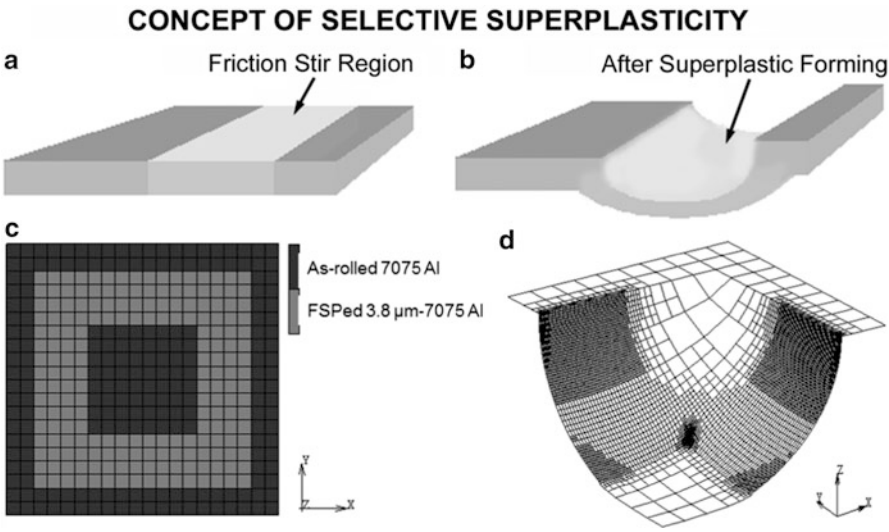

Fig. 9.8 (**a**) A schematic illustration of 'selective superplasticity,' where only the region undergoing superplastic deformation will be friction stir processed. (**b**) Brighter areas in the commercial 7075 Al rolled sheet are selected to be FSPed to become superplasticity instead of making the whole sheet superplastic. (**c**, **d**) Finite element mesh after adaptive remeshing (Wang and Mishra 2007, reprinted with permission from Elsevier)

9.1.3.1 Selective Superplastic Forming

In many components, only selected regions require superplastic deformation. The concept of such a superplastically formed component is shown in Fig. 9.8. In essence, only the region undergoing superplastic deformation needs the fine grained microstructure. However, conventional processing cannot be used to produce microstructural refinement on a 'selective' basis. FSP provides such an opportunity. Using FSP, a selected portion of the sheet can be processed for superplastic behavior. The difference in microstructure would result in selective deformation of the grain-refined region (Fig. 9.8). The FSP region with finer grain size undergoes superplastic deformation. This provides a versatile method to produce gas formed components with an intricate design.

9.1.3.2 Superplastic Forming of Thick Sheets

In conventional thermo-mechanical processing involving rolling of sheets, the sheet thickness reduces with every pass. To provide sufficient total strain for grain refinement, a number of passes are required resulting in thin sheets (<3 mm). On the other hand, when using FSP, the sheet thickness does not change. High strain rate and thick section superplasticity are two material properties never before demonstrated on a practical scale and are made possible only by FSP. For example, Mahoney et al. (2001) demonstrated high uniform elongation (>500 %) at strain rates

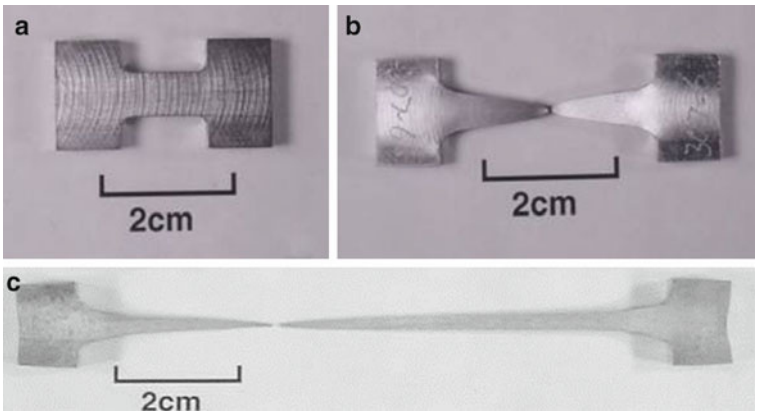

Fig. 9.9 (**a**) 5 mm thick tensile sample, (**b**) limited tensile elongation and severe necking without FSP, and (**c**) 800 % superplastic elongation in 5 mm thick FSP 7075 Al (Mishra and Mahoney 2007, reprinted with permission from ASM International)

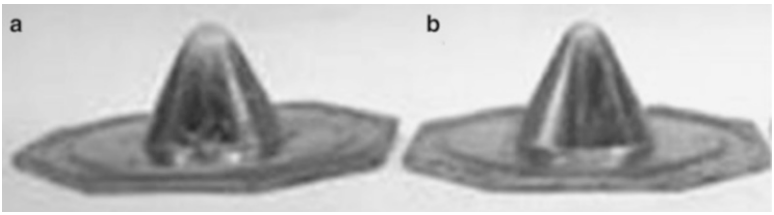

Fig. 9.10 Example of gas pressure cone tests for (**a**) a conventional superplastic 7475 Al alloy, 150 psi, 95 min, and (**b**) FSP 7475 Al 150 psi, 18 min (Mishra and Mahoney 2007, reprinted with permission from ASM International)

$>1 \times 10^{-3}$ s^{-1} at temperatures <460 °C. This offers the potential to form complex shaped parts at a higher strain rate and in section thickness never before possible. Figure 9.9 illustrates superplastic tensile elongation of ~800 % at 460 ºC following FSP in 5 mm thick FSP 7050 Al. The thickness limit for superplasticity has not been established but results up to 12 mm thick specimens have been published. Figure 9.10 shows cones formed by gas forming and make the important point of reduction in forming time. While a conventional superplastic 7475 Al alloy, i.e., the sheet was processed to a fine grain size (~15 μm grain size) via special thermomechanical processing, completely formed the cone at 150 psi in 95 min, the FSP 7475 Al (~3–4 μm grain size) completely formed the cone in a reduced time of 18 min. This type of reduction in forming time is exceptional from the energy saving point of view.

9.1.3.3 One Step Processing for Superplasticity from Cast Sheet or Hot-Pressed Powder Metallurgy Sheet

A conventionally cast microstructure can be converted to a superplastic microstructure in many steps. The present process of microstructural refinement can be

used directly on cast sheets. This leads to very economical manufacturing. Ma et al. (2004) have demonstrated superplasticity in A356 cast alloy. They were able to obtain a maximum superplastic elongation of 650 % at 530 °C for an initial strain rate of 1×10^{-3} s^{-1}. Charit and Mishra (2005) observed exceptional superplastic properties in an as-cast Al-8.9Zn-2.6 Mg-0.09Sc (wt%) alloy which is shown in Fig. 9.7. FSP with a smaller pin tool led to ultrafine grains (0.68 μm grain size) from the as-cast state. The ultrafine grained alloy exhibited superplasticity at relatively low temperatures and higher strain rates. An optimum ductility of 1,165 % at a strain rate of 3×10^{-2} s^{-1} and 310 °C was obtained. Enhanced superplasticity was also achieved at a temperature as low as 220 °C. A similar approach can be taken for direct chill cast or continuous cast sheet, thereby eliminating several steps. Similarly, powder metallurgy processed aluminum alloys require extensive thermomechanical processing to break down the prior particle boundaries that contain an alumina film. The friction stir process results in a very uniform microstructure from the hot pressed sheet. For example, FSP of a nanophase Al-Ti-Cu alloy results in a remarkable combination of high strength and ductility (Berbon et al. 2001). Again, the economical benefits of eliminating several steps are likely to be substantial. This approach will involve cast or PM sheet + FSP + SPF to produce high-strength, low-cost, unitized structures. These concepts can be applied to many metallic materials and metal matrix composites, but they have maximum impact on aluminum and magnesium alloys and components.

9.1.3.4 Superplastic Forming of Multisheet Structures

Multisheet structures are commercially fabricated by combining diffusion bonding and superplastic forming of titanium alloys. The key issue that helps titanium alloys and hinders aluminum alloys is diffusion bonding. Because of the surface oxide layer, diffusion bonding of aluminum alloys is difficult. This has limited the development of aluminum alloy multisheet structures. The work of Grant et al. (2006) has demonstrated the feasibility of making multisheet structures by combining FSW and FSSW with SPF. Figure 9.11 shows an example of a three-sheet structure created by FSW through two and three sheets. Fusion welding of aluminum alloys leads to a complete loss of superplasticity in the welded region because of microstructural changes. As noted earlier, the FSW microstructure consists of fine grains and superplastic properties are not degraded. A new opportunity involves microstructural tailoring by controlled heat input during FSW. The grain size can be varied by changing the thermal input. By controlling the microstructure, one can make the superplastic flow stress of the FSW region lower, higher, or equal to the parent sheet. Grant et al. (2006) have also used FSSW to create different types of multisheet structures. Their work is opening up new possibilities of sandwich structures using aluminum alloy sheets.

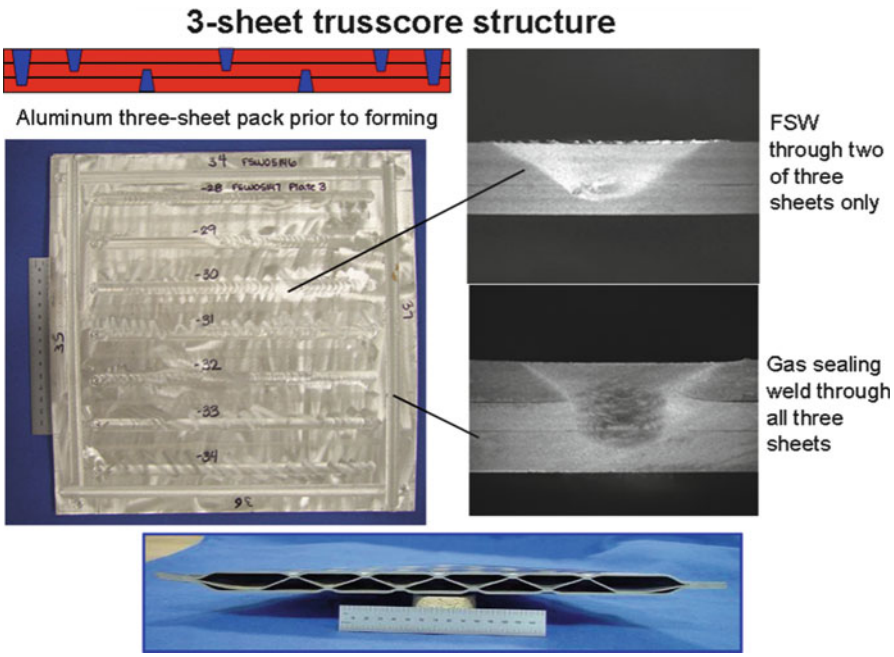

Fig. 9.11 An example of multisheet structure created by a combination of FSW and superplastic forming (figure courtesy Glenn Grant)

9.2 Enhanced Room Temperature Formability via FSP

Sheet metal forming is a very common technique for shaping of metallic components. An easy example is bending which is relatively simple operation. Smith and Mishra (2014) and Mishra and Mahoney (2007) have reviewed enhanced room temperature formability after friction stir processing. A relatively short discussion is presented to illustrate the potential of this approach. Datsko and Yang (1960) presented a very simple correlation between tensile properties and bending of a material as,

$$\frac{R}{t} = \frac{50}{A_r} - 1 \tag{9.2}$$

where R is the radius of bend (also referred as bend radius), t is the thickness of sheet/plate and A_r is the reduction of area during a tensile test. In this example, we just cover the basics with a solid solution strengthened aluminum alloy (Al 5083) and a precipitation strengthened alloy (Al 2519). The conventional tempers for Al 5083 aluminum alloys are O (annealed condition), F (as fabricated) and H (work hardened) tempers. The relevant temper for Al 2519 is T8 (solution treated, cold worked and artificially aged to peak hardness) and T3 (solution treated, cold worked and

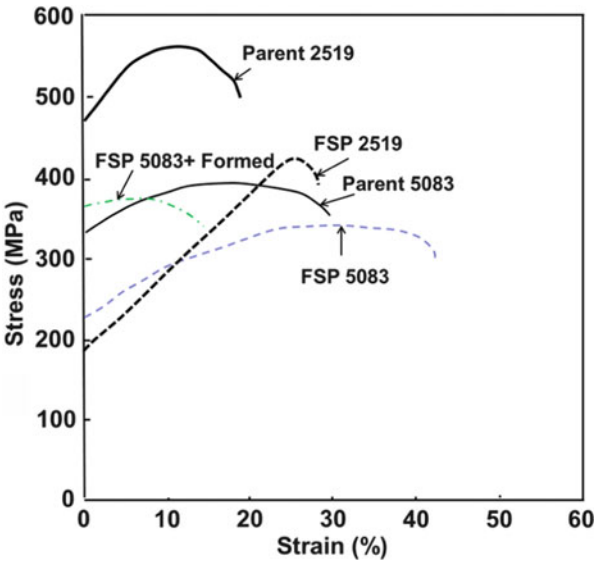

Fig. 9.12 Stress-strain curves for AA5083 and AA2519 in as-received and FSP conditions. Also, included is stress-strain curve of AA5083 specimen after FSP and room temperature bending

naturally aged to substantially stable condition). For friction stir processing, it is also important to consider definition of some other tempers that would not be conventionally used; T1 (cooled for elevated temperature shaping process and naturally aged to stable condition), T5 (cooled for elevated temperature shaping process and artificially aged).

Figure 9.12 shows stress-strain curves for AA5083 and AA2519 alloys. The AA5083 is a solid solution strengthened Al-Mg alloy. In this alloy, the relevant strengthening mechanisms are (a) solid solution strengthening, (b) dislocation storage based strain (or work) strengthening, and (c) grain boundary strengthening. The original material was in H temper and has high strength because of high retained dislocation density. FSP lowers the strength and increases the overall elongation. It is important to note that the net loss of strength reflects decrease in strength due to reduction in stored dislocation density and increase in strength due to grain refinement. After forming of such a solid solution strengthened alloy, the stored dislocation density increases. The stress-strain curve for AA5083 in formed condition reflects that. In the case of AA2519 alloy, the major strengthening component comes from Cu containing precipitates. The starting material for this alloy was in T8 temper. After friction stir processing the strength decreases and elongation increases because of the dissolution of precipitates in the nugget zone.

Figure 9.13 shows a cross-section of the friction stir processed region of AA5083 alloy after forming to an 8 mm (5/16″) internal radius. The bend axis was parallel to the rolling direction and centered about the FSP zone. However, one important note is the lack of any visible cracking, indicating the ability of FSP to locally enhance ductility, consistent with the stress-strain curve in Fig. 9.12. Little, if any, difference is noted in the macro cross-section other than obvious fact of the overall shape of the macro cross-section.

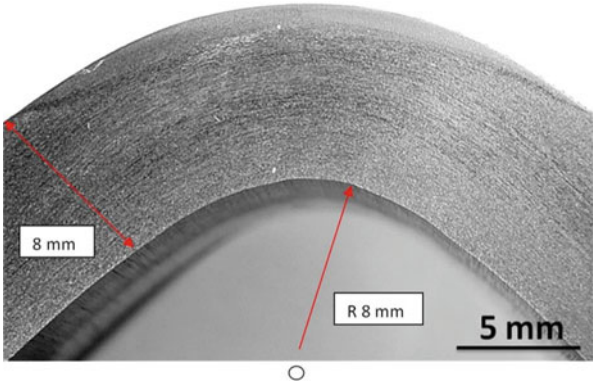

Fig. 9.13 A cross-section of the friction stir processed region of AA5083 after forming to an 8 mm (5/16″) internal radius (Smith and Mishra 2014, reprinted with permission from Elsevier)

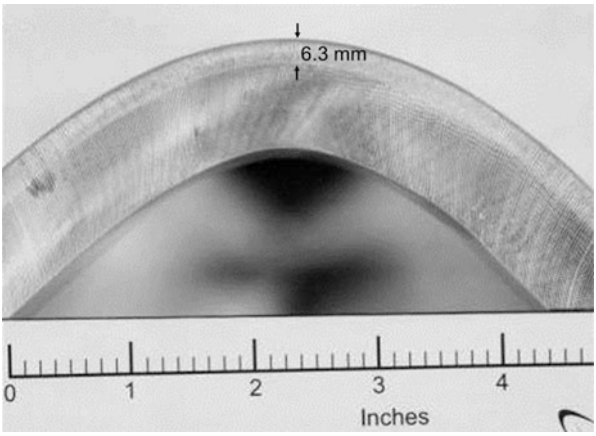

Fig. 9.14 Illustration of the FSP depth (6.3 mm) and the ability to bend 2519-T87 Al ~85° at room temperature (Mishra and Mahoney 2007, reprinted with permission from ASM International)

Figure 9.14 illustrates a transverse cross-section of the 25 mm thick 2519 Al plate following FSP to a depth of 6.3 mm. This depth was chosen somewhat arbitrarily and the same results may have been attained with less tool penetration. It demonstrates a concept of partial penetration friction stir processing of the surface experiencing tensile stresses during forming. The FSP zone is essentially annealed and below the FSP zone, there will be a heat affected zone (HAZ) with reduced mechanical properties. The sample shown in Fig. 9.14 has been bent 85° (limit of the die) at room temperature without any indication of impending failure.

The examples shown so far in the chapter showed enhanced formability of material due to microstructural refinement and modification. In Fig. 9.2, five design limited approaches are listed, namely, stiffness limiting, strength limiting, fatigue

limiting, toughness limiting and creep limiting. The next two sections deal with localized microstructural modification to deal with some of these design approaches.

9.3 Friction Stir Processing of Surface Composites and Powder Processing: Approach for Stiffness Limiting Design

Metal matrix composites (MMCs) are used because they allow combinations of the properties of metals and ceramics. Compared to unreinforced metals, metal-matrix composites reinforced with ceramic phases exhibit high strength, high elastic modulus, and improved resistance to wear, creep and fatigue. For example, the modulus of a metal can be increased by adding ceramic particulates (or fibers or whiskers). Typically ceramics have much higher moduli than metals and a combination of the two can lead to composites with tailored values of the modulus. Materials with higher moduli are desirable for components that are designed for high stiffness. The guiding principle for these composites for density and modulus has been the rule of mixtures (Ashby 2003),

$$P_{comp} = fP_r + (1 - f)P_m \tag{9.3}$$

where P represents property of interest (density or modulus), f is the volume fraction of reinforcement, and subscripts comp, r and m denote composite, reinforcement and matrix, respectively. The theoretical prediction based on the rule of mixture, gives an upper estimate of the property that can be obtained. Although a more precise limit can be predicted (Eshelby 1957; Hashin and Strikman 1962), these values are always lower than that predicted by the rule of mixtures. Therefore, for the purposes of this chapter, Eq. (9.3) can be used to benchmark for further discussion and will be referred to as 100 % of the predicted value.

The enhanced properties make MMCs promising structural materials for the aerospace and automobile industries. However, MMCs also suffer from a great loss in ductility and toughness due to incorporation of non-deformable ceramic reinforcements, and are relatively costly. These restrictions limit their wider utilization. For many applications, the useful life of components often depends on surface properties such as wear-resistance. In these situations, only the surface layer needs to be reinforced by ceramic phases while the bulk of the component could retain the original composition and structure with higher toughness. There is also an emphasis on added functionality. For example, a structural component can be designed to serve additional non-structural functions. This approach has the possibility of integrating subsystems.

Table 9.1 Some examples of properties that can be tailored by localized surface modification (Mishra and Mahoney 2007, reprinted with permission from ASM International)

Property	Approach
Elastic modulus	Addition of ceramic particles or intermetallic particles
Wear resistance	Addition of second phase particles and microstructural refinement can enhance wear properties
Fatigue	Addition of shape memory particles can alter the residual stresses, thereby influencing the fatigue properties
Magnetic	Magnetic particles can be added in local regions to obtain magnetic properties in otherwise non-magnetic materials
Electrical conductivity	Second phase additions can be used to enhance or lower the electrical conductivity
Thermal conductivity	Second phase particles can be used to enhance or lower thermal conductivity based on the thermal conductivity of matrix and reinforcement
Damping	Shape memory particles and piezoelectric particles can be added to enhance the damping capabilities

9.3.1 Localized Surface Modification

Localized surface modifications can be a very powerful tool to achieve the right combination of properties, i.e., a gradient of properties within a monolithic structure. The potential exists to broaden design possibilities using metal matrix composites surfaces. Some examples of properties that can be influenced are listed in Table 9.1. A number of these approaches require particles of a stoichiometric nature. The properties of these particles can degrade or change if they undergo chemical reaction with the matrix. The short thermal cycle and relatively low temperature during FSP can help to avoid or eliminate reaction products. This is a key distinction compared to other techniques like laser processing that involves melting of matrix phase. Some examples from early efforts are summarized in Table 9.2 to illustrate the range of particles and phases that can be added. The second phase particles can be added in various geometrical configurations. Figure 9.15 gives a few simple examples, but a variety of combinations are possible and have been reported in literature. There are two aspects: (a) type of addition configuration, and (b) frequency. The shape, size and frequency of these features control how much second phase can be added. This interacts with the tool pin features in terms of nugget cross-section. Both combined together control the volume fraction in the embedded region. Each method has some inhomogeneity associated with it. A pre-processed strip would be good, but it adds to number of steps.

Figure 9.16a, b show examples of SiC distributed using the surface addition method (Mishra et al. 2003; Ma et al. 2003). The uniform SiC distribution is demonstrated and a reaction and defect free composite/matrix interface illustrated. Figure 9.16c shows the fracture surface of a single wall carbon nanotube-aluminum composite tested in tension (Johannes et al. 2006). The survivability following large processing strains and the thermal cycle is noteworthy. This illustrates the

Table 9.2 A summary of some examples of surface modification and in-situ composite efforts (Mishra and Mahoney 2007, reprinted with permission from ASM International)

Material system	Remarks
5083 Al-SiC (Mishra et al. 2003)	SiC particles were put on the surface and stirred into the matrix
A356 Al-SiC (Ma et al. 2003)	SiC particles were put on surface and stirred into the matrix
7050 Al-WC (Newkirk et al. 2003)	WC particles were put a machined surface slot and stirred
1100 Al-SiO_2 and TiO_2 (Howard et al. 2005)	Introduced the concept of reaction processing during FSP. The reaction product was placed sub-surface with a three-layer set-up and friction stir processed
7050 Al and 6061 Al-WC, SiC, Al_2O_3, MoS_2, Fe, Zn, Cu (Ramadorai et al. 2005)	Powders were placed in sub-surface drilled holes. The hole geometry provided good control of the volume fraction. A number of ceramic and metallic phases were explored, including a combination of SiC and MoS_2
AZ61-SiO_2 (Lee et al. 2006a, b)	Distributed nano-particles by using repeated runs
Al-SWCNT (Johannes et al. 2006)	Demonstrated the survivability of single wall carbon nanotubes (SWCNT) during FSP. The nanotubes were placed sub-surface by drilling a hole from top and using a plug
AZ31-MWCNT (Morisada et al. 2006)	Multi-wall carbon nanotubes (MWCNT) were distributed in a Mg alloy
Al-NiTi (Dixit et al. 2007)	Shape memory alloy (NiTi) was distributed using the hole method without any interfacial reaction with Al

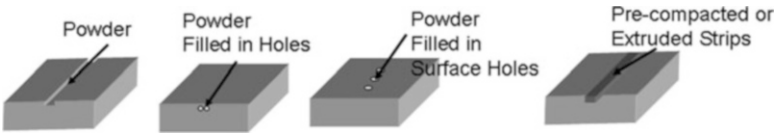

Fig. 9.15 An illustration of a few ways of adding powder during FSP surface modification. Note that all approaches lead to some inhomogeneity

possibility of developing sensors and actuators by locally embedding functional particles. In another attempt to embed functional particles, Dixit et al. (2007) have observed clean Al-NiTi interfaces after friction stir processing (Fig. 9.16d).

9.3.2 Processing of Powder Metallurgy Alloys

Powder metallurgy processed aluminum alloys suffer from three major microstructural problems that limit their full potential: (a) prior particle boundaries with an aluminum oxide film, (b) microstructural inhomogeneity, and (c) remnant porosity. These microstructural features particularly hamper the ductility in very high strength

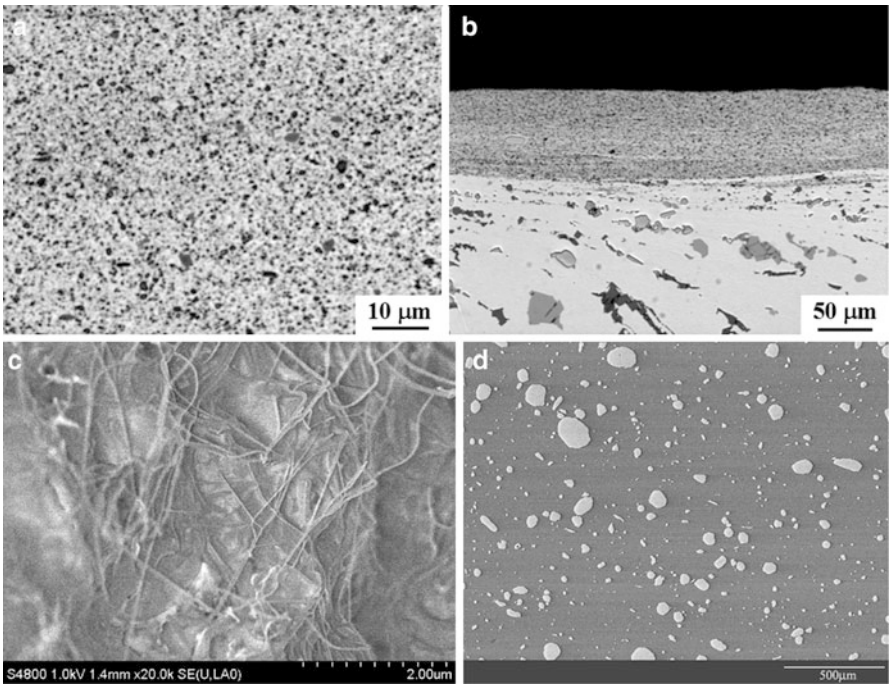

Fig. 9.16 Optical micrograph showing (**a**) uniform distribution of SiC particles (~15 vol.%) in A356 matrix, and (**b**) perfect bonding between surface composite and aluminum alloy substrate (600 rpm rotation rate and 6.4 mm/min traverse speed) (Ma et al. 2003). (**c**) SEM image showing SWCNTs bundles on the fracture surface of a friction stir processed aluminum matrix (Johannes et al. 2006). (**d**) SEM image showing uniformly distributed NiTi particles in Al matrix (Dixit et al. 2007) (Mishra and Mahoney 2007, reprinted with permission from ASM International)

aluminum alloys. Berbon et al. (2001) and Zheng et al. (2001) have shown that FSP can be used a homogenization tool. Figure 9.17 shows the microstructural difference in an Al-Ti-Cu alloy processed by extrusion and by FSP. The FSP microstructure is remarkably different from the as-extruded microstructure. This leads to an excellent combination of strength and ductility. Spowart et al. (2003) have highlighted the effect of spatial heterogeneity on mechanical properties. They used FSP to modify the homogeneity of three aluminum matrix composites produced with controlled inhomogeneity. Figure 9.18 shows the relationship between homogeneous length scale and ductility in aluminum matrix composites. Results clearly demonstrate that FSP can be a very useful tool to enhance the mechanical properties of high strength alloys and composites. Combining the trends observed by various studies cited in this section, the potential of FSP as a tool to create homogeneous composites on a local scale can be visualized. Designers and fabricators can take this approach to design components and sub-systems to take advantage of localized property enhancements to augment conceptual design elements.

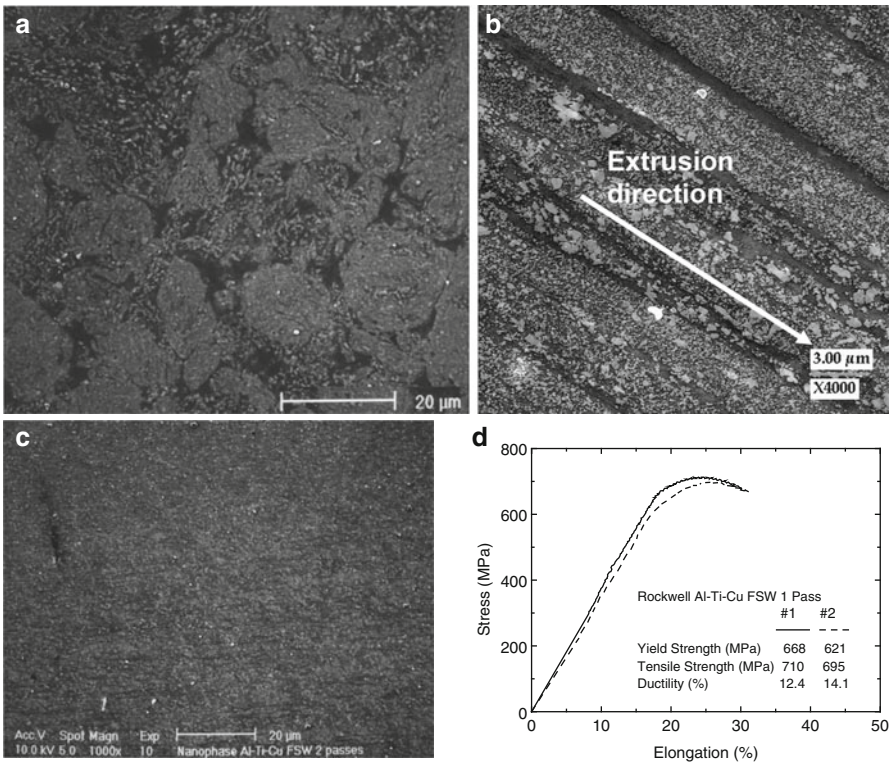

Fig. 9.17 (**a**) Typical microstructure in the as-HIPed condition. Dark regions consist of pure Al, grey regions consist of fine intermetallics dispersed in an Al matrix, and light regions consist of coarse intermetallics in an Al matrix. (**b**) Typical as-extruded microstructure shows the same three microstructural features, now elongated in the extrusion direction. (**c**) Typical microstructure observed in the FSP nugget. The three different microstructural features seen in the starting material have been homogenized. (**d**) Tensile tests of the Friction Stir processed material show an excellent strength and more than 10 % ductility (Berbon et al. 2001) (Mishra and Mahoney 2007, reprinted with permission from ASM International)

9.3.3 Synergistic Design: Concept of Embedded Structures for Higher Efficiency

This concept has two aspects to it. The first one is a generic concept dealing with the question: Can more than 100 % structural efficiency be obtained by synergistic design of composites? In what follows, it is argued that it is possible to combine two design features, volume fraction of reinforcement and location of reinforcement, to obtain synergistic enhancement that leads to >100 % efficiency. The second aspect relates to economical manufacturing of such composites. FSP has the potential to provide such a processing route.

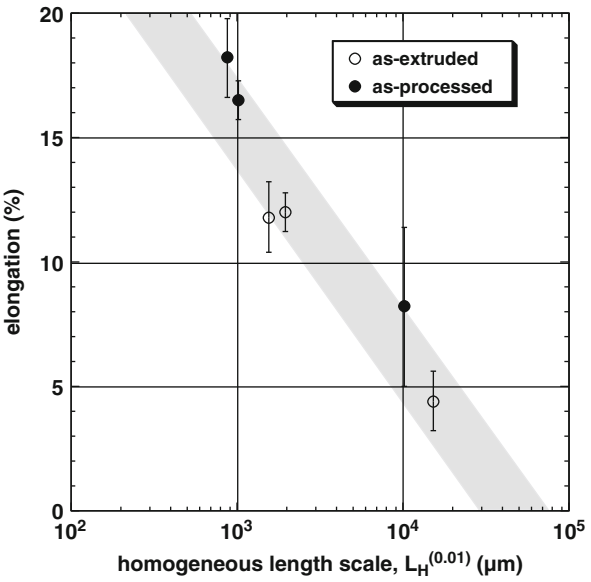

Fig. 9.18 A relationship between tensile elongation and level of spatial heterogeneity, as characterized by the homogeneous length scale, $L_H^{(0.01)}$ (Spowart et al. 2003)

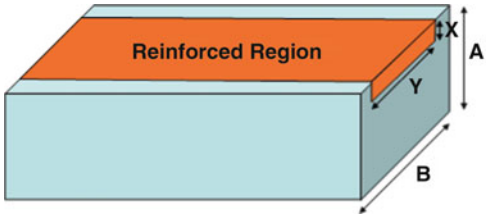

Fig. 9.19 An illustration of the concept of selective reinforcement for synergistic enhancement

Figure 9.19 illustrates the concept of selective reinforcement. The idea of synergistic enhancement is based on interaction between two length scales of materials design. At the microstructural level, mixing of two phases will lead to property enhancement following the rule of mixture. At the meso or macro-scale, the product can be designed to maximize the property at strategic locations. To illustrate this concept we select stiffness as an example, although a similar strategy will work for several other properties as well. In Fig. 9.19, the overall cross section of the beam is A × B. For the selectively reinforced concept, only the region with cross-section of X × Y has particles. For this design two other considerations can be brought in, (a) during bending of beams, the stresses are maximum at the surface and go through the neutral axis in the center, and (b) metal matrix composites suffer from poor tensile ductility, but have excellent compressive properties. If we want to have 30 vol.% reinforcement in this region for a specific level of stiffness of the beam, it can be put on the compressive side of the beam. The equivalent volume fraction of particles in a monolithic composite (material with uniform distribution of particles) can be computed as $0.3 \times \{(X \times Y)/(A \times B)\}$. If we now apply a force

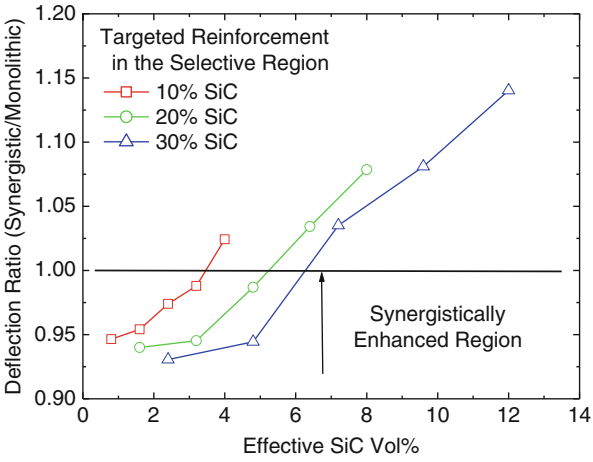

Fig. 9.20 Enhancement in stiffness results from synergistic design (Tandon and Mishra, unpublished)

Table 9.3 Summary of equivalent vol.% SiC in monolithic beam for different depth of selectively reinforced layer

Vol.% of SiC in selective region	Reinforced layer depth—X (mm)				
	0.5	1.0	1.5	2.0	2.5
10	0.8	1.6	2.4	3.2	4.0
20	1.6	3.2	4.8	6.4	8.0
30	2.4	4.8	7.2	9.6	12.0

on these beams with different designs, but an equivalent overall reinforcement phase, the level of deflection would indicate the effectiveness of the design. It should also be recognized that poor bonding between the reinforcement phase and matrix lowers the load transfer and therefore leads to lower stiffness.

Figure 9.20 shows the efficiency of synergistic design. Three curves are presented for different volume fractions of SiC in the selective region of an AA5083 beam. The following dimensions of the beam and selective layers were used: A = 5 mm; B = 10 mm; Y = 8 mm. Table 9.3 shows the equivalent SiC fraction in a monolithic composite beam given the mixed beam composite's strip fraction of SiC and the strip depth. The value of X was varied between 0.5 and 2.5 mm. It is very interesting to note that the best results are obtained for thin selectively reinforced region. In fact when the depth is such that it touches the neutral line (center of beam), the selectively reinforced composite is worse than the monolithic beam (uniformly reinforced beam). This is an important factor to consider on component design. The enhancement for thinner layers can be as much as 7 %. The implication is that for the same design stiffness, up to 7 % weight saving can result from synergistic design within the range considered here. Further improvement can be obtained by optimizing the modulus and density of the reinforcement phase.

9.4 Friction Stir Casting Modification: Examples of Approaches for Strength Limiting, Fatigue Limiting and Toughness Limiting Designs

Casting is the most cost efficient way to produce complex shaped parts. However, castings suffer from many microstructural issues that limit its performance. Forging on the other hand is a preferred manufacturing technique for high performance components. The basic difference of course lies in the microstructure; wrought microstructure in forgings vs. solidification microstructure in castings. So, the paradigm shift that friction stir processing offers is to have 'wrought microstructure in localized regions of a cast component'; a balance between cost, complexity and performance of a component. Critical microstructural features in a casting can be listed as,

- Large oxide films
- Large dendritic porosity (larger than 1 mm)
- Small dendritic porosity (smaller than 1 mm)
- Particulate oxides/inclusions
- Secondary dendritic arm spacing (SDAS). The high stress regions are frequently the slowest to solidify, with larger SDAS.
- Silicon modification and iron-phase intermetallics
- Non-dendritic (~spherical) hydrogen gas porosity

Conventional approach in casting is to increase the cross-section of high stress regions. This leads to lower cooling rate in those areas and the microstructure is actually inferior in the critical regions. Rest of this section shows examples of friction stir processing induced microstructural refinement and its influence on strength, ductility, fatigue and toughness.

9.4.1 Microstructural Refinement

Figure 9.21 shows a comparison of cast and friction stir processed microstructure for three commercially cast components of A356 alloy. The level of porosity and dendritic arm spacing is different in all the specimens. Also the particles in interdendritic regions have different sizes because of the practice of adding Si modifier. After friction stir processing, the obvious microstructural changes include, elimination of porosity, refinement of particles and homogenization of microstructure. The effect of FSP on particle size can be quantitatively seen from distribution histograms shown in Fig. 9.22. It is important to focus on the larger particles. In as-cast condition, more than 10 % particles are above 15 μm. During mechanical loading such as tensile test or fatigue test, larger particles are the local area where failure starts. Table 9.4 summarizes the microstructural refinement and changes in the context of critical features in castings discussed above. It reemphasizes the refinement of particles, homogenization of microstructure and elimination of porosity.

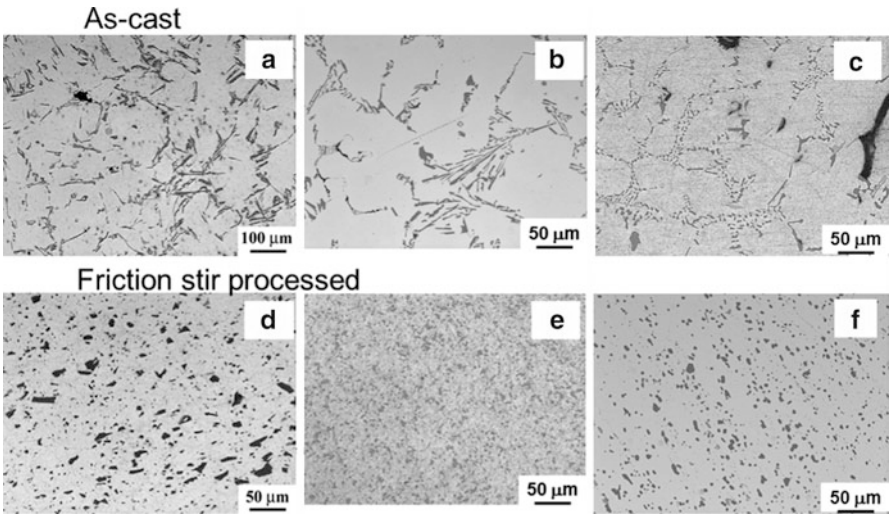

Fig. 9.21 A comparison of as-cast (**a**, **b**, **c**) and friction stir processed (**d**, **e**, **f**) microstructures of A356 alloy from three commercial casting. Note the dendritic arm spacing, large particles and porosity in as-cast condition. FSP refines and homogenizes the microstructure as well close all the porosity

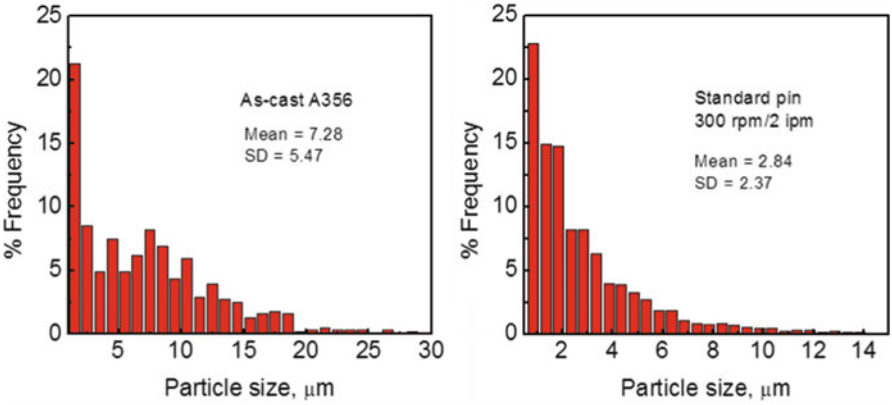

Fig. 9.22 Distribution of particle size in as-cast and after FSP for A356 alloy in one cast condition. Note the reduction in maximum particle size. More than 10 % of particles in as-cast condition were above 15 μm

A206 is an Al-Cu casting alloy that is capable of much higher strength levels, but suffers from higher level of porosity. Figure 9.23 shows microstructure of A206 alloy before and after FSP. The strengthening phase in this alloy is Al_2Cu. The microstructural summary after refinement is listed in Table 9.5. The volume fraction of large particles in this alloy is significantly lower than A356, but the size of coarser phase is quite similar.

Table 9.4 A summary of the influence of FSP on critical microstructural features

	As-cast A356	Friction stir processed
Porosity	0.005–0.03 %	Almost 0 %
Fe rich intermetallics	11.1 mm	3.0 mm
Si size	3.6 mm	1.0 mm
Si aspect ratio	2–7	1–2
Oxide inclusion	Non-uniform	Fine and distributed
Homogenize	No	Yes

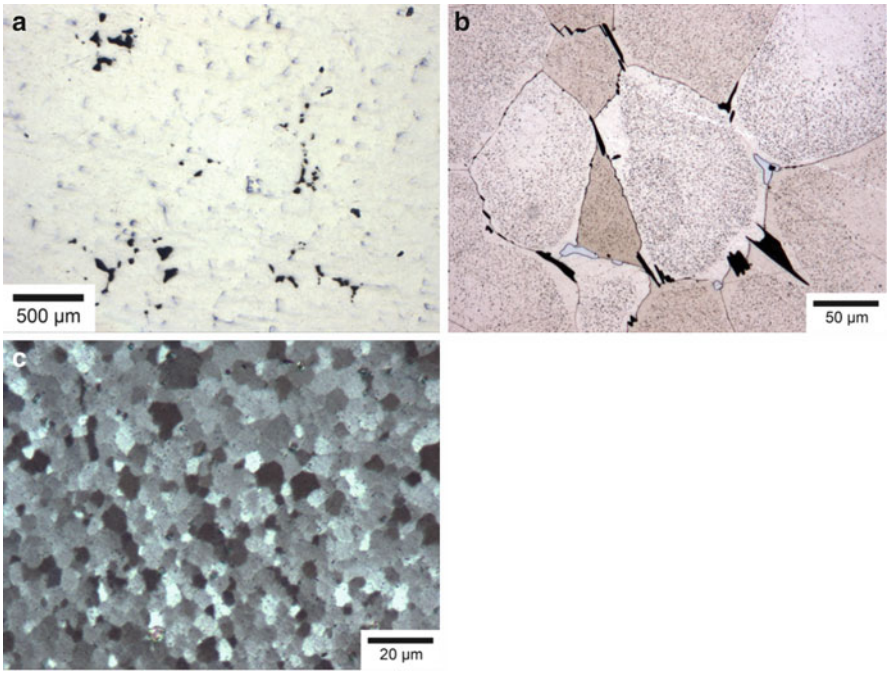

Fig. 9.23 Optical microscopy of A206 in cast + T4 condition showing pores (**a**), needle shaped Cu_2FeAl_7 intermetallics (**b**), and grain distribution after FSP (**c**) (Kapoor et al. 2011, reprinted with permission from Elsevier)

Table 9.5 Comparison of microstructural features, pores, particles, grains and precipitates in different heat treatment conditions

Name	Pores (μm)	Particles (μm)	Grains (μm)	Precipitates
Cast + T4	14.7 ± 2	5.6 ± 2.5	210 ± 6	Coherent
As-FSP	None	2.9 ± 1.4	3.5 ± 1.5	Coherent
FSP + 190C	None	2.9 ± 1.4	3.5 ± 1.5	Incoherent
FSP + T4	None	2.9 ± 1.4	350 ± 200	Coherent
FSP + T6	None	2.9 ± 1.4	350 ± 200	Semi-coherent
FSP + T7	None	2.9 ± 1.4	350 ± 200	Incoherent

The average values with standard deviation for pores, particles and grains are listed along with the type of precipitates present in the different conditions (Kapoor et al. 2013, reprinted with permission from Elsevier)

Table 9.6 A summary of A356 room temperature tensile properties from an average of five specimens. The differences between Cast+T6 and FSP+T6 are highlighted

Condition	UTS (MPa)	YS (MPa)	% E
As cast (handbook)	159	84	6
Cast + T6 (handbook)	278	207	6
Cast	169 ± 8	132 ± 3	3 ± 1
Cast + T6	$\mathbf{231 \pm 30}$	$\mathbf{225 \pm 20}$	$\mathbf{0.6 \pm 0.4}$
Cast + FSP	264 ± 3	168 ± 9	13 ± 2
Homogenized + FSP	262 ± 7	168 ± 4	12 ± 2
T6 + FSP	228 ± 9	144 ± 7	14 ± 4
FSP + T6	$\mathbf{328 \pm 12}$	$\mathbf{288 \pm 9}$	$\mathbf{10 \pm 1}$
Homogenized + FSP + Aged	311 ± 15	277 ± 17	4 ± 1

9.4.2 Influence on Mechanical Properties

9.4.2.1 Tensile Behavior

A number of papers have reported mechanical behavior of castings before and after FSP. We focus on only a few results which are adequate to illustrate the point. A356 and A357 are very popular Al-Si-Mg alloys which have Si for fluidity and Mg_2Si precipitates for strengthening. Table 9.6 gives one set of data from sand cast A356 alloy. It is important to focus on both the average values and the standard deviation. As the components are designed to some minimum guaranteed property value, we can take (Mean YS-3σ) values in cast + T6 (165 MPa) and FSP + T6 conditions (261 MPa). This represents nearly 58 % increase in the design stress if the design guideline is based on yield strength. This table also shows various pathways for insertion of FSP. For example, a typical production of cast component involves; casting, homogenization and aging, then final machining. A question that comes up is on insertion of FSP step. What is the most prudent stage to do it? Based on the basic value addition proposition, one can think of many pathways. Let us discuss a few scenarios. Bear in mind that all the discussion is based on the premise that casting modification would be done in local regions where in the current context, higher strength or higher fatigue life is desired. The selection of the region is based on some form of stress analysis, say finite element modeling of the entire component. The most conservative approach would be to insert it after homogenization and perform T6 treatment after FSP. The machining would still be the last step. A paradigm changing approach would be to declare that FSP takes care of homogenization and solution treatment. Then the production can be simplified to casting, FSP and aging. This would result in significant energy saving associated with homogenization and solution treatment. Of course, several other paths in between these two limits can be used to insert FSP step in production.

A206 alloy is an Al-Cu casting alloy that is significantly stronger. Kapoor et al. (2013) have published detailed tensile behavior in many conditions. Figure 9.24 shows stress-strain curves as well as summary of strength-ductility variation.

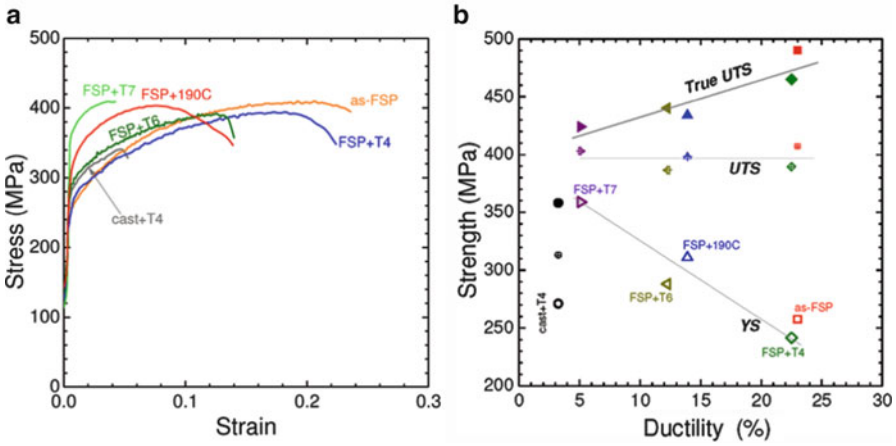

Fig. 9.24 (**a**) Stress-strain plot for A206 alloy in different conditions. The strength and ductility data from these curves is plotted in (**b**). Note that while engineering UTS values are constant for various FSP specimens, the true UTS values are higher for specimens with higher ductility. Kapoor et al. (2013), reprinted with permission from Elsevier

There are several interesting trends in this. This alloy is similar to 2XXX alloys in wrought condition unlike A356 alloy, which has no equivalent wrought composition. So, the first aspect that needs comparison is the strength level. The yield strength after FSP and aging is in the range of 350 MPa and UTS values are around 400 MPa. These values are very consistent with AA2XXX alloys. The yield strength-ductility relationship has a typical profile of structural materials, i.e. the ductility decreases as the strength increases. However, an interesting aspect is that the engineering values of UTS are constant. When plotted as true UTS vs. ductility, it shows that FSP and FSP + T4 specimens which have lower yield strength show highest UTS because of high strain hardening as high uniform elongation.

The casting industry uses strength and ductility data to define 'quality index'. Drouzy et al. (1980) have proposed a simple relationship to represent quality index (Q) as,

$$Q = \sigma_{UTS} + 150 \log E \tag{9.4}$$

where σ_{UTS} is the ultimate tensile strength and E is the elongation. Figure 9.25 shows a quality index plot for A356 alloy that was discussed earlier. The improvement in Weibull modulus after FSP is quite obvious and this suggests high reliability after FSP.

9.4.2.2 Fatigue Behavior

A number of fatigue behavior papers have been published on friction stir processing of aluminum and titanium alloys, but we focus on just a few to lay out the basic foundation behind the improved fatigue behavior. Figure 9.26 illustrates fatigue

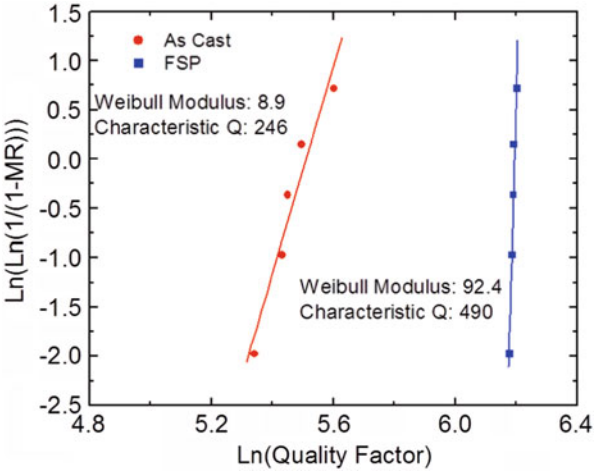

Fig. 9.25 A plot of quality index showing significant in Weibull modulus after friction stir processing of A356 alloy

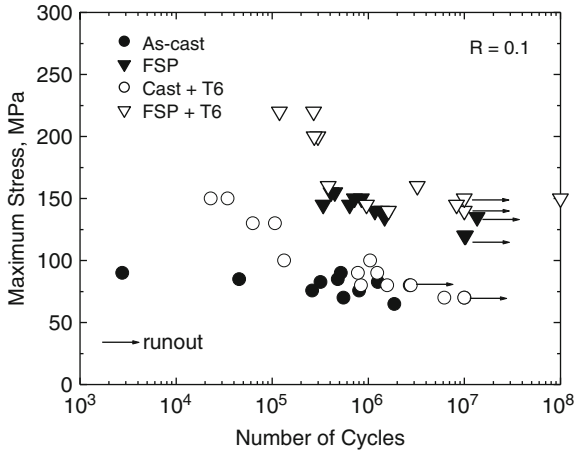

Fig. 9.26 Plot of fatigue lifetime vs. maximum stress for as-cast and FSP A356 samples (Sharma et al. 2004, reprinted with permission from Elsevier)

results for A356 plates before and after FSP (Sharma et al. 2004). For processed plates, the samples were machined completely from the stir zone. The arrows in Fig. 9.26 indicate specimens that did not fail. As shown, the fatigue strength threshold stress increased by >80 % after FSP. This fatigue strength improvement is attributed to both a reduction in silicon particle size and reduced porosity volume fraction. The fatigue life N_f has been related to the positive component of cyclic stress, σ*, and the pore size a_o, by:

$$\sigma^* = C\left(a_o N_f\right)^{-\frac{1}{m}} \tag{9.5}$$

where m is the Paris exponent for fatigue crack growth and C is a constant that depends on the Paris pre-exponential constant and on the pore shape and position. From the above analysis, it was concluded that fatigue life is influenced more by the

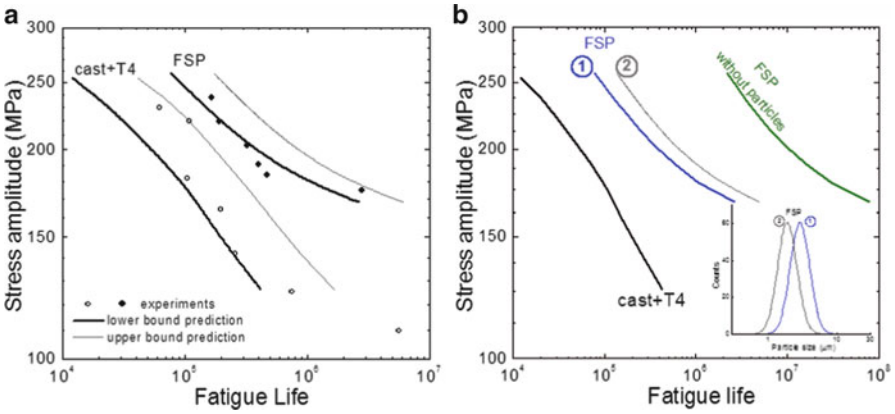

Fig. 9.27 (**a**) A comparison between the experimental and predicted stress amplitude vs. fatigue life for both cast + T4 and FSP conditions. The lower and upper bounds of the prediction are shown on the plot. (**b**) Stress amplitude vs. lower bound of computed fatigue life showing cast + T4 and FSP conditions from actual defect distribution labeled 1. Also shown is the predicted lower bound of life for distribution of smaller particles labeled 2 and the predicted lower bound of life for a condition without particles. The *inset* shows the corresponding particle distribution marked as 1 and 2. (Kapoor et al. 2011, reprinted with permission from Elsevier)

size of the largest pore rather than porosity volume fraction or mean pore size. In addition to porosity, fracture characteristics of Al-Si-Mg castings are influenced by size, orientation and local distribution of Si particles as well as by the Si-matrix interface strength. Larger Si particles present in the as-cast material accelerate crack nucleation due to stress concentration effects. Murakami and Endo (1994) have proposed the following equation for the fatigue limit in metals with 3-D defects:

$$\sigma_w = \frac{1.43(H_V + 120)}{\left(\sqrt{A}\right)^{\frac{1}{6}}} \tag{9.6}$$

where σ_w is the fatigue limit (MPa), A is the area obtained by projecting a defect or a crack onto the plate perpendicular to the maximum tensile stress (mm), and H_v is Vickers hardness (kgf mm^{-2}) between 70 and 720 H_v. Based on Eq. (9.6), a 30 % reduction is particle size alone would contribute to a 25 % improvement in the fatigue limit. FSP significantly refines the microstructure leading to a homogeneous distribution of smaller Si particles with smaller aspect ratios when compared to the as-cast microstructure. This refined microstructure also leads to increased plastic deformation in the aluminum matrix during cyclic crack tip propagation resulting in a concurrent increase in crack energy dissipation and a consequent increase in crack growth resistance. Plastic deformation during fatigue leads to crack nucleation either by separation of the silicon aluminum interface or by particle cracking or both.

Figure 9.27 shows experimental and modeling results from Kapoor et al. (2011) on fatigue of A206 alloy. This comprehensive paper on probabilistic modeling not

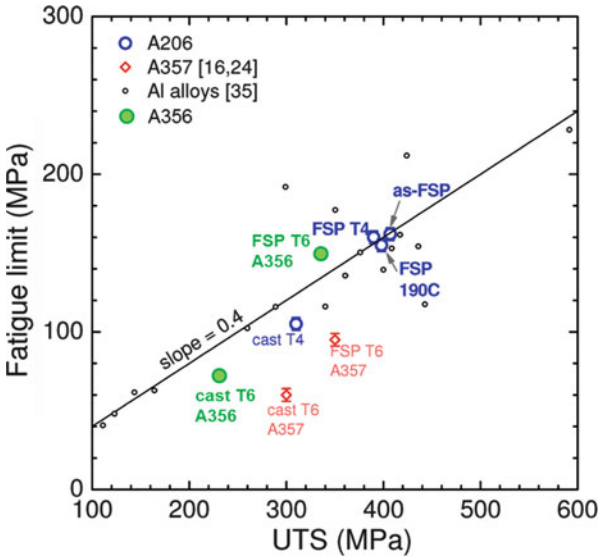

Fig. 9.28 Fatigue limit vs. UTS for A356, A357 and A206 aluminum alloys before and after FSP with different heat treatments. Compared are general data for other Al alloys (Figure taken from Kapoor et al. 2013, reprinted with permission from Elsevier, and modified to include A356 alloy data)

only focused on modeling prediction of the fatigue life of A206 specimens, but considered hypothetical specimens without any particles. Figure 9.27a shows the experimental and predicted data for A206 alloy. Clearly FSP leads to improvement in fatigue life. As discussed earlier, the fatigue life after FSP is controlled by largest flaw size, which in this case becomes broken down intermetallic particles. Then a hypothetical question arises; what is the maximum potential of FSP for fatigue life enhancement? In other words, if there were no flaws or large intermetallic particles, what would be the predicted life? The answer would then set the maximum limit of fatigue life enhancement that can be expected. Figure 9.27b has four curves. The cast + T4 data is the baseline and we are interested in the extent of improvement possible with FSP. The first two predicted lines are for two level of particle size distribution shown in inset. The assumption here is that FSP condition dictates the refinement of particles and these two examples are based on this. Again, a clear expectation is that the fatigue life would improve, which is consistent with all the experimental data. The last curve is for a material that has no particles. This condition represents the best case scenario where the FSP was so effective that it refined the entire particles to very small sizes where they are no longer fatigue crack nucleation sites, i.e. fatigue crack nucleation shifts to other types of sites.

The last point that we consider in this section is also taken from Kapoor et al. (2013). Figure 9.28 shows a plot of fatigue limit (stress for 10^7 cycles) with UTS for A356, A357 and A206. It is quite clear that FSP enhances the UTS and fatigue limit. This is the type of information that can be taken for design consideration.

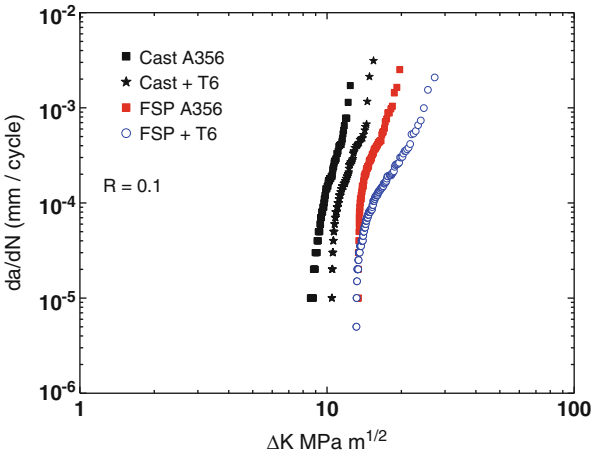

Fig. 9.29 Crack growth rates in A356 under various processing conditions at stress ratio R = 0.1 (Sharma and Mishra 2008, reprinted with permission from Elsevier)

Table 9.7 Comparison of "pseudo" fracture toughness of A356 under various processing conditions

	Cast	Cast + T6	FSP	FSP + T6
K_Q(MPa $\sqrt{m}$)	14.6 ± 2	15.8 ± 4	19.5 ± 1	24.4 ± 1

9.4.2.3 Fatigue Crack Growth and Fracture Toughness

There is not much data on fatigue crack growth. Figure 9.29 shows a comparison between the crack growth rates of cast A356 and friction stir processed region using compact tension specimen (Sharma and Mishra 2008). To achieve similar crack growth rates in FSP A356, compared to cast A356, a greater than 36 % increase in load was required. Also, the friction stir processed alloy follows region II in the da/dN vs. ΔK plot at higher ΔK values. The slower crack growth rates in FSP A356 are attributed to the finer microstructure developed during FSP. Results from tests conducted at higher stress ratios indicate that crack closure is the dominant mechanism in increasing crack growth resistance in FSP samples in the threshold region.

The upper limit of the crack driving force was assumed to be the "pseudo" fracture toughness of the materials. Because the CT specimens in that study did not meet plane strain fracture toughness requirements of ASTM E399, the measured fracture toughness values were referred to as "pseudo" fracture toughness. Pseudo fracture toughness was determined using the crack length and critical load at the onset of unstable fracture. The "pseudo" fracture toughness is only slightly influenced by the T6 heat treatment for the as-cast A356, while FSP samples show higher toughness than cast A356 samples, Table 9.7. The pseudo fracture toughness of FSP samples improved by over 30 % when compared to cast samples and in the T6 condition, FSP samples showed >50 % improvement in toughness.

9.5 Friction Stir Channeling (FSC)

During FSW, a defect referred to as a "wormhole" is generated if the processing parameters and tool shoulder contact are not proper. FSC is based on converting this defect formation process into a manufacturing technique for heat exchanger applications. Mishra (2005) has shown that a continuous hole in a single plate can be achieved by selecting the right processing conditions and reversing the material flow. Balasubramanian et al. (2009) published first paper on this concept and this section is taken from that paper. The main aspects of FSC are as follows:

(a) a profiled tool is rotated such that the material flow is upwards towards the tool shoulder,
(b) an initial clearance is provided between the shoulder and the workpiece, where the material from the base of the pin is deposited, and
(c) this distance between the tool shoulder and the workpiece can be adjusted to control the shape, size, and integrity of the channel.

The presence of the gap between the shoulder and the workpiece is a major difference between the FSC and the normal FSW or FSP practices where the back of the shoulder touches the workpiece to generate the forging action required to produce defect-free welding or processing. During channeling, an upward force is generated by rotating a right-hand threaded tool clockwise (or a left-hand threaded tool counter-clockwise). A channel is formed because of the separation of the plasticized material around the pin from the plasticized material at the base of the pin. This separated material is moved upwards by the rotation of the pin and the orientation of the threads, and it is deposited on the top of the nugget underneath the shoulder surface. The shape and size of the channel can be controlled by varying the following parameters: The clearance between the shoulder and the work material; the tool rotation speed; the tool traverse rate and the tool design.

The generation of a continuous channel by FSC has the potential to open a wide range of applications in heat exchanger industry. Heat exchangers are devices that are used to transfer thermal energy between two or more fluids, or between a solid surface and a fluid, at different temperatures and in thermal contact. Typical applications of heat exchangers involve heating or cooling of a fluid stream and evaporation or condensation of fluid streams, with an objective to reject or recover heat. Heat exchangers are usually classified on the basis of the transfer process, as either direct contact type or indirect contact type. The heat exchangers are also classified on the basis of the number of process fluids, or on the basis of the construction or flow arrangements or the heat transfer mechanisms. Another basis for classification of the heat exchangers is on the basis of surface compactness. The main objectives of compact heat exchangers are to maximize the efficiency of a heat exchanger and also to reduce the size of the heat exchanger for a given duty. Compact heat exchangers are generally used in industry, especially in gas-to-gas or liquid-to-gas heat exchangers. For example, vehicular heat exchangers, condensers and evaporators in air-condition and refrigeration industry, aircraft oil-coolers, automotive radiators, and intercoolers or compressors.

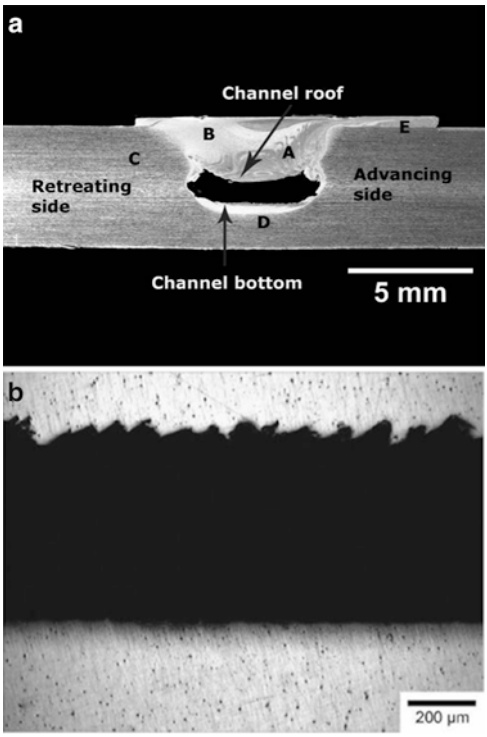

Fig. 9.30 (**a**) Cross-sectional image of a channel showing the different process regions: (A + B) channel nugget, (C) parent material, (D) channel, and (E) material from the channel nugget deposited on the surface. (**b**) Longitudinal cross section of the channel showing the roughness on the roof of the channels (800 rpm, 1.27 mm/s) (Taken from Balasubramanian et al. 2009, reprinted with permission from Elsevier)

Figure 9.30 shows the cross section of the channel nugget, and depicts clearly the material flow pattern during the process, after the tool has passed the region. The direction of tool rotation is counter clockwise and the traverse direction is into the plane of the paper. To understand the channel formation requires distinguishing among the different regions of the channel cross section. Regions A and B are collectively referred to as the stir zone. Region C is the unprocessed parent material, and region D is the channel. Region E represents the material deposited from the channel nugget region above the original surface of the material, underneath the shoulder. To allow a channel to form, material must be removed from the stir zone. This is accomplished by having a space between the tool shoulder and top surface of the workpiece, and allows the pin features to move the material in this gap. Because of the orientation of the threads on the pin and the direction of tool rotation, the plasticized region at the bottom of the channel is pushed upward on the advancing side (the side where the tool surface velocity vector is opposite to the tool traverse direction). The upward force produced by the threads causes the plasticized material to be pushed upward and deposited by the shoulder on the surface (region E). Region A represents the part of the nugget processed by the pin. The pattern seen in region A depicts the flow path of the material moving from the pin base to the shoulder-workpiece clearance.

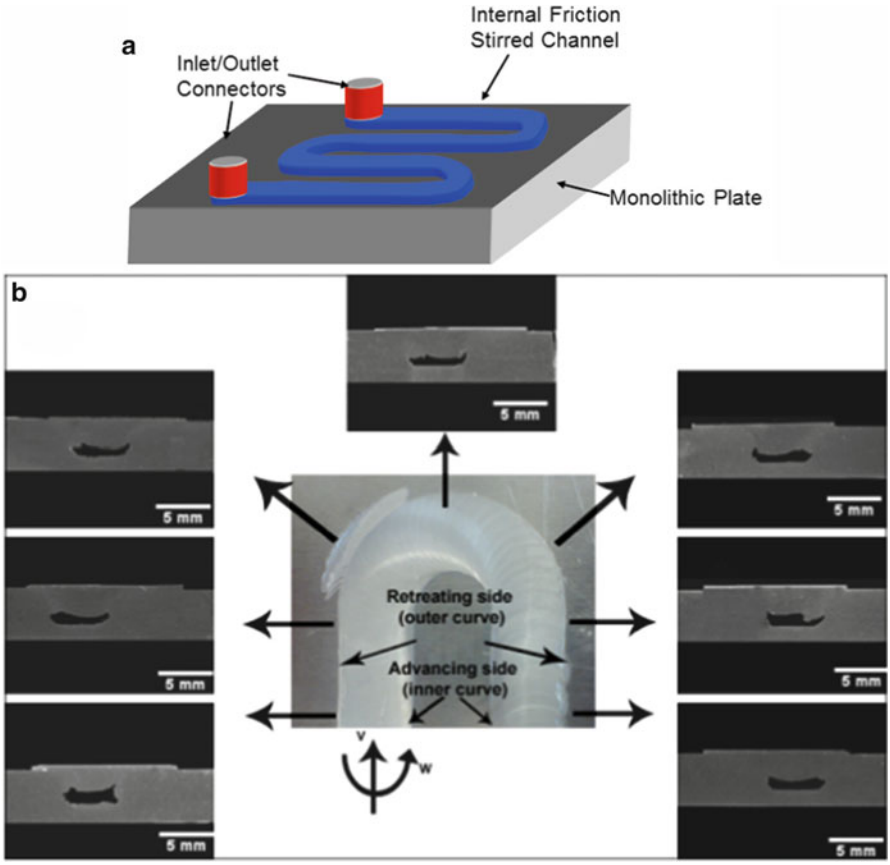

Fig. 9.31 (**a**) Conceptual depiction of a heat exchanger fabricated by robotic machine. (**b**) Also included is a curved channel example from Balasubramanian et al. (2009), reprinted with permission from Elsevier

The deposition of the material underneath the shoulder results in a downward resultant force on the channel roof behind the pin (trailing side of the tool). Also, due to the shoulder rotation, the material in the upper region of the workpiece is pushed inward and deposited in region B, mainly on the retreating side. An additional layer surrounds the nugget, referred to as a thermo-mechanically affected zone (TMAZ), where the amount of grain refinement is insignificant. TMAZ is unclear in Fig. 9.30. The surface roughness at the upper surface of the channel is uniformly spaced, and the periodicity of the roughness at the top surface matches the amount of material that is being displaced with each rotation, i.e., the process pitch. In the case of Fig. 9.30b, the pitch of the run is 0.095 mm/rot, and the actual spacing is 0.091 mm.

Figure 9.31 shows a conceptual drawing of a heat exchanger from a single plate. Also included is a figure from Balasubramanian et al. (2009), which shows the channel along a curved friction stir channeling run with a robotic machine. This is a technique that shows friction stir processing as a manufacturing technique.

9.6 Ultrafine Grained Materials via Friction Stir Processing

Ultrafine grained materials (UFG) are of interest because it provides a balance between strength, ductility and other properties. It also provides unique opportunities to investigate dislocation based plasticity mechanisms. Some reference to ultrafine grained microstructure (referred as average grain size below 1 μm) has come in earlier chapter and in this chapter in the context of powder metallurgy alloys and superplasticity. In this section, we capture a few examples of microstructure and room temperature behavior.

Figure 9.32 shows an ultrafine grained Al-4 Mg- 1 Zr alloy with truly random grain misorientation distribution. Such microstructure is unheard of from conventional thermo-mechanical processing (TMP) techniques. The average grain size of this UFG alloy is ~700 nm with >97 % HAGB in FSP Al-Mg-Zr specimen. For comparison, conventional TMP for superplastic sheet leads to ~60 % HAGB and equal channel angular pressing (ECAP) leads to around 80 % HAGB in eight passes. ECAP is routinely used to obtain UFG microstructure and severe plastic deformation community relies heavily on this technique. FSP has proven to a very effective severe plastic deformation technique because of unique combination of high strain, high strain rate and high processing temperature.

A scientifically important result was published by Kumar et al. (2011) on critical grain size for dislocation plasticity and intragranular dislocation storage. Figure 9.33 shows two ultrafine grained conditions designated as UFG-1 and UFG-2. The average grain size only changed from 0.63 to 0.39 μm, however the stress-strain curves are quite different in terms of uniform elongation and strain hardening (Fig. 9.34). Kumar et al. (2011) explained this on the basis of dislocation-dislocation interaction within the grain and possibility of dislocation storage.

Similar behavior was also reported by Panigrahi et al. (2012) as shown in Fig. 9.35. The stress-strain curves in four conditions are very illustrative of change

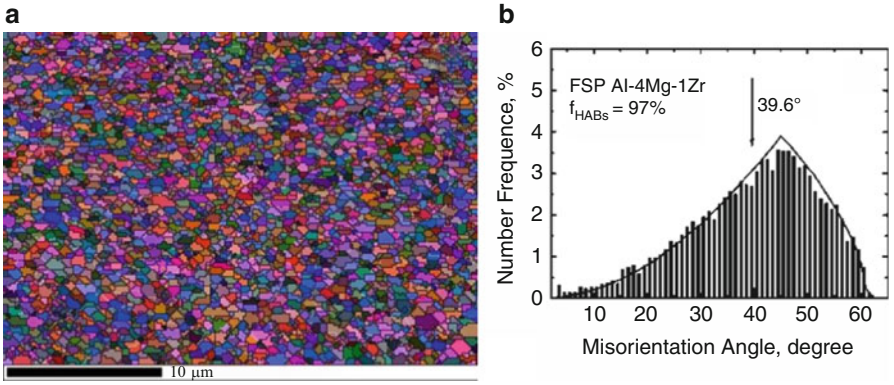

Fig. 9.32 (**a**) An orientation imaging map of Al-4 Mg-1 Zr alloy showing ultrafine grained microstructure and (**b**) a truly random misorientation distribution (Ma et al. 2010, reprinted with permission from Elsevier)

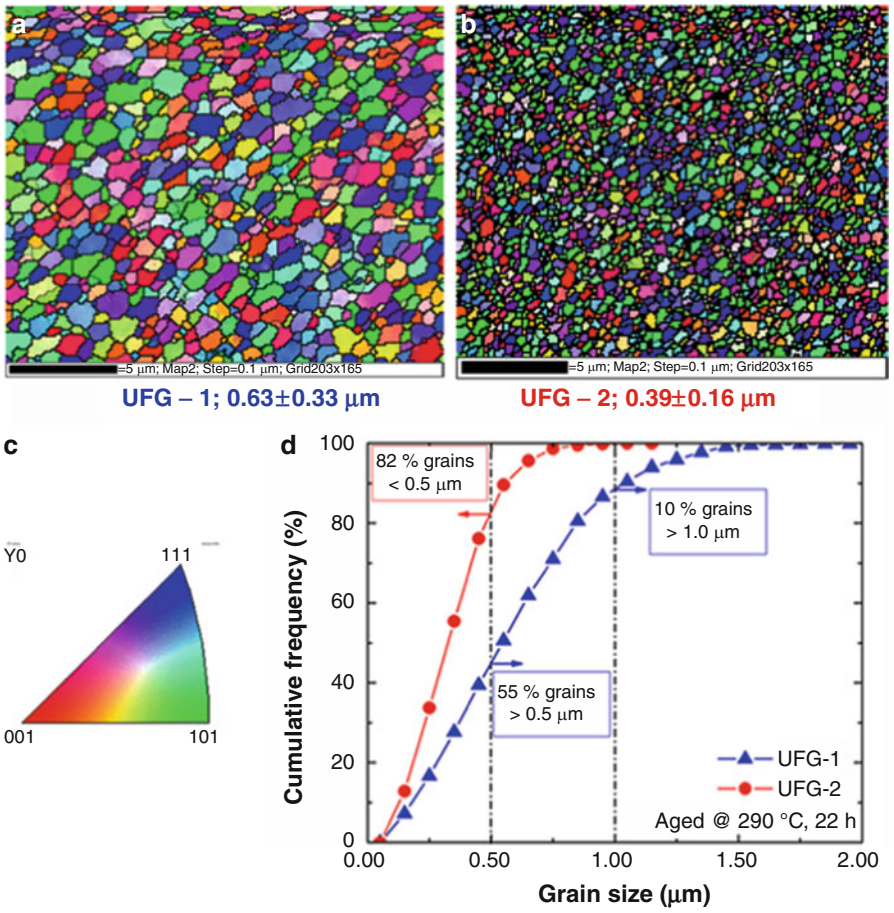

Fig. 9.33 (**a**, **b**) Micrographs of Al-Mg-Sc alloy in two ultrafine grained conditions. (**c**) Inverse pole figures with colors used for figures in (**a**) and (**b**). (**d**) Cumulative frequency distribution of grain size for both conditions (Kumar et al. 2011, reprinted with permission from Elsevier)

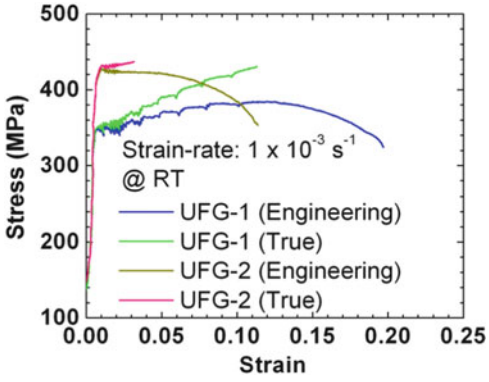

Fig. 9.34 The stress-strain behavior for the microstructures shown in Fig. 9.33. Note the difference in the work hardening and uniform elongation. The true stress-true strain curve is only plotted till uniform elongation (Kumar et al. 2011, reprinted with permission from Elsevier)

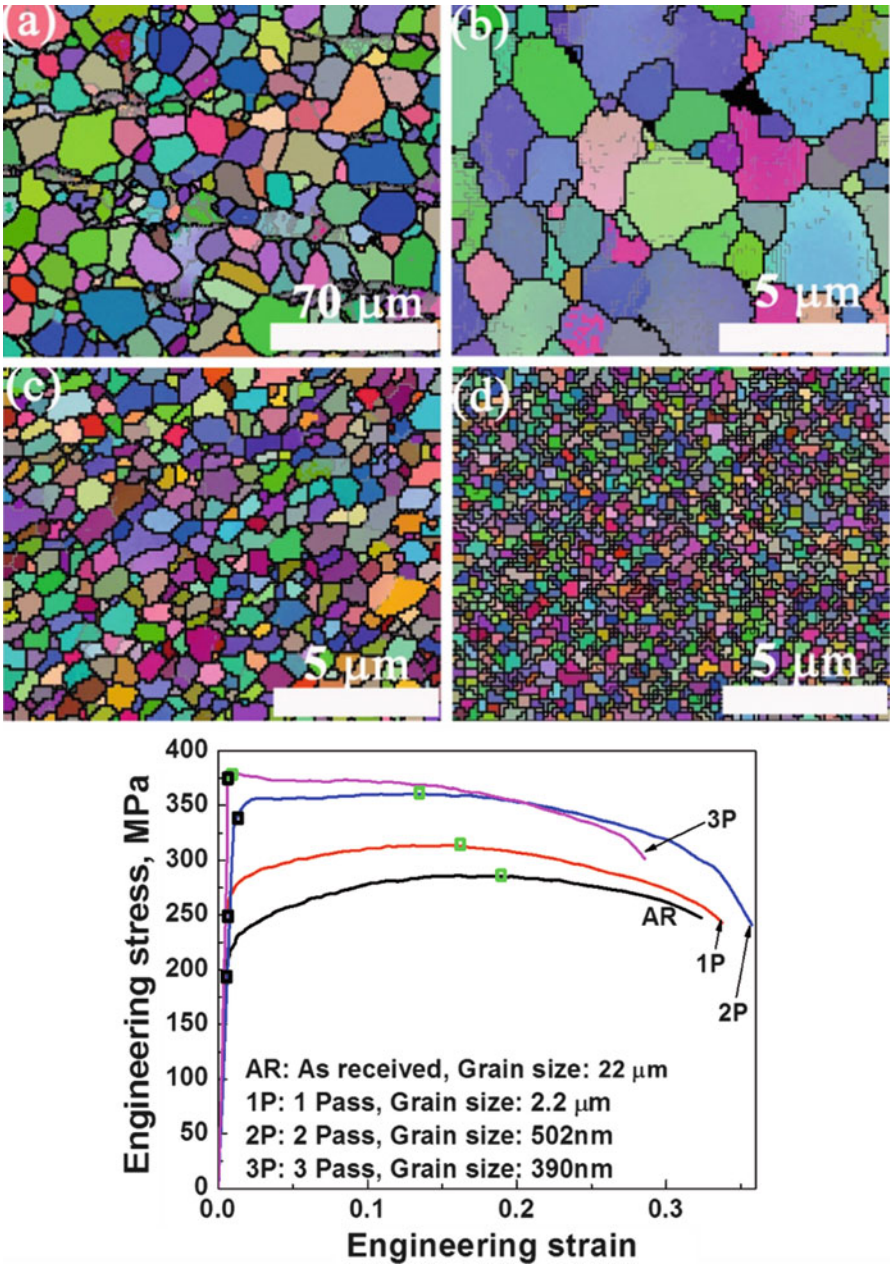

Fig. 9.35 (**a**)–(**d**) Microstructure of a WE43 magnesium alloy in four conditions and (**e**) associated stress-strain curves. Note the lack of work hardening in the UFG material with 390 nm average grain size (Panigrahi et al. 2012, reprinted with permission from Elsevier)

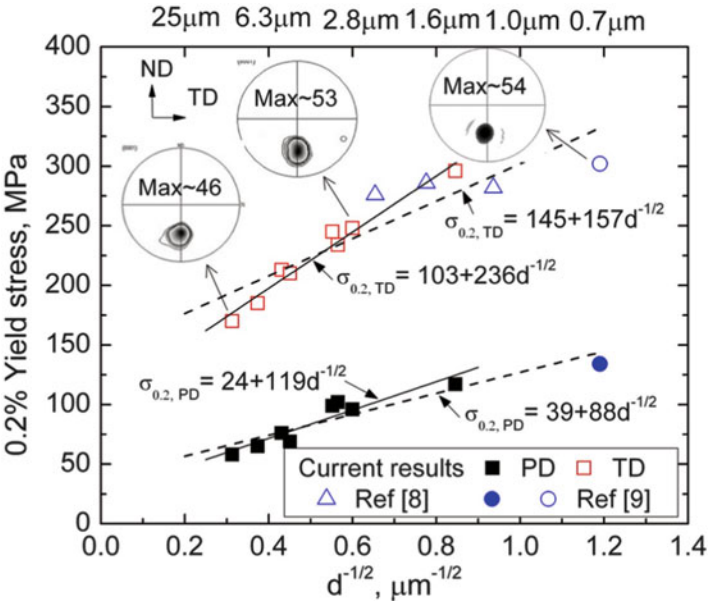

Fig. 9.36 Variation of yield strength with grain size in FSP AZ31 magnesium alloy. These specimens exhibited significantly strong texture as shown in the *inset* pole figures (Yuan et al. 2011, reprinted with permission from Elsevier)

in deformation mechanisms. It can be noted that the finest UFG material with 390 nm average grain size, the yield stress is quite high and there is no work hardening. Still the specimen exhibited significant overall ductility. This is a common trend now among FSP materials. Panigrahi et al. (2012) also correlated this transition to deformation by twinning in Mg alloys. They observed that UFG alloys showed no twinning. An interesting aspect in magnesium alloys is the extent of texture during FSP. The OIM micrographs in Fig. 9.35 show random orientation of grains. On the other hand, a study by Yuan et al. (2011) on single phase AZ31 magnesium alloy showed that texture can be very significant as shown in the inset of Fig. 9.36. They took advantage of this to investigate the role of grain size and texture on the Hall-Petch relationship (grain boundary strengthening). The approach used to obtain ultrafine grain size without any external cooling involved using overlapping passes with reduced heat during successive passes by lowering the tool rotation rate. This shows that the processing parameters can be controlled to obtain microstructure with different level of texture and grain refinement.

References

M.F. Ashby, Designing hybrid materials. Acta Mater. **51**, 5801 (2003)
W.A. Backofen, I.R. Turner, D.H. Avery, Superplasticity in an Al-Zn alloy. Trans. ASM **57**, 980–989 (1964)
N. Balasubramanian, R.S. Mishra, K. Krishnamurthy, Friction stir channeling: characterization of the channels. J. Mater. Process. Technol. **209**(8), 3696–3704 (2009)
P.B. Berbon, W.H. Bingel, R.S. Mishra, C.C. Bampton, M.W. Mahoney, Friction stir processing: a tool to homogenize nanocomposite aluminum alloys. Scr. Mater. **44**, 61 (2001)
I. Charit, R.S. Mishra, Low temperature superplasticity in a friction-stir-processed ultrafine grained Al-Zn-Mg-Sc alloy. Acta Mater. **53**(15), 4211–4223 (2005)
J. Datsko, C.T. Yang, Correlation of bendability of materials with their tensile properties. Trans. ASME B **82**(4), 309–313 (1960)
M. Dixit, J.W. Newkirk, R.S. Mishra, Properties of friction stir-processed Al 1100-NiTi composite. Scr. Mater. **56**, 541–544 (2007)
M. Drouzy, S. Jacob, M. Richard, Interpretation of tensile results by means of a quality index. AFS Int. Cast Metal J. **5**, 43–50 (1980)
J.D. Eshelby, Proc. Roy. Soc. Lond. **A241**, 376 (1957)
G.J. Grant, D. Herling, W. Arbegast, C. Allen, C. Degen, *2006 International Conference on Superplasticity in Advanced Materials*, Chengdu, China, 23 June 2006
Z. Hashin, S. Strikman, J. Appl. Phys. **33**, 3125 (1962)
S.M. Howard, B.K. Jasthi, W.J. Arbegast, G.J. Grant, D.R. Herling, Friction surface reaction processing in aluminum substrates. Friction stir welding and processing III as held at the 2005 TMS annual meeting, San Francisco, CA, 2005, pp. 139–146
L.B. Johannes, L.L. Yowell, E. Sosa, S. Arepalli, R.S. Mishra, Survivability of single-walled carbon nanotubes during friction stir processing. Nanotechnology **17**, 3081–3084 (2006)
R. Kapoor, V.S.H. Rao, R.S. Mishra, J.A. Baumann, G. Grant, Probabilistic fatigue life prediction model for alloys with defects: applied to A206. Acta Mater. **59**(9), 3447–3462 (2011)
R. Kapoor, K. Kandasamy, R.S. Mishra, J.A. Baumann, G. Grant, Effect of friction stir processing on the tensile and fatigue behavior of a cast A206 alloy. Mater. Sci. Eng. A **561**, 159–166 (2013)
N. Kumar, R.S. Mishra, C.S. Huskamp, K.K. Sankaran, Critical grain size for change in deformation behavior in ultrafine grained Al-Mg-Sc alloy. Scr. Mater. **64**(6), 576–579 (2011)
C.J. Lee, J.C. Huang, P.J. Hsieh, Mg based nano-composites fabricated by friction stir processing. Scr. Mater. **54**, 1415–1420 (2006a)
C.J. Lee, J.C. Huang, P.L. Hsieh, Compos. Mater. **313**, 69 (2006b)
Z.Y. Ma, R.S. Mishra, Friction stir surface composite fabrication. Surface engineering: in materials science II, TMS, Warrendale, PA, 2003, p. 243
Z.Y. Ma, R.S. Mishra, M.W. Mahoney, Superplasticity in cast A356 induced via friction stir processing. Scr. Mater. **50**(7), 931–935 (2004)
Z.Y. Ma, F.C. Liu, R.S. Mishra, Superplastic deformation mechanism of an ultrafine-grained aluminum alloy produced by friction stir processing. Acta Mater. **58**(14), 4693–4704 (2010)
M. Mahoney, R.S. Mishra, T. Nelson, J. Flintoff, R. Islamgaliev, Y. Hovansky, High strain rate, thick section superplasticity created via friction stir processing. Friction stir welding and processing, Indianapolis, IN, 4–8 Nov 2001, pp. 183–194
R.S. Mishra, M.W. Mahoney, S.X. McFadden, N.A. Mara, A.K. Mukherjee, High strain rate superplasticity in a friction stir processed 7075 al alloy. Scr. Mater. **42**, 163 (1999)
R.S. Mishra, M.W. Mahoney, in *Friction Stir Processing: A New Grain Refinement Technique To Achieve High Strain Rate Superplasticity in Commercial Alloys*. Superplasticity in Advanced Materials, ICSAM-2000 Materials Science Forum, 357–3 (2001), p. 507
R.S. Mishra, M.W. Mahoney, U.S. Patent (6,712,916) on "Metal superplasticity enhancement and forming process," 30 Mar 2004

R.S. Mishra, M.W. Mahoney, *Friction Stir Processing, in Friction Stir Welding and Processing,* ed. by R.S. Mishra, M.W. Mahoney (ASM International, Materials Park, 2007), pp. 309–350. ISBN-13: 978-0-87170-840-3

R.S. Mishra, Friction stir processing for superplasticity. Adv. Mater. Process. **162**(2), 45–47 (2004)

R.S. Mishra, Integral channels in metal components, U.S. Patent 6,923,362, 2005

R.S. Mishra, Z.Y. Ma, I. Charit, Friction stir processing: a novel technique for fabrication of surface composite. Mater. Sci. Eng. A **A341**, 307 (2003)

R.S. Mishra, M.W. Mahoney, Metal superplasticity enhancement and forming process, U.S. Patent 6,712,916, 30 March 2004

Y. Morisada, H. Fujii, T. Nagaoka, M. Fukusumi, Structural materials properties microstructure and processing. Mater. Sci. Eng. **419**, 344 (2006)

Y. Murakami, M. Endo, Effects of defects, inclusions and inhomogeneities on fatigue strength. Int. J. Fatig. **16**, 163–182 (1994)

J.W. Newkirk, R. Mishra, J. Thomas, J.A. Hawk, Friction stir processing to create surface composites. Advances in powder metallurgy & particulate materials, MPIF, Princeton, NJ, 2003, pp. 6.60–6.70

T.G. Nieh, J. Wadsworth, O.D. Sherby, *Superplasticity in Metals and Ceramics* (Cambridge University Press, Cambridge, UK, 1997)

S.K. Panigrahi, K. Kumar, N. Kumar, W. Yuan, R.S. Mishra, R. DeLorme, B. Davis, R.A. Howell, K. Cho, Transition of deformation behavior in an ultrafine grained magnesium alloy. Mater. Sci. Eng. A **549**, 123–127 (2012)

U. Ramadorai, J.W. Newkirk, R.S. Mishra, J.A. Hawk, *Surface Modification of Aluminum Alloys to Create in Situ Surface Composites*. 4th ASM International Surface Engineering Congress and 19th International Conference on Surface Modification Technologies, August 2005

S.R. Sharma, R.S. Mishra, Fatigue crack growth behavior of friction stir processed aluminum alloy. Scr. Mater. **59**(2008), 395–398 (2008)

S.R. Sharma, Z.Y. Ma, R.S. Mishra, Effect of friction stir processing on fatigue behavior of A356 alloy. Scr. Mater. **51**(3), 237–241 (2004)

C.B. Smith, R.S. Mishra, *Friction Stir Processing for Enhanced Low Temperature Formability: A Volume in the Friction Stir Welding and Processing Book Series* [Paperback] (2014). ISBN-10: 012420113X

J.E. Spowart, Z.-Y. Ma, R.S. Mishra, The effect of friction stir processing (FSP) on the spatial heterogeneity of discontinuously-reinforced aluminum (DRA) microstructures. Friction stir welding and processing II, 2003 TMS annual meeting, San Diego, CA, 2–6 Mar 2003, pp. 243–252

S. Tandon and R. S. Mishra, unpublished research

Y. Wang and R.S. Mishra, Finite element simulation of selective superplastic forming of friction stir processed 7075 Al alloy, Materials Science and Engineering A, **463**, 245–248. (2007)

W. Yuan, S.K. Panigrahi, J.-Q. Su, R.S. Mishra, Influence of grain size and texture on Hall-Petch relationship for a magnesium alloy. Scr. Mater. **65**(11), 994–997 (2011)

J. Zheng, R.S. Mishra, P.B. Berbon, M.W. Mahoney, Microstructure and mechanical behavior of friction stir processed Al-Ti-Cu alloy. Friction stir welding and processing, Indianapolis, IN, 4–8 Nov 2001, pp. 235–242

Chapter 10
Residual Stresses and Mitigation Strategies

10.1 Introduction

10.1.1 Definition

The stresses existing in an elastic body in the absence of external forces or loads (thermal or mechanical) are termed as residual stresses. This can be appreciated further from the schematic illustrated in Fig. 10.1 which shows an irregular externally loaded two dimensional body. The external forces or loads are denoted by symbol F_i, where $i = 1–5$ and acts on a small region indicated by A. After removal of external forces or loads, two possible scenarios for the region denoted by letter A are: (a) there are no internal stresses, and (b) there are internal stresses present in the absence of external loads F_i. The stresses within the body in state (b) are termed as residual stresses.

10.1.2 Causes of Residual Stress

Residual stresses are a consequence of inhomogeneous thermal distribution and plastic deformation of different regions during processing of a component. This can arise due to complex thermal-metallurgical-mechanical interactions during processing of an elastic body. This aspect of residual stress is pictorially depicted in Fig. 10.2 (Inoue and Wang 1985). For the introduction of residual stresses in a given component it is not necessary for all the factors mentioned in Fig. 10.2 to be present simultaneously. For example, the heating and cooling of a plate may lead to generation of thermal stresses which can eventually lead to residual stresses. In general, uneven or inhomogeneous heating and cooling leads to the generation of residual stresses. However, microstructural changes due to transformations during isothermal heat treatment can also lead to residual stresses.

R.S. Mishra et al., *Friction Stir Welding and Processing: Science and Engineering*, 297
DOI 10.1007/978-3-319-07043-8_10, © Springer International Publishing Switzerland 2014

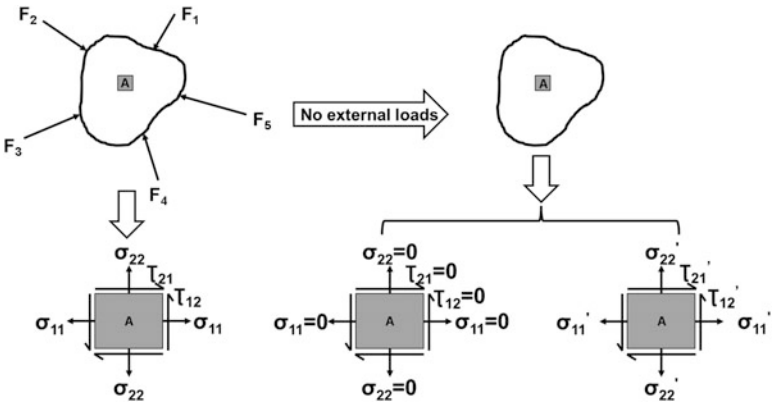

Fig. 10.1 A schematic illustration of definition of residual stresses

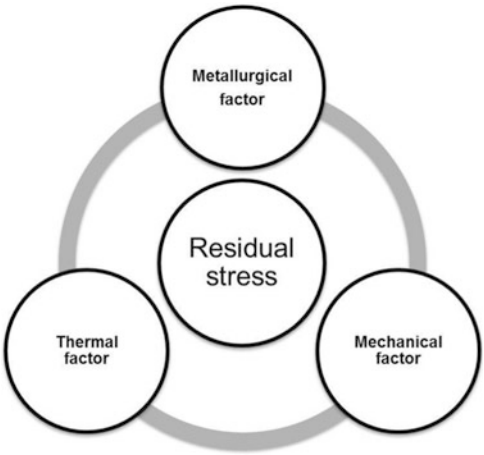

Fig. 10.2 Schematic illustration of residual stress development in an elastic body as a result of coupling between metallurgical, thermal, and mechanical factors

10.1.3 Types of Residual Stresses

Almost all manufacturing processes lead to generation of residual stresses which can differ in nature and scale. Figure 10.3 very broadly classifies residual stresses into two categories—macrostresses and microstresses. It further illustrates how industrial processes such as peening, cold hole expansion, bending and welding can lead to generation of macrostresses. Microstressess occur at much smaller scale than that of macrostresses. Processes which can lead to generation of microstresses are also illustrated in Fig. 10.3. All thermo-mechanical treatments which introduce macrostresses can also generate microstresses. In some cases it is quite possible that the two types of stresses coexist.

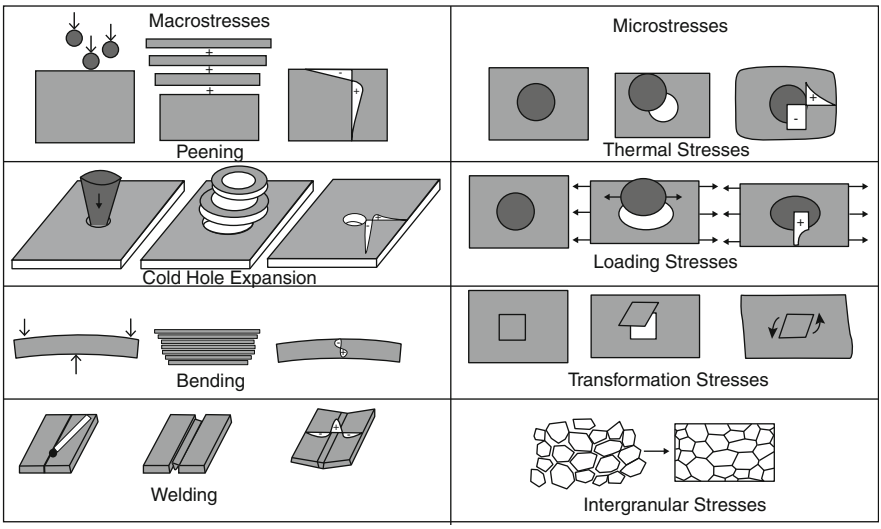

Fig. 10.3 A schematic of some industrial processes which lead to generation of residual stresses (adapted from Withers 2001)

Depending on the length scale residual stresses are again categorized based on the dimension over which they equilibrate: (a) Type I (equilibrium exists over the scale of the structure), (b) Type II residual stresses equilibrate over tens of grains, and (c) Type III exists at atomic scale (see Fig. 10.4). A rectangular box filled with grey color represents a component and shows the variation of Type I residual stress over the length of the entire structure. To represent Type II and Type III residual stresses, which are microscopic and submicroscopic in scale, a magnified image of a small white colored region in the grey colored rectangular box is shown next to it. Below this is shown variations of such stresses over the length of a few grains. These are type II residual stresses and an average value is also shown over the same dimension. Type III stresses are shown as variation of residual stresses within a grain and can exist due to the presence of defects like dislocations, precipitates, etc.

Type II and Type III are beyond the scope of the present book and only Type I residual stresses would be discussed which is relevant to welding processes in general and friction stir welding in particular.

10.1.4 Implications of Residual Stresses

Residual stresses can be beneficial or deleterious depending on the nature of stresses and the conditions considered. For example, the growth rate of a crack is accelerated when residual stresses are tensile and retards under compressive conditions (See Chap. 5 Figs. 5.12 and 5.15). This is a consequence of the effect on stress intensity at the crack tip given by

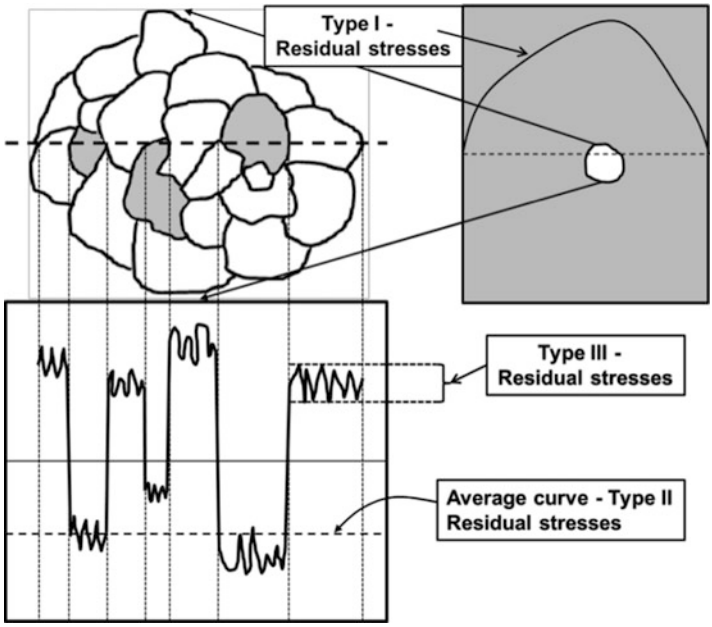

Fig. 10.4 A schematic illustration of different types of residual stresses commonly observed in functional materials (Adapted from Withers and Bhadeshia (2001))

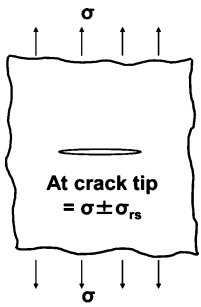

Fig. 10.5 A through crack in an infinite plate illustrating the effect of residual stress on crack intensity factor; σ_{rs} = residual stress

$$K_I = \sigma\sqrt{\pi a} \tag{10.1}$$

where K_I and σ are stress intensity factor and applied stress, respectively (Fig. 10.5). Depending on the magnitude and direction of residual stress σ reduces or increases by an equal amount. If K_I exceeds the K_{IC} (critical stress intensity factor—a material property), the crack propagates triggering a failure of the component. In such instances compressive residual stresses are beneficial, although the same is not true where buckling strength of the structure is of prime importance. Other properties which are influenced by the presence of residual stress include fatigue life, fracture toughness, stress corrosion cracking, etc. (Fig. 10.13).

10.2 Residual Stresses in Welding

During welding a concentrated heat source is applied along the weld centerline to form a joint. This heat source results in an intense thermal gradient in the material which causes inhomogeneous deformation of the workpiece being welded. Figure 10.6 schematically shows the temperature and thermal stress distribution at different positions (Fig. 10.6a) of the plate for a fusion welding process. Compared to other locations the peak temperature is highest at OO (Fig. 10.6c) which is just under the heat source and thermal stresses are close to zero. In case of friction stir welding, the region in close proximity to the tool has thermal stresses close to the yield stress of the alloy at that temperature. In the vicinity of the weld centerline along OO, the thermal stresses are compressive and on moving further towards the edge they turn tensile before tapering down to zero. Along the line BB (Fig. 10.6d) which is behind the moving heat source, the welded zone begins to cool down. The welded material tries to contract. However, the material surrounding the weld zone restricts it from doing so. Hence, this results in the generation of tensile stresses. The tensile thermal stress magnitude at location AA (Fig. 10.6e) is even higher since temperature at this location has reduced even further. Finally, at line CC (Fig. 10.6b) ahead of the heat source the plate is still at its initial temperature and thermal stresses are still zero.

At the end of welding cycle when the workpiece has cooled down sufficiently, the clamps restraining the workpiece are released and the thermal stresses

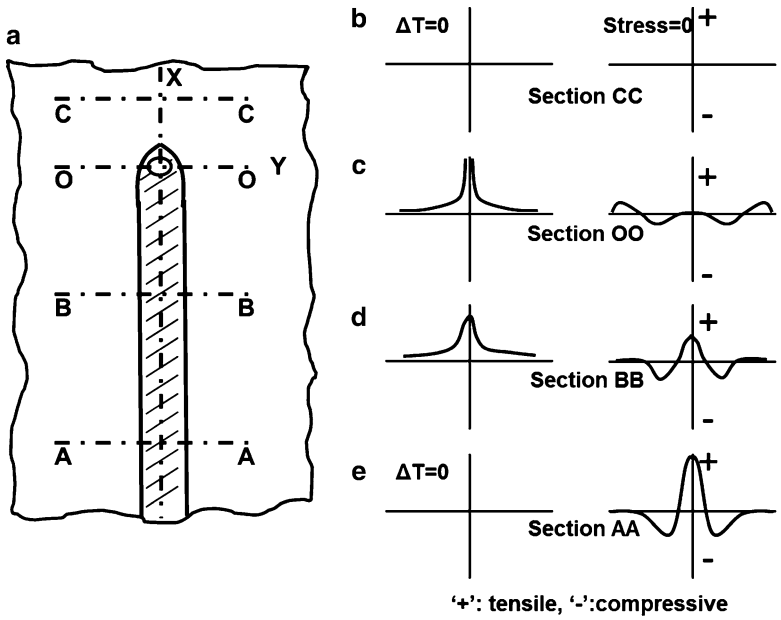

Fig. 10.6 Schematic showing temperature and thermal stress distribution at different regions of the plate being fusion welded (adapted from Masubuchi 1980a)

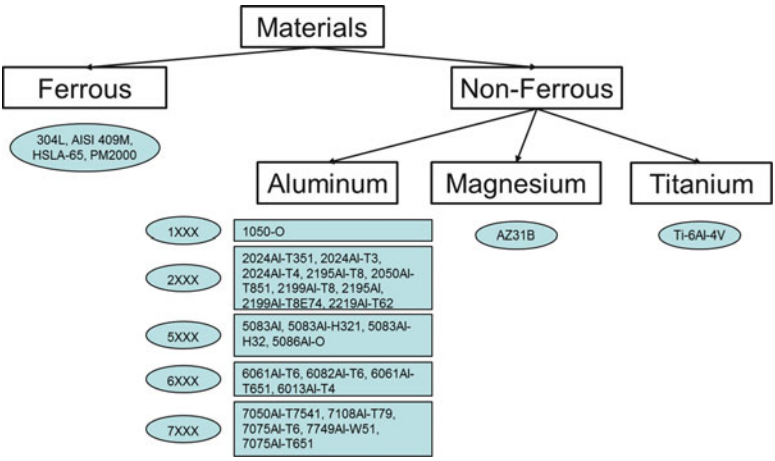

Fig. 10.7 An overview of the materials investigated for residual stress and distortion study in friction stir welding

redistribute themselves and result in residual stresses (and resulting in distortion). This generic description of thermal and residual stress development provides an insight in how such stresses develop during welding process. Later in this chapter, a schematic model is included to discuss the origin of residual stress during friction stir welding.

10.2.1 Residual Stresses in Friction Stir Welding

At the early stages of friction stir welding research, due to the solid state nature of the process the residual stress generated during joining was considered to be nominal. But, subsequent research indicates that a significant amount of residual stresses, sometime approaching the yield strength of the alloy can exist. The choice of friction stir welding process parameters controls the magnitude and distribution of residual stresses in friction stir welded structure. Section 10.5 discusses this aspect in greater detail. Among various parameters, one parameter is heat input which is defined as weld power per unit length. However, compared to other commercially available techniques, it is not possible to carry out friction stir welding at very high speed. So, even if the weld power requirement is low compared to other welding techniques, heat input becomes significant. Hence, consideration of total heat input per unit length suggests significant level of residual stresses.

Due to historical reason, the early research in residual stress and distortions is predominantly for aluminum alloys. Figure 10.7 provides an overview of the materials investigated for residual stress studies. Table 10.1 lists some of the aluminum alloys investigated so far. In addition, the processing parameters details and peak value of residual stresses observed along with the techniques used to

Table 10.1 A summary of processing parameters and residual stress measurement of friction stir welded aluminum alloys

Alloy	YS (MPa)	Tensile stress (max), MPa	Tensile RS (weld centerline), MPa	Tool traverse speed (mm/min)	Tool rotation rate (rpm)	Plate dimension (after joining)			Measurement technique	References
2024Al-T3	345	185	150	200	800	500	700	5	Neutron and synchrotron diffraction	Altenkirch et al. (2009a)
2195Al	215 (weld plate)	150	100	150	300	910	300	12.5	X-ray diffraction	Hatamleh (2009)
2024Al-T351	470	56	40	71.5	750	100	140	3	Cut-compliance technique	Fratini et al. (2009)
5083Al-H321	228	155	120	160	600	1,000	200	3.5	Slot sectioning stress relaxation method	Han et al. (2011
6061Al-T6	276	140	50	279		300	300	6	Neutron diffraction	Wang et al. (2000)
6013Al-T4	203	200	80	1,000	1,500			1.8	X-ray diffraction	Lemmen et al. (2010)
7075Al-T6	510	92	40	100	715				Cut-compliance technique	Buffa et al. (2008)
7449Al		200	200	250	225	1,000	300	12	Synchrotron diffraction	Altenkirch et al. (2008)
7075Al-T6	525 (BM), 390 (Nugget)	225	200	300	280			2	X-ray diffraction	Lemmen et al. (2010)
7108Al-T79	400	200	120	600					Ultrasonic wave technique	Gachi et al. (2009)

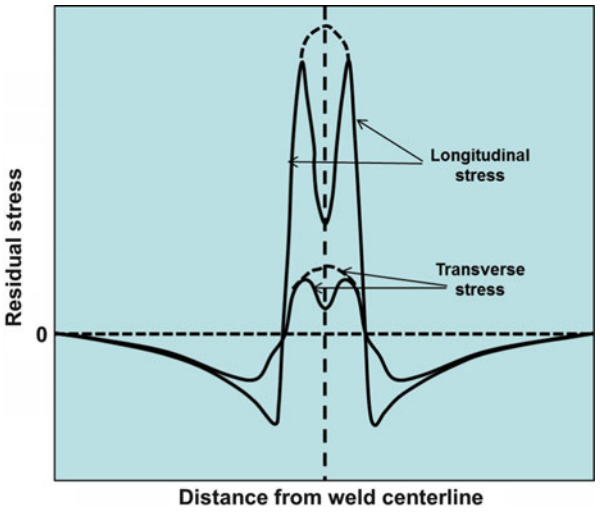

Fig. 10.8 Schematic showing the distribution and shape of residual stresses across the width of friction stir welded components

measure such stresses are included. Evidently, residual stresses in the welded structure are of considerable proportion with respect to the yield strength of the welded alloy. Such a level of residual stress in the friction stir welded structure is a matter of some concern from application point of view. Hence, every effort should be made to mitigate magnitude of residual stresses.

The general trend observed in terms of distribution and shapes of residual stress curves across the width of the weldments are shown in Fig. 10.8. Salient features of this distribution with respect to friction stir welded ferrous and non-ferrous alloys are:

- In general, longitudinal residual stresses are tensile in nature in welded region. Outside of the welded region it is compressive. It becomes asymptotically zero on moving towards the edge of workpiece.
- Overall, transverse residual stresses are also tensile in nature. The variation across the width of the weldments can be similar. However, in general, the magnitude of these stresses is smaller than the longitudinal residual stresses.
- Maximum longitudinal tensile stress mostly occur either in thermo-mechanically or heat-affected zones. In few instances, maximum longitudinal stresses have been found at weld centerline also.
- It leads to two different types of residual stress profile—M-shaped and inverted V- shaped profiles (Fig. 10.8).
- The residual stress curves can be approximated using following expression:

$$\sigma_x(y) = \sigma_{\mathrm{m}}\left\{1 - \left(\frac{y}{b}\right)^2\right\}\exp\left\{-\frac{1}{2}\left(\frac{y}{b}\right)^2\right\} \tag{10.2}$$

where σ_{m}, y, and b are peak tensile longitudinal RS, distance along y coordinate, and width of the tensile residual stress zone. Above expression for residual stress

is valid for fusion welded structures. But, given the similarity between the profiles of residual stresses in friction stir welding and fusion welding, the expression is expected to hold good for friction stir welded material also.

10.3 Measurement of Residual Stresses

Table 10.2 summarizes the techniques available to measure residual stresses and is classified into three groups: destructive, semi-destructive, and non-destructive. The intention here is to introduce some of the techniques used for residual stress measurement. Destructive methods involve the removal of material in a pre-conceived manner to assess uniaxial, biaxial, or triaxial stresses. In this method a priori knowledge of stress distribution is essential for selection of measurement technique to determine the stress state. Hole drilling and indentation are considered semi-destructive due to insignificant amount of material removal for residual stress measurements. X-ray diffraction, neutron diffraction, synchrotron diffraction, and ultrasonic wave velocity techniques are considered non-destructive since no material removal is required.

Although we are interested in residual stress distribution in essence all the techniques measures strain. The essential difference between destructive (or semi-destructive) and non-destructive methods is the manner in which the strains are measured for stress determination. To illustrate this point further, a schematic is drawn in Fig. 10.9. Here atoms and atomic bonds are represented by circles and springs. Figure 10.9a shows the material in relaxed state, i.e., in the absence of residual stress. Figure 10.9b represents a situation where residual stresses are present in the material. It is quite conceivable that the presence of stress in the material stretches the bonds, i.e., elastic strain exists. The non-destructive methods measure this strain. It is also possible to measure the strain by relaxing the stress. The stress relaxation is done by sectioning or material removal of the pre-stressed component. The material removal or sectioning results in relaxation of stretched bond, which is measured by strain gages. In relaxed state the state of the strain in a

Table 10.2 Residual stress measurement techniques

Method						
Destructive	Semi-destructive		Non-destructive			
Excision, sectioning, layer removal, tube splitting, crack compliance	Hole drilling, ring core	Indentation	X-ray diffraction	Neutron diffraction	Synchrotron diffraction	Ultrasonic wave velocity

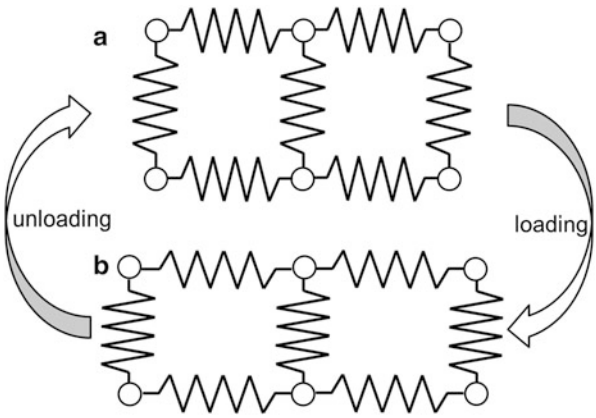

Fig. 10.9 Schematic to illustrate the change in state of strain in the material having residual stress. (**a**) relaxed state (**b**) loaded Circles and springs represent atoms and atomic bonds, respectively, between the atoms

material can be expressed by either Fig. 10.9a (when fully relaxed) or a state in-between Fig. 10.9a and b (when partially relaxed). Measurement of this change in elastic strain is the principle behind residual stress measurement using destructive or semi-destructive techniques.

Hole drilling and X-ray diffraction are by far the most widely used techniques for residual stress estimation and will be discussed below in some detail.

10.3.1 Hole Drilling

It is considered semi-destructive residual stress measurement technique and its widespread use stems from its simplicity and the use of inexpensive equipment in during the measurement. Two variants exist for this particular technique. In one procedure, a strain gage rosette is put around the region where stress measurement is to be done (Fig. 10.10a). A very small hole is drilled which results in relaxation of strain due to redistribution of stress in the region surrounding the hole. In another method, an annular groove is drilled around the strain gage rosette (Fig. 10.10a). It results in relaxation of strain in the material volume to which strain gages are attached. For a situation where there is no variation of stress along the depth of the specimen, the residual stresses at hole location can be measured using following expression for rectangular strain gage rosette (Schajer 2001),

$$\sigma_{\max}, \sigma_{\min} = -\frac{E}{2}\left(\frac{\varepsilon_3 + \varepsilon_1}{(1+\nu)\overline{a}} \mp \sqrt{\frac{(\varepsilon_3 - \varepsilon_1)^2 + (\varepsilon_3 + \varepsilon_1 - 2\varepsilon_2)^2}{\overline{b}}}\right) \tag{10.1}$$

Here, ε_1, ε_2, and ε_3 are elastic strain values measured using three strain gages in rectangular rosette. E and ν are elastic modulus and Poisson's ratio, respectively, of the specimen. $\overline{a}$ and $\overline{b}$ are calibration parameters which depend on the diameter and

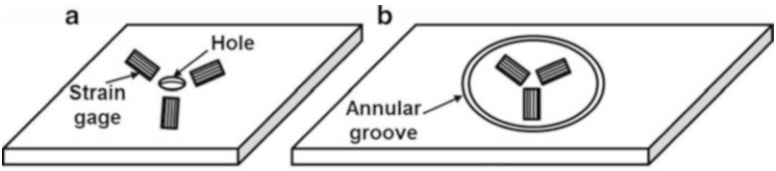

Fig. 10.10 A schematic showing strain gage rosette (**a**) around a hole drilled at the geometric center of the rosette and (**b**) within annular ring

depth of the drilled hole. For the situation where annular ring is drilled around the strain gage rosette and as a result complete relaxation of strain has taken place, the residual stresses is given by the expression (Schajer 2001),

$$\sigma_{\max}, \sigma_{\min} = -\frac{E}{2}\left(\frac{\varepsilon_3 + \varepsilon_1}{(1-\nu)} \mp \sqrt{\frac{(\varepsilon_3 - \varepsilon_1)^2 + (\varepsilon_3 + \varepsilon_1 - 2\varepsilon_2)^2}{(1+\nu)}}\right) \tag{10.2}$$

For the cases where significant stress gradient exists along the depth of the specimen other formulations of stress calculation based on strain measurements is used.

10.3.2 X-Ray Diffraction

As mentioned before, this is considered as a non-destructive technique, and is the most widely used method for residual stress measurement (Withers 2001). As explained using Fig. 10.9, in this case the strain is measured in the specimen in pre-stressed condition, which in turn is used to calculate stress. The strain is measured by measuring the interplanar spacings of different planes. For such purpose, X-rays are focused on the surface of the specimen on which residual stress measurement is to be done and intensity versus diffraction angle is recorded. Figure 10.11 shows the basic principle involved in the measurement of residual stresses using X-ray diffraction technique. It shows that once diffraction condition is met, X-ray gets diffracted from a set of crystallographic planes at an angle 2θ. This condition is given by the relationship proposed by Bragg,

$$\lambda = 2d_{hkl} \sin(\theta) \tag{10.3}$$

where λ, d_{hkl}, and θ are X-ray wavelength, interplanar spacing of plane {hkl}, and Bragg's angle, respectively. Equation (10.3) indicates that depending on the interplanar spacing the Bragg's angle would change. The interplanar spacing of a particular family of planes {hkl} depends on various factors such as composition, temperature, residual stress, etc. Hence, with regard to residual stress, the Bragg's angle for a set of planes {hkl} increases or decreases depending on whether the

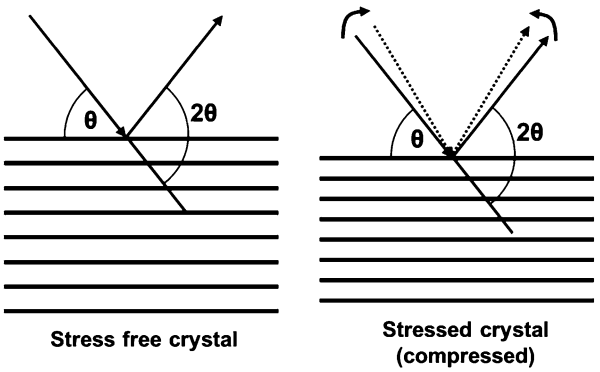

Fig. 10.11 Schematic illustration of basic principle X-ray diffraction in the measurement of residual stresses

existing stress has decreased or increased the interplanar spacing. Figure 10.11 shows how Bragg's angle increases for a sample under compressive loading. The strain perpendicular to the diffracting plane is calculated using following expression,

$$\varepsilon_i = \frac{d_{\mathrm{hkl}} - d_{0,\mathrm{hkl}}}{d_{0,\mathrm{hkl}}} \tag{10.4}$$

where $i = \mathrm{x}$, y coordinates. $d_{0,\mathrm{hkl}}$ is interplanar spacing of {hkl} family of planes in stress-free condition. The calculation of $d_{0,\mathrm{hkl}}$ should be performed in a region which is free from residual stress. As mentioned before, compositional changes and temperature might also affect the interplanar spacing. Hence, in a process like welding the interplanar spacing {hkl} across weld line is expected to be different even in the absence of residual stresses due to difference in microstructure in different regions. Therefore, interplanar spacing is measured in stress free condition in different microstructural states at multiple locations. Finally, the stresses are calculated using following relationship,

$$\sigma_{\mathrm{x}} = \frac{E}{(1-\nu^2)}\left(\varepsilon_{\mathrm{x}} + \nu\varepsilon_{\mathrm{y}}\right) \tag{10.5}$$

$$\sigma_{\mathrm{y}} = \frac{E}{(1-\nu^2)}\left(\varepsilon_{\mathrm{y}} + \nu\varepsilon_{\mathrm{x}}\right) \tag{10.6}$$

where ν is Poisson's ratio. Since, X-ray diffraction measures the stress at the surface of a component where essentially biaxial stress of state exists, Eqs. (10.5) and (10.6) are adequate to compute both components of the residual stress. There are situations where stresses within the penetration depth of X-rays (~100 μm), may exist perpendicular to the plane of residual stress measurement. In such cases, biaxial assumptions might not hold good. In such cases, triaxial method should be invoked to calculate all three components of stresses.

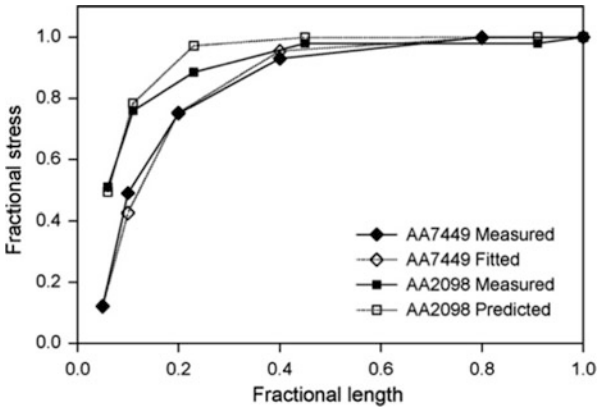

Fig. 10.12 Effect of sectioning on the longitudinal residual stress distribution in the weldments (Altenkirch et al. 2008, 2009b, reprinted with permission from Elsevier)

10.3.3 Role of Sample Size in the Measurement of Residual Stresses

The literature shows that different sample sizes have been used for measurement of residual stresses. In this section we will see how the sample size used for the measurement purposes can affect the outcome of the measurement. Different size samples are chosen either due to the constraint imposed by the measurement devices or a correlation needs to be established between residual stress and a particular property of the material. It is well-documented in literature that sectioning of the welded samples lead to relaxation of residual stresses. To illustrate this point further, the work done by Altenkirch et al. (Altenkirch et al. 2008, 2009b) on AA7449 and AA2098 alloys are included in Fig. 10.12. It shows the stress remaining (fractional stress defined as the ratio of stress remaining and stress at the weld centerline in as-welded condition) at weld centerline as a function of fractional length of the plate. It is evident that the original stress level is maintained up to 40 % fractional length of the plate. When fraction length reaches below 10 % of the original length, the remnant residual stresses at weld centerline were ~50 % and ~10 % for AA2098 and AA7449 alloys, respectively.

The experimentally measured curve can be curve fitted with following empirical expression,

$$\sigma_{relax} = \sigma_o \left[1 - \exp\left(-\frac{l_r - l_{relax}}{l_{char}}\right)\right] \tag{10.7}$$

where σ_{relax}, σ_0, l_r, l_{relax}, and l_{char} are stress at the weld centerline after sectioning, stress at the weld centerline in as-welded condition, remaining length, length at which RS becomes zero, and characteristics distance beyond which sectioning does not influence RS distribution, respectively.

This example exemplifies the role sample dimensions play in the measurement of residual stresses. Therefore, a careful selection of sample size to obtain representative residual stress measurement is required.

10.4 Effect of Residual Stress on Properties

Figure 10.13 shows pictorially the properties which may get influenced by the presence of residual stresses. However, the evaluation of the influence of the residual stress on these properties is very difficult because these properties (except dimensional stability) are not only dependent on the level of such stresses but also on the microstructural state of the alloy. Any welding technique including friction stir welding modifies the microstructure in the welded zone. Hence, a great care should be exercised while interpreting the results on the influence of residual stresses on the properties mentioned in Fig. 10.13.

Figure 10.14 shows how presence of residual stresses can alter the buckling strength of a material. Figure 10.14a shows a slender cylindrical bar under compressive load. The bar contains a compressive residual stress oriented along the loading direction. The material shows elastic-perfectly plastic deformation behavior. Figure 10.14b shows two different stress-strain curves. In the absence of any residual stress, the bar being made of elastic-perfectly plastic material, follows the path OA'AB'B. However, in the presence of a compressive residual stress of magnitude

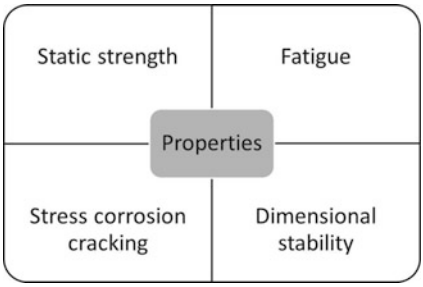

Fig. 10.13 Some properties which may get affected by the presence of residual stresses

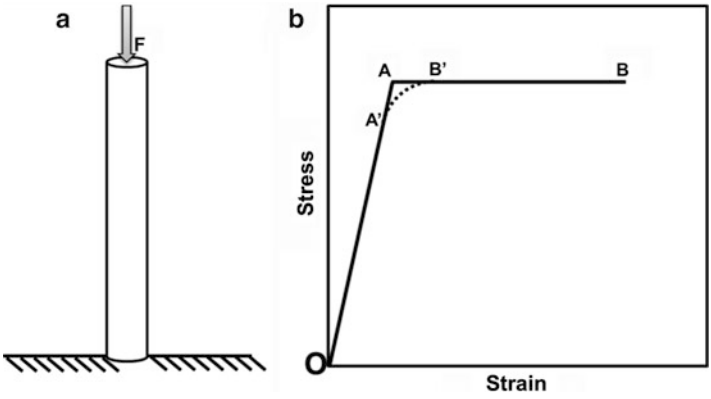

Fig. 10.14 (**a**) A cylindrical bar containing compressive residual stress along the axis of the cylinder experiencing compressive loading. (**b**) Modification of stress-strain curve due to the presence of residual stresses (Adapted from Masubuchi 1980b)

σ_{rs} the material takes the path OA'B'B during deformation. Point A in the stress-strain curve represents yield strength (σ_Y) of the material. However, in the presence of residual stress, the yield strength of the material is below point A, i.e., when $\sigma + \sigma_{rs}$ equals to σ_Y. It implies that applied stress σ is lower than σ_Y. This point corresponds to A' in the stress-strain curve in Fig. 10.14b. Another interesting feature which can be noted is decreasing influence of residual stress with continued plastic deformation. At point B' the influence of residual stress on flow stress vanishes completely.

Similarly, fatigue properties are strongly affected by the presence of residual stresses. However, quantification of such change is not an easy task. Welding process not only introduces residual stresses in a component but also modifies microstructure in the welded zone. Residual stress and change in microstructure both modify the fatigue deformation behavior of welded materials. Researchers have tried deconvoluting these two components and studied impact of each on fatigue crack growth rate (Bussu and Irving 2003; Pouget and Reynolds 2008; Fratini et al. 2009). To study the effect of microstructure on fatigue crack growth rate, it can be subjected to heat treatment to relieve the stresses. However, it should be ensured that the microstructure does not change to the extent that it changes the properties of the material significantly from the one obtained in as-welded condition. Another means by which residual stresses can be relieved is by deforming the welded workpiece plastically. This also should be done in such a way that microstructure and hence mechanical properties are still representative of as-welded condition. The difference in the crack growth rates in as-welded and stress-relieved conditions can be used to elucidate the role of residual stresses on the fatigue deformation behavior. In friction stir welded plates, it has been found that crack growth rate is slower in heat-affected zone and faster in nugget compared to base material. Data contradicting the trend observed for crack growth rate in different zone have also been reported in literature.

10.5 Dependence of Residual Stresses on Friction Stir Welding Parameters

As mentioned before there are number of processing parameters which affect the state of residual stresses and resulting distortion of a friction stir welded plate. Figure 10.15 summarizes all the parameters which may affect generation of residual stresses in friction stir weldments. It is evident that all these parameters can affect the thermal profile during friction stir welding process. As we know thermal excursion has profound impact on the generation of residual stresses and any modification in it would have bearing on the thermal stresses and hence residual stresses. Although all the parameters mentioned in Fig. 10.15 may affect the residual stresses, the role of tool traverse speed and tool rotation rate are most widely studied in this context.

Figure 10.16 illustrates the effect of tool rotation rate on residual stresses. In this particular example a 5083Al-H321 plate was used for welding. Feed rate (tool

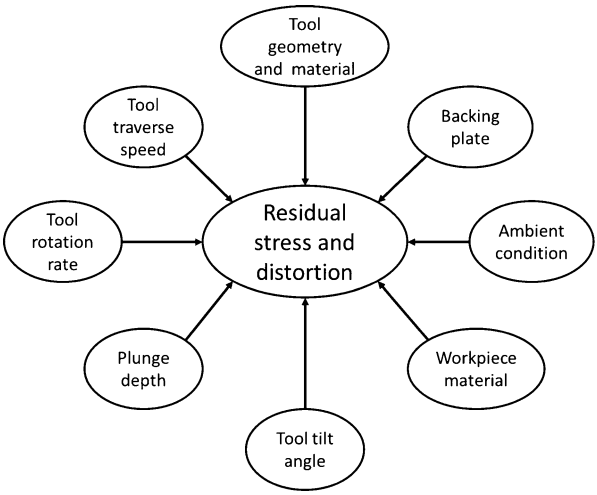

Fig. 10.15 Schematic illustration of the parameters affecting residual stresses and distortions in the welded component

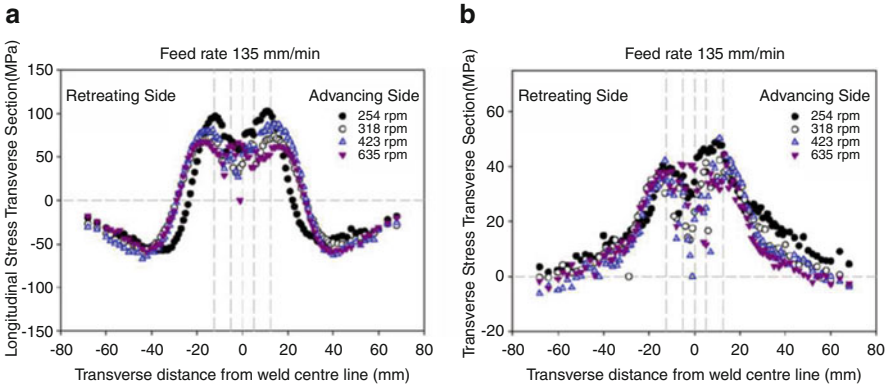

Fig. 10.16 Effect of tool rotation rate on (**a**) longitudinal and (**b**) transverse residual stresses in 5083Al alloy (Lombard et al. 2009, reprinted with permission from Elsevier)

traverse speed) and tool rotation rates were variables (Lombard et al. 2009). Figure 10.16 shows the variation in longitudinal and transverse residual stress for tool rotation rates ranging from 254 to 635 rpm at a constant feed rate of 135 mm/min. It shows a systematic decrease in peak and weld centerline longitudinal residual stress values (Fig. 10.16a) with increase in tool rotation rate. Other point which can be noted is increase in the width of welded region containing longitudinal tensile residual stresses. However, the increase of the width is not monotonic. For tool rotation rate 318 rpm and above, no increase in the width of the zone containing longitudinal tensile residual stresses. The variation of transverse residual stress across the weld centerline as a function of tool rotation rate is not

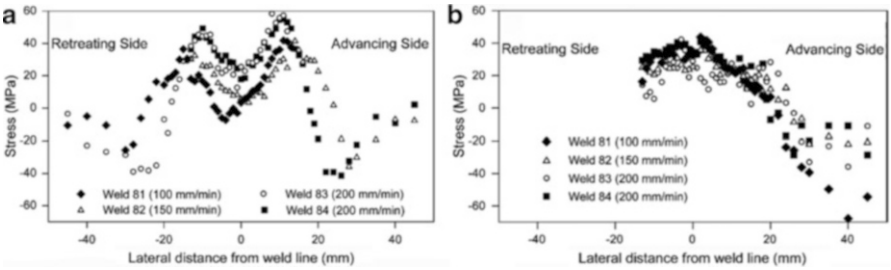

Fig. 10.17 Effect of tool traverse speed on the distribution of (**a**) longitudinal and (**b**) transverse residual stresses across the width of 5083Al weld (Peel et al. 2003, reprinted with permission from Elsevier)

well defined. However, as reported in literature, here also overall the longitudinal residual stresses are greater than the transverse residual stresses.

The observed trend as a function of tool rotation rate can be rationalized as follows. In general, increasing tool rotation rate causes the peak temperature in the plate being welded to rise. The degree of annealing and consequently thermal stress relieving is more at higher peak temperature for the material volume on the trailing side in the wake of the friction stir welding tool. This results in a decrease in residual stress. Higher peak temperature may also cause higher width of the nugget which will, in turn, increase the width of the zone containing tensile longitudinal residual stresses.

Similar to the tool rotation rate, the variation in the feed rate or the tool traverse speed also brings about changes in the distribution of residual stresses in the welded specimens. Figure 10.17 shows changes in the distribution of residual stresses as a function of tool traverse speed (Peel et al. 2003). Overall, a decrease in longitudinal residual stresses can be noted from Fig. 10.17a with decrease in tool rotation rate. As was the case with the change in tool rotation rate, in this case also no general trend could be observed in the case of transverse residual stresses with change in tool traverse speed.

A decreasing tool traverse speed causes higher heat input in the material during welding. It causes temperature to go up in the sample being welded. As mentioned before, a higher peak temperature would have higher thermal stress relieving effect on the material volume on the trailing side of the friction stir welding tool. Hence, thermal stress relieving effect would cause a lower residual stresses at lower tool rotation rate.

Figure 10.17 also includes effect of tool geometry on residual stresses. The weld number 83 and 84 were made at 200 mm/min tool traverse speed. However, the diameter and pitch of the thread of the tool pin were 5.0 mm and 0.8 mm, respectively for weld 83. For weld 84, the tool pin was 6 mm in diameter and had 1.0 mm pitch of the thread. The careful observation of the results presented for these cases suggest not much dependence of residual stress distribution on pin geometries. Given that the contribution of the tool pin to the total heat input is very small compared to the contribution made by the shoulder of the tool, such a small

variation in the geometry may not cause much change in the distribution and values of the residual stresses.

Section 10.3.3 discussed the effect of sample dimensions on the measurement of residual stresses. The sectioning of the welded samples for residual stress measurement results in stress relaxation due to reduced stiffness of the welded materials. Similarly, if a relatively smaller component is welded, it will impose less constraint on the contracting welded zone (to be discussed in Sect. 10.6). It, therefore, results in the development of residual stresses of smaller magnitude. As sample dimensions are increased, the material surrounding welded zone will impose increasingly higher level of constraints, thereby making contraction of the welded zone more difficult. Hence, it would result in the development of higher level of residual stresses. Although larger samples may introduce very high level of residual stresses, they present higher resistance to distortion due to higher cross-section or geometry related stiffness.

There is complete lack of a systematic study involving role of welding coupon size on the development of residual stresses. It is also worth mentioning that the experimental approach to address this issue would be a painstaking task. Given the current state-of-the-art of numerical methods, it would be a viable option to explore the role of coupon size numerically on the residual stresses and resulting distortions (Section 10.9).

10.6 Understanding Development of Residual Stresses in Friction Stir Welding

An understanding about the origin of residual stresses in welded components is of paramount importance and is key to mitigating residual stresses in the weldments and hence distortions. For this purpose a conceptual model is presented in Fig. 10.18. A rectangular bar of length l_o and width w is shown to be sandwiched between two rigid constraints (no deformation of the constraints) at the opposite end of the bar. When the temperature of an unconstrained bar is raised by T (Fig. 10.18b), it will elongate and the change in length is given by

$$\Delta l = l_o(1 + \alpha \Delta \mathrm{T}) \tag{10.8}$$

where Δl, l_o, α, and ΔT are change in length, initial length, coefficient of thermal expansion, and difference between final and initial temperature of the bar, respectively. In the absence of any constraints, the bar is free to expand. However, when constraints are present, $\Delta l = 0$. Due to which the bar would be subjected to compressive stress and strain. If temperature is raised sufficiently the bar might undergo plastic deformation.

Figure 10.18c, d describe a situation where such constraints have been removed at the end and $\Delta \mathrm{T} = 0$. If during heating ΔT was such that it deformed the bar only elastically, it will regain original dimension once $\Delta \mathrm{T} = 0$ (Fig. 10.18c). However, if

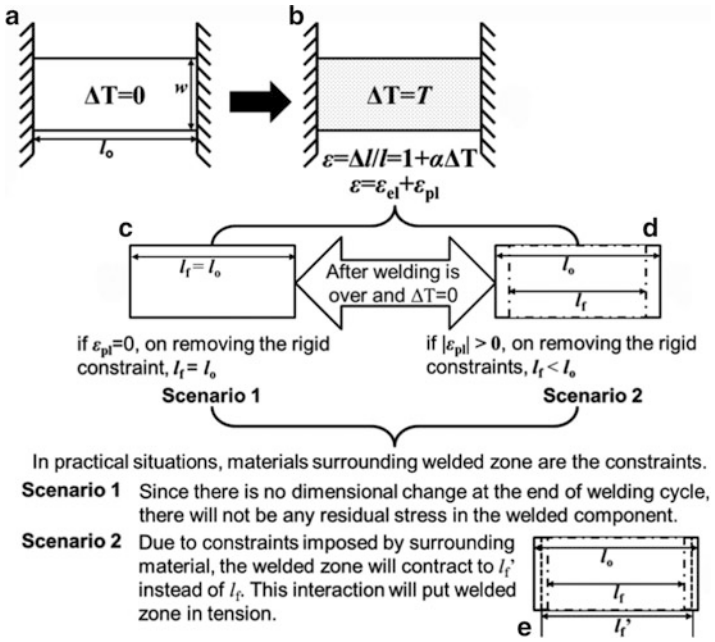

Fig. 10.18 A conceptual model to understand the development of residual stresses in friction stir welding, (**a**) A workpiece at room temperature, (**b**) workpiece heated to a temperature T, (**c**) workpiece showing original length regained after the welding, if $\varepsilon_{pl} = 0$, (**d**) workpiece comparing the length before and after welding if $|\varepsilon_{pl}| > 0$, (e) effect of constraints on the dimensional change

the change in ΔT (Fig. 10.18b) leads to plastic deformation of the bar, it would like to contract on removal of the constraint as it cools down so that eventually $\Delta T = 0$ (Fig. 10.18d). It contracts because the presence of rigid constraints places the bar in compressive state of stress and it results in compressive plastic strains in the bar. Hence, on removal of such constraints during cooling of the bar, it tries to contract. In both the cases since bar is allowed to achieve it equilibrium shape, it will be free from any residual stresses. In actual situations, for example, during welding, it is not possible to get rid of constrains completely. The material surrounding the welded zone will always impose some level of constraint on welded zone and would lead to introduction of residual stresses. The level of residual stresses will now depend of the extent of constraints imposed on the welded zone.

Scenario 1 in Fig. 10.18 describes a situation where bar was subjected to elastic compressive strain due to heating of the bar. If this strain is relaxed completely, there should not be any residual stress when all the external forces have been removed. In scenario 2 which refers to the case presented in Fig. 10.18d, it is shown in Fig. 10.18e that if the contraction of the bar takes place in constrained condition (constraints not shown), it will lead to tensile stresses in the welded zone.

This conceptual model suggests that compressive plastic strains accumulated during the thermal cycle, where flow stress of the material is lower than the thermal

stresses, in the welded zone are responsible for tensile residual stresses developed in the welded zone. Hence, mitigation strategies should be directed towards reduction or removal of such tensile stresses due to dimensional mismatch between welded zone and surrounding materials. In Sect. 10.8 where mitigation efforts have been presented, it will be discussed how those techniques help reduce such dimensional mismatch in different regions of the weld and hence influence the residual stress and distortion of the weldments.

10.7 Difference Between Residual Stress Generation in Friction Stir Welding and Fusion Welding

There are a few subtle differences in the manner in which residual stresses develop during fusion welding and friction stir welding. Figure 10.19 illustrates the deformation of the plate being welded using friction stir and fusion welding techniques. Figure 10.19a, b show that compressive plastic deformation (equivalent plastic strain) of the plate during welding starts when thermal stresses (Mises stress) become equal (point B) to the yield stress of the material. It is shown that thermal stresses increase and yield stress of the material decreases as temperature rises in the material. As long as thermal stresses are equal to the yield strength of the material, plastic strain keeps on accumulating in the welded region. During cooling cycle yield strength of the material starts to rise and a point is reached where it is higher than thermal stresses in the material. From this point onward the plastic deformation of the plate stops at the location under consideration.

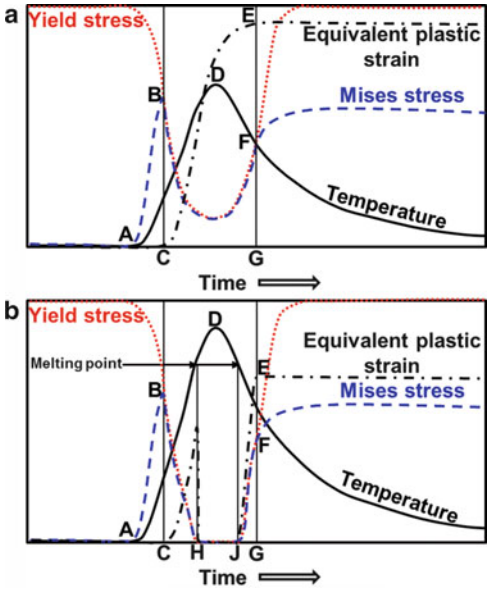

Fig. 10.19 Schematic illustrating the possible difference in residual stress generation between friction stir welding (solid state) and fusion welding; (**a**) Friction stir welding and (**b**) fusion welding

Friction stir welding being a solid-state joining technique peak temperature in the processed zone never exceeds melting point of the material. As name implies, in fusion welding temperature reaches well above melting point of the material. Comparison of Fig. 10.19a, b indicate that the compressive plastic strain continues to accumulate until thermal stresses become smaller than yield strength of the material in FSW (point F). For fusion welding it drops to zero when temperature exceeds the melting point of the material. In this case plastic strain again starts accumulating once solidification of melt pool starts and continues as along as yield strength and thermal stresses are equal (up to point F in Fig. 10.19b).

The compressive plastic deformation leads to a geometrical misfit between welded region and the material surrounding it. It eventually results in generation of tensile stresses in the welded region and compressive stresses in the regions away. Another source which adds to geometrical misfit emanates from solidification shrinkage of the melt pool. Shrinkage takes place due to material loss as a result of evaporation, spattering, etc. Hence, in friction stir welding the misfit occurs mostly due to compressive plastic deformation of the welded region, whereas it occurs due to combined effect of compressive plastic strain and solidification shrinkage in fusion welded structures.

10.8 Mitigation of Residual Stresses

A number of techniques such as thermal tensioning, active cooling, weld sequencing, precambering, post-weld heat treatment, etc. have been employed to mitigate residual stresses and resulting distortions of the welded structures using fusion welding. Some of these techniques have been utilized in friction stir welding also for the management of residual stresses and distortions. Some of these techniques will be described here.

10.8.1 Active Cooling

It is an in-situ technique used for mitigating residual stresses and hence distortion. As the name suggests, the mitigation is effected by modifying the existing thermal field due to friction stir welding by imposing an external source of cooling (active cooling).

The active cooling technique is described schematically in Fig. 10.20. Liquid nitrogen, liquid CO_2, and water are few examples of cooling media. Although, Fig. 10.20 shows location of the cooling nozzle on the trailing side of FSW tool, it can be anywhere in the vicinity of the tool. But, limited research has shown that location of the tool with respect to FSW tool is very important. In Sect. 10.9 the results of finite element analysis on the effect of location and number of nozzles are discussed. The use of cooling media basically modifies the thermal field (favorably) around the tool thereby reducing geometrical misfit between the welded zone and

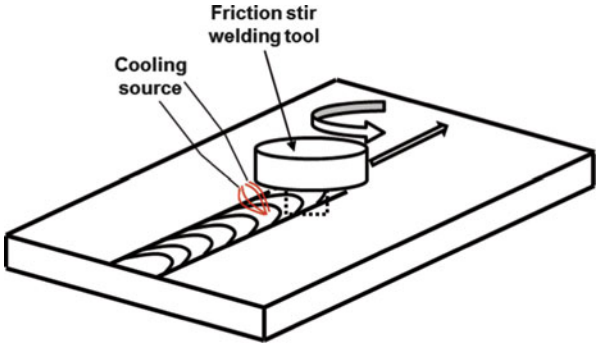

Fig. 10.20 Schematic illustration of deployment of active cooling source to mitigate residual stress

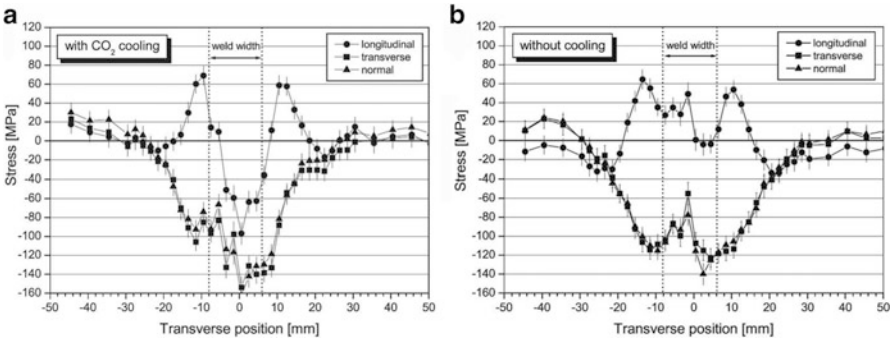

Fig. 10.21 Residual stress mitigation by the use of active cooling (in-situ cooling using liquid CO_2) on the trailing side of the tool; material: 2024Al-T351; residual stress distribution (**a**) with cooling and (**b**) without cooling (Staron et al. 2002, reprinted with permission from Springer)

the surrounding material. The reduction results in lower level of residual stresses in the welded structure.

Figure 10.21 provides an example of the effect of deployment of such active cooling media on the residual stress distribution (Staron et al. 2002). Figure 10.21a corresponds to the case where liquid CO_2 was used to mitigate residual stress. In the welded region all three (x, y, and z) components of the residual stress are compressive. However, for the case where welding was done without the aid of active cooling medium (Fig. 10.21b) the longitudinal residual stresses are tensile in nature. Evidently, the use of cooling medium during friction stir welding is an effective means of managing the distribution of residual stresses in welded structures.

10.8.2 Mechanical Tensioning

This is also a very effective technique for managing the distribution of residual stresses in welded components. A schematic of this technique is illustrated in Fig. 10.22. In this technique the plates being welded are subjected to tensile loading. The magnitude of

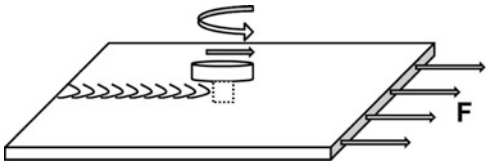

Fig. 10.22 Schematic illustration of mechanical tensioning technique

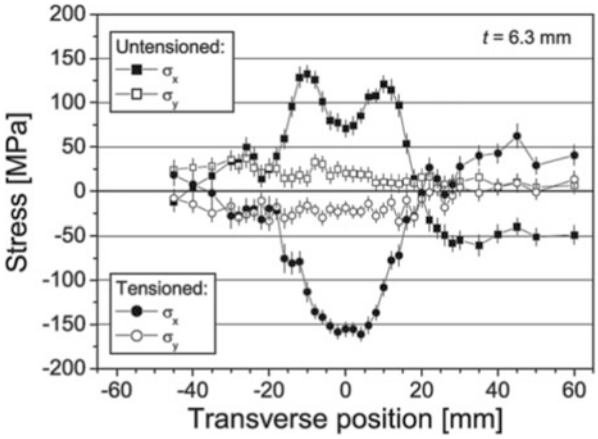

Fig. 10.23 Residual stress management in 2024Al-T351 alloy by the use of roller tensioning technique (Staron et al. 2004, reprinted with permission from Elsevier)

loading can be from a small fraction to a significant proportion of the yield strength of the material. Due to in-situ loading compressive plastic deformation ahead of FSW tool decreases whereas tensile plastic deformation or yielding behind the tool increases. It results in lower misfit between welded zone and surrounding materials. This technique can be applied after welding also. However, the load requirement increases due to higher strength of the welded zone at low temperature.

Figure 10.23 illustrates the effect of mechanical tensioning on the components of residual stress in 2024Al plate (Staron et al. 2004). Clearly, both longitudinal and transverse residual stresses are tensile in nature in major parts of the plate. However, after subjecting it to a tensile load 70 % of yield strength of 2024Al-T351 at room temperature, the nature of residual stresses change from tensile to compressive for both the components of the residual stress.

10.8.3 Roller Tensioning

The mechanical tensioning method described above is also known as global mechanical tensioning method because entire weld plate is loaded simultaneously. As opposed to this, roller tensioning technique is regarded as local mechanical tensioning method as it stretches weld material at the location the rollers are present.

Figure 10.24 describes roller tensioning technique. Use of single roller right in the welded zone is shown in Fig. 10.24a. This particular situation can be implemented either in-situ or post welding. Instead of directly moving the roller

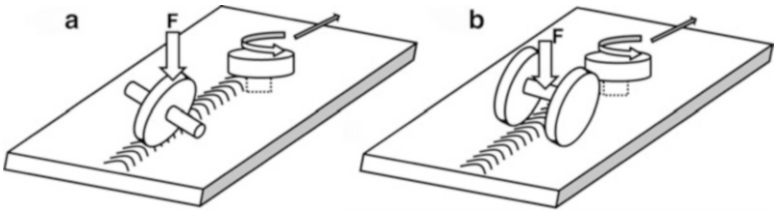

Fig. 10.24 Schematic illustration of roller tensioning technique; (**a**) rolling of the weld beam—in-situ and post-weld both possible and (**b**) rolling of the material adjoining welded zone (adapted from Altenkirch et al. 2009a)

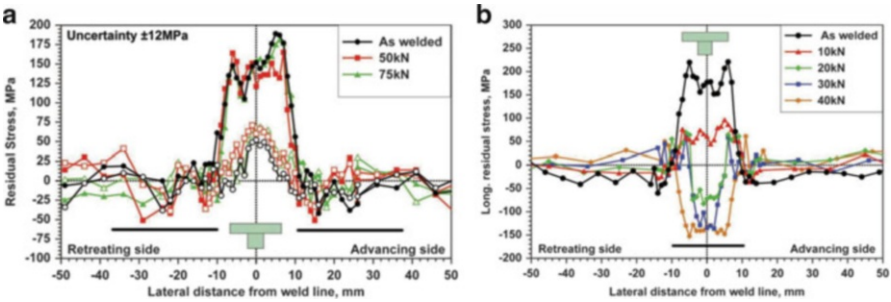

Fig. 10.25 (**a**) In-situ roller tensioning (Fig. 10.24b) and (**b**) post-weld roller tensioning (Fig. 10.24a) (Altenkirch et al. 2009a, reprinted with permission from Maney Publishing)

over the welded zone, it can also be made to move in the zone next to it. This particular scenario is shown in Fig. 10.24b where two rollers are moving just next to the welded region.

Figure 10.25 shows experimental results following roller tensioning technique to mitigate residual stress (Altenkirch et al. 2009a). It shows that in-situ roller tensioning (Fig. 10.24b) did not cause any change in the distribution of residual stresses across the width of the plate. However, when roller tensioning was applied post-weld, it resulted in not only reduction in the magnitude of residual stresses in welded zone but also changed the nature of the residual stress at sufficiently higher loads.

10.9 Modeling and Simulation of Residual Stresses in Friction Stir Welding

With the advent of modern computers, modeling and simulation has become an integral tool in many engineering applications. In parallel there has been a great deal of development activities in the area of commercial numerical codes which are assisting in many engineering design and development works in various disciplines. The application of modeling and simulation technique in the study of residual stress

and resulting distortion is no exception. Although, in last two decades or so, there has been a surge in modeling activities relating to weld residual stress and distortion, it has been actively pursued for last four decades (Michaleris 2011).

The residual stress and distortion study of fusion welding processes carried out through modeling and simulation has greatly benefitted similar studies in friction stir welding. In fusion welding techniques mostly Eulerian frame of reference where material and mesh are not associated is used for this purpose using computational fluid dynamics (CFD) technique. Although, CFD is capable of providing us with thermal history and profile of the weld pool during fusion welding, it does not provide any information on residual stresses. However, the thermal history obtained in CFD can be used as an input to another finite element code utilizing elastoplastic material model in Lagrangian frame of reference. Friction stir welding being a solid-state joining technique directly utilizes conventional elastoplastic analysis technique in the prediction of residual stresses and distortions. It is worth mentioning that similar to that in fusion welding technique, use of CFD followed by elastoplastic model has been incorporated in friction stir welding also to study residual stresses (Richards et al. 2010).

Despite significant improvement in computational speed, the computational cost is still very high due to complexity of the processes like friction stir welding. Hence, during the modeling of the process a great number of assumptions are made to keep the size of the problem as minimum as possible. But, at the same time efforts are directed towards keeping all the essential components of a process intact so that the output of the modeling still remains meaningful. Chao and Qi (1998) were first to study the residual stress and distortions in 6061Al. In the plate only conduction mode of heat transfer was considered. The heat transfer to ambient air from top surface and to the backing plate from bottom of the plate were modeled using appropriate heat transfer coefficients. The heat transfer to the tool was not considered. A moving heat source was considered to model the actual friction stir tool. Such a heat source is capable of mimicking the heat generated by frictional and adiabatic plastic deformation of the material surrounding the tool. However, the actual plastic deformation cannot be modeled. In this particular case total heat input was varied until computational and thermal temperature profiles matched well. It was a sequentially coupled thermo-mechanical analysis. Thermal analysis was followed by stress analysis in the plate. Recent finite element models are able to introduce more sophistication in the analysis with reduced time for the analysis (Buffa et al. 2006, 2011). For example, it is now possible to include plunge stage, tool extraction stage, and plastic deformation by the tool during different stages of friction stir welding process. However, it should be mentioned that for residual stress modeling it is not important to include plastic deformation due to the tool movement. The incorporation of plastic deformation may become important in cases where knowledge of strain, strain rate, and adiabatic heat generated due to plastic deformation may be necessary. Although, it is possible to consider volumetric heat generation to include the heat generation at tool pin/workpiece interface, this part also can be ignored for residual stress modeling purpose leading to further simplification of the analysis. Buffa et al. (2008) showed by processing 7075Al-T6 with pin and pinless tool that

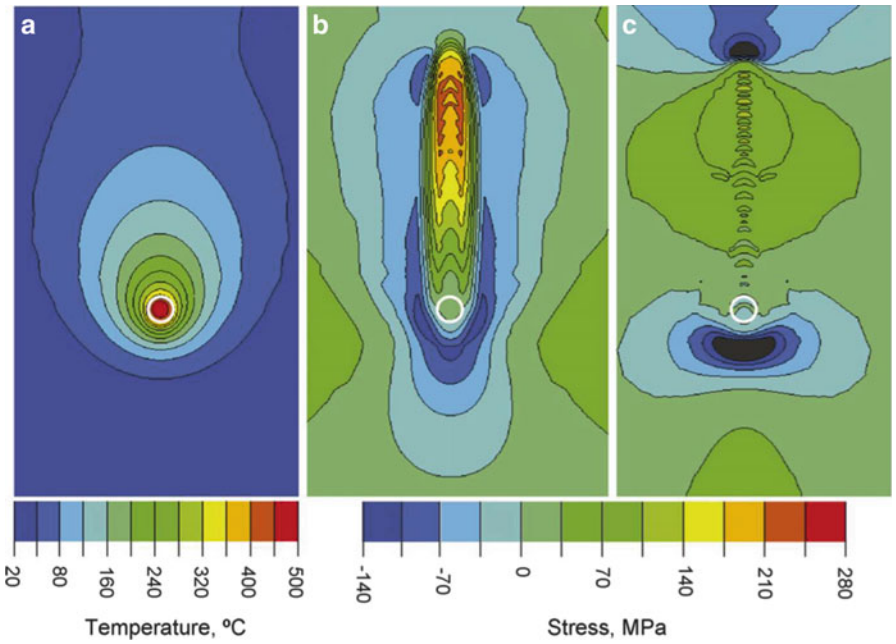

Fig. 10.26 Contour plots of temperature and thermal stresses in 2024Al-T6 plate. A heat input of 958 W was used in the simulation. (**a**) Temperature contour plot, (**b**) longitudinal stress distribution, and (**c**) transverse stress distribution (Richards et al. 2008, reprinted with permission from Elsevier)

the longitudinal residual stress distribution was same in both the cases. The main conclusion of this work was that the residual stress is mainly affected by heat generated at tool shoulder/workpiece interface. In fact, a very good correlation between modeling based on surface heat source and experimental residual stress measurement results is another validity of such assumptions.

Figure 10.26 shows the two-dimensional contour plot of temperature and thermal stress in a 2024Al-T6 plate (Richards et al. 2008). The temperature profile and residual stress distribution corresponds to 770 rpm and 195 mm/min friction stir welding parameters. It corresponds to a weld power of 958 W. The power was obtained using a heat transfer model using CFD technique. The thermal profile obtained from the CFD based heat transfer model was used as an input in a three dimensional stress analysis model designed to compute residual stresses. It should be noted that away from the tool (shown by white circular region in the figure) stresses are tensile and ahead of the tool thermal stresses are compressive in nature. Experimentally it is possible to get the knowledge on the thermal stress evolution only at selected locations. However, this example shows that computationally we get far greater insight into the evolution of thermal and, as will be shown next, residual stresses.

Figure 10.27 shows distribution of computed residual stress (longitudinal and transverse) in SS 304L. The processing condition of the stainless steel sheet is

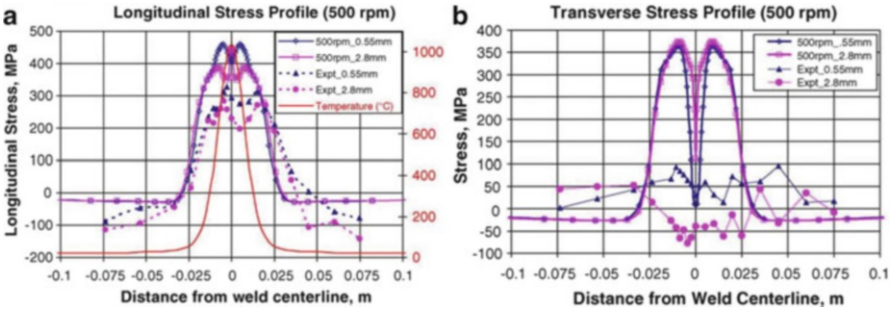

Fig. 10.27 Residual stress distribution in a stainless steel 304L; (**a**) Longitudinal and (**b**) transverse stresses. Experimental condition: Plate thickness 3.2 mm, tool rotation rate 500 rpm, tool traverse speed 4 ipm (102 mm/min), length of the welded region 279 mm (Khandkar et al. 2006, reprinted with permission from Elsevier)

provided in the caption of Fig. 10.27. The residual stress values are reported for different depths: 0.55 and 2.8 mm below top surface of the sheet. The experimental residual stress data are also superimposed to compare them with computed stress distribution profile. As can be noted here the longitudinal residual stress prediction is quite well. However, the predicted transverse residual stress varies significantly in the close vicinity of the weld centerline. Boundary conditions used at weld centerline (or plane of symmetry), neglecting tool movement assisted plastic deformation, and lack of some temperature dependent physical and mechanical properties for the alloy are a few possible reasons for the deviation of predicted transverse residual stresses from the experimentally measured one.

Previous couple of examples demonstrated how modeling and simulation work is assisting us in visualizing thermal and residual stress generation during friction stir welding. In next couple of examples it will be demonstrated how residual stress simulation work is assisting in taking steps to mitigate residual stresses and resulting distortion. Section 10.8 discussed various experimental approaches undertaken to mitigate residual stresses in welded components. Here finite element study of global mechanical tensioning and the role of active cooling in addressing the issue of residual stress and resulting distortions of welded components will be illustrated. Active cooling (use of cooling media such as liquid CO_2, liquid nitrogen, etc.) has been used for reducing or eliminating residual stresses in friction stir welded components by many. Richards et al. (2010) studied this aspect using finite element method in a 2024Al-T3 plate. The effect of the location of a cooling nozzle on the thermal contour profiles are shown in Fig. 10.28. Figure 10.28a is a contour plot without any active cooling. Figure 10.28b represents a situation where the cooling nozzle was placed in front of the heat source which is equivalent of placing it ahead of friction stir welding tool. The effect of the presence of cooling nozzle on thermal profiles is quite evident from these images. The effect of active cooling and its position with respect to the heat source is illustrated in Fig. 10.29. It is quite remarkable to note the inversion of the nature of longitudinal residual stress at the weld centerline. It changes from a tensile value close to 130–135 MPa to compressive 20 MPa.

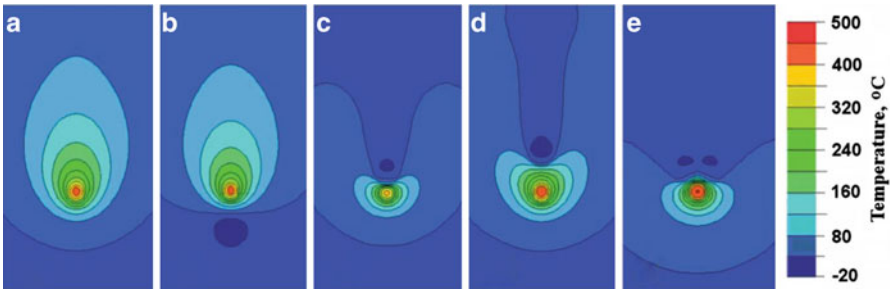

Fig. 10.28 Temperature contour plot as a function of distance of cooling nozzle from heat source; (**a**) no cooling, (**b**) 20 mm in front of the heat source; in rest of the cases heat cooling source behind the heat source (**c**) 20 mm, (**d**) 40 mm, and (**e**) two heat sinks at 20 mm (Richards et al. 2010, reprinted with permission from Maney Publishing)

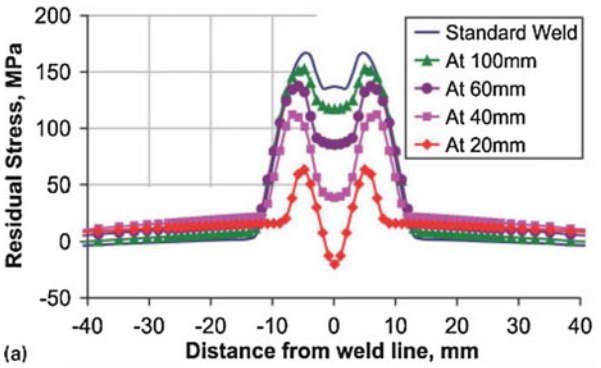

Fig. 10.29 Effect of active cooling and the position of the cooling medium on the longitudinal residual stress distribution. The distribution is at mid-thickness level halfway along the length of the plate (Richards et al. 2010, reprinted with permission from Maney Publishing)

As mentioned before global mechanical tensioning is another method of reducing residual stresses in the welded components, and this has been studied using finite element methods. As an example the result of the study done by Richards et al. (2008) is included here in Fig. 10.30. It shows two dimensional longitudinal stress and plastic strain distributions as a function of applied in-situ tensile load. After tensioning to 35 % of the yield strength of 2024Al-T6 at room temperature, Fig. 10.30b shows close to zero plastic strain. At this level of tensioning the longitudinal stresses are also very small. The tensioning level with respect to room temperature yield strength might change depending on the exact processing condition. Experimentally also it has been observed that at tensioning level ranging from 25 to 50 % of room temperature yield strength, the residual stresses were close to zero (Staron et al. 2004; Altenkirch et al. 2008; Price 2007).

Hence, it is quite evident from above examples that finite element simulation study of residual stresses in friction stir welding is assisting not only in developing an understanding of process parameter affecting the residual stresses but also suggesting means of mitigating such stresses.

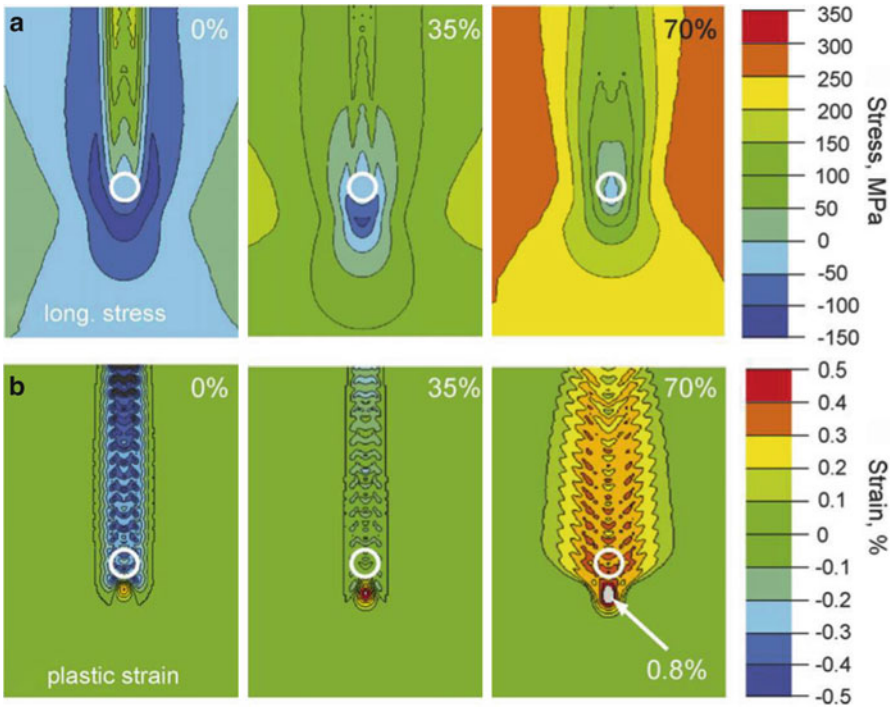

Fig. 10.30 Effect of mechanical tensioning on longitudinal stress (**a**) and plastic strain (**b**). 35 and 70 % represent fraction of yield strength of 2024Al-T6 at room temperature applied as mechanical tensioning during friction stir welding simulation (Richards et al. 2008, reprinted with permission from Elsevier)

References

J. Altenkirch, A. Steuwer, M. Peel, D.G. Richards, P.J. Withers, The effect of tensioning and sectioning on residual stresses in aluminium AA7749 friction stir welds. Mater. Sci. Eng. **488**, 16–24 (2008)

J. Altenkirch, A. Steuwer, P.J. Withers, S.W. Williams, M. Poad, S.W. Wen, Residual stress engineering in friction stir welds by roller tensioning. Sci. Technol. Weld. Join. **14**, 185–192 (2009a)

J. Altenkirch, A. Steuwer, M.J. Peel, P.J. Withers, The extent of relaxation of weld residual stresses on cutting out cross-weld test-pieces. Powder Diffr. **24**, S31–S36 (2009b)

G. Buffa, J. Hua, R. Shivpuri, L. Fratini, A continuum based fem model for friction stir welding–model development. Mater. Sci. Eng. A **419**, 389–396 (2006)

G. Buffa, L. Fratini, S. Pasta, R. Shivpuri, On the thermo-mechanical loads and the resultant residual stresses in friction stir processing operations. CIRP Ann. Manuf. Technol. **57**, 287–290 (2008)

G. Buffa, A. Ducato, L. Fratini, Numerical procedure for residual stresses prediction in friction stir welding. Finite Elem. Anal. Des. **47**, 470–476 (2011)

G. Bussu, P.E. Irving, The role of residual stress and heat affected zone properties on fatigue crack propagation in friction stir welded 2024-T351 aluminum joints. Int. J. Fatig. **25**, 77–88 (2003)

Y.J. Chao, X. Qi, Thermal and thermo-mechanical modeling of friction stir welding of aluminum alloy 6061-T6. J. Mater. Process. Manuf. Sci. **7**, 215–233 (1998)
L. Fratini, S. Pasta, A.P. Reynolds, Fatigue crack growth in 2024-T351 friction stir welded joints: longitudinal residual stress and microstructural effects. Int. J. Fatig. **31**, 495–500 (2009)
S. Gachi, F. Belahcene, F. Boubenider, Residual stresses in AA7108 aluminium alloy sheets joined by friction stir welding. Nondestr. Test. Eval. **24**, 301–309 (2009)
W.T. Han, F.R. Wan, G. Li, C.L. Dong, J.H. Tong, Effect of trailing heat sink on residual stresses and welding distortion in friction stir welding Al sheets. Sci. Technol. Weld. Join. **16**, 453–458 (2011)
O. Hatamleh, A comprehensive investigation on the effects of laser and shot peening on fatigue crack growth in friction stir welded AA 2195 joints. Int. J. Fatig. **31**, 974–988 (2009)
T. Inoue, Z. Wang, Coupling between stress, temperature, and metallic structures during processes involving phase transformations. Mater. Sci. Technol. **1**, 845–850 (1985)
M.Z.H. Khandkar, J.A. Khan, A.P. Reynolds, M.A. Sutton, Predicting residual thermal stresses in friction stir welded metals. J. Mater. Process. Technol. **174**, 195–203 (2006)
H.J.K. Lemmen, R.C. Alderliesten, R.R.G.M. Pieters, R. Benedictus, J.A. Pineault, Yield strength and residual stress measurements on friction-stir-welded aluminum alloys. J. Aircr. **47**, 1570–1583 (2010)
H. Lombard, D.G. Hattingh, A. Steuwer, M.N. James, Effect of process parameters on the residual stresses in AA5083-H321 friction stir welds. Mater. Sci. Eng. **501**, 119–124 (2009)
K. Masubuchi, in *The Strength of Welded Structures: Fundamentals, in Analysis of Welded Structures*, ed. by D.W. Hopkins (Pergamon Press, Oxford, 1980), p. 328
K. Masubuchi, Transient thermal stresses and metal movement during welding, in *Analysis of Welded Structures*, ed. by D.W. Hopkins (Pergamon Press, Oxford, 1980a), p. 148
P. Michaleris, Modelling welding residual stress and distortion: current and future research trends. Sci. Technol. Weld. Join. **16**, 363–368 (2011)
M. Peel, A. Steuwer, M. Preuss, P.J. Withers, Microstructure, mechanical properties and residual stresses as a function of welding speed in aluminium AA5083 friction stir welds. Acta Mater. **51**, 4791–4801 (2003)
G. Pouget, A.P. Reynolds, Residual stress and microstructure effects on fatigue crack growth in AA2050 friction stir welds. Int. J. Fatig. **30**, 463–472 (2008)
D.A. Price, S.W. Williams, A. Wescott, C.J.C. Harrison, A. Rezai, A. Steuwer, M. Peel, P. Staron, M. Kocak, Distortion control in welding by mechanical tensioning. Sci. Technol. Weld. Join. **12**(7), 620–633 (2007)
D.G. Richards, P.B. Prangnell, S.W. Williams, P.J. Withers, Global mechanical tensioning for the management of residual stresses in welds. Mater. Sci. Eng. **489**, 351–362 (2008)
D.G. Richards, P.B. Prangnell, P.J. Withers, S.W. Williams, T. Nagy, S. Morgan, Efficacy of active cooling for controlling residual stresses in friction stir welds. Sci. Technol. Weld. Join. **15**, 156–165 (2010)
G.S. Schajer, *Residual Stresses: Measurement by Destructive Testing, Encyclopedia of Materials: Science and Technology* (Elsevier, Oxford, 2001), pp. 8152–8158
P. Staron, M. Kocak, S. Williams, Residual stresses in friction stir welded Al sheets. Appl. Phys. Mater. Sci. Process. **74**, S1161–S1162 (2002)
P. Staron, M. Kocak, S. Williams, A. Wescott, Residual stress in friction stir-welded Al sheets. Phys. B Condens. Matter **350**, E491–E493 (2004)
X. Wang, Z. Feng, S. David, S. Spooner, C. Hubbard, Neutron diffraction study of residual stresses in friction stir welds, in *Proceedings of the 6th International Conference on Residual Stress*, IOM Communications, London, UK, 2000, pp. 1408–1415
P.J. Withers, *Residual Stresses: Measurement by Diffraction, Encyclopedia of Materials: Science and Technology* (Elsevier, Oxford, 2001), pp. 8158–8169
P. Withers, H. Bhadeshia, Residual stress Part 1—measurement techniques. Mater. Sci. Technol. **17**, 355–365 (2001)

Index

A
AA356, 59, 60
Abnormal grain growth, 264
Acicular, 119, 203
Activation energy, 40, 52, 65, 67
Active cooling, 317–318, 323, 324
Adhesive bonding, 1, 2
Advance per revolution (APR), 4, 24, 32, 33, 44, 45, 47, 49, 105
Advancing side, 4, 6, 14, 30, 31, 44, 45, 54, 55, 97, 98, 103, 115, 123– 125, 132, 162, 177, 201, 202, 241, 243, 245–248, 255, 289
Aged, 111, 169, 206, 269, 270, 282
Aging, 80, 111, 115, 118, 120, 121, 129–137, 140, 195, 282, 283
Aircraft, 1, 9, 288
AISI. *See* American Iron and Steel Institute (AISI)
Al alloys. *See* Aluminum (Al) alloys
ALE technique. *See* Arbitrary Lagrangian-Eulerian (ALE) technique
Allotropic transitions, 189
Alloy chemistry, 190–193, 264
Alloying, 151, 209, 210, 212–214, 230
Alloying elements, 9, 70, 109, 110, 116, 151–153, 190–192, 200, 206, 210, 212, 240
α alloys, 200, 206
α+β alloys, 195
α-/β-stabilizer, 190, 195
Aluminum, 7, 9, 109, 119, 149, 151, 189, 190, 199, 217, 227, 228, 230, 238–240, 243, 245, 251–255, 268, 275, 283, 285
Aluminum (Al) alloys, 3, 7–9, 14, 25, 32, 33, 35, 42, 46, 59, 77, 89–91, 99, 109–145, 151, 154, 161, 163, 164, 168, 169, 172, 181, 182, 189, 202, 216, 230, 237, 239–243, 245–257, 262–265, 267–269, 274, 275, 286, 302, 303
Aluminum Association, 110, 151
American Iron and Steel Institute (AISI), 28, 210–212, 216, 224, 225
Angular velocity, 22, 47, 145
Anodic reaction, 143
Anvil, 19, 26, 28, 29, 31, 97
Applications, 3, 9, 37, 50, 77, 100, 109, 112, 119, 153, 163, 233, 259, 268, 272, 288, 304, 320
APR. *See* Advance per revolution (APR)
Arbitrary Lagrangian-Eulerian (ALE) technique, 40, 47
Assembly processes, 1
ASTM, 144, 145, 151, 152, 212, 287
Athermal, 66, 86
Atomic diffusivity, 70
Austenite, 60, 83–88, 208, 210, 212–215, 222–224, 226, 229, 230
Austenitic stainless steel, 216–218, 220, 230–232, 255
Autogenous, 98, 238
Automotive, 3, 9, 11, 149, 151, 210, 237, 238, 288
Avrami, 70, 71

B
Bainite, 210, 212, 221
Bars, 25, 52, 53, 192, 310, 314, 315

R.S. Mishra et al., *Friction Stir Welding and Processing: Science and Engineering*,
DOI 10.1007/978-3-319-07043-8,

Basal plane, 170, 171, 183
Base material, 30, 122, 164, 169, 170, 175, 177, 183, 202, 203, 206, 207, 217, 221–224, 226, 227, 229, 230, 232, 237, 243, 249
Basin, 162
b.c.c. *See* Body centered cubic (b.c.c.)
Bending, 49, 142, 269, 270, 277, 298
Bending fatigue, 103
Bend property, 127
β alloys, 195, 198, 200, 205
Beta transus temperature, 190–194, 199–205
Body centered cubic (b.c.c.), 63, 86
Bonding, 1–3, 142, 154, 253, 268, 275, 278
Boundary conditions, 28, 29, 38, 39, 323
Brazing, 1, 2
Butt, 4, 7–9, 95–98, 174, 221, 224, 225, 252

C
Casting, 59, 60, 119, 132, 153, 279–287
Cast magnesium, 41
Cast sheet, 267–268
Cells, 73, 121, 126, 145, 168
Cellular automata, 76
Cementite, 59, 61, 83, 84, 208, 210, 213, 229, 230
Center-crack specimen, 138
Ceramic phases, 272
Ceramic tools, 101
Cermets, 102, 195
Cermet tools, 100, 101, 104
CFD. *See* Computational fluid dynamics (CFD)
Channel, 288–291
Characterization, 121
Chemical, 21, 37, 38, 61, 99, 102, 196, 197, 273
Chemical compositions, 144, 237, 244
Chemistry, 161, 173, 181, 190–194, 212, 214, 217, 233, 237, 238, 243, 244, 254, 264
Chill cast, 268
Classifications, 1, 64, 72, 151–153, 189, 190, 208–211, 288
Clearance, 288, 289
Cobalt base superalloy, 195
Coefficient of static/dynamic friction, 18
Cold run, 95, 97
Cold working, 72, 111, 116
Components, 16, 21, 37, 54, 55, 61, 62, 65, 88, 95, 97, 104, 105, 149, 151, 153, 155, 167, 172, 179, 206, 259, 261, 266, 268, 270, 272, 275, 278, 279, 282, 284, 297, 299, 300, 304, 305, 308, 311, 312, 314, 318, 319, 321, 323, 324
Composition, 7, 60–63, 65, 67, 69, 70, 80–82, 85, 86, 87, 110, 114, 116, 119, 120, 144, 152, 153, 192, 212, 237, 238, 244, 261, 272, 283, 307, 308
Compositional fluctuations, 65, 75, 81, 82
Compressive, 52, 53, 89, 112, 125, 128, 129, 170, 181, 277, 299–301, 304, 308, 310, 314–319, 322, 323
  forces, 6, 64
  strain, 315
Computational fluid dynamics (CFD), 44, 321, 322
Concave shoulder, 5, 112, 141, 144, 240
Concentration, 38, 69, 70, 82, 83, 120, 195, 240, 285
Consolidation processes, 1
Constant shear model, 21, 34, 35, 47
Constituent particles, 99, 115–116
Constitutive behavior, 34, 37, 38
Constitutive equation, 39, 50–53, 76, 78, 88
Constitutive relation, 88, 261–262
Contact pressure, 16
Contamination, 195, 217
Continuous cast sheet, 268
Continuous precipitation, 80, 82
Convective coefficient, 28, 29
Convective heat transfer, 26, 28, 29
Cooling, 43, 59–61, 63, 80, 92, 93, 140, 163, 193–195, 200, 203, 208, 213, 221, 225, 229, 233, 288, 294, 297, 315, 317, 318, 323, 324
  cycle, 43, 89, 90, 201, 213, 222, 229, 316
  rates, 59, 60, 90, 92, 159, 189, 192, 200, 203, 205, 214, 215, 221, 223–228, 230, 233, 279
Corrosion, 109, 111, 120, 143–145, 151, 152, 181–184, 212, 237, 238, 260, 300
Coulomb friction, 18, 21, 34, 35
Covex shoulder, 5, 102, 104, 141, 143, 196, 216
Crack, 124, 125, 128, 129, 132, 138, 183, 245, 250, 285–287, 299, 300, 305
  growth, 98, 124, 142, 145, 284, 285, 287, 311
  initiation, 119, 124, 142
  propagation, 124, 125, 128, 129, 132, 134, 137–139, 143, 145
  tip, 183, 285, 299
Creep, 37, 272
Critical free energy, 65, 87

Critical grain size, 291
Critical nuclei radius, 65
Critical temperature, 13, 15, 104, 200, 208, 221, 228, 233
Cross-section, 5, 28, 53, 54, 95, 104–106, 155, 164, 179, 188, 199, 200, 202, 223, 226, 227, 232, 238, 241, 245, 246, 248, 250–253, 270, 271, 273, 277, 279, 289, 314
Crystallographic texture, 33
Crystal structure, 63, 75, 80, 88, 190, 205, 208, 217, 230
Cut-compliance technique, 125, 126, 303
Cyclic stress, 284
Cyclic variation, 47
Cylindrical pin, 21, 53, 54, 95, 104, 106, 144, 155, 170, 172

D

Defects, 8, 37, 40, 54, 64–66, 70, 95–98, 103, 105, 114, 119, 141, 154, 155, 161, 162, 189, 273, 285, 288, 299
  energy, 63, 65
  formation map, 96
Deflection zone, 41, 42
Deformation, 2–7, 15–18, 21, 24–25, 27–31, 34, 36, 37, 40, 41, 43, 44, 47, 50, 52, 53, 59, 73, 76, 88, 89, 91, 92, 100, 104, 123, 168–171, 175, 178, 179, 200, 202, 203, 212, 229, 249, 250, 255, 261, 262, 266, 285, 291, 294, 297, 301, 310, 311, 314–319, 321, 323
  bonding, 3
  kinetics, 263
  zone, 31, 34, 92, 170
Dendritic microstructure, 60
Dendritic porosity, 279
Density, 26, 30, 37, 50, 73, 75, 109, 116, 120, 121, 123, 160, 168, 169, 182, 190, 270, 272, 278
Dependent process variables, 16, 89
Design, 1, 4–6, 8, 53, 54, 95, 97, 101, 102, 104, 106, 107, 112–114, 141, 153, 155, 184, 237, 238, 240, 261, 262, 266, 271–287
Design approach, 259, 260, 264, 272
Destructive, 305, 306
Die-cast(ing), 119, 151, 153
Diffusion, 2, 37, 60, 66, 69, 70, 81–83, 85, 86, 190, 192
Diffusion bonding, 3, 154, 268
Diffusion-limited coarsening, 83
Diffusive flux, 37
Diffusive phase transformation, 63
Digital image correlation, 122–123
Discontinuous precipitation, 80, 82
Dislocations, 37, 50, 65, 66, 70, 73–75, 77, 79, 82, 88, 91, 109, 116, 120, 121, 126, 130, 168, 169, 182, 201, 223, 230, 270, 291, 299
Dislocation strengthening, 219
Dispersoids, 116, 119, 120, 129, 169, 182, 263
Displacement, 13, 32, 33, 41, 47, 48, 104–106, 142
Displacement controlled mode, 14
Dissimilar, 7, 33, 69, 240, 241, 243–245, 250
  joints, 237, 238
  metals, 36, 237–257
  weld, 33, 240–242, 245, 246–250, 253
  welding, 238, 240, 242, 244, 246
Distortions, 8, 9, 189, 302, 311, 312, 314, 316, 317, 321, 323
Distribution, 4, 16, 26, 34, 44, 59, 61, 63, 65, 75, 103, 115, 117–119, 126–128, 144, 150, 161, 169, 172, 179, 180, 183, 203, 230, 232, 233, 262, 273, 275, 279–281, 285, 286, 291, 297, 301, 302, 304–306, 309, 313, 314, 318, 320, 322–324
Drop-weight testing, 52
Dubé system, 214
Ductility, 109, 173–176, 182, 194, 195, 206–208, 218, 232, 249, 262, 268, 270, 272, 275–277, 279, 282, 283, 291, 294
Duplex, 194, 206, 216, 230, 233
Dwell phase, 13, 139
Dynamic recovery, 37, 71, 76–77, 91, 92, 118, 120, 126, 168
Dynamic recrystallization, 71, 72, 77–78, 92, 116, 163

E

EBSD. *See* Electron-backscattering diffraction (EBSD)
ECA, 291
Elastic body, 297, 298
Elastic modulus, 272, 273, 306
Electrical resistance, 109
Electrochemical impedance test, 145
Electromagnetic welding, 154, 155
Electron-backscattering diffraction (EBSD), 116, 118, 221, 222

Electron beam welding, 154, 237
Elements, 9, 36, 70, 91, 109, 110, 116, 120, 143, 149, 151–152, 189–192, 200, 206, 208, 210, 212, 217, 237, 238, 240, 243, 261, 266, 275, 282, 317, 321, 323, 324
Ellingham diagram, 100, 101
Elliptical, 30, 162, 169
Elongation, 122, 175, 176, 195, 198, 206, 207, 217, 249, 250, 261, 263–268, 270, 277, 283, 291, 292
Empirical, 50, 112, 192, 309
  based, 50
  laws, 18
Enabling technology, 189
Energy, 7, 9, 16, 20, 21, 24, 25, 37, 40, 52, 61–67, 70, 74, 75, 78, 80, 82, 84, 86–88, 96, 109, 161, 168, 245, 264, 267, 282, 285, 288
  benefits, 9
  flow, 16
Engineering, 51, 97, 232, 237, 249, 260, 261, 283, 320
Engineering materials, 208
Environmental benefits, 9
Equiaxed, 5, 60, 182, 194, 199, 201, 202, 206, 213, 262
Equilibrium, 59, 61, 67–69, 84, 85, 90, 117, 120, 145, 244, 299, 315
Eulerian, 38, 40, 41, 321
Eutectoid, 60–61, 83–85, 190, 195
Eutectoid microstructure, 60, 82
Eutectoid steel, 60–61
Exit hole, 97, 106
Explosive welding, 3
External force, 92, 297, 315
Extrusion forces, 89

F

Face-centered cubic (f.c.c.), 63, 86
Failure, 1, 15, 103, 104, 124, 133, 138, 142, 144, 177, 178, 208, 249, 261, 271, 279, 300
Fatigue, 5, 99, 100, 102, 103, 119, 124, 125, 127–129, 132–134, 137–140, 142, 145, 179–181, 208, 256, 271, 273, 279–287, 300, 311
  behavior, 124, 127, 139, 283–287
  life, 99, 124, 127, 128, 132, 139, 142, 179, 181, 282, 284–286, 300
  properties, 5, 100, 119, 128, 132, 179, 256, 273, 311
Faying surface, 8, 30, 31, 55, 95, 97, 98, 105
Feed rate, 311–313
Ferrite, 59, 60, 83–86, 208, 210, 213, 219, 221–224, 226, 227, 229–231, 255
Ferrous alloys, 208–233, 237, 238, 251–257
Filler material, 2, 3, 238
Fillet, 7, 8, 95, 96, 98
Fine grain, 4, 5, 66, 116, 259, 262, 267, 268
Fine grained, 128, 132, 138, 183, 263, 266
Finite element, 36, 261, 266, 282, 317, 321, 323, 324
Finite element analysis (FEA), 40
Finite element models(ing), 282, 321
Flats, 6, 84, 97, 100, 101, 103, 105, 106, 139, 141–143, 155, 157, 216
Flaw size, 128, 286
Flow arm, 103
Flow pattern, 30, 31, 205, 289
Flow strength, 202, 238
Flow stress, 37, 50, 51, 88, 102, 104, 190, 216, 261, 263, 268, 311, 315
Flow zones, 40–41
Fluid, 36–41, 44, 46, 282, 288, 321
  dynamics, 44, 46, 321
  flow, 36, 37, 39–41
  particle, 38
Flutes, 6, 105, 106
Flux, 7, 37, 67, 68
Forces, 6, 7, 13, 15–17, 21–23, 29, 34, 37, 46–49, 53–55, 63, 64, 66, 73–76, 78, 86, 89, 91, 97–100, 102–104, 106, 112, 113, 217, 227, 244, 256, 277, 287–290, 297, 315
  controlled
    FSW, 46
    mode, 14
Forge welding, 3
Forging load, 97
Fracture, 113, 169, 173, 175, 177–179, 215–217, 243, 245, 254, 273, 275, 285, 287
Fracture toughness, 99, 102, 113, 287, 300
Free surfaces, 61, 65
Frequency, 47, 49, 67, 273
Friction, 18
Frictional force, 18, 21
Frictional heat(ing), 13, 15, 18–24, 27, 34
Friction stir attributes, 259
Friction stir channeling (FSC), 288–290
Friction stirs joints, 95
Friction stirs microstructure, 264
Friction stir process(ing) (FSP), 4, 5, 7, 13–55, 59, 66, 72, 95, 96, 99, 105, 112–114, 119, 132, 135, 164, 189, 193, 195, 207, 208, 259–29, 260, 262, 268
Friction stir spot weld(ing) (FSSW), 9, 11, 14, 33, 35, 139–144, 268

Friction stirs tool, 13, 321
Friction stirs welds(ing) (FSW), 34, 49, 88, 120, 123–125, 138, 173, 183, 189, 200, 223, 230, 232, 233, 241, 245, 251
Friction stress, 217
FSP. *See* Friction stir process(ing) (FSP)
FSSW. *See* Friction stir spot weld(ing) (FSSW)
Fusion, 1, 2, 7, 8, 13, 70, 109, 154, 155, 189, 237, 238, 268, 301, 305, 316–317, 321
Fusion-based joining processes, 13
Fusion welding, 1, 2, 7, 8, 70, 154, 155, 189, 237, 238, 268, 301, 305, 316–317, 321

G

Galvanic series, 181, 182
Gas forming, 261, 267
Gas metal arc welding, 177
Geometrical configurations, 273
Geometries, 7, 216, 276, 307, 317
Gibbs free energy, 61, 62
Gleeble®, 89
Glissile interface, 66
GP zones. *See* Guinier-Preston (GP) zones
Gradient, 4, 5, 18, 70, 74, 75, 95, 98, 102, 202–204, 273, 301, 307
Grain boundary, 63, 65, 66, 76, 83, 84, 86, 88, 110, 116, 120, 126, 128, 143, 153, 183, 203, 205, 206, 214, 219, 223, 261, 262, 270, 294
  allotriomorphs, 86, 214
  sliding, 262
  strengthening, 126, 153, 206, 219, 223, 270, 294
Grain growth, 43, 66, 71–79, 82, 88, 91, 92, 107, 110, 116, 202, 264
Grain refinement, 163, 164, 182, 223, 230, 232, 262, 270, 290, 294
Grain size, 4, 30, 34, 43, 78, 79, 92, 123, 128, 129, 132, 163–168, 189, 195, 203, 206, 223, 229, 232, 259, 261, 262, 264, 266–268, 291–294
Guinier-Preston (GP) zones, 82, 115, 118, 120, 121, 130, 131

H

Habit plane, 87, 88
Hall-Heroult process, 149
Hall-Petch strengthening, 153, 219
Hardness, 112–114, 121–123, 126, 129, 130, 132, 133, 139–141, 151, 156, 163, 172, 173, 177, 195, 206, 223, 226–228, 232, 243, 285
Hardness profile, 126, 129, 133, 173, 206, 223
Heat, 6, 7, 14–17, 19–36, 43, 47, 59–61, 72, 89, 96, 97, 101, 107, 110, 111, 113, 120, 122, 132, 138, 140, 152, 154, 159, 160, 172, 177, 189, 199–201, 212, 217, 222, 227, 229, 252, 268, 271, 281, 286–288, 290, 294, 297, 301, 302, 304, 311, 313, 317, 321–324
  affected zone, 7, 89, 97, 177, 200, 271, 311
  capacity, 21, 26, 154, 160, 199
  energy, 21, 25, 96
  exchanger, 288, 290
  generation, 15–29, 47, 321
  input, 16, 24, 101, 107, 140, 189, 222, 227, 268, 302, 313, 321, 322
  loss, 28, 113
  source, 16, 159, 301, 321–324
  transfer, 25–29, 43, 59, 288, 321, 322
  treatable, 110, 172
  treatment, 59, 61, 111, 120, 122, 132, 229, 281, 286, 287, 297, 311, 317
Heating, 4, 13, 18, 23, 59–61, 89, 100, 102, 111, 159, 200, 208, 212, 217, 230, 288, 297, 314, 315
  cycle, 212, 230
  rate, 60, 159
Heterogenous nucleation, 65, 66
High angle boundary, 74
High angle grain boundaries, 75, 116, 118, 262
High-carbon steel, 157, 209, 215, 220, 224–229
High cycle fatigue, 127, 139
High strain band, 30, 123
High strain rate, 37, 52–53, 255, 261–265, 291
High strength aluminum alloys, 8, 189
High temperature materials, 104
Holed-drilling, 305–307
Homogenization, 183, 230, 259, 275, 279, 282
Homogenous nucleation, 65, 76, 81, 82, 87, 88
Hook defect, 98, 141
Hot pressure welding, 3
Hot run, 95
Hot working, 72, 91
Hydrogen diffusivity, 183

I

Impurity, 181, 261
Incipient melting, 238, 244
Inclusions, 210, 279, 281

Incoherent, 64, 69, 74, 83, 84, 86, 115, 281
Independent process variables, 16
Industry, 8, 14, 114, 151, 237, 283, 288
Inhomogeneity, 5, 273–275
Initial microstructure, 167, 221, 229–230
Interdendritic region, 279
Interface, 3, 13–15, 21, 22, 27, 29, 31, 32, 34, 39, 53, 66–71, 73, 75, 81–86, 106, 133, 172, 178, 245, 246, 250, 253, 256, 273, 274, 285, 322
Interfacial adhesion, 21
Intergranular corrosion, 143, 145
Interlamellar, 84, 195
Intermetallic compounds, 238, 244, 245, 250–251, 255
Intermetallic layer, 245
Intermetallic particles, 273, 286
Internal stresses, 297
International Magnesium Association, 149, 150
Interphase boundary, 65
Interstitial-free steel (IF-steel), 216, 221–223
Isomorphous, 190, 195
Isothermal phase transformation, 71

J
Johnson-Mehl-Avrami/Johnson-Mehl-Avrami-Kolgomorov (JMAK), 70, 76
Joining, 1–5, 7–9, 13–15, 18, 36, 46, 106, 109, 153, 154, 177, 217, 237, 240, 243, 244, 255, 257, 302, 303
Joining technique, 1, 3, 95, 153, 155, 238, 317, 321
Joint configurations, 4, 7, 8, 95–98
Joint efficiency, 113, 114, 126, 156, 172, 177, 178, 250

K
Keyhole, 139, 141
Kinetics, 23, 60–72, 76, 79, 82, 83, 86, 90, 228, 254, 263
Kolsky bar, 25, 52

L
Lagrangian, 38, 40, 321
Lamellar, 83–85, 194, 195, 203, 204, 206, 230
Lap, 7–8, 95–98, 141, 142, 224–226, 250, 252
Laser beam welding (LBW), 154
Lazy S, 95, 122, 127
Leading edge, 6
Leading side, 42, 54, 98, 201
Lever rule, 81
Light metals, 237
Limited solubility, 253
Liquation cracking, 244
Loads, 17, 18, 21, 97, 100, 124, 151, 177, 245, 278, 287, 297, 310, 319, 320, 324
Location, 18, 63, 64, 98, 124, 125, 130, 133, 138, 143, 159–161, 164, 173, 179, 199–201, 204–206, 238, 240, 243, 245, 254, 276, 277, 301, 306, 308, 316, 317, 319, 322, 323
Longitudinal, 41, 53, 116, 125, 126, 128, 134, 136, 137, 232, 253, 289, 304, 309, 312, 313, 319, 322, 323
Low angle boundary, 69, 74, 121
Low angle grain boundaries, 118, 168, 222, 223
Low-carbon steel, 88, 182, 210, 223–224
Low strain band (LSB), 123

M
Machining process, 13, 17
Macrostress, 298
Macrostructure, 33, 59, 60, 130, 139, 141, 142, 246, 252, 253
Magnesium alloys, 149–184, 189, 217, 230, 237, 240, 243, 245–251, 268, 293, 294
Manufacturing, 1, 151, 153, 259, 268, 276, 279, 288, 290
Manufacturing process, 1, 2, 13, 17, 261, 298
Marker, 30–33, 124
Martensite, 59, 86–88, 210, 213, 215, 221, 223, 224, 226, 228–230
  finish temperature, 86
  start temperature, 86, 214, 215
Mass conservation, 37, 38
Massive transformation, 86
Material density, 26
Material flow, 3, 5, 6, 16, 29–50, 53–55, 91, 95, 97, 98, 101, 103–105, 141, 189, 192, 202, 241, 244, 245, 259, 288, 289
Material mixing, 107, 238, 241–243, 246, 248
Measurement, 24, 25, 34–36, 121, 122, 126, 139, 145, 160, 220–222, 226, 229, 230, 243, 303, 305–310, 314, 322
Mechanic(al), 1, 17, 50, 53, 61, 97, 104, 109, 111, 113, 129, 133, 143, 181, 200, 279, 297, 298, 318–319, 323–325
  behavior, 122, 205–208, 282
  properties, 5–7, 9, 119, 121–143, 153, 172–181, 195–199, 206, 212, 217–219, 221–232, 243, 248, 250, 256–257, 275, 282–287, 311
Mechanism, 13, 25, 80, 82, 100, 112, 116, 153, 189, 205, 217, 219, 261, 270, 287, 288, 291

Medium-carbon steel, 209, 220, 228, 229
Melting, 1–3, 5, 7, 13, 36, 99, 238, 244, 245, 273
Melting point, 13, 14, 16, 36, 101, 155, 177, 216, 237, 238, 240–257, 317
Metal, 1, 13, 59, 100, 109, 151, 212, 237, 268
  forming, 15–17, 269
  matrix composites, 268, 272, 273, 277
Metal inert gas (MIG), 154
Metallurgical band, 30, 34, 47, 49, 115, 122–124
Metallurgical tool, 259
Micrographs, 169, 202–204, 223–226, 228, 246–248, 251, 275, 292, 294
Microhardness, 122, 130, 131, 135, 139, 140, 223, 226, 227, 232, 243
Microscopic plastic deformation, 21
Microstress, 298
Microstructural change, 1, 18, 73, 89, 90, 112, 171, 268, 279, 297
Microstructural framework, 194–195, 210–215
Microstructural modification, 232, 272
Microstructure, 2, 16, 59, 95, 112, 162, 189, 244, 261, 308
Microstructure(al) evolution(al), 59, 69, 89–92, 107, 114–121, 159, 194, 195, 200–205, 207, 210, 212, 217, 221–233, 259
Migration, 66
Mild steel, 226, 253
Mixing, 62, 105, 107, 238, 241, 245, 246, 248, 277
Modeling, 16, 36, 50, 51, 88, 91, 113, 261, 282, 285, 286, 320–325
Modification, 75, 92, 151, 152, 228, 232, 271–274, 279–287, 310, 311
Momentum conservation, 37, 38
Monte Carlo simulation, 76
Morphology, 59, 141, 169, 193, 194, 203, 214, 228–230, 233

N

Near-α alloys, 190, 193
Near-β alloys, 190, 194, 195, 206
Newton's law of viscosity, 38
Non-destructive, 114, 305, 307
Non-equilibrium, 50, 59, 63, 69, 228, 230, 244
Non-fusion, 237
Non-glissile interface, 67
Non-weldable, fusion welding, 70
Normal force, 7, 14, 53, 103
Nucleation, 63, 65, 66, 70, 71, 76, 78, 81–84, 86, 87–90, 171, 183, 285
  kinetics, 63–66, 90
  rate, 66, 71
  site, 66, 76, 78, 286
Nugget, 5–7, 30, 31, 35, 36, 55, 72, 91, 92, 98, 101, 103, 105, 106, 115–118, 120–123, 126, 128, 129, 132, 134, 136, 138–142, 144, 145, 159, 161–164, 167–169, 171, 172, 175, 177, 181, 200–203, 213, 217, 218, 221, 223–233, 243–249, 262, 270, 273, 278, 288–290, 303, 311, 313
Numerical simulations, 24, 40

O

Onion ring, 30, 34, 47, 115, 162, 241, 243
Open-circuit potential, 144
Organizations, 210
Orientation gradient, 74, 75
Over-aged, 169
Oxide film, 95, 98, 105, 274
Oxide particles, 127

P

Parent material, 9, 113, 114, 121, 138–140, 200, 206, 289
Particle coarsening, 117
Particles, 30, 38, 70, 74, 76, 83, 99, 115–117, 119, 120, 123, 127, 133, 145, 169, 171, 183, 194, 195, 253, 259, 261, 262, 264, 265, 268, 273–275, 277, 279–281, 284–286
Peak stress, 100
Peak temperature, 16, 35, 43, 89, 92, 155, 159–161, 189, 192, 193, 199–203, 205, 220–222, 224, 226–230, 232, 233, 301, 313, 317
Pearlite, 84, 86, 210, 212, 223, 224, 226, 227, 229, 230
Peierls-Nabarro stress, 217
Performance, 98, 153, 189, 209, 216, 260, 279
Phases, 9, 13, 59, 99, 109, 171, 189, 238, 262
  diagram, 61–63, 69, 80, 85, 89, 190, 191, 195, 208, 209, 212, 213, 238, 239, 244, 251, 254
  distribution, 34, 61
  field, 86, 194, 195, 212
  growth, 69, 70, 86
  growth kinetics, 66–70, 76

Phases (*cont.*)
transformation, 50, 59, 61–71, 75, 83, 86, 189–194, 213, 215, 222, 226, 230, 232, 233
Physical effects, 15, 16, 19, 20, 50, 89
Physical metallurgy, 59–92, 189–195, 208–215
Physical simulation, 88–89
Pin, 4, 13, 92, 95, 112, 155, 196, 240, 263, 313
diameter, 33, 44, 45, 101, 112, 113, 115, 155, 156, 163, 196, 197, 201, 241
features, 95, 102, 104, 106, 273, 289
geometry, 216
height, 155, 156, 240, 241
profile, 97, 104, 141, 175
shape, 54, 104
surface, 6, 13, 30, 33, 39, 53–55, 170, 172, 202, 216
Pitting corrosion, 143, 145, 148, 183
Plain carbon steel, 209, 213, 220, 221, 232, 233
Plastic deformation, 3–5, 7, 17, 21, 24–25, 27, 36, 47, 73, 91, 168, 169, 178, 249, 250, 285, 291, 297, 310, 314–317, 319, 321
Plastic deformation energy, 24, 25
Plastic strain, 7, 51, 106, 123, 315–317, 324, 325
Plate impact, 52
Plunge depth, 6, 103, 143
Plunge force, 6, 99, 104, 217
Plunge phase, 13
Plunge rate, 6, 13, 14, 100, 217
Plunge stage, 13, 100, 217, 321
Pole figures, 170, 171, 294
Polycrystalline cubic boron nitride, 189
Pore size, 284, 285
Porosity, 119, 154, 274, 279–281, 284, 285
Position, 5–7, 13–15, 28, 30, 31, 38, 41, 42, 44, 50, 67, 71, 97, 117, 118, 123, 124, 126, 131, 132, 138, 142, 145, 160, 170, 241, 245, 246, 252, 255–256, 284, 301, 324
Post-weld aging, 118, 122, 129, 130, 137
Post-weld heat treatment, 317
Pourbaix diagram, 181, 183
Powder metallurgy, 267–268, 274–276, 291
Power control, 14
Prebending,
Precambering, 317
Precipitate free zones, 120, 143
Precipitates, 65, 79, 82, 83, 89–91, 114, 117–121, 126, 132, 143–145, 169, 182, 189, 210, 246, 270, 281, 282, 299
Precipitation, 79–83, 90, 114–117, 120, 129–131, 145, 153, 195, 206
hardening, 80, 89, 114, 117, 120, 122, 126, 133, 139
strengthened, 153, 169
strengthened alloy, 77, 110, 269
strengthening, 205, 206, 219
Probabilistic
modeling, 285
Probe, 5, 32, 33
Processing
history, 152, 181, 212
parameters, 89, 91, 92, 159, 161, 163, 164, 169, 173, 174–178, 196, 203, 220, 224–227, 229, 233, 246, 288, 294, 302, 303, 311
route(s), 151, 181, 217, 219, 276
strain, 98
window, 161–162
Process pitch, 290
Process window, 96, 159, 161
Production, 2, 4, 100, 149, 150, 282
Proeutectoid, 213, 229
Projectile, 53
Propagation, 124, 125, 128, 129, 132, 134, 137–139, 143, 145, 183, 285
Properties, 2, 18, 61, 95, 109, 152, 189, 237, 260, 300

R

Reaction product, 100, 217, 254, 255, 273, 274
Reactivity, 100, 122, 190, 196, 197
Recovery, 37, 66, 71–79, 89, 91, 92, 107, 134, 168, 201
Recrystallization, 7, 36, 43, 66, 72–79, 89, 91, 92, 107, 110, 116, 163, 201
Refinement, 183, 200, 226, 232, 259, 264–267, 271, 273, 279–282, 286
Reflected wave, 53
Reinforcement, 272, 273, 276–278
Relative velocity, 21
Relaxation, 303, 305–307, 309, 314
Reliability, 1, 114
Residual stress, 8, 28, 29, 40, 124–126, 128, 132, 134, 137–139, 189, 199, 273, 297–325
Resistance spot welding, 14
Retract phase, 13
Retreating side, 4, 6, 30, 31, 44, 45, 95, 103, 162, 201, 202, 243, 245, 247, 248, 255, 256, 290
Roller tensioning, 319–320

Roll welding, 3
Rotation axis, 8, 13, 31
Rotation zone, 41, 42
R ratio, 124, 132, 138
Rupture, 181

S
SAE. *See* Society of Automotive Engineers (SAE)
Sample size, 309–310
Scroll shoulder, 104, 216
Second phase, 34, 75, 79, 116, 171, 183, 240, 273
Second phase particles, 75, 76, 183, 262, 264, 273
Sectioning, 303, 305, 309, 314
Semicoherent, 83, 84
Semi-empirical, 112
Servo-hydraulic testing, 25
Shape(s), 5, 7, 28–30, 42, 54, 55, 59, 79, 103, 104, 119, 120, 122, 162–163, 172, 262, 270, 273, 274, 284, 288, 304, 315
Shear force, 53, 55, 66, 100, 103, 106, 244, 256
Shear force vectors, 55
Shearing force, 37
Shear layer, 41, 53, 92, 101, 104, 201
Shear stress, 16, 21, 22, 34–37, 50, 74
Shipbuilding, 1, 3, 114
Shoulder, 4–7, 13–15, 22, 23, 27, 30–34, 39, 41, 46, 49, 53–55, 89, 91, 95, 98, 101–104, 106, 112, 113, 141–144, 161, 170, 171, 179, 180, 196, 197, 200, 201, 216, 223, 224, 288–290, 313, 322
  diameter, 16, 21, 34, 101, 112, 113, 155, 161, 180, 240, 241
  generated heat, 15, 322
Si modification, 279
Simulation, 24, 28, 38–40, 43, 44, 46, 47, 76, 88–89, 113, 201, 320–325
Single edge tension specimen, 138
Slow strain rate tensile test polarization, 144
Small crack, 128
Society of Automotive Engineers (SAE), 210–212
Softening characteristics, 238
Soldering, 1, 2
Solid, 9, 18, 37, 53, 64, 89, 109, 110, 136, 161, 288, 302
  solution, 89, 109, 110, 116, 126, 244
    strengthened, 153, 269, 270
    strengthening, 116, 195, 205, 206, 217, 270
  state joining, 3, 5, 317, 321
Solid-state, 1–3, 5, 36, 83, 116, 153–155, 238, 240, 302
Solutes, 79, 80, 82, 85, 89, 110, 169
Solute strengthened, 77
Source-limited coarsening, 83
Space, 2, 9, 38, 41, 74, 95, 98, 155, 192, 198, 289
Specific heat capacity, 26, 154, 160, 199
Speckle interferometry, 178, 180
Spindle, 6, 16, 34, 49
Spindle speed, 16
Spinodal decomposition, 80–82
Split-Hopkinson pressure bars, 52
Stable, 17, 62, 65, 70, 74, 80, 82, 83, 111, 115, 152, 208, 228, 264, 265, 270
Stacking fault energy, 168
Static recovery, 73–76, 89, 91, 92
Static recrystallization, 72, 73, 75–76, 91, 92
Static strength, 141–143
Steel(s), 14, 16, 27, 30, 59–61, 83–88, 99, 100, 102, 109, 112, 151, 155–157, 182, 189, 190, 208–233, 237–239, 241, 252–257, 323
Sticking coefficient, 201
Stiffness, 6, 97, 112, 271–278, 314
Stir zone, 7, 33, 53, 54, 89, 141, 144, 169, 177, 200, 201, 206, 284, 289
Stop-action technique, 41–42, 171
Strain, 5, 25, 64, 97, 111, 151, 201, 249, 261, 301
  energy, 64, 75, 81
  gage, 305–307
  hardening, 51, 283, 291
  rate, 5, 25, 26, 37, 39–46, 50, 52–53, 76, 88, 89, 91, 144, 164, 233, 255, 261–265, 267, 268, 291, 321
  rate sensitivity, 52, 262
Strain-free grains, 75, 77
Streamlines, 41
Strength, 3, 4, 8, 9, 21, 51, 77, 79, 83, 99, 100, 102, 109–114, 116, 120, 123, 131, 133, 134, 137, 144, 151, 153, 161, 173–178, 181, 182, 189, 190, 194, 195, 198, 202, 206–208, 211, 216–219, 223, 227, 228, 232, 238–240, 243, 249, 250, 253, 256, 270–272, 275, 279–287, 294, 300, 302, 310
Strengthening mechanisms, 153, 205, 217, 219, 270
Stress-corrosion cracking, 143, 144, 182, 183, 300
Stress intensity factor, 129, 132, 300
Stress ratios, 287
Stress wave, 53

Structural, 1, 7, 105, 109, 179, 189, 190, 216, 237, 259, 261, 272, 276, 283
Structure(s), 4, 18, 30, 60, 63, 69, 74, 75, 76, 79, 80, 82, 86, 88, 89, 103, 116, 118, 120, 121, 126, 163, 174, 177, 178, 190, 205, 208, 217, 224, 226, 230, 233, 237, 241, 251, 260, 262, 264, 268–269, 272, 273, 291, 299, 300, 302, 304, 317
Subgrain boundary, 74
Subgrains, 43, 73–79, 121
Superalloy, 99, 102, 195
Superplastic forming, 261–269
Superplasticity, 4, 5, 259, 261–268, 291
Supersaturated, 82, 114, 115
Surface composites, 272–278
Surface energy, 64, 73–75, 78, 84
Surface modification, 273–274
Symmetrical, 14
Synergistic, 276–278

T
Technology enabler, 264–269
Temperature, 3, 13, 60, 95, 110, 155, 189, 237, 259, 301
  control, 14, 233
  cycle, 28, 72, 119
  distribution, 16, 26, 161
  gradient, 95, 102
Temper designation(s), 111, 151, 152
Tempering, 112, 113
Tensile, 52, 112, 122, 123, 125, 133, 174, 177, 182, 207, 249, 250, 254, 256, 257, 267, 269, 276, 282–283, 299, 301, 303, 304, 312, 316, 318, 319, 322, 324
  failure, 249
  property, 114, 122, 127, 131–134, 136, 269, 282
  specimens, 122, 123
  test, 24, 51, 52, 134, 142, 144, 207, 243, 269, 276, 279
  thermal stress, 301
Texture, 30, 33, 34, 79, 169–172, 177, 183, 203, 219, 294
Texture strengthening, 219
Thermal
  conductivity, 21, 26, 29, 102, 160, 199, 237, 273
  cycle, 6, 7, 27, 34, 89–92, 199, 200, 273, 315
  gradient, 301
  model, 27
  profile, 159, 160, 199, 220, 221, 223, 311, 322
  properties, 199
  stability, 99, 190, 264
  stresses, 297, 301, 311, 313, 316, 317, 322
  tensioning, 317
Thermocouple, 28, 35, 36, 160, 199, 220, 228
Thermodynamics, 60–63, 80, 181
Thermo-mechanical, 15, 18, 59, 112, 152, 208, 213, 217, 219, 252, 266, 291, 298, 321
Thermo-mechanically affected zone (TMAZ), 7, 42, 89, 91, 92, 115–122, 124, 126, 129, 130, 133, 139, 144, 145, 159, 163, 167, 169, 172, 175, 177, 179, 182, 200–205, 213, 228, 233, 290
Thermo-mechanical metalworking, 15
Thermo-mechanical process(ing) (TMP), 18, 59, 152, 208, 213, 217, 219, 266, 291
Threshold stress intensity, 145
Tilt angle, 6, 97, 102–104, 240, 241
Time, 3, 13, 14, 17, 18, 22, 24, 28, 31, 33, 35, 37, 38, 40, 41, 53, 60, 63, 67, 68, 71, 72, 83, 92, 96, 103, 114, 121, 131, 139, 140, 161, 193, 195, 196, 207, 219, 224, 227, 229, 230, 252, 254, 264, 267, 321
Titanium alloys, 100, 104, 189–208, 268, 283
TMAZ. *See* Thermo-mechanically affected zone (TMAZ)
TMP. *See* Thermo-mechanical process(ing) (TMP)
Tools, 3, 13, 59, 95, 112, 155, 189, 240, 259, 301
  design, 8, 54, 101, 102, 106, 112–113, 141, 155, 288
  forces, 102, 106, 113
  geometry, 101, 163, 165, 166, 196, 313
  holder, 49
  life, 208
  material(s), 5, 26, 29, 99–102, 104, 112, 155, 156, 189, 190, 195, 196, 215–217, 318
  offset, 248–250, 252–254, 256
  pin, 4–7, 22, 31, 40–41, 44, 45, 49, 92, 97, 99, 104, 106, 139, 141, 174, 196, 197, 240, 252, 256, 273, 313, 321
  rotation, 23, 35, 44, 45, 47, 92, 95, 113, 126, 256, 288, 289
    axis, 8, 31, 34
    rate, 4, 6, 24, 46, 103, 105, 155, 159, 161–164, 167, 173–177, 199, 220–230, 241, 242, 245, 247–250, 294, 303, 311–313, 323

run-out, 47, 49
selection, 95–107
shoulder, 4–6, 13, 15, 16, 21–23, 31, 34, 101, 102, 104, 161, 171, 288, 289, 322
steel, 99, 100, 102, 112, 155–157, 212, 217, 252
travel speed, 6, 16
traverse speed, 6, 24, 92, 96, 103, 113, 155, 159, 162–164, 167, 173–177, 195, 221–227, 240–242, 245, 247, 248, 303, 311, 313, 323
wear, 106, 196, 215–217, 243, 252, 256
Torque, 16, 23–25, 27, 34, 46, 47
Torque control, 14
Torsional deformation, 89
Trailing edge, 6
Trailing side, 44, 54, 92, 98, 170, 171, 201, 225, 290, 313, 317, 318
Transformation, 63, 65, 66, 71, 79–83, 190, 200, 202, 203, 206, 208, 213–215, 229, 233, 297
Transformation kinetics, 70–71
Transition region (TR), 162, 169
Transition zone (TZ), 41, 42, 164, 202
Transmission electron microscope, 120
Transmitted wave, 53
Transportation, 149, 179
Transverse, 5, 15, 30, 34, 41, 106, 116, 125, 126, 128, 134, 136, 137, 164, 175, 179, 180, 223, 226, 227, 232, 240, 241, 243, 245, 247, 248, 250–253, 271, 304, 312, 313, 319, 322, 323
Traverse phase, 15
Traverse speed, 4, 46, 77, 155, 165, 166, 275
Tungsten inert gas (TIG), 154
Turbocharger impeller, 237, 238
Twinning, 50, 294
TZ. *See* Transition zone (TZ)

U
UFG. *See* Ultrafine grained materials (UFG)
Ultimate tensile strength, 174, 177, 283
Ultrafine grained, 255, 264, 265, 268, 291, 292
Ultrafine grained materials (UFG), 291, 293, 294
Ultrahigh-carbon steel, 209
Ultrasonic welding, 3, 154, 155
Unbonded region, 141
Unconstrained lattice misfit, 64, 81
Unified numbering system (UNS), 151, 210, 212
Unintended microstructure, 260, 261
Unstable, 65, 152, 287

V
Vacancies, 65, 73, 120
Vertical flow, 30, 104
Vertical force, 6, 13, 47, 97
Viscosity, 37, 38, 40
Volume fraction, 75, 79, 99, 115–118, 169, 171, 200, 204, 249, 263, 273, 274, 276, 278, 285
Volumetric defects, 98, 103
Volumetric energy, 63

W
Wear, 99, 100, 106, 190, 195–197, 208, 215–218, 243, 252, 253, 256, 272, 273
Wear resistance, 102, 272, 273
Weld, 1, 15, 59, 95, 112, 154, 189, 237, 268, 301
cycle, 3
nugget, 6, 7, 163, 217, 218, 220, 223, 225–227, 229, 230, 232, 245–249
seam, 15
Weldability, 109, 252
Welded structure, 174, 177, 178, 302, 304, 317
Welding
phase, 14
sequencing, 317
speed, 24, 47, 60, 154, 221
techniques, 1, 5, 14, 154, 155, 177, 189, 217, 237, 238, 310, 316, 321
Widmanstatten, 205, 214
Widmanstatten plates, 214
Work angle, 6
Work hardenable material, 90
Work-hardening, 111, 291–293
Workpiece, 1, 3–7, 13–18, 20–21, 24, 26–29, 31, 34–36, 41, 42, 47, 54, 79, 89, 96, 97, 99–102, 104, 106, 140, 159, 175, 199–201, 216, 217, 220, 288–290, 301, 304, 311
Workpiece/tool interface, 14, 15, 22, 31, 34, 39, 53, 106
World production, 149
Wormhole, 97, 288
Wrought alloys, 151
Wrought magnesium, 151, 153

X
X-ray diffraction (XRD), 128, 303, 305–308

Y
Yield strength, 3, 79, 110, 174, 175, 178, 181, 198, 206, 219, 232, 238, 239, 282, 283, 294, 302, 304, 311, 316–318, 319, 324, 325
Yield stress, 21, 34, 35, 291, 301, 316

Z
Zener drags effect, 74
Zener-Hollomon parameter, 40, 43
Zener limit, 79